frontiers | Research Topics

# Evolution mechanism and prevention technology of karst geological engineering disasters

**Edited by**
Pengfei Liu, Zhang Cong, Guotao Ma, Jae-Joon Song, Tongming Qu and Weibing Gong

**Published in**
Frontiers in Earth Science

ISSN 1664-8714
ISBN 978-2-8325-7378-5
DOI 10.3389/978-2-8325-7378-5

**Generative AI statement**
Any alternative text (Alt text) provided alongside figures in the articles in this ebook has been generated by Frontiers with the support of artificial intelligence and reasonable efforts have been made to ensure accuracy, including review by the authors wherever possible. If you identify any issues, please contact us.

## About Frontiers

Frontiers is more than just an open access publisher of scholarly articles: it is a pioneering approach to the world of academia, radically improving the way scholarly research is managed. The grand vision of Frontiers is a world where all people have an equal opportunity to seek, share and generate knowledge. Frontiers provides immediate and permanent online open access to all its publications, but this alone is not enough to realize our grand goals.

## Frontiers journal series

The Frontiers journal series is a multi-tier and interdisciplinary set of open-access, online journals, promising a paradigm shift from the current review, selection and dissemination processes in academic publishing. All Frontiers journals are driven by researchers for researchers; therefore, they constitute a service to the scholarly community. At the same time, the *Frontiers journal series* operates on a revolutionary invention, the tiered publishing system, initially addressing specific communities of scholars, and gradually climbing up to broader public understanding, thus serving the interests of the lay society, too.

## Dedication to quality

Each Frontiers article is a landmark of the highest quality, thanks to genuinely collaborative interactions between authors and review editors, who include some of the world's best academicians. Research must be certified by peers before entering a stream of knowledge that may eventually reach the public - and shape society; therefore, Frontiers only applies the most rigorous and unbiased reviews. Frontiers revolutionizes research publishing by freely delivering the most outstanding research, evaluated with no bias from both the academic and social point of view. By applying the most advanced information technologies, Frontiers is catapulting scholarly publishing into a new generation.

## What are Frontiers Research Topics?

Frontiers Research Topics are very popular trademarks of the *Frontiers journals series*: they are collections of at least ten articles, all centered on a particular subject. With their unique mix of varied contributions from Original Research to Review Articles, Frontiers Research Topics unify the most influential researchers, the latest key findings and historical advances in a hot research area.

Find out more on how to host your own Frontiers Research Topic or contribute to one as an author by contacting the Frontiers editorial office: frontiersin.org/about/contact

# Evolution mechanism and prevention technology of karst geological engineering disasters

**Topic editors**

Pengfei Liu — CCCC Second Harbor Engineering Co., Ltd., China
Zhang Cong — Central South University Forestry and Technology, China
Guotao Ma — University of Warwick, United Kingdom
Jae-Joon Song — Seoul National University, Republic of Korea
Tongming Qu — Hong Kong University of Science and Technology, Hong Kong, SAR China
Weibing Gong — Missouri University of Science and Technology, United States

**Citation**

Liu, P., Cong, Z., Ma, G., Song, J.-J., Qu, T., Gong, W., eds. (2026). *Evolution mechanism and prevention technology of karst geological engineering disasters*. Lausanne: Frontiers Media SA. doi: 10.3389/978-2-8325-7378-5

# Table of contents

frontiers | Frontiers in Earth Science

TYPE Editorial
PUBLISHED 06 January 2026
DOI 10.3389/feart.2025.1768763



OPEN ACCESS

EDITED AND REVIEWED BY
Gordon Woo,
Risk Management Solutions, United Kingdom

*CORRESPONDENCE
Pengfei Liu,
pfliu0229@foxmail.com

RECEIVED 16 December 2025
ACCEPTED 16 December 2025
PUBLISHED 06 January 2026

CITATION
Liu P, Chen P, Song X, Feng X and Zhang C (2026) Editorial: Evolution mechanism and prevention technology of karst geological engineering disasters.
*Front. Earth Sci.* 13:1768763.
doi: 10.3389/feart.2025.1768763



# Editorial: Evolution mechanism and prevention technology of karst geological engineering disasters

Pengfei Liu[1]*, Peishuai Chen[1], Xiangrong Song[1], Xin Feng[1] and Cong Zhang[2]

[1]Technology Center, CCCC Second Harbor Engineering Co., Ltd., Wuhan, China, [2]School of Civil Engineering, Central South University Forestry and Technology, Changsha, China

KEYWORDS

**construction project, karst exploration, karst geological engineering disasters, karst region, karst treatment**

Editorial on the Research Topic
Evolution mechanism and prevention technology of karst geological engineering disasters

## Introduction

Soluble rocks such as limestone and dolomite can form karst features, including caves, sinkholes, and solution grooves through prolonged groundwater erosion (Parise et al., 2015). Karst landscapes are widespread globally. Construction in karst areas often faces sudden and severe ground collapse risks, endangering project safety, structural integrity, and personnel well-being. Therefore, the detection, assessment, and treatment of karst formations are crucial in engineering.

## Karst detection

Geotechnical investigation in karst regions necessarily includes karst detection. Current methods are diverse, primarily comprising geological mapping, engineering drilling, and geophysical exploration (Li and Xiao, 2006; Goldscheider et al., 2011; Kaufmann, 2014). Among these, geophysical techniques impose relatively fewer constraints and are more widely applied. Wang et al. detailed the principles and data processing methods of four geophysical exploration approaches for karst detection: multi-electrode resistivity, cross-hole electromagnetic wave computed tomography, microtremor survey, and ground-penetrating radar. They compared the applicability of each method through case studies. A novel one-shaped layout 3D electrical exploration model has been proposed for detecting karst groundwater channels, improving exploration efficiency by 85.9% over conventional methods while maintaining high accuracy (Wang et al.).

## Geological assessment in karst areas

Karst collapse, a common hazard in such regions, is characterized by strong concealment, abrupt occurrence, and high destructiveness, capable of causing sudden surface subsidence and damage to structures. Thus, assessing and predicting karst collapse is essential.

Machine learning has been a transformative tool in addressing various science and technology problems (Qu et al., 2021; Qu et al., 2023). For example, it has been used for predicting potential hazards in tunnel engineering (Zhang et al.; Qu et al., 2025; Yuan et al., 2026). To address the need for high-precision karst collapse assessment, Wang et al. proposed a prediction model based on an optimized sparrow search algorithm combined with an extreme learning machine. The model uses Singer chaotic mapping to improve the sparrow search algorithm, enhancing population diversity and global search capability to avoid local optima. The optimized ISSA automatically adjusts the initial weights and thresholds of the ELM, while five-fold cross-validation determines the optimal hidden layer structure, forming an adaptive intelligent prediction framework.

## Karst treatment

Karst features, often concealed, complex, and challenging to treat, can easily lead to engineering accidents if improperly managed during construction. Consequently, karst treatment remains a key research focus.

Grouting is a common technique in karst treatment. To overcome the limitations of traditional cement grouts in complex environments with high water flow and pressure, Liang et al. developed a high-performance modified clay-cement grouting material. Laboratory tests verified its performance, and field application in a water conservancy project demonstrated its suitability and effectiveness.

Addressing water inrush in karst formations and seepage at diaphragm wall joints, Jiang et al. proposed a treatment method combining geophysical exploration with grouting. For karst water inrush, electrical methods identify the flow channels, which are then sealed with clay-cement paste grouting. For diaphragm wall joint seepage, sonar detects leakage points, treated with cement-sodium silicate double-fluid grouting. Xu et al. developed a catastrophe theory-based grouting reinforcement control standard for underwater karst shield tunnels by analyzing instability mechanisms and modeling reinforcement ranges. The mechanism of dynamic grouting with self-expanding slurry for water plugging in karst tunnels was examined by Zhan et al. Tang et al. revealed that karst water erosion causes grouting curtain leakage mainly due to severe degradation of cement-clay composites, which are less durable than pure cement grouts. The pressure filtration effect in karst areas significantly enhances the initial consolidation strength of grouted curtains, necessitating a revised life prediction model that incorporates this effect for accurate service life forecasting, as validated through experiments and field application (Yan et al.). Yao et al. demonstrated that integrating high-density resistivity and frequency-division electrical resistivity tomography with geological methods provides an accurate, practical, and broadly applicable approach for diagnosing leakage risks in karst reservoir dams.

## Construction cases in karst formations

Shield tunneling through karst strata poses risks such as shield machine sinking, head pitching, ground settlement or collapse, and excessive post-construction settlement (Cheng et al., 2017), which can cause serious hazards, significant economic loss, and even casualties (Xie et al., 2025; Ou et al., 2025a; Ou et al., 2025b).

Based on a shield tunneling project in Shenzhen, China, Li et al. proposed a membrane-sleeve valve pipe grouting technique for reinforcing karst strata, building on conventional sleeve valve pipe grouting. They detailed its key construction points and process, with field tests confirming its applicability. A combined short straight-hole and wedge compound cut blasting scheme was proposed and tested in a hard rock tunnel (Tu et al.). Various machine learning techniques have been leveraged to integrate geological records and tunneling parameters for predicting rock grades (Dang et al.). Mechanistic analysis of TBM cutterhead–ground interaction under the mud build-up effect was explored by Wang et al.

Finally, we extend our gratitude to everyone who contributed to this Research Topic. Their contributions include not only theoretical breakthroughs but also the accumulation and sharing of practical engineering experience. Through their dedicated efforts, challenges in karst construction are being progressively overcome, providing valuable references and insights for similar projects.

## Author contributions

PL: Writing – original draft, Conceptualization. PC: Writing – review and editing, Investigation. XS: Writing – review and editing. XF: Writing – review and editing. CZ: Writing – original draft.

## Funding

The author(s) declared that financial support was not received for this work and/or its publication.

## Conflict of interest

Authors PL, PC, XS, and XF were employed by CCCC Second Harbor Engineering Company Ltd.

The remaining author(s) declared that this work was conducted in the absence of any commercial or financial relationships that could be construed as a potential conflict of interest.

## Generative AI statement

The author(s) declared that generative AI was not used in the creation of this manuscript.

Any alternative text (alt text) provided alongside figures in this article has been generated by Frontiers with the support of artificial intelligence and reasonable efforts have been made to ensure accuracy, including review by the authors wherever possible. If you identify any issues, please contact us.

## Publisher's note



## References

Cheng, W-C., Cui, Q-L., Shen, JS-L, Arulrajah, A, and Yuan, D-J (2017). Fractal prediction of grouting volume for treating karst caverns along shield tunneling alignment. *Appl. Sci.* 7 (7), 652–665. doi:10.3390/app7070652

Goldscheider, N., Plagnes, V., Guerin, R., Valois, R., and Bosch, F. P. (2011). Contribution of geophysical methods to karst-system exploration: an overview. *Hydrogeol. J.* 19 (6), 1169–1180. doi:10.1007/s10040-011-0746-x

Kaufmann, O. (2014). Geophysical mapping of solution and collapse sinkholes. *J. Appl. Geophys.* 111, 271–288. doi:10.1016/j.jappgeo.2014.10.011

Li, D., and Xiao, K. H. (2006). High density electrical resistance exploration in the NO.2 TieFengShan tunnel. *J. Eng. Geol.* 14 (3), 197–200. doi:10.3969/j.issn.1672-7940.2006.03.008

Ou, X., Zhou, Y., Kong, Y., Qu, T., Xu, S., Liao, W., et al. (2025a). Predicting floor heave risk in road tunnels with machine learning. *J. Rock Mech. Geotechnical Eng.* 17 (10), 6428–6438. doi:10.1016/j.jrmge.2024.12.034

Ou, X., Tang, C., Qu, T., Xu, S., Zhou, Y., and Tian, J. (2025b). Towards digitalized maintenance of operating tunnels: a text documents-based defect evaluation and visualization. *Tunn. Undergr. Space Technol.* 157, 106345. doi:10.1016/j.tust.2024.106345

Parise, M., Closson, F.D., Gutierrez, F., and Stevanović, Z. (2015). Anticipating and managing engineering problems in the complex karst environment. *Environ. Earth Sci.* 74 (12), 7823–7835. doi:10.1007/s12665-015-4647-5

Qu, T., Di, S., Feng, Y. T., Wang, M., and Zhao, T. (2021). Towards data-driven constitutive modelling for granular materials via micromechanics-informed deep learning. *Int. J. Plasticity* 144, 103046. doi:10.1016/j.ijplas.2021.103046

Qu, T., Zhao, J., Guan, S., and Feng, Y. T. (2023). Data-driven multiscale modelling of granular materials *via* knowledge transfer and sharing. *Int. J. Plasticity* 171, 103786. doi:10.1016/j.ijplas.2023.103786

Qu, T., Zhao, J., and Feng, Y. T. (2025). Artificial intelligence for computational granular media. *Comput. Geotechnics* 185, 107310. doi:10.1016/j.compgeo.2025.107310

Xie, Y., Qu, T., Yang, J., Wang, S., and Zhao, J. (2025). Multiscale insights into tunneling-induced ground responses in coarse-grained soils. *Comput. Geotechnics* 185, 107319. doi:10.1016/j.compgeo.2025.107319

Yuan, X., Wang, S., Qu, T., Zeng, J., Liu, P., and Chen, X. (2026). Knowledge-assisted deep transfer learning for muck clogging identification during mechanized shield tunneling. *Tunn. Undergr. Space Technol.* 168, 107124. doi:10.1016/j.tust.2025.107124

frontiers | Frontiers in Earth Science

TYPE Original Research
PUBLISHED 21 February 2025
DOI 10.3389/feart.2025.1559663



OPEN ACCESS

EDITED BY
Tongming Qu,
Hong Kong University of Science and Technology, Hong Kong SAR, China

REVIEWED BY
Lidong Sun,
Chongqing University, China
Lin Li,
Chang'an University, China

*CORRESPONDENCE
Chu Jiang,
827173049@qq.com

RECEIVED 13 January 2025
ACCEPTED 05 February 2025
PUBLISHED 21 February 2025

CITATION
Jiang H, Jiang C, Chen D and Qiu X (2025) Technology and application of treating water inrush disasters in underground engineering with the method of physical detection combined with grouting.
*Front. Earth Sci.* 13:1559663.
doi: 10.3389/feart.2025.1559663



# Technology and application of treating water inrush disasters in underground engineering with the method of physical detection combined with grouting

Huangbin Jiang[1,2], Chu Jiang[1,2]*, Di Chen[1,2] and Xiang Qiu[1,2]

[1]Hunan Institute of Water Resources and Hydropower Research, Changsha, Hunan, China, [2]Hunan Dam Safety and Disease Prevention Engineering and Technology Research Centre, Changsha, Hunan, China

The water gushing disaster in karst unfavorable geology has always been one of the difficult problems to be solved in the engineering field. In view of engineering problems such as water gushing in karst geology with relatively high-water flow velocity and water seepage at the joints of the underground diaphragm wall which is concealed, a treatment method for water gushing disasters in karst geology based on physical detection combined with grouting is proposed. The main steps of this method are as follows: Firstly, according to the analysis results of engineering geological investigations, by selecting appropriate physical detection means, accurately locate the hidden danger positions such as underground water gushing channels and cracks. Then, based on the results of physical detection, select appropriate grouting materials and techniques to conduct water blocking treatment at the water gushing points and effectively block the water gushing paths. In addition, the feasibility of the above method has also been verified through engineering applications. For the water gushing problem in the limestone area with extensive karst development, the electrical method of geophysical exploration technology was adopted to clarify the karst water gushing channels. And combined with the clay-cement paste grouting blocking technology to block them. The results show that the water blocking effect is obvious, and the water gushing volume has been drastically reduced from 103,900 to 8,600 $m^3$/d, with a reduction rate as high as 91.72%. Moreover, for the concealed water gushing disasters at the joints of the underground diaphragm wall, the sonar detection method was selected to explore the positions of water gushing. Then the cement-water glass double-liquid grouting method was used to conduct anti-seepage treatment at the water gushing positions. An inspection of the water gushing situation after treatment found that the leakage phenomenon at the joints was significantly reduced. The research results can provide certain references for the design of treatment schemes for similar water gushing disasters in karst unfavorable geology.

KEYWORDS

**karst geology, water inrush disasters, physical detection, grouting, engineering application**

# 1 Introduction

Karst geology is mainly composed of caves and fissures, which have the characteristics of high-water content in fissures, high rock permeability, and easy collapse (Zhang et al., 2017). Along with unpredictable groundwater flow, these special geological forms and hydrological conditions bring many hidden dangers to the production and construction of karst areas, especially in the process of underground construction, which is prone to water inrush disasters (Bai et al., 2022; Wang et al., 2017; Li et al., 2013; Lan et al., 2021), causing serious economic losses and casualties (Zhang et al., 2022). For example, in 2007, a major water leakage accident occurred in the Yesanguan Tunnel of the Yiwan Railway, resulting in 52 casualties. China has karst landforms that account for one-third of its total land area, making it one of the countries with the widest distribution of karst landforms in the world. When carrying out production and construction in provinces such as Yunnan, Sichuan, Hunan, and Guangxi in China, it is inevitable to deal with karst geological problems (Wang et al., 2022; Zhao et al., 2013; Qiu et al., 2023). Therefore, it is urgent to carry out research on the treatment methods for geological disasters caused by foundation pit water inflow in karst areas.

Currently, the treatment techniques for water inflow in karst areas mainly include methods such as foundation pit dewatering, grouting reinforcement, and anti-seepage treatment (Liu et al., 2022; Lu et al., 2013; Parise et al., 2008; Zhang et al., 2019). Foundation pit dewatering uses pumping equipment to lower the groundwater level, thereby reducing water inflow, and is commonly used for water level control in the initial stage. However, precipitation methods are often only temporary solutions and will have a certain impact on surrounding water resources (Liu et al., 2021; Peng et al., 2020; Wan et al., 2021). Grouting reinforcement technology, as the core means of preventing water inflow in karst areas, uses high-pressure grouting and other processes to seal the cracks and caves around the foundation pit, forming a strong waterproof barrier (Ma et al., 2022; Xu et al., 2021; Li et al., 2019). In recent years, new grouting materials and processes such as micro grouting and chemical grouting have gradually been applied, which can form effective sealing in finer cracks and significantly improve the anti-seepage effect (Liu et al., 2018; Gutiérrez et al., 2014; Liu et al., 2019). The anti-seepage technology further prevents water flow into the foundation pit area by setting up anti-seepage walls, geomembranes and other facilities, ensuring the stability of the foundation pit (Qiu et al., 2022; Li et al., 2024; Li X. F. et al., 2018).

The existing prevention and control technologies have to some extent solved the problem of water inflow, but due to the limitations of specific geological conditions on the application effects of various technical means, the most suitable systematic construction plan still needs to be selected according to the actual situation. For this reason, scholars at home and abroad have begun to conduct a series of systematic studies on the treatment of water inrush disasters under different geological conditions (Li S. C. et al., 2018; Song et al., 2021; Zheng et al., 2019). For example, Li et al. (2021) proposed a new type of pipeline water spraying geological disaster treatment technology and construction technology in karst areas, effectively solving the karst water inrush disasters in limestone mines; Yang et al. (2020) described the pre grouting reinforcement technology for underwater karst areas of Changsha Xiangjiang shield tunnel, which is a systematic grouting reinforcement technology for tunnel excavation in underwater karst areas; Cui et al. (2015) explored a geological hazard prevention measure for shield tunneling in karst geology and cave karst areas, and verified the applicability of the measure through on-site cases. There have been many achievements in the systematic treatment of water inrush disasters in karst areas, but due to the complexity of karst areas, there are many special geological landforms, and the above water inrush disaster engineering treatment schemes have poor adaptability to these special sections.

Based on the foregoing, this study proposes a treatment approach that combines physical detection and grouting techniques for water inrush disasters in underground engineering projects with diverse geological formations. Through practical engineering applications, the suitability and effectiveness of this method have been demonstrated, thereby establishing a foundation for similar engineering projects and contributing to the further enhancement and refinement of the treatment technologies and construction methodologies for water inrush disasters in underground engineering.

# 2 Water inrush situation in underground engineering

## 2.1 Water inrush disasters in karst geology

A limestone mine affiliated with a certain cement production company in Hunan, China, employs a depressed open-pit mining approach. This limestone mine occupies an area of 327,000 $m^2$ and has a perimeter of 2,527 m, with a designed excavation depth of 100 m. Since 2016, a karst cave at the elevation of +27 m on the south pit wall has experienced a sudden water inrush (designated as water inrush point No. 1), and the daily water inrush volume has reached 20,000 $m^3$. As the mining depth further extends, a water inrush occurs in a karst fracture at the +9-m platform (termed water inrush point No. 2), and the water inrush volume exhibits a steadily increasing tendency. By October 2018, the maximum water inrush volume has reached 103,900 $m^3$/d. The actual scene photographs of the mine and the water inrush locations are presented in Figure 1. This geological disaster has consequently led to an increment of six million yuan in the monthly cement production cost.

## 2.2 Water inrush disasters at the joints of diaphragm walls

A particular subway station in Guangxi, China, adopts a four-story underground double-column three-span structural design, with shield lifting shafts located at both the northern and southern ends. The depth of the foundation pit for the main structure of the station is 30.8 m, and that of the foundation pit at the enlarged end is 32 m. The construction method adopted is the cut-and-cover method. The foundation pit support system utilizes 1,200 mm diaphragm walls and an internal support structure to guarantee stability during the construction process. The construction site is illustrated in Figure 2. It is worth noting that the project is located in a karst developed area, and the surrounding high-rise buildings are close to the station foundation pit, with a horizontal distance of


FIGURE 1
Realistic photos of mining areas and water inflow points.

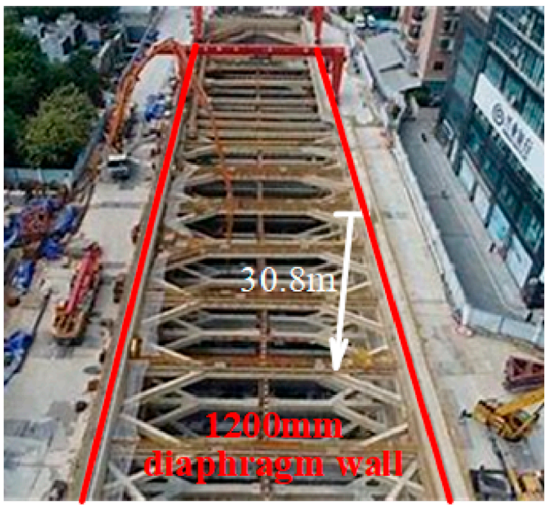


FIGURE 2
Construction site.

about 31.5 m between these buildings and the station foundation pit. Additionally, the bottom of the section of Line 1 is situated above the gravel layer and silty-fine sand layers. Hence, if water leakage occurs during the foundation pit construction process, it will exert a substantial impact on the surrounding buildings and the currently operating Line 1.

# 3 Treatment method for water inrush disasters combining physical detection and grouting

## 3.1 Technical process

To begin with, preliminary investigation and analysis are of crucial importance to guarantee the safety of construction and the formulation of treatment measures. Subsequently, in order to ascertain the water inrush circumstances and define the grouting scope, it is requisite to pick out suitable and dependable physical exploration techniques from a variety of methods. Once the actual state of the water inrush is acquired, the coordinated grouting mode is implemented, with appropriate grouting standards, materials and processes being selected. Eventually, the efficacy of the method is verified by means of core drilling, unconfined compressive strength testing, and groundwater level monitoring. The specific procedure is illustrated in Figure 3.

## 3.2 Exploration methods

To provide accurate data and a scientific basis for anti-water inflow measures in the construction of karst geological water inrush disasters, this study used electrical exploration instruments and three-dimensional velocity vector sonar measuring instruments as shown in Figures 4, 5 to detect geological information of limestone mining areas and seepage at the joints of diaphragm wall. Electrical exploration and sonar detection are commonly used comprehensive detection techniques for dealing with water inrush disasters in karst areas. Electrical exploration can be used to identify large-scale geological structures and geological disasters (such as karst caves, water-rich areas, fractured rock layers, aquifers, etc.). Sonar detection, by emitting sound waves and measuring echo signals, can accurately identify the direction, velocity, and flow changes of water flow, including revealing hidden leakage points that are difficult to detect by other methods.

## 3.3 Drilling standards

Drilling operations should strictly follow China's Code for Engineering Geological Drilling (DZ/T0017-1991). The error between the drilling azimuth and inclination during the drilling process should be controlled within 2°. After the installation of the grouting casing, cement slurry should be used for fixation, and a hydrostatic test should be conducted after solidification. The test pressure should reach 1.5 times or more than the final grouting design pressure. At the same time, detailed records should be kept of the number, specific location, and filing status of water inrush or cave recharge runoff zones in karst areas.

## 3.4 Grouting materials

The grouting materials should be selected according to the specific engineering geological conditions. This article selects the following two commonly used low-cost and environmentally friendly underground water blocking and grouting materials.

### 3.4.1 Clay-cement paste slurry

The clay-cement paste slurry is applicable to grouting reinforcement projects in unfavorable geological conditions

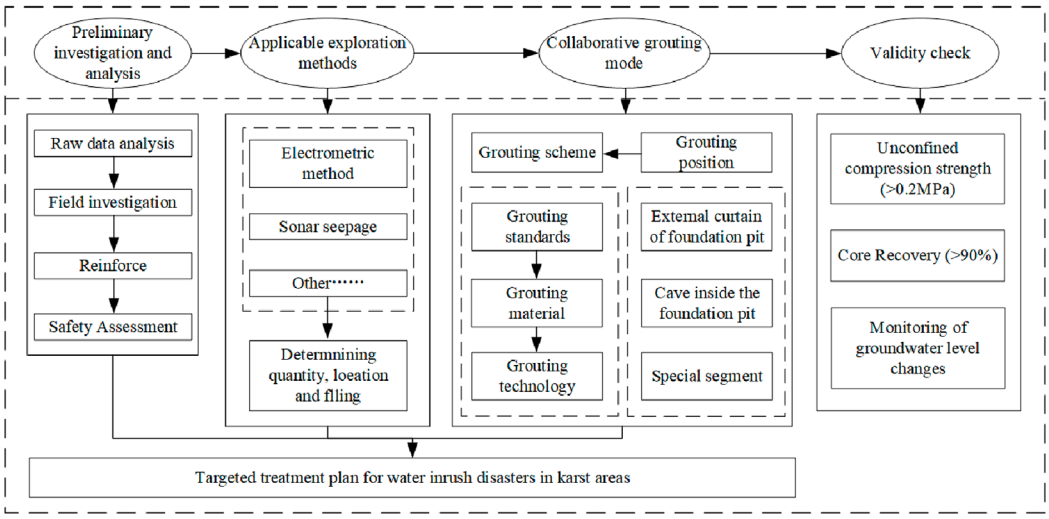


FIGURE 3
Technology flowchart.

FIGURE 4
Electrical exploration instruments.

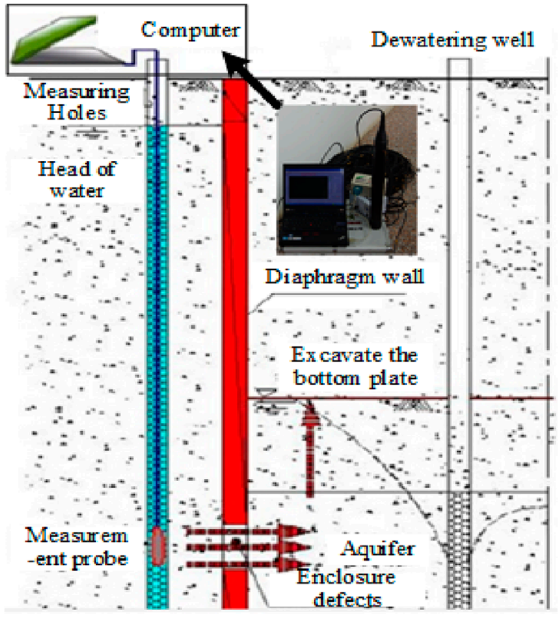


FIGURE 5
Schematic diagram of three-dimensional velocity vector sonar measuring instrument and detection principle.

such as large karst caves, dissolution fractures, fracture zones and joint fracture development zones. Its physical properties like fluidity, setting time and flow time can be adjusted according to the actual situation, demonstrating strong adaptability. The grouting method of "from bottom to top with small-interval lifting" can be adopted for grouting, as specifically shown in Figure 6.

### 3.4.2 Cement-sodium silicate two-liquid grouting materials

The cement-sodium silicate two-liquid grouting materials are composed of cement, sodium silicate and other admixtures. The mass ratio of water: cement: sodium silicate is generally 1.5: 1: 0.2. The types and dosages of admixtures can also be adjusted according to the actual grouting parameters required. The cement-sodium silicate two-liquid grouting materials are suitable for grouting anti-seepage projects in unfavorable geological conditions such as filled dissolution areas and narrow and long fractures. The grouting method of "sectional grouting from bottom to top, hole mouth sealing and circulation grouting inside the hole" should be adopted for grouting, as specifically shown in Figure 7.

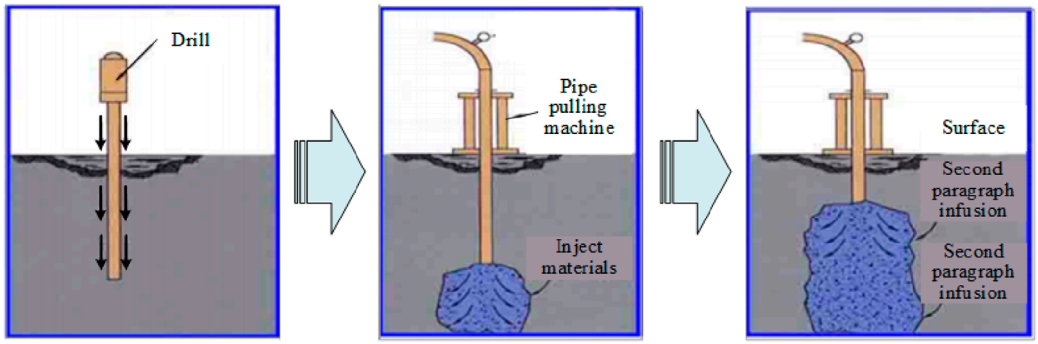


FIGURE 6
Construction schematic diagram of clay cement paste from bottom to top.

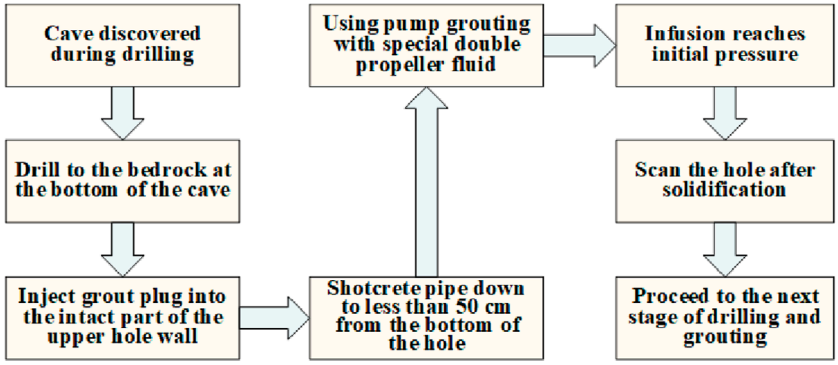


FIGURE 7
Double slurry construction process diagram.

TABLE 1 Grouting parameters (Zhang et al., 2018).

| Crack size | Slurry diffusion radius (m) | Length of grouting section (m) |
|---|---|---|
| Fine cracks (0.3–3 mm) | >3 | 15~30 |
| Medium crack (3–6 mm) | 3~10 | 10~20 |
| Large crack (6–13 mm) | 5~15 | 5~15 |
| Broken zone (13~500 mm) | <20 | 5~10 |
| Small karst cave (0.2~2m) | 30~50 | Filling all |
| Large karst cave (greater than 2 m) | 30~100 | — |

## 3.5 Grouting parameters

### 3.5.1 Grouting of curtain

For curtain grouting, the parameters mainly include the thickness of the curtain body (spacing, number of rows, pressure), the anti-seepage strength of the stone body and filling material (grout, pressure), etc. Specifically, the diffusion radius corresponding to different fracture magnitudes, and the length of the grouting section are presented in Table 1.

### 3.5.2 Grouting of karst caves

When it comes to grouting unfilled karst caves, clay-cement paste slurry is employed for consolidation and filling purposes (see Figure 8). In the case of grouting fully filled and semi-filled karst caves, a relatively high grouting pressure should be applied to ensure that the clay-cement paste slurry can effect compacted filling of the fillings. Moreover, for karst caves with a diameter exceeding 0.5 m or relatively large dissolution fractures, due to the excessive absorption

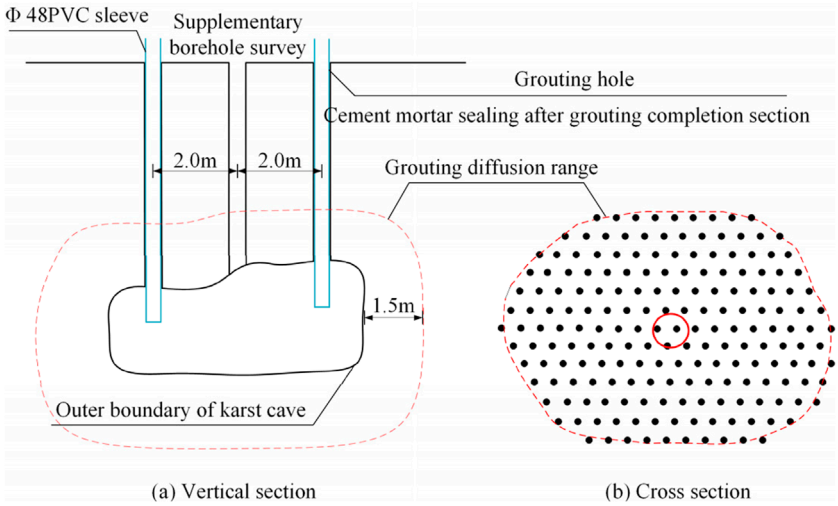


FIGURE 8
Schematic diagram of unfilled karst cave treatment.

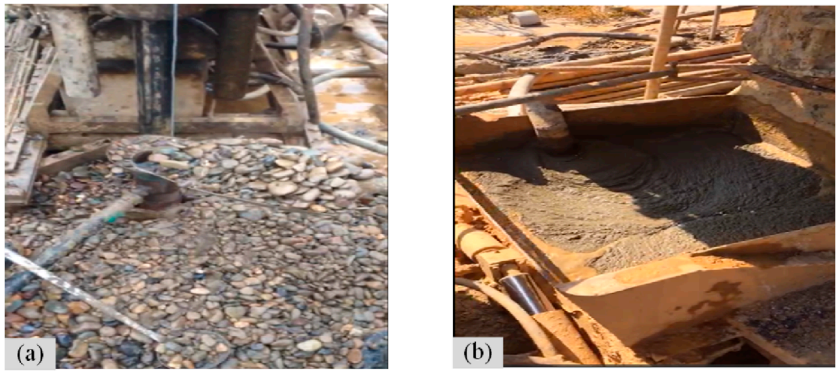


FIGURE 9
Measures for hole filling **(A)** filling sand and gravel material; **(B)** pouring cement mortar.

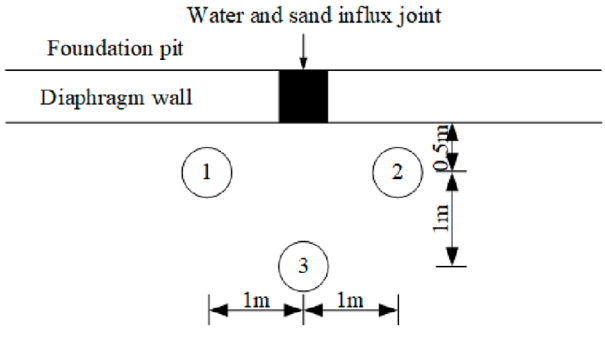


FIGURE 10
Layout of reserved grouting holes for the joints of the diaphragm wall.

of grout, the treatment principle of "prior filling followed by compaction" ought to be adhered to. Use PVC sleeves with a diameter of 48 mm and a spacing of 4m for grouting, and complete a supplementary survey between the two grouting holes.

### 3.5.3 Special segment

#### 3.5.3.1 Dynamic water conditions with high flow velocity

When the velocity of the underground water flow is relatively high, the approach of constructing measure holes can be utilized for grouting. Initially, measure holes are added approximately 1.5 m beside the grouting holes, and the diameter of the drilled holes is expanded to 110–150 mm. Inert materials such as sand and gravel are first filled into the measure holes (as illustrated in Figure 9), and subsequently, low-slump paste slurry is injected. The grouting pipe is required to be a large-diameter one with a diameter of no less than 75 mm, and the rated pressure of the grouting pump should be no lower than 20 MPa.

#### 3.5.3.2 Joints of diaphragm wall

Upon the completion of karst grouting both inside and outside the foundation pit, reserved holes should be arranged at the joints

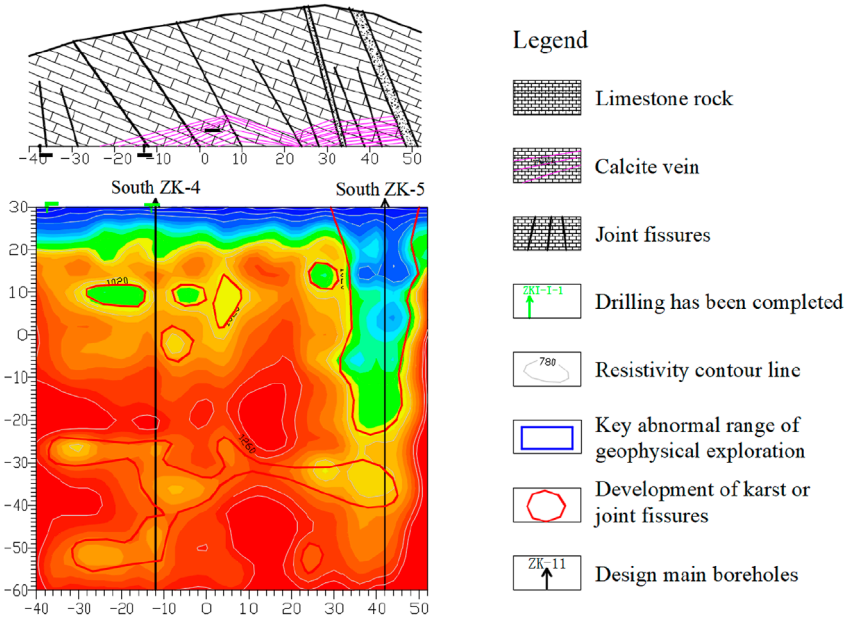


FIGURE 11
Geophysical exploration results of south ZK-4~South ZK-5 drilling holes.


FIGURE 12
Schematic diagram of mine fault.

of the underground diaphragm wall, with a hole spacing of 1 m, as depicted in Figure 10. When water inrush occurs in the upper overburden layer, the cement-sodium silicate two-liquid grouting materials can be used for anti-seepage and consolidation grouting.

## 3.6 Effectiveness check system

To assess the effectiveness of curtain grouting, it is necessary to conduct a spot check on 10% of the total number of grouting holes, with the number of checked holes being not less than three. Samples should be obtained using the core drilling method in line with the Specification for Geological Core Drilling DZ/T 0227 - 2018. The core recovery rate is required to exceed 90%. Additionally, the unconfined compressive strength of the core samples taken 28 days after the karst cave treatment should be greater than 0.2 MPa.

# 4 Engineering application

## 4.1 Treatment of water inrush disasters in karst geology

### 4.1.1 Preliminary investigation and analysis

According to existing hydrogeological data and field investigations of limestone mining areas, it is known that there is an ancient river channel within the working area, which is 3.5 km wide from east to west and 4 km long from north to south. The lower sand and gravel aquifer is in direct contact with the underlying carbonate rock, with strong hydraulic connections and abundant water content. At the same time, the mining area is covered with karst water, with a karst cave rate of 66% in boreholes and an average linear karst rate of 1.54%. Karst development is relatively extensive, with dense karst caves. Groundwater is closely connected to the hydraulic system of the bedrock layer, providing continuous replenishment for sudden water disasters.

### 4.1.2 Electrical exploration

To accurately obtain the geological structure information of the mining area, the geological exploration method was used to scan the mining area, and the joint surface structure map and resistivity scan map of the mining area were obtained. Due to space limitations, only geological information near South ZK-4 and South ZK-5 will be presented (see Figure 11). As shown in the figure, there are many steeply inclined conjugate torsional joints in the mining area, and multiple fault structures such as limestone layers are cut by horizontal structures. As shown in Figure 12, the summary of drilling information indicates that the mining area has formed strong structural dissolution in the south and northwest, including northeast trending compression torsional faults F1-1, F1-2, F1-3,

TABLE 2 Basic information of main inlet channels.

| Hole number | Leakage section hole depth (m) | Section top elevation (m) | Section low elevation (m) | Remarks |
|---|---|---|---|---|
| K361# | 40~60 | 8.27 | −11.73 | Fracture |
| K369# | 35~50 | 13.44 | −1.56 | Fracture |
| K373# | 47~47.5 | 1.67 | 1.17 | Karst cave |
| K377# | 25~42 | 23.75 | 6.75 | Fracture |
| K419# | 45~63 | 5.53 | −12.47 | Fracture |
| K437# | 30~50 | 19.42 | −0.58 | Fracture |
| K485# | 40~52 | 9.32 | −2.68 | Fracture |
| K489# | 50~65 | −0.63 | −15.63 | Fracture |

FIGURE 13
Photo of leakage at the water inflow point during K373# grouting.

FIGURE 14
Photo of leakage at the water inflow point during K485# grouting.

and northwest-trending fault F2. Various karst channels and joint fissures are interconnected, and groundwater forms a strong runoff zone along the bedrock fissures and fault fracture zones in the south of the mining area. At the same time, it is discharged into the mine pit through the north, resulting in three water inflow points: South No.1, Southwest No.2, and North No.3 (later added).

### 4.1.3 Treatment schemes

Based on precise geophysical information, the following combined grouting modes are adopted for the karst development section and nonkarst development section: the karst development section adopts a double row hole design with a hole spacing of 3 m and a row spacing of 2.5 m; Single row holes with a spacing of 3 m are used in nonkarst development sections; The drilling depth is 10 m below the karst floor. The selection of slurry materials is based on geological conditions, using clay composite slurry with a flowability of 110 mm and clay composite slurry with a flowability of 75 mm, ensuring good permeability and stability of the slurry. The grouting pressure is set at 0.8–3.5 MPa to ensure that the slurry can effectively penetrate and seal cracks and voids. In the grouting operation, low slump grout and pulsating grouting methods are used to ensure uniform injection of grout into karst voids and avoid uneven seepage. Slurry with higher fluidity can quickly cover and fill larger cracks and voids, while slurry with lower fluidity helps to form a stable sealing layer and enhance the reinforcement effect.

After the first phase of curtain grouting treatment (with a total of 334 grouting holes completed, curtain grouting footage of 34,272.9 m, and a total injection volume of 35,757 $m^3$), the water inflow within the curtain line range in the southern part of the mine is about 5,000 $m^3$/d, and the water inflow within the unexecuted curtain grouting range in the northern part is about 8,000 $m^3$/d. The water inflow in the entire mine is about 13,000 $m^3$/d, which is 87% lower than the initial water inflow disaster. But after the formation of the first curtain for a period of time, the total water inflow of the mine gradually increased again. The possible reason for this may be that water flows around the formed curtain body, causing seepage and water influx from the fault fracture zone or karst development zone in the north and northwest of the mine. Through the excavation of the F2 fault zone in the northwest by groundwater and the damage


FIGURE 15
Comparison of the effect of core sample and limestone mining area water inflow treatment after grouting before and after grouting construction.

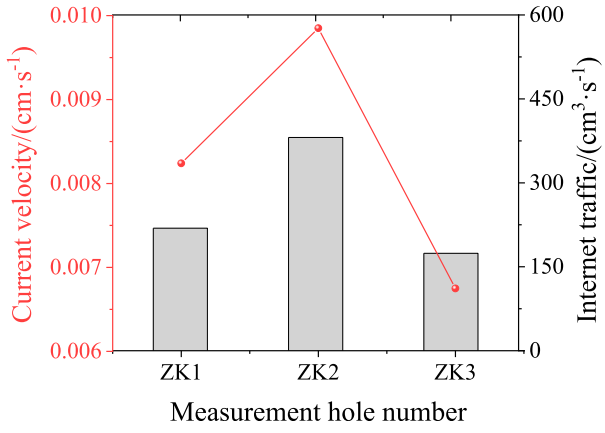


FIGURE 16
Flow velocity and flow distribution of sonar seepage detection test hole.

caused by blasting to certain parts of the original curtain body, the total water inflow of the mine gradually increases.

Based on the analysis of grouting conditions, the basic information such as the hole numbers of the main inlet channels has been sorted out as shown in Table 2. The boreholes in the table all show varying degrees of grout leakage at the water inflow points during grouting (see Figures 13, 14), suspected to be small fissure channels or small lava pipelines, which are the main permeable pathways outside the curtain line of the mine pit. The curtain line from K361# to K489# is about 387 m long, indicating that the leakage range and fissure distribution are mainly in this section, which should be the focus of treatment.

Therefore, the second phase grouting project mainly carries out curtain grouting treatment on the northern and western parts of the mining area (from 0 + 808 on the west side of the curtain line to 0 + 420 on the east side). Starting from the ZK270 hole in the last section of the first phase curtain, it overlaps parallel to the red line of the mining area to the original old mining area, forming a closed curtain anti-seepage body with the curtain of the first phase project and improving the overall stability of the curtain. The total length of the curtain line is 864 m, with a total of 299 grouting holes completed. The curtain grouting footage is 26,580.7 m, and the total injected grout volume is 10,544.89 $m^3$.

### 4.1.4 Effect inspection

After grouting, the single-point water pressure method is used for construction effect inspection, and the single-point water pressure test is carried out in accordance with Appendix A of DL/T5148-2012. The water pressure test of the inspection hole shows that the permeability value is basically less than 3 Lu, with an average permeability of 2.27 Lu, which meets the anti-seepage standard. Compared with the permeability value before grouting of the pilot hole, it has decreased by 72.0%, and the permeability of the rock mass has significantly decreased, indicating that the permeability conditions of the rock mass have been well improved after grouting treatment.

Figure 15 shows the comparison of the effects of grouting on the core sample after grouting and the treatment of water inflow in limestone mining areas before and after grouting construction. The slurry stone body extracted from hole J372 at 36.5 m–37.2 m showed good integrity, and the UCS and core recovery rate of the drilling samples met the requirements. After the sealing construction of key water inflow channels near WK133 and WK221 was completed, the water-blocking effect was significant, and the subsequent water inflow in the mine remained stable at 8600 $m^3$/d. This combined grouting mode successfully addresses the complex geological conditions of limestone rock dissolution and effectively improves the waterproofing and reinforcement effect of foundation pits.

## 4.2 Treatment of water inrush disasters at the joints of diaphragm walls

### 4.2.1 Sonar seepage detection

The sonar detection technology was adopted to detect the flow rate and velocity distribution of the seepage test holes, and the results are shown in Figure 16. It can be seen that the flow velocity of ZK1~3

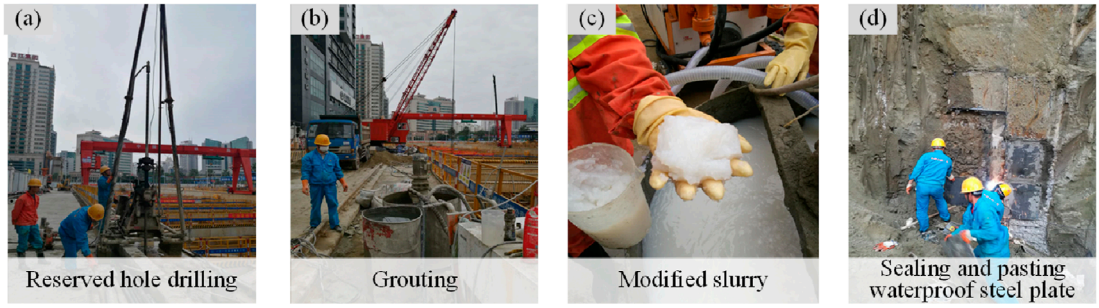


FIGURE 17
Grouting construction process for water inflow treatment of diaphragm wall joints. **(A)** Reserved hole drilling. **(B)** Grouting. **(C)** Modified slurry. **(D)** Sealing and pasting waterproof steel plate.

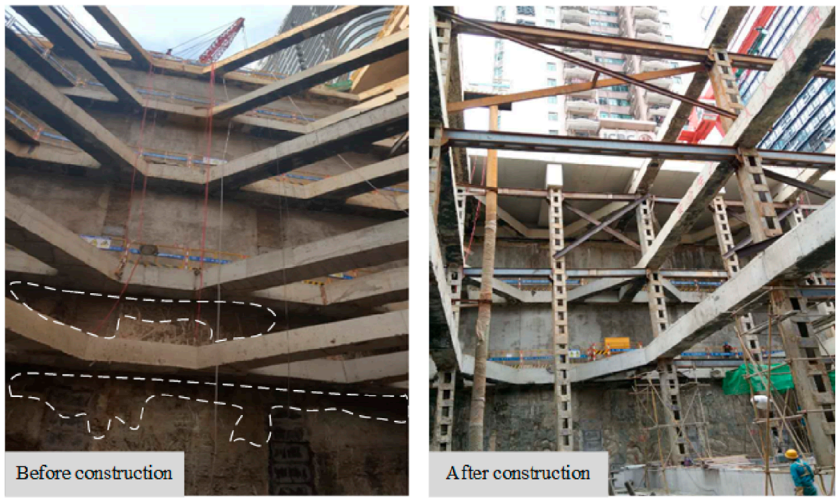


FIGURE 18
Construction effect of grouting treatment for water inflow at the joints of diaphragm walls.

directly facing the joint is much higher than the infiltration flow velocity warning line ($2 \times 10^{-4}$ cm $s^{-1}$), and the flow rate of ZK2 test hole has reached 381 $cm^3$ $s^{-1}$. Therefore, waterproofing construction should be carried out at the joint. Meanwhile, since the ZK1~3 test holes are located in the round gravel layer and silty-fine sand layers. To ensure uniform slurry permeation in the gravel and silty-fine sand layers, the cement-sodium silicate two-liquid grouting material can be chosen for grouting.

### 4.2.2 Effect inspection

The water-cement ratio of the slurry is 1:1. The mixing ratio of the cement slurry to the mixed solution is 1:1. The mixed solution consists of a water reducing agent, an early strength agent and sodium silicate, and their mixing ratio is 4%: 6%: 90%. The dilution ratio of sodium silicate is 1:3. The sleeve valve pipe grouting process is adopted, and the grouting pressure is 0.3–0.5 MPa. During the foundation pit excavation process, trench excavation is carried out, and active protective water-stop steel plates are pasted at the joints (see Figure 17).

### 4.2.3 Validity check

As shown in Figure 18, there are obvious signs of water seepage in the lower layer of the diaphragm wall joint before treatment. Long-term infiltration will erode the protective structure of the foundation pit and soften the rock and soil mass, seriously threatening the safety of subway station foundation pit construction. After processing, the water flow leakage phenomenon in the figure significantly decreased, and almost no water flow penetrated along the joint. A strong waterproof barrier has been formed by using grouting reinforcement and sealing materials at the joints. This indicates that through reasonable joint treatment measures, water seepage disasters can be effectively avoided, ensuring the safety of foundation pit construction.

## 5 Conclusion

The paper presents two water inrush scenarios in underground engineering, specifically water inrush in karst geology and water inrush at the joints of underground diaphragm walls. To address

these two types of water inrush disasters, a method combining physical detection and grouting has been put forward for their remediation. Through practical engineering applications, the effectiveness of this method has been verified. The specific conclusions are as follows:

The electrical detection technique can clearly identify the distribution of underground karst caves and fractures. Precise curtain grouting is then carried out based on the results of physical detection. After grouting, the water inrush volume has dropped sharply from 103,900 $m^3$/d to 8,600 $m^3$/d, effectively controlling the water inrush disasters in karst geology.

The sonar detection technique can effectively detect the distribution of flow rate and velocity at the joints of underground diaphragm walls. Similarly, the cement-sodium silicate two-liquid grouting method, which has good grouting permeability, is employed for joint grouting, effectively controlling the seepage flow at these joints.

For different water inrush situations in underground engineering, appropriate physical detection methods can be selected to accurately locate the positions of water inrush, followed by grouting to block the water. It has been proven that this method is highly efficient.

## Data availability statement

The original contributions presented in the study are included in the article/supplementary material, further inquiries can be directed to the corresponding author.

## Author contributions

HJ: Conceptualization, Methodology, Writing–original draft, Writing–review and editing. CJ: Conceptualization, Investigation, Methodology, Resources, Writing–original draft, Writing–review and editing. DC: Data curation, Writing–original draft. XQ: Data curation, Validation, Writing–original draft.

## Funding

The author(s) declare that financial support was received for the research, authorship, and/or publication of this article. The research was supported by the Key R & D project of Hunan Province (2024AQ2044), the Natural Science Foundation Project of Hunan Province (2024JJ6282) and the Major projects of water conservancy science and technology in Hunan Province (XSKJ2023059-02, XSKJ2024064-2, XSKJ2024064-10, XSKJ2024064-9, XSKJ2024064-6).

## Conflict of interest

The authors declare that the research was conducted in the absence of any commercial or financial relationships that could be construed as a potential conflict of interest.

## Generative AI statement

The author(s) declare that no Generative AI was used in the creation of this manuscript.

## Publisher's note



## References

Bai, Y., Wu, Z., Huang, T., and Peng, D. (2022). A dynamic modeling approach to predict water inflow during karst tunnel excavation. *Water* 14, 2380. doi:10.3390/w14152380

Cui, Q., Wu, H. N., Shen, S. L., Xu, Y. S., and Ye, G. L. (2015). Chinese karst geology and measures to prevent geohazards during shield tunnelling in karst region with caves. *Nat. Hazards* 77, 129–152. doi:10.1007/s11069-014-1585-6

Gutiérrez, F., Parise, M., Waele, J. D., and Jourde, H. (2014). A review on natural and human-induced geohazards and impacts in karst. *Earth Sci. Rev.* 138, 61–88. doi:10.1016/j.earscirev.2014.08.002

Lan, X., Zhang, X., Yin, Z., Li, X., and Yang, T. (2021). Mitigation of karst tunnel water inrush during operation in seasonal variation zone: case study in nanshibi tunnel. *Constr. Facil.* 35, 4021010. doi:10.1061/(asce)cf.1943-5509.0001573

Li, J., Fu, H., Qiu, X., Wu, Y., and Chen, J. (2024). Research on dynamic response characteristics of red clay low embankment with different road structures under vehicle load. *Transp. Geotech.* 49, 101427. doi:10.1016/j.trgeo.2024.101427

Li, S., Gao, C., Zhou, Z., Li, L., Wang, M., Yuan, Y., et al. (2019). Analysis on the precursor information of water inrush in karst tunnels: a true triaxial model test study. *Rock Mech. Rock Eng.* 52, 373–384. doi:10.1007/s00603-018-1582-2

Li, S., Qi, Y., Li, Z., Li, H., and Zhang, J. (2021). A novel treatment method and construction technology of the pipeline gushing water geohazards in karst region. *Tunn. Undergr. Space Technol.* 113, 103939. doi:10.1016/j.tust.2021.103939

Li, S., Zhou, Z., Li, L., Xu, Z., Zhang, Q., and Shi, S. (2013). Risk assessment of water inrush in karst tunnels based on attribute synthetic evaluation system. *Tunn. Undergr. Space Technol.* 38, 50–58. doi:10.1016/j.tust.2013.05.001

Li, S. C., Xu, Z. H., Huang, X., Lin, P., Zhao, X. C., Zhang, Q. S., et al. (2018). Classification, geological identification, hazard mode and typical case studies of hazard-causing structures for water and mud inrush in tunnels. Chin. J. *Rock Mech. Eng.* 37, 1041–1069. doi:10.13722/j.cnki.jrme.2017.1332

Li, X. F., Sun, J. T., Chen, W. Z., Yuan, J. Q., Liu, J. Q., and Zhang, Q. Y. (2018). Strength and anti-washout property of fibre silica fume cement grout. *Rock Soil Mech.* 39, 3157–3164. doi:10.16285/j.rsm.2016.2844

Liu, J., Chen, W., Liu, T., Yu, J., Dong, J., and Nie, W. (2018). Effects of initial porosity and water pressure on seepage-erosion properties of water inrush in completely weathered granite. *Geofluids* 2018, 1–11. doi:10.1155/2018/4103645

Liu, J., Chen, W., Nie, W., Yuan, J., and Dong, J. (2019). Experimental research on the mass transfer and flow properties of water inrush in completely weathered granite under different particle size distributions. *Rock Mech. Rock Eng.* 52, 2141–2153. doi:10.1007/s00603-018-1719-3

Liu, J., Li, Z., Zhang, X., and Weng, X. (2021). Analysis of water and mud inrush in tunnel fault fracture zone—a case study of yonglian tunnel. *Sustainability* 13, 9585. doi:10.3390/su13179585

Liu, N., Pei, J., Cao, C., Liu, X., Huang, Y., and Mei, G. (2022). Geological investigation and treatment measures against water inrush hazard in karst tunnels: a case study in Guiyang, southwest China. *Space Technol.* 124, 104491. doi:10.1016/j.tust.2022.104491

Lu, Y. R., Liu, Q., and Zhang, F. E. (2013). Environmental characteristics of karst in China and their effect on engineering. *Carbonates Evaporites* 28, 251–258. doi:10.1007/s13146-013-0158-1

Ma, G. M., Zhang, X. L., and Yang, H. Q. (2022). Study on water inrush mechanism and safety critical conditions of karst tunnels. *Saf. Environ. Eng.* 29, 64–70. doi:10.13578/j.cnki.issn.1671-1556.20210786

Parise, M., Waele, J. D., and Gutierrez, F. (2008). Engineering and environmental problems in karst—an introduction. *Eng. Geol.* 99, 91–94. doi:10.1016/j.enggeo.2007.11.009

Peng, Y., Wu, L., Zuo, Q., Chen, C., and Hao, Y. (2020). Risk assessment of water inrush in tunnel through water-rich fault based on AHP-cloud model. *Geomat. Nat. Hazards Risk* 11, 301–317. doi:10.1080/19475705.2020.1722760

Qiu, X., Li, J., Jiang, H., Ou, J., and Ma, J. (2022). Evolution of the transient saturated zone and stability analysis of slopes under rainfall conditions. *KSCE J. Civ. Eng.* 26, 1618–1631. doi:10.1007/s12205-022-0733-x

Qiu, X., Li, J., and Zeng, B. (2023). Study on the wetting deformation characteristics of high liquid limit red clay under low stress conditions. *Geotech. Mech.* 44 (07), 2028–2040. doi:10.16285/j.rsm.2022.1222

Song, J., Chen, D. Y., Wang, J., Bi, Y. F., Liu, S., Zhong, G. Q., et al. (2021). Evolution pattern and matching mode of precursor information about water inrush in a karst tunnel. *Water* 13, 1579. doi:10.3390/w13111579

Wan, F., Xu, P., Zhang, P., Qu, H., and Wang, L. (2021). Quantitative inversion of water-inrush incidents in mountain tunnel beneath a karst pit. *Adv. Civ. Eng.* 2021, 9971944. doi:10.1155/2021/9971944

Wang, M., Yang, W., Zhou, Z., Li, L., Deng, D., and Zhou, Q. (2022). Research on the evolution mechanism of water inrush in karst tunnel and the safety thickness of water-resisting rock mass. *Geotech. Geol. Eng.* 40, 4539–4549. doi:10.1007/s10706-022-02169-8

Wang, Z. M., Rawal, K., Hu, L. B., Yang, R. D., and Yang, G. L. (2017). A study of dissolution and water-bearing characteristics of the restricted platform dolomite facies in the karst areas of Guizhou, China. *China. Environ. Earth Sci.* 76, 124. doi:10.1007/s12665-017-6419-x

Xu, Z., Lin, P., Xing, H., Pan, D., and Huang, X. (2021). Hydro-mechanical coupling response behaviors in tunnel subjected to a water-filled karst cave. *Rock Mech. Rock Eng.* 54, 3737–3756. doi:10.1007/s00603-021-02423-0

Yang, J., Zhang, C., Fu, J., Wang, S., Ou, X., and Xie, Y. (2020). Pre-grouting reinforcement of underwater karst area for shield tunneling passing through Xiangjiang River in Changsha, China. *Tunn. Undergr. Space Technol.* 100, 103380. doi:10.1016/j.tust.2020.103380

Zhang, C., Fu, J., Yang, J., Ou, X., Ye, X., and Zhang, Y. (2018). Formulation and performance of grouting materials for underwater shield tunnel construction in karst ground. *Constr. Build. Mater* 187, 327–338. doi:10.1016/j.conbuildmat.2018.07.054

Zhang, K., Zheng, W., Xu, C., and Chen, S. (2019). An improved extension system for assessing risk of water inrush in tunnels in carbonate karst terrain. *KSCE J. Civ. Eng.* 23, 2049–2064. doi:10.1007/s12205-019-0756-0

Zhang, L. K., Qin, X. Q., Tang, J. S., Liu, W., and Yang, H. (2017). Review of arsenic geochemical characteristics and its significance on arsenic pollution studies in karst groundwater, Southwest China. *Appl. Geochem.* 77, 80–88. doi:10.1016/j.apgeochem.2016.05.014

Zhang, W., Zhou, X., Wei, W., and Cheng, X. (2022). Risk assessment of water inrush in tunnels: a case study of a tunnel in guangdong province, China. *Sustainability* 14, 11443. doi:10.3390/su141811443

Zhao, Y., Li, P., and Tian, S. (2013). Prevention and treatment technologies of railway tunnel water inrush and mud gushing in China. *Rock Mech. Geotech. Eng.* 5, 468–477. doi:10.1016/j.jrmge.2013.07.009

Zheng, W., Wang, D., Li, G., Qin, L., Luo, K., and Liu, J. (2019). Optimizing the grouting design for groundwater inrush control in completely weathered granite tunnel: an experimental and field investigation. *Sustainability* 11, 3636. doi:10.3390/su11133636

frontiers | Frontiers in Earth Science

TYPE Original Research
PUBLISHED 03 March 2025
DOI 10.3389/feart.2025.1544650



OPEN ACCESS

EDITED BY
Zhang Cong,
Central South University Forestry and Technology, China

REVIEWED BY
Yu Liang,
Sun Yat-sen University, China
Xuefeng Ou,
Changsha University of Science and Technology, China

*CORRESPONDENCE
Jing Zhang,
hnpfliu@qq.com

RECEIVED 13 December 2024
ACCEPTED 10 February 2025
PUBLISHED 03 March 2025

CITATION
Zhang Q, Xu P, Zhang J, Yang Z, Li Y, Kong X and Yuan X (2025) TBM shield mud cake prediction model based on machine learning. *Front. Earth Sci.* 13:1544650. doi: 10.3389/feart.2025.1544650



# TBM shield mud cake prediction model based on machine learning

Qi Zhang[1], Peng Xu[2], Jing Zhang[3]*, Zhao Yang[1], Yu Li[1], Xintong Kong[4] and Xiao Yuan[5]

[1]CCCC Second Harbor Engineering Company Ltd., Wuhan, China, [2]CCCC South China Construction and Development Co., Ltd., Shenzhen, China, [3]Sichuan Tibet Railway Co., Ltd., Chengdu, China, [4]School of Civil Engineering, Southeast University, Nanjing, Jiangsu, China, [5]School of Civil Engineering, Central South University, Changsha, China

**Introduction:** During tunnel boring machine (TBM) shield tunneling in clayey strata, the excavated soil consolidates on the cutter head or cutting tools, forming mud cakes that significantly impact the efficiency of shield tunneling.

**Methods:** To predict mud cakes during shield tunneling, four distinct supervised machine learning models, including logistic regression, support vector machine, random forest, and BP neural network were employed. The optimal predictive model for mud cake formation was determined by assessing the precision, recall, and F1 scores of the models. Further analysis of feature dependencies and shapley additive explanations (SHAP) is conducted to pinpoint the critical risk factors associated with mud cake formation.

**Results:** The results indicate that among the four supervised machine learning models, the random forest model exhibited the best performance in predicting mud cake formation during shield tunneling, with an F1 score as high as 0.9934. Feature dependencies and SHAP information showed that the shield tunneling chamber temperature and average excavation speed had the most significant impact on mud cake formation, serving as crucial factors in determining mud cake formation. The rear earth pressure of the screw conveyor and the cutterhead penetration depth followed, constituting important elements in mud cake formation. The introduction of the interpretable method SHAP for analyzing the relationships between various factors extends beyond simple linear relationships, allowing for the examination of nonlinear patterns among factors.

KEYWORDS

**shield tunnel, mud cake, tunneling parameter, machine learning, prediction model**

## 1 Introduction

China is one of the countries with the largest distribution of karst in the world (Yang et al., 2020). Due to the long-term dissolution of surface water and groundwater on soluble rocks, karst caves, grooves and other unique karst landforms have been formed (Zhang et al., 2018; Ou et al., 2024). With the acceleration of urbanization and the increasing demand for transportation, the rational development and utilization of urban underground space have become key to alleviating urban traffic pressure. Due to its high safety level and excavation efficiency, the TBM shield tunneling method has become the preferred

construction method for urban subway tunnels (Ou et al., 2025). However, caves are often filled with clayey soil in some karst areas. When the shield passes through soil layers with a high clay mineral content and weathered rock layers, the soil is prone to adhere to the surface of cutterheads and cutters made of metal, which forms mud cakes on the surface under the thrust of the shield. In milder cases, this will cause the cutter to lose its cutting ability, affecting the efficiency of shield tunneling. More severe consequences include surface subsidence, which endangers the safety of buildings and personnel. The shield mud cake formation is, in essence, the process of continuous soil compression and consolidation. In the early stage, the mud cake has a relatively low strength and is easier to handle. When the formation is complete, it may cause damage to the shield cutter, lower the efficiency of shield tunneling, and become much harder to treat (Langmaack and Lee, 2016; Yang et al., 2023). Therefore, early prediction of mud cakes is a prerequisite for ensuring safe and efficient shield tunneling and is also a hot topic actively studied by scholars. Some investigations indirectly determined the formation of shield mud cakes by monitoring the temperature or main tunneling parameters of shield tunneling (Zumsteg et al., 2016; Li et al., 2022). However, these methods failed to achieve early-stage prediction. Benefiting from the applications of emerging technologies such as machine learning and image recognition in civil engineering (Jin et al., 2022; Gao et al., 2021; Liu et al., 2020; Suwansawat and Einstein, 2006; Kohestani et al., 2017; Mahmoodzadeh et al., 2021), some studies developed early warning and monitoring systems for mud cake monitoring and identification. For instance, Fu et al. (2021) developed an early warning and monitoring system based on the Internet of Things technology, which monitored the temperature of TBM cutters in real time to identify the formation of mud cakes, thereby improving the shield machine's operating efficiency and reducing construction risks. Zhai et al. (2022) analyzed the influencing factors of mud cake formation based on machine learning, established a mud cake prediction and early warning model, and developed a real-time mud cake early warning system. Most existing studies on the formation and prevention of mud cakes rely on traditional theories (Li et al., 2022), such as the summary of construction site experience, while the analysis of mud cake formation based on emerging machine learning technologies is still in its infancy and lacks methods with model interpretability (Kang and Chois, 2020). Beyond the model prediction accuracy, the reason for generating such prediction data also requires in-depth understanding since reasonable interpretability conclusions can help technicians apply the model more confidently and enhance generalization. Some commonly used model interpretability tools include permutation importance, SHAP, local interpretable model-agnostic explanations (LIME), and partial dependence plot (PDP).

This study targets one section of the Fuzhou Metro Binhai Express where a TBM shield passes through clayey strata in China. Based on the tunneling parameters before and after in-chamber processing of shield mud cakes, the model prediction results are analyzed using the SHAP analysis tool. The effects on a shield mud cake dataset of four supervised machine learning models, i.e., logistic regression, support vector machine (SVM), random forest (RF), and back propagation (BP) neural network, are compared. The optimum prediction model is selected for further feature dependency and SHAP analysis to identify key risk factors for mud cake formation. A mud cake formation prediction model is established to provide a reliable theoretical judgment basis for mud cake prevention in shield tunneling.

# 2 Project background and data preparation

## 2.1 Project background

As an essential intercity rail transit line in Fujian Province in China, the Fuzhou Metro Binhai Express connects the railways, Changle airport, and the urban rail transit network. As an inter-city railway tunnel project from Fuzhou to Changle Airport, the shield passes through dense ground structures multiple times along the route. The ground construction environment is complex, and the strata are diverse. The excavation diameter of the shield tunnel in this section is 8.6 m, and the tunnel cover soil has a thickness of 8.8–15.3 m. The shield tunneling section of this project is located in an alluvial plain with marine-terrigenous facies. The site surface is mostly covered by sand filling layers. The geology along the line is complex and diverse, mainly composed of silty clay and muddy fine sand, with a high content of clay particles. The shield section primarily passes through the strata of mucky soil, muddy fine sand, silty clay, and strongly weathered silty sand. The overlying soil is dominated by soft soil, such as shallow silt and fill. The compositions of soil mechanics particles in the strata are displayed in Table 1. Considering the high content of clay particles, an earth pressure balance (EPB) shield machine was used for excavation construction. The cutterheads and cutters often exhibit mud cakes during the construction process, greatly reducing the excavation efficiency. Moreover, multiple pressurized in-chamber mud cake treatment increase the risk of the project.

## 2.2 Data preparation

The original data before and after cutterhead mud cake treatment from three shield tunneling sections were selected for analysis, with a total of 4,525 samples. Based on the existing research results about the influencing factors of shield mud cakes (Alberto-Hernandez et al., 2018; Zumsteg et al., 2016), characteristic factors related to the formation of shield mud cakes were screened. Each sample included ten numerical features, namely, total thrust of the propulsion cylinder, torque of the screw machine, front soil pressure of screw conveyor, rear soil pressure of screw conveyor, temperature of the sealed cabin, cutterhead torque, average driving speed, temperature of the motor cooling water, gear oil temperature, and cutterhead penetration. In addition, a binary label was used to indicate whether a mud cake was produced, where 0 indicated no presence of mud cake and 1 indicated the generation of mud cakes. Sorting and analysis of the original dataset finds 3,710 entries labeled as a normal class and 815 items labeled as mud cakes. Randomly divide the original 4,525 pieces of data into training and testing sets in an 8:2 ratio, with 3,620 data points in the training set and 905 in the testing set. The schematic diagram of the prediction model is presented in Figure 1.

Statistical analysis of the shield tunneling parameters before and after mud cake treatment was performed. Measurement data

TABLE 1 Soil mechanics parameters of strata.

| Stratum | Compositions of stratum particles (μm) | | | | | |
|---|---|---|---|---|---|---|
| | 0–10 (%) | 10–20 (%) | 20–45 (%) | 45–74 (%) | 74–200 (%) | 200–460 (%) |
| Mucky soil | 8.33 | 10.61 | 18.49 | 24.62 | 35.18 | 2.77 |
| Silt | 8.56 | 13.34 | 21.75 | 30.75 | 24.09 | 1.51 |
| Muddy fine sand | 4.77 | 7.43 | 11.45 | 24.32 | 35.22 | 16.81 |
| Silty clay | 6.88 | 9.50 | 15.24 | 21.43 | 46.02 | 0.93 |

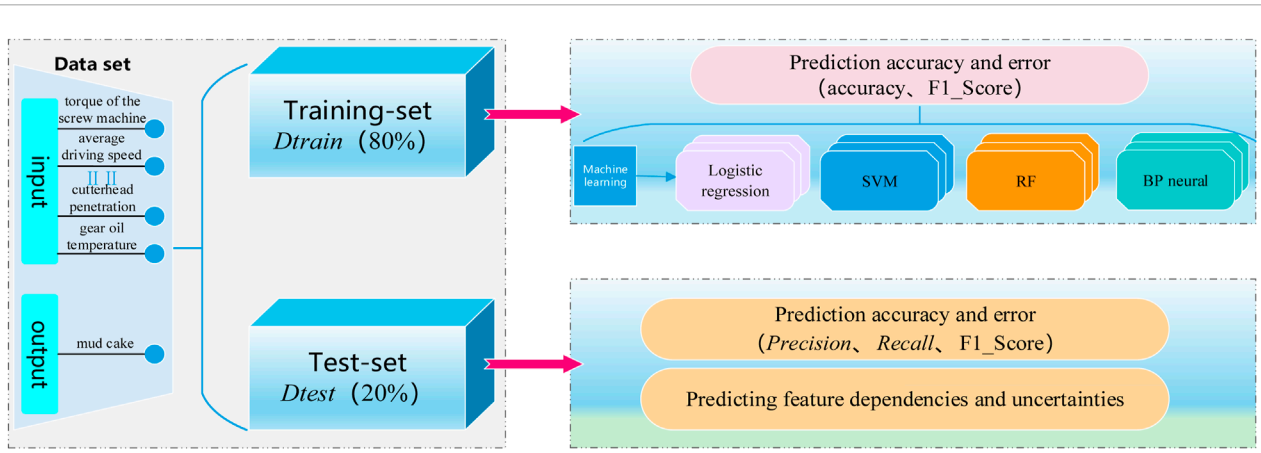


FIGURE 1
Schematic diagram of the prediction model.

that conformed to a normal distribution was expressed as mean ± standard deviation ($\bar{x} \pm s$), and the t-test was adopted for comparison among groups. Non-normally distributed measurement data was represented by its median [M($P_{20}$, $P_{80}$)], and the non-parametric test was used for comparison among groups. Count data was expressed by the number of cases and percentage (%). Comparison between categorical data adopted the $\chi^2$ test. The test level was $\alpha = 0.05$, and $P < 0.05$ indicated a statistically significant difference.

# 3 Establishment and evaluation of machine learning model

This study adopted the tools of Python 3.10 and Sklearn to establish the four different supervised machine learning models, i.e., logistic regression (Bisong et al., 2019), SVM (Cervantes et al., 2020), RF (Denisko and Hoffman, 2018), and BP neural network (Rumelhart et al., 1986), thereby evaluating the prediction accuracy of each model on the data validation set.

## 3.1 Logistic regression

As one of the most classic machine learning models, logistic regression is widely used in binary classification problems. It has advantages such as low computational complexity, rapid learning and prediction, and easy model interpretation, and its analysis model is:

$$Z = W_0 + W_1X_1 + W_2X_2 + \cdots + W_nX_n \quad (1)$$

$$F(z) = \frac{1}{1 + e^{-z}} \quad (2)$$

In Equation 1, $X_1$, $X_2$ … represent the features, while $W_1$, $W_2$ … represent the corresponding weights. Equation 2 is called the Sigmoid function, which features a monotonic increase, and its inverse function is also a monotonic increasing function. It is often used as a threshold function for neural networks, mapping variables to [0,1], and can be used for binary classification, which has good compatibility with logistic regression. When analyzing, substitute the calculated result $Z$ from Equation 1 into Equation 2 to achieve data classification, where the output of $Z$ is in the range of [0,1].

## 3.2 Support vector machine (SVM)

As a classic binary machine learning method, SVM can handle high-dimensional and nonlinear data well. It can obtain the optimum hyperplane in the sample feature space that separates all data points and maximizes their distance to it. Nonlinear SVM can

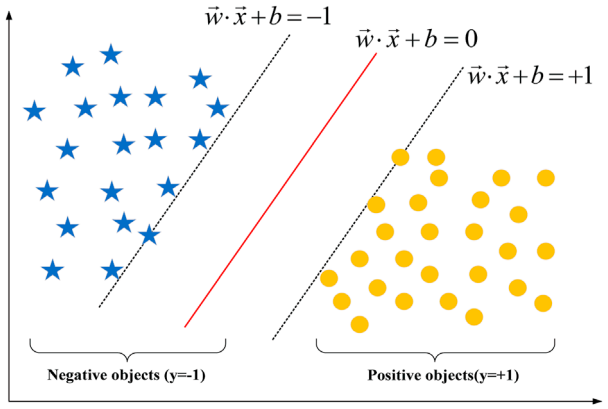


FIGURE 2
Operating principle diagram of SVM.

solve nonlinear problems by introducing kernel functions to map data onto higher dimensional spaces. The operating principle of SVM is displayed in Figure 2.

The left and right samples closest to the red solid line at the center in Figure 2 are support vectors, and the goal of SVM is to maximize the distances from the support vectors to the center red line. SVM uses the hinge loss function (*HingeLoss*) as the objective function for optimizing the model, where $f(x)$ represents the predicted results of SVM. The formula for calculating the hinge loss function is:

$$HingeLoss(y, f(x)) = \sum_{0}^{\infty} [1 - y * (f(x))]+ = |z|+ \tag{3}$$

Equation 3 indicates that when $z$ is greater than 0, the function has a value of 0. When $z$ is smaller than 0, the function equals $z$.

## 3.3 Random forest (RF)

As an ensemble learning algorithm, RF is a widely used classifier in machine learning and has the advantages of anti-overfitting, anti-data noise, and high accuracy. Its core idea is to summarize the classification results of all independent small classifiers, namely, decision trees, and set the category with the most classification results as the final classification result, as displayed in Figure 3. Each decision tree adopts the Bootstrap class analysis method, which randomly selects a fixed number of samples from the training set with replacement and then takes them as the training set.

The core idea of RF classification decision-making can be represented by

$$RF(X) = ArgMax(Ti(X)) \tag{4}$$

In Equation 4, $Ti(x)$ denotes the prediction result of the $i$-th tree in the forest for the sample with input X; $RF(X)$ represents the statistical analysis of all decision tree results where the highest result is taken as the final classification result of the entire RF for the sample with input $X$. Meanwhile, the Gini index is used as the basis for decision tree bifurcation to ensure higher dataset accuracy after each bifurcation. The formulas for the Gini index and RF algorithm bifurcation basis are

$$\text{Gini(D)} = 1\text{-}\sum_{k=0}^{y} P_k^2 \tag{5}$$

$$Gini\_Index(D,x) = \sum_{v=0}^{n} \frac{D^v}{D} \text{Gini}(D) \tag{6}$$

$$Argmin\, Gini\_Index(D,x) \tag{7}$$

In Equation 5, $Gini(D)$ represents the overall Gini index of dataset $D$. In this example, $k$ takes the value of 2, representing a normal label and a label that displays the presence of mud cakes. $P_k$ represents the probability of class $k$, which is the proportion of class $k$ in the overall sample $D$. In Equation 6, $Gini\_Index\ (D,x)$ represents the Gini index after selecting feature $x$ as the basis for bifurcation, $D^v$ denotes the size of the dataset obtained by using feature $x$ as the basis for bifurcation. Finally, according to Equation 7, the working condition with the smallest Gini index is taken as the basis for the bifurcation of each decision tree.

## 3.4 BP neural network

BP neural network is a supervised machine learning algorithm, the core idea of which is the forward propagation of data and the backward propagation of errors. It continuously adjusts the weight of each feature through gradient descent to improve model accuracy. Its outstanding advantages are its strong nonlinear mapping capability and flexible network structure. The forward propagation structure of the BP neural network is presented in Figure 4.

This study is based on the neural network module of PyTorch. The input feature X has 10 dimensions, the output category Y includes 2 classes, and the hidden layer has a total of 13 neurons (Karsoliya, 2012). The rectified linear unit (ReLU) function is used as the activation function, the cross entropy loss is used as the loss function, the learning rate is set to 0.01, and the model is trained 1,000 times. As shown in Figure 5, overfitting does not occur.

The cross entropy loss function is used in machine learning to show the difference between the real sample label and the predicted probability, which is expressed by

$$L = -\frac{1}{n}\sum_{x} |ylogx + (1-y)\,log\,(1-x)| \tag{8}$$

In Equation 8, $y$ represents the true label type, and $x$ represents the predicted probability in the range of [0,1].

## 3.5 Model evaluation metrics

### 3.5.1 F1 Score

The F1 score is an accuracy metric used in statistics to measure the results of binary classification problems, considering the precision and recall of the model. The F1 score is in the range of [0,1]. The closer it is to 1, the higher the prediction accuracy. The F1 score is calculated by

$$\text{F1} = 2 \times \frac{Precision \cdot recall}{Precision + recall} \tag{9}$$

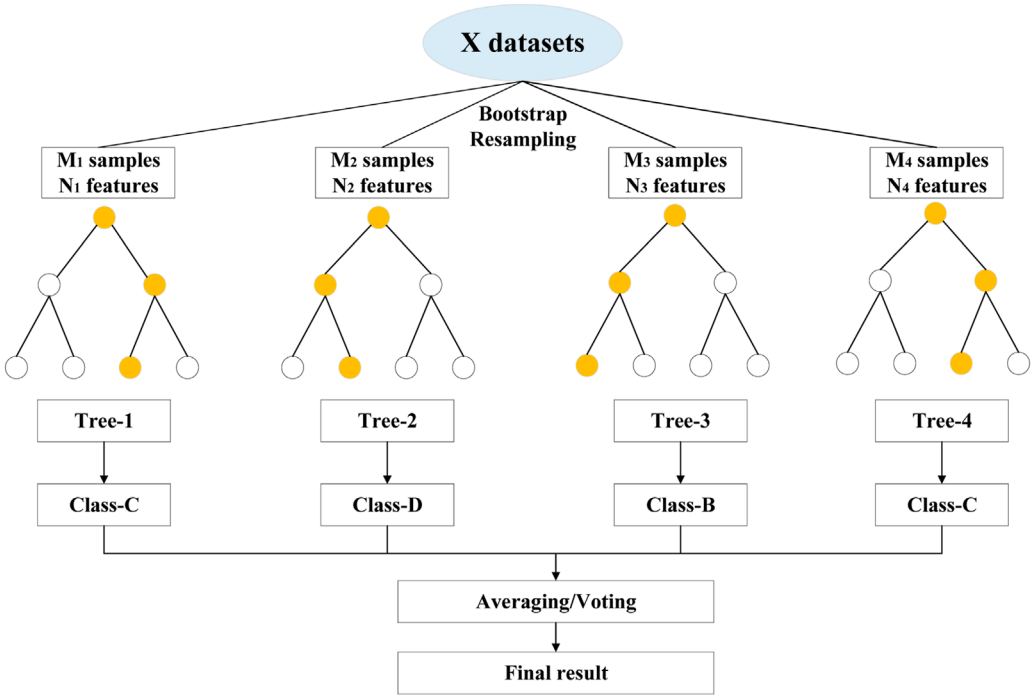


FIGURE 3
Structural diagram of the core idea of RF.

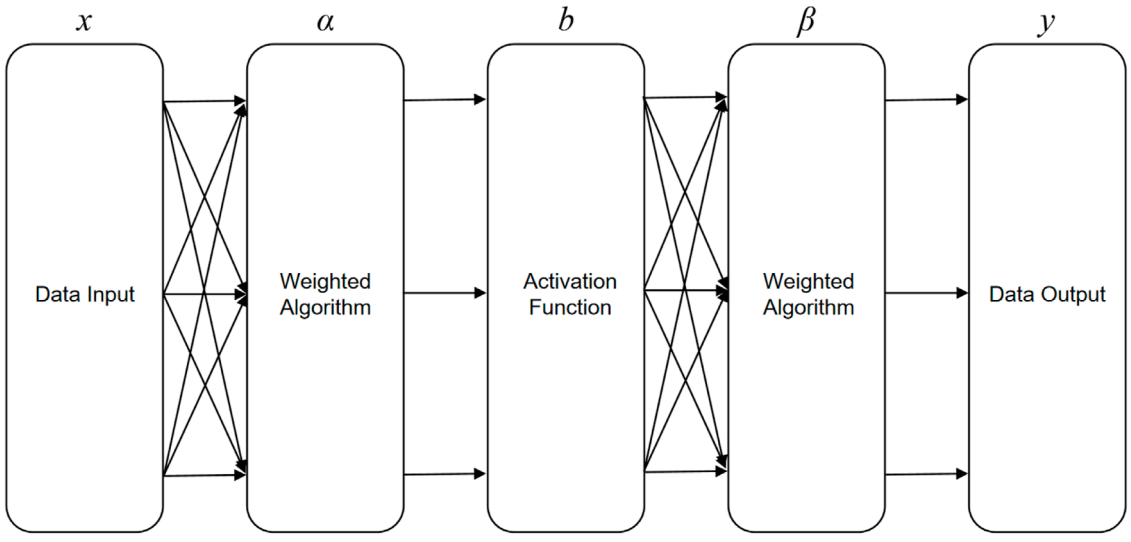


FIGURE 4
Forward propagation structure diagram of BP neural network.

$$Precision = \frac{TP}{TP + FP} \tag{10}$$

$$Recall = \frac{TP}{TP + FN} \tag{11}$$

In Equation 9, Precision represents the proportion of true positive cases among the samples predicted as positive by the model, Recall represents the proportion of samples correctly predicted as positive by the model to all true positive cases. In Equation 10, TP represents true cases (the number of samples correctly predicted as positive by the model), FP represents false positive cases (the number of samples incorrectly predicted as positive by the model). In Equation 11, FN represents false negative cases (the number of samples incorrectly predicted as negative by the model).

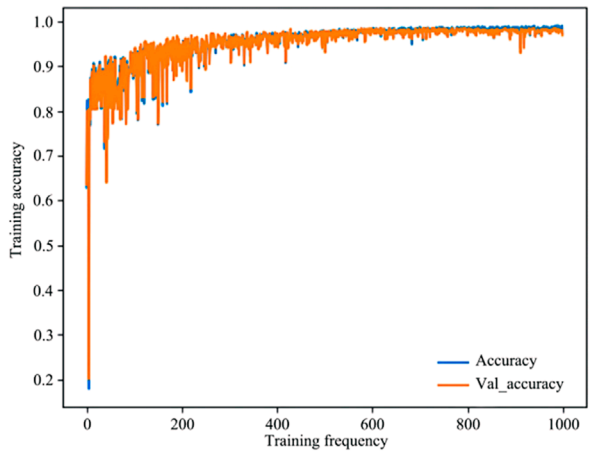


FIGURE 5
Variation graph of training loss using the cross entropy loss function.

Taking the shield mud cake category as an example, *Precision* represents the proportion of samples that truly belong to the mud cake category among all the samples predicted by the model as mud cakes, and *Recall* represents the proportion of samples correctly predicted by the model as mud cakes among all samples that truly belong to the mud cake category.

### 3.5.2 Shapley additive explanations (SHAP)

SHAP is a game theory-inspired method for explaining the predictions of machine learning models. It was first proposed by Lundberg and Lee (2017). Its essence is the average marginal contribution of feature values in all possible alliances, which can reflect the influence of each feature in the sample. As a powerful model interpretability method, SHAP can transform the results calculated by the model into a more easily understandable one, which helps interpret the model. The SHAP value of each feature reflects its contribution to the final model prediction result; the larger the SHAP value, the greater the contribution.

$$\phi i = \sum_{S \in N} \frac{|S|!(n - |S| - 1)!}{n!} [v(S \cup \{i\}) - v(S)] \quad (12)$$

where $n$ denotes the total number of features, $\phi i$ denotes the contribution of feature $i$ to prediction, and $S$ denotes all subsets that use feature $i$. Therefore, $\frac{|S|!(n-|S|-1)!}{n!}$ in Equation 12 represents the weight of subset $S$, and $v(S)$ represents the prediction for $S$.

# 4 Experimental analysis

## 4.1 Overall experimental analysis

Using the metrics module in Sklearn, the statistics for the prediction accuracy of the four machine learning models are produced, as shown in Table 2, where the recall and precision of normal and mud cake categories are compared. The final experimental analysis results are shown in Figure 6.

According to Table 2 and Figure 6, the overall accuracy of the four models is above 90%. Among them, the RF algorithm performs the best, showing the highest prediction accuracy on the dataset, especially in terms of recall and precision of the normal category. The precision and recall of SVM and logistic regression in the mud cake category are significantly lower than those of the RF model and the BP neural network. Specifically, the recall of logistic regression in the mud cake category is 26% lower than that in the normal category, and a gap of over 7% in precision also appears. Similar phenomena also occur in SVM, where the recall of the mud cake category is 25% lower than that of the normal category, and there is a 13% difference in precision. The analysis results are consistent with the results obtained by Zhai et al (2022).

## 4.2 Model interpretability analysis

After model evaluation, the best prediction model for mud cake formation, i.e., RF, is selected for further analysis. Figure 7 displays the SHAP value feature importance map, the overall sample heat map, and the overall sample swarm plot of the RF model. In the heat map, the horizontal axis represents the specific samples, while the vertical axis represents the SHAP value of each feature. The importance of features decreases from top to bottom, with red indicating a positive impact on mud cake formation and blue the opposite. The swarm plot presents each sample in the form of points, and the importance of each feature for mud cake formation also decreases from top to bottom.

As shown in Figure 7, according to the SHAP value, the features in terms of importance are ranked as follows: temperature of the sealed cabin, average driving speed, cutterhead penetration, soil pressure behind the screw machine, soil pressure before the screw machine, cutterhead torque, temperature of the motor cooling water, gear oil temperature, total thrust of the propulsion cylinder, and torque of the screw machine. The temperature of the sealed cabin is the most important factor for the final judgment of the model since its increase facilitates the solidification of soils, such as crushed rock and soil, and their adherence to the cutter and cutterhead, increasing the probability of shield mud cake formation. The average driving speed of shield tunneling also plays an essential role in the final model prediction result. As can be seen from the overall feature distribution map in Figure 7, the average driving speed is positively correlated with mud cake formation. In the overall sample swarm plot in Figure 7C, a higher average driving speed corresponds to easier mud cake formation. This is mainly because as the shield tunneling speed increases, the shear rate generated by cutterhead rotation also increases. This increase in shear force will increase the contact area and adhesive force between soil particles, thereby increasing the probability of mud cake formation at the cutterhead. In addition, as the average driving speed increases, the soil is subjected to a large shear force, resulting in soil fluidization and a corresponding decrease in soil pressure. As for the feature of soil pressure behind the screw machine, its decrease increases the risk of mud cake formation. The factor that follows in terms of the influence on the final model judgment is the cutterhead penetration. With the increase of penetration, the compression and friction conditions for forming the cutterhead mud cake become more mature, so the formation probability increases. One reason is the increased contact area between the cutterhead and the soil. Meanwhile, the damage to soil particles increases the soil porosity,

TABLE 2 Statistics of prediction accuracy for the four machine learning models.

| Category | F1 score | Normal precision | Normal recall | Mud cake precision | Mud cake recall |
|---|---|---|---|---|---|
| Logistic regression | 0.9151 | 0.9301 | 0.9711 | 0.8571 | 0.7039 |
| SVM | 0.9038 | 0.9290 | 0.9559 | 0.7975 | 0.7039 |
| RF | 0.9934 | 0.9945 | 0.9972 | 0.9887 | 0.9777 |
| BP neural network | 0.9712 | 0.9808 | 0.9835 | 0.9322 | 0.9218 |

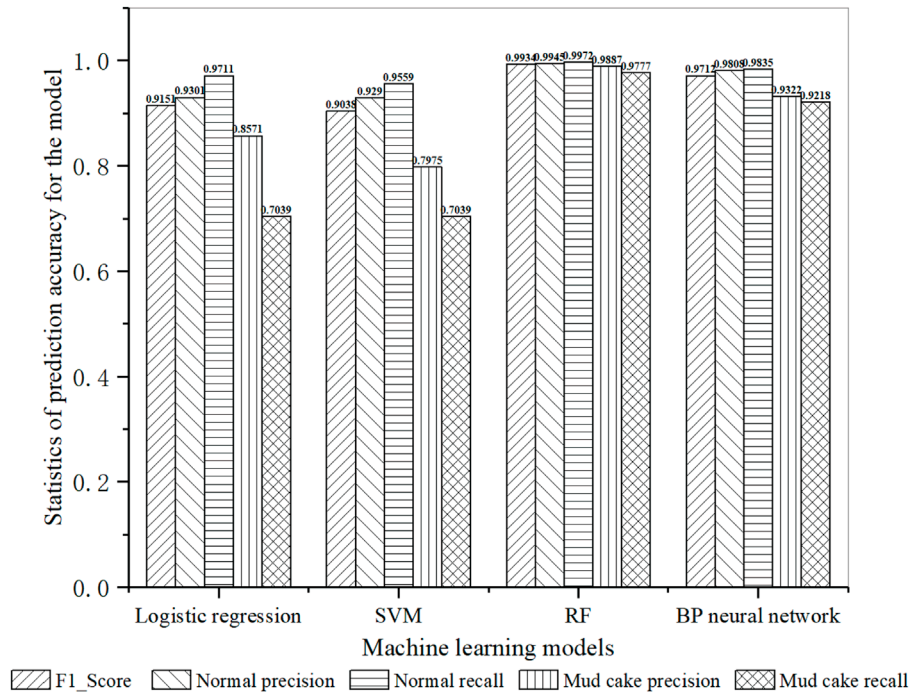


FIGURE 6
Statistical bar charts of prediction accuracy for the four machine learning models.

which promotes the entry of water into the soil and facilitates the generation of the cutterhead mud cake.

Besides these four most influential features, other factors have no decisive impact on the formation of mud cakes, most of which have a relatively small absolute SHAP value. For instance, the total thrust of the propulsion cylinder is nearly positively correlated with the probability of mud cake formation, but it is not a decisive factor. The same rule also applies to the soil pressure in front of the screw machine. As shown in Figure 8, the higher the soil pressure before the screw machine, the lower the risk of mud cake formation. This is mainly because the increase of this feature constrains the movement of soil particles and thus reduces the formation of mud cakes. Meanwhile, influenced by the soil moisture content, the increase in soil pressure before the screw machine will remove some water from the soil, indirectly reducing the risk of mud cake formation.

Figure 8 shows the contribution and influence direction (positive or negative) and the predicted value of each feature in the selected individual sample for mud cake formation, which can be used to determine the risk of mud cake formation in this sample. The base value represents the average of all model training samples, while f(x) represents the predicted risk of mud cake formation for a given sample. An f(x) below the sample average indicates a decreased mud cake formation risk, and an f(x) above average signifies an increased risk. The size of each arrow corresponds to a weight, indicating the level of impact of the feature on the prediction result. The red features and red arrows indicate a positive contribution to the formation of mud cakes, while the blue ones correspond to a negative contribution. The value of the weight characterizes the impact of the feature on sample prediction results.

Specifically, the average value of the overall sample set is 0.1752, as shown in Figure 8. In the first normal sample, the main influencing factors that turn the model prediction value from the base value to 0 include the temperature of the sealed cabin, the average driving speed, and the soil pressure after the screw machine. For a randomly selected mud cake sample, the main influencing

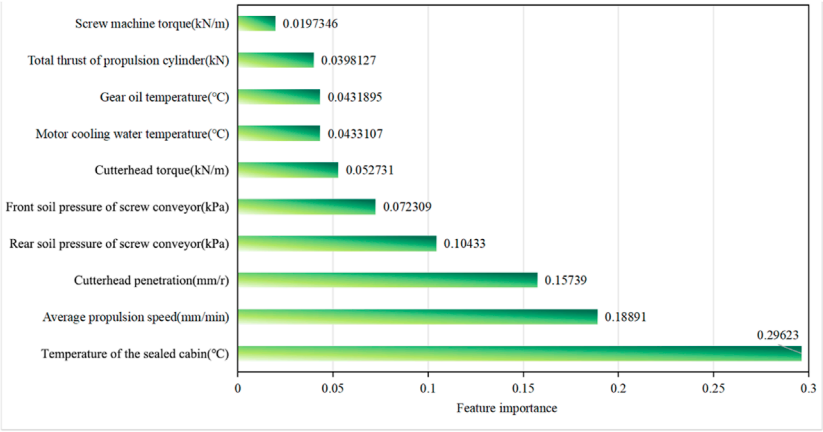


(a) Feature importance map in terms of SHAP value

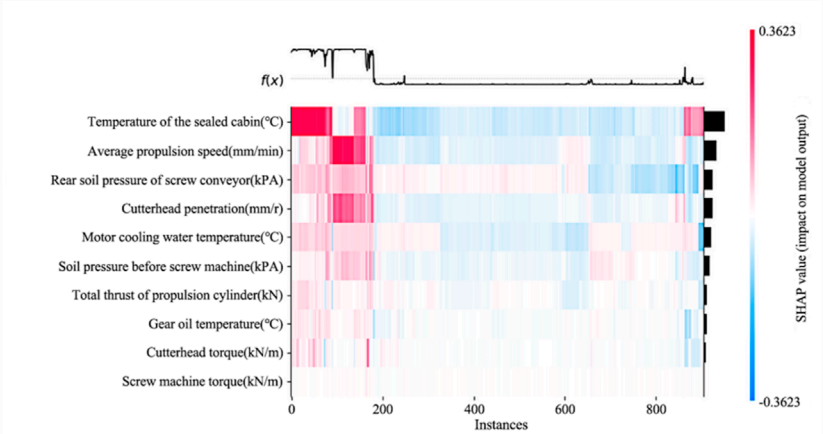


(b) Overall sample heat map

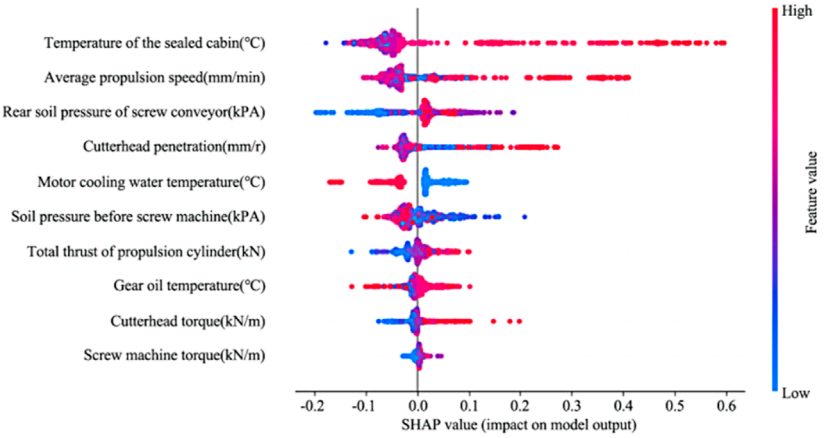


(c) Overall sample swarm plot

FIGURE 7
Analysis of various features of the RF model using the SHAP method. **(A)** Feature importance map in terms of SHAP value, **(B)** Overall sample heat map, **(C)** Overall sample swarm plot.

factors that change the predicted value from the baseline to 1 are the temperature of the sealed cabin, the soil pressure behind the screw machine, and the penetration. These results mean that the temperature of the sealed cabin, the average driving speed, the soil pressure behind the screw machine, and the penetration are the primary influencing factors for the generation of shield mud cakes,

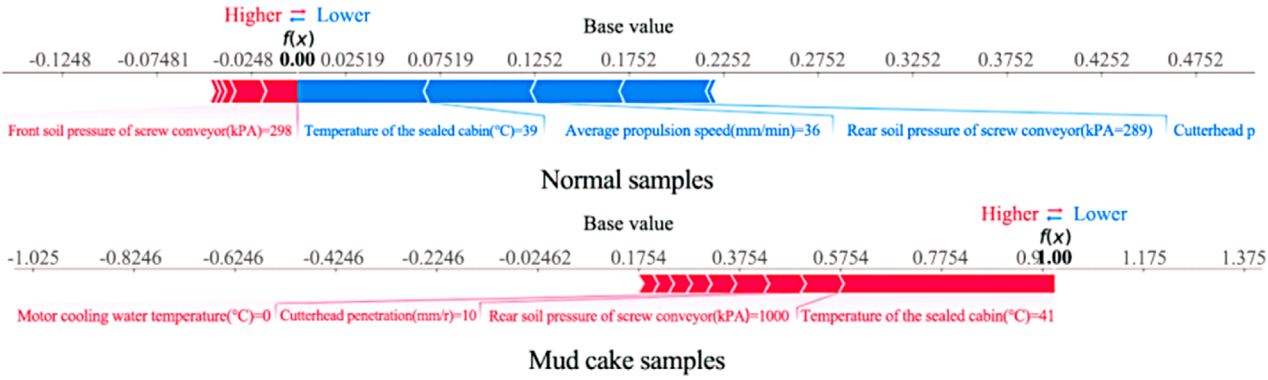


FIGURE 8
The overall heat map of mud cake and normal categories.

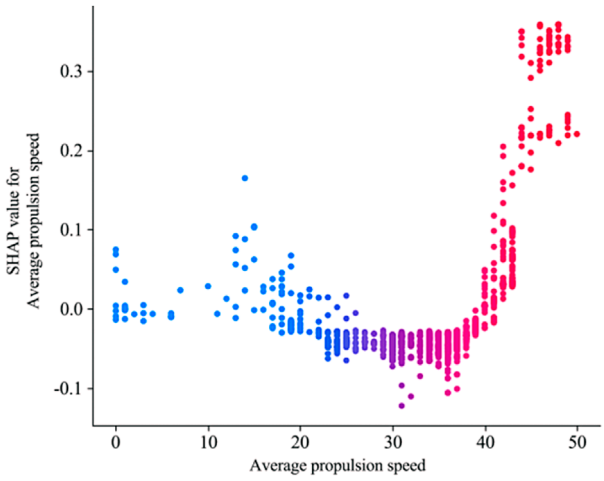


FIGURE 9
Feature dependence analysis on average driving speed.

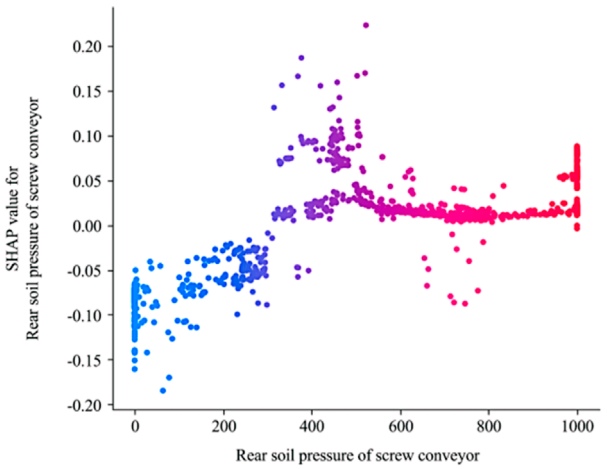


FIGURE 10
Feature dependence analysis on soil pressure after the screw machine.

which is consistent with the prediction results based on the SHAP value feature importance analysis shown in Figure 7.

## 4.3 Feature dependency analysis

As mentioned earlier, the temperature of the sealed cabin has a direct linear impact on the formation of mud cakes; the higher the temperature, the greater the risk of cutterhead mud cake formation. The second most important feature is the average driving speed, which does not show a clear gradient change pattern with mud cake formation. This is also true for the feature of soil pressure behind the screw machine. Therefore, it is necessary to conduct a feature dependency analysis for these two features. The analysis cloud maps are shown in Figures 9, 10, respectively.

Figures 9, 10 visualize the curve distribution relationships between the two features and the SHAP value. The left vertical axis represents the SHAP value of the feature, and each sample corresponds to a feature point in the figure. The color changing from blue to red indicates that the feature size gradually increases. According to the feature dependency analysis on the average driving speed in Figure 9, when the average driving speed of the shield machine is slower than 20 mm/min, the SHAP value of most samples is greater than 0. However, when the average driving speed is between 20 and 40 mm/min, the SHAP value is smaller than 0, indicating that the shield cutterhead is not prone to mud cakes. However, when the driving speed increases to above 40 mm/min, the SHAP value jumps to above 0, indicating a significant increase in the probability of mud cake formation within this speed range. A similar distribution pattern of feature points also appears for the feature of penetration. As known from the swarm plot in Figure 7C, the variations of the penetration and driving speed are consistent, both showing a linear pattern. This relationship can be explained by Equation 13.

$$\text{Penetration} = \text{Driving speed}/\text{Cutterhead rotation speed} \quad (13)$$

Figure 10 shows the SHAP value variations of soil pressure behind the screw machine. The overall distribution of the curve

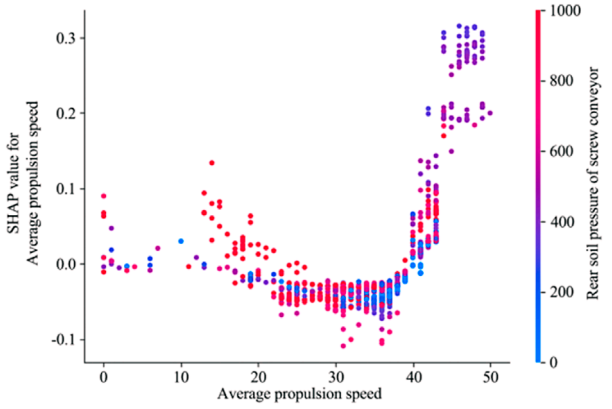


FIGURE 11
Relationship between the average driving speed and the soil pressure behind the screw machine.

demonstrates that as the soil pressure behind the screw machine increases, the SHAP value also increases. The feature distribution pattern reveals that the SHAP value is mostly smaller than 0 when the soil pressure behind the screw machine is in the range of 0–400 kPa. However, when this pressure is between 400 and 600 kPa, the SHAP value suddenly increases, peaking for some samples, which indicates that the soil pressure behind the screw machine has a positive effect on mud cake formation. When this pressure rises to above 600 kPa, the overall SHAP value is still greater than 0, though the absolute value is less than that in the range of 400–600 kPa. This indicates a pattern of first increasing and then decreasing effect for mud cake formation as the soil pressure behind the screw machine increases, which reaches the maximum at 400–500 kPa.

Figure 11 shows the distribution relationship between the average driving speed of the shield machine and the soil pressure behind the screw machine. According to Figures 9, 10, a nonlinear relationship exists between the average driving speed or the soil pressure behind the screw machine and the formation of shield mud cakes, but there is no relevant data to indicate the existence of an intrinsic relationship between these two features. Therefore, it is necessary to consider the curve distribution shown in Figure 11 to analyze the intrinsic relationship between the two. As can be seen from Figure 11, no intuitive relationship between the two features is present. However, when the soil pressure behind the screw machine is high, the SHAP value of the corresponding average driving speed is small. This may be because the excavated soil soil is squeezed around the screw machine during shield tunneling. When the shield tunneling speed is low, the soil soil will stay inside the screw machine for a relatively long time, which will lead to an increase in soil pressure behind the screw machine.

## 5 Conclusion and outlook

This study is conducted based on the original excavation parameters of a double shield tunneling machine passing through the viscous strata in a section of the Fuzhou Metro Binhai Express before and after in-cabin shield mud cake treatment. By comparing four different supervised machine learning models (logistic regression, SVM, RF, and BP neural network), the best prediction model for mud cake formation, RF, is selected. Further feature dependence and SHAP analyses for the RF algorithm are conducted to identify key risk factors for mud cake formation, and the risk prediction model for mud cake formation is established. The research results have some guiding significance for preventing mud cake formation in shield cutterheads and controlling shield tunneling parameters. The main conclusions are as follows:

(1) Among the four supervised machine learning models, the RF model has good adaptability and the highest accuracy in predicting the formation of shield mud cakes. The high precision and recall metrics in normal and mud cake classes verify the robustness of the RF model.
(2) Among the ten listed features that affect the formation of mud cakes, the sealed cabin temperature and the average driving speed of the shield machine have the strongest impact on the formation of mud cakes, which are deemed the key factors in mud cake formation, followed by the soil pressure behind the screw machine and cutterhead penetration. It is recommended to monitor the real-time temperature of in-cabin soils during shield tunneling and dynamically adjust the tunneling speed to reduce the risk of mud cake formation.
(3) The interpretability method SHAP is introduced to analyze the relationships, linear or nonlinear, between the various factors. For example, the average driving speed is a key factor that has a nonlinear relationship with mud cake formation. This provides a new approach for preventing mud cake formation in shield tunneling by adjusting the driving speed.

There are two limitations to this study. (1) Only ten strongly related parameters are considered, so more features need to be integrated in the future to establish a more comprehensive analysis model of mud cake formation. (2) There are only 4,525 samples in the dataset, so more experimental samples need to be collected to complete a more accurate prediction model.

## Data availability statement

The original contributions presented in the study are included in the article/supplementary material, further inquiries can be directed to the corresponding author.

## Author contributions

QZ: Conceptualization, Data curation, Investigation, Methodology, Writing–original draft. PX: Resources, Validation, Writing–review and editing. JZ: Conceptualization, Methodology, Software, Writing–review and editing. ZY: Data curation, Project administration, Writing–review and editing. YL: Data curation, Formal Analysis, Writing–review and editing.

XK: Resources, Validation, Writing–review and editing. XY: Formal Analysis, Visualization, Writing–review and editing.

## Funding

The author(s) declare that financial support was received for the research, authorship, and/or publication of this article. The financial support from the China Postdoctoral Science Foundation (Grant No. 2022M723536) is acknowledged and appreciated.

## Conflict of interest

Authors QZ, ZY and YL were employed by CCCC Second Harbor Engineering Company Ltd. PX was employed by CCCC South China Construction and Development Co., Ltd. JZ was employed by Sichuan Tibet Railway Co., Ltd.

The remaining authors declare that the research was conducted in the absence of any commercial or financial relationships that could be construed as a potential conflict of interest.

## Generative AI statement

The author(s) declare that no Generative AI was used in the creation of this manuscript.

## Publisher's note

All claims expressed in this article are solely those of the authors and do not necessarily represent those of their affiliated organizations, or those of the publisher, the editors and the reviewers. Any product that may be evaluated in this article, or claim that may be made by its manufacturer, is not guaranteed or endorsed by the publisher.

## References

Alberto-Hernandez, Y., Kang, C., Yi, Y., and Bayat, A. (2018). Clogging potential of tunnel boring machine (TBM): a review. *Int. J. Geotechnical Eng.*, 12 (3): 316, 323. doi:10.1080/19386362.2016.1277621

Bisong, E. (2019). Building machine learning and deep learning models on google cloud platform: a comprehensive guide for beginners. 2019: 243–250. doi:10.1007/978-1-4842-4470-8

Cervantes, J., Garcia-Lamont, F., Rodríguez-Mazahua, L., and Lopez, A. (2020). A comprehensive survey on support vector machine classification: applications, challenges and trends. *Neurocomputing* 408, 189–215. doi:10.1016/j.neucom.2019.10.118

Denisko, D., and Hoffman, M. (2018). Classification and interaction in random forests. *Proc. Natl. Acad. Sci. U. S. A.* 115 (8), 1690–1692. doi:10.1073/pnas.1800256115

Fu, J., Xia, Y., Lan, H., Wu, D., and Lin, L. (2021). A case study on TBM cutterhead temperature monitoring and mud cake formation discrimination method. *Sci. Rep.* 11 (1), 19983. doi:10.1038/s41598-021-99439-x

Gao, B., Wang, R., Lin, C., Guo, X., Liu, B., and Zhang, W. (2021). TBM penetration rate prediction based on the long short-term memory neural network. *Undergr. Space* 6 (6), 718–731. doi:10.1016/j.undsp.2020.01.003

Jin, Y., Qin, C., Tao, J., and Liu, C. (2022). An accurate and adaptative cutterhead torque prediction method for shield tunneling machines via adaptative residual long-short term memory network. *Mech. Syst. Signal Process.* 165, 108312. doi:10.1016/j.ymssp.2021.108312

Kang, T.-H., Choi, S.-W., Lee, C., and Chang, S.-H. (2020). A study on prediction of EPB shield TBM advance rate using machine learning technique and TBM construction information. *Tunn. Undergr. Space* 30 (6), 540–550. doi:10.7474/TUS.2020.30.6.540

Karsoliya, S. (2012). Approximating number of hidden layer neurons in multiple hidden layer BPNN architecture. *Int. J. Eng. Trends and Technol.*

Kohestani, V., Bazargan-Lari, M., and Marnani, J. (2017). Prediction of maximum surface settlement caused by earth pressure balance shield tunneling using random forest. *J. AI Data Min.* 5, 127–135. doi:10.22044/jadm.2016.748

Langmaack, L., and Lee, K. (2016). Difficult ground conditions? Use the right chemicals! Chances–limits–requirements. *Tunn. Undergr. Space Technol.* 57, 112–121. doi:10.1016/j.tust.2016.01.011

Li, X., Yang, Y., Li, X., and Liu, H. (2022). Criteria for cutting head clogging occurrence during slurry shield tunneling[J]. *Appl. Sci.*, 12(3): 1001–1001. doi:10.3390/app12031001

Liu, Q., Wang, X., Huang, X., and Yin, X. (2020). Prediction model of rock mass class using classification and regression tree integrated Ada Boost algorithm based on TBM driving data. *Tunn. Undergr. Space Technol.* 106, 103595. doi:10.1016/j.tust.2020.103595

Lundberg, S., and Lee, S. (2017). A unified approach to interpreting model predictions. *Statistics* 63, 4765–4774. doi:10.48550/arXiv.1705.07874

Mahmoodzadeh, A., Mohammadi, M., Ibrahim, H., Abdulhamid, S., Mahmud, H., Mohammed Hasan, A., et al. (2021). Machine learning forecasting models of disc cutters life of tunnel boring machine. *Automation Constr.* 128, 103779. doi:10.1016/j.autcon.2021.103779

Ou, X., Ouyang, L., Zheng, X., and Zhang, X. (2024). Hydrogeological analysis and remediation strategies for water inrush hazards in highway karst tunnels. *Tunn. Undergr. Space Technol.* 152, 105929. doi:10.1016/j.tust.2024.105929

Ou, X., Tang, C., Qu, T., Xu, S., Zhou, Y., and Tian, J. (2025). Towards digitalized maintenance of operating tunnels: a text documents-based defect evaluation and visualization. *Tunn. Undergr. Space Technol.* 157, 106345. doi:10.1016/j.tust.2024.106345

Rumelhart, D., Hinton, G., and Williams, R. (1986). Learning representations by back-propagating errors. *Nature* 323, 533–536. doi:10.1038/323533a0

Suwansawat, S., and Einstein, H. (2006). Artificial neural networks for predicting the maximum surface settlement caused by EPB shield tunneling. *Tunn. Undergr. Space Technol.* 21 (2), 133–150. doi:10.1016/j.tust.2005.06.007

Yang, J., Zhang, C., Fu, J. Y., Wang, S., Ou, X., and Xie, Y. (2020). Pre-grouting reinforcement of underwater karst area for shield tunneling passing through Xiangjiang River in Changsha, China. *Tunn. Undergr. Space Technol.* 100, 103380. doi:10.1016/j.tust.2020.103380

Yang, Z., Liu, P., Chen, P., Li, S., and Ji, F. (2023). Clogging prevention of slurry - earth pressure balance dual-mode shield in composed strata with medium - coarse sand and argillaceous siltstone. *Appl. Sci.* 13, 2023. doi:10.3390/app13032023

Zhai, J., Wang, Q., Yuan, D., Zhang, W., Wang, H., Xie, X., et al. (2022). Clogging risk early warning for slurry shield tunneling in mixed mudstone–gravel ground: a real-time self-updating machine learning approach[J]. *Sustainability*, 14(3): 1368–1368. doi:10.3390/su14031368

Zhang, C., Fu, J., Yang, J., Ou, X., Ye, X., and Zhang, Y. (2018). Formulation and performance of grouting materials for underwater shield tunnel construction in karst ground.*Constr. Build. Mater.* 187, 327, 338. doi:10.1016/j.conbuildmat.2018.07.054

Zumsteg, R., Puzrin, A., and Anagnostou, G. (2016). Effects of slurry on stickiness of excavated clays and clogging of equipment in fluid supported excavations. *Tunn. Undergr. Space Technol.* 58, 197–208. doi:10.1016/j.tust.2016.05.006

frontiers | Frontiers in Earth Science

TYPE Original Research
PUBLISHED 20 March 2025
DOI 10.3389/feart.2025.1556061



OPEN ACCESS

EDITED BY
Pengfei Liu,
CCCC Second Harbor Engineering Co., Ltd., China

REVIEWED BY
Kaiwen Liu,
Southwest Jiaotong University, China
Xi Jiang,
Hong Kong Polytechnic University, Hong Kong SAR, China
Changyi Yang,
Hong Kong University of Science and Technology, Hong Kong SAR, China

*CORRESPONDENCE
Zilong Song,
76581437@qq.com

RECEIVED 06 January 2025
ACCEPTED 24 February 2025
PUBLISHED 20 March 2025

CITATION
Liang J, Song Z, Fan Z and Wang X (2025) Study and application of a novel high-performance grouting material in the management of karst water inrush disasters. *Front. Earth Sci.* 13:1556061. doi: 10.3389/feart.2025.1556061



# Study and application of a novel high-performance grouting material in the management of karst water inrush disasters

Jingwei Liang[1,2], Zilong Song[1,2]*, Zezhong Fan[1,2] and Xiang Wang[1,2]

[1]Hunan Institute of Water Resources and Hydropower Research, Hunan, Changsha, China, [2]Hunan Dam Safety and Disease Prevention Engineering and Technology Research Centre, Hunan, Changsha, China

Grouting technology is a crucial method for mitigating karst water inrush disasters. However, traditional grouting materials face significant limitations when addressing catastrophic karst water inrush under conditions of high-water pressure, large water inflow, and complex hydraulic environments. To overcome these challenges, this study developed a high-performance modified clay-cement grouting material. A series of indoor experiments were conducted to investigate the effects of the water-to-solid ratio, clay content, and modifier dosage on the material's grouting performance. The optimal mix ratio was identified as water: cement: clay = 2:1:1, with an admixture dosage of 0.75%, by comparing the engineering performance of the new material against pure cement and traditional cement-clay grouting materials. The applicability and effectiveness of the developed grouting material were further validated in a practical engineering application within a water conservancy hub project in Guiping City, Guangxi Province. Results indicate that the new material not only effectively mitigates the risk of catastrophic karst water inrush but also offers advantages such as low cost, ecological benefits, and environmental sustainability. This study provides reliable technical support for emergency grouting applications and demonstrates potential for wider use.

KEYWORDS

**grouting, karst water gushing, grouting material, admixture, rheological properties**

## 1 Introduction

With the rapid advancement of society and industrialization, changes in the hydrogeological environment and issues related to karst water inflow have increasingly become significant challenges in engineering construction (Zhang et al., 2018a; Li Y. et al., 2020; Cui and Tan, 2021; Cui et al., 2015; Yang and Zhang, 2016; Xu Z. et al., 2024). Karst water inflow is prevalent in regions with highly mobile groundwater, especially in fractured zones and areas with well-developed fissures in limestone and dolomite (Veress, 2020; De Waele et al., 2011; Li et al., 2016). Karst water inflow can result in sudden water and mud ingress during construction, increasing both construction

difficulty and risk. Additionally, it poses long-term threats to the stability and durability of infrastructure (Gutiérrez et al., 2014; Song et al., 2012). Furthermore, dissolved minerals that are carried by inflowing water accelerate the erosion of engineering structures, potentially leading to foundation settlement, tunnel leakage, dam instability, and other serious issues (Cui et al., 2015). These hazards not only significantly increase remediation costs but also necessitate higher safety standards in engineering projects. Therefore, effectively controlling karst water inflow and mitigating its destructive impact on engineering works has become a pressing technical challenges in the field of geotechnical engineering.

Grouting technology is considered an effective solution for controlling karst water inflow. Its primary mechanism involves filling karst fractures and cavities with grouting materials to block the formation of water inflow channels and enhance rock mass stability (Zhang et al., 2018b; Li H. et al., 2020). Researchers have developed various grouting materials that are tailored to address karst water inflow issues (Cui et al., 2017; Shi et al., 2017; Zhenjun et al., 2024). Among these materials, cement-based grouting materials are widely used due to their high strength, broad availability, and adaptability. However, these materials also have several disadvantages, including high material consumption, difficulties in controlling diffusion, and poor environmental adaptability. These challenges are particularly evident in highly erosive karst water environments, where maintaining the long-term effectiveness of cement-based grouting is often challenging (Li Y. et al., 2020; Xu C. et al., 2024; Li et al., 2021). Additionally, the high carbon emissions that are associated with traditional cement-based materials conflict with current objectives of green and low-carbon development in the engineering sector (Zhang et al., 2019; Zhang et al., 2024). In recent years, modified cement materials have emerged as an important class of green building materials, and they are widely applied in underground engineering due to their low cost, ease of construction, high mechanical strength, and superior durability. In particular, the combination of cement and clay significantly improves grout fluidity and setting performance while enhancing filling capacity and compactness. However, traditional cement-clay grouts still exhibit limitations in erosion resistance and impermeability under high water pressure and fast-flowing water conditions, making them insufficient for effectively managing karst water inflow.

This study aims to optimize the performance of cement-clay grouting materials by incorporating modifiers to increase their adaptability under complex hydrogeological conditions. Based on the practical requirements of karst water inflow management, a novel high-performance modified cement-clay grouting material was developed. The research systematically analyzed the effects of the water-solid ratio, clay content, and modifier dosage on grouting material performance, and its effectiveness and feasibility were validated through practical engineering applications. This study not only introduces an innovative, efficient, economical, and environmentally friendly solution for managing karst water inflow but also provides theoretical and technical support for addressing engineering challenges under complex geological conditions.

# 2 Engineering background

The Datengxia Water Conservancy Project (Figure 1), approved by the State Council, is a flood control hub project for the Pearl River Basin and a landmark infrastructure project for the Pearl River–Xijiang Economic Belt and the "Xijiang Hundred-Million-Ton Golden Waterway." It is a significant cooperative effort between Guangdong and Guangxi provinces and between Guangxi and Macao. Located at the outlet of the Datengxia Gorge on the Qianjiang River section of the Xijiang River system in the Pearl River Basin, approximately 6.6 km from the Qianjiang Bridge in Guiping, the Datengxia Water Conservancy Project is a large-scale multifunctional water conservancy project. Its functions include flood control, navigation, power generation, freshwater replenishment to combat saltwater intrusion, and irrigation, with the ship lock being one of its primary structures.

The ship lock foundation primarily comprises an upper Quaternary overburden layer and a lower bedrock layer. The bedrock consists of limestone and dolomite from the lower and middle sections of the Yujing Formation (D1y1-3 and D1y2 layers). The strata strike northeast, dip southeast, and have dip angles ranging from 20° to 22°, with interbedded formations as the dominant structure, along with minor thick-bedded and thin-bedded formations. Karst development is prominent in the limestone and dolomite of the Yujing Formation, characterized as a broad-valley-type buried karst system.

As the excavation of the ship lock foundation approached the designed foundation level, the volume of karst water inflow within the foundation pit showed a continuous increase. Three major water inflows were observed at the left slope toe of the pit, while one significant inflow occurred at the right slope toe, with a combined water inflow rate of approximately 3,800 $m^3$/h. The high drainage volume required for the foundation pit led to elevated pumping costs and posed a risk of catastrophic karst water inflow. To prevent catastrophic water inflow that could flood the foundation pit and ensure construction safety, it was essential to implement emergency rescue measures and comprehensive karst water seepage management.

# 3 Grouting material test

## 3.1 Test material

### 3.1.1 Cement

Cement primarily serves as a binder in grouting materials, generating strength and enhancing material stability through hydration reactions. The cement used in this study is Grade 42.5 ordinary Portland cement produced by the Hunan Biluo Cement Plant, meeting the national standards for Portland cement. The main performance indicators are shown in Table 1.

### 3.1.2 Clay

Clay primarily serves as a thickening agent in grouting materials, enhancing slurry viscosity, stability, and water retention while improving rheological properties. This contributes to better

FIGURE 1
Datengxia water conservancy project.

TABLE 1 Properties of cement.

| Parameter | Value |
|---|---|
| Specific gravity | 3.09 |
| Stability | Qualified |
| Initial setting time/min | 95 |
| 28 days compressive strength/MPa | 46.7 |
| w (CaO)/% | 61.9 |
| W($SiO_2$)/% | 20.3 |
| W($Al_2O_3$)/% | 5.6 |
| Bal./% | 12.2 |

TABLE 2 Properties of clay.

| Parameter | Value |
|---|---|
| Specific gravity | 2.65 |
| Water content | 25.1 |
| Initial setting time/min | 90 |
| Liquid limit/% | 42.4 |
| Plastic limit/% | 22.7 |
| Liquid index/% | 0.12 |
| pH | 5.8 |
| Silicon dioxide ($SiO_2$)/% | 46.3 |
| Aluminium oxide ($Al_2O_3$)/% | 39.5 |
| Iron oxide ($Fe_2O_3$)/% | 0.8 |
| Magnesium oxide (MgO)/% | 0.13 |
| Calcium oxide (CaO)/% | 0.12 |

workability and filling performance of the slurry (Cui and Tan, 2021; Zhang et al., 2017). The clay used in this study was sourced from Changsha, Hunan Province, and its chemical composition is shown in Table 2.

### 3.1.3 Modifier

The modifier in grouting materials enhances the compatibility between cement and clay, ensuring uniformity of the slurry. This effectively improves grouting performance and soil stability (Zhang et al., 2018b; He et al., 2020). The primary component of the modifier is meta-aluminate, and its dosage complies with relevant Chinese regulations. Due to its hygroscopic nature, the modifier must be stored in a dry environment.

## 3.2 Test scheme

The water-to-solid ratio, clay content, and modifier dosage are the primary factors influencing the rheological properties of grouting materials. In this study, the water-to-solid ratio (by mass) was set at 0.6, 1.0, and 1.5 (see Table 3), while the clay content was selected as 0%, 10%, 30%, and 45% of the cement mass. Based on prior laboratory experiments and field engineering practices (Güllü,

TABLE 3 Experimental schemes of cement clay grouting material (CCGM).

| Number | A1 | A2 | A3 | A4 | A5 | A6 | A7 | A8 | A9 | A10 | A11 | A12 |
|---|---|---|---|---|---|---|---|---|---|---|---|---|
| Water: solid ratio | 0.6:1 | | | | 1.0:1 | | | | 1.5:l | | | |
| Clay dosag/% | 0 | 15 | 30 | 45 | 0 | 15 | 30 | 45 | 0 | 15 | 30 | 45 |

TABLE 4 Experimental schemes of modified cement clay grouting material (MCCGM).

| Number | B1 | B2 | B3 | B4 | B5 |
|---|---|---|---|---|---|
| Water: cement: clay | 2:1:1 | 2:1:1 | 2:1:1 | 2:1:1 | 2:1:1 |
| Modifier dosage/% | 0.25 | 0.5 | 0.75 | 1.0 | 1.25 |

2015; Anagnostopoulos, 2014), the modifier dosage was set between 0.5% and 3.0% of the cement mass. Accordingly, in Table 4 the modifier dosages in this study were 0.25%, 0.5%, 0.75%, 1.0%, and 1.25% of the cement mass. To minimize experimental error, each scheme was tested three times, and the median value of the three results was used for final analysis. Where cement grouting material (CGM) was used as a control experiment.

## 3.3 Experimental test

### 3.3.1 Rheological test

Figure 2 shows the experimental testing. The rheological testing of grouting materials is used to evaluate their fluidity and injectability, providing a basis for optimizing construction parameters and predicting the material's diffusion and coverage performance in soil. This helps improve grouting effectiveness and ensures construction quality. The rheological tests were conducted using an RSX SST rheometer (Brookfield Engineering, United States of America), which operates in controlled shear rate (RPM) and controlled shear stress (torque) modes. It characterizes the creep behavior, yield stress, and viscosity distribution of slurries, muds, and particulate materials. The accompanying Rheo3000 software supports PC control, enabling data acquisition and analysis, and allows for the processing of multiple test files.

### 3.3.2 Scouring resistance test

Grouting materials applied to karst water inflows must possess anti-erosion capabilities to resist the scouring or dilution caused by high water flow velocities and quickly solidify in dynamic water environments to maintain stability. To evaluate the anti-erosion performance, the grouting materials were subjected to experiments under varying flow velocities in a water tank. The flow velocity was controlled using a water pump and set to 0.3 m/s, 0.6 m/s, 0.9 m/s, and 1.2 m/s, with a scouring duration of 60 s. The experimental procedure was as follows: first, the flow velocity was adjusted to the target value. Once the flow stabilized, the grouting material was placed in the water tank to begin the anti-erosion test. After 60 s, the experiment was stopped, and the remaining slurry was weighed to calculate the erosion retention rate.

### 3.3.3 Consistency and setting time test

Consistency and setting time are key parameters that affect grouting activities. Consistency is an important indicator for evaluating the fluidity of the slurry during the pumping process, while setting time directly influences the control of the grouting process. By assessing the consistency and setting time of the slurry, the diffusion radius can be effectively controlled. In this study, the consistency and setting time of the slurry were measured using a mortar consistency tester. The initial setting time of the slurry was determined by pouring the slurry into a beaker inclined at 45° and recording the time required for the slurry to stop flowing.

### 3.3.4 Compressive strength test

The mechanical properties of the hardened slurry, including compressive strength and permeability coefficient, are important indicators for evaluating grouting quality. In this experiment, a concrete compression testing machine was used to test the compressive strength of cubic samples with a side length of 70.7 mm. The hardened slurry was tested at three different curing periods: 3 days, 7 days, and 28 days, under standard curing conditions.

# 4 Results and discussion

## 4.1 Rheological properties

### 4.1.1 Rheological curves

#### 4.1.1.1 CCGM

Figure 3 shows the rheological curves of the cement-clay slurry at different water-solid ratios. The results indicate that when the water-solid ratio is 0.6:1, the cement-clay slurry behaves as a Bingham fluid, with yield stress gradually increasing as clay content increases (Choi et al., 2016). When the water-solid ratio is 1:1, the rheological behavior of slurries with 0% and 15% clay content is similar, and both exhibited shear-thinning characteristics typical of a power-law fluid (expanding fluid), where shear stress increases with shear rate. As the clay content increases to 30% and 45%, the slurry transitions to a Bingham fluid, with shear-thinning behavior observed only when the clay content is 30%. At a water-to-solid ratio of 1.5:1, the cement-clay slurry continues to exhibit Bingham fluid behavior. Although clay content significantly influences the slurry's rheological curve, its overall rheological behavior remains consistent with the Bingham fluid model. When the shear rate is below 15 $s^{-1}$, the slurry's initial viscosity approaches that of water (0 Pas) due to the higher water-solid ratio, resulting in a shear stress

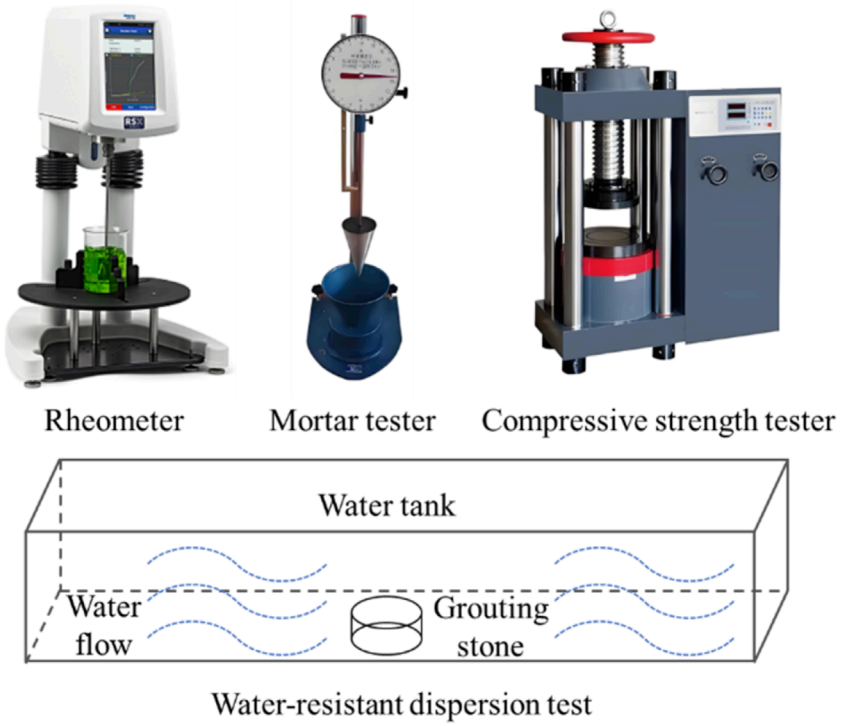


FIGURE 2
Experimental testing.

of 0 Pa. As the slurry begins to set, both viscosity and shear stress gradually increase.

#### 4.1.1.2 MCCGM

Figure 4 presents the rheological curves of modified cement-clay slurry with different amounts of modifier. When the modifier content is 0.25% and 0.50%, the slurry exhibits Bingham fluid characteristics. As the modifier content increases to 0.75%, 1.0%, and 1.25%, the slurry transitions to a pseudoplastic fluid (Herschel-Bulkley fluid) (Rahman et al., 2017), with an initial shear yield value exceeding 20 Pa. When the modifier content exceeds 0.75%, the shear stress of the slurry first decreases before stabilizing as the shear rate increases. This phenomenon may be attributed to the disruption of the internal structure of the slurry at higher shear rates, which reduces structural resistance and ultimately leads to a decrease in viscosity. As structural breakdown continues, shear stress stabilizes at a constant value. A comparison of static yield stress and dynamic yield stress can further clarify this mechanism. When the modifier content exceeds 0.75%, the stable shear stress of the slurry tends to become consistent. At a specific shear rate, increasing the modifier content initially increases shear stress, but further increases result in little significant change.

### 4.1.2 Viscosity

#### 4.1.2.1 CCGM

Figure 5 illustrates the viscosity curves of cement-clay slurry at different water-solid ratios. When the water-solid ratio is 0.6:1 and the clay content is 0% or 15%, the slurry viscosity shows minimal variation over time. However, as the clay content increases to 30% and 45%, viscosity increases rapidly before stabilizing at approximately 40 min. At a water-solid ratio of 1:1, viscosity initially decreases before increasing, with higher initial viscosity observed with higher clay contents. For a water-solid ratio of 1.5:1, the viscosity of the slurry with 0% clay remains at zero initially but gradually increases over time. Other slurries follow a trend of decreasing viscosity followed by increased viscosity. Except for the slurry with 45% clay content, all the others exhibit an initial viscosity of zero.

The observed trend of viscosity decreasing and then increasing over time can be attributed to the instability of slurries with higher water-solid ratios, which promote rapid separation of water from the slurry. During this segregation process, slurry viscosity decreases. Once water segregation is complete, the slurry begins to coagulate, leading to a subsequent increase in viscosity.

#### 4.1.2.2 MCCGM

Figure 6 shows the effect of different modifier dosages on the viscosity changes of modified clay-cement slurry over time. The viscosity of the modified slurry initially increases before gradually stabilizing. The trend indicates that the continuous generation of hydration products leads to a progressive increase in viscosity throughout the hydration process, with a sustained increase as the hydration time extends. Additionally, the time required for viscosity stabilization is delayed with increasing modifier dosage.

The results indicate that viscosity stabilization time is closely related to hydration duration. Additionally, slurries with the same clay content but varying modifier dosages exhibit similar viscosity trends, suggesting that clay content is the primary factor influencing slurry viscosity.

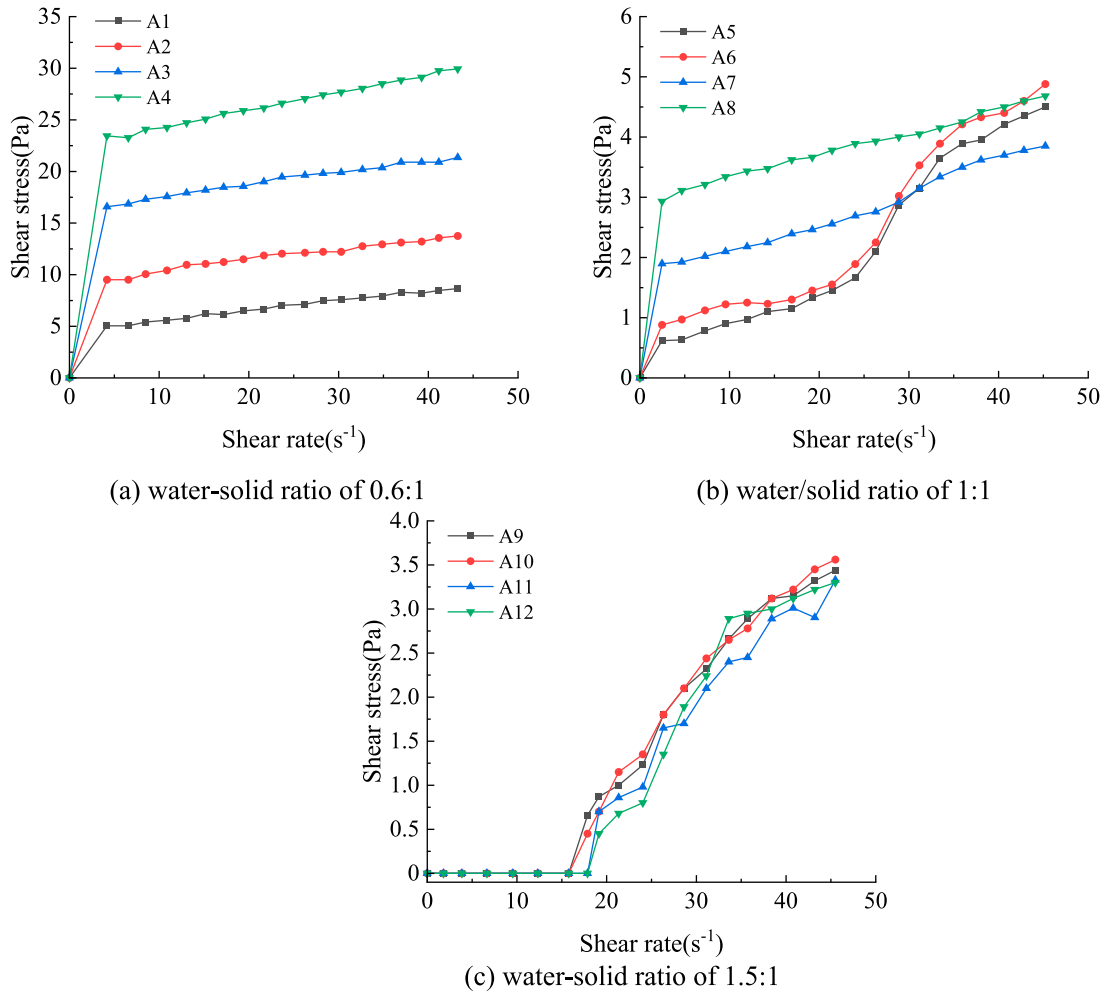


FIGURE 3
Rheological curves of CCGM with different water-solid ratios. **(A)** Water-solid ratio of 0.6:1. **(B)** Water/solid ratio of 1:1.**(C)** water-solid ratio of 1.5:1.

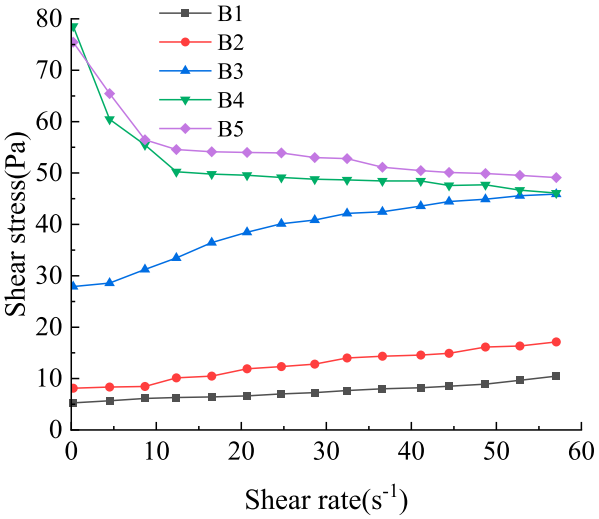


FIGURE 4
Rheological curves of MCCGM with different modifier dosages.

## 4.2 Thixotropy

### 4.2.1 MCCGM

When a suspension is at rest, particles collide due to shear forces and Brownian motion, eventually forming flocs. However, under shear stress, these flocs break apart, decreasing in size as shear rate increases, leading to a reduction in viscosity. This phenomenon, known as thixotropy, has also been observed in other fluids (Wallevik, 2009; Mardani-Aghabaglou et al., 2021). Figure 7 illustrates the thixotropic behavior of modified clay-cement slurries prepared with different dosages of modifiers. The modifier dosage significantly affects the slurry's thixotropy, resulting in complex changes.

The effect of modifier dosage on the thixotropy of modified cement-clay slurry is evident in several aspects. When the modifier dosage is relatively high (≥1.25%), the slurry exhibits coagulation behavior and transitions into a plastic state. Under external forces, such as sustained shear stress, intermolecular forces weaken or disappear, leading to structural degradation within the slurry. This structural degradation reduces strength and consistency. When the external force is removed, molecular recombination occurs, but the slurry

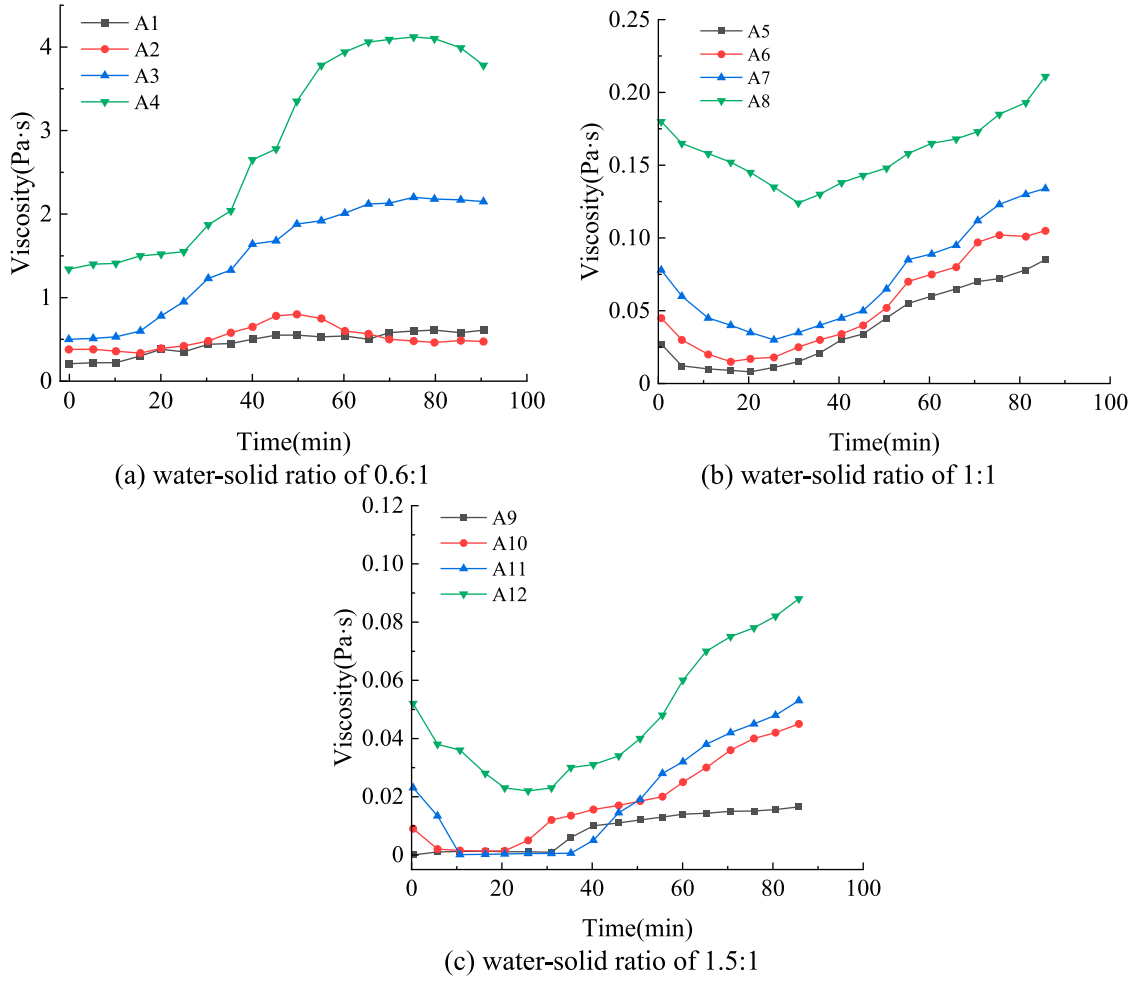


FIGURE 5
Viscosity of CCGM with different water-solid ratios. **(A)** Water-solid ratio of 0.6:1. **(B)** Water-solid ratio of 1:1. **(C)** Water-solid ratio of 1.5:1.

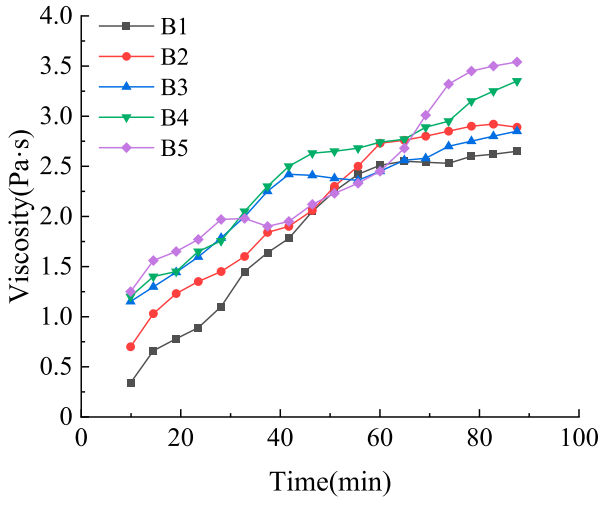


FIGURE 6
Viscosities of MCCGM with different modifier dosages.

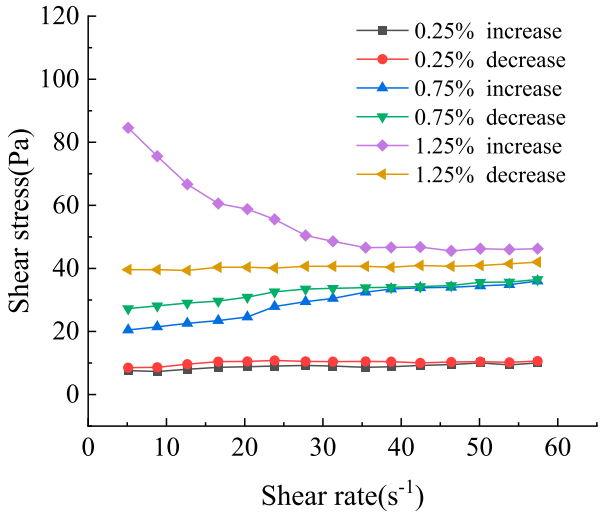


FIGURE 7
Thixotropy of MCCGM with different modifier dosages.

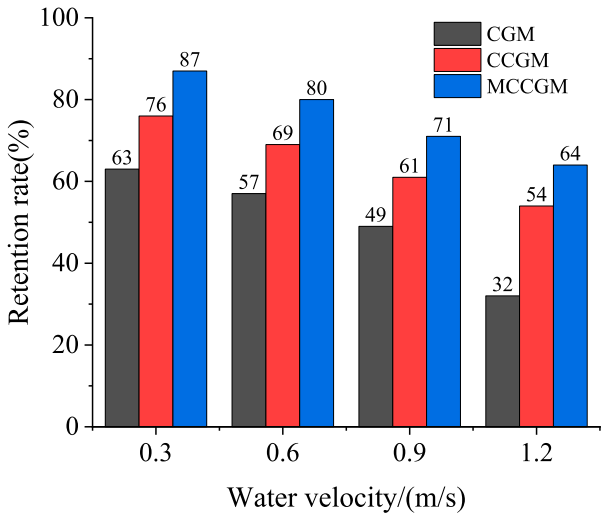


FIGURE 8
Retention rates of different grouting materials.

strength does not fully recover to its original state, demonstrating typical thixotropic behavior. In contrast, when the modifier dosage is relatively low (<0.75%), intermolecular bonding forces within the slurry are weaker, and Brownian motion is more pronounced. As the cement hydration reaction progresses, the consistency of the slurry gradually increases. At the same shear rate, the shear stress of the upward flow curve is consistently lower than that of the downward flow curve, reflecting the rheological characteristics of the slurry.

## 4.3 Scouring resistance

The results of the erosion resistance experiments are shown in Figure 8. As shown in the figure, cement slurry exhibits the poorest erosion resistance, with a retention rate of only 32% at a flow velocity of 1.2 m/s. In contrast, the retention rate of cement-clay slurry is 22% higher than that of cement slurry, which can be attributed to clay particles filling the voids within the slurry. Additionally, the water absorption and slight swelling of clay particles reduce the porosity and enhance the compactness of the hardened material, thereby improving erosion resistance. The modified cement-clay slurry, with the addition of modifiers, demonstrates superior erosion resistance across all flow velocities compared to the other two slurries. This improvement is attributed to the modifier reducing slurry dispersibility, thereby minimizing particle loss and peeling in erosive environments. Furthermore, the modifier optimizes the internal microstructure of the slurry, resulting in a more compact and uniform hardened material, significantly enhancing its erosion resistance. Based on this analysis, modified cement-clay slurry is well-suited for high-flow velocity conditions, such as karst water inrush conditions.

## 4.4 Setting time

Table 5 presents the setting times of various grouting materials. The results indicate that cement-clay slurry has the longest setting time, followed by pure cement slurry, while the modified cement-clay slurry exhibits a significantly reduced setting time compared to the other two materials. Specifically, the setting time of CCGM increased by 16.2%, whereas that of MCCGM decreased by 50.7% compared to CGM. The prolonged setting time of cement-clay slurry is primarily due to its lower cementitious material content and the strong water absorption capacity of clay. Clay particles absorb free water, slowing the hydration rate of cement particles and extending the setting time. In contrast, the modifier in the modified cement-clay slurry rapidly stimulates the hydration reactions of both cement and clay, accelerating the formation of C-S-H gel. This promotes the rapid development of a stable gel network within the slurry, thereby significantly shortening its setting time.

## 4.5 Bleeding rate and bulk shrinkage rate

Table 5 presents the bleeding rates of various grouting materials, showing that the incorporation of clay and modifiers significantly reduces the bleeding rate. Compared to pure cement grouting material, the bleeding rates of cement-clay grouting material and modified cement-clay grouting material decreased by 50.6% and 84.7%, respectively. This reduction can be attributed to the properties of clay, including pore-filling and water-absorbing expansion. The fine clay particles fill microvoids within the grouting material and swell upon water absorption, sealing channels and enhancing the material's compactness. Furthermore, the modifier accelerates cement hydration, generating denser hydration products that further reduce the bleeding rate. Table 5 also presents the volumetric shrinkage rates of the grouting materials, which follow a trend consistent with the bleeding rates. The modified cement-clay grouting material exhibits a significantly lower volumetric shrinkage rate than the other two materials. This is because the modifier not only promotes the generation of additional cementitious materials but also enhances the uniformity and anti-segregation properties of the slurry, thereby minimizing volumetric shrinkage. In conclusion, the modified cement-clay grouting material offers significant advantages for engineering applications, particularly in managing karst water inflow environments.

## 4.6 Compressive strength

Figure 9 shows the compressive strength of the solidified bodies of each slurry at different curing ages. As shown in the figure, the compressive strength of the cement slurry solidified bodies is significantly higher than that of the other two slurries at all curing ages. Additionally, the solidified bodies of the modified cement-clay slurry exhibit higher early compressive strength than those of the cement-clay slurry. The decrease in compressive strength of the cement-clay slurry solidified bodies can be attributed to the partial replacement of cement with clay, which reduces the effective cement content in the paste. This leads to a lower generation of hydration products, thereby decreasing compressive strength. However, the addition of the modifier accelerates early hydration reactions, enabling the modified cement-clay slurry to achieve a compressive strength of 1.4 MPa at the 3-day curing age,

TABLE 5 Performance parameters of different grouting materials.

| Material type | Setting time/min | Water bleeding rate/% | Bulk shrinkage rate/% |
|---|---|---|---|
| CGM | 136 | 8.5 | 4.8 |
| CCGM | 158 | 4.2 | 2.7 |
| MCCGM | 67 | 1.3 | 0.5 |

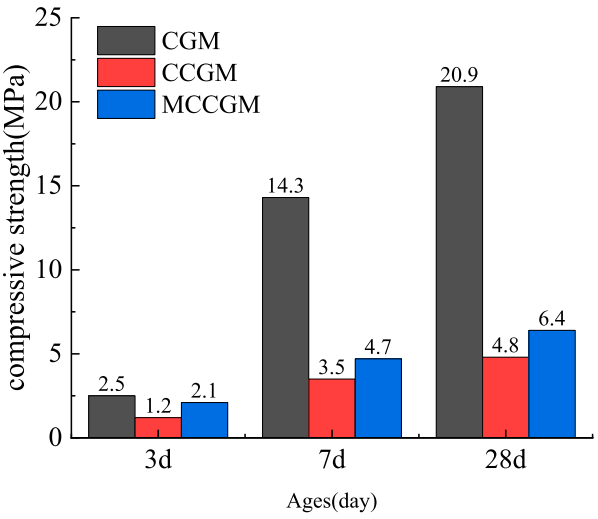


FIGURE 9
Compressive strength of different grouting materials.


FIGURE 11
Concrete compression weight.


FIGURE 10
Pipe layout.

surpassing the cement-clay slurry, which has a strength of 2.1 MPa. Thus, the modified cement-clay slurry exhibits a higher early strength gain.

## 5 Field application

The treatment of karst groundwater inflow was influenced by geological conditions and the overall project schedule. The treatment was carried out using methods that involved blocking inflow points and reverse grouting. The grouting process was carried out as follows: First, loose debris and silt at each inflow point were removed to expose the karst water channels or fractures as much as possible. The removal area was determined based on the actual conditions at each inflow point on-site. Next, a diversion (grouting) pipe was inserted into the karst water channel. The diversion (grouting) pipe was selected, and different diameters of steel pipes were used depending on the channel size. The length of the steel pipe was adjusted based on the inflow volume and burial depth of each inflow point. The underground section of the steel pipe and its mouth were wrapped with two layers of nonwoven geotextile to maximize water redirection into the pipe. A gate valve was installed at the exposed outlet of the steel pipe. Subsequently, as can be seen in Figure 10, concrete was applied to add weight, while a setting accelerator and dispersant were incorporated to minimize slurry loss. As shown in Figure 11, during the initial grouting phase, cement slurry was used to establish a channel for subsequent grouting, preventing excessive plugging pressure in later stages that could lead to the lifting of the sealing concrete.

FIGURE 12
Effect of grouting after construction.

It can be seen from Figure 12, after backfilling the centralized seepage points, the gushing water in the pit was reduced from 4,200 $m^3$/h to 1,400 $m^3$/h. Additionally, the quality of the gushing water improved, becoming clearer. The reduction in total water inflow by more than two-thirds resulted in the distribution of water entry points no longer being centralized, significantly lowering the risk of catastrophic water inflow and ensuring that the lock pits remained under control. Through this counter-irrigation treatment, the water surge problem was effectively solved. Following the completion of the construction, excavation in the treated area resumed without any recurrence of sudden water influx, confirming that the counter-irrigation treatment effectively sealed the water influx channel. This construction method offers an effective approach for addressing similar water influx issues, especially in cases of sudden water influx during pit excavation. By effectively reducing water inflow, the method can ensure pit construction safety. The pit karst surge water backfilling treatment method is especially suitable for managing sudden groundwater surges in projects of a similar engineering nature.

## 6 Conclusion

To address challenging issues such as sudden karst water influx, which is common in engineering, this paper develops a kind of inexpensive, low-carbon, and environmentally friendly modified clay-cement grouting material using cement, clay, and a modifier. The main conclusions are as follows:

1. Experimental research determined that the optimal ratio for the modified clay-cement grouting materials is water:cement:clay = 2:1:1, with a modifier dosage of 0.75%. This ratio improves the fluidity and compressive strength of the material, making it suitable for grouting under high water pressure and complex hydraulic conditions.
2. The modified cement-clay slurry exhibited better scour resistance than traditional cement-based materials under varying water flow rates. The addition of the modifier effectively reduces slurry dispersion, thereby enhancing scour resistance. This characteristic makes it particularly suitable for rapid water flow scenarios, such as karst surges.
3. The study shows that the percolation rate of the modified cement-clay grouting material is significantly lower than that of traditional cement grouting material, by 50.6% and 84.7%, respectively. This indicates that the modified material exhibits superior densification and durability in karst water surge management, effectively preventing water infiltration and improving the durability and stability of the grouting material.
4. In the actual application of the project, the modified cement-clay grouting material shows good applicability and effectiveness, providing an efficient, economical, and environmentally friendly solution for controlling karst water influx. Moreover, this material has a wide range of potential applications.

## Data availability statement

The raw data supporting the conclusions of this article will be made available by the authors, without undue reservation.

## Author contributions

JL: Conceptualization, Investigation, Methodology, Writing–original draft. ZS: Conceptualization, Methodology, Writing–review and editing. ZF: Data curation, Writing–review and editing. XW: Data curation, Writing–review and editing.

## Funding

The author(s) declare that no financial support was received for the research, authorship, and/or publication of this article.

## Conflict of interest

The authors declare that the research was conducted in the absence of any commercial or financial relationships that could be construed as a potential conflict of interest.

## Generative AI statement

The author(s) declare that no Generative AI was used in the creation of this manuscript.

## Publisher's note

All claims expressed in this article are solely those of the authors and do not necessarily represent those of their affiliated

organizations, or those of the publisher, the editors and the reviewers. Any product that may be evaluated in this article, or claim that may be made by its manufacturer, is not guaranteed or endorsed by the publisher.

## References


Anagnostopoulos, C. A. (2014). Effect of different superplasticisers on the physical and mechanical properties of cement grouts. *Constr. Build. Mater* 50, 162–168. doi:10.1016/j.conbuildmat.2013.09.050

Choi, M., Park, K., and Oh, T. (2016). Viscoelastic properties of fresh cement paste to study the flow behavior. *Int. J. Concr. Struct. M.* 10, 65–74. doi:10.1007/s40069-016-0158-3

Cui, Q., Wu, H., Shen, S., Xu, Y., and Ye, G. (2015). Chinese karst geology and measures to prevent geohazards during shield tunnelling in karst region with caves. *Nat. Hazards* 77, 129–152. doi:10.1007/s11069-014-1585-6

Cui, W., Huang, J., Song, H., and Xiao, M. (2017). Development of two new anti-washout grouting materials using multi-way ANOVA in conjunction with grey relational analysis. *Constr. Build. Mater* 156, 184–198. doi:10.1016/j.conbuildmat.2017.08.126

Cui, Y., and Tan, Z. (2021). Experimental study of high performance synchronous grouting materials prepared with clay. *Materials* 14, 1362. doi:10.3390/ma14061362

De Waele, J., Gutiérrez, F., Parise, M., and Plan, L. (2011). Geomorphology and natural hazards in karst areas: a review. *Geomorphology* 134, 1–8. doi:10.1016/j.geomorph.2011.08.001

Güllü, H. (2015). On the viscous behavior of cement mixtures with clay, sand, lime and bottom ash for jet grouting. *Constr. Build. Mater* 93, 891–910. doi:10.1016/j.conbuildmat.2015.05.072

Gutiérrez, F., Parise, M., De Waele, J., and Jourde, H. (2014). A review on natural and human-induced geohazards and impacts in karst. *Earth-Sci Rev.* 138, 61–88. doi:10.1016/j.earscirev.2014.08.002

He, S., Lai, J., Wang, L., and Wang, K. (2020). A literature review on properties and applications of grouts for shield tunnel. *Constr. Build. Mater* 239, 117782. doi:10.1016/j.conbuildmat.2019.117782

Li, H., Zhang, Y., Wu, J., Zhang, X., Zhang, L., and Li, Z. (2020b). Grouting sealing mechanism of water gushing in karst pipelines and engineering application. *Constr. Build. Mater* 254, 119250. doi:10.1016/j.conbuildmat.2020.119250

Li, S., Liu, R., Zhang, Q., and Zhang, X. (2016). Protection against water or mud inrush in tunnels by grouting: a review. *J. Rock Mech. Geotech.* 8, 753–766. doi:10.1016/j.jrmge.2016.05.002

Li, S., Ma, C., Liu, R., Chen, M., Yan, J., Wang, Z., et al. (2021). Super-absorbent swellable polymer as grouting material for treatment of karst water inrush. *Int. J. Min. Sci. Techno* 31, 753–763. doi:10.1016/j.ijmst.2021.06.004

Li, Y., Zhang, G., Jiang, H., Liu, Y., and Kuang, C. (2020a). Performance assessment of a newly developed and highly stable sandy cementitious grout for karst aquifers in China. *Environ. Earth Sci.* 79, 153–211. doi:10.1007/s12665-020-8894-8

Mardani-Aghabaglou, A., Kankal, M., Nacar, S., Felekoğlu, B., and Ramyar, K. (2021). Assessment of cement characteristics affecting rheological properties of cement pastes. *Neural Comput. Appl.* 33, 12805–12826. doi:10.1007/s00521-021-05925-8

Rahman, M., Wiklund, J., Kotzé, R., and Håkansson, U. (2017). Yield stress of cement grouts. *Tunn. Undergr. Sp. Tech.* 61, 50–60. doi:10.1016/j.tust.2016.09.009

Shi, H., Bai, M., and Xing, S. (2017). Mechanics parameter optimization and evaluation of curtain grouting material in deep, water-rich karst tunnels. *Adv. Mater Sci. Eng.* 2017, 1853951–1854012. doi:10.1155/2017/1853951

Song, K., Cho, G., and Chang, S. (2012). Identification, remediation, and analysis of karst sinkholes in the longest railroad tunnel in South Korea. *Eng. Geol.* 135, 92–105. doi:10.1016/j.enggeo.2012.02.018

Veress, M. (2020). Karst types and their karstification. *J. Earth Sci-China* 31, 621–634. doi:10.1007/s12583-020-1306-x

Wallevik, J. E. (2009). Rheological properties of cement paste: thixotropic behavior and structural breakdown. *Cem. Concr. Res.* 39, 14–29. doi:10.1016/j.cemconres.2008.10.001

Xu, C., Lei, X., Han, L., Lang, L., Chen, Z., Fu, S., et al. (2024b). Investigation the engineering properties and environmental impact of electrolytic manganese residue-based grouting materials for karst application. *Constr. Build. Mater* 457, 139344. doi:10.1016/j.conbuildmat.2024.139344

Xu, Z., Zhang, Z., Cao, C., Wu, Z., and Dong, T. (2024a). Progressive assessment of water inrush disasters in pre-construction and construction phases based on Chinese tunnels research. *Carbonate Evaporite* 39, 50. doi:10.1007/s13146-024-00958-1

Yang, Z., and Zhang, J. (2016). Minimum safe thickness of rock plug in karst tunnel according to upper bound theorem. *J. Cent. South Univ.* 23, 2346–2353. doi:10.1007/s11771-016-3293-8

Zhang, C., Fu, J., Yang, J., Ou, X., Ye, X., and Zhang, Y. (2018b). Formulation and performance of grouting materials for underwater shield tunnel construction in karst ground. *Constr. Build. Mater* 187, 327–338. doi:10.1016/j.conbuildmat.2018.07.054

Zhang, C., Yang, J., Fu, J., Ou, X., Xie, Y., Dai, Y., et al. (2019). A new clay-cement composite grouting material for tunnelling in underwater karst area. *J. Cent. South Univ.* 26, 1863–1873. doi:10.1007/s11771-019-4140-5

Zhang, C., Yang, J., Ou, X., Fu, J., Xie, Y., and Liang, X. (2018a). Clay dosage and water/cement ratio of clay-cement grout for optimal engineering performance. *Appl. Clay Sci.* 163, 312–318. doi:10.1016/j.clay.2018.07.035

Zhang, C., Zhou, J., Zheng, X., Yang, J., Zhan, S., and Yang, L. (2024). A novel water-swelling grouting material formulation and its performance for water rushing in karst strata. *Constr. Build. Mater* 416, 135245. doi:10.1016/j.conbuildmat.2024.135245

Zhang, G., Liu, J., Li, Y., and Liang, J. (2017). A pasty clay–cement grouting material for soft and loose ground under groundwater conditions. *Adv. Cem. Res.* 29, 54–62. doi:10.1680/jadcr.16.00079

Zhenjun, W., Zhang, Q., Bing, H., Rentai, L., Daoguo, T., and Yueqi, Z. (2024). New materials for controlling water inrush and sealing tunnel karst pipes. *Mater Sci+* 30, 351–359. doi:10.5755/j02.ms.36078

frontiers | Frontiers in Earth Science

TYPE Original Research
PUBLISHED 22 April 2025
DOI 10.3389/feart.2025.1578357



OPEN ACCESS

EDITED BY
Pengfei Liu,
CCCC Second Harbor Engineering Co., Ltd., China

REVIEWED BY
Youjun Guo,
Geological Survey Institute of Hunan Province, China
Jiabin Yan,
Central South University, China

*CORRESPONDENCE
Mingwei Yang,
hniwhr@163.com

RECEIVED 17 February 2025
ACCEPTED 19 March 2025
PUBLISHED 22 April 2025

CITATION
Wang X, Yang M, Zhu Y, Liang J and Jiang H (2025) New exploration model and engineering application of urban karst groundwater channel based on the 3D electrical method.
*Front. Earth Sci.* 13:1578357.
doi: 10.3389/feart.2025.1578357



# New exploration model and engineering application of urban karst groundwater channel based on the 3D electrical method

Xiang Wang[1,2], Mingwei Yang[1,2]*, Yuan Zhu[1,2], Jingwei Liang[1,2] and Huangbin Jiang[1,2]

[1]Hunan Institute of Water Resources and Hydropower Research, Changsha, Hunan, China, [2]Hunan Dam Safety and Disease Prevention Engineering and Technology Research Centre, Changsha, Hunan, China

The detection of karst groundwater channels is of great significance for the development of underground cities and the prevention and control of geological disasters. Aiming at the characteristics of high spatial variability of karst geological groundwater channels, a new exploration model based on the three-dimensional (3D) electrical method is proposed. Combined with an urban exploration project in Hunan Province, China, the exploration efficiency and effect of the new mode of one-shaped layout arrangement exploration and conventional three-dimensional electric method exploration are compared and analyzed. The main process of this model is as follows: Firstly, determine the X and Y directions of electrophysical exploration according to the direction of the geological anomalies in the exploration area. Then, according to the exploration length and measuring point spacing in X and Y directions, the electrical grid parameters are determined. Finally, the coordinates of all power supply grids and the actual relative coordinates of the exploration area are calculated, and the power supply points are arranged in a pattern of one. The feasibility of the above model has been verified through the exploration project, and the results show that the exploration efficiency of this exploration model has been significantly improved compared with the conventional three-dimensional electric method, and the effect is excellent and highly applicable.The comparison of data shows that the number of power supplies and data acquisition of conventional 3D electrical method are 121 and 14520 respectively, while the number of new mode of one-shaped layout is only 17 and 2046 respectively, with a reduction of 85.9%. The research results can provide some reference for the exploration scheme design of urban karst groundwater channels.

KEYWORDS

**3D electrical method, one-shaped layout, karst groundwater channel, detection efficiency, engineering application**

## 1 Introduction

Given the increasing global population and acceleration of urbanization, the demand for groundwater resources has increased steadily (Asaue et al., 2021; Adamson et al., 2021; Reza and Singh, 2023). In karst areas, atmospheric precipitation seeps underground rapidly through surface sinkholes and fissures, resulting in a scarcity of surface water.

The groundwater resources also demonstrate temporal non-uniformity under the influence of seasonal rainfall. These have caused water shortages as well as karst-related droughts and floods. In karst areas, groundwater is the primary source of water supply. Hence, exploration and utilization of karst groundwater is crucial for addressing the water supply demands for local industrial, agricultural, and domestic purposes. However, the exploration and development of karst groundwater entail significant challenges owing to the complex urban terrain, deep groundwater burial, and uneven karst development (Gong et al., 2024; Dai et al., 2024). The historical success rate of karst groundwater exploration has been approximately 30% (Bian et al., 2024). Therefore, accurately identifying the distribution of groundwater is crucial to the success of water exploration.

There are significant similarities and commonalities between the methods used for karst groundwater exploration. Typically, investigations of the groundwater pathways are conducted using geological or geophysical methods, followed by verification through drilling (Wu et al., 2024; Zhao et al., 2024; Lu et al., 2024). The geological methods include hydrogeological surveys, geological mapping, and remote sensing technologies. The geophysical methods include conventional direct current and electromagnetic methods (Yuan et al., 2024; Permanasari et al., 2019; Ou et al., 2020). The primary rock-forming minerals comprising the rocks possess high resistivity, while the pore water within the rocks is essentially a saline solution containing various conductive particles. This pore water exhibits good conductivity and makes electrical exploration a key method for locating and assessing groundwater resources (Xiong et al., 2019; Huang et al., 2023; Chirindja et al., 2016). Such electrical exploration methods have numerous successful applications in groundwater exploration worldwide and can be categorized into one-dimensional (1D), two-dimensional (2D), and three-dimensional (3D) methods (Chirindja et al., 2016; Kouadio et al., 2020). The 1D electrical method is rarely applied given its low precision and poor efficacy (Kevin et al., 2021; Rupesh and Sharma, 2021). In comparison, the 2D electrical method offers higher precision and better effects, but its exploration precision is still lower than that of the 3D method. The 3D electrical method has been widely adopted in geological exploration owing to its high accuracy and efficacy (Pilla and Torrese, 2022; Cardarelli et al., 2018). Han et al. (2023) compared and analyzed the influences of different electrode devices on the exploration effects based on engineering projects, and their results showed that the 3D high-density electrodynamic method is more effective at detecting low-resistance anomalies. Gong et al. (2019) found that 3D inversion could highlight the interface areas of the rock layers as well as the spatial distribution and continuity of the rock layers in the stratigraphic division; these were in agreement with the actual stratigraphy when performing 3D inversion on the exploration data. Yuan et al. (2024) conducted a comparative analysis of the electrical and drilling methods and found that the electrical methods can accurately detect underground water. Although the 3D electrical method has clear advantages in terms of precision and efficacy, its low efficiency, high cost, and strict terrain requirements limit the extent of application in practical field explorations. Hence, there is an urgent need to develop a precise exploration technology suitable for karst terrains.

The present study is based on a mineral water resources monitoring project in an urban area of Hunan Province; herein, we investigated the groundwater resources under the strong development characteristics of karst in this area. Based on the geological and geomorphological characteristics of the study area, a new model of urban groundwater exploration based on the 3D electrical method is proposed. The accuracy and effectiveness of this new exploration model were verified using the complete 3D electrical method and drilling results as the standard. The results of the exploration are intended to provide a reliable basis for urban groundwater exploration as well as for the development and utilization of water resources. This exploration model is also expected to provide guidance for the design of urban karst groundwater channel exploration programs.

# 2 Engineering background

## 2.1 Overview of the study area

The study area is located in the central urban region of Hexi District, Yiyang City (Figure 1). To address the issue of water supply for residents in the area, an exploration of underground karst water and fracture water pathways was undertaken. Owing to interference from nearby buildings, there were some challenges to implementing the conventional 3D electrical method, such as difficulties with grid distribution, limited measurement accuracies, and extended construction periods. To enhance the efficiency and accuracy of urban underground water channel exploration, we propose a layout for the 3D electrical method in the shape of the number one that was tailored for complex environments, such as urban areas.

## 2.2 Hydrological conditions

According to the stratum lithology, geological structure, and hydrodynamic conditions, the groundwater in the study area can be divided into loose rock-like pore water, clastic rock-like pore water, carbonate fissure cavern water, and fissure water; here, the fissure water includes fracture tectonic water, tectonic fissure or dyke fissure water, and weathering fissure water. The stratigraphy of the study area is simple, and the lithology is single (Table 1). The Quaternary sediment strata in this area include clay and sandy soils that exhibit low resistivity values ranging from 10 to 50 Ω·m. The resistivity of basic volcanic rocks ranges from 100 to 500 Ω·m and is similar to that of the Quaternary strata, as shown in Table 1. The resistivity of the semi-weathered strata is between those of the Quaternary strata and volcanic rocks. If faults develop within the Quaternary strata and weathered strata of volcanic rocks, the resistivity will decrease further. If faults develop in relatively intact basic volcanic rocks, then it is more likely to result in a trend of resistivity decline. There are two categories of caves, of which the water- and mud-filled caves typically have resistivities of less than 50 Ω·m while the unfilled caves generally have resistivities exceeding 3,000 Ω·m.

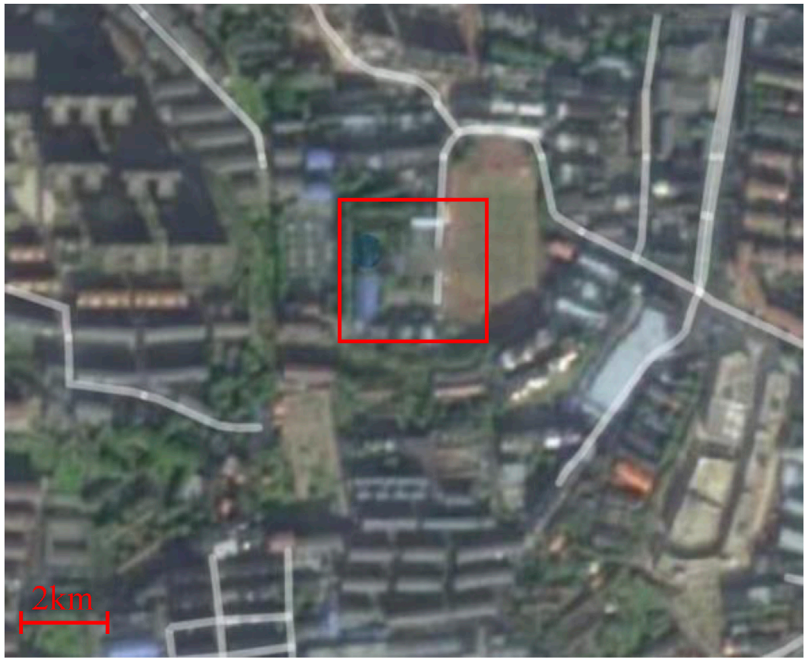


FIGURE 1
Geographic location of the project.

TABLE 1 Electrical characteristics in the survey area.

| Strata | Lithology | Electrical value (Ω·m) |
|---|---|---|
| Quaternary | Clay, sandy soil, and silt | 10~50 |
| Bedrock | Volcanic rock | 100~500 |
| Karst cave | Water- and mud-filled caves | <50 |
| | Unfilled caves | >3,000 |

# 3 Detection method and survey line layout

## 3.1 One-shaped 3D electrical method

Based on the topographical characteristics, the one-shaped 3D electrical method was designed. Here, the electrical exploration transmitter injects current into the ground through the electrodes of the power supply point. Simultaneously, the electrical exploration receiver synchronously collects electric field signals at each measurement point. By analyzing the apparent resistivity and induced polarization parameters at each measurement point upon activation of each power supply point, we achieved effective implementation of the one-shaped 3D electrical exploration. The specific descriptions of the measurements are as follows.

(1) Analysis of previous geological results and setting of exploration direction

Based on the preliminary geological results of the exploration area, the direction of the main geological anomalies in the area is inferred. Then, the direction that is approximately perpendicular to that of the geological anomalies is set as the X direction (the angle between the X direction and main geological anomalies is in the range of 60°–120° and as close to or equal to 90° as possible), while the direction parallel to the geological anomalies is set as the Y direction (the angle between the Y direction and main geological anomalies is in the range of −30° to 30° and as close to or equal to 0° as possible). These directions are perpendicular to each other and are both horizontal.

(2) Determination of exploration length and grid parameters

Based on the exploration objectives and requirements, we established the exploration lengths $L$ for the X direction and $M$ for the Y direction. Concurrently, we determined the measurement point spacings $c$ in the X direction and $d$ in the Y direction. Using the center of the exploration area as the reference point, we next calculated the grid parameters $a$ in the X direction and $b$ in the Y direction through Equation 1.

$$a = \frac{L}{2c}, \quad b = \frac{M}{2d}. \tag{1}$$

(3) Grid layout of the power supply point

Based on the topographical characteristics, we arranged the 3D electrical exploration measurement points reasonably. When the length of the measurement line in the X direction of the rectangular exploration area reaches or exceeds twice the predicted width of the exploration target, the layout of the power supply points should adhere to the following guidelines.

Assuming that the coordinates of the lower-left and upper-right corners of the rectangular exploration area are (-*a*, -*b*) and (*a*, *b*), respectively, the grid coordinates (*x*, *y*) of the power supply points are calculated by Equation 2. Thus, the actual relative coordinates ($X_C$, $Y_C$) of the electrical grid points can be determined by Equation 3.

$$(x,y) = \begin{cases} (x,0) & |x| \le a \\ (a+2^i,0) & a < x \le (3a+1), i \in [1,2,...[\log_2(2a+1)]] \\ (-a-2^i,0) & -(3a+1) \le x < -a, i \in [1,2,...[\log_2(2a+1)]] \end{cases}, \tag{2}$$

$$(X_C, Y_C) = (x \times c, y \times d) = (x \times c, 0), \tag{3}$$

where *x*, *y*, *a*, and *i* are all integers.

To reduce the boundary effects of the boundary measurement points and improve the exploration accuracy, when the length of the measurement line in the X direction is less than twice the predicted width of the exploration target, all the electrical grid points should be arranged at the same interval as the measurement points. Thus, the coordinates (*x*, *y*) of the electrical grid points are calculated using Equation 4.

$$(x,y) = (x,0); |x| \le 2a. \tag{4}$$

Combining the aforementioned rules with the conversion relationship between grid coordinates (*x*, *y*) and actual relative coordinates ($X_C$, $Y_C$), the positions of all power supply points are determined. Then, these points are reasonably arranged within the exploration area to ensure accuracy and efficiency.

(4) Arrangement of the measurement points

Based on the exploration requirements and calculated grid parameters, including the spacing and measurement points in the X and Y directions, the layout scheme for the 3D electrical measurement points is established.

(5) Data acquisition and measurements

On the preset grid lines, the power supply points are activated sequentially using a multichannel electrical measurement system or multiple independent measurement systems to collect the electrical data from all measurement points within the exploration area.

(6) Data processing and integration of results

The collected electrical data are organized and processed through the one-shaped 3D electrical method to generate the electrical exploration results for the surveyed area.

## 3.2 Survey line arrangement

The field layout diagram of the one-shaped 3D electrical method is presented in Figure 2. A total of six 3D electrical measurement lines are arranged within the site area, as illustrated in Figure 3. Owing to constraints from the terrain and topography, the layout of the measurement points and power supply points is primarily a grid of 20 × 40 m. In addition, some measurement points were adjusted and shifted based on the unique topography of the urban area. Within this measurement area, the one-shaped 3D electrical survey line was arranged along both east–west and north–south orientations, resulting in a total of 121 measurement points. Owing to the presence of obstacles, such as buildings, the spacing between the measurement points and lines is adjusted flexibly according to the actual on-site conditions. The distances between the measurement points range from 10 to 20 m, while the line spacing is approximately 40 m. The working frequencies of the dual-frequency electrical instrument are 4 Hz and 4/13 Hz, where the supply current is maintained above 800 mA. The obtained data are completely devoid of human electromagnetic interference in the measurement area, meaning that the data are reliable.

Within the measurement area, the complete 3D electrical method was employed for exploration, where the exploration area was divided into 11 × 11 grids. The lengths of the measurement lines in the X direction exceeded twice the predicted width of the exploration target. Hence, a total of 121 complete 3D electrical measurement points and power supply points were calculated using Equation 5, 6, and the number of electrical data acquisitions was 14,520.

$$M = P = m \times n. \tag{5}$$

Here, *M* and *P* are the numbers of measurement points and power supply points, respectively; *m* and *n* are the number of grids of measurement lines in the X and Y directions, respectively.

$$D = m \times n \times (m \times n - 1), \tag{6}$$

where *D* is the amount of data collected.

# 4 Effect analysis

## 4.1 Effect analysis of the one-shaped 3D electrical method

The 3D electrical exploration cross-section and contour map of the measurement area are shown in Figure 4. It can be observed that the southern part of the measurement area exhibits an overall low-resistivity anomaly in a "funnel" shape, suggesting the presence of a near east–west-trending fault or fracture zone inclined to the south. The 3D electrical exploration cross-section and contour map of the measurement area as viewed from the east are shown in Figure 5. It can be inferred that the low-resistivity anomaly between the measurement points −100 and 0, with point 0 as the boundary, is indicative of a near east–west-trending fault or fracture zone. The section from 0 to 70 mainly exhibits high resistivity, which is presumed to represent relatively intact volcanic rocks. Between measurement points 70 and 100, there is a trend of low-resistivity anomalies presumed to be caused by the presence of a fracture zone or karst caves in the measurement area.

The results of the 3D electrical exploration section and isosurface from the perspective of the north of the survey area are shown in Figure 6. It is seen that the resistivity trend is generally nearly east–west, indicating relatively complete volcanic rocks and a near east–west fracture zone. The 3D electrical exploration section and isosurface results of the survey area viewed from the west are shown in Figure 7; here, the shallow high-resistance body is

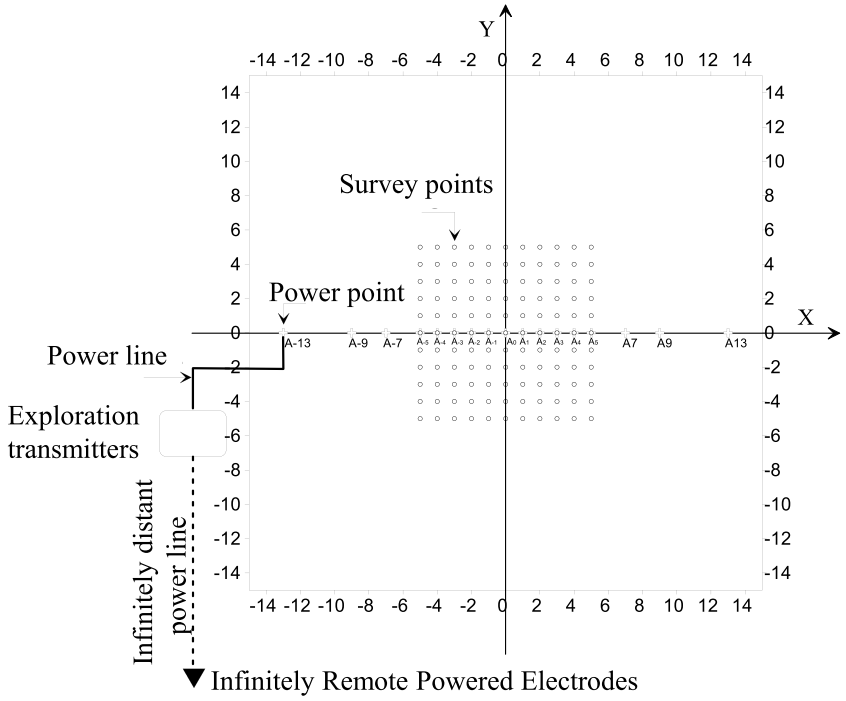


FIGURE 2
Schematic illustration of the survey field.


FIGURE 3
Layout of the exploration survey lines.

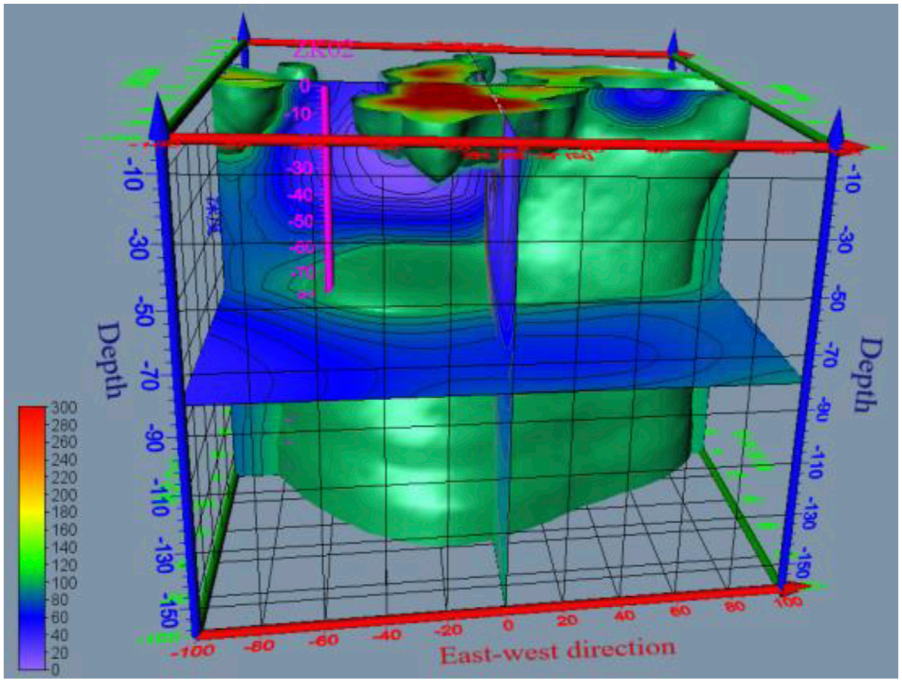


FIGURE 4
Three-dimensional view of the electrical exploration section and isosurface results map of the detection area (viewed from the south).

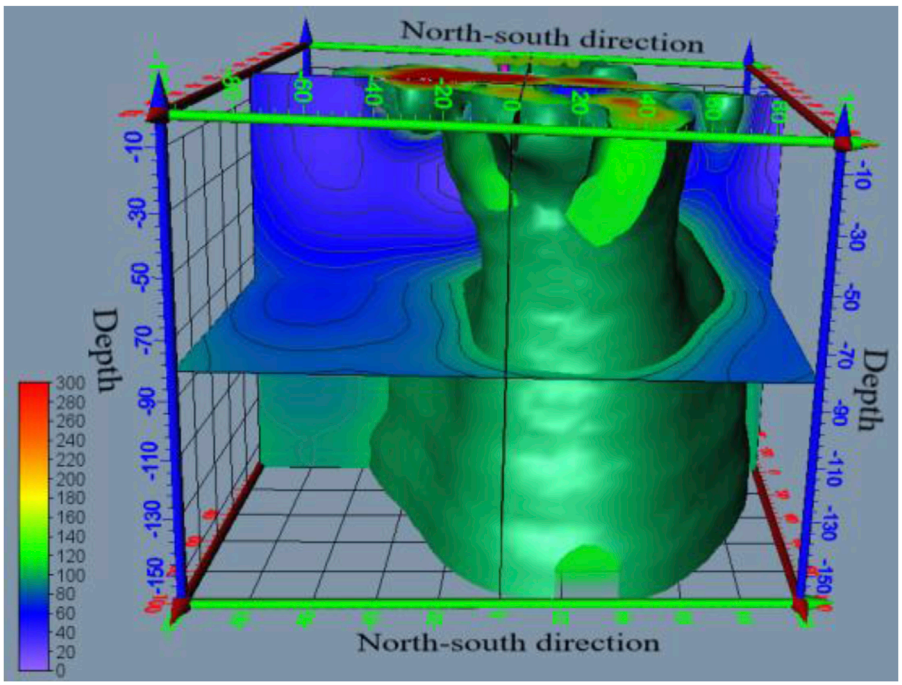


FIGURE 5
Three-dimensional view of the electrical exploration section and isosurface results map of the detection area (viewed from the east).

inferred to be the influence of the cement floor of the basketball court. There is a relatively thick low-resistance anomaly underneath the high-resistance body, which is speculated to be the response of the near north–south faults, fracture zones, or karst caves in the west of the survey area. The southwest corner generally shows a low-resistance anomaly from shallow to deep, and it is speculated

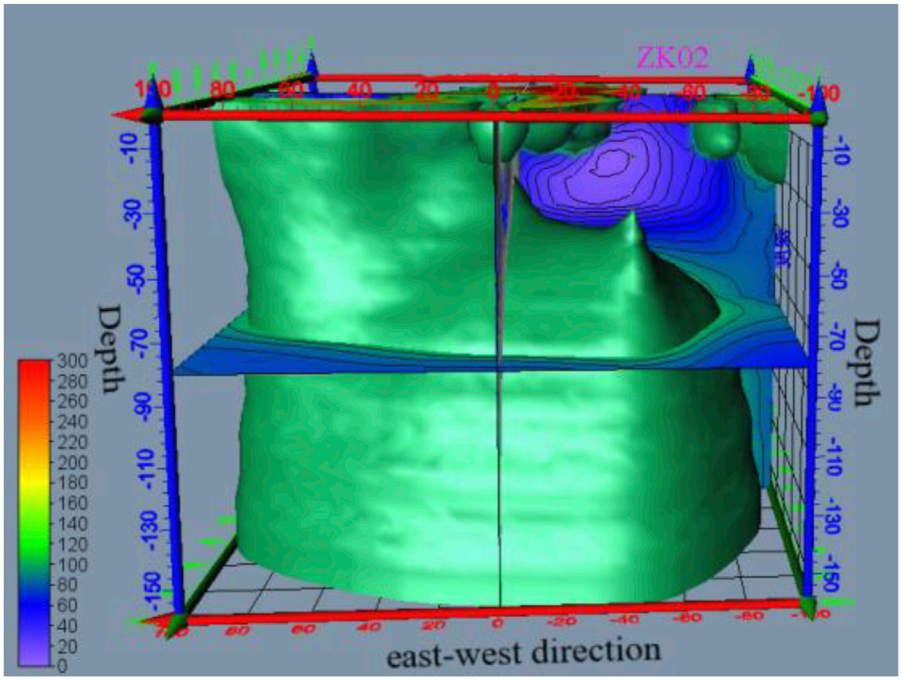


FIGURE 6
Three-dimensional view of the electrical exploration section and isosurface results map of the detection area (viewed from the north).

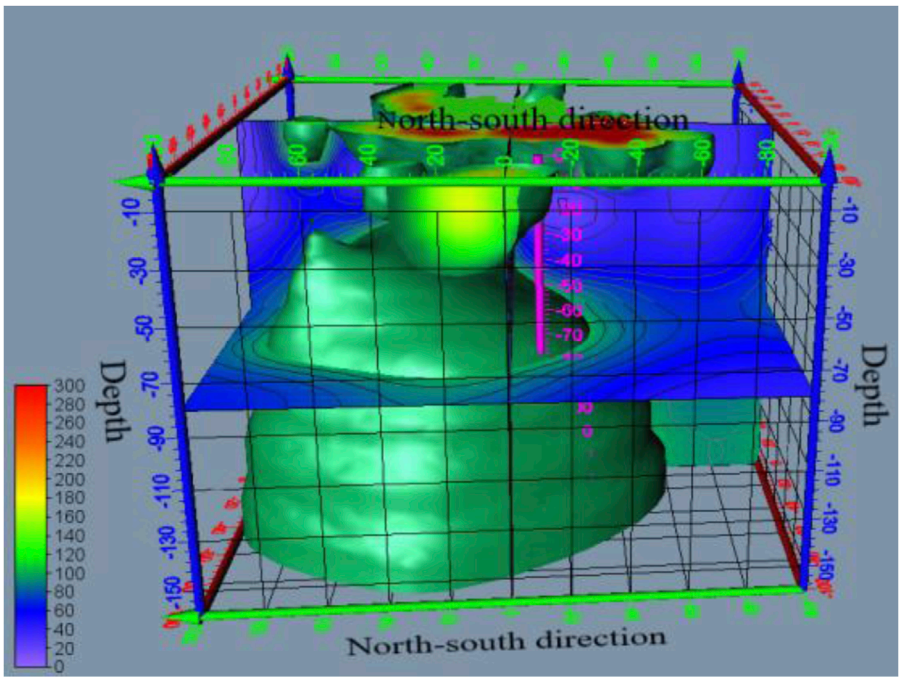


FIGURE 7
Three-dimensional view of the electrical exploration section and isosurface results map of the detection area (viewed from the west).

that this part is the intersection of the north–south-trending fault or fracture zone in the west with the nearly east–west-trending fault or fracture zone in the south.

From the electrical exploration results map of the measurement area (Figure 8), it is seen that three faults or fracture zones are developed within this area. The overall trend in the

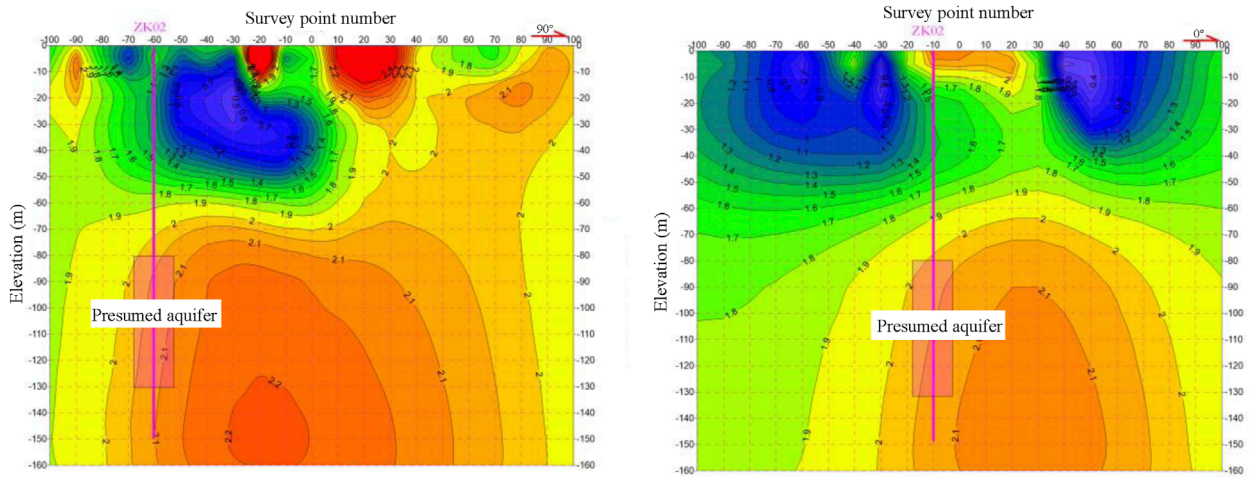


FIGURE 8
Three-dimensional electrical prospecting resistivity inversion result diagram of one-shaped layout.

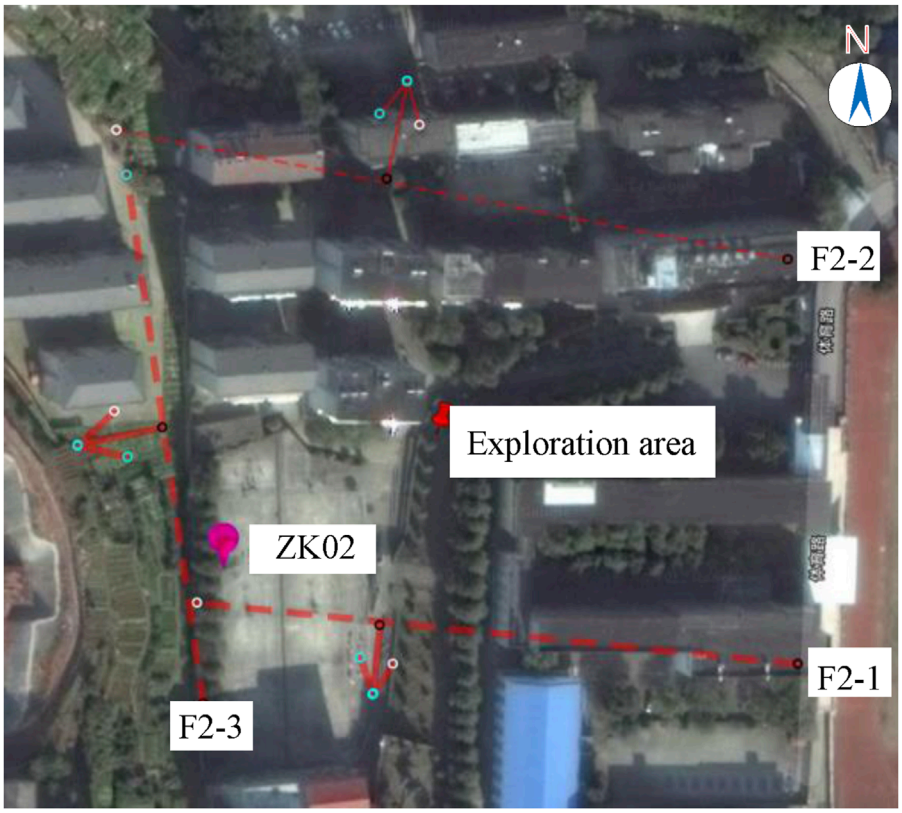


FIGURE 9
Three-dimensional electrical exploration plane results of the survey area.

southern area indicates a low-resistivity anomaly from shallow to deep, implying the existence of a fault or fracture zone (referred to as F2-1); the orientation of this is nearly east–west, with a southward dip at a steep angle, suggesting a development depth of greater than 200 m. The overall trend in the northern area indicates a high-resistivity anomaly from shallow to deep, implying that the thickness

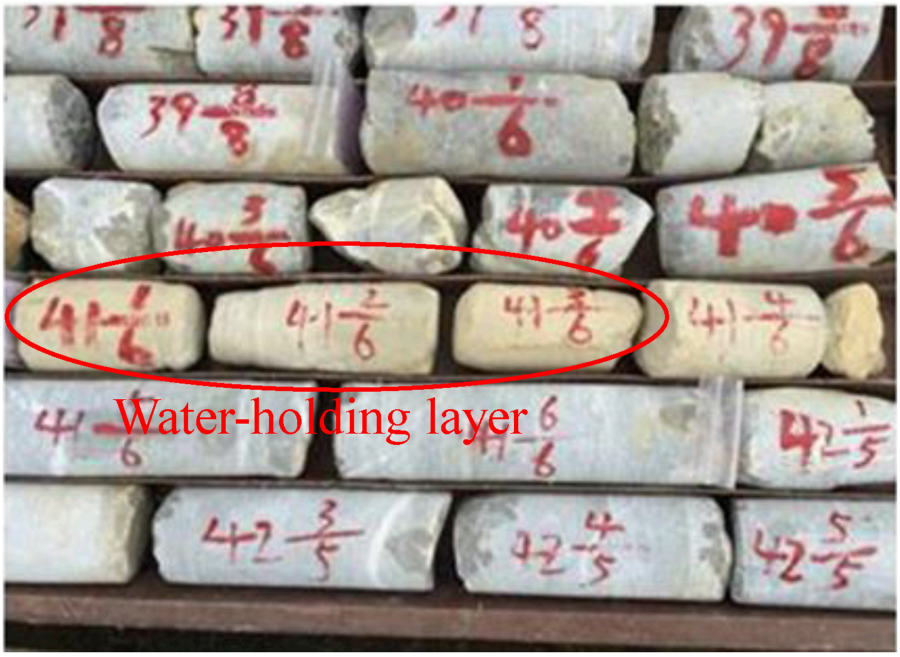


FIGURE 10
Resistivity inversion maps obtained with the conventional 3D electrical method.

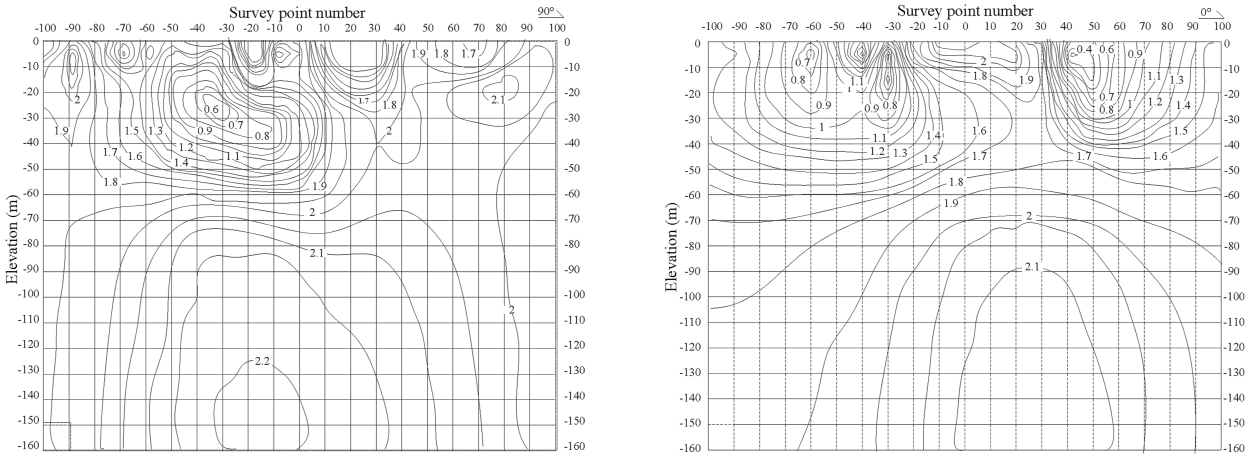


FIGURE 11
Drill-hole coring diagram.

of the Quaternary and highly weathered layers decreases in the north as this fracture zone is situated at the boundary of the measurement area (referred to as F2-2).

The eastern part of the survey area exhibits generally higher resistivity, suggesting that the Quaternary and strongly weathered layers in this region are relatively thin. In contrast, the shallow resistivity in the western part is generally lower, indicating that the Quaternary and strongly weathered layers in the west are thicker than those in the east. The western area is characterized by faults, fracture zones, or caverns, where these structures are typically inclined to the west. They exhibit a gentle angle in the shallow sections and steepen at greater depths (designated as F2-3), as illustrated in Figure 9. The depth of the development exceeds 200 m, leading to the inference that this structure serves as a primary water-controlling feature.

## 4.2 Conventional 3D electrical application analysis

The inversion results of the complete 3D electrical exploration resistivity for the survey area are illustrated in Figure 10. A

comparative analysis reveals that the resistivity variations obtained from both methods are similar in this area. This implies that the one-shaped layout of the 3D electrical method exhibits comparable accuracy to that of the complete 3D electrical method. However, the complete 3D electrical method requires 121 measurement points and 121 power supply points, resulting in a total of 14,520 electrical data collection points. In contrast, the application of the one-shaped layout with the 3D electrical method allows a reduction of up to 85.9% in terms of both the number of power supply points and volume of electrical data collected, which is more efficient for exploration compared to the conventional 3D electrical method.

### 4.3 Setting and verification of drilling

Based on the results obtained with the 1D and 3D electrical methods, three faults or fractures were identified in the survey area. The fissures developed in the upper bedrock create channels to facilitate the infiltration and replenishment of surface water. Furthermore, the gradually increasing resistivity at greater depth indicates the limited development of deep fractures within the fracture zone, which acts as a barrier to water and creates conditions favorable for groundwater accumulation. Consequently, a drilling hole is planned at ZK02 to target the aquifers beneath the Quaternary and highly weathered layer, primarily at depths below 80 m, as illustrated in Figure 11. These plans align with the results obtained from the aforementioned 3D electrical method.

## 5 Conclusion

The 3D electrical method is a key technique for groundwater exploration as it can effectively detect groundwater channels. In this paper, a new one-shaped layout is proposed for exploration based on the 3D electrical method, and its validity is assessed through practical engineering application to provide a reliable basis for the development and utilization of water resources in areas with complex topographical and geomorphological conditions. The specific conclusions of the present study are as follows:

(1) A new one-shaped layout model for the 3D electrical method is proposed. Initially, the X and Y directions of the electrical exploration are determined using the primary orientation of the geological anomalies in the exploration area. Then, the electrical grid parameters are established based on the measurement lengths in the X and Y directions as well as spacing between the measurement points in the exploration area. Finally, the coordinates of all power supply grids and their actual relative coordinates are calculated by arranging the power supply points in a one-shaped layout.

(2) Based on a groundwater exploration project in an urban area of Hunan Province, the feasibility of the proposed model layout was verified based on the results of the complete 3D electrical method and drilling. The reduction in the number of power supply points and data collection volume with the one-shaped 3D electrical method was 85.9% compared to the complete 3D electrical method. This indicates that the proposed model significantly improves exploration efficiency and produces excellent results compared to the traditional 3D electrical method.

(3) The new model offers considerable flexibility by allowing the selection of appropriate measurement line arrangements and point spacing based on different geological and geomorphological features of the survey area to accommodate various exploration zones effectively.

## Data availability statement

The raw data supporting the conclusions of this article will be made available by the authors without undue reservation.

## Author contributions

XW: conceptualization, methodology, and writing – original draft. MY: conceptualization, data curation, writing – original draft, and writing – review and editing. YZ: data curation, software, and writing – original draft. JL: data curation and writing – review and editing. HJ: data curation and writing – original draft.

## Funding

The author(s) declare that financial support was received for the research and/or publication of this article. The research was supported by the Key R&D project of Hunan Province (no. 2024AQ2044), Natural Science Foundation Project of Hunan Province (no. 2024JJ6282), and Major Projects of Water Conservancy Science and Technology in Hunan Province (nos. XSKJ2023059-02, XSKJ2024064-2, XSKJ2024064-10, XSKJ2024064-9, and XSKJ2024064-6).

## Conflict of interest

The authors declare that the research was conducted in the absence of any commercial or financial relationships that could be construed as a potential conflict of interest.

## Generative AI statement

The authors declare that no Generative AI was used in the creation of this manuscript.

## Publisher's note

# References

Adamson, J., LaVanchy, T., Stone, B., Clark, J., and Taylor, M. (2021). Geological and hydrogeological assessment of the Brito Formation: Municipio de Tola, Nicaragua. *Hydrogeol. J.* 29 (6), 2285–2304. doi:10.1007/s10040-021-02360-w

Asaue, H., Koike, K., Yoshinaga, T., Tada-nori, G., and Yoshida, H. (2021). Development and application of a variable-frequency-based electric sounding system for increasing the accuracy of aquifer detection. *Nat. Resour. Res.* 30 (4), 3017–3034. doi:10.1007/s11053-020-09791-4

Bian, C., Lü, G., Zhang, H., Liu, J., Feng, C., Chen, T., et al. (2024). Hydrochemical characteristics and variation in karst groundwater in the Baiquan spring area of Xingtai over the last 30 years. *Huan Jing Ke Xue* 45 (9), 5277–5289. doi:10.13227/j.hjkx.202309208

Cardarelli, E., Donno, D., Uliveti, I., and Scatigno, C. (2018). Three-dimensional reconstruction of a masonry building through electrical and seismic tomography validated by biological analyses. *Near Surf. Geophys* 16 (1), 53–65. doi:10.3997/1873-0604.2017040

Chirindja, F., Dahlin, T., Juizo, D., and Steinbruch, F. (2016). Reconstructing the formation of a costal aquifer in Nampula Province, Mozambique,from ERT and IP methods for water prospection. *Environ. Earth Sci.* 76 (1), 36. doi:10.1007/s12665-016-6364-0

Dai, J., Wei, Z., Pan, Z., Yin, R., Wu, Y., and Guan, Z. (2024). Research on environmental geological problems caused by water and mud inrush in tunnels and long-term drainage: taking Chaoyang tunnel of Guinan high-speed railway as an example. *Carbonate Evaporite* 39 (4), 115. doi:10.1007/s13146-024-01036-2

Gong, C., Dai, J., Wan, Z., Zeng, H., and Zhang, H. (2024). Simulation of nitrate nitrogen concentrations and DOM characteristics in groundwater from southwest China's karst wetlands using an improved GMS model. *Environ. Monit. Assess.* 197 (1), 44. doi:10.1007/s10661-024-13473-6

Gong, S., Yang, Y., Lin, P., Wu, W., Zheng, C., Shi, F., et al. (2019). Three-dimensional electrical exploration methods for the mapping of polymetallic targets in Gansu Province, China. *Geophys Prrospec* 67 (7), 1929–1947. doi:10.1111/1365-2478.12787

Han, Y., Wang, Y., Tan, C., and Du, L. (2023). Research and application of 3D high density electrical method. *J. Phys. Conf. Ser.* 2651 (1), 012091. doi:10.1088/1742-6596/2651/1/012091

Huang, W., Sui, L., Wang, Y., Zhang, C., Jiang, D., Cai, X., et al. (2023). Study of the mining and aquifer interactions in complex geological conditions and its management. *Sci. Rep.* 13 (1), 9462. doi:10.1038/s41598-023-34947-6

Kevin, T., Abdurrahman, W., Nugroho, S., and Mariyanto, M. (2021). Analytical comparison of electrode configuration on 2D geoelectric method for identification of water seepage in the lake body. *J. Phys. Conf. Ser.* 1825 (1), 012019. doi:10.1088/1742-6596/1825/1/012019

Kouadio, K., Xu, Y., Liu, C. ; M., and Boukhalfa, Z. (2020). Two-dimensional inversion of CSAMT data and three-dimensional geological mapping for groundwater exploration in Tongkeng Area, Hunan Province, China. *J. Appl. Geophys* 183, 104204. doi:10.1016/j.jappgeo.2020.104204

Lu, C., Cheng, W., Yin, H., Li, S., Zhang, Y., Dong, F., et al. (2024). Study on inverse geochemical modeling of hydrochemical characteristics and genesis of groundwater system in coal mine area-a case study of Longwanggou Coal Mine in Ordos Basin. *Environ. Sci. Pollut. R.* 31 (11), 16583–16600. doi:10.1007/s11356-024-32153-z

Ou, Y., Zhang, P., Liu, C., Tan, L., and Sun, B. (2020). Comparative study of 3D joint inversion based on multi-section resistivity data. *Aip Adv.* 10 (8), 085102. doi:10.1063/5.0015601

Permanasari, P., Akbar, F., Handayani, G., and Hendarajaya, L. (2019). Determination of the type of soil using 2D geoelectric method and laboratory analysis for landslide area cililin west java. *J. Phys. Conf. Ser.* 1127 (1), 012042. doi:10.1088/1742-6596/1127/1/012042

Pilla, G., and Torrese, P. (2022). Hydrochemical-geophysical study of saline paleo-water contamination in alluvial aquifers. *Hydrogeol. J.* 30 (2), 511–532. doi:10.1007/s10040-021-02446-5

Reza, A., and Singh, S. (2023). Delineation of optimal locations for artificial groundwater recharge utilizing MIF and GIS in a semi-arid area. *Environ. Earth Sci.* 83 (1), 33. doi:10.1007/s12665-023-11338-8

Rupesh, P., and Sharma, S. (2021). High-resolution quasi-3D electric resistivity tomography for deciphering groundwater potential zones in lateritic terrain. *Nat. Resour. Res.* 30 (5), 1–15. doi:10.1007/S11053-021-09888-4

Wu, Z., Wang, X., Li, J., Cui, J., and Zhang, B. (2024). Hydrochemical constraints on the flowing paths of groundwater in limestone reservoirs beneath the Pingdingshan coalfield in north China. *Acta Geol. Sin-Engl* 98 (6), 1615–1636. doi:10.1111/1755-6724.15255

Xiong, Z., Tang, X., Li, D., and Zhao, C. (2019). Numerical simulation of 3D borehole-to-surface electrical method. *Acta Geol. Sin-Engl* 93 (s1), 340–341. doi:10.1111/1755-6724.14125

Yuan, K., Liu, H., Yao, Y., and Chen, X. (2024). Research on precise detection of landfill based on high density resistivity method. *J. Phys. Conf. Se* 2895 (1), 012021. doi:10.1088/1742-6596/2895/1/012021

Zhao, J., Wang, J., Cui, B., Zhai, B., Hu, C., Liu, Y., et al. (2024). Mixed irrigation affects the composition and diversity of the soil bacterial community. *Open Geeosci* 16 (1), 20220659. doi:10.1515/geo-2022-0659

frontiers | Frontiers in Earth Science

TYPE Methods
PUBLISHED 24 April 2025
DOI 10.3389/feart.2025.1578017



OPEN ACCESS

EDITED BY
Pengfei Liu,
CCCC Second Harbor Engineering Co., Ltd., China

REVIEWED BY
Yong Huang,
Hohai University, China
Wenbing Zhang,
Shanghai Maritime University, China

*CORRESPONDENCE
Yuanli Yang,
836460069@qq.com

RECEIVED 17 February 2025
ACCEPTED 10 April 2025
PUBLISHED 24 April 2025

CITATION
Yao J, Yang Y, Yang M, Shen Z, He X and Chen X (2025) Research on the diagnosis of leakage hazards in a karst reservoir based on integrated electrical method and geological method.
*Front. Earth Sci.* 13:1578017.
doi: 10.3389/feart.2025.1578017



# Research on the diagnosis of leakage hazards in a karst reservoir based on integrated electrical method and geological method

Jihua Yao[1,2], Yuanli Yang[1,2]*, Mingwei Yang[1,2], Zhigao Shen[1,2], Xiangjian He[1,2] and Xiang Chen[1,2]

[1]Hunan Institute of Water Resources and Hydropower Research, Changsha, China, [2]Hunan Dam Safety and Disease Prevention Engineering Technology Research Center, Changsha, China

**Objective:** Due to the dual influence of karst features in the dam site area and the unique characteristics of the dam soil, leakage issues in the dam body and dam foundation of a certain reservoir have persisted, limiting the effectiveness of the reservoir. Despite multiple attempts at anti-leakage reinforcement, the leakage problems have not been completely resolved and have worsened in recent years. The detection and identification of karst reservoir leakage should be conducted more accurately and simply.

**Methods:** This paper integrates the use of High-density resistivity method and Frequency-Division and Electrical Resistivity Tomography method for the detection and identification of leakage in the karst reservoir, complemented by geological surveys and geological drilling for verification.

**Results:** The leakage areas at the left and right ends of the dam base are caused by bypass seepage and contact leakage at the dam abutments. The perpetual water inflow in the sump wells at the middle and toe of the dam is mainly due to karst leakage in the dam foundation, leakage from the surface alluvial and depositional layers of the dam foundation, and contact leakage between the dam body and the dam foundation. Water seepage from within the culvert pipe body and its contact leakage with the dam body are the primary causes of scattered seepage on the fourth-level dam slope at the top of the power generation and irrigation culvert.

**Conclusion:** Integrated electrical method and geological methods can accurately diagnose the leakage risks in karst reservoirs. This comprehensive detection method is easy to operate, highly accurate, and widely applicable for identifying leakage risks in similar earth-rock dam karst reservoirs.

KEYWORDS

**high-density resistivity method, frequency-division and electrical resistivity tomography method, geological method, karst reservoir, karst leakage, leakage**

# 1 Introduction

The benefits of karst reservoirs are often not effectively utilized due to issues such as dam body leakage, dam foundation leakage, bypass seepage at dam abutments, or reservoir leakage, resulting in insufficient water retention throughout the year during operation. Among them, dam foundation seepages, dam abutment seepages and reservoir area seepages are mostly caused by karst seepages, while dam body seepages are mainly due to issues such as poor local impermeability of the filled soil or quality defects within the dam. These seepage risks can cause significant damage to dams, including infiltration, slope instability, and breaches that result in catastrophic disasters. The comprehensive geophysical exploration method can effectively detect the leakage risks in karst reservoirs and carry out targeted anti-leakage reinforcement measures, ensuring the safe operation of the dam.

For this purpose, many scholars have conducted theoretical and practical research on the identification and diagnosis of leakage problems in karst reservoirs based on single geophysical exploration methods (Jiang et al., 2020; Zhang et al., 2018) or comprehensive geophysical exploration methods (Peng, 2016; Yao et al., 2014). The main research objects include leakage sources in the dam site area (He, 2000; Jian and Sun, 2020; Yao et al., 2020), leakage channels within the dam body (Zhang et al., 2023; Zhao et al., 2022; Cui et al., 2024), quality defects (Wang et al., 2024; Yao et al., 2023; Liu et al., 2023), and leakage outlets (Bukowska-Belniak and Lesniak, 2017; Xu et al., 2020). The development and application of comprehensive geophysical exploration techniques for detecting hidden dangers in water conservancy and hydropower engineering are analyzed and summarized (Xu et al., 2022; Liu et al., 2019). Karst leakage issues in some karst reservoirs have been successfully resolved during construction or operation phases.

However, after the construction of a reservoir dam in a karst area, the identification and diagnosis of its leakage hazards not only require considering the uncertainty, diversity, and complexity of karst development in the dam site area (Zhen, 2018), but also necessitate addressing issues such as quality defects within the dam body, as well as leakage at the contacts between the dam body and its internal structures, and between the dam body and the dam foundation. These factors render the diagnosis of leakage hazards particularly challenging (Ren et al., 2014; Liu, 2022). Therefore, it is highly necessary and urgent to explore an effective, accurate, and operable multi-source fusion identification and diagnosis method for leakage hazards in karst reservoirs.

The occurrence of leakage often results in changes and anomalies in the physical characteristics of the dam (Sun et al., 2024). Due to the inherent limitations of a single geophysical exploration method, the revealed physical characteristics of the site are often one-sidedness and ambiguity, which leading to deviations or errors in the spatial location information of leakage hazards in reservoirs. The integrated geophysical exploration method can obtain multiple physical property detection results for karst reservoirs, it can reduce ambiguity, eliminate the false and retain the true, and serve as a mutual complement. This allows for a more accurate inversion of leakage hazards in karst reservoirs.

This paper comprehensively employs High-density resistivity method and Frequency-Division and Electrical Resistivity Tomography method (FD-ERT method), complemented by geological surveys and geological drilling results for verification, to diagnose and expose the developmental characteristics and causes of these leakage hazards. It is hoped to provide practical application experience for similar projects.

# 2 Methods

## 2.1 High-density resistivity method

High-density resistivity method is an array-based resistivity measurement method that combines electrical exploration techniques with computer digital technology. It integrates the characteristics of both electrical profiling and electrical sounding, enabling the revelation of lateral and vertical electrical variations in the rock and soil mass within a certain depth range underground (Peng et al., 2024). When leakage channels, voids, defects, or significant differences from the surrounding area exist in the buried rock and soil mass, the resistivity in these areas will exhibit obvious anomalies, with results significantly higher or lower than normal. Therefore, this method can be used to detect the approximate locations of leakage channels or defects in the rock and soil mass (Zhang et al., 2024; Li et al., 2024).

## 2.2 FD-ERT method

The operational principle diagram of instrument of FD-ERT method is shown in Figure 1. Firstly, instrument of FD-ERT method is set up to arrange the receiving electrodes in an array. An electrical transmitter capable of simultaneously emitting three independent current signals of different frequencies is used to send three current signals of different frequencies at one time. Three power supply points A1, A2, A3, and three infinite power supply electrodes B1, B2, B3 are arranged. Then, the electrical receiver collects the total electric field signals from each adjacent receiving electrode M and N, and separates these signals. By inputting the three-dimensional coordinates of each electrode and the current values of different frequencies, the apparent resistivity values can be calculated according to Equation 1. During the electrode movement, by shifting the three power supply electrodes A1, A2, and A3 collectively to the right, apparent resistivity data at different depths can be obtained, ultimately forming a measurement profile (Liu, 2022).

FFD-ERT method primarily employs a three-pole array, utilizing copper electrodes with a diameter of 50 mm, a length of 300 mm, and spacing ranging from 0.5 to 1.0 m. The three distinct current signal frequencies are 10Hz, 4Hz, and 1Hz, respectively. The signal separation algorithm adopts the extraction of odd harmonic signals from the received signals, and employs the difference quotient formula to obtain electric field information of the same frequency at different measurement points.

According to the formula for calculating apparent resistivity in the direct current resistivity method:

$$\rho_{si} = K_i \frac{\Delta U_i}{I_i} (i = 1, 2, 3) \quad (1)$$

Where: $\Delta U_i$ are the potential values for each frequency after separation, with units of V; $I_i$ are the current values for each

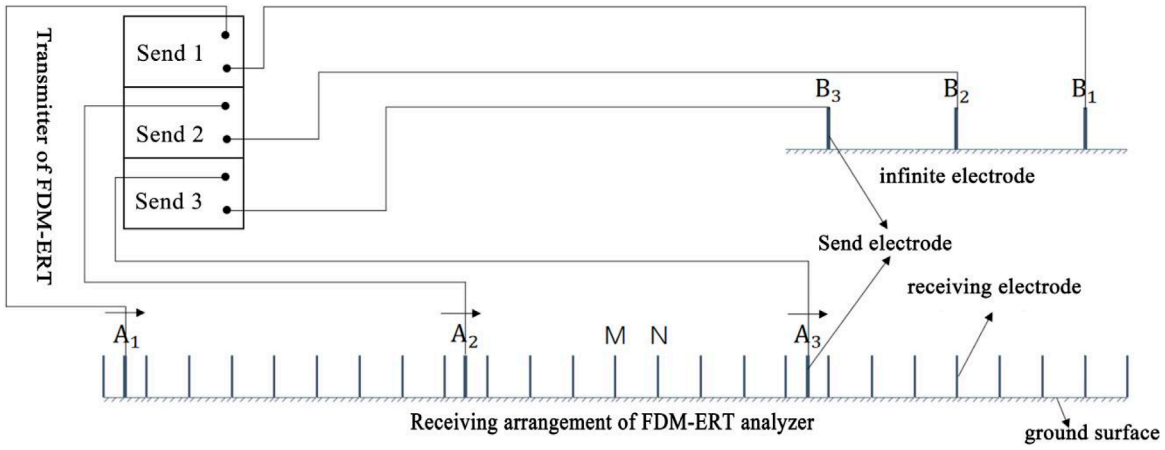


FIGURE 1
Operational principle diagram of FD-ERT method.

frequency, with units of A; $\rho_{si}$ are the apparent resistivity values for each frequency after separation, with units of Ω.m.

It is evident that simultaneous power supply from multiple points in the frequency-division electrical method can significantly enhance the efficiency and accuracy of identifying and diagnosing leakage issues in dam bodies and foundations. Based on the significant differences in resistivity among dam fill, leakage pathways, and the rock masses of dam foundations and abutments, the interpretation of leakage issues within the dam body, foundation, and abutments can be achieved. Generally, relatively low-resistivity areas indicate the presence of leakage issues.

## 2.3 Geological method

Geological methods employ techniques such as geological surveys, geological drilling, and water injection tests within boreholes to obtain information about the landform characteristics, stratigraphic lithology, geological structure, hydrogeological conditions, dam stability, and current state of leakage under the dam within the project area. It also involves drilling to ascertain the composition, compactness, and permeability of the dam fill soil. Additionally, laboratory soil tests are conducted to obtain the physical parameters of the rock and soil mass in the dam site area, which are then used to analyze the locations of leakage inlets, leakage pathways, and leakage exit zones in the dam.

Geological surveys are guided by geology and related sciences. Through observation and research, they investigate information such as leakage, cracking, deformation and landslides of the exposed surface, karst development, and hydrogeological conditions within the dam site area.

Geological drilling involves using drilling rods, drilling tools, and other equipment to bore vertically downwards from the dam crest into the dam body and foundation. This process aims to obtain core samples of the geotechnical materials (soil and rock) within the dam body and foundation, as well as to gather information about their properties, structure, composition, and water content.

The water injection test within boreholes refers to a test where water is injected into boreholes drilled in the dam. By regularly measuring relevant parameters such as the injection rate, time, and water level, the permeability coefficients of the dam body, the contact zone between the dam body and foundation, and the rock mass of the dam foundation can be determined.

# 3 Engineering applications and experimental scheme

## 3.1 Project overview

A reservoir is located upstream of the Songbai River, a tributary of the Youshui River, which is a first-tier tributary of the Yuanjiang River. It is a karst reservoir with a dam made of homogeneous red clay. The dam crest elevation is 741.64 m, the normal water level is 738.08 m, the maximum dam height is 31.64 m, and the dam crest axis is 434 m long. It is a key medium-sized water conservancy project with comprehensive benefits, primarily focusing on flood control and irrigation, while also accommodating power generation, water supply, aquaculture, and other functions. The bedrock in the dam area is composed of dolomitic limestone belonging to the middle-upper Loushanguan Group of the Cambrian System (∈2 + 3Ls), Karstification is extremely developed, with solution channels, solution holes, and caves visible on the surface, accompanied by karst pinnacles. The dam fill soil is red clay, which exhibits characteristics such as swelling upon water absorption, shrinking upon water loss, high liquid limit and plastic index, and difficulty in controlling compaction. Numerous desiccation cracks have been found on the downstream dam slope, some of which extend approximately 30–80 cm into the dam. Since its completion and operation, the reservoir has been plagued by issues such as dam body leakage, dam foundation leakage, and bypass seepage at the dam abutments. Despite multiple risk removal and reinforcement efforts, serious leakage problems still persist, hindering the full utilization of the reservoir's benefits. The plan view and profile view of the dam are detailed in Figures 2, 3.

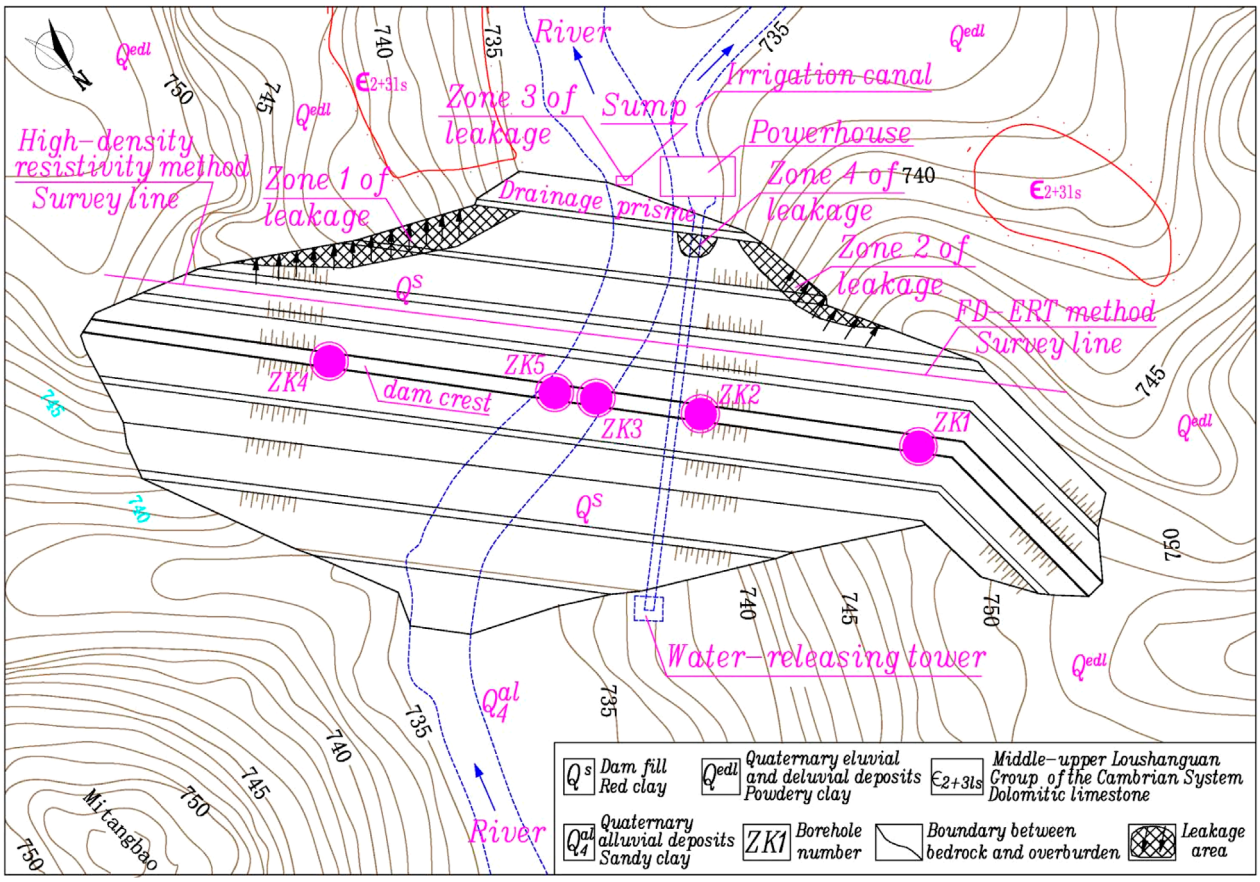


FIGURE 2
Layout diagram of survey lines and location map of leakage risks in the dam.

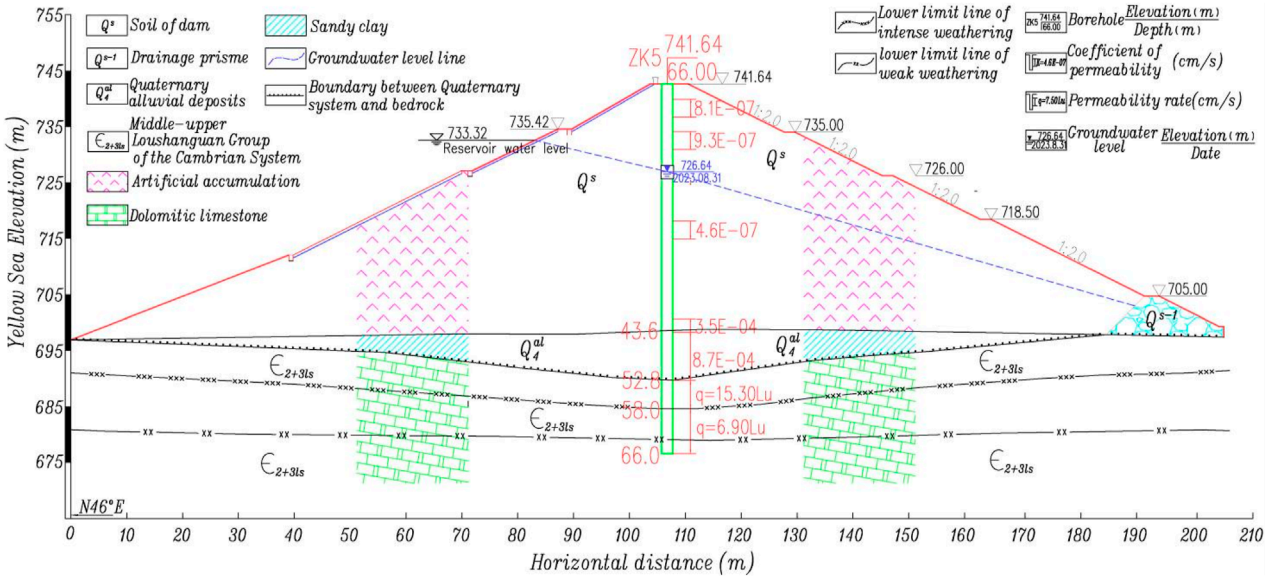


FIGURE 3
Longitudinal section at the centerline of the dam body.

On 18 August 2023, when the reservoir water level was at 733.32 m, we conducted an exhaustive geological survey and inspection of the leakage risk indications in the dam site area. Field geological investigations revealed that there was abutment seepage around both the left and right dam abutments below elevations of approximately 728.0 m and 724.0 m, respectively. The total seepage volumes amounted to approximately 0.5 L/s and 0.3 L/s, respectively. Additionally, near the areas of concentrated abutment seepage, there were large areas of dispersed seepage with multiple concentrated leakage points on the third and fourth-grade downstream slopes at both ends of the dam body. The dispersed seepage areas measured approximately 30 $m^2$ and 18 $m^2$, with total seepage volumes of 0.25 L/s and 0.1 L/s, designated as Leakage Area 1 and Leakage Area 2, respectively. Meanwhile, there was a sump well at the middle of the dam toe from which water flowed continuously throughout the year, with a seepage rate of approximately 0.8 L/s, labeled as Leakage Area 3. There was also a dispersed wet area measuring approximately 12 $m^2$ on the fourth-grade downstream slope at the top of the power conveyance culvert outlet section, though no concentrated leakage points were observed, designated as Leakage Area 4. Notably, the leakage volumes at these leakage risk points exhibited a high correlation with the reservoir water level, disappearing partially during low water levels but significantly increasing in terms of both dispersed seepage area and concentrated leakage volumes during high water levels, posing a serious threat to dam safety.

Therefore, there are issues such as dam body leakage, dam foundation leakage, and bypass leakage at the dam abutments within the dam site area. Traditional geological methods struggle to interpret information about leakage sources, leakage pathways, and leakage outlets in the dam site area, making it difficult to implement targeted anti-leakage reinforcement measures for the leakage hazards. However, the integrated geophysical exploration method based on High-density resistivity method and frequency-division electrical method can effectively and accurately diagnose the spatial information of potential leakage hazards. Coupled with field geological surveys and geological drilling results for verification, it can ascertain the developmental characteristics and causes of various leakage hazards.

## 3.2 Geophysical and lithological characteristics of the engineering projects

To obtain the electrical characteristics of the rock and soil in the dam site area, undisturbed samples were taken by drilling cores from the dam body fill, dam foundation, and dam abutment rock masses. Resistivity measurements were conducted on the rock and soil masses in the dam site area. The sampling locations for the dam body soil cores were evenly distributed from the dam top to the dam bottom and from the left bank to the right bank. Similarly, the dam foundation and dam abutment rock cores were evenly distributed from highly weathered to slightly weathered materials. The geophysical exploration parameters are shown in Table 1.

The electrical characteristics of the rock and soil masses in the dam site area are as follows: the dolomitic limestone of the middle-upper Loushanguan Group of the Cambrian System (∈2 + 3) exhibits medium to high resistivity, with an average resistivity of 803.7 Ω m; the red clay of the dam body exhibits low resistivity, with an average resistivity of 47.2 Ω m. It can be seen that there are significant electrical differences between different rock and soil masses, providing a prerequisite for electrical exploration.

## 3.3 Experimental scheme

A comprehensive approach was employed at the site, utilizing frequency-division electrical method, high-density resistivity method, and infrared thermography to identify the location information of leakage hazards in the dam area and analyze their causes.

(1) The equipment used in this experiment includes high-density resistivity meters and frequency-division electrical method instruments. All measurement points were laid out using high-precision RTK-GPS. Due to the lack of control points at the site, the GPS parameters adopted the China Geodetic 2000 (CGCS 2000) coordinate system, with a central meridian of 111°. The high-density resistivity meter used was manufactured by Chongqing Geological Instrument Factory, with the model number DUK-2A. For this experiment, one high-density resistivity survey line and one frequency-division electrical survey line were set up. In order to enable comparison between the results of the two measurement methods, the survey lines for both methods were arranged at the same locations, extending from the mountain at the right abutment downstream of the dam to the first-level downstream slope of the dam body, until reaching the mountain at the left abutment. The point spacing for the high-density resistivity survey line was 5 m, and for the frequency-division electrical survey line, it was 20 m. The primary objective was to detect the spatial locations of leakage hazards within the dam body, dam foundation, and both dam abutments. The details are shown in Figure 2.

(2) Based on the suspected problematic areas in the dam site zone diagnosed by the integrated electrical method, geological drilling was conducted for exposure and verification to further identify the sources of leakage in the dam body, dam foundation, and dam abutments. The drilling results were then compared, verified, and complemented with the detection results from the two electrical methods to thoroughly ascertain the causes of leakage in various seepage areas within the dam site zone.

# 4 Results and discussion

## 4.1 Results and analysis of high-density resistivity method

The detection results of the high-density resistivity survey line are shown in Figure 4.

(1) Low resistivity zones exist at measurement points 415 to 455 with elevations ranging from 730 m to 720 m, and at measurement points 455 to 515 with elevations from 725 m to 715 m. A high resistivity zone that lifts upwards is found

TABLE 1 Resistivity of rock and soil masses in the engineering area.

| Stratigraphic code | Number | Name of rock and soil mass | Range of resistivity/(Ω·m) | Average resistivity |
|---|---|---|---|---|
| $Q_4$ | 32 | Red clay | 21.6–95.4 | 47.2 |
| $\epsilon_{2+3Ls}$ | 20 | Dolomitic limestone | 392.6–1,546.5 | 803.7 |

near measurement point 525. Low resistivity zones also exist at measurement points 520 to 570 with elevations ranging from 730 m to 725 m, and at measurement points 555 to 580 with elevations from 715 m to 705 m. A high resistivity zone that lifts upwards is observed near measurement point 645. Low resistivity zones are present at measurement points 590 to 625 with elevations ranging from 720 m to 712 m, and at measurement points 630 to 675 with elevations from 723 m to 718 m. Based on pre-dam construction data, the dam between measurement points 380 and 700 was originally formed by connecting three small hilltops. Specifically, the vicinity of measurement point 470 is a low saddle on the right bank, the area near measurement point 560 is the old riverbed of Songbai River, and the vicinity of measurement point 645 is a small hill on the left side.

(2) The overall dam body exhibits low resistivity zones dominated by yellow, yellow-green, and green colors, with a resistivity approximately ranging from 30 to 150 Ω m, which is relatively consistent with the resistivity measured in the dam's soil core. However, the resistivity in the low saddle area of the right dam abutment, the old riverbed of Songbai River in the middle, and the small hill area of the left dam abutment is significantly lower. Among these, the resistivity in the small hill area of the left dam abutment is the lowest, with some local areas already appearing as blue zones. This indicates that the water content in the dam fill at these locations is significantly higher, leading to enhanced electrical conductivity. These areas may represent leakage zones within the dam, and their elevations are relatively consistent with the leakage zones at the left and right ends of the dam.

(3) From the left dam abutment to the right dam abutment, a yellow-orange low-resistivity zone with a resistivity of approximately 200–300 Ω m exists on the surface of the dolomitic limestone at the bottom of the contact surface between the dam and its foundation. This resistivity is significantly lower than the measured resistivity of dolomitic limestone cores obtained from laboratory tests. The thickness of this low-resistivity zone is approximately 3.0 m, within which the water content of the dolomitic limestone and the activity of groundwater are significantly higher than those in the deeper rock mass. Preliminary speculation suggests that karst or joint fissures may have developed within the dolomitic limestone in this area, leading to a higher water content, more active groundwater, enhanced conductivity, and lower rock resistivity at this location. However, based on the exposed rock mass and stone buds in the dam site area, the joint fissures are not well developed, but karst is extremely developed. Therefore, it can be further determined that karst development exists within the rock mass with a thickness of approximately 3.0 m at the shallow surface of the dam foundation, and there are karst leakage pathways.

(4) The deep rock mass of the dam foundation is mostly composed of high resistivity zones with orange-red and red hues, featuring a resistivity greater than 500 Ω m. This indicates that the deep rock mass of the dam foundation is well-integrated, with low water content in the rock mass. The groundwater is inactive, exhibiting weak conductivity. Karst development is minimal, and the possibility of the development of caves and underground rivers within the rock mass is extremely low.

(5) A low resistivity zone appears at an elevation of approximately 670 m within the deep part of the small hill on the left dam abutment, indicating that groundwater is relatively active at this location. This suggests the presence of a karst cave or an underground river.

## 4.2 Results and analysis of FD-ERT method

The detection results of FD-ERT method survey lines are shown in Figure 5.

(1) The diagnostic results are generally consistent with those obtained by High-density resistivity method, but the frequency-division electrical method demonstrates significantly better detection accuracy for the deep dam body, dam foundation, dam abutment rock and soil mass, and their interfaces, especially in revealing the original topography of the dam foundation. However, High-density resistivity method offers superior detection accuracy for shallow rock and soil masses compared to the frequency-division electrical method. The main reason for this is that the measuring point spacing for High-density resistivity method is 5 m, while it is 20 m for the frequency-division electrical method. Therefore, the latter has lower sensitivity to shallow features compared to the former.

(2) There is a green low-resistivity zone at measurement points 425 to 460 with an elevation of approximately 730 to 724 m, and at measurement points 445 to 510 with an elevation of approximately 726 to 714 m in the right dam section. Similarly, in the left dam section, there are low-resistivity zones at measurement points 580 to 610 with an elevation of approximately 714–724 m, and at measurement points 630 to 640 with an elevation of approximately 715–721 m. Preliminary speculation suggests that these areas have high water content in the fill soil within the dam body, resulting in strong conductivity, and may represent leakage disease zones within the dam.

(3) There are noticeable relatively low-resistivity zones in both the dam body and dam foundation at measurement points

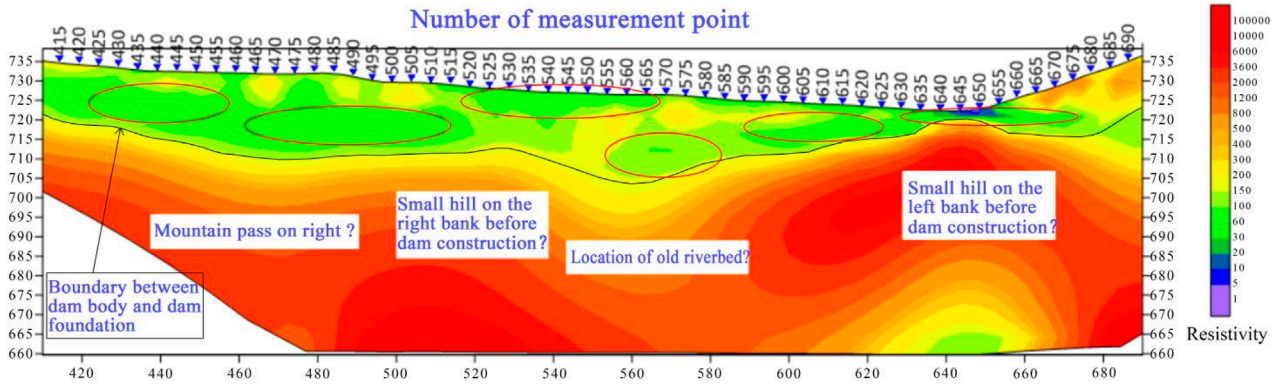


FIGURE 4
Inversion map of diagnostic results obtained by high-density resistivity method in the dam (The red circles in the diagram indicate leakage zones).

535 to 560 in the middle of the dam. At an elevation of approximately 725 to 718 m, there is a leakage disease in the dam body. Within the range of approximately 718 to 660 m in elevation, there exists an ancient low-lying corrosive gully in the dam foundation, which was an old riverbed. Before the dam was constructed, it was filled with Quaternary overburden, leaving behind permeable weak zones or pathways. These are located roughly in the same longitudinal position as the water collection well behind the dam. Preliminary speculation suggests that the continuous water inflow in the water collection well behind the dam may originate from the leakage in the dam foundation and dam body at the location of this old riverbed.

(4) Beneath the contact surface between the dam body and the dam foundation, there exists a continuous layer of yellow to orange-yellow low-resistivity zone with a thickness of approximately 3.0 m on the surface of the dam foundation rock and soil. This may be due to the development of karst features such as solution pores, caves, solution holes, or sinkholes in the dolomitic limestone at the surface of the dam foundation. The presence of karst leakage pathways results in high water content in the surface rock mass of the dam foundation, active groundwater, and enhanced conductivity.

## 4.3 Results and analysis of geological method

Based on the comprehensive analysis results of the two electrical methods, five boreholes were drilled on the dam crest, located at the right dam abutment, the top of the power generation and irrigation culvert, the old riverbed in the middle of the dam, and the left dam abutment, numbered ZK1 to ZK5 respectively (specific locations are shown in Figure 1). The objectives were to ascertain the soil composition and permeability of the dam body, the permeability of the contact zone between the dam body and the dam foundation, the permeability of the rock mass in the dam foundation, and the permeability of the contact zone between the dam body and the culvert pipe. By combining the locations and scales of Leakage Areas 1 to 4 obtained from the field geological survey, as well as the karst development of the exposed rock mass near the dam area, a comprehensive assessment of the leakage situation in the dam site area was conducted, and the causes of the leakage were analyzed.

(1) Based on the results of the geological drilling and water injection tests conducted at the site, the fill structures of the dam body revealed by ZK1, ZK3, ZK4, and ZK5 were relatively dense, with permeability coefficients all less than 1.0E-6 cm/s, indicating low permeability and good anti-seepage performance. Therefore, the possibility of leakage risks and pathways existing in the dam body (excluding the area surrounding the culvert within the dam) is relatively low. However, the permeability coefficients of the contact zones between the dam body and the dam foundation for ZK1 to ZK5 were 7.2E-4 cm/s, 2.3E-4 cm/s, 3.1E-4 cm/s, 2.8E-4 cm/s, and 8.6E-4 cm/s, respectively, all indicating moderate permeability and poor anti-seepage performance. Especially at the locations of ZK1 and ZK4, it was evident that the anti-seepage performance of the contact zones between the dam body and the dam foundation was poor, resulting in leakage at these contact zones. Additionally, the permeability coefficient of the dam body soil in the section from an elevation of 705 m–700 m at ZK2 was 4.9E-4 cm/s, indicating moderate permeability and poor anti-seepage performance. The permeability coefficients of the dam body soil in other sections were all less than 1.0E-6 cm/s, indicating low permeability and good anti-seepage performance. The elevation of the culvert floor adjacent to the left side of ZK2 was approximately 702.43 m, revealing poor fill quality and anti-seepage performance around the culvert within the dam, which resulted in leakage at the contact between the culvert and the dam body.

(2) During the investigation, the reservoir water level was recorded at 733.32 m, while the stable water levels within boreholes ZK1 to ZK5 were 727.28 m, 726.76 m, 726.62 m, 727.52 m, and 726.64 m, respectively. Combining these data with the elevations of low-resistivity zones revealed by two electrical methods, as well as the locations and elevations of leakage zones 1 to 4, it can be inferred that there is a significant gradient descent and clear connectivity among the reservoir water level,

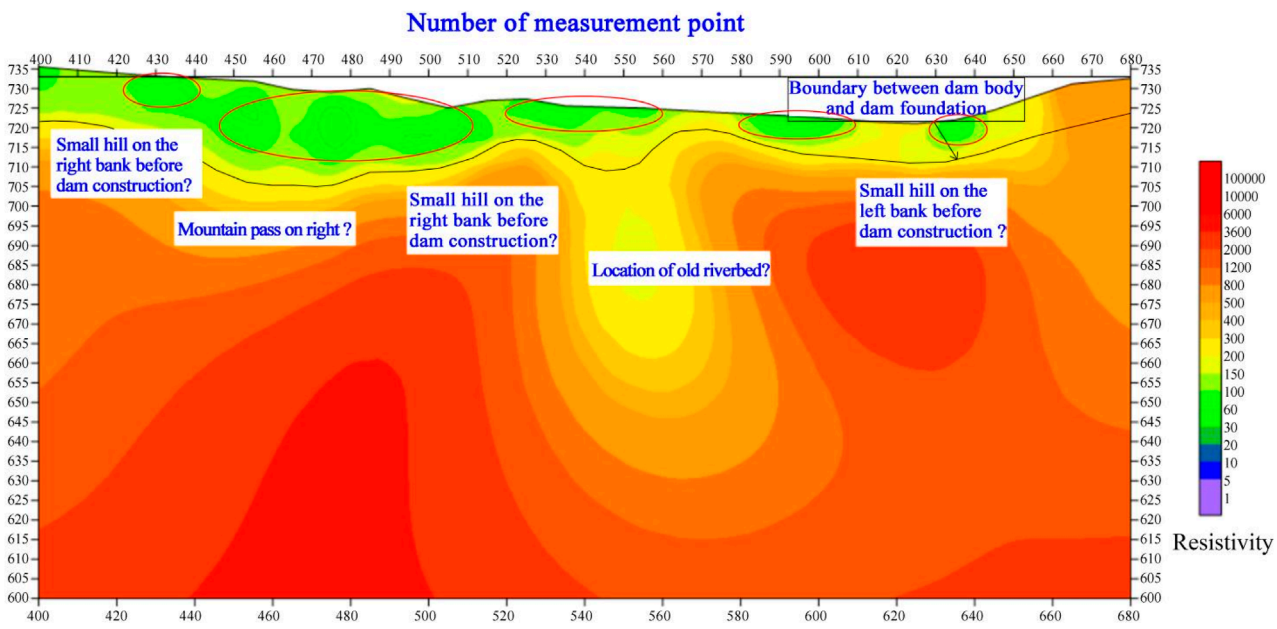


FIGURE 5
Inversion map of diagnostic results obtained by FD-ERT method in the dam (The red circles in the diagram indicate leakage zones).

stable borehole water levels, low-resistivity zone elevations from electrical profiling, and the elevations of leakage zones 1 to 4. Evidently, the detection results from the two electrical methods are in good agreement with the actual conditions.

(3) Based on the results of the field geological survey, karst development in the exposed bedrock surface at the dam site is extremely pronounced, with karst gullies, cavities, and caves visible on the surface, accompanied by stone sprouts. It can be inferred that karst development in the surface rock mass of the dam foundation and abutments is also extremely pronounced. There are many well-connected karst leakage channels within the surface rock mass, indicating potential risks of leakage in the dam foundation and abutments.

(4) The low resistivity zones revealed by the two electrical methods within the downstream dam slope and dam body align well with the locations of leakage zones 1 to 4. Combining the results of in-hole water injection tests conducted on-site at the dam body and the contact zone between the dam body and dam foundation, it is likely that the leakage water in zones 1 to 4 does not solely originate from the dam body itself, but rather is a combined result of bypass leakage from the dam abutments, dam foundation leakage, leakage at the contact between the dam body and culverts, and leakage at the contact between the dam body and dam foundation. Additionally, some leakage water bypasses and infiltrates into the shrinkage cracks of the shallow red clay within the dam body, subsequently overflowing from the downstream slope surface of the dam body. This results in the presence of low resistivity zones within the dam body as shown in the profiles of the two electrical survey lines.

(5) ZK2 did not penetrate the power generation and irrigation culvert but passed through approximately 0.1 m to the left of the culvert pipe. However, when the borehole was drilled to an elevation of around 704.0 m, pressurized groundwater surged into the borehole, despite the dam body fill being of low permeability. Preliminary speculation suggests that there may be leakage channels at the contact zone between the culvert pipe and the dam body, and that there are quality defects in the culvert pipe itself. The groundwater within the borehole may originate from leakage channels at the contact zone between the culvert pipe and the dam body, as well as from water seepage within the culvert pipe.

(6) Drilling holes ZK1 to ZK5 reached the contact zone between the dam body and the dam foundation rock mass, and water inflow was observed in all holes. Significant dissolution was visible in the rock cores with thicknesses of approximately 3.2 m and 3.6 m respectively from the surface layer of the dam foundation rock mass. In particular, a drill dropout of about 40 cm occurred at ZK4. These observations are relatively consistent with the detection results from two types of electrical methods, indicating the presence of leakage hazards and pathways in the contact zone between the dam body and dam foundation, as well as within the surface layer of the dam foundation rock mass at both the left and right ends of the dam.

(7) ZK3 revealed that the top elevation of the dam foundation rock mass is approximately 712 m, which differs significantly from the detection results of the two electrical methods. To address this, we added ZK5 approximately 6 m to the left of ZK3. ZK5 revealed that the top elevation of the bedrock is approximately 688 m, with a height difference of about 24 m. Additionally, the soil layer below an elevation of approximately 698 m in ZK5 is loose, with a high void ratio and high water content. It has a grayish-yellow color, which is significantly

different from the brownish-red color of the red clay in the dam body. Preliminary speculation suggests that there may be a towering clint in the old riverbed within the dam, with loose Quaternary alluvial deposits on both sides of the clint. This is relatively consistent with the detection results of the two electrical methods.

(8) The relationship between the leakage conditions in the four leakage areas downstream of the dam and the reservoir water level indicates the following:

1) When the reservoir water level is below approximately 725 m, leakage areas 1 and 2 will disappear. When the water level exceeds 725 m, leakage areas 1 and 2 begin to appear, with leakage occurring in a diffuse manner. When the water level rises above 730 m, the leakage form changes to a combination of diffuse and concentrated leakage. As the water level continues to rise, both the diffuse leakage area and the number and flow rate of concentrated leakage points in areas 11 and 2 increase significantly.
2) In leakage area 3, leakage persists long-term and increases significantly as the reservoir water level rises.
3) In leakage area 4, diffuse leakage is more severe during water release for irrigation or power generation through the irrigation and power generation culvert. This leakage becomes more pronounced as the reservoir water level increases during culvert operation. When the culvert is closed, only minor diffuse leakage occurs in this area when the reservoir water level exceeds 735 m.
4) In recent years, there has been a clear trend of increasing total leakage measured in the four leakage areas at the same reservoir water levels.

It is evident that the leakage scale and volume in these four areas are highly correlated with the reservoir water level.

## 5 Discussion

Based on the results of two different electrical methods and geological methods, further discussion can be conducted in the following aspects.

(1) The water injection tests conducted in boreholes ZK1 to ZK5 revealed that the dam fill (excluding the area around the culverts) is composed of slightly permeable zones, which are also indicated as medium to high resistivity zones by the results of both electrical methods. In contrast, the contact surfaces between the dam body and dam foundation, as well as the surface rock mass areas of the dam foundation at these five boreholes, are all moderately permeable zones. These areas are shown as low resistivity zones by both electrical methods, and the higher the permeability coefficient, the lower the resistivity. It is evident that there is a strong correlation between the permeability of the dam's geomaterials and their resistivity.

(2) There are mainly two reasons for the occurrence of leakage in the contact zone between the dam body and the dam foundation, as well as in the dam foundation itsel:

1) Long-term seepage in the contact zone between the dam body and the dam foundation removes fine soil particles, resulting in an increase in porosity ratio within the contact zone. This, in turn, connects isolated seepage channels, forming leakage in the contact zone.
2) The dam foundation rock mass located beneath the contact zone is composed of dolomitic limestone, which is susceptible to leakage-induced chemical dissolution. This leads to the dissolution of the surface rock mass of the dam foundation. Consequently, dissolution fractures, pores, grooves, cavities, and karst caves form in the upper part of the dam foundation rock mass. These features then develop into interconnected dissolution leakage channels, triggering leakage in both the contact zone between the dam body and the dam foundation and in the karst features of the dam foundation.
3) The detection results of both electrical methods indicate the presence of a continuous low-resistivity anomaly zone with a thickness of approximately 3.0 m on the surface layer of the dam foundation. The dam foundation rock mass is composed of dolomitic limestone with a calcite content exceeding 50%. Over 95% of the calcite is calcium carbonate. The groundwater in the dam foundation contains dissolved carbon dioxide and is in a state of long-term runoff. This results in continuous chemical dissolution and hydromechanical erosion of the calcite in the dolomitic limestone, forming permeable and interconnected karst leakage channels in the surface layer of the dam foundation rock mass. These channels create a high-water-content, low-resistivity zone.
4) During the field data collection process using the two electrical methods, the influence of topographic relief can complicate the electrical measurement curves and increase the difficulty in identifying resistivity anomaly zones. Especially when encountering valleys or ridges, multiple peaks may appear, making identification even more challenging. Additionally, steep terrain or dense vegetation can affect the grounding quality of the electrodes, leading to abnormal data.

## 6 Conclusion

Based on the geophysical exploration results of High-density resistivity method and frequency-division electrical method, supplemented by field geological investigations and additional geological drilling verifications, the main conclusions obtained are as follows.

(1) The concentrated leakage and distributed seepage in leakage zones one and 2 downstream of the dam mainly originate from the leakage in the contact zone between the dam body and the dam foundation at the left and right ends of the dam, karst leakage in the surface rock mass of the dam foundation, and bypass seepage through the dam abutments.

(2) The water-gushing leakage in leakage zone 3 mainly comes from the leakage in the Quaternary alluvial deposits in the old riverbed gullies within the dam, karst leakage in shallow

bedrock, and leakage at the contact between the dam body and the dam foundation.

(3) The diffuse seepage in leakage zone 4 is caused by leakage in the contact zone between the power and irrigation culvert body and the dam body, as well as water leakage from within the culvert, rather than from the dam body itself.

## Data availability statement

The original contributions presented in the study are included in the article/supplementary material, further inquiries can be directed to the corresponding author.

## Author contributions

JY: Conceptualization, Data curation, Formal Analysis, Funding acquisition, Investigation, Methodology, Project administration, Resources, Software, Supervision, Validation, Visualization, Writing – original draft, Writing – review and editing. YY: Data curation, Formal Analysis, Investigation, Supervision, Validation, Writing – original draft. MY: Conceptualization, Funding acquisition, Resources, Validation, Writing – review and editing. ZS: Methodology, Project administration, Writing – review and editing. XH: Investigation, Project administration, Validation, Writing – review and editing. XC: Data curation, Validation, Writing – review and editing.

## Funding

The author(s) declare that financial support was received for the research and/or publication of this article. This research is supported by Hunan Provincial key research and development plan project (NO. 2024AQ 2044), the Natural Science Foundation of Changsha (NO. kq2502135 and NO. kq220 2,358), the Major water conservancy technology project in Hunan Province (NO. XSKJ2024064-10, NO. XSKJ2023059-02), the Excellent Personnel Training Support Project of Hunan Water Resources and hydropower Research Institute (NO. 2021–11), and the Open Foundation of the Hunan Province Dam Safety and Disease Prevention and Control Engineering Technology Research Center (NO. Hndam 2023kf02).

## Conflict of interest

The authors declare that the research was conducted in the absence of any commercial or financial relationships that could be construed as a potential conflict of interest.

## Generative AI statement

The author(s) declare that no Generative AI was used in the creation of this manuscript.

## Publisher's note

All claims expressed in this article are solely those of the authors and do not necessarily represent those of their affiliated organizations, or those of the publisher, the editors and the reviewers. Any product that may be evaluated in this article, or claim that may be made by its manufacturer, is not guaranteed or endorsed by the publisher.

## References

Bukowska-Belniak, B., and Lesniak, A. (2017). Image processing of leaks detection in sequence of infrared images. *Pomiary Autom. Kontrola* 63 (4), 131–134. doi:10.1016/j.measurement.2017.04.003

Cui, Z., Zhu, Z., Feng, Y., and Hao, M. (2024). Application of comprehensive geophysical exploration method and detection technology in dam seepage detection. *Chin. J. Eng. Geophys.* 21 (02), 205–210. doi:10.3969/j.issn.1672-7940.2024.02.003

He, J. (2000). "Flowingfield"technology to detect surge leakage in dam. *Copp. Eng.* 1, 5–4. doi:10.3969/j.issn.1009-3842.2000.01.002

Jian, C., and Sun, H. (2020). Application of pseudo-random flow field fitting method to leakage detection on clay core dam. *Chin. J. Eng. Geophys.* 17 (3), 373–377. doi:10.3969/j.issn.1672-7940.2020.03.016

Jiang, S., Zuo, S., Zhao, F., and Jin, Y. (2020). Application of high density method to estimate the development scale of karst cave in a certain site. *J. Hebei Univ. Water Resour. Electr. Eng.* 30 (1), 41–49. doi:10.16046/j.cnki.issn2096-5680.2020.01.008

Li, C., Min, G., Liu, K., Shu, R., Si, F., and Sun, Y. (2024). Three-dimensional numerical simulation and case analysis of deep leakage channel based on multi-electrode resistivity method. *Comput. Tech. Geophys. Geochem. Explor.*, 1–12. doi:10.3969/j.issn.1001-1749.2024.04.002

Liu, K., Tong, G., Duan, W., and Zhao, W. (2019). Analysi on the development of geophysical exploration in water conservancy and hydropower projects. *J China Three Gorges Univ.(NaturalSciences)* 41 (S1), 185–194.

Liu, W., Liu, S., and Liu, K. (2023). Application study of integrated geophysical prospecting to dam foundation survey in a certain reservoir. *J. Hebei Univ. Water Resour. Electr. Eng.* 33 (02), 7–5. doi:10.16046/j.cnki.issn2096-5680.2023.02.002

Liu, Z. (2022). "Development of FDM-ERT measurement and control system based on IoT," in Master's thesis. June: Central South University.

Peng, B., Qiang, S., and Shi, X. (2024). Optimization of 4D hydrogeological processes monitoring through cross-hole electrical resistivity Tomography (CHERT) using bayesian experimental design. *Bull. Geol. Sci. Technol.* (07), 1–10. doi:10.19509/j.cnki.dzkq.tb20230600

Peng, C. (2016). The combined application of seismic imaging method and high-density electric method to the survey of karst collapse areas. *Chin. J. Eng. Geophys.* 13 (01), 60–64. doi:10.3969/j.issn.1672-7940.2016.01.010

Ren, A., Ke, B., Cheng, J., Sun, P., Duan, Q., and Shao, Y. (2014). Analysis of the causes for the leakage of reseroir in karst area and nondestructive testing verification. *J. Hydraulic Eng.* 45 (S2), 119–126.

Sun, J., Deng, C., Tang, L., Wang, H., and Wen, J. (2024). Accurate identification technology for leakage channels in earth-rock dams through threedimensional reconstruction and inversion. *Hydro-Science Eng.* 4, 71–79. doi:10.12170/20231017001

Wang, Y., Lv, M., and Zhang, J. (2024). Application of integrated geophysical prospecting in the detection of hidden leakage of reservoir dam. *Comput. Tech. Geophys. Geochem. Explor.* 46 (01), 118–119. doi:10.3969/j.issn.1001-1749.2024.01.14

Xu, L., Gao, Y., Zhang, J., Yu, Y., and Guo, W. (2020). Identification method of dam leakage and layered diseases based on infrared imaging technology. *Electron. Technol. and Softw. Eng.* (08), 134–142. doi:10.20109/j.cnki.etse.2020.08.057

Xu, L., Zhang, G., and Ma, Z. (2022). Development of comprehensive geophysical prospecting technology for hidden danger detection of earth rock dams. *Prog. Geophys.* 37 (04), 1769–1811. doi:10.6038/pg2022ff0444

Yao, J., Luo, S., Song, W., Liu, Y., Zhao, W., and Lv, H. (2020). Application of comprehensive geophysical exploration method in leakage detection of reservoir.

*Geophys. Geochem. Explor.* 44 (2), 456–457. doi:10.3969/j.issn.1672-7940.2023.05.003

Yao, J., Song, H., Luo, S., Wu, Z., and Liu, W. (2014). Application of comprehensive tracing method in the leakage detection of a karst reservoir. *Geotech. Investig.* 4, 93–96.

Yao, J., Wu, Y., Song, Z., Liu, Y., Liang, J., and Wang, X. (2023). Research on identifying leakage defects of plastic concrete cutoff walls in dams by ground penetrating radar and high density electrical method. *ChineseJournalofEngineeringGeophysics* 20 (5), 599–606.

Zhang, J., Ma, F., and Huo, J. (2024). Application of high density electrical method based on BP neural network in detection of desilting coffer dam in reservoir. *Water Resour. Powe* 42 (05), 174–175. doi:10.20040/j.cnki.1000-7709.2024.20230652

Zhang, K., Gao, W., and Fang, Z. (2018). Leakage detection of earth and rockfill dam in karst area by pseudo-random flow field method. *China Water Conserv.* 20, 46–54. doi:10.3969/j.issn.1000-1123.2018.20.012

Zhang, T., Jiang, J., Li, Z., Fan, G., and Bi, C. (2023). Comprehensive geophysical detection and evaluation of quality of "stepped" concrete cut-off wall of Hejiagou Reservoir Dam. *Water Resour. Power* 41 (01), 96–104. doi:10.20040/j.cnki.1000-7709.2023.20220871

Zhao, L., Huo, J., Yu, Y., and Zhou, H. (2022). Comprehensive geophysical prospecting analysis of the main dam of Changzhuang Reservoir after the torrential rainstorm of July 20,2021 in Zhengzhou. *Yellow River* 44 (11), 152–154. doi:10.3969/j.issn.1000-1379.2022.031

Zhen, Y. (2018). Application of comprehensive geophysical exploration in the detection of karst cavities in dams. *Eng. Technol. Appl.* 16, 59–63.

frontiers | Frontiers in Earth Science

TYPE Original Research
PUBLISHED 30 April 2025
DOI 10.3389/feart.2025.1583402



OPEN ACCESS

EDITED BY
Tongming Qu,
Hong Kong University of Science and Technology, Hong Kong SAR, China

REVIEWED BY
Dengguo Li,
Jiaxing University, China
Xiong Wang,
Shanghai Jiao Tong University, China

*CORRESPONDENCE
Zeliang Li,
525065355@qq.com

RECEIVED 25 February 2025
ACCEPTED 10 April 2025
PUBLISHED 30 April 2025

CITATION
Dang P, Li Z, Zou D, Li H, Cheng Z, Chang L and Lu Y (2025) Monitoring data-driven dynamic safety assessment framework for deep foundation pit construction based on grey clustering and moment method. *Front. Earth Sci.* 13:1583402. doi: 10.3389/feart.2025.1583402



# Monitoring data-driven dynamic safety assessment framework for deep foundation pit construction based on grey clustering and moment method

Pengliang Dang[1], Zeliang Li[2]*, Dehai Zou[1], Hangjun Li[1], Zilong Cheng[2], Le Chang[1] and Yadong Lu[1]

[1]Sinohydro Bureau 14 Co., Ltd., Kunming, China, [2]College of Civil and Transportation Engineering, Shenzhen University, Shenzhen, China

To address the safety challenges of deep foundation pit construction under complex conditions, this study proposes a dynamic assessment framework based on grey clustering theory and a moment estimation composite weighting method. A three-level indicator system was constructed, integrating subjective and objective weights through order relationship and entropy weight methods. Grey clustering was employed to classify real-time monitoring data and assess safety levels dynamically. Application to a large-scale water diversion shaft project in Shenzhen verified the model's effectiveness, with assessment results closely matching observed risks during excavation. The framework improves accuracy and responsiveness in uncertain monitoring environments and supports intelligent risk management.

KEYWORDS

**deep foundation pit, monitoring data, dynamic safety assessment, grey clustering theory, composite weights**

## 1 Introduction

When there is a need to build underground structures such as shaft foundations, basements, or tunnels, a foundation pit is usually excavated. As urbanization continues to advance and calls for constructing more underground infrastructures, the scale and depth of deep foundation pit engineering are continuously expanding, and their safety issues are receiving increasing attention, especially in densely populated urban areas and karst-prone regions. The pit excavation triggers significant unloading effects and usually negatively disturbs the greenfield ground, which imposes high risks to the surrounding environment and may lead to the disastrous collapse of pit bracing structures and damage to adjacent buildings (Chen et al., 2023). In recent years, multiple foundation pit accidents have occurred, such as the collapse of a metro station project in Hangzhou in 2008 (Gong and Zhang, 2012), the failure of foundation pit support in Nanchang in 2015 (Feng and Lu, 2016), and the pit collapse accident in Nanning in 2019 (Chin et al., 2019), many of which were exacerbated by karst-induced instability (Lv et al., 2020). Causing substantial property losses and casualties. It should be pointed out that these incidents are attributed to unqualified field monitoring or untimely responses to alert monitoring data. Studies emphasize that accurate field monitoring, effective data analysis,

and timely risk management are crucial in preventing foundation pit accidents. For example, numerical analyses have highlighted the importance of understanding the seismic responses of underground structures in complex soil conditions such as liquefiable soils and marine soft soils (Bao et al., 2025), and karst regions (Li et al., 2023). Therefore, performing accurate field monitoring and further effective monitoring data analysis and timely risk management are effective ways to prevent foundation pit accidents. With the advancement of technology, modern deep foundation pit engineering has introduced advanced monitoring techniques and computational models to ensure safety during construction and structural stability. For instance, seismic responses of underground structures in liquefiable soils necessitate precise monitoring and design optimizations to enhance safety during seismic events (Shen et al., 2025; Bao et al., 2024). Similarly, Xu et al. explored the monitoring and assessment methods for ultra-deep diaphragm walls during excavation, providing critical insights into structural stability under high-stress conditions (Xu et al., 2024). In karst regions, unique challenges arise due to hidden cavities, water-filled voids, and unpredictable soil mechanics, which amplify risks of sudden collapses and water inrush during excavation (Xu and Wang, 2022). Recent advancements in machine learning have shown promise in detecting hidden defects in complex geological environments. For example, Bao et al. developed an improved YOLOv8 model with attention mechanisms to detect voids in rebar-affected areas using ground-penetrating radar (GPR) data, demonstrating enhanced accuracy in noisy and cluttered datasets (Bao et al., 2025).

With advancements in monitoring technologies and equipment, effectively utilizing data for risk assessment and prediction has become essential for ensuring safety during deep foundation pit construction. To address this need, several scholars have proposed various methods to predict and assess safety risks throughout the construction process. For instance, Wei et al. introduced a fuzzy analytic hierarchy process (FAHP) combined with evidence reasoning algorithms to evaluate the overall risk level of deep foundation pits, enabling reasonable risk assessments even with insufficient monitoring data (Wei et al., 2020). Similarly, Zhou et al. developed risk prediction models based on support vector machines (SVM) (Zhou et al., 2017) and random forest algorithms (Zhou et al., 2019), both of which have demonstrated reliable validation. Moreover, Wu et al. presented a rapid convergence and high-reliability multi-source data fusion method for assessing subway foundation pit collapse risk, utilizing cloud models (CM) and improved Dempster-Shafer evidence theory to integrate and quickly converge multi-source data under various factors (Wu et al., 2024). Furthermore, Sun applied digital twin technology for real-time risk prediction and control during deep foundation excavation, improving the precision and timeliness of risk management; however, the complexity of the technology and high equipment costs currently hinder large-scale implementation (Sun et al., 2023). Shen established the cloud model theory by using the parameters such as expectation, entropy and super-entropy to represent uncertainty, which provided a new perspective for multi-index comprehensive evaluation (Shen et al., 2025).

With the emergence of an increasing number of safety assessment methods for deep foundation pit construction, the selection of assessment indicators has become more diverse. As a structured framework for assessment methods, assessment indicators directly impact the accuracy and reliability of assessment results. Previous studies have made significant strides in developing safety assessment frameworks for deep foundation pits. However, these methods face notable limitations. FAHP introduces subjectivity due to reliance on expert judgment, whereas SVM struggles with incomplete or uncertain data. Additionally, existing approaches often focus narrowly on structural deformation indicators while neglecting critical factors such as structural internal forces and environmental impacts. This oversight can lead to incomplete risk assessments, particularly in complex geological conditions where multi-factor interactions dominate.

To address the aforementioned issues and provide solutions, this study innovatively proposes a dynamic safety assessment method for deep foundation pit construction based on gray clustering theory and moment estimation composite weights. The innovations of this assessment method include: (1) the introduction of gray clustering theory effectively addresses the uncertainty and incompleteness of monitoring data in practical engineering, enhancing computational efficiency and ensuring the accuracy and timeliness of assessment results; (2) the incorporates monitoring projects from current standards as assessment indicators, eliminating the need for additional resource investment and ensuring the economic viability and applicability of the assessment approach; (3) a multi-layer composite weights approach based on moment estimation is proposed for assigning weights to each assessment indicator, ensuring objectivity and scientific rigor in the distribution of weights.

The rest of this paper is divided into five main sections: Section 2 will elaborate on the theoretical foundations of this research, including the principles of gray clustering theory and moment estimation methods, as well as their application context in safety assessments; Section 3 details the construction process of the assessment model, covering the selection of assessment indicators, the methodology for weight allocation, and the mathematical representation of the model; Section 4 presents the application process and practical effects of the assessment model through specific engineering cases, validating its effectiveness and applicability; Section 5 summarizes the main contributions and practical value of the assessment method, while also discussing the limitations of the study and potential future research directions.

## 2 Methodology

As a multi-attribute decision-making (MADM) problem (Li et al., 2015), the dynamic safety assessment of deep foundation pit construction needs to consider the interaction between multiple factors, and finally obtain a safety index comprehensively. The assessment of safety indicators requires scientific weight coefficients allocation and reasonable assessment methods to obtain accurately fit actual results.

A scientific and reasonable weight determination method should consider subjective and objective factors. Common subjective weight determination methods include expert evaluation method, analytic hierarchy process (AHP) and order relationship analysis method. The expert evaluation method directly assigns weights to each evaluation indicator through the experience and knowledge of professionals; the AHP quantifies the relative

importance of different factors by constructing a hierarchical model, and determines the weights through a series of comparative judgments; and the order relationship analysis method determines the weights for each indicator by judging the relationship between sequences, which is suitable for situations where clear data is lacking. The calculation of objective weights is usually based on some theoretical methods based on data, among which the entropy weight method is the most universal method. The entropy weight method is based on the objectivity of data and determines the objective weights of each indicator by analyzing the uncertainty of the data. This process is completely based on the inherent characteristics of the data, reducing the possibility of human intervention and errors.

Given the diversity of assessment indicators of deep foundation pit construction and the implicit relationships among them, it is more practical to calculate composite weights by integrating both subjective and objective aspects.

## 2.1 Weight coefficients

### 2.1.1 Order relationship analysis method

The Order Relationship Analysis Method (ORAM) is a subjective weight assignment method proposed based on the AHP. This method first qualitatively sorts the indicators and then quantitatively assigns values with comparing adjacent indicators (Ye et al., 2023). After arranging the importance of the assessment indicators in order, the relative importance of other assessment indicators is also uniquely determined, and so are the weights. Compared to the AHP method, when there are many assessment indicators, ORAM does not require a one-time check, solving the problem of inconsistent judgment matrices and greatly improving the computational efficiency of the model. The detailed process of this method include.

Step 1: Determine the order relationship

Establish the set of indicators based on the dynamic safety assessment index system, perform a Delphi method ranking (usually by experts in this area), and ultimately establish a unique order based on importance from the highest to the lowest, as in Equation 1:

$$X_1 > X_2 > \ldots > X_{i-1} > X_i > X_{i+1} > \ldots > X_p \tag{1}$$

Step 2: Calculate the relative importance coefficient

Set Equation 2 as $r_I$, the ratio of the relative importance of indicator $X_{i-1}$ to $X_I$ and refer to Table 1 for the meaning of $r_i$:

$$r_i = \frac{x_{i-1}}{x_i} \, (i = 2, 3, \ldots, p) \tag{2}$$

In the formula, *i* represents the relative importance.

Step 3: Weight coefficient calculation

Within the context of sequential relational indicators, designate the weight of the j indicator as $w_j'$ as presented in Equation 3.

$$w_j' = \frac{\alpha_i \prod_{i=j+1}^{p} r_i}{\sum_{k=1}^{p} \alpha_k \prod_{i=k+1}^{p} r_i} \tag{3}$$

TABLE 1 Relative importance of indicators.

| $r_i$ | Meanings |
|---|---|
| 1.0 | The indicator $X_{i-1}$ is just as important as the indicator $X_i$ |
| 1.2 | The indicator $X_{i-1}$ is slightly more important than the indicator $X_i$ |
| 1.4 | The indicator $X_{i-1}$ is significantly more important than the indicator $X_i$ |
| 1.6 | The indicator $X_{i-1}$ is more important than the indicator $X_i$ |
| 1.8 | The indicator $X_{i-1}$ is extremely important than the indicator $X_i$ |

Note: 1.1, 1.3, 1.5, and 1.7 respectively indicate importance between neighboring two.

In the formula, $\alpha_I$ is an adjustment factor, which is set in reverse order based on the importance of the indicator.

### 2.1.2 Entropy weight method

The entropy weight method (EWM) is an important objective weighting method that develops from the concept of entropy, a term mostly used to describe a state of disorder, randomness, or uncertainty. The term is first recognized and used in classical thermodynamics (Akih-Kumgeh, 2016). Generally, the lower the information entropy $H_j$ of an indicator, the greater the variability of its values and the more information it provides. When using the characteristic of entropy to express information quantity, the greater the difference of an indicator among various assessment objects, the greater its role in the comprehensive assessment, and consequently, its weight should also be greater (Wu et al., 2022). As an objective weighting method, EWM calculates weights from the judgment matrix, and it is considered more precise compared to other objective weighting assessment methods (Ahn, 2011). The general process of entropy weight method includes the below key steps:

Step 1: Data standardization.

Formulate the data of each indicator into an i × j judgment matrix, defined as the raw matrix A, and then obtain matrix B through standardization processing Equation 4.

$$b_{ij} = \frac{a_{ij} - \min(a_{ij})}{\max(a_{ij}) - \min(a_{ij})} \tag{4}$$

Here, $a_{ij}$ refers to the data in the j row of the i indicator in the judgment matrix, $\max(a_{ij})$ is the maximum value of all elements in matrix A, and $\min(a_{ij})$ is the minimum value of all elements in matrix A.

Step 2: Proportion of the indicator.

The purpose of proportion is to measure the importance of each assessment objects in that indicator. For standardized data, Equation 5 is used to calculate the proportion of each assessment objects under each index.

$$p_{il} = \frac{b_{ij}}{\sum_{i=1}^{m} b_{ij}} \tag{5}$$

Here, m is the number of assessment objects, pil represents the proportion of the i object in the j index.

Step 3: Calculate the information entropy.

The information entropy for each indicator is calculated utilizing Equation 6.

$$H_j = -k\sum_{i=1}^{m} p_{ij} \ln\left(p_{ij}\right), k = \frac{1}{\ln(m)} \tag{6}$$

Here, k is the normalization coefficient, ensuring that the value of information entropy is between $[0, 1]$. The information entropy reflects the uncertainty of the data. The greater the entropy, the smaller the variability of the data and the lower the differentiation of the index.

Step 5: Calculate objective weights.

Information entropy is introduced into Equation 7 to obtain the objective weight of the index.

$$w_j'' = \frac{1 - H_j}{m - \sum_{j=1}^{m} H_j} \tag{7}$$

### 2.1.3 Entropy weight method

To balance subjective judgment with objective data in the MADM process, this study employs the moment estimation composite weights method (MECWM) for composite weights, aiming to minimize the influence of subjectivity on the assessment of indicator importance. MECWM is a widely used parameter estimation technique in statistics. This method quantifies the importance of indicators by calculating sample moments and matching them with theoretical population moments (Wooldridge, 2001). This method was first proposed by British statistician Karl Pearson in the late 19th century, estimating the parameters of a probability distribution by matching sample moments with population moments (Pearson, 1936).

In the process of composite weights, MECWM allows us to combine the analysis results of objective data with the subjective judgment of decision-makers. By adjusting parameter estimates to reflect the importance of different indicators, this approach not only enhances the transparency of the decision-making process but also strengthens the reliability of the decision outcomes.

Therefore, this paper will apply MECWM to optimize the combination of weights for the indicators, based on the optimal subjective and objective weight values determined by the ORAM and the EWM, respectively. Employing Equation 8, the composite weights coefficient $\beta_j$ is ascertained. Thereafter, by integrating the subjective and objective weights into Equation 9, the composite weights $w_j$ for each indicator is ultimately derived. The weight coefficient $\beta_j$, determined according to the moment method, primarily reflects the relative importance of subjective and objective factors in decision-making.

$$\beta_j = \frac{w_j'}{w_j' + w_j''} \tag{8}$$

$$w_j = \frac{\beta_j w_j' + \left(1 - \beta_j\right) w_j''}{\sum_{j=1}^{p}\left[\left(1 - \beta_j\right) w_j' + \beta_j w_j''\right]} \tag{9}$$

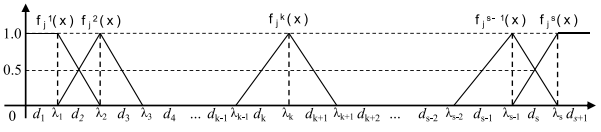


FIGURE 1
Whitening functions of S assessment gray classes.

## 2.2 Grey clustering theory

The dynamic safety assessment of deep foundation pit construction is a MADM problem. In such scenarios, decision-makers often aim to develop the most reasonable assessment plan in an objective and impartial manner. In deep foundation pit construction, monitoring data often exhibits characteristics such as incompleteness, uncertainty, and variability due to complex geological conditions and construction activities. These uncertainties pose significant challenges in accurately assessing safety risks. Gray clustering theory, based on the whitening weight function of gray numbers, effectively addresses these challenges by integrating the analysis of various indicators to categorize observed objects into predefined classes. It demonstrates good adaptability in addressing multi-attribute decision-making challenges (Li et al., 2015), especially when dealing with uncertain and incomplete data that are common in foundation pit monitoring processes. As an unsupervised learning method, the core idea of gray clustering theory is to effectively manage the grayness of both known and unknown information within a system, thereby revealing the behavioral patterns and intrinsic connections of the system. This method is particularly suitable for situations involving incomplete or highly uncertain information (Li et al., 2015; Liu and Yang, 2017).

Grey clustering theory, rooted in grey system theory, is a powerful tool for addressing uncertainty and incompleteness in data. It operates on the concept of grey numbers' that values with partially known and partially unknown information and employs whitening weight functions to transform ambiguous data into interpretable metrics. The core principle involves dividing data into predefined grey classes' using triangular or trapezoidal membership functions, which inherently accommodate data vagueness. This approach surpasses traditional methods by allowing partial membership in multiple classes, reflecting real-world ambiguities in monitoring data. For example, a displacement value near a safety threshold can be assigned fractional membership to both 'Alert' and 'Warning' classes, capturing transitional states not accounted for in binary systems. This contrasts sharply with binary classification methods, which force data into discrete categories, potentially masking critical transitional risks.

While grey clustering excels in dynamic, uncertain environments, it also outperforms other advanced clustering techniques in critical aspects. k-means clustering, for instance, relies on Euclidean distance and assumes spherical cluster shapes, making it ineffective for non-linear relationships often observed in foundation pit data. Fuzzy C-means introduces

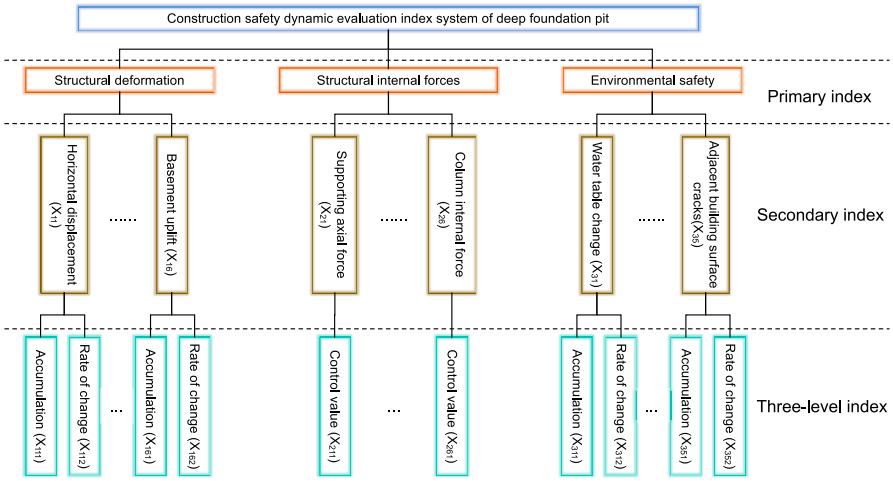


FIGURE 2
The diagram of the dynamic safety assessment index system for deep foundation pit construction.

probabilistic memberships but requires predefined cluster numbers and Gaussian assumptions, which are rarely valid in complex geological settings. Hierarchical clustering lacks scalability for large datasets and is prone to error propagation from early merge decisions, limiting its use in real-time monitoring. In contrast, grey clustering dynamically adapts to data patterns without rigid distribution assumptions, making it uniquely suited for incomplete or evolving datasets typical of deep foundation pit construction.

As a specific application of gray clustering theory, gray clustering analysis primarily includes two types: gray relational clustering and gray whitening weight function clustering (Liu et al., 2017). Gray relational clustering is based on the gray relational matrix, which classifies the observed indicators or objects into predefined categories by calculating the gray relational degree among the assessment objects. In contrast, gray whitening weight function clustering is used to determine whether the observed objects belong to a specific category. This involves establishing a whitening weight function to convert gray data into meaningful whitening values, allowing for appropriate differentiation and processing (Chen et al., 2019). Both the two clustering analysis types offer unique advantages in addressing multi-attribute decision-making problems, particularly in situations with incomplete or highly uncertain information. For the analysis of monitoring data in deep foundation pit construction, the gray whitening weight function clustering method can effectively identify the risks and trends of various factors, particularly in key monitoring indicators such as settlement, displacement, and stress. In contrast, gray correlation clustering focuses more on recognizing the similarities between different data points. Therefore, this study employs the gray whitening weight function clustering method for gray clustering analysis.

Notably, the gray whitening weight function is a piecewise function. Depending on the nature of the observed indicators, different ranges of indicator values correspond to different expressions of the weight function. Let $x_{ij}$ be the observation value of the i assessment object regarding the j indicator (where $i = 1,2,3,\ldots,n$ and $j = 1,2,3,\ldots,p$). $f_i^k(x_{ij})$ denotes the whitening weight function value for the k subclass of the j indicator (where $k = 1,2,3$). According to gray clustering theory, the design of the whitening weight function must meet the following requirements as in Equation 10:

$$\sum_{k=1}^{s} f_i^k(x_{ij}) = 1 \quad \forall x_{ij} \in \otimes \tag{10}$$

Here, $\otimes$ denotes the value range of $x_{ij}$. The value range of the indicator $x_j$ is divided into S subintervals $[d_1, d_{s+1}]$. The geometric midpoint $\lambda$ of each subinterval is calculated using the following Equation 11:

$$\lambda_k = \frac{d_{k-1} + d_k}{2} \quad (k \in 1,2,3,\ldots,s) \tag{11}$$

Next, the whitening weight function is constructed as illustrated in Figure 1. Let $\lambda_k$ represent the whitening weight function value for the k gray class ($k = 2,3,\ldots,s-1$). By connecting point $(\lambda_k, 1)$ with the geometric midpoints $\lambda_{k-1}$ and $\lambda_{k+1}$ of the $k-1$ and $k+1$ gray classes, respectively, the triangular whitening weight function $f_i^k(x)$ for indicator $X_j$ concerning the k gray class is obtained, and its expression is given by the following Equation 12:

$$f_j^k(x) = \begin{cases} 0 & x \notin [\lambda_{k-1}, \lambda_{k+1}] \\ \dfrac{x - \lambda_{k-1}}{(\lambda_k - \lambda_{k-1})} & x \in [\lambda_{k-1}, \lambda_k] \\ \dfrac{\lambda_{k+1} - x}{(\lambda_{k+1} - \lambda_k)} & x \in [\lambda_k, \lambda_{k+1}] \end{cases} \tag{12}$$

The triangular whitening weight function for the first gray class is expressed as following Equation 13, the triangular whitening weight function for the s Gy class is expressed as following Equation 14:

$$f_j^k(x) = \begin{cases} 1 & x \in [d_1, d_2] \\ \dfrac{\lambda_2 - x}{\lambda_2 - \lambda_1} & x \in [d_2, \lambda_2] \\ 0 & x \notin [d_1, \lambda_2] \end{cases} \tag{13}$$

TABLE 2 Construction safety dynamic assessment index system of deep foundation pit.

| Primary index | Secondary index | Three-level index | unit |
|---|---|---|---|
| Structural deformation ($X_1$) | Horizontal displacement at the top of bracing and retaining structure ($X_{11}$) | Accumulation ($X_{111}$) | mm |
| | | Rate of change ($X_{112}$) | mm/d |
| | Vertical displacement at the top of the bracing and retaining structure ($X_{12}$) | Accumulation ($X_{121}$) | mm |
| | | Rate of change ($X_{122}$) | mm/d |
| | Lateral wall deflection ($X_{13}$) | Accumulation ($X_{131}$) | mm |
| | | Rate of change ($X_{132}$) | mm/d |
| | Vertical displacement of column ($X_{14}$) | Accumulation ($X_{141}$) | mm |
| | | Rate of change ($X_{142}$) | mm/d |
| | Vertical surface displacement ($X_{15}$) | Accumulation ($X_{151}$) | mm |
| | | Rate of change ($X_{152}$) | mm/d |
| | Basement uplift ($X_{16}$) | Accumulation ($X_{161}$) | mm |
| | | Rate of change ($X_{162}$) | mm/d |
| Structural internal forces ($X_2$) | Supporting axial force ($X_{21}$) | Control value ($X_{211}$) | kPa |
| | Axial force of bolt ($X_{22}$) | Control value ($X_{221}$) | kPa |
| | Earth pressure ($X_{23}$) | Control value ($X_{231}$) | kN |
| | Pore water pressure ($X_{24}$) | Control value ($X_{241}$) | kN |
| | Internal Force of Retaining wall ($X_{25}$) | Control value ($X_{251}$) | kPa |
| | Column internal force ($X_{26}$) | Control value ($X_{261}$) | kPa |
| Environmental safety ($X_3$) | Water table change ($X_{31}$) | Accumulation ($X_{311}$) | mm |
| | | Rate of change ($X_{312}$) | mm/d |
| | Pipeline displacement ($X_{32}$) | Accumulation ($X_{321}$) | mm |
| | | Rate of change ($X_{322}$) | mm/d |
| | Adjacent building displacement ($X_{33}$) | Accumulation ($X_{331}$) | mm |
| | | Rate of change ($X_{332}$) | mm/d |
| | Adjacent road settlement ($X_{34}$) | Accumulation ($X_{341}$) | mm |
| | | Rate of change ($X_{342}$) | mm/d |
| | Adjacent building surface cracks ($X_{35}$) | Accumulation ($X_{351}$) | mm |
| | | Rate of change ($X_{352}$) | mm/d |

10.3389/feart.2025.1583402

TABLE 3 Construction safety dynamic assessment index system of deep foundation pit.

| Index | Safety level | | | |
|---|---|---|---|---|
| | U1 | U2 | U3 | U4 |
| $X_{111}$ | (−∞,10] | (10.20] | (20.30] | (30, +∞) |
| $X_{112}$ | (−∞,1] | (1,2] | (2,3] | (3, +∞) |
| $X_{121}$ | (−∞,5] | (5.10] | (10.20] | (20, +∞) |
| $X_{122}$ | (−∞,1] | (1,2] | (2,3] | (3, +∞) |
| $X_{131}$ | (−∞,15] | (15.30] | (30.50] | (50, +∞) |
| $X_{132}$ | (−∞,1] | (1,2] | (2,3] | (3, +∞) |
| $X_{141}$ | (−∞,10] | (10.20] | (20.30] | (30, +∞) |
| $X_{142}$ | (−∞,1] | (1,2] | (2,3] | (3, +∞) |
| $X_{151}$ | (−∞,15] | (15.25] | (25.35] | (35, +∞) |
| $X_{152}$ | (−∞,1] | (1,2] | (2,3] | (3, +∞) |
| $X_{161}$ | (−∞,30] | (30.45] | (45.60] | (60, +∞) |
| $X_{162}$ | (−∞,4] | (4,7] | (7.10] | (10, +∞) |
| $X_{211}$ | $(f_y,60\%f_2]$ | $(90\%f_y,f_y]\cup(60\%f_2,70\%f_2]$ | $(80\%f_y,90f_y]\cup(70\%f_2,80\%f_2]$ | $<80\%f_y\cup>0\%f_2$ |
| $X_{221}$ | $(f_y,60\%f_2]$ | $(90\%f_y,f_y]\cup(60\%f_2,70\%f_2]$ | $(80\%f_y,90f_y]\cup(70\%f_2,80\%f_2]$ | $<80\%f_y\cup>0\%f_2$ |
| $X_{231}$ | $(0.60\%f_1]$ | $(60\%f_1,70\%f_1]$ | $(70\%f_1,80\%f_1]$ | $(80\%f_1, +\infty)$ |
| $X_{241}$ | $(0.60\%f_1]$ | $(60\%f_1,70\%f_1]$ | $(70\%f_1,80\%f_1]$ | $(80\%f_1, +\infty)$ |
| $X_{251}$ | $(0.60\%f_2]$ | $(60\%f_2,70\%f_2]$ | $(70\%f_2,80\%f_2]$ | $(80\%f_2, +\infty)$ |
| $X_{261}$ | $(0.60\%f_2]$ | $(60\%f_2,70\%f_2]$ | $(70\%f_2,80\%f_2]$ | $(80\%f_2, +\infty)$ |
| $X_{311}$ | (01,000] | (1000,1500] | (1,500,2000] | (2000, +∞) |
| $X_{312}$ | (−∞,400] | (400,450] | (450,500] | (500, +∞) |
| $X_{321}$ | (−∞,10] | (10.15] | (15.20] | (20, +∞) |
| $X_{322}$ | (−∞,1] | (1,5] | (1.5,2] | (2, +∞) |
| $X_{331}$ | (−∞,10] | (10.20] | (20.30] | (30, +∞) |
| $X_{332}$ | (−∞,1] | (1,2] | (2,3] | (3, +∞) |
| $X_{341}$ | (−∞,10] | (10.20] | (20.30] | (30, +∞) |
| $X_{342}$ | (−∞,1] | (1,2] | (2,3] | (3, +∞) |
| $X_{351}$ | (−∞,10] | (10.13] | (13.15] | (15, +∞) |
| $X_{352}$ | (−∞,1] | (1,2] | (2,3] | (3, +∞) |

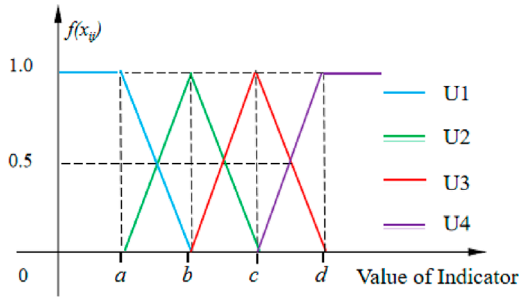


FIGURE 3
Image of whitening weight function of three-level indicators.

$$f_j^k(x) = \begin{cases} 1 & x \in [\lambda_s, d_{s+1}] \\ \dfrac{x-\lambda_{s-1}}{\lambda_s-\lambda_{s-1}} & x \in [\lambda_{s-1}, \lambda_s] \\ 0 & x \notin [\lambda_{s-1}, d_{s+1}] \end{cases} \tag{14}$$

If the weight $w_j^k$ of the k subclass of the j indicator is independent of k (where $w_j^1 = w_j^2 = \ldots = w_j^s$), let $\sigma_i^k$ denote the gray fixed weight clustering coefficient for the i assessment object in the k subclass. Then as following Equation 15:

$$\sigma_i^k = \sum_{j=1}^{p} f_i^k(x_{ij}) w_j \quad (i = 1, 2, \ldots, m; k = 1, 2, 3) \tag{15}$$

If $\sigma_i^{k^*} = \max(\sigma_i^k) = \max\left[\sum_{j=1}^{p} f_i^k(x_{ij}) w_j\right]$ is satisfied, then the i assessment object belongs to the $k^*$ subclass. Based on Equations 13–15, we can derive the following Equation 16:

$$\sum_{k=1}^{s} \sigma_i^k = 1 \tag{16}$$

This means that the sum of the gray fixed weight clustering coefficients for all subclasses of the i assessment object is equal to 1.

# 3 Dynamic safety assessment methods for deep foundation pits

## 3.1 Dynamic safety assessment index system

The selection of proper assessment indicators is a critical aspect determining the effectiveness of the dynamic assessment method of deep foundation pit construction. In this study, the proposed assessment index system is based on the relevant standards (MOHURD, 2019), in order to closely align with actual engineering practices. The selection of assessment indicators must, on one hand consider the complexity of the foundation pit's environment, such as geological conditions, groundwater levels, and the status of surrounding buildings and infrastructure, and on the other hand, carefully weigh the difficulty of data acquisition to ensure the feasibility of equipment deployment and the continuity of data collection. Moreover, the chosen indicators should have a strong ability to reflect the safety status of the foundation pit, capturing changes with adequate sensitivity and accuracy, particularly key indicators like vertical retaining structure deformation and stress or strain responses of the horizontal support structures, which are critical early warning signals of foundation pit instability. Additionally, environmental safety indicators, such as the ground settlement and tilting of nearby structures, should not be overlooked, as they provide insights into the construction's impact on the surrounding environment, allowing decision-makers to intervene in a timely manner (Tan et al., 2023; Zhao et al., 2022). In conclusion, by selecting and designing a rational assessment index system has to incorporate both the bracing structures of pits and also the surrounding influential environment, while balancing the ease of on-site data acquisition (Ye et al., 2021; Qiao et al., 2024).

Based on the classification of deep foundation pit monitoring items, a dynamic safety assessment index system is established to include three primary level indicators and seventeen secondary level process indicators. The three primary level indicators are: structural deformation indicators ($X_1$), structural internal forces indicators ($X_2$), and environmental safety indicators ($X_3$), each incorporates several secondary level indicators, and each secondary level indicator further considers several three-level control indicators. The assessment objectives, assessment criteria, and assessment indicators are at different levels, forming a progressive hierarchical structure. The diagram of the dynamic assessment index system is partially demonstrated here in Figure 2, while the detailed descriptions of indicators are included in Table 2.

## 3.2 Classification of safety levels

The determination of threshold ranges for the dynamic assessment of deep foundation pit construction safety is based on an analysis of monitoring data from actual projects, combined with references to domestic and international research findings and industry standards (MOHURD, 2019; MOHURD, 2012). The threshold setting also takes into account the specific characteristics of foundation pit projects, including geological conditions, pit excavation depth, retaining structure types, and the complexity of the surrounding environment.

In establishing the threshold ranges for each level, initial reference values were derived from empirical monitoring data on foundation pit deformation, mechanical response of bracing structures, and environmental disturbance monitoring. Significant correlations between foundation pit deformation and instability informed the setting of critical limits for horizontal displacement and vertical settlement of retaining structures such as the diaphragm walls and the sheet pile walls. The mechanical response of support structures during construction also served as a basis for adjusting the alert and warning thresholds for stress-strain indicators of support systems. Additionally, precision of monitoring equipment, dynamic changes during construction, and the influence of the surrounding environment on monitoring data were considered in the threshold determination. For indicators of environment impacts, such as settlement and tilting of adjacent buildings, data from project cases were analyzed to help define appropriate alert and warning thresholds.

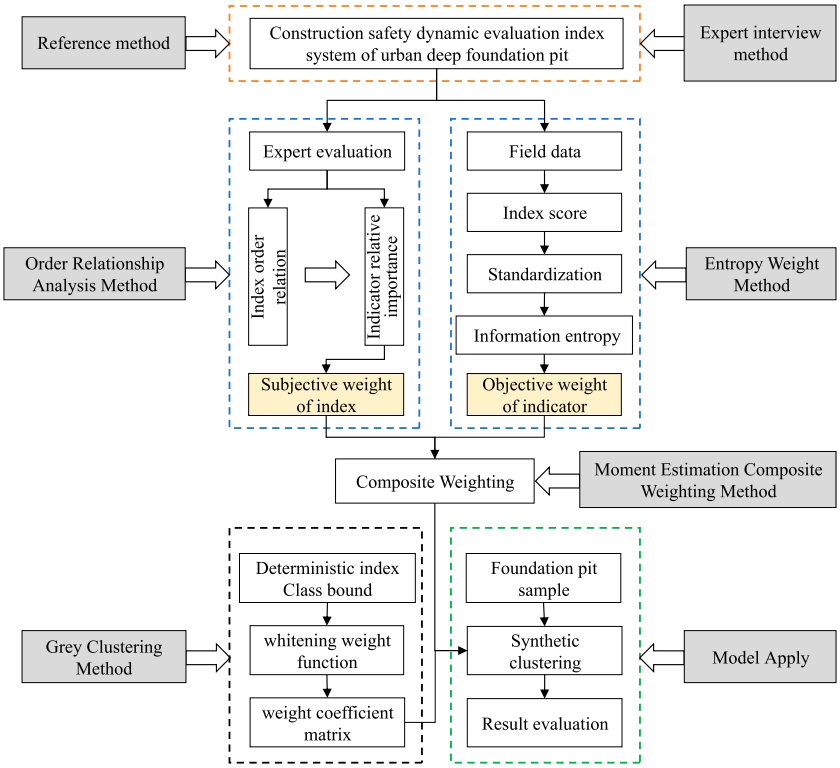


FIGURE 4
Construction dynamic safety assessment model of deep foundation pit.


FIGURE 5
Project routing diagram.

Based on this multi-dimensional analysis, the safety assessment index system U of the deep foundation pit construction is divided into four levels: Safe (U1), Alert (U2), Warning (U3), and Dangerous (U4). Due to space limitations, the final value ranges for each assessment level are detailed in Table 3. According to the divisions of the safety levels, each indicator has three boundary conditions. From these, the four category boundary values (a, b, c, d) can be calculated using Equation 3. Subsequently, combining Equations 4–6, the whitening power functions for each third-level indicator are constructed, resulting in the corresponding weight coefficient matrix. The whitening power functions between different indicators differ only in the category boundary values, with the overall function plots being similar, as shown in Figure 3.

As shown in the figure, the whitening weight function graph of grey clustering theory visually represents how indicator values are mapped to assessment levels, with the horizontal axis denoting indicator values and the vertical axis $f(x_{ij})$ indicating membership weights (0–1). Unlike traditional binary classification methods that impose strict thresholds, this graph inherently reflects the theory's strength in handling uncertainty: adjacent intervals allow partial membership overlaps rather than absolute exclusivity. For instance, an indicator value near threshold b would simultaneously hold fractional membership in both U2 level and U3 level, capturing transitional states typical of incomplete or ambiguous monitoring data. The key points serve as flexible classification boundaries, enabling adaptive quantification of risk levels while accommodating data vagueness. This design ensures the graph provides a robust foundation for the comprehensive evaluation model by translating complex uncertainty into interpretable membership degrees.

## 3.3 Establishing the dynamic safety assessment model

Based on the determination of the assessment index system and the weight coefficient calculation method, this paper integrates grey

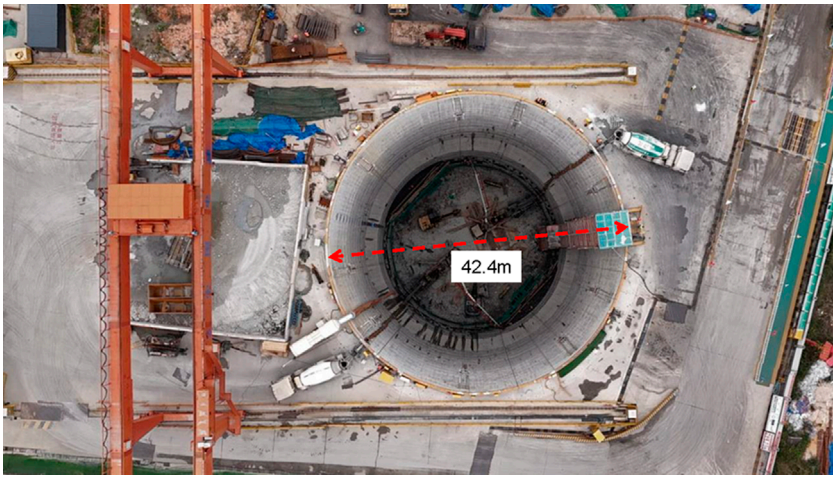


FIGURE 6
Bird-view of the excavated deep shaftLife Science Identifiers.

TABLE 4 Physical and mechanical parameters of soil layer.

| Soil layer | $\rho/(g \cdot cm^{-3})$ | $c/kPa$ | $\varphi/(°)$ | $E_e/MPa$ | $v$ | Thickness/m |
|---|---|---|---|---|---|---|
| Gravel clay | 2.66 | 20 | 20 | 12.6 | 0.35 | 12 |
| Heavily weathered granite | 2.53 | 350 | 25 | 6,200 | 0.32 | 21 |
| Rock mass fracture zone | 2.58 | 40 | 25 | 2,400 | 0.32 | 34 |
| Aeolian granite | 2.62 | 720 | 25 | 22,300 | 0.26 | 33 |

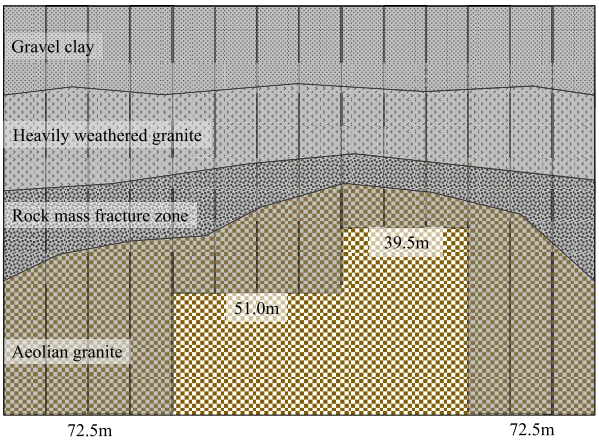


FIGURE 7
Stratum conditions and diaphragm wall layout.

clustering theory to establish a dynamic safety assessment model for deep foundation pit construction as shown in Figure 4. The model combines quantitative and qualitative analyses and relies on real-time monitoring data to dynamically assess the safety status of deep foundation pit construction through grey clustering analysis. It aims to effectively integrate data from multiple sources and expert knowledge, providing a comprehensive dynamic assessment of foundation pit safety through scientific weight allocation and clustering analysis.

The innovative aspect of this model lies in its integration of both quantitative and qualitative analyses, subjective and objective weight allocation, and the application of grey clustering theory to address the complex and variable environment of foundation pit construction and the uncertainty of monitoring data. By leveraging this model, accurate, real-time dynamic assessments of deep foundation pit construction safety can be achieved, providing robust support for risk management and decision-making in the construction process.

Compared to existing methods, our framework offers distinct advantages. Unlike FAHP, which relies on subjective expert judgment, our composite weighting method dynamically balances subjective and objective inputs, enhancing objectivity. In contrast to SVM, which requires large, clean datasets, grey clustering handles incomplete or uncertain data inherent in foundation pit monitoring. Furthermore, our comprehensive three-level index system integrates deformation, internal forces, and environmental factors, addressing the narrow indicator focus of prior studies. These advancements position our framework as a robust tool for real-time, data-driven safety assessment in deep foundation pit construction.

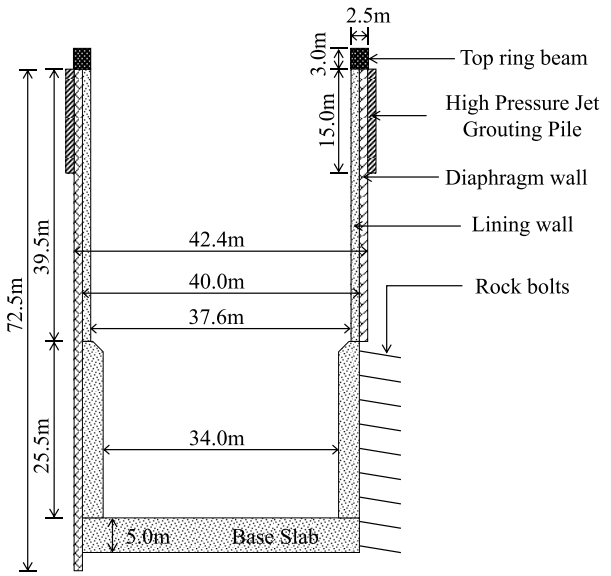


FIGURE 8
Profile of the shaft foundation pit.

To prevent the distortion that a single indicator might cause in the dynamic safety assessment results of the foundation pit, it is necessary to combine the assessment with the prominent primary factor method. Specifically, if any single dynamic monitoring data of the foundation pit exceeds the extreme value of the dangerous situation, the weight of that assessment factor is stipulated to be 1, and the weights of other factors are set to 0. The risk value is then calculated to determine the current danger level of the pit. If none of the deep foundation pit assessment indicators exceed the extreme values of the dangerous situation, proceed to the dynamic safety assessment calculation process. This involves using the assessment index system and the composite weighting values to conduct a dynamic safety assessment calculation for the deep foundation pit construction.

# 4 Case study

## 4.1 Project overview

The Luotian-Tiegang Reservoir water diversion tunnel is an important large-scale water conservancy project in Shenzhen (Figure 5), with a designed capacity of 2.6 million cubic meters per day. The main task of the project is to reasonably distribute and use the water from the West River in Shenzhen, optimize the allocation of new foreign water, ensure water supply to the western area of Shenzhen, and meet the long-term urban living and production water needs of Bao'an District and part of Nanshan District. The whole line of the project is located in Bao'an District and Guangming District in the west of Shenzhen, with a total length of 21.68 km and a cross-section diameter of 5.2 m. The main line includes three working diversion shafts, each with an outer diameter exceeding 30 m and a depth of over 60 m.

A dynamic assessment will be conducted on the Wuzhiba diversion shaft, which features the most complex geological conditions. The Wuzhiba diversion shaft is classified as a first-class ultra-deep circular foundation pit, with a final excavation depth of 72.5 m and an internal diameter of 42.4 m (Figure 6).

### 4.1.1 Geological conditions

The site is located in the western part of Shenzhen, consisting primarily of plain fill, gravelly clay, and granite. The soil profile consists of several distinct layers. Gravel clay at the surface extends to a depth of 12 m, characterized by low density and cohesion which could influence surface stability and water infiltration rates. Heavily weathered granite starts from 12 m down to 33 m, where the rock has degraded substantially, impacting its structural integrity and load-bearing capacity. Between 35.5 and 69.5 m, the fractured rock mass zone contains fragmented rock that could pose challenges for excavation construction. Aeolian granite below 69.5 m is less weathered, offering better stability. Based on the results of exploration and testing, combined with the experience of related local projects, the different mechanical and physical parameters of each soil layer are depicted in Table 4. The geological conditions within the pit area are average, with issues such as low strength, significant variations in weathering, and multiple layers of fractured rock.

### 4.1.2 Foundation pit excavation and support

In this shaft construction, a 1.2-m-thick diaphragm wall is utilized for retaining structure, but along circumferential direction the wall depths changes with detailed geological conditions, as shown in the layout diagram of the diaphragm wall in Figure 7. The entire diaphragm wall is divided into 30 sections along the circumference. High-pressure jet grouting piles are constructed at the joints of each segment for seepage prevention and reinforcement, with each pile extending 15 m in depth. The shaft will be excavated layer-wises from top to down, and the reinforced concrete shaft walls will be constructed for each newly excavated layer using the bottom-up method. The thickness of the upper part of the lining wall is 1.2 m, which increases to 3 m after reaching the fractured rock layer at a depth of 37.5 m. To ensure the stability and safety of the deep excavation, rock bolts are installed within the fractured rock zones. These bolts, made of HRB400 steel rebar with a diameter of 28mm, are installed at a 15-degree angle to penetrate 6 m depth into the rock, with 2 m spacing in vertical direction. The dimensions of the shaft pit are detailed in Figure 8.

After constructing the diaphragm wall and high-pressure jet grouting piles, excavation of the shaft foundation pit began on 1 May 2023, and the base slab was completed on 24 September 2023, with a total duration of about 147 days. The pit excavation of 75 m deep was divided into 21 layers, with each layer around 3.0 m. Following the excavation of each pit layer, the reinforcement concrete lining was constructed. And the next pit layer excavation was proceeded once the concrete strength (of the previous layer) had reached 80% of the design value, continuing this cycle until reaching the base slab. Specific pit excavation and lining construction parameters are detailed in Table 5.

TABLE 5 Construction parameters at different stages of deep foundation pit.

| Stage | Lining Height/m | Lining Thickness/m | Excavation Depth/m |
|---|---|---|---|
| First Layer (Top ring Beam) | 3 | 2.5 | 3.4 |
| Second Layer | 3 | 1.2 | 3.9 |
| Third to 13th Layer | 3 | 1.2 | 3 |
| Fourteenth Layer | 3 | 3 | 3.3 |
| Fifteenth Layer | 2.5 | 3 | 2.5 |
| Sixteenth to 20th Layer | 3 | 3 | 3 |
| Twenty-first Layer | 3 | 3 | 6.4 |
| Twenty-second Layer (Base Slab) | 5 | 5 | |

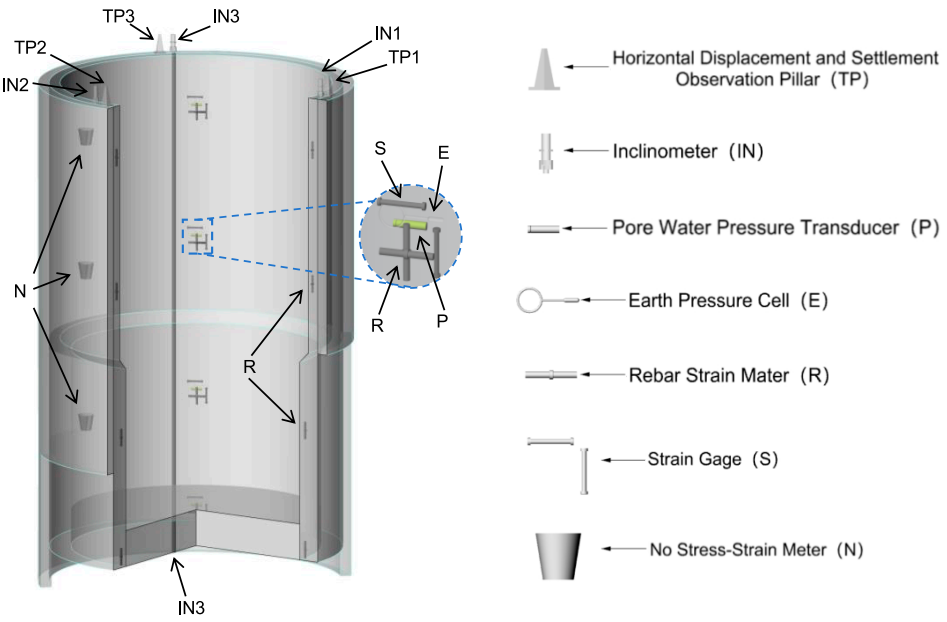


FIGURE 9
Axonometric view of monitoring facilities.

### 4.1.3 Monitoring plan and data acquisition

To ensure the safety of the deep shaft foundation pit construction, deformation monitoring is conducted simultaneously. Monitoring lines (L1-L3) are laid out at three different depths of the diaphragm wall, as shown in Figures 9, 10. The full monitoring plan is demonstrated in Figure 11 with details described as below.

#### 4.1.3.1 Bracing structural deformation indicators

Three observation piers (TP1~TP3) are set at the top of diaphragm wall to measure the horizontal displacement ($X_{11}$) and the vertical displacement ($X_{12}$) at the top of the retaining diaphragm wall. Adjacent to each observation pier, a total of three inclinometer casing (IN1~IN3) is embedded vertically within the diaphragm wall to monitor the lateral wall deflection ($X_{13}$) during the excavation process. IN1 to IN3 are installed at three different sections of the diaphragm wall, ranging from shortest to longest. For measuring surrounding ground deformation, three monitoring sections are set around the perimeter of the foundation pit, with each section comprising a radial measurement line. Each line has six settlement observation points arranged concentrically from the center of the pit outwards, monitoring the vertical ground displacement ($X_{15}$). The first observation point is located next to the P1 observation pier, 2 m away from the second point, with subsequent points spaced 8 m apart, totaling 24 observation points (BM1~BM18). Two monitoring holes, each 65 m deep (H1, H2), are set up to monitor the uplift of the shaft pit base ($X_{16}$). H1 is located near the shaft lining,

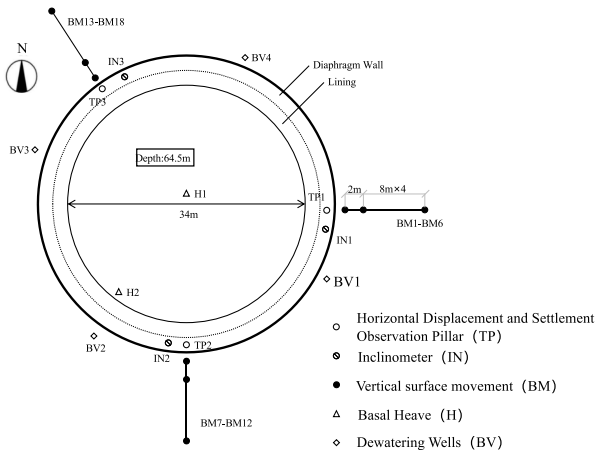


FIGURE 10
Plan view of monitoring facilities.

while H2 is at the center of the shaft. Each hole is equipped with ten magnetic ring-type stratification settlement markers at depths of 10, 18, 26, 34, 40, 46, 52, 56, 60, and 64 m. These rings are removed along with ongoing excavation progresses. Measurements are taken twice at each excavation depth, with one just at completion of layer excavation and the other later just before the subsequent excavation begins.

#### 4.1.3.2 Structural internal forces indicators

Five monitoring sections are set up on the horizontal plane of the foundation pit, with each section having four embedment depths and the base slab. Strain gauges, stress meters, and stress-free meters are installed on the reinforcement bars inside and outside the diaphragm wall, and at the base slab to monitor the supporting axial force ($X_{21}$), column internal force ($X_{26}$), anchor axial force ($X_{22}$), and the internal force of the retaining structure at different depths ($X_{25}$). Besides, soil and water pressures are measured at designated locations. Four sets of gauges, with each set combining one piezometer and one soil pressure gauge, are installed at four different depths on the outer surface of the diaphragm wall. Two piezometers are placed at the bottom and top of shaft base slab, and two earth pressure gauges are placed at the interface of the shaft base slab and the underlying rock soil to monitor the soil pressure ($X_{23}$) and pore water pressure ($X_{24}$) borne by different embedment sections of the diaphragm wall and the base slab.

#### 4.1.3.3 Environmental safety indicators

Groundwater monitoring holes (BV1~BV4) are arranged outside the foundation pit at every 90° to monitor the changes in groundwater level ($X_{31}$) around the shaft. These holes are drilled and installed outside the settlement observation points, 2.5 m away from them. Additionally, within a 100-m range beyond the edge of the foundation pit, monitoring is conducted for the surrounding environment, including residential houses, roadbeds, pipelines, and other protected facilities along the line. Deformation data is collected for pipeline displacement ($X_{32}$), adjacent roadbed settlement ($X_{34}$), adjacent building displacement ($X_{33}$), and ground surface cracks ($X_{35}$).

The lateral wall displacements from different excavation stages were collected and demonstrated in Figure 11. In Figure 11A, the shortest segment of the diaphragm wall (IN1) exhibits a gradual increase in lateral wall displacement during various excavation stages. This increase predominantly occurs as the wall traverses vertically through gravel clay and heavily weathered granite layers, which, despite their differing mechanical properties, both possess some degree of flexibility and compressibility, effectively dispersing lateral pressure. However, during the baseplate phase, as the wall transitions from heavily weathered granite to aeolian granite, there is a sudden significant increase in displacement. This surge is due to the high elastic modulus and stiffness of aeolian granite, which causes a drastic change in the properties of the soil layers, concentrating stress in this region, coupled with the maximum vertical pressure induced by increased excavation depth, collectively exacerbating the lateral displacement of the wall at this stage.

In Figure 11B, the medium-length diaphragm wall (IN2) shows a lateral wall deflection curve that transitions gradually from being relatively flat to significantly increasing from the early excavation stage to the baseplate phase. Initially, the displacement is minimal, indicating that the wall is well-supported by the upper soil layers. However, as the excavation depth increases, particularly at the onset of the baseplate phase, there is a noticeable surge in the curve, likely due to construction disturbances such as soil excavation and heavy equipment operation, which dynamically impact the wall in the absence of sufficient lower soil support. This change illustrates that the lateral pressure on the wall increases with excavation depth, directly affecting the stability of the wall due to construction activities.

In Figure 11C, the lateral wall deflection of the longest segment of the diaphragm wall demonstrates a trend of gradual increase with excavation depth, with the most significant displacement occurring during the baseplate phase. Notably, significant displacement anomalies at a depth of 2–5 m are especially prominent, primarily due to the installation of a construction pathway on the lining wall in this region of the diaphragm wall. The establishment and use of the construction pathway led to significant construction disturbances, generating intense vibrations and dynamic loads directly near the retaining structure.

This comprehensive analysis reveals that as excavation depth increases, the displacement of the diaphragm walls gradually increases, especially in areas where soil conditions change or construction activities are concentrated.

## 4.2 Safety assessment results

### 4.2.1 Weights of indicators

Ten experts evaluated the primary indices of the deep foundation pit construction safety dynamic assessment system using the Delphi method. The indices were ranked in descending order of importance as structural deformation indicators, structural internal forces indicators, and environmental safety indicators. The relative importance levels between adjacent indicators were set as $r_2 = 1.2$ and $r_3 = 1.3$. Subjective weights for the primary, secondary, and tertiary indices were calculated accordingly, with tertiary indices within the same category assigned equal weight proportions of 0.5.

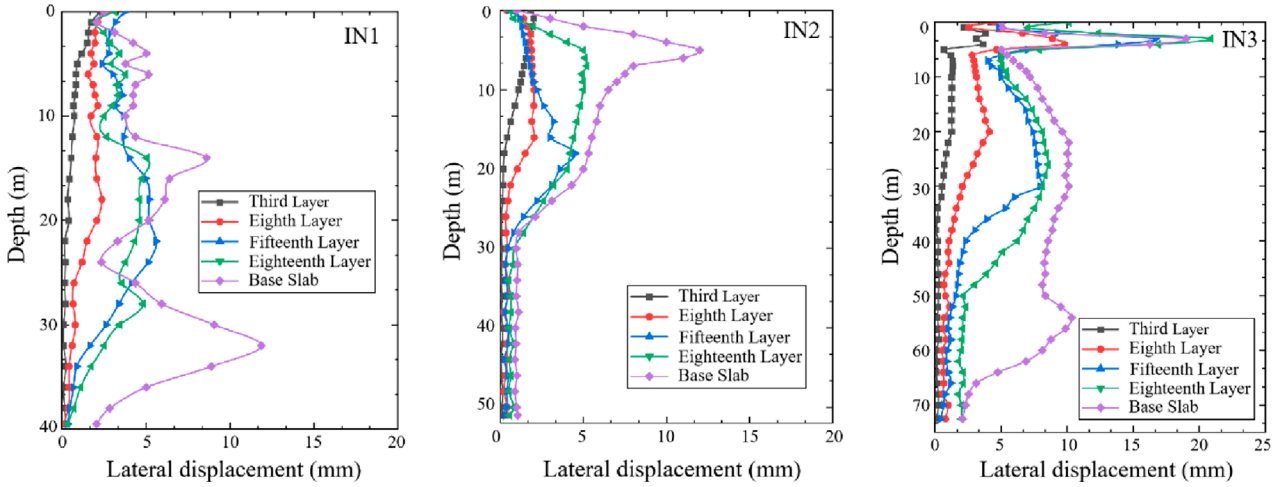


FIGURE 11
Lateral wall deflection at different excavation stages.

Onsite monitoring provided data for the assessment system, which was standardized and used to calculate information entropy and objective weights. Finally, combined weights were determined by integrating subjective and objective weights, and the comprehensive weights of tertiary indicators were calculated. The results are summarized in Table 6.

### 4.2.2 Dynamic safety assessment

Grey clustering analysis is employed to evaluate the current safety level of the foundation pit construction using real-time monitoring data. An assessment matrix is established based on the on-site monitoring data. By substituting the data of the third-level indicators of the foundation pit into the whitening power functions, the weight coefficient matrix is obtained. Ultimately, the level to which the indicator belongs is determined based on the principle of maximum membership degree, as shown in Appendix. By determining the level through the membership degree, we can clearly observe the varying safety conditions of each monitoring indicator.

Three groups of representative monitoring data were selected respectively, analyzed through the dynamic evaluation of deep foundation pit construction safety, and finally selected the safety data collected during the excavation of the eighth layer, the 15th layer and the Twenty-second Layer. These layers correspond to distinct geological formations and have unique characteristics and risks associated with their excavation. The eighth layer is within the heavily weathered granite, the 15th layer is within the rock mass fracture zone, and the base layer reaches down to the aeolian granite.

The excavation of the eighth layer occurs early in the project timeline, a period when the overall pit stability is comparatively high. This layer consists of heavily weathered granite, which is relatively unstable and prone to crumbling. The weathered nature of the granite increases the risk of sudden soil shifts and collapses. The safety level of foundation pit excavated on the eighth layer is obtained by summarizing the data, as shown in Figure 12. During the excavation of this layer, monitoring focused on structural deformation indicators due to the unstable nature of the soil. The safety indices during this phase showed elevated levels of deformation, indicating stress within the excavation walls.

The eighth layer's elevated deformation risks are directly linked to the geological properties of heavily weathered granite. This layer's low stiffness and high compressibility, combined with the transition from initial diaphragm wall support to permanent concrete lining, created stress concentrations. Monitoring data showed cumulative horizontal displacement of 18 mm and lateral wall deflection of 22 mm. These trends align with the layer's interspersed weathered rock fragments and clay matrix, which reduced load-bearing capacity and amplified deformation under excavation unloading.

The high membership degree value of the top horizontal displacement of the retaining structure (X11) in the safety level U1 indicates that the stability of this indicator is currently good. The membership degree of the deep horizontal displacement (X13) shows that it is mostly in a safe state but with a certain warning trend, suggesting that we need to pay close attention and adjust the support structure in a timely manner. The membership degree analysis of the internal force of the retaining wall (X25) shows that it remains within the safe range in the vast majority of cases, but the membership degree of the warning level should not be ignored, implying that additional monitoring and preventive measures may be needed during the construction process. The high membership degree value of the neighboring building displacement (X33) in U1 provides us with confidence, indicating that the impact of foundation pit construction on the surrounding environment has been effectively controlled.

The 15th layer's fractured rock zone posed significant challenges due to uneven stress distribution and groundwater infiltration. Monitoring data showed a sudden increase in lateral wall deflection, coinciding with the transition to 3 m-thick lining walls. This structural modification altered load transfer mechanisms, reflected in internal force indicators: supporting axial force increased by 25% compared to the previous layer, while earth pressure reached 72% of design capacity. The fractured zone's fragmented rock matrix amplified stress concentrations.

10.3389/feart.2025.1583402

TABLE 6 Comprehensive weight calculation results of indicators at all levels primary index.

| Primary index (local weights) | Secondary index (local weights) | Three-level index (comprehensive weight) |
|---|---|---|
| Structural deformation (0.438) | $X_{11}$ (0.201) | $X_{111}$ (0.054) |
| | | $X_{112}$ (0.044) |
| | $X_{12}$ (0.209) | $X_{121}$ (0.028) |
| | | $X_{122}$ (0.020) |
| | $X_{13}$ (0.256) | $X_{131}$ (0.032) |
| | | $X_{132}$ (0.028) |
| | $X_{14}$ (0.108) | $X_{141}$ (0.026) |
| | | $X_{142}$ (0.025) |
| | $X_{15}$ (0.125) | $X_{151}$ (0.026) |
| | | $X_{152}$ (0.024) |
| | $X_{16}$ (0.131) | $X_{161}$ (0.023) |
| | | $X_{162}$ (0.021) |
| Structural internal forces (0.342) | $X_{21}$ (0.160) | $X_{211}$ (0.032) |
| | $X_{22}$ (0.147) | $X_{221}$ (0.029) |
| | $X_{23}$ (0.226) | $X_{231}$ (0.044) |
| | $X_{24}$ (0.164) | $X_{241}$ (0.026) |
| | $X_{25}$ (0.165) | $X_{251}$ (0.021) |
| | $X_{26}$ (0.109) | $X_{261}$ (0.019) |
| Environmental safety (0.22) | $X_{31}$ (0.262) | $X_{311}$ (0.023) |
| | | $X_{312}$ (0.021) |
| | $X_{32}$ (0.226) | $X_{321}$ (0.011) |
| | | $X_{322}$ (0.010) |
| | $X_{33}$ (0.229) | $X_{331}$ (0.016) |
| | | $X_{332}$ (0.013) |
| | $X_{34}$ (0.163) | $X_{341}$ (0.008) |
| | | $X_{342}$ (0.006) |
| | $X_{35}$ (0.140) | $X_{351}$ (0.009) |
| | | $X_{352}$ (0.007) |

The 15th Layer Excavation represents a pivotal stage in the construction process, not only because it lies within a fracture zone but also due to changes in the lining wall thickness and construction methodologies. The rock mass fracture zone is characterized by fragmented rock layers with potential voids and uneven stress distribution. This can lead to unpredictable movements and a higher risk of localized failures. The safety level of foundation pit excavated on the 15th layer is obtained by summarizing the data, as shown in Figure 13.

The 20-s layer is also the excavation of the base slab signifies the conclusion of the pit's excavation stages. This final layer provides a comprehensive view of the impacts of construction disturbances

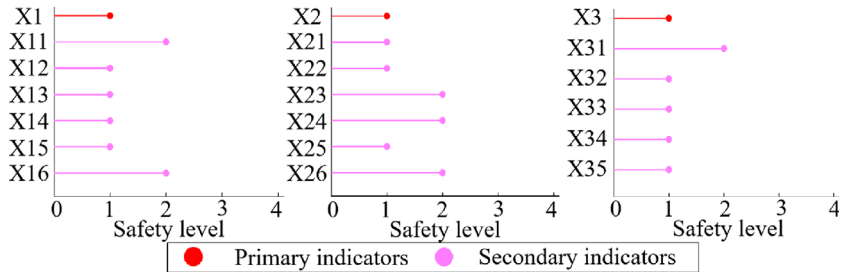


FIGURE 12
Safety dynamic assessment of the eighth layer excavation.

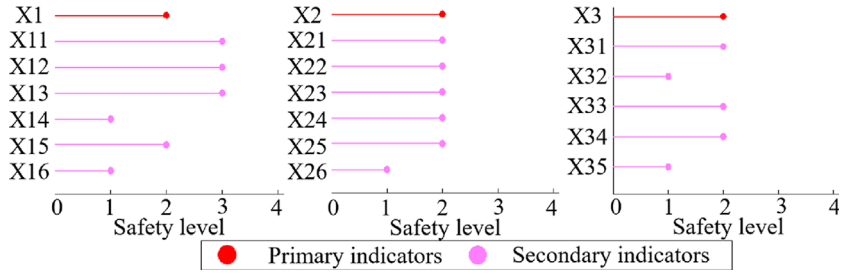


FIGURE 13
Safety dynamic assessment of the 15th layer excavation.

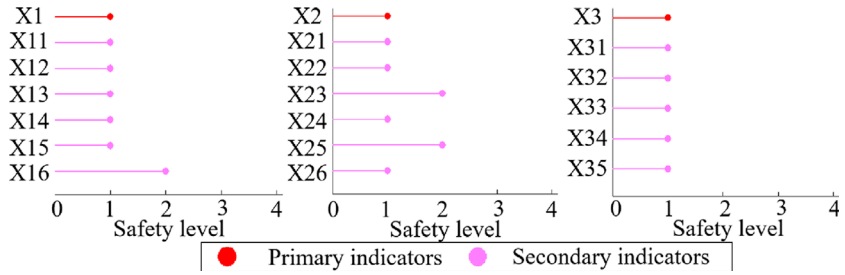


FIGURE 14
Safety dynamic assessment of the base slab excavation.

on the pit's stability throughout the project. By this stage, the data collected offers a complete picture of how well the excavation and support strategies have performed against initial projections and across varying geological conditions. Monitoring at this depth is crucial for ensuring that the base of the pit remains stable and that any signs of undue stress or deformation can be promptly addressed. Finally, the safety level when the excavation of the foundation pit is completed is shown in Figure 14.

## 4.3 Limitations of this study

In-depth exploration of the effectiveness and application value of the proposed dynamic assessment method for deep foundation pit construction safety, based on gray clustering and moment estimation, leads us to discuss some limitations encountered during the research process. These limitations may include data availability, potential biases in subjective assessments, and the need for further validation in diverse scenarios. Addressing these challenges will be essential for enhancing the robustness and applicability of the proposed methodology.

(1) The safety risk levels established by this research model are based on current regulations used for evaluating deep foundation pit construction safety risks. These regulations often incorporate significant safety margins to ensure absolute project safety, indicating that the assessment method still has room for refinement and enhancement.

Further calibration of the model could provide more precise risk assessments tailored to specific project conditions.

(2) In this study, the construction of the whitening weight function in the application of gray clustering analysis primarily relies on data generated from numerical simulations rather than directly sourced from actual engineering monitoring databases. While numerical simulations provide a relatively controlled and systematic environment for testing and validating the assessment method, they may not fully capture the complexities and uncertainties inherent in real-world construction processes. This limitation suggests the need for further integration of field data to enhance the model's applicability and accuracy.

(3) A notable limitation of this study is the absence of dynamic threshold optimization for monitoring indicators, which could be addressed by integrating data-driven frameworks such as the multi-objective expected value optimization (MEVO) method (Wang et al., 2024). This approach standardizes monitoring data and refines early-warning thresholds through grey relational analysis and Monte Carlo simulations, reducing false alarms and improving risk classification accuracy. For instance, the vertical displacement rate of the retaining structure ($X_{112}$) could benefit from threshold optimization to better reflect its safety boundaries. Future research should explore this integration to enhance the adaptability of the assessment model under complex geological conditions.

## 5 Conclusion

This study develops a dynamic safety assessment model for deep foundation pit construction, utilizing a combination of gray clustering and moment estimation weighting. Validation through engineering case studies indicates the model's strong applicability and accuracy. Key findings include.

(1) A comprehensive three-level safety assessment index system comprising 21 indicators is established, incorporating both subjective and objective weight calculations. The gray clustering algorithm categorizes these indicators into structural, mechanical, and environmental safety aspects;

(2) The model's reliability is corroborated by comparisons between numerical simulations and on-site monitoring data from a water diversion well project in Shenzhen, demonstrating consistent trends;

(3) The resilience assessment reveals that the foundation pit is currently at level U1, indicating a safe condition that aligns with actual project observations.

This model provides a scientific basis for optimizing construction strategies and formulating effective risk control measures, highlighting its significant contribution to engineering practices.

The study has confirmed the dynamic assessment method's efficacy for deep foundation pit construction safety and pinpointed areas for future enhancement. Future work should refine safety risk assessment criteria to account for diverse geological and construction factors, promoting more efficient resource use. Additionally, it is essential to gather more real-world engineering data to enhance the accuracy and applicability of the assessment models.

## Data availability statement

The original contributions presented in the study are included in the article/supplementary material, further inquiries can be directed to the corresponding authors.

## Author contributions

PD: Conceptualization, Methodology, Writing – original draft, Writing – review and editing. ZL: Conceptualization, Investigation, Methodology, Resources, Writing – original draft, Writing – review and editing. DZ: Data curation, Writing – original draft. HL: Data curation, Validation, Writing – original draft. ZC: Investigation, Software, Validation, Writing – original draft. LC: Formal Analysis, Project administration, Writing – original draft. YL: Investigation, Project administration, Writing – original draft.

## Funding

The author(s) declare that no financial support was received for the research and/or publication of this article.

## Conflict of interest

Authors PD, DZ, HL, LC, and YL were employed by Sinohydro Bureau 14 Co., Ltd.

The remaining authors declare that the research was conducted in the absence of any commercial or financial relationships that could be construed as a potential conflict of interest.

## Generative AI statement

The author(s) declare that no Generative AI was used in the creation of this manuscript.

## Publisher's note

All claims expressed in this article are solely those of the authors and do not necessarily represent those of their affiliated organizations, or those of the publisher, the editors and the reviewers. Any product that may be evaluated in this article, or claim that may be made by its manufacturer, is not guaranteed or endorsed by the publisher.

# References


Ahn, B. S. (2011). Compatible weighting method with rank order centroid: maximum entropy ordered weighted averaging approach. *Eur. J. operational Res.* 212 (3), 552–559. doi:10.1016/j.ejor.2011.02.017

Akih-Kumgeh, B. (2016). Toward improved understanding of the physical meaning of entropy in classical thermodynamics. *Entropy* 18 (7), 270. doi:10.3390/e18070270

Bao, X., Huang, J., Shen, J., Wu, X., Wang, T., Chen, X., et al. (2025). A novel method of void detection in rebar-affected areas based on transfer learning and improved YOLOv8. *Tunn. Undergr. Space Technol.* 158, 106440. doi:10.1016/j.tust.2025.106440

Bao, X., Li, J., Shen, J., Chen, X., Zhang, C., and Cui, H. (2025). Comprehensive multivariate joint distribution model for marine soft soil based on the vine copula. *Comput. Geotechnics* 177, 106814. doi:10.1016/j.compgeo.2024.106814

Bao, X., Yuan, H., Shen, J., Liu, C., Chen, X., and Cui, H. (2024). Numerical analysis of seismic response of a circular tunnel-rectangular underpass system in liquefiable soil. *Comput. geotechnics* 174, 106642. doi:10.1016/j.compgeo.2024.106642

Chen, K., Chen, P., Yang, L., and Jin, L. (2019). Grey clustering evaluation based on AHP and interval grey number. *Int. J. Intelligent Comput. Cybern.* 12 (1), 127–137. doi:10.1108/ijicc-04-2018-0045

Chen, X., Shen, J., Bao, X., Wu, X., Tang, W., and Cui, H. (2023). A review of seismic resilience of shield tunnels. *Tunn. Undergr. Space Technol.* 136, 105075. doi:10.1016/j.tust.2023.105075

Chin, Y., Shen, S., Zhou, A., and Chen, J. (2019). Foundation pit collapse on 8 june 2019 in nanning, China: a brief report. *Safety* 5, 68. doi:10.3390/safety5040068

Feng, S. J., and Lu, S. F. (2016). Failure of a retaining structure in a metro station excavation in Nanchang City, China. *J. Perform. Constr. Facil.* 30 (4), 04015097. doi:10.1061/(asce)cf.1943-5509.0000855

Gong, X. N., and Zhang, X. C. (2012). Excavation collapse of Hangzhou subway station in soft clay and numerical investigation based on orthogonal experiment method. *J. Zhejiang Univ. Sci. A* 13 (10), 760–767. doi:10.1631/jzus.a1200120

Li, B., Lin, Z., Chen, Y., Xu, C., Li, P., and Ding, H. (2023). Numerical analysis for supporting and deformation of complex foundation pit groups in unstable areas of karst strata. *Front. Earth Sci.* 11, 1283184. doi:10.3389/feart.2023.1283184

Li, C., Chen, K., and Xiang, X. (2015). An integrated framework for effective safety management evaluation: application of an improved grey clustering measurement. *Expert Syst. Appl.* 42 (13), 5541–5553. doi:10.1016/j.eswa.2015.02.053

Li, D., Liao, F., Wang, L., Lin, J., and Wang, J. (2024). Multi-stage and multi-parameter influence analysis of deep foundation pit excavation on surrounding environment. *Buildings* 14 (1), 297. doi:10.3390/buildings14010297

Li, X., Hipel, K. W., and Dang, Y. (2015). An improved grey relational analysis approach for panel data clustering. *Expert Syst. Appl.* 42 (23), 9105–9116. doi:10.1016/j.eswa.2015.07.066

Liu, S., and Yang, Y. (2017). Explanation of terms of grey clustering evaluation models. *Grey Syst. Theory Appl.* 7 (1), 129–135. doi:10.1108/gs-11-2016-0046

Liu, W., Zhang, J., Jin, M., Liu, S., Chang, X., Xie, N., et al. (2017). Key indices of the remanufacturing industry in China using a combined method of grey incidence analysis and grey clustering. *J. Clean. Prod.* 168, 1348–1357. doi:10.1016/j.jclepro.2017.09.078

Lv, Y., Jiang, Y., Hu, W., Cao, M., and Mao, Y. (2020). A review of the effects of tunnel excavation on the hydrology, ecology, and environment in karst areas: current status, challenges, and perspectives. *J. Hydrology* 586, 124891. doi:10.1016/j.jhydrol.2020.124891

Ministry of Housing and Urban-Rural Development of the People's Republic of China (2019). *Technical code for construction safety of deep building foundation excavations; jgj311-2013*. Beijing, China: China Architecture and Building Press, 4.

Ministry of Housing and Urban-Rural Development of the People's Republic of China (2019). *Technical specification for retaining and protection of building foundation excavations; jgj120-2012*. Beijing, China: China Architecture and Building Press, 6.

Ministry of Housing and Urban-Rural Development of the People's Republic of China (2019). *Technical Standard for Monitoring of building excavation engineering; GB 50497-2019*. Beijing, China: China Plans Publishing House, 34–36.

Pearson, K. (1936). Method of moments and method of maximum likelihood. *Biometrika* 28 (1/2), 34–47. doi:10.1093/biomet/28.1-2.34

Qiao, Y., Xie, F., Bai, Z., Lu, J., and Ding, W. (2024). Deformation characteristics of ultra-deep circular shaft in soft soil: a case study. *Undergr. Space* 16, 239–260. doi:10.1016/j.undsp.2023.09.006

Shen, J., Bao, X., Chen, X., Wu, X., Qiu, T., and Cui, H. (2025). Seismic resilience assessment method for tunnels based on cloud model considering multiple damage evaluation indices. *Tunn. Undergr. Space Technol.* 157, 106360. doi:10.1016/j.tust.2024.106360

Shen, J., Bao, X., Li, J., Chen, X., and Cui, H. (2025). Study on the mechanism of EPWP dissipation at the joints of shield tunnel in liquefiable strata during seismic events. *Soil Dyn. Earthq. Eng.* 188, 109089. doi:10.1016/j.soildyn.2024.109089

Sun, Z., Li, H., Bao, Y., Meng, X., and Zhang, D. (2023). Intelligent risk prognosis and control of foundation pit excavation based on digital twin. *Buildings* 13 (1), 247. doi:10.3390/buildings13010247

Tan, Y., Lu, Y., and Wang, D. (2023). Interactive behaviors of four closely spaced mega excavations in soft clays: case study on an excavation group in Shanghai, China. *Tunn. Undergr. Space Technol.* 138, 105186. doi:10.1016/j.tust.2023.105186

Wang, X., Pan, Y., Li, M., and Chen, J. (2024). A novel data-driven optimization framework for unsupervised and multivariate early-warning threshold modification in risk assessment of deep excavations. *Expert Syst. Appl.* 238, 121872. doi:10.1016/j.eswa.2023.121872

Wei, D., Xu, D., and Zhang, Y. (2020). A fuzzy evidential reasoning-based approach for risk assessment of deep foundation pit. *Tunn. Undergr. Space Technol.* 97, 103232. doi:10.1016/j.tust.2019.103232

Wooldridge, J. M. (2001). Applications of generalized method of moments estimation. *J. Econ. Perspect.* 15 (4), 87–100. doi:10.1257/jep.15.4.87

Wu, B., Zeng, J., Zhu, R., Yang, F., Liu, C., and Xie, Y. (2024). A collapse risk assessment method for subway foundation pit based on cloud model and improved Dempster–Shafer evidence theory. *Sci. Rep.* 14 (1), 2653. doi:10.1038/s41598-024-52643-x

Wu, R. M., Zhang, Z., Yan, W., Fan, J., Gou, J., Liu, B., et al. (2022). A comparative analysis of the principal component analysis and entropy weight methods to establish the indexing measurement. *PloS one* 17 (1), e0262261. doi:10.1371/journal.pone.0262261

Xu, J., and Wang, Y. (2022). Stability analysis and support design methods for rock foundation pit with combination of structural plane and karst cave. *Adv. Civ. Eng.* 2022 (1), 5662079. doi:10.1155/2022/5662079

Xu, Q., Xie, J., Zhu, H., and Lu, L. (2024). Supporting behavior evolution of ultra-deep circular diaphragm walls during excavation: monitoring and assessment methods comparison. *Tunn. Undergr. Space Technol.* 143, 105495. doi:10.1016/j.tust.2023.105495

Ye, F., Sun, J., Wang, Y., Nedjah, N., and Bu, W. (2023). A novel method for the performance evaluation of institutionalized collaborative innovation using an improved G1-CRITIC comprehensive evaluation model. *J. Innovation and Knowl.* 8 (1), 100289. doi:10.1016/j.jik.2022.100289

Ye, S., Zhao, Z., and Wang, D. (2021). Deformation analysis and safety assessment of existing metro tunnels affected by excavation of a foundation pit. *Undergr. Space* 6 (4), 421–431. doi:10.1016/j.undsp.2020.06.002

Zhao, J., Tan, Z., Yu, R., Li, Z., Zhang, X., and Zhu, P. (2022). Deformation responses of the foundation pit construction of the urban metro station: a case study in Xiamen. *Tunn. Undergr. Space Technol.* 128, 104662. doi:10.1016/j.tust.2022.104662

Zhou, Y., Li, S., Zhou, C., and Luo, H. (2019). Intelligent approach based on random forest for safety risk prediction of deep foundation pit in subway stations. *J. Comput. Civ. Eng.* 33 (1), 05018004. doi:10.1061/(asce)cp.1943-5487.0000796

Zhou, Y., Su, W., Ding, L., Luo, H., and Love, P. E. (2017). Predicting safety risks in deep foundation pits in subway infrastructure projects: support vector machine approach. *J. Comput. Civ. Eng.* 31 (5), 04017052. doi:10.1061/(asce)cp.1943-5487.0000700

frontiers | Frontiers in Earth Science

TYPE Original Research
PUBLISHED 06 May 2025
DOI 10.3389/feart.2025.1581090



OPEN ACCESS

EDITED BY
Zhang Cong,
Central South University Forestry and Technology, China

REVIEWED BY
Yi Chang,
East China University of Technology, China
Pengjiao Jia,
Soochow University, China
Fei Huang,
Flinders University, Australia

*CORRESPONDENCE
Ying Yang,
493662400@qq.com

RECEIVED 21 February 2025
ACCEPTED 01 April 2025
PUBLISHED 06 May 2025

CITATION
Wang J, Yang Y, Yang X, Lu Y, Liu Y, Hu D and Hu Y (2025) The prediction of karst-collapse susceptibility levels based on the ISSA-ELM integrated model.
*Front. Earth Sci.* 13:1581090.
doi: 10.3389/feart.2025.1581090



# The prediction of karst-collapse susceptibility levels based on the ISSA-ELM integrated model

Jiaxin Wang[1], Ying Yang[2]*, Xian Yang[3], Yulong Lu[4], Yang Liu[4], Da Hu[3] and Yongjia Hu[5]

[1]Department of Natural Resources, Hunan Vocational College of Engineering, Changsha, China, [2]Department of Discipline Inspection and Supervision,, Hunan Vocational College of Engineering, Changsha, China, [3]Hunan Engineering Research Center of Structural Safety and Disaster Prevention for Urban Underground Infrastructure, Hunan City University, Yiyang, China, [4]School of Earth Sciences and Spatial Information, Hunan University of Science and Technology, Xiangtan, China, [5]School of Resources and Safety Engineering, Central South University, Changsha, China

Karst collapse, a sudden geological hazard with complex mechanisms and low predictability, presents significant threats to urban safety and sustainable development by jeopardizing human lives and infrastructure. To address the limitations of conventional prediction methods, in this study, we introduce an enhanced predictive model, the improved sparrow search algorithm-optimized extreme learning machine (ISSA-ELM), for accurate karst-collapse susceptibility assessment. The methodology incorporates two key innovations: first, it applies a Singer chaotic mapping technique to enhance the sparrow search algorithm (SSA), effectively mitigating local optima entrapment by increasing population diversity and enhancing global search capabilities. Second, the optimized ISSA automatically adjusts the initial weights and thresholds of the ELM, whereas a five-fold cross-validation is used to determine the optimal hidden layer configuration, forming an adaptive and intelligent prediction framework. When validated against 20 datasets from a representative karst region, the proposed model achieved exceptional performance, with a mean absolute error (MAE) of 0.0544 and a coefficient of determination ($R^2$) of 0.9914, significantly surpassing the prediction accuracy of conventional ELM and SSA-ELM models. The results underscore the ISSA-ELM's superior nonlinear fitting capability, enhanced generalization performance, and outstanding stability in practical engineering applications. This research offers a solid scientific foundation for risk classification and hazard mitigation strategies while introducing a novel methodological framework through the integration of innovative algorithms. The proposed technical pathway provides significant theoretical advancements and practical engineering values for geological disaster prediction systems.

KEYWORDS

**karst collapse, susceptibility prediction, improved sparrow search algorithm, extreme learning machine, ISSA-ELM integrated model**

## 1 Introduction

Karst collapse, a prominent geological hazard, arises from the interaction between karst formation processes and groundwater dynamics. It often results in sudden surface subsidence or structural failure which occurs due to the

progressive development of subsurface voids and fractures (Bouzerda et al., 2024; Wang et al., 2024; Xiaozhen et al., 2024). With its concealed nature, intricate triggering mechanisms, and significant destructive potential, karst collapse poses substantial challenges to urban development and infrastructure security in vulnerable regions. Conducting an accurate susceptibility assessment is crucial for enhancing disaster prevention frameworks and guiding sustainable land-use planning.

The development of karst collapse prediction methodologies has progressed through distinct phases, evolving from qualitative evaluations (Gao et al., 2009; Luo and Shen, 2018) to more sophisticated quantitative analyses. Early research primarily established qualitative models based on genetic mechanism analysis. Subsequent interdisciplinary advancements introduced semi-quantitative approaches, including Fisher discriminant analysis (Huang et al., 2011; Jiang and Jiang, 2012) and the Analytic Hierarchy Process (AHP) (Jiyuan et al., 2021; YanHua et al., 2022). Additionally, quantitative frameworks such as fuzzy logic systems (Zhang et al., 2021; Zhuang, 2022) and grey system theory (Qiu, 2004; Meng et al., 2009; Gao et al., 2018; Ding et al., 2019) were developed. More recently, machine learning techniques have significantly enhanced prediction accuracy by modeling complex nonlinear relationships. Techniques such as backpropagation neural networks (BPNNs) (Bao and Hu, 2002; Chen et al., 2005; Yang et al., 2023; Journal of Chemistry, 2023), entropy-weighted cloud models (Chen et al., 2019; Wei et al., 2021), support vector machines (SVMs) (Lai and Qiao, 2008; En et al., 2011; Zhou et al., 2020), random forests (RFs) (Wang et al., 2022; Ren et al., 2023), and extreme learning machines (ELMs) (Xie et al., 2021) have been widely applied. Despite these advancements, current methodologies face several limitations. First, conventional statistical methods (e.g., AHP and fuzzy analysis) rely heavily on expert judgment, leading to subjective biases and challenges in determining objective weights. Second, data-driven models (e.g., BPNN and RF) often experience optimization challenges, including convergence to local minima and sensitivity to parameter selection. Additionally, traditional ELM implementations suffer from instability due to random weight initialization, compromising their reliability in engineering applications.

To address these constraints, in this study, we propose an optimized prediction framework (ISSA-ELM) that integrates an improved sparrow search algorithm (ISSA) with the extreme learning machine architecture. The method uses a three-fold optimization strategy: First, principal component analysis (PCA) reduces the dimensionality of collapse-influencing factors, minimizing multicollinearity while retaining essential diagnostic information. Second, Singer chaotic mapping enhances the standard sparrow search algorithm (SSA) by improving population diversity, expanding the search space, and preventing premature convergence. Third, an adaptive optimization framework combines the refined ISSA with K-fold cross-validation to optimize ELM hyperparameters, ensuring robust model generalization. Empirical validation through case studies in representative karst regions demonstrates that the ISSA-ELM outperforms conventional methods in predictive accuracy, particularly for susceptibility zonation. This methodological advancement offers a novel paradigm for regional-scale geological risk management, providing both theoretical insights and practical values for geological disaster prevention and land-use planning.

# 2 Theory of the ISSA-ELM integrated model

## 2.1 Principal component analysis

PCA, initially proposed by Pearson (1901), is a widely adopted dimensionality reduction technique. It converts multiple indicators into a smaller set of comprehensive variables (Zhou et al., 2020; Cao et al., 2015). This approach not only reduces data complexity but also preserves key relationships among variables. The main steps of PCA are as follows.

### 2.1.1 Data standardization

Given $n$ samples and $p$ influencing factors, the original data matrix is represented as shown in Equation 1:

$$Z = \left(z_{ij}\right)_{n\times p}, (i = 1,2,3,\cdots,n; j = 1,2,3,\cdots,p). \tag{1}$$

Standardization is applied using the formula as shown in Equation 2:

$$Z^* = \left(z_{ij}{}^*\right)_{n\times p}, (i = 1,2,3,\cdots,n; j = 1,2,3,\cdots,p), \tag{2}$$

where

$$z^* = \frac{z_{ij} - \frac{1}{n}\sum_{i=1}^{n} z_{ij}}{\sqrt{\frac{1}{n-1}\sum_{i=1}^{n}\left(z_{ij} - \overline{z_j}\right)^2}}, (i = 1,2,3,\cdots,n; j = 1,2,3,\cdots,p). \tag{3}$$

In Equation 3, $z_{ij}$ is the observed value of the $j$th variable of the $i$th sample, and $\overline{z_j}$ is the sample mean of the $j$th variable.

### 2.1.2 Correlation coefficient matrix calculation

The correlation coefficient matrix $R$ can be calculated using Equation 4:

$$\mathrm{R} = \frac{1}{n-1}\boldsymbol{Z}^{*T}\boldsymbol{Z}^*, \tag{4}$$

where $\mathrm{Z}^*$ represents the standardized data matrix.

### 2.1.3 Eigenvalue and eigenvector computation

The eigenvalues $\lambda_1 \geq \lambda_2 \geq \lambda_3 \geq \ldots \geq \lambda_p$ of the correlation coefficient matrix $\boldsymbol{R}$ are calculated, and their corresponding orthogonal eigenvectors are as follows:

$$a_i = \left(a_{i1}, a_{i2}, a_{i3}, \ldots, a_{ip}\right)^T, (i = 1,2,3,\ldots,p).$$

### 2.1.4 Variance contribution rate and cumulative Variance contribution rate

The variance contribution rate $\beta_i$ and the cumulative variance contribution rate $\beta(i)$ can be calculated using Equations 5, 6:

$$\beta_i = \frac{\lambda_i}{\sum_{i=1}^{p}\lambda_i}, \ (i = 1,2,3,\cdots,p), \tag{5}$$

$$\beta(i) = \sum_{i=1}^{p}\beta_i, \ (i = 1,2,3,\cdots,p). \tag{6}$$

### 2.1.5 Principal component selection

Principal components are selected when the cumulative variance contribution rate reaches 85% or higher, ensuring most of the original data information is retained (Zhou et al., 2020).

## 2.2 Sparrow search algorithm

The SSA is a swarm intelligence optimization algorithm introduced by Xue and Shen (2020). It simulates the foraging and anti-predation behaviors of sparrow flocks to find optimal solutions. The sparrow population consists of discoverers, followers, and sentinels, represented by an n × d matrix (as shown in Equation 7), where n is the number of sparrows, d denotes the dimension, and $x_{nd}$ represents the *j*th dimension of the *i*th sparrow. The fitness value for each sparrow is represented as $F_x$ (as shown in Equation 8).

$$\boldsymbol{X} = \begin{bmatrix} x_{11} & x_{12} & \cdots & x_{1d} \\ x_{21} & x_{22} & \cdots & x_{2d} \\ \vdots & \vdots & \ddots & \vdots \\ x_{n1} & x_{n2} & \cdots & x_{nd} \end{bmatrix}, \tag{7}$$

$$\boldsymbol{F}_x = \begin{bmatrix} f([x_{11} \quad x_{12} \quad \cdots \quad x_{1d}]) \\ f([x_{21} \quad x_{22} \quad \cdots \quad x_{2d}]) \\ \vdots \\ f([x_{n1} \quad x_{n2} \quad \cdots \quad x_{nd}]) \end{bmatrix}. \tag{8}$$

### 2.2.1 Discoverer update

Discoverers locate new food sources using Equation 9:

$$X_{i,j}^{t+1} = \begin{cases} X_{i,j}^{t} \cdot exp\left(\dfrac{-i}{\alpha \cdot iter_{max}}\right), & R_2 < ST \\ X_{i,j}^{t} + Q \cdot \boldsymbol{L}, & R_2 \geq ST \end{cases}, \tag{9}$$

where $iter_{max}$ denotes the maximum number of iterations; $X_{i,j}^{t}$ is the position of the *i*th sparrow in the *j*th dimension at the t-th iteration; $\alpha \in (0,1]$, $Q \in [0,1]$, and $R_2 \in [0,1]$ are random numbers, representing the warning values, respectively; L is a matrix of ones; and ST takes values between [0.5,1], representing the safety value.

When $R_2 \geq ST$, it indicates that the foraging area is not safe, and all sparrows need to fly to other safe foraging locations.

#### 2.2.1.1 Follower update

Followers adjust their positions by tracking discoverers to accelerate convergence using Equation 10:

$$X_{i,j}^{t+1} = \begin{cases} Q \cdot exp\left(\dfrac{X_{worst}^{t} - X_{i,j}^{t}}{i^2}\right), & i > \dfrac{n}{2} \\ X_{p}^{t+1} + \left|X_{i,j}^{t} - X_{p}^{t+1}\right| \boldsymbol{A}^{+} \cdot \boldsymbol{L}, & i \leq \dfrac{n}{2} \end{cases}, \tag{10}$$

where $X_{p}^{t+1}$ is the best position where the discoverers are located, $X_{worst}^{t}$ is the current globally worst position, and $A^{+} = A^{T} \cdot \left(A \cdot A^{T}\right)^{-1}$ is a matrix, with each element being 1 or −1.

When $i > \frac{n}{2}$, it indicates that the *i*th follower has not obtained food and needs to move to other places to forage.

#### 2.2.1.2 Sentinel update

Sentinels monitor threats and adjust their positions using Equation 11:

$$X_{i,j}^{t+1} = \begin{cases} X_{best}^{t} + \theta\left|X_{i,j}^{t} - X_{best}^{t}\right|, & f_i > f_g \\ X_{i,j}^{t} + K\left|\dfrac{X_{i,j}^{t} - X_{worst}^{t}}{(f_i - f_w) + \varepsilon}\right|, & f_i = f_g \end{cases}, \tag{11}$$

where $X_{best}^{t}$ is the global optimal position in the sparrow population at the t-th generation, ε is a constant, θ is the step–size control coefficient, $K \in [-1,1]$ is a random number, $f_i$ is the fitness value of the ith sparrow currently, $f_g$ is the current global best fitness value, and $f_w$ is the current global worst fitness value.

When $f_i > f_g$, it indicates that the sparrow is currently at the edge of the population and is vulnerable to predator attacks; when $f_i = f_g$, it indicates that the sparrows in the middle of the population are aware of the danger of being preyed upon and need to move closer to other sparrows.

## 2.3 Improved sparrow search algorithm

The conventional SSA often experiences issues related to local convergence and reduced population diversity in later iterations (Lv et al., 2021; Liu et al., 2022). To mitigate these challenges, the Singer chaotic mapping is introduced to enhance population initialization. The formula for Singer chaotic mapping is shown in Equation 12:

$$X_{k+1} = u\left(7.86x_k - 23.32x_k^2 + 28.75x_k^3 - 13.3.2875x_k^4\right), \tag{12}$$

where $u \in (0.9, 1.08)$ is a control parameter and $x_k \in [0,1]$ is a random number.

As shown in Figure 1, the value range of the Singer mapping lies within the interval [0, 1]. By replacing the random initialization method with its chaotic characteristics, the search space can be made more uniform, enhancing the uniformity and diversity of the sparrow population, and thereby improving the global search ability.

The steps of the improved SSA are outlined as follows:

(1) Use the chaotic mapping to initialize the population, the number of iterations, and the proportions of discoverers and followers.
(2) Compute the fitness values, and arrange them in order.
(3) Update the positions of discoverers.
(4) Update the positions of followers.
(5) Update the positions of sentinels.
(6) Recalculate the fitness values, and update the positions of the sparrows.
(7) Repeat until the maximum number of iterations is reached.

The flowchart of the improved SSA is presented in Figure 2.

## 2.4 Extreme learning machine

The ELM is a computationally efficient algorithm designed for training single-hidden-layer feedforward neural networks (SLFNs).

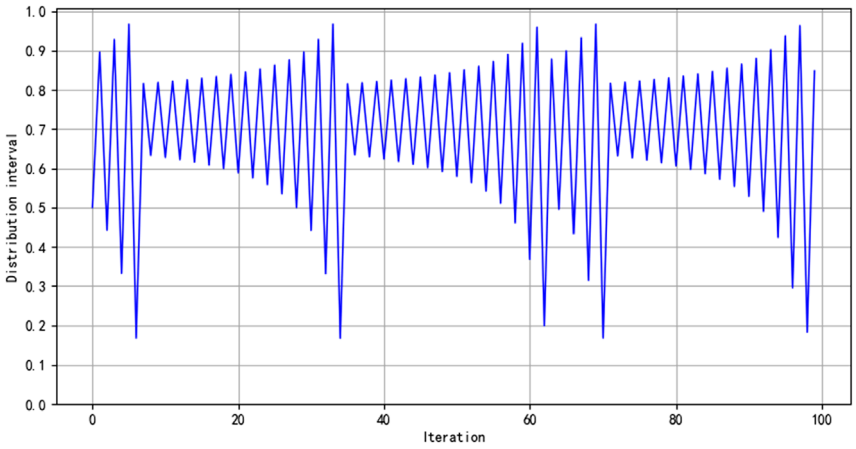


FIGURE 1
Distribution of the Singer map after 100 iterations.

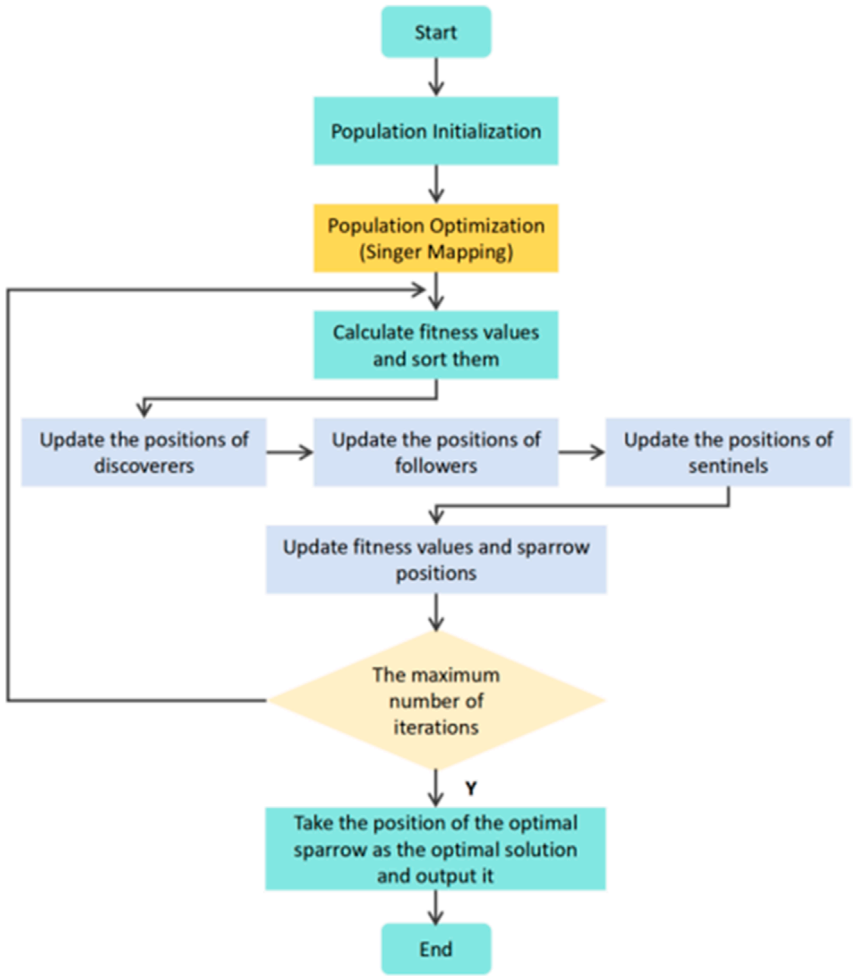


FIGURE 2
Flowchart of the ISSA.

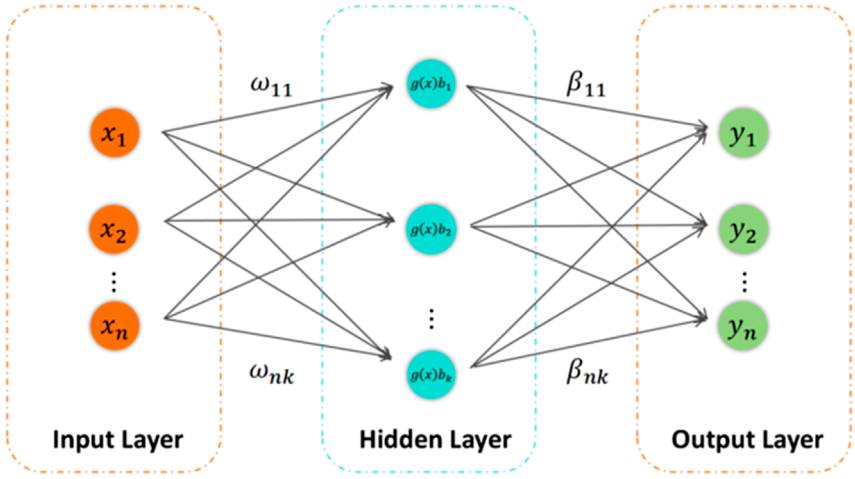


FIGURE 3
ELM structure.

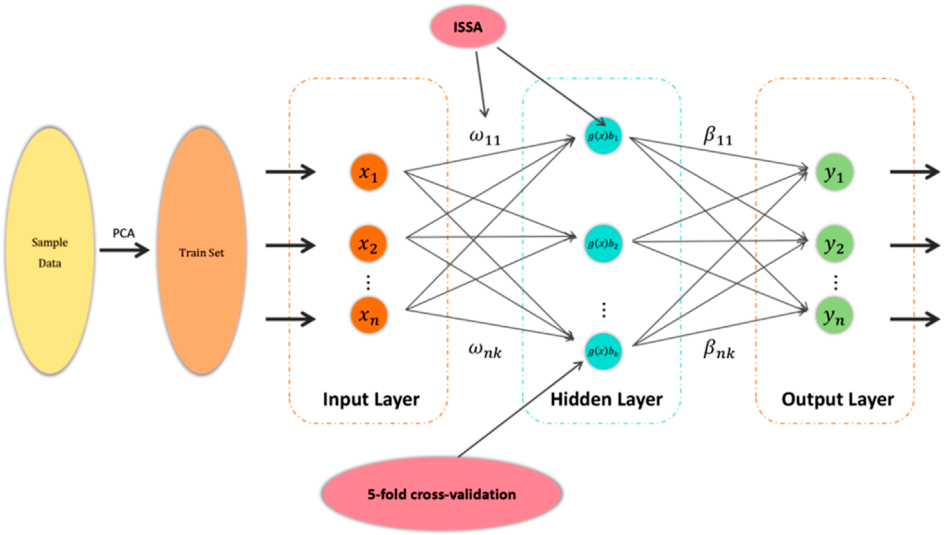


FIGURE 4
Framework of the karst-collapse susceptibility prediction model based on the ISSA-ELM model.

First introduced by Huang et al. (2006), ELM offers significant improvements in training speed and generalization capability. Its applications are widespread across various domains, including classification, regression, and prediction tasks.

The ELM algorithm follows a simple structure, as illustrated in Figure 3, comprising an input layer, a hidden layer, and an output layer. Unlike traditional neural networks, ELM assigns random values to the input-layer weights and hidden-layer threshold. The output-layer weights are then calculated using a generalized matrix, enabling efficient and accurate chaotic recognition outcomes.

The mathematical representation of the output model for a single-hidden-layer neural network with $L$ hidden-layer nodes and an activation function g($x$) is given in Equation 13:

$$y_j = \sum_{i=1}^{L} \beta_i g\left(\omega_i \cdot x_j + b_i\right), (j = 1, 2, 3, \cdots, n), \tag{13}$$

where $x_j$ denotes the input value, $y_j$ represents the actual output value, $\omega_i$ is the input weight matrix, $b_i$ denotes the hidden-layer threshold, $\beta_i$ is the output weight matrix, and g(x) is typically a sigmoid function (Jiang and Shi, 2023)

The primary objective of the ELM algorithm is to minimize the output error, which can be expressed in Equation 14:

$$\|\boldsymbol{H\beta} - \boldsymbol{T}\| = min, \tag{14}$$

where there exist $\beta_i$, $\omega_i$, and $b_i$ such that

$$\boldsymbol{H\beta} = \boldsymbol{T}. \tag{15}$$

This relationship shown in Equation 15 consists of $N$ equations that can be represented in a matrix form as shown in Equation 16:

$$\boldsymbol{H} = \begin{bmatrix} g(\omega_1 \cdot x_1 + b_1) & \cdots & g(\omega_L \cdot x_1 + b_L) \\ g(\omega_1 \cdot x_2 + b_1) & \cdots & g(\omega_1 \cdot x_2 + b_1) \\ \vdots & \ddots & \vdots \\ g(\omega_1 \cdot x_N + b_1) & \cdots & g(\omega_L \cdot x_1 + b_L) \end{bmatrix}, \tag{16}$$

where $H$ is the hidden-layer output matrix, $\beta$ is the weight matrix connecting the hidden and output layers, and $T$ represents the desired output.

The least-squares solution for the output-layer weights can be efficiently obtained using the Moore–Penrose generalized inverse matrix $\boldsymbol{H}^{+}$, as shown in Equation 17:

$$\boldsymbol{\beta} = \boldsymbol{H}^{+}\boldsymbol{T}. \tag{17}$$

A notable limitation of ELM is its sensitivity to the random initialization of input-layer weights and hidden-layer threshold, leading to potential instability. To mitigate this issue, the ISSA is applied for parameter optimization. By enhancing the search process and avoiding local optima, the ISSA improves both the accuracy and robustness of the ELM model.

## 2.5 Hyperparameter optimization of the prediction model

The ELM algorithm randomly assigns input-layer weights and hidden-layer threshold. Without appropriate adjustment, this randomness may reduce the functionality of certain hidden-layer nodes, leading to algorithmic instability. Furthermore, although a larger number of hidden-layer nodes can enhance performance, an excessive number of nodes may result in overfitting, whereas too few nodes can cause underfitting, thereby reducing the prediction accuracy (Xie et al., 2021).

To mitigate these issues, in this study, we employ a combined approach using the ISSA and K-fold cross-validation to optimize the hyperparameters of the ELM prediction model. The optimized parameters include input-layer weights, hidden-layer thresholds, and the number of hidden nodes (N). The hyperparameter optimization process consists of the following steps:

(1) Initialization: set the sparrow population size, maximum number of iterations, proportions of initial discoverers and followers, and the number of hidden nodes.
(2) Fitness function calculation: define the mean squared error (MSE) between the predicted and actual values as the model's fitness function, represented in Equation 18:

$$\text{Fitness} = \frac{1}{n}\sum_{i=1}^{n}(y_i - \overline{y_i})^2, \tag{18}$$

where $y_i$ represents the actual grade of karst-collapse susceptibility of the ith sample, $\overline{y_i}$ denotes the predicted value for the i-th sample, and $n$ is the number of samples.

(3) Ranking and selection: compute the fitness values and rank individuals. Those with higher fitness values are designated as discoverers in the sparrow population.
(4) Position update: update the positions of discoverers, followers, and vigilant individuals using Formulas 9–11, and then, recalculate fitness values.
(5) Iteration check: assess whether the maximum number of iterations is reached. If so, terminate training and output the global optimal parameters (optimal weights, hidden-layer biases, and N). Otherwise, repeat steps (2–4).
(6) K-fold cross-validation: perform five-fold cross-validation to determine the optimal number of hidden nodes. The data are split into five subsets, with each subset used once as a validation set, whereas the remaining subsets form the training set. The optimal number of hidden nodes is determined by minimizing the average error across the five models, as shown in Equation 19:

$$\text{MAE} = \frac{1}{5}\sum_{i=1}^{n}(y_i - \overline{y_i}). \tag{19}$$

(7) Output: provide the final optimal parameter combination, including input-layer weights, hidden-layer threshold, and the number of hidden nodes.

## 2.6 Prediction process of karst collapse susceptibility using the ISSA-ELM model

The ISSA-ELM-based karst-collapse susceptibility prediction model is illustrated in Figure 4, with its overall flowchart depicted in Figure 5. The prediction process consists of the following steps:

(1) Data collection and preprocessing: Real-world data are collected from key karst collapse exploration areas. Data preprocessing is performed by removing outliers and imputing missing values using the mode. PCA is then applied for dimensionality reduction.
(2) Data division: The dataset is split into a training set and a test set. The training set is used to train the ISSA-ELM model, whereas the test set is used for prediction and model evaluation.
(3) Hyperparameter optimization: The ELM model's hyperparameters, including the sparrow population size, maximum iterations, proportions of discoverers and followers, and the number of hidden nodes, are initialized. The initial model is trained and evaluated using MSE and MAE. The optimal hyperparameters are determined when the error reaches its minimum.
(4) Prediction: The ISSA-ELM model, with the optimized hyperparameters, is used to predict karst-collapse susceptibility. The final model parameters are applied for prediction tasks.

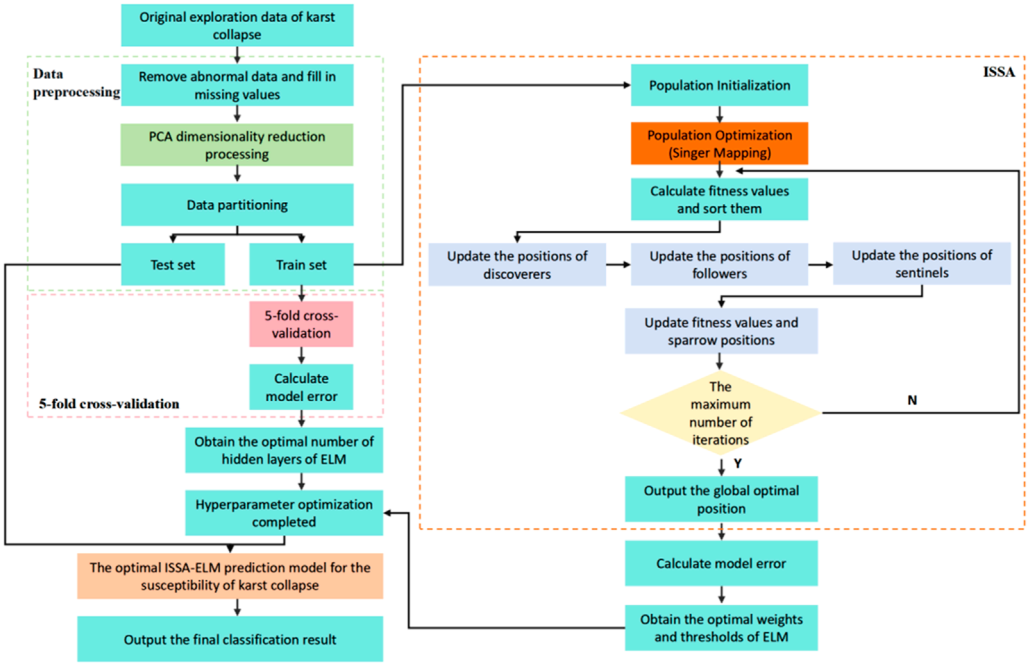


FIGURE 5
Overall flowchart of the karst-collapse susceptibility prediction model based on the ISSA-ELM model.

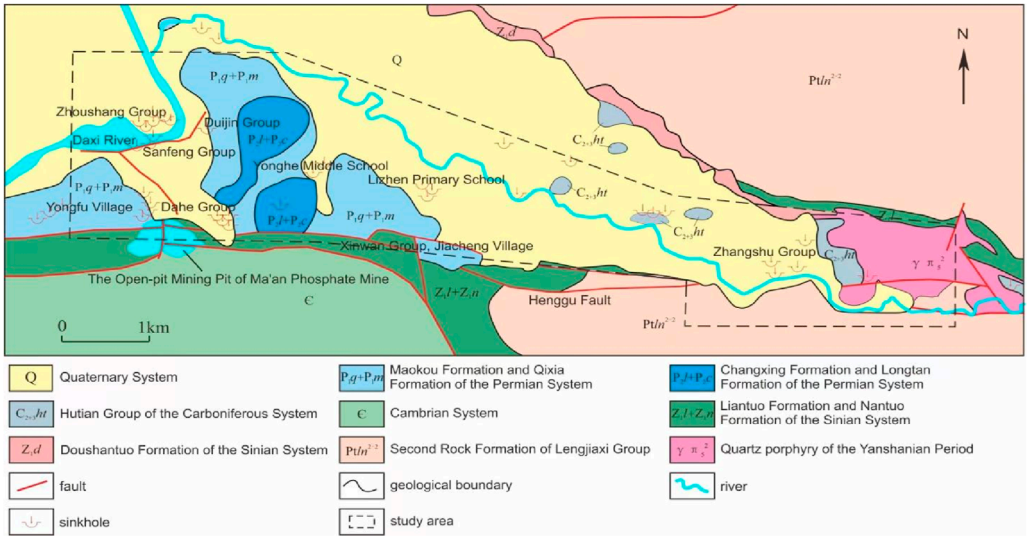


FIGURE 6
Relationship diagram among karst development, strata, and faults in the study area.

## 2.7 Evaluation methods

To comprehensively evaluate the predictive performance of various karst-collapse susceptibility models, the following indicators are applied.

### 2.7.1 Coefficient of determination ($R^2$)

$$R^2 = 1 - \frac{\sum_{i=1}^{n}(y_i - \hat{y}_i)^2}{\sum_{i=1}^{n}(y_i - \bar{y})^2}. \quad (20)$$

In Equation 20, $y_i$ is the actual value of the *i*th sample, $\hat{y}_i$ is the predicted value of the *i*th sample, $\bar{y}$ is the mean of the actual values, and *n* is the total number of samples. A coefficient value closer to 1 indicates a better model fit.

### 2.7.2 Mean squared error

$$MSE = \frac{1}{n}\sum_{i=1}^{n}(y_i - \hat{y}_i)^2. \quad (21)$$

### 2.7.3 Mean absolute error

$$MAE = \frac{1}{n}\sum_{i=1}^{n}|y_i - \hat{y}_i|. \quad (22)$$

Smaller MSE (Equation 21) and MAE (Equation 22) values indicate a more accurate model, with the predicted values closely matching the actual values.

# 3 General situation of the project

## 3.1 Overview of the geological environment

The study area is located in Yonghe Town, in the northeastern part of Liuyang City, Hunan Province. The terrain generally slopes from higher elevations in the south and northeast to lower elevations in the central and western regions. The primary geological and environmental conditions are as follows:

(1) Physical geography: the region is characterized by denudation–erosion hilly landforms and dissolution–erosion valley landforms. The hills are primarily located in the southern part and the Qibaoshan area to the east. These positive landforms are composed mainly of sandstones, slates, and dolomites from the Upper Sinian System (Zb), Cambrian System (∈), Longtan Formation ($P_2$l), and Changxing Formation ($P_2$c) of the Upper Permian System. In contrast, negative landforms composed of dolomites, marls, and limestones interbedded with shales are prevalent in the northern and western parts. These belong to the Hutian Group ($C_{2+3}$ht) of the Middle and Upper Carboniferous Systems and the Qixia Formation ($P_1$q) of the Lower Permian System.

Dissolution–erosion valley landforms are dominant in the northern and western regions, characterized by broad valleys and alluvial plains formed through erosional and depositional processes. These areas are covered by upper silty clay and sandy gravel layers from the Holocene Series ($Q_h^{al}$) of the Quaternary System. The underlying bedrock mainly comprises marls, limestones interbedded with shales, and dolomites. The area experiences an average annual rainfall of 1574.7 mm, with maximum and minimum recorded rainfalls of 2096.1 mm and 1079.1 mm, respectively. Rainfall is most concentrated in June, contributing over 16% of the annual total. The Daxi River, the second largest tributary of the Liuyang River, flows from north to west across the study area (Figure 7).

(2) Stratigraphic lithology: the stratigraphic sequence in the study area, from the oldest to the youngest, includes the second segment of the second lithologic unit of the Lengjiaxi Group ($Ptln^{2\text{-}2}$), the Liantuo Formation ($Z_1$l) and Nantuo Formation ($Z_1$n) of the Lower Sinian System, the Doushantuo Formation ($Z_2$d) of the Upper Sinian System, the Cambrian System (∈), the Hutian Group ($C_{2+3}$ht) of the Middle and Upper Carboniferous Systems, the Qixia Formation ($P_1$q) and Maokou Formation ($P_1$m) of the Lower Permian System, the Longtan Formation ($P_2$l) and Changxing Formation ($P_2$c) of the Upper Permian System, and the Quaternary System (Q) (Figure 6).

Soluble rock strata are predominantly found in the Changxing Formation, the Qixia Formation, and the Hutian Group. The Hutian Group and the first ($P_1q^1$) and second ($P_1q^2$) segments of the Qixia Formation consist of interbedded limestones, shales, argillaceous limestones, and dolomites, displaying well-developed karst features.

(3) Geological structure: the Yonghe Syncline is a minor fold structure oriented in a north-northwest direction. The syncline core consists of the Changxing Formation, with the wings comprising the Longtan Formation, the Maokou Formation, and the Qixia Formation. The strata dip gently, with angles ranging from 10° to 20°.

Several faults are present, including two strike-slip faults, two reverse faults, one transverse thrust fault, and two unidentified faults. The most prominent is the transverse thrust fault, which traverses the northern edge of the Ma'anling Phosphate Mine (Figure 6).

(4) Hydrogeological conditions: the groundwater in the area consists of karst water, bedrock weathering fissure water, and pore water within loose rock formations.

## 3.2 Overview of karst collapses

A total of 38 karst collapses were documented within the 14-km$^2$ exploration area (Figure 7), resulting in a collapse density of 2.71 occurrences per km$^2$. These collapses are primarily concentrated in regions with well-developed soluble rocks, significant fault activity, and strong surface water–groundwater interactions. The most affected areas include the Yueshan-Ou's-Dahe area of Yongfu Village; the Juxiang Community, Yonghe Old Street, Huayuan Village of Yanxi Town; and the Nanshan-Jiacheng Village, Li Zhen Primary School (Old), Xinwan-Xinping regions.

Most collapses are small-scale, with long-axis lengths ranging from 1 to 7 m, accounting for 73% of incidents (Figure 8).

Xinwu Group, Jiacheng Village collapse (Figure 9a): this circular collapse pit has a long-axis length of approximately 3.5 m, a short-axis length of 2.5 m, and a depth of 1.2 m. The pit contains water, with the water level approximately 0.2 m below the surface. Bedrock is not visible, and the surrounding area consists of alluvial gravel-bearing silty clay, negatively impacting agricultural activities.

Xinwan Group, Jiacheng Village collapse (Figure 9b): this collapse is nearly circular, with a long-axis length of 2.3 m, a short-axis length of 2.2 m, and a depth of 10 m. The water level inside the pit is approximately 5 m. The primary triggering factors were

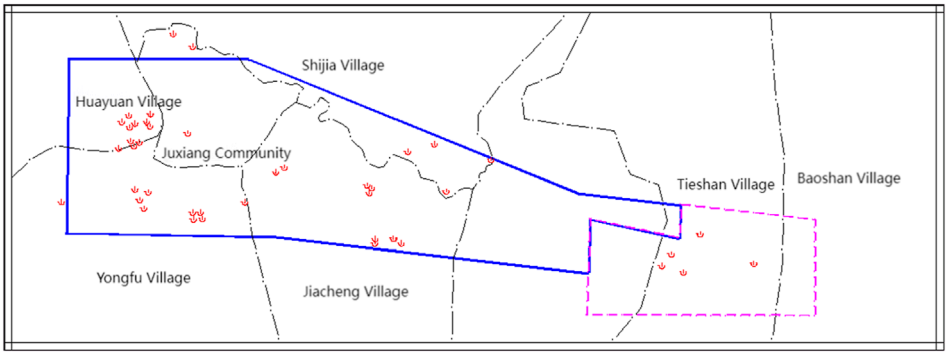


FIGURE 7
Distribution map of karst-collapse points in the exploration area (the blue solid line represents the scope of the exploration area, and the dotted line represents the scope of the prediction area).

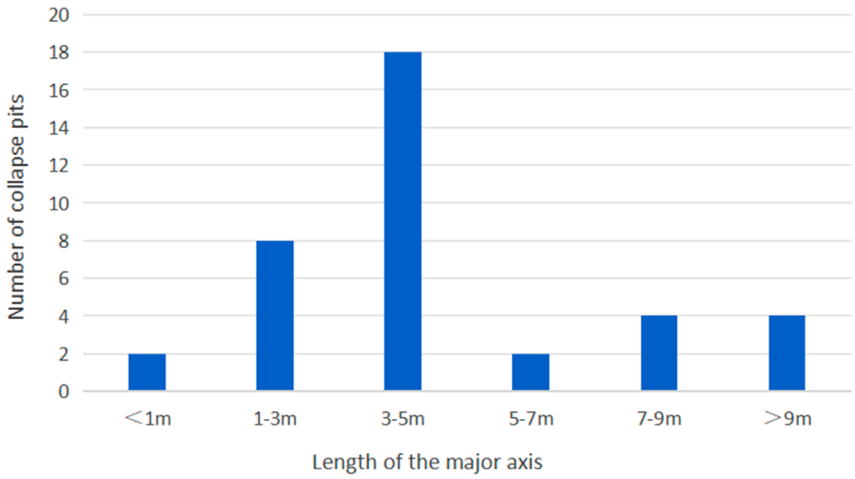


FIGURE 8
Scale situation of the long axis of the collapse pits.

groundwater extraction and heavy rainfall. Situated on a river terrace, the surrounding soil consists of silty clay with pebbles, forming a single-layer structure approximately 1 m thick. The underlying bedrock is limestone. Due to its instability, this collapse presents a continuous risk to local production and daily life.

## 3.3 Formation mechanism of karst collapses

The occurrence of karst collapses results from the complex interplay and cumulative effects of multiple formation mechanisms (Hu et al., 2001; Chen and Cao, 2023; Feng, 2025). Based on comprehensive investigations, in-depth research, and detailed exploration within the study area, the primary formation conditions include karst development characteristics, overburden properties, and hydrodynamic features.

(1) Impact of the karst development degree on karst collapses: karst development serves as the essential foundation and prerequisite for the occurrence of karst collapses. Statistical analysis indicates that most collapse pits in the study area are located within or near intense karst development zones. Notably, collapses are most prevalent in strata with well-developed karst, particularly within the second segment of the Qixia Formation ($P_1q^2$) of the Lower Permian System and the Hutian Group ($C_{2+3}$ht) of the Middle and Upper Carboniferous Systems. This strong correlation underscores the critical influence of karst development on the formation of collapses.

(2) Influence of overburden characteristics on karst collapses: the overburden comprises Quaternary loose soil layers that cover the bedrock surface. Collapse pits are primarily concentrated in covered karst regions, where the thickness of the Quaternary loose layer generally does not exceed 20 m. Areas with alluvial and diluvial deposits that lack a clay layer at the base are particularly vulnerable to collapse formation. From a geotechnical perspective, these soil layers exhibit low shear strength and limited resistance to seepage-induced


FIGURE 9
Examples of planar morphological characteristics of karst-collapse pits. **(a)** Karst collapse in the Xinwu Group of Jiacheng Village (T23). **(b)** Karst collapse in the Xinwan Group of Jiacheng Village (T27). **(c)** Karst collapse in the Xinping Group of Jiacheng Village (T30). **(d)** Karst collapse in the Shixing Group of Shijia Village (T32).

deformation, making them susceptible to piping processes and subsequent collapses.

For instance, in the collapse-affected section spanning the Zhoushang Group of Huayuan Village, Juxiang Community, Yonghe Old Street, Mingshan Group of Yongfu Village, Yueshan, Ou's Group, and Dahe Group, the soil structure consists predominantly of gravel-bearing silty clay formed through alluvial and diluvial processes, along with residual slope-derived crushed stone soil. The total thickness of the soil layer ranges from 5.5 to 13.5 m. In these areas, the upper silty clay layer is relatively thin, and the absence of a water-retaining clay layer at the base facilitates the infiltration of atmospheric precipitation, surface water seepage, and the upward movement of water and sand during the increase in the karst water level. Consequently, the thickness and physical properties of the overburden significantly regulate the collapse process.

(3) Effect of hydrodynamic characteristics on karst collapses: the study area contains two distinct groundwater layers: the upper-layer Quaternary pore water and the lower-layer karst water. The upper-layer pore water is primarily stored in silty clay, pebble-bearing soil, and residual crushed stone soil from Quaternary alluvial and diluvial facies. Recharge sources include atmospheric precipitation and seepage from nearby surface water bodies such as the Daxi River. During recharge, seepage forces can trigger piping within the soil layer, leading to cavity formation, which may expand and eventually result in collapse.

The lower-layer karst water mainly originates from the limestone aquifer of $P_1q$ and the limestone karst–cave aquifer of $C_{23}ht$, both exhibiting significant karst development and high water-bearing capacity. Groundwater extraction often lowers the karst water level, prompting the continuous recharge of upper-layer pore water into the karst aquifer. Fine-grained soil particles are transported by the flowing water, further accelerating the collapse process. In conclusion, the coexistence of the two-layer groundwater system, the presence of a significant hydraulic gradient, and the infiltration of surface water bodies jointly alter the hydrodynamic characteristics of the region, playing a pivotal role in the formation of karst collapses.

## 3.4 Determination of influencing factors for the susceptibility of karst collapses

The development of karst collapses is influenced by the combined effects of multiple factors. Nonlinear relationships exist not only among these factors but also between each factor and the occurrence of karst collapses (Chen and Cao, 2023). Through extensive on-site investigations and comprehensive analyses of the formation mechanisms of numerous karst collapses, this study identified the key factors for predicting karst-collapse susceptibility.

### 3.4.1 Karst development degree

Soluble rocks provide the material basis for karstification, with their solubility directly impacting the extent of karst development. In the region extending from the Zhoushang Group of Huayuan Village to Juxiang Community, Yonghe Old Street, Yueshan Group, Ou's Group, and Dahe Group, 29 karst collapses have occurred. Borehole data from 15 boreholes revealed karst caves in five of them, yielding a karst–cave encounter rate of 33.3%. Among the six identified caves, five developed within the second member of the Lower Permian Qixia Formation ($P_1q^2$), characterized by thick-bedded dark gray limestone with a faint flesh-red tinge, interbedded with thin layers of marl and dolomite. Geophysical interpretation indicated that 76.98% of the 505 detected anomalies were karst related, predominantly in the Qixia Formation.

### 3.4.2 Distance from intra-area faults

Fault structures provide conduits for groundwater flow and play a decisive role in karst development. On-site investigations revealed that karst collapses are concentrated along concealed and unidentified faults on both sides of the NW-trending secondary faults within the northern plate of the Henggu Fault. Notably, four collapses in Yongfu Village, Yonghe Town, occurred approximately 200 m west of a concealed fault. This positive correlation highlights the influence of fault zones on collapse occurrence.

### 3.4.3 Thickness of the overlying soil layer

The development and distribution of karst collapses are closely linked to the thickness of the Quaternary layer. Survey results

indicated that the Quaternary layer in the Dahe Group, Yueshan Group, Ou's Group, and Mingshan Group of Yongfu Village, as well as in the Zhoushang Group, Juxiang Community, and Yonghe Old Street in Huayuan Village, ranged from 5.50 to 13.5 m. Additionally, the thickness of the upper silty clay layer was generally ≤3 m. The presence of a thin silty clay layer facilitates water infiltration and groundwater-level fluctuations, increasing the likelihood of collapses.

#### 3.4.4 Groundwater fluctuation range

Karst water fluctuates between confined and unconfined states near the bedrock surface, contributing to collapse occurrence. Survey data from the Yueshan Group and Ou's Group regions indicated that groundwater levels ranged from 9.27 to 25.90 m during the wet season, with the bedrock surface buried at depths of 15.00–30.70 m. During the dry season, groundwater levels decrease by 5–10 m, maintaining their position near the bedrock surface. This fluctuation promotes the "bellows effect," characterized by piping and suction erosion of the overlying soil, which increases the risk of collapse.

#### 3.4.5 Distance from the center of the artificial pumping funnel

Before October 2016, mining at the Ma'an Phosphate Mine reached an elevation of approximately ±0 m, affecting an area within a 2-km radius, primarily around Huayuan Village, Juxiang Community, Yongfu Village, and Yonghe Middle School. Investigations documented 89 instances of house and ground cracking, accounting for 44.9% of all cases, alongside 22 collapse pits (57.9%). Since the cessation of mining activities, a significant decrease in collapses and cracking incidents has been observed, underscoring the impact of groundwater extraction on collapse susceptibility.

#### 3.4.6 Development density of existing ground collapses

A total of 38 ground collapses were identified within the study area, distributed as follows: 16 collapses in the Mingshan Group, Yueshan Group, Ou's Group, and Dahe Group of Yongfu Village; 12 in the Zhoushang Group, Juxiang Community, and Yonghe Old Street in Huayuan Village; three in the Yonghe Middle School and Nanshan Group area of Jiacheng Village; seven in the Li Zhen Primary School (Old), Xinwan Group, and Xinping Group area; and four in the Tieshan Village and Qibaoshan Village area. The density of existing collapses was considered a key predictive indicator.

Following the relevant guidelines (Ministry of Natural Resources of the People's Republic of China, 2023) and building on previous studies (Huang et al., 2011; YanHua et al., 2022), in this study, we integrated field survey results, geophysical exploration data, and borehole data to identify six key factors influencing karst-collapse susceptibility (Table 1). Through a comprehensive analysis of the field survey data, the susceptibility levels of karst collapse were assessed. To effectively represent the likelihood of collapse occurrences, the susceptibility levels were classified into three categories: low susceptibility, medium susceptibility, and high susceptibility, corresponding to category labels 1, 2, and 3, respectively (Table 2).

## 4 Case analysis

### 4.1 Data collection and preprocessing

The karst-collapse-affected area in Yonghe Town, Liuyang City, Hunan Province, was selected as the research subject. A total of 20 sets of sample data were collected within the exploration zone, comprising 16 samples from collapsed pits and four samples from non-collapsed pits representing locations with no recent collapses within 1 km of the sampling points and also considered similar geological settings (like lithology and stratigraphy) and hydrogeological conditions (groundwater levels, flow, and quality) (Table 3). This dataset was used to evaluate the feasibility of the ISSA-ELM model for predicting the karst-collapse susceptibility.

Given the complex interrelationships among various influencing factors of karst collapses, using all factors as inputs could introduce information redundancy. To mitigate this, PCA was applied to reduce the dimensionality and remove correlations among six key factors: the degree of karst development, the distance from faults, the thickness of the overlying soil layer, the groundwater fluctuation range, the distance from the center of the artificial pumping funnel, and the development density of preexisting ground collapses. This approach retained the essential information while minimizing redundancy.

The original data were standardized to eliminate the impact of differing units and magnitudes. A standardized covariance matrix was then calculated (Table 4), followed by an in-depth correlation analysis to explore the relationships among the influencing factors. Eigenvalues and contribution rates were derived from the covariance matrix, and principal components were selected based on a cumulative contribution rate exceeding the widely accepted threshold of 85% (Table 5).

As shown in Table 5, the cumulative contribution rate of the first five principal components was 96.87%, surpassing the 85% threshold. Therefore, these five principal components were chosen to represent the original six variables.

Based on the eigenvector matrix (Table 6), the principal components were expressed as follows:

The karst-collapse-affected area in Yonghe Town, Liuyang City, Hunan Province, was selected as the research subject. A total of 20 sets of sample data were collected within the exploration zone, comprising 16 samples from collapsed pits and four samples from non-collapsed pits representing locations with no recent collapses within 1 km of the sampling points (Table 3). This dataset was used to evaluate the feasibility of the ISSA-ELM (improved sparrow search algorithm-extreme learning machine) model for predicting karst-collapse susceptibility.

Given the complex interrelationships among various influencing factors of karst collapses, using all factors as inputs could introduce information redundancy. To mitigate this, PCA was applied to reduce dimensionality and remove correlations among six key factors: the degree of karst development, the distance from faults, the thickness of the overlying soil layer, the groundwater fluctuation range, the distance from the center of the artificial pumping funnel, and the development density of preexisting ground collapses. This approach retained essential information while minimizing redundancy.

TABLE 1 Classification of influencing factors for karst-collapse susceptibility.

| Factor | Karst-collapse susceptibility levels | | |
|---|---|---|---|
| | Low-susceptibility criteria | Medium-susceptibility criteria | High-susceptibility criteria |
| Drilling saturation/% | <3 | 3~10 | >10 |
| Distance to faults/m | >100 | 50~100 | 0~50 |
| Overburden thickness/m | Total >20 m; upper clay >3 m | 10< Total ≤20 m; upper clay ≤3 m | Total ≤10 m; upper clay ≤3 m |
| Groundwater fluctuation/m·a$^{-1}$ | <3 | 3~8 | >8 |
| Distance to pumping center/m | >500 | 200~500 | 0~200 |
| Collapse density (per 10 km$^2$) | <2 | 2~10 | >10 |

TABLE 2 Class labels for the grading of expected output parameters.

| Susceptibility level | Low | Medium | High |
|---|---|---|---|
| Label | 1 | 2 | 3 |

The original data were standardized to eliminate the impact of differing units and magnitudes. A standardized covariance matrix was then calculated (Table 4), followed by an in-depth correlation analysis to explore the relationships among the influencing factors. Eigenvalues and contribution rates were derived from the covariance matrix, and principal components were selected based on a cumulative contribution rate exceeding the widely accepted threshold of 85% (Table 5).

As shown in Table 5, the cumulative contribution rate of the first five principal components was 96.87%, surpassing the 85% threshold. Therefore, these five principal components were chosen to represent the original six variables.

Based on the eigenvector matrix, the principal components were expressed as follows:

$$X_1 = -0.0407Z_1^* + 0.6521Z_2^* - 0.0783Z_3^* + 0.3718Z_4^* + 0.6459Z_5^* + 0.1069Z_{6,}^*$$

$$X_2 = -0.5044Z_1^* - 0.0975Z_2^* - 0.6139Z_3^* + 0.4390Z_4^* - 0.2019Z_5^* - 0.3543Z_{6,}^*$$

$$X_3 = 0.3891Z_1^* - 0.1321 + 0.2367Z_3^* + 0.1785Z_4^* + 0.2218Z_5^* - 0.8330Z_{6,}^*$$

$$X_4 = -0.0242Z_1^* - 0.2971Z_2^* + 0.4789Z_3^* + 0.7582Z_4^* - 0.1295Z_5^* + 0.2999Z_{6,}^*$$

$$X_5 = 0.1712Z_1^* + 0.6665Z_2^* + 0.1441Z_3^* + 0.1148Z_4^* - 0.6869Z_5^* - 0.1431Z_{6,}^*$$

where $Z_1^*$, $Z_2^*$, $Z_3^*$, $Z_4^*$, $Z_4^*$, $Z_5^*$, and $Z_6^*$ represent the standardized values of the degree of karst development, the distance from faults, the thickness of the overlying soil layer, the groundwater fluctuation range, the distance from the pumping funnel center, and the development density of existing ground collapses, respectively.

The principal components were subsequently calculated using these expressions (Table 7) and used for training the ISSA-ELM model.

## 4.2 Optimization of model parameters

From the PCA-processed dataset, 14 samples were designated as the training set, whereas the remaining six samples were used as the test set. This 7:3 split ensured a balanced approach, maintaining sufficient data for training while reserving a representative subset for evaluating the model's generalization performance.

The ISSA-ELM model parameters were configured as follows: population size N = 20, maximum iterations = 100, warning threshold ST = 0.6, proportion of discoverers PD = 0.7, and proportion of scouts SD = 0.2.

The number of hidden-layer nodes significantly affects model performance. In the ELM model, the number of input-layer nodes was set to 5, corresponding to the number of principal components. The sigmoid function was applied as the activation function. The number of hidden-layer nodes was selected within the range [2n+1, N] (where n is the number of nodes in the input layer n = 5, and N denotes the total number of input samples N = 20), resulting in a range of [11, 20] (Jiang and Shi, 2023). A five-fold cross-validation approach was used to determine the optimal number of hidden-layer nodes, balancing computational efficiency and robust evaluation. The MAE index results (Figure 10) indicated that the optimal number of hidden layers was 12 as it produced a concentrated MAE distribution without significant outliers.

The PCA-processed data were input into the ISSA-ELM and SSA-ELM models for iterative comparisons. The resulting optimization curves (Figure 11) showed that the ISSA-ELM model achieved rapid convergence. After 63 iterations, its fitness value stabilized at approximately 0.0047. In contrast, the SSA-ELM model exhibited a slower convergence rate, requiring 70 iterations to reach a fitness value of approximately 0.009. These findings demonstrate that the ISSA-ELM model is closer to the global optimal solution

TABLE 3 Sample dataset.

| Sample | Degree of karst development/% | Distance to faults/m | Overburden thickness/m | Groundwater fluctuation/m·a$^{-1}$ | Distance to pumping center/m | Collapse density (per 10 km$^2$) | Label |
|---|---|---|---|---|---|---|---|
| 1 | 12.3 | 32 | 18.3 | 7.64 | 12 | 7 | 3 |
| 2 | 9.8 | 55 | 15 | 8.6 | 35 | 20 | 3 |
| 3 | 15.6 | 33 | 18 | 8.87 | 56 | 19 | 3 |
| 4 | 8.5 | 42 | 8 | 13.7 | 78 | 12 | 3 |
| 5 | 11.2 | 28 | 11 | 17 | 90 | 11 | 3 |
| 6 | 13.7 | 47 | 10 | 2.8 | 110 | 8 | 3 |
| 7 | 10.1 | 120 | 65 | 10.2 | 520 | 2 | 1 |
| 8 | 7.9 | 150 | 37 | 11.76 | 650 | 14 | 1 |
| 9 | 14.4 | 48 | 20 | 15 | 132 | 9 | 3 |
| 10 | 12.9 | 33 | 15 | 11 | 155 | 13 | 3 |
| 11 | 16.2 | 200 | 28.3 | 12.1 | 710 | 11 | 1 |
| 12 | 9.2 | 31 | 12.5 | 5.37 | 178 | 13 | 3 |
| 13 | 11.8 | 45 | 6.7 | 8.3 | 19 | 16 | 3 |
| 14 | 10.7 | 37 | 14 | 11.13 | 45 | 5 | 3 |
| 15 | 13.1 | 350 | 37 | 15.4 | 830 | 12 | 1 |
| 16 | 8.8 | 39 | 14 | 11.67 | 67 | 12 | 3 |
| 17 | 15.3 | 35 | 17 | 10.06 | 89 | 18 | 3 |
| 18 | 12.6 | 48 | 14 | 3.12 | 123 | 14 | 3 |
| 19 | 9.5 | 44 | 18 | 5.7 | 145 | 7 | 3 |
| 20 | 14.7 | 37 | 19 | 2.57 | 107 | 15 | 3 |





10.3389/feart.2025.1581090

TABLE 4 Covariance matrix of six variables.

| Variable | $Z_1^*$ | $Z_2^*$ | $Z_3^*$ | $Z_4^*$ | $Z_5^*$ | $Z_6^*$ |
|---|---|---|---|---|---|---|
| $Z_1^*$ | 1.0526 | −0.1031 | 0.1103 | −0.1029 | 0.1080 | 0.0525 |
| $Z_2^*$ | −0.1031 | 1.0526 | −0.0776 | 0.2224 | 0.7858 | 0.1873 |
| $Z_3^*$ | 0.1103 | −0.0776 | 1.0526 | −0.2154 | 0.0873 | 0.0397 |
| $Z_4^*$ | −0.1029 | 0.2224 | −0.2154 | 1.0526 | 0.3014 | −0.0652 |
| $Z_5^*$ | 0.1080 | 0.7858 | 0.0873 | 0.3014 | 1.0526 | 0.0141 |
| $Z_6^*$ | 0.0525 | 0.1873 | 0.0397 | −0.0652 | 0.0141 | 1.0526 |

TABLE 5 Eigenvalues of the covariance matrix for each variable.

| Principal component variable | $X_1$ | $X_2$ | $X_3$ | $X_4$ | $X_5$ | $X_6$ |
|---|---|---|---|---|---|---|
| Eigenvalue | 2.00 | 1.34 | 1.06 | 0.97 | 0.76 | 0.20 |
| Variance contribution rate, % | 31.74 | 21.16 | 16.73 | 15.28 | 11.96 | 3.13 |
| Cumulative variance contribution rate, % | 31.74 | 52.90 | 69.63 | 84.91 | 96.87 | 100.00 |

TABLE 6 Eigenvectors corresponding to the eigenvalues of the covariance matrix of six variables.

| Variable | $X_1$ | $X_2$ | $X_3$ | $X_4$ | $X_5$ |
|---|---|---|---|---|---|
| $Z_1^*$ | −0.0407 | −0.5044 | 0.3891 | −0.0242 | 0.1712 |
| $Z_2^*$ | 0.6521 | −0.0975 | −0.1321 | −0.2971 | 0.6665 |
| $Z_3^*$ | −0.0783 | −0.6139 | 0.2367 | 0.4789 | 0.1441 |
| $Z_4^*$ | 0.3718 | 0.4390 | 0.1785 | 0.7582 | 0.1148 |
| $Z_5^*$ | 0.6459 | −0.2019 | 0.2218 | −0.1295 | −0.6869 |
| $Z_6^*$ | 0.1069 | −0.3543 | −0.8330 | 0.2999 | −0.1431 |

and outperforms the SSA-ELM model in terms of both optimization capabilities and search speed.

## 4.3 Prediction of karst-collapse susceptibility

The optimal parameter combination was identified using the ISSA in conjunction with a five-fold cross-validation technique. These optimized parameters were then applied to the ELM model, resulting in the ISSA-ELM model. To comprehensively evaluate the effectiveness of PCA for data preprocessing and to assess the predictive capability of the ISSA-ELM model in karst-collapse susceptibility prediction, validation experiments were conducted using two independent datasets. One dataset consisted of 20 sets of raw field-measured data from the exploration area, whereas the other contained PCA-processed data to reduce dimensionality and mitigate redundancy.

The training datasets were used to develop the ISSA-ELM model, which was subsequently applied to the test datasets to generate predictions. The predicted values were then compared to the actual values to assess the model's predictive accuracy (refer to Figures 12–14). A comparative analysis was also performed to evaluate the relative performance of the ISSA-ELM model, the SSA-ELM model, and the conventional ELM model.

The fitting results demonstrated that the predicted and actual values for all three models exhibited a generally linear relationship, indicating a reasonable degree of accuracy. However, the coefficient of determination ($R^2 = 0.9914$) for the PCA-processed ISSA-ELM model was significantly higher than that for both the non-PCA-processed ISSA-ELM model ($R^2 = 0.8945$) and the SSA-ELM model ($R^2 = 0.9837$). This finding suggests that applying PCA preprocessing effectively enhances the predictive accuracy by reducing noise and eliminating redundant information.

Furthermore, the ISSA-ELM model's predicted values displayed a superior alignment with actual values, reflecting the model's ability to capture complex nonlinear relationships among the influencing factors of karst collapse. This improvement in predictive capability highlights the robustness and reliability of the ISSA-ELM model as an effective tool for karst-collapse susceptibility assessment. Its strong performance offers valuable insights for practical applications in geological hazard management and regional risk assessment.

## 4.4 Analysis of error metrics

To further evaluate the performance of the ISSA-ELM model, three quantitative metrics were applied: $R^2$, MSE, and MAE, as

TABLE 7 Sample principal components of 20 sets of original data.

| Sample | $X_1$ | $X_2$ | $X_3$ | $X_4$ | $X_5$ | Label |
|---|---|---|---|---|---|---|
| 1 | 0.1951 | 0.8412 | 0.2243 | 0.8250 | 0.4164 | 3 |
| 2 | −1.1088 | −0.8936 | −0.6128 | −1.1902 | −0.1288 | 3 |
| 3 | −1.1156 | 1.1636 | −1.8450 | −0.4318 | 0.2906 | 3 |
| 4 | 1.0692 | −1.4289 | −0.3521 | 0.2497 | −0.4030 | 3 |
| 5 | 0.1672 | −1.0043 | −0.9085 | 1.4766 | 0.2303 | 3 |
| 6 | 0.8426 | 1.6515 | 1.0372 | −0.4781 | 0.3287 | 3 |
| 7 | −0.3019 | −1.1554 | −0.5059 | −1.5938 | −0.8299 | 1 |
| 8 | 0.3988 | −2.0851 | 1.5171 | −0.6149 | −0.3268 | 1 |
| 9 | −0.1935 | 0.3527 | −0.7559 | 1.8877 | 0.5824 | 3 |
| 10 | 0.3567 | 0.2279 | −0.5183 | 0.2046 | −0.1037 | 3 |
| 11 | −0.5726 | 0.2954 | 1.2158 | 0.6263 | 1.3463 | 1 |
| 12 | −0.8876 | −0.1501 | 1.1124 | −0.2751 | −0.8738 | 3 |
| 13 | −0.6103 | −0.4283 | 0.0356 | −0.9649 | 0.9998 | 3 |
| 14 | 0.7837 | 0.2155 | 0.0255 | 1.6396 | −0.1804 | 3 |
| 15 | −0.0526 | −1.2964 | 1.6167 | 0.4785 | 0.8863 | 1 |
| 16 | 0.0057 | −1.3587 | 0.4027 | 0.1493 | 0.1907 | 3 |
| 17 | −0.9001 | 0.8008 | −1.4816 | −0.2934 | 0.4536 | 3 |
| 18 | 1.9534 | 1.9457 | −1.1564 | −1.2251 | −1.8506 | 3 |
| 19 | 0.6418 | 0.7898 | 0.5852 | 0.7657 | −1.5597 | 3 |
| 20 | −0.6714 | 1.5165 | 0.3638 | −1.2357 | 0.5313 | 3 |

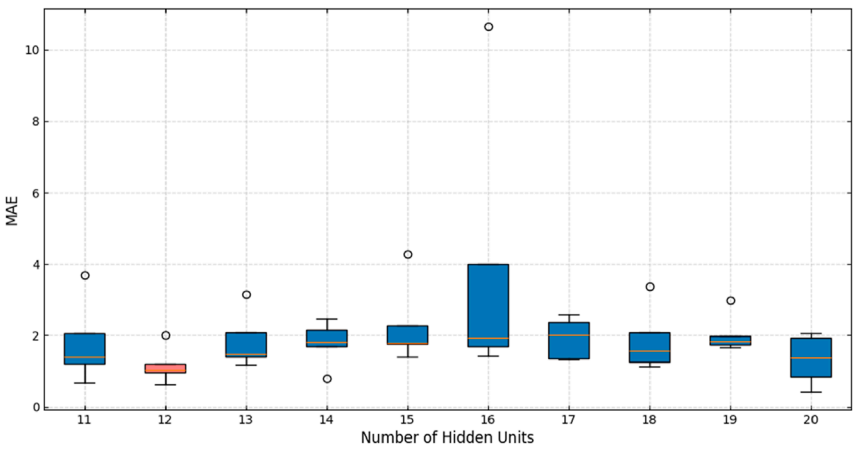


FIGURE 10
Error graph of five-fold cross-validation.

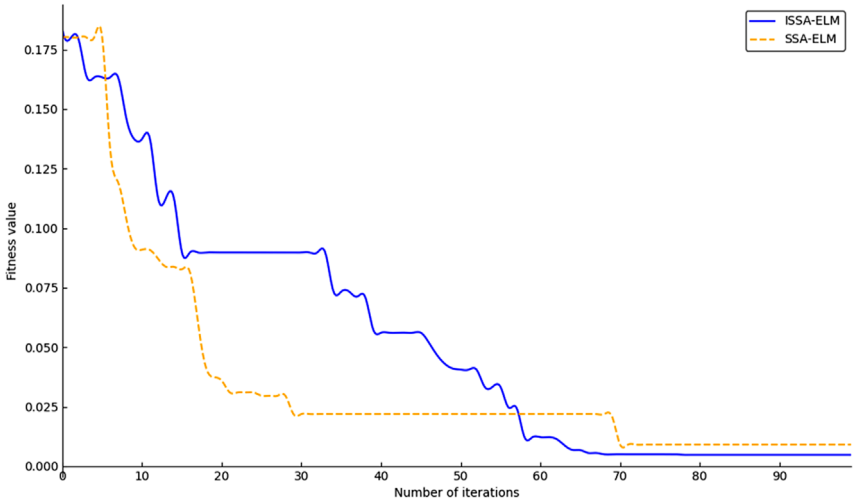


FIGURE 11
Adaptation graph.

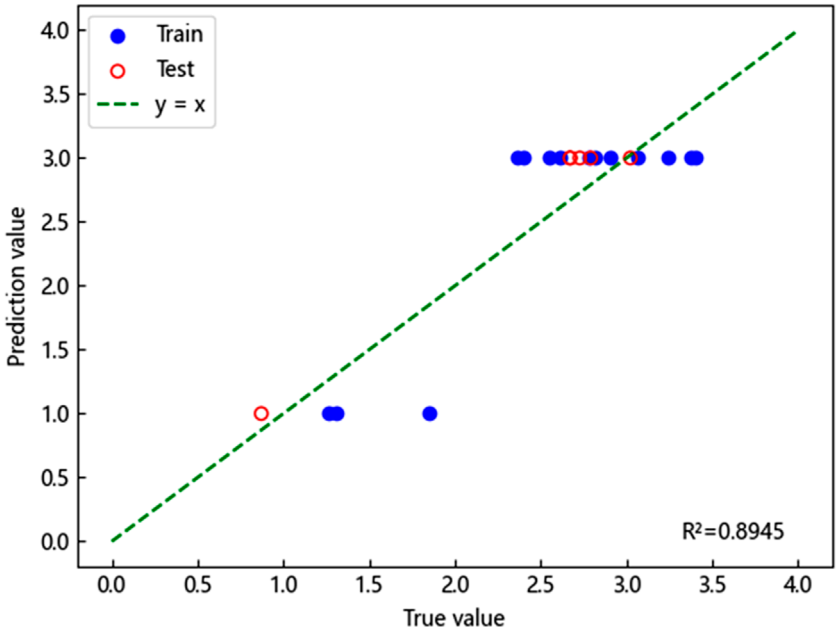


FIGURE 12
Prediction results of the ISSA-ELM model (without PCA processing).

described in Section 2.7. A comprehensive comparative analysis was conducted to assess the predictive accuracy and generalization capability of the ISSA-ELM model against the SSA-ELM model and the conventional ELM model (Figure 15)

The results presented in Figure 15 indicate that the ISSA-ELM model achieved the lowest MSE (0.0047) and MAE (0.0544) among all models. In comparison, the SSA-ELM model reported an MSE of 0.0091 and an MAE of 0.0766, whereas the ELM model exhibited a significantly higher MSE of 0.9988 and an MAE of 0.6903. These results clearly demonstrate the superior predictive accuracy and robustness of the ISSA-ELM model. The enhanced convergence of the ISSA, facilitated by the integration of the Singer chaotic map, effectively mitigated the limitations of traditional sparrow search algorithms, preventing premature convergence and ensuring optimal parameter selection.

Furthermore, the goodness-of-fit coefficient ($R^2$) of the ISSA-ELM model was markedly higher than those of the SSA-ELM and ELM models. This result reflects the ISSA-ELM model's excellent generalization performance, indicating its ability to make accurate predictions across diverse datasets. The reduced error values and

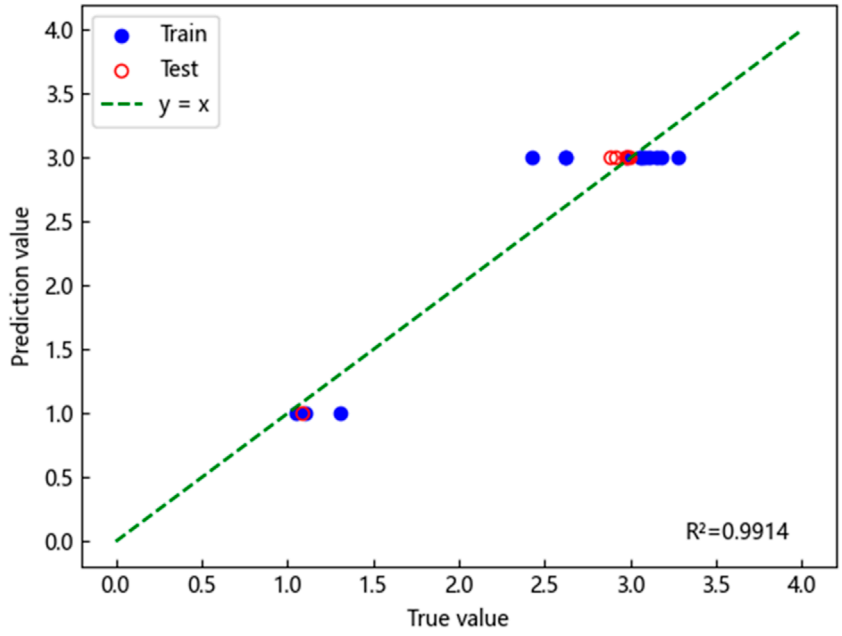


FIGURE 13
Prediction results of the ISSA-ELM model (with PCA processing).

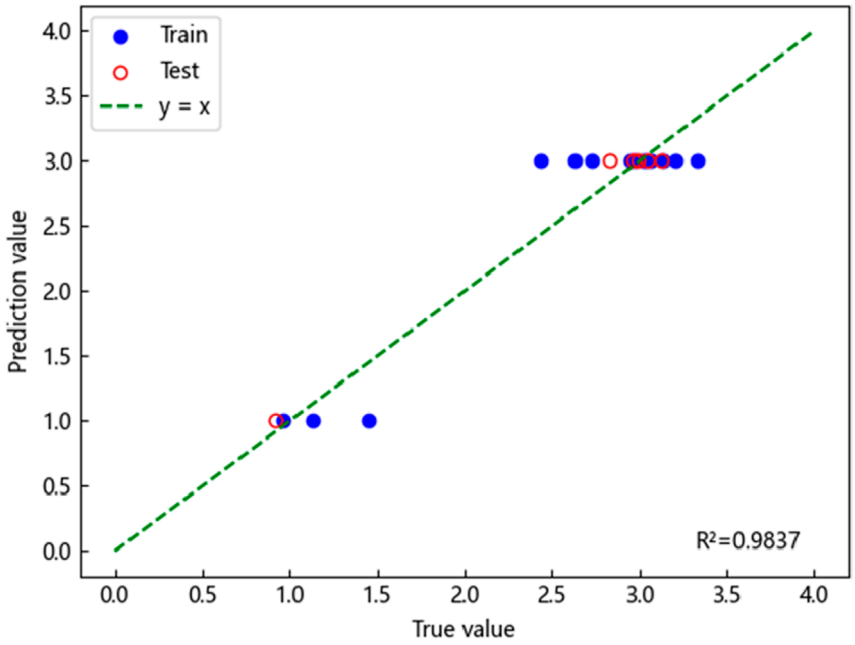


FIGURE 14
Prediction results of the SSA-ELM model.

consistent prediction accuracy further validate the model's reliability and stability.

In summary, the ISSA-ELM model exhibits substantial advantages in karst-collapse susceptibility prediction. Its remarkable accuracy, minimized prediction errors, and robust generalization capacity make it an effective and reliable tool for geohazard risk assessment. Consequently, the model can serve as a valuable decision-support system for policymakers, urban planners, and geotechnical engineers engaged in geological disaster prevention and management.

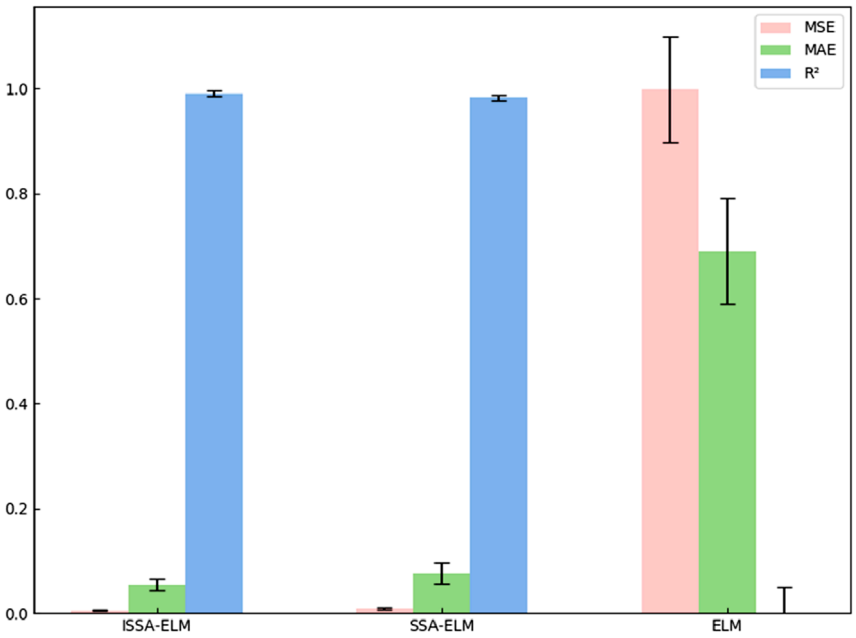


FIGURE 15
Comparison of error metrics among various models.

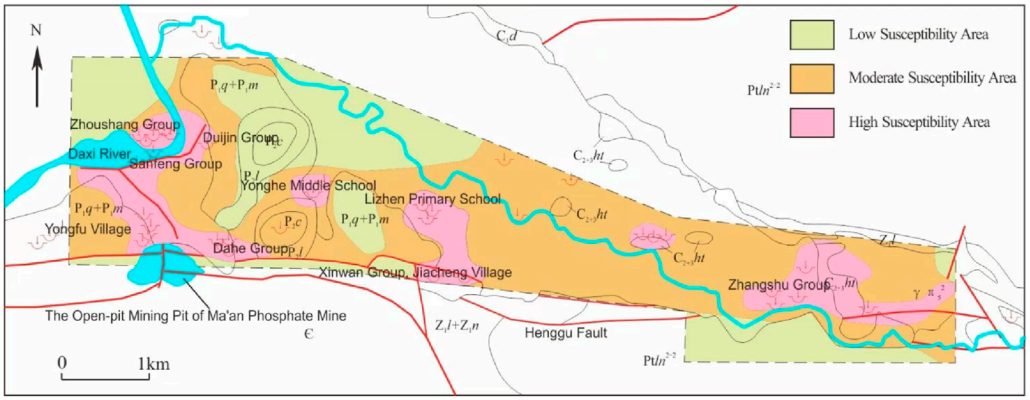


FIGURE 16
Zoning map of karst-collapse susceptibility grades in Yonghe Town, Liuyang City, Hunan Province conclusions.

## 4.5 Model validation

To comprehensively evaluate the effectiveness and accuracy of the ISSA-ELM model in predicting the karst-collapse susceptibility, the evaluation area shown in Figure 7 was designated as the primary study region. Subsequently, the prediction scope was expanded to cover the entire Yonghe Town. A karst-collapse susceptibility zoning map was generated using MAPGIS software, as illustrated in Figure 16.

The results reveal that Yonghe Middle School, Lizhen Primary School—Xinwan Group of Jiacheng Village, Sanfeng Group—Dahe Group, and Zhangshu Group are classified as high-susceptibility zones. Conversely, Duijin Group and Zhoushang Group are identified as low-susceptibility areas, with other regions falling under medium-susceptibility zones.

Notably, numerous collapse pits were identified in Jingquan Village, Tieshan Village, and Qibaoshan Village, all located in proximity to the Qibaoshan mining area. Although most pits have been backfilled, a substantial secondary collapse occurred in the Zhangshu Group of Tieshan Village. This incident further substantiates the predictive reliability of the ISSA-ELM model, which accurately identified high-susceptibility regions. The model's capacity to predict secondary collapses post-backfilling highlights its practical applicability in real-world scenarios.

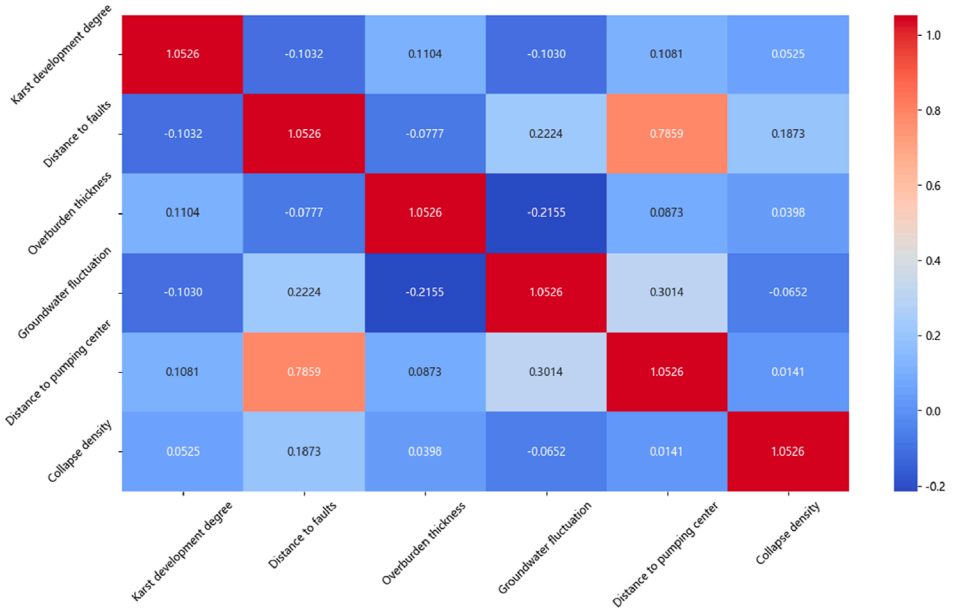


FIGURE 17
Correlation diagram of influencing factors of karst collapses.

The correlation analysis of influencing factors, presented in Section 4.1 (Figure 17), further corroborates these findings. Proximity to intra-area faults and the distance from the pumping funnel center were identified as primary determinants of karst-collapse susceptibility. These insights provide a strong basis for the implementation of targeted disaster prevention and mitigation measures.

To mitigate the risk of karst collapses effectively, comprehensive monitoring and preventive measures are essential in high-susceptibility regions. Advanced remote sensing, geophysical exploration techniques, and real-time monitoring systems can provide early warnings and facilitate rapid response efforts. Additionally, evidence-based management strategies, including regulated groundwater extraction and optimized land-use planning, should be prioritized to minimize collapse incidents.

Furthermore, this research provides valuable theoretical support for urban planning, particularly in the determination of disaster-avoidance distances. Policymakers and urban planners can utilize the susceptibility zoning map to make informed decisions, ensuring that critical infrastructure and densely populated areas are located outside high-susceptibility zones.

## 5 Conclusion

(1) In this study, we used PCA for dimensionality reduction in karst-collapse susceptibility factors. Comparative analysis confirmed that the application of PCA significantly enhanced the predictive accuracy of the ISSA-ELM model, resulting in a 10.83% increase in $R^2$. This demonstrates the effectiveness of PCA in reducing data redundancy and extracting critical features.

(2) To overcome the limitations of the traditional SSA, including local optima convergence and slow convergence speed, the Singer chaotic map was introduced for population initialization. This enhancement resulted in the development of the ISSA, which was integrated with the ELM model. The ISSA-ELM model exhibited superior predictive performance across 20 measured datasets, achieving an MAE of 0.0544, an MSE of 0.0047, and an $R^2$ of 0.9914. These results highlight the model's exceptional accuracy and robust generalization capability compared to conventional ELM and SSA-ELM models.

(3) The optimal number of hidden-layer nodes in the ELM model was determined through a rigorous five-fold cross-validation approach. This method effectively mitigated the risks of underfitting and overfitting while maximizing the use of limited data. The selected optimal number of nodes (N = 12) further demonstrated the effectiveness of this approach in fine-tuning model hyperparameters.

(4) The ISSA-ELM model was applied for the first time to predict karst-collapse susceptibility. The generated susceptibility zoning map showed a significant spatial correlation between high-susceptibility zones and densely populated areas, including schools and villages. Through correlation analysis, the primary influencing factors were identified, offering a solid theoretical foundation for determining disaster-avoidance distances in urban planning. The findings provide essential guidance for policymakers in

developing evidence-based disaster prevention and mitigation strategies.

(5) Despite its promising results, this study has certain limitations:
   ① Limited dataset: the dataset used for model training and validation was relatively small, which may affect the model's generalizability.
   ② Activation function selection: only the sigmoid activation function was applied, with no comparative analysis involving other functions. Future studies could explore Tanh or ReLU activation functions to assess their impact on model performance.
   ③ Data imbalance: the dataset contained limited non-disaster-point data, potentially resulting in an incomplete representation of non-disaster areas. Techniques such as the synthetic minority over-sampling technique (SMOTE) could be applied to address this imbalance.
   ④ Normalization methods: the study did not investigate the effects of different normalization methods, leaving the potential impact of alternative approaches unexplored.

(6) To further refine and validate the ISSA-ELM model, future research should focus on the following aspects:
   ① Dataset expansion: incorporating additional data from various karst regions will improve model training and validation.
   ② Activation function evaluation: comparative studies of different activation functions, including Tanh and ReLU, can optimize model performance.
   ③ Algorithmic enhancements: developing hybrid optimization strategies could further mitigate the risk of local optima in the sparrow algorithm.
   ④ Data balancing: applying algorithms like SMOTE will balance the sample distribution and enhance model robustness.
   ⑤ Normalization analysis: evaluating the impact of different normalization methods will provide insights into their influence on prediction accuracy.
   ⑥ Generalizability assessment: applying the ISSA-ELM model to other karst regions with diverse geological and hydrological conditions will assess its broader applicability.

By addressing these aspects, future research can further enhance the predictive accuracy, stability, and practical applicability of the ISSA-ELM model. Ultimately, this will contribute to more effective karst-collapse prevention and improved risk management strategies.

## Data availability statement

The original contributions presented in the study are included in the article/supplementary material; further inquiries can be directed to the corresponding author.

## Author contributions

JW: conceptualization, data curation, and writing – original draft. YY: methodology, supervision, and writing – review and editing. XY: data curation, supervision, validation, and writing – original draft. YuL: data curation, investigation, and writing – review and editing. YaL: data curation, investigation, and writing – review and editing. DH: software, validation, and writing – review and editing. YH: software and writing – review and editing.

## Funding

The author(s) declare that no financial support was received for the research and/or publication of this article.

## Acknowledgments

The authors are grateful to the Hunan Institute of Territorial Spatial Survey and Monitoring, providing access to field data and technical support.

## Conflict of interest

The authors declare that the research was conducted in the absence of any commercial or financial relationships that could be construed as a potential conflict of interest.

## Generative AI statement

The author(s) declare that no Generative AI was used in the creation of this manuscript.

## Publisher's note



## Supplementary material

The Supplementary Material for this article can be found online at: https://www.frontiersin.org/articles/10.3389/feart.2025.1581090/full#supplementary-material.

# References


Bao, H. M., and Hu, C. S. (2002). Neural network prediction of karst ground collapse. *J. Eng. Geol.* 10 (3), 299–304. doi:10.3969/j.issn.1004-9665.2002.03.014

Bouzerda, M., Mehdi, K., Boualla, O., Fadili, A., Najib, S., and Saied, M. (2024). Inventory and geomorphological analysis of karstic collapse dolines in Sahel-Doukkala (Morocco). *Carbonates Evaporites* 39 (4), 93. doi:10.1007/s13146-024-01007-7

Cao, B., Bai, G., and Li, H. (2015). Prediction and analysis of gas content based on PCA-GA-BP neural network. *J. Saf. Sci. Technol.* (5), 84–90. doi:10.11731/j.issn.1673-193x.2015.05.013

Chen, D., and Cao, Y. (2023). Numerical simulation of karst collapse in qingling Town, wuhan. *J. Phys. Conf. Ser.* 2565 (1), 012034. doi:10.1088/1742-6596/2565/1/012034

Chen, X. J., Chen, L. J., Song, Y., and Pengyan, B. (2019). Prediction and analysis of karst collapse with entropy - normal cloud model. *J. Eng. Geol.* 27 (6), 1389–1394. doi:10.13544/j.cnki.jeg.2018-347

Chen, H. F., Zhu, M. Q., Xia, R. Y., Tang, J. S., and Liang, B. (2005). Analysis on epikarst spring with BP ANN in Luota, Hunan Province. *Carsologica Sin.* (4), 300–304 doi:10.3969/j.issn.1001-4810.2005.04.008

Ding, H., Wu, Q., Zhao, D., Mu, W., and Yu, S. (2019). Risk assessment of karst collapse using an integrated fuzzy analytic hierarchy process and grey relational analysis model. *Geomechanics Eng.* 18 (5), 515–525. doi:10.12989/gae.2019.18.5.515

En, W., Long-Cang, S., Li-Hong, L., and Bi-Juan, H. (2011). Prediction model for water level of sinkholes in karst region based on improved SVM. *J. Hohai Univ. Nat. Sci.* 39 (1), 20–23. doi:10.1007/s12182-011-0118-0

Feng, T. (2025). *Mechanism and stability analysis of karst collapse in jingquan water source area of tengzhou city*. Singapore: Springer. doi:10.1007/978-981-97-7251-3_20

Gao, C., Li, S., Wang, J., Li, L., and Lin, P. (2018). The risk assessment of tunnels based on grey correlation and entropy weight method. *Geotech. Geol. Eng.* 36, 1621–1631. doi:10.1007/s10706-017-0415-5

Gao, Z. J., Ma, H. H., Wang, M., and Cheng, S. C. (2009). Preliminary exploration of the prediction model for karst ground collapse. *Chin. J. Geol. Hazard Control.* 20 (4), 66–71. doi:10.3969/j.issn.1003-8035.2009.04.014

Hu, R., Yeung, M., Lee, C., S., W., and J., X. (2001). Regional risk assessment of karst collapse in Tangshan, China. *Environ. Geol.* 40 (11), 1377–1389. doi:10.1007/s002540100319

Huang, G. B., Zhu, Q. Y., and Siew, C. K. (2006). Extreme learning machine: theory and applications. *Neurocomputing* 70 (1/3), 489–501. doi:10.1016/j.neucom.2005.12.126

Huang, R. D., Han, M., Zhang, X. J., Zhang, H., Jin, H., and Hua, Z. (2011). Classification and prediction of karst collapse tendency grade based on Fisher discriminant method. *China Saf. Sci. J.* 21 (9), 70–76. doi:10.3969/j.issn.1003-3033.2011.09.012

Jiang, C. L., and Jiang, Z. Q. (2012). Prediction of karst collapse based on Fisher discriminant analysis method. *J. Earth Sci. Environ.* 34 (1), 5. doi:10.3969/j.issn.1672-6561.2012.01.012

Jiang, S. Q., and Shi, B. (2023). Prediction of failure pressure of pipelines with corrosion defects based on the ISSA-ELM model. *Hot Work. Technol.* 52 (12), 70–75 + 80. doi:10.14158/j.cnki.1001-3814.20221045

Jiyuan, H., Mahdi, M., Jiayao, W., Qin, F., Zhang, J., Wu, W., et al. (2021). Karst collapse risk zonation and evaluation in wuhan, China based on analytic hierarchy process, logistic regression, and InSAR angular distortion approaches. *Remote Sens.* 13 (24), 5063. doi:10.3390/rs13245063

Journal of Chemistry (2023). Retracted: study on early warning of karst collapse based on the BP neural network. 1. doi:10.1155/2023/9818621

Lai, Y. B., and Qiao, C. S. (2008). An intelligent prediction model for karst collapse based on support vector machine. *J. Beijing Jiaot. Univ.* 32 (1), 5. doi:10.3969/j.issn.1673-0291.2008.01.009

Liu, C. A., Feng, X. L., Sun, C. H., and Zhao, L. J. (2022). Maximum 2 - D entropy image segmentation method based on improved sparrow algorithm. *Laser Technol.* 46 (2), 274–282. doi:10.7510/jgjs.issn.1001-3806.2022.02.020

Luo, X. J., and Shen, J. (2018). Research progress and prospect of karst ground collapse in China. *Carsologica Sin.* 37 (1): 101–111. doi:10.11932/karst20180106

Lv, X., Mu, X. D., Zhang, J., and Wang, Z. (2021). Chaotic sparrow search optimization algorithm. *J. Beijing Univ. Aeronautics Astronautics* 47 (8), 1712–1720. doi:10.13700/j.bh.1001-5965.2020.0298

Meng, Y., Huang, J. M., Lei, M. T., Li, Y., and Dai, J. L. (2009). Quantitative forecasting method of karst collapse based on grey Verhulst model. *Carsologica Sin.* (1), 17–22. doi:10.3969/j.issn.1001-4810.2009.01.004

Ministry of Natural Resources of the People's Republic of China (2023). DZ/T 0447-2023 specification for karst collapse survey. 1. Beijing: China Standard Press. 10–31.

Pearson, K. (1901). LIII. On lines and planes of closest fit to systems of points in space. *Philosophical Magazine Series 6.* 2 (11), 559–572. doi:10.1080/14786440109462720

Qiu, X. R. (2004). Grey - fuzzy comprehensive evaluation on the stability of karst collapse. *Hydrogeology and Eng. Geol.* 31 (4), 4. doi:10.3969/j.issn.1000-3665.2004.04.010

Ren, T., Tian, G. L., Ning, Z. J., Zhou, A. H., Li, K., and Chen, S. (2023). Evaluation of karst collapse susceptibility based on geographical detector and random forest. *J. Catastrophology* 38 (3), 227–234. doi:10.3969/j.issn.1000-811X.2023.03.035

Wang, G., Hao, J., Wen, H., and Cao, C. (2022). A random forest model of karst ground collapse susceptibility based on factor and parameter coupling optimization. *Geocarto Int.* 37 (27), 15548–15567. doi:10.1080/10106049.2022.2102216

Wang, Z. Z., Zhuang, Z. H., Hu, F. Y., and Huang, W. L. (2024). Formation conditions and susceptibility assessment of karst collapses in the northern hilly area of Guangzhou City. *J. China Geol. Hazard Control* 35 (4), 163–172. doi:10.16031/j.cnki.issn.1003-8035.202311008

Wei, A., Li, D., Zhou, Y., Deng, Q., and Yan, L. (2021). A novel combination approach for karst collapse susceptibility assessment using the analytic hierarchy process, catastrophe, and entropy model. *Nat. Hazards* 105, 405–430. doi:10.1007/s11069-020-04317-w

Xiaozhen, J., Jianling, D., Zhiwen, Z., Li, X. J., Ma, X., Zhou, W., et al. (2024). An overview on karst collapse mechanism in China. *Carbonates and Evaporites* 39 (3), 71. doi:10.1007/s13146-024-00986-x

Xie, J. F., Tan, F., Jiao, Y. Y., Zou, J., and Mao, Z. (2021). Prediction of karst ground collapse based on factor analysis-GA-ELM model. *J. Eng. Geol.* 29 (2), 236–544. doi:10.13544/j.cnki.jeg.2020-219

Xue, J. K., and Shen, B. (2020). A novel swarm intelligence optimization approach: sparrow search algorithm. *Systems Science and Control Engineering* 8 (1), 22–34. doi:10.1080/21642583.2019.1708830

Yang, Z., Li, B., Wu, H., Li, M., Fan, J., Chen, M., et al. (2023). Water consumption prediction and influencing factor analysis based on PCA-BP neural network in karst regions: a case study of Guizhou Province. *Environmental Science and Pollution Research* 30 (12), 33504–33515. doi:10.1007/s11356-022-24604-2

YanHua, X., BingHui, Z., YuXin, L., Liu, B. C., Zhang, C. F., and Lin, Y. S. (2022). Evaluation of the karst collapse susceptibility of subgrade based on the AHP method of ArcGIS and prevention measures: a case study of the quannan expressway, section K1379+300-K1471+920. *Water* 14 (9), 1432. doi:10.3390/w14091432

Zhang, J., Bi, P., Wei, A. H., Tao, Z. B., and Zhu, H. C. (2021). Assessment of susceptibility to karst collapse in the Qixia Zhongqiao district of Yantai based on fuzzy comprehensive method. *Carsologica Sinica* (2), 215–220. doi:10.11932/karst2021y07

Zhou, A. H., Niu, P. F., Yuan, Y., and Huang, H. C. (2020). Prediction of karst surface collapse risk in Fankou lead - zinc mine area based on PCA-PSO-SVM. *Carsologica Sinica* (4), 622–628. doi:10.11932/karst2020y30

Zhuang, S. Y. (2022). Assessment of karst collapse susceptibility in yongding district, Longyan city using the fuzzy analytic hierarchy process. *Geology of Fujian* 41 (4), 323–331. doi:10.3969/j.issn.1001-3970.2022.04.008

frontiers | Frontiers in Earth Science

TYPE Brief Research Report
PUBLISHED 07 May 2025
DOI 10.3389/feart.2025.1593528



OPEN ACCESS

EDITED BY
Pengfei Liu,
CCCC Second Harbor Engineering Co., Ltd., China

REVIEWED BY
Xiangcou Zheng,
Central South University, China
Yipeng Xie,
Ocean University of China, China
Yunpeng Hu,
Chengdu University of Technology, China

*CORRESPONDENCE
Liu Yinglin,
461272650@qq.com

RECEIVED 14 March 2025
ACCEPTED 10 April 2025
PUBLISHED 07 May 2025

CITATION
Yan Z, Jihong D, Yinglin L, Mengshan X and Wen L (2025) Study on strength prediction of grouting filling body in karst areas considering pressure filter effect.
*Front. Earth Sci.* 13:1593528.
doi: 10.3389/feart.2025.1593528



# Study on strength prediction of grouting filling body in karst areas considering pressure filter effect

Zhao Yan[1,2], Duan Jihong[1], Liu Yinglin[2,3]*, Xie Mengshan[2,4] and Li Wen[1]

[1]Yunnan Honghe Hydropower Survey and Design Institute, Mengzi, Yunan, China, [2]Central South University of Forestry and Technology, Changsha, Hunan, China, [3]The Administration Bureau of Large-scale Irrigation Areas in Honghe Prefecture, Mengzi, Yunan, China, [4]Changsha Building Engineering School, Changsha, Hunan, China

The slurry within the grouting pressure and karst boundary constraints produces a pressure filtration effect, resulting in the initial consolidation strength of the embankment curtain stone body in karst areas being significantly higher than the natural consolidation strength of the slurry. Consequently, using the natural consolidation strength of the slurry as the initial condition for constructing the curtain life prediction model often leads to substantial deviations from engineering practice. To address this issue, this paper first derives a theoretical formula for calculating the initial consolidation strength of the grouted curtain body, taking into account the erosive effects of karst water ions and the pressure-filtering effect. Secondly, a life prediction model for grouting curtains in karst areas, which incorporates the pressure-filtering effect, is developed, and its feasibility is demonstrated through indoor accelerated testing. Finally, the research findings were successfully applied to guide the curtain de-reinforcement project at the Yingpan Reservoir in Yunnan Province. The results indicate that the theoretical formula for the initial consolidation strength of the grouted curtain body, which considers the pressure-filtering effect, more accurately characterizes the initial conditions of the curtain. Additionally, the theoretical values derived from the curtain life prediction model closely align with the accelerated experimental test values, with an error margin of less than 15%. This demonstrates that the theoretical prediction model can effectively forecast the service life of the curtain body under conditions of karst water erosion. The successful engineering application further confirms the feasibility and practicality of the theoretical prediction model. Given the increasing number of similar cases, the research findings hold significant application potential and practical value.

KEYWORDS

**karst area embankment, pressure-filtration effect, grouted curtain body, strength calculation, life prediction**

## 1 Introduction

In the 1950s–1970s, many dam projects were constructed in China. Due to the design standards, construction conditions, and level of mechanization at that time,

numerous dams experienced varying degrees of seepage, either during the initial stages of operation or after several years. This seepage significantly affected the operational safety of the dams (Ge et al., 2024; Jian et al., 2024; Xiang et al., 2022). Consequently, over the past decade, large-scale danger removal and reinforcement work has been conducted on dams in China. Grouting has played a crucial role in these projects due to its advantages, including simple construction, low environmental impact, and high construction efficiency (Fazeli, 2007; ZHANG et al., 2021; Dou et al., 2020). However, after a period of operation, some dams that underwent danger removal and reinforcement experienced seepage again, primarily in the areas of the grouting anti-seepage body. This issue is particularly pronounced in karst dams. Numerous studies have shown (Mozafari et al., 2021; Romanov et al., 2003) that the grouting anti-seepage body is susceptible to erosion and damage under the combined effects of high water pressure and karst water ions, leading to a significant reduction in its service life. Given the large number of dams in China and the widespread distribution of karst areas, researching the service life prediction of grouting curtains for dams in karst regions is of great practical significance and engineering value. This research can guide subsequent dam danger removal and reinforcement projects, as well as the design and construction of new dams.

At this stage, scholars have conducted extensive research on the life prediction of grouting curtains in karst areas through numerical simulation, model testing, and theoretical analysis, yielding significant results. In numerical simulations, Nagihara (1996), Wang et al. (2020), and others explored the deterioration of slurry crenellations in erosive environments by establishing a multivariate grey prediction model, a mechanical damage model for grouting plus solids under seepage, and a service life-cycle prediction model. Meanwhile, Dafny et al. (2015), Chen et al. (2022), and Huo et al. (2019) employed multi-coupled physical field software to investigate the decay processes and characteristics of service performance and impermeability in embankment curtains within karst areas. Although the numerical simulation results provide valuable insights for predicting the lifespan of grouted curtains in karst environments, these studies often simplify the karst water erosion process, leading to discrepancies between predicted lifespans and actual project outcomes. In terms of model testing, researchers have employed dry-and-wet cyclic deterioration tests (Muntaha, 2017; Zhou et al., 2022), accelerated erosion experiments (Paglia et al., 2003; Wang et al., 2021), drenching tests, and uniaxial compression tests (He et al., 2021; Ran et al., 2021) to investigate the performance deterioration of karst fillers, producing supportive findings for life prediction studies. However, due to limitations of model tests, it is challenging to conduct large-sample and long-cycle tests that comprehensively represent the entire service life of grouting curtains in karst areas. The theoretical analysis method, which can circumvent many shortcomings of model testing through specific assumptions and straightforward derivation processes, is increasingly being adopted by scholars for life prediction research on grouting curtains in karst areas. For instance, Dong et al. (2022) enhanced the initial weights and thresholds of a BP neural network using genetic algorithms to create a GA-BP model for predicting compressive strength; Peng (2012) developed a GA-BP model based on acid-base test methods to assess the service life of slurry-cemented bodies; and Hou et al. (2020) established a life-cycle prediction model for slurry-cemented body specimens based on deformation modulus measurements from indoor tests. Literature reviews indicate that these studies advance theoretical research on life prediction for grouted curtains in embankment dams situated in karst areas. However, existing research often neglects the impact of the pressure-filtering effect on the performance of grouted curtains during formation, resulting in significant discrepancies between the initial conditions of life prediction models and engineering realities. Specifically, the slurry subjected to grouting pressure and constrained by karst boundaries produces a pressure-filtering effect (Chen et al., 2021), which precipitates free water and solidified water in the slurry. This results in the initial consolidation strength of the curtain stone body being significantly higher than that of the natural-state slurry consolidation strength (Axelsson et al., 2009; Eklund and Stille, 2008; Bouchelaghem et al., 2007). Therefore, using the natural consolidation strength of the slurry as the initial condition in life prediction models for curtains is unlikely to effectively guide engineering practice.

This paper first derives the theoretical formula for the initial consolidation strength of the grouting curtain body under karst water ion erosion, considering the filtering effect. Based on this theoretical formula, a life prediction model for the grouting curtain in karst areas is constructed. Next, the feasibility and practicality of the life prediction model are validated through indoor accelerated erosion tests of the cemented stone body, conducted using a self-developed filter-pressing grouting device. Finally, the grouting curtain life prediction model, which accounts for the pressure-filtering effect, is applied to the Zhumashao Reservoir in Kaiyuan City to determine the optimal grouting pressure during the design and construction stages of the reservoir. The results of this study aim to provide a reference for real-world projects.

## 2 Grouted curtain body life prediction model under pressure-filtration effect

### 2.1 Basic assumptions of the model

(1) The slurry is an incompressible fluid, and its properties remain consistent throughout the diffusion process, adhering to Darcy's law.
(2) The slurry undergoes cylindrical diffusion, resulting in a grout curtain body structure that is uniform, isotropic, and composed of incompressible homogeneous material.
(3) During the filtration process, the structure and number of capillary pores within the grout curtain remain unchanged, allowing water in the slurry to precipitate freely.
(4) The pressure-filtering effect is present throughout the entire grouting process; however, its influence varies along the horizontal direction of the grouting curtain.
(5) The primary component of the cement slurry forming the curtain is calcium silicate, with hydrated calcium silicate gel playing a crucial role in determining the curtain's properties.
(6) The hydration of cement in the grouting curtain is complete, and there is no air present in the pore spaces of the curtain.

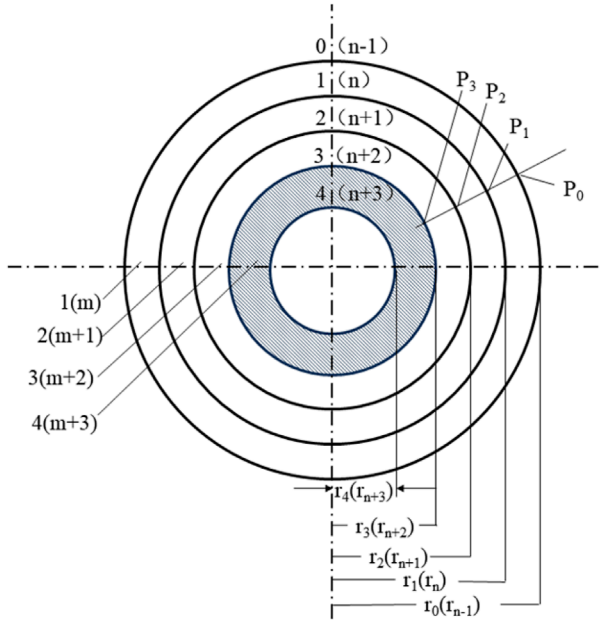


FIGURE 1
Radial load calculation diagram.

## 2.2 Model construction and solution

Based on the above assumptions and references (Chen et al., 2021), it is evident that during the formation stage of the grout curtain, the cement slurry in the grouting process is influenced by a pressure-filtering effect. This effect causes the free and combined water in the slurry to continuously precipitate, resulting in the initial consolidation strength of the curtain body being significantly higher than the natural consolidation strength of the slurry. In the operational stage, the grout curtain body interacts with erosive ions present in the karst water. The calcium oxide within the grout curtain is gradually dissolved, which diminishes its seepage control and reinforcement capabilities until the grout curtain ultimately fails, marking the end of its service life. Therefore, during the formation stage of the grout curtain, and in accordance with assumptions (Equations 2–4), this paper performs a force analysis on a unit body within the curtain. The radial load calculation sketch is illustrated in Figure 1.

As shown in Figure 1, a cylindrical model of the curtain body is cut into rings of varying heights using a circular cross-section. Here, $m$ denotes the number of rings, $n$ denotes the number of demarcation surfaces, and $r_n$ represents the radius of the rings. The radial pressure acting on the demarcation surface is $P$, the modulus of elasticity of the circular body is $E$, and the Poisson's ratio is $\mu$. The equilibrium condition at the interface between the rings (Equation 1) is given by He (1990).

$$\begin{cases} U_{m,n} = U_{(m+1),n}\,(\text{Equilibrium equation of radial displacement U}) \\ P_{m,n} = P_{(m+1),n}\,(\text{Equilibrium equation of radial force P}) \end{cases} \tag{1}$$

If the height of the curtain is assumed to be $h$, the radial $\sigma_r$ and tangential stresses $\sigma_\tau$ are related to the same radius by the equation.

$$\sigma_r = \frac{\frac{1-\mu}{Eh} \times \frac{r_1}{2}(r_2 - r_1)E}{1-\mu} + \frac{\frac{1-\mu}{Eh} \times \frac{r_2}{2}(r_3 - r_2)E}{(1+\mu)r^2} \tag{2}$$

$$\sigma_\tau = \frac{\frac{1-\mu}{Eh} \times \frac{r_1}{2}(r_2 - r_1)E}{1-\mu} + \frac{\frac{1-\mu}{Eh} \times \frac{r_2}{2}(r_3 - r_2)E}{(1+\mu)r^2} \tag{3}$$

The equilibrium differential equation for a planar circular ring under uniform external radial pressure is simplified as follows:

$$U = \sigma_1 r + \frac{\sigma_2}{r} \tag{4}$$

Two adjacent rings of circular cross-section, the m-th and the (m+1)-th, are selected for analysis. The m-th ring is bounded by the radii $r_{n-1}$ and $r_n$, and the (m+1)-th ring is bounded by $r_n$ and $r_{n+1}$. Then, the equilibrium differential equations of the planar circular rings under radial pressure for the m-th rings (Equations 5, 6) and (m+1)-th rings (Equations 7, 8) are obtained from Equation 4 as:

$$\begin{cases} U_{m,(n+1)} = \dfrac{1-\mu}{Eh} \times \dfrac{r_{1,m}}{2}(r_{2,m} - r_{1,m})r_{n+1} + \dfrac{\frac{1-\mu}{Eh} \times \frac{r_{2,m}}{2}(r_{3,m} - r_{2,m})}{r_{n+1}} \\ U_{m,n} = \dfrac{1-\mu}{Eh} \times \dfrac{r_{1,m}}{2}(r_{2,m} - r_{1,m})r_n + \dfrac{\frac{1-\mu}{Eh} \times \frac{r_{2,m}}{2}(r_{3,m} - r_{2,m})}{r_n} \end{cases} \tag{5}$$

$$\begin{cases} \sigma_{r,m,(n+1)} = \dfrac{\frac{1-\mu}{Eh} \times \frac{r_{1,m}}{2}(r_{2,m} - r_{1,m})E}{1-\mu} - \dfrac{\frac{1-\mu}{Eh} \times \frac{r_{2,m}}{2}(r_{3,m} - r_{2,m})E}{(1+\mu)r_{n+1}^2} \\ \sigma_{r,m,n} = \dfrac{\frac{1-\mu}{Eh} \times \frac{r_{1,m}}{2}(r_{2,m} - r_{1,m})E}{1-\mu} - \dfrac{\frac{1-\mu}{Eh} \times \frac{r_{2,m}}{2}(r_{3,m} - r_{2,m})E}{(1+\mu)r_n^2} \end{cases} \tag{6}$$

$$\begin{cases} U_{(m+1),n} = \dfrac{1-\mu}{Eh} \times \dfrac{r_{1,m+1}}{2}(r_{2,m+1} - r_{1,m+1})r_n + \dfrac{\frac{1-\mu}{Eh} \times \frac{r_{2,m+1}}{2}(r_{3,m} - r_{2,m+1})}{r_n} \\ U_{(m+1),(n+1)} = \dfrac{1-\mu}{Eh} \times \dfrac{r_{1,m+1}}{2}(r_{2,m+1} - r_{1,m+1})r_{n+1} + \dfrac{\frac{1-\mu}{Eh} \times \frac{r_{2,m+1}}{2}(r_{3,m} - r_{2,m+1})}{r_{n+1}} \end{cases} \tag{7}$$

$$\begin{cases} \sigma_{\tau,(m+1),n} = \dfrac{\frac{1-\mu}{Eh} \times \frac{r_{1,m+1}}{2}(r_{2,m+1} - r_{1,m+1})E}{1-\mu} - \dfrac{\frac{1-\mu}{Eh} \times \frac{r_{2,m+1}}{2}(r_{3,m} - r_{2,m+1})E}{(1+\mu){r_n}^2} \\ \sigma_{\tau,(m+1),(n+1)} = \dfrac{\frac{1-\mu}{Eh} \times \frac{r_{1,m+1}}{2}(r_{2,m+1} - r_{1,m+1})E}{1-\mu} - \dfrac{\frac{1-\mu}{Eh} \times \frac{r_{2,m+1}}{2}(r_{3,m} - r_{2,m+1})E}{(1+\mu){r_{n+1}}^2} \end{cases} \tag{8}$$

When $U_{m,n} = U_{(m+1),n}$,then there were:

$$r_n(\sigma_{1,m} - \sigma_{1,m+1}) + \frac{1}{r_n}(\sigma_{2,m} - \sigma_{2,m+1}) = 0 \tag{9}$$

According to the system of Equation 6, the stress balance equations for m and m+1 neighboring rings can be obtained as

Equations 10, 11.

$$\begin{cases} \sigma_{1,m} = \dfrac{1-\mu}{E(r_{n-1}^2 - r_n^2)} \times \left( \dfrac{r_{n-1}^2 P_{n-1} - r_n^2 P_n}{h} \right) \\ \sigma_{2,m} = \dfrac{(1+\mu) r_{n-1}^2 r_n^2}{E(r_{n-1}^2 - r_n^2)} \times \dfrac{P_{n-1} - P_n}{h} \end{cases} \tag{10}$$

$$\begin{cases} \sigma_{1,(m+1)} = \dfrac{1-\mu}{E(r_n^2 - r_{n+1}^2)} \times \left( \dfrac{r_n^2 P_n - r_{n+1}^2}{h} \right) \\ \sigma_{2,(m+1)} = \dfrac{(1+\mu) r_n^2 r_{n+1}^2}{E(r_n^2 - r_{n+1}^2)} \times \left( \dfrac{P_n - P_{n+1}}{h} \right) \end{cases} \tag{11}$$

Bringing $\sigma_{1,m}$, $\sigma_{2,m}$, $\sigma_{1,(m+1)}$, $\sigma_{2,(m+1)}$ into Equation 9. The stress balance equations at the m and m+1 contact surfaces are shown in Equation 12.

$$l_m P_{n-1} - (l_m + l_m + 1 + b_n) P_{\mathrm{n}} + l_m \cdot P_{n+1} = 0 \tag{12}$$

where $P_{n-1}$, $P_n$ and $P_{n+1}$ are the radial pressures acting on the ring at the separating interface ($P_0$ is the hydrostatic pressure, $P_0 = \rho g h$).

According to Reference He (1990), the expressions for the coefficients $l_m$, $l_{m+1}$ and $b_n$ are as follows:

$$l_m = \frac{r_{n-1}^2 r_n^2}{Eh(r_{n-1}^2 - r_n^2)} \tag{13}$$

$$l_{m+1} = \frac{r_n^2 r_{n+1}^2}{Eh(r_n^2 - r_{n+1}^2)} \tag{14}$$

$$b_n = \frac{r_n^2}{2} \times \frac{1-\mu}{Eh} \tag{15}$$

Expression of coefficients in Equations 13–15, where $r_{n-1}$, $r$ and $r_{n+1}$ are the radii of the interfaces when the number of interfaces is $n$.

According to the assumption condition (Equation 2), the trinomial system of equations is obtained as follows:

$$\begin{cases} P_0 - (l_1 + l_2 + \sigma_1) P_1 + l_2 P_2 = 0 \\ P_1 - (l_2 + l_3 + \sigma_2) P_2 + l_3 P_3 = 0 \\ l_3 P_2 - (l_3 + l_4 + \sigma_2) P_3 = 0 \\ l_{\mathrm{n}} = \dfrac{r_{n-1}^2 r_n^2}{Eh(r_{n-1}^2 - r_n^2)} \end{cases} \tag{16}$$

Substitute $l_1, l_2, l_3, l_4, \sigma_1, \sigma_2, \sigma_3$ into Equation 16 to find the pressure $P$ at the contact surface of the ring as follows:

$$\begin{cases} P_1 = \dfrac{(a_2 a_3 - l_3^2) l_1}{a_1 a_2 a_3 - (a_1 l_3^2 + l_2^2 a_3)} \cdot P_0 \\ P_2 = \dfrac{l_1 l_2 a_3}{a_1 a_2 a_3 - (a_1 l_3^2 + l_2^2 a_3)} \cdot P_0 \\ P_3 = \dfrac{l_1 l_2 l_3}{a_1 a_2 a_3 - (a_1 l_3^2 + l_2^2 a_3)} \cdot P_0 \\ a_1 = l_1 + l_2 + O_1 \\ a_2 = l_2 + l_3 + O_2 \\ a_3 = l_3 + l_4 + O_3 \end{cases} \tag{17}$$

Take the average value of $P_1$, $P_2$, and $P_3$ as the natural consolidation strength $f_0$ of the grouted curtain body. Then,

$$f_0 = \frac{P_1 + P_2 + P_3}{3} \tag{18}$$

According to the assumption condition (Equation 5) and in combination with the research findings of POWERS (1960), Equation relationship between the initial consolidation strength $f$ of the grouted curtain body considering the pressure-filtering effect and the gel-void ratio $X$ of the curtain body:

$$f = f_0 \cdot X^{\mathrm{n}} \tag{19}$$

where $X$ is the gel-void ratio; $n$ is an experimental constant ranging from 2.6 to 3.0, which is related to the type of cement and experimental conditions.

According to Reference (Chen et al., 2021), the calculation formula for the gel-void ratio is as follows:

$$X = \frac{V_{\mathrm{p}}}{V_{\mathrm{s}}} \tag{20}$$

$$V_p = V_s + V_d + V_h \tag{21}$$

where $V_p$ represents the pore volume of the curtain body filling the fractures after drainage and hydration under the grouting pressure ($m^3$); $V_s$ is the volume of the grout curtain body, which is also the volume of the grout filling the fractures ($m^3$); $V_d$ is the volume of the drained water from the grout filling the fractures during the grouting project ($m^3$); $V_h$ is the volume of the hydration water in the grout ($m^3$).

The volume $V_s$ of the grout curtain body can be calculated by Equation 22:

$$V_{\mathrm{s}} = \pi r^2 h \tag{22}$$

During a variable time interval $dt$ in the grouting process, the reduction in the pore volume within the unit body should be equal to the amount of water seeped out, that is Equation 23:

$$\frac{\partial V_{\mathrm{s}}}{\partial t} dt = \frac{\partial q}{\partial h} dh dt \tag{23}$$

where $t$ is the time (s); $q$ is the amount of water seeped out from the pores ($m^3$). Generally, the pore diameter of the cement curtain body ranges from $10^{-5}$ to $10^{-10}$ m. Based on the assumption condition (Equation 3), it can be deduced that:

$$q = \frac{p r^4}{g h} J \tag{24}$$

where $r$ is the radius of the pore (m), which gradually decreases as the pore water is discharged; $J$ is the hydraulic gradient in the pore ($MPa \cdot m^{-1}$); $\eta$ is the viscosity coefficient of water (Pa·s).

After the grouting time $t$, the total amount of water seeped out from the pores is:

$$V_d = \int \frac{\pi r^4}{g\eta} J t N dt \tag{25}$$

where $N$ is the number of pores on the calculation cross-section.

According to Reference Chen et al. (2021), the amount of water required for the hydration reaction with cement particles during complete hydration is 0.227 times the mass of the cement particles. Therefore, the formula for calculating the volume $V_h$ of hydration water in the Equation 26:

$$V_h = 0.227 \times \frac{V_s \rho_s m_c}{1 + (m_w / m_c) \rho_w} \tag{26}$$

where $\rho_s$ is the density of the grout (kg·cm$^{-3}$); $\rho_w$ is the density of water (kg·cm$^{-3}$); $m_c$ and $m_w$ are the masses of cement particles and water in a unit volume of the grout (kg), respectively.

Therefore, according to the different durations of pressure application during the grouting process, the initial consolidation strength $f$ of the curtain body considering the pressure-filtration effect can be obtained as follows:

$$f = f_0 \times \left[ \frac{\pi r^2 h + \int \frac{\pi r^4}{g\eta} t N dt + 0.227 \times \frac{\pi r^2 h \rho_s m_c}{1+(m_w/m_c)\rho_w}}{\pi r^2 h} \right]^n \tag{27}$$

During the operational stage of the grouted curtain body, ion erosion from karst water causes continuous dissolution of calcium oxide within the grouting material. As calcium oxide dissolves, solid-phase calcium hydroxide begins to dissolve as well. Subsequently, high-alkaline hydrated silicates and hydrated aluminates decompose into low-alkaline hydrates, ultimately transforming into substances such as gaseous silicon dioxide, which lacks cementing ability (Gao et al., 2024). Additionally, the consumption rate of calcium oxide is closely related to the pH of the environment (Peng, 2012). Consequently, the degree of strength attenuation in the curtain body varies with different pH levels.

The standard curve of the strength-pH of the calcified body is fitted using the plotting software SPSS (Version 19.0), and the Equation 28 of the standard curve is obtained.

$$F = f + \frac{A}{w\sqrt{\frac{\pi}{2}}} e^{-2\frac{(pH-pH_0)^2}{w_1^2}} \tag{28}$$

where $F$ is the residual strength of the curtain body after being eroded by karst water; $f$ is the initial consolidation strength; $pH_0$ is the initial $pH$ of the solution; $A$ and $w_1$ are constants obtained from the curve fitting.

Based on the unconfined compressive strength of the calcified body obtained from the experimental tests, a relationship curve between the strength and the service life of the calcified body is plotted. Then, the plotting software is used to fit the standard curve of the strength-service life of the calcified body, and the calculation formula of the standard curve is obtained as follows:

$$F = f + Be^{\frac{(T-T_c)^2}{2w_2^2}} \tag{29}$$

where $T_c$ is the initial time constant of the solution; $B$ and $w_2$ are constants obtained from the curve fitting.

According to Reference Peng (2012), the strength of the grouting curtain body and the $pH$ of the karst water satisfy the following relationship:

$$pH = pH_0 + \zeta(R) \tag{30}$$

where $R$ is the attenuation rate of the compressive strength.

Combining Equations 18, 27, 30, we can obtain the residual strength of the curtain body's initial consolidation strength after erosion by karst water:

$$F = \frac{P_1 + P_2 + P_3}{3} \cdot \left( \frac{\pi r^2 h - \int \frac{\pi r^4}{g\eta} t N dt - 0.227 \times \frac{\pi r^2 h_s \rho_s m_c}{1+(m_w/m_c)\rho_w}}{\pi r^2 h} \right)^n \cdot R \tag{31}$$

Taking the reaction between hydrochloric acid and cement stone as an example, $m$ moles of $Ca(OH)_2$ will consume $2m$ moles of hydrochloric acid. When the volume of the corrosive solution is $n$ liters and the initial $pH$ is $pH_0$, the consumption of $Ca(OH)_2$ and the $pH$ of the solution satisfy the following relationship:

$$pH = \lg\left( \frac{n}{n10^{-pH_0} - 2m} \right) \tag{32}$$

where $n$ is the volume of the corrosive solution; $m$ is the cumulative consumption of CaO; $pH_0$ is the initial $pH$ of the corrosive solution.

Combining Equation 30 and Equation 31 and substituting the critical $pH_T$ calculated from Equation 32 into the combined formulas, the service life $T$ of the grouted calcified body can be calculated.

Numerous studies have shown (Huo et al., 2019; Peng, 2012) that the consumption rate of calcium oxide in the grouted curtain body (i.e., the ratio of the consumed amount to the original internal total amount) is closely related to the strength of the grouted curtain body. Especially when the cumulative consumption rate of calcium oxide exceeds 25%, the strength of the curtain body will decline sharply, indicating that the grouted curtain has failed. Therefore, the failure of the curtain body, defined as reaching the critical value of its service life, occurs when its initial consolidation strength diminishes to 50% in a karst water environment.

There is the following relationship between the compressive strength of the curtain body and its service life:

$$R = \eta(t) \tag{33}$$

where $R$ is the attenuation rate of the compressive strength decay rate versus erosion time equation.

Therefore, by combining Equations 28–31, the service-life prediction model for the grouted curtain in karst areas considering the pressure-filtration effect can be obtained as follows:

$$\begin{cases} f = \frac{P_1 + P_2 + P_3}{3} \cdot \left( \frac{V_p}{V_s} \right)^n \cdot R \\ pH - pH_0 = \zeta(R)、\ pH = \lg\left( \frac{n}{n10^{-pH_0} - 2m} \right) \\ R = \eta(t)、\ T = t|\mathrm{CaO} = 25\% \end{cases} \tag{34}$$

## 2.3 Determination of model formula parameters

(1) In the formula, the elastic modulus $E$ and Poisson's ratio $\mu$ of the grouting curtain body can be obtained through tests using a triaxial stress testing machine. Specifically, the specifications in the Standard for Geotechnical Test Methods (Ministry of Water Resources of the People's Republic of China, 2019) should be referred to.

(2) The hydraulic gradient (MPa·m$^{-1}$) in the pores is equal to the ratio of the water head difference $p$ to the drainage length $h$. The calculation can be seen in Equation 35:

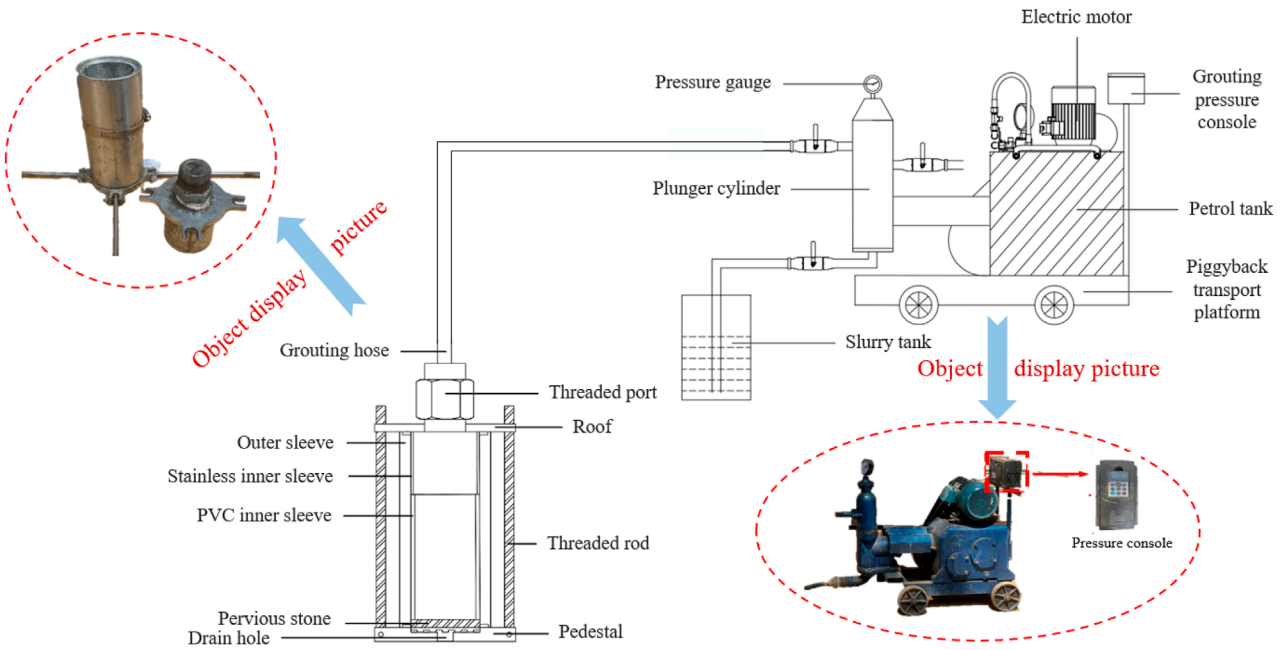


FIGURE 2
Sample preparation device for grouting stone test blocks in karst areas.

$$J = \frac{p}{h} \tag{35}$$

(3) The $\eta$ is defined as the viscosity coefficient of water at 20°C, which is generally taken as 1.0087.
(4) The density of the grout $\rho_s$ is equal to the ratio of the average saturated mass in the initial state to the volume of the specimen. The density of water $\rho_w$ is generally taken as $1 \times 10^3$ kg·m$^{-3}$.
(5) The *N*-values of grouts with different water-cement ratios can be calculated by referring to the test method in Reference You (2010).

# 3 Verification of the service - life prediction model

## 3.1 Pressure-filtration sample preparation system

To verify the feasibility of the derived service-life prediction model for the grouting curtain under the pressure filtration effect, a set of sample preparation equipment was developed for creating grouting test blocks of calcified bodies in karst areas, as shown in Figure 2. This equipment comprises two main components: a constant-pressure grouting machine and a sample preparation mold. By utilizing the properties of filter paper and permeable stones, which permit water to pass through while preventing grout from doing so, specimens of grouting-reinforced bodies can be created using different grouting materials and construction parameters under the pressure-filtration effect.

## 3.2 Specimen preparation and curing

### 3.2.1 Specimen preparation

In this test, pure cement grout was selected to create specimens of the grouting calcified body. The grout was prepared according to the commonly used mix proportions for grouting curtains in karst areas. Specifically, the water-to-cement ratio of the pure cement grout was 1:2, the grouting pressure was set at 1 MPa, and the grouting time was 6 s.

### 3.2.2 Specimen curing

Curing was conducted in accordance with the standard requirements outlined in the Standard for Test Methods of Mechanical Properties of Ordinary Concrete (Ministry of Construction of the People's Republic of China, 2019). These standards specify a temperature of 20°C ± 1°C and a humidity level of at least 95%.

## 3.3 Design of accelerated deterioration of specimens

To determine the service life of the grouting curtain body in a karst water environment within a short time frame, this paper accelerates the deterioration process of the grouting calcified body by adjusting the concentration of corrosive

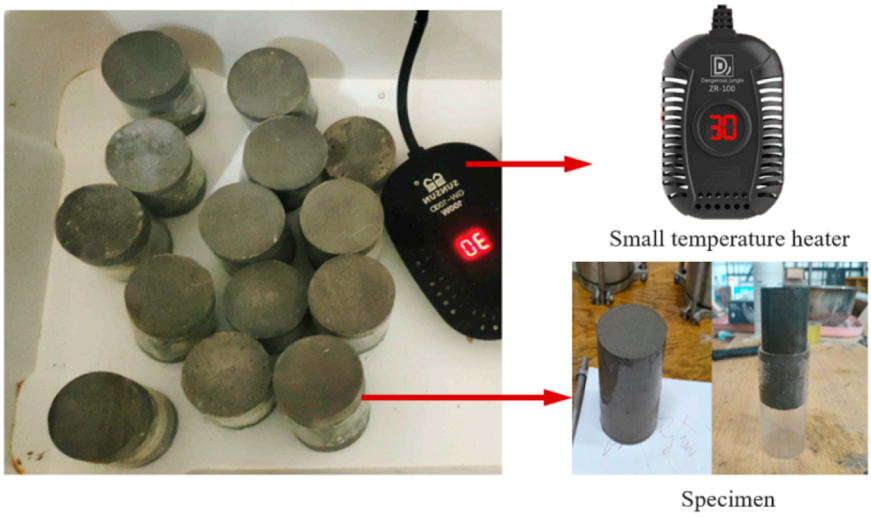


FIGURE 3
Accelerated curing of grouting stone body.

ions in the karst water and the curing temperature. The accelerated deterioration curing of the specimens is illustrated in Figure 3.

### 3.3.1 Acceleration by ion concentration

When the influence of the binding capacity of aggressive ions within the grouted stone body and the time-dependent structural defects on the diffusion coefficient is not considered, the diffusion theoretical model of aggressive ions (Equation 36) can be obtained based on Fick's second law (Zuo et al., 2012):

$$c = c_s\left(1 - erf\frac{x}{2\sqrt{Dt}}\right) \tag{36}$$

where $c_s$ is the concentration of aggressive ions on the exposed surface of the grouted stone body (mol·L$^{-1}$); $erf$ is the error function, $erf_u = \frac{2}{\pi}\int_0^u e^{-t^2}dt$.

If the concentration $c_s$ of aggressive ions on the exposed surface of the grouted stone body is increased by 20 times, then the test acceleration factor $s_1 = 20$.

### 3.3.2 Temperature acceleration

In the test, the grouting reinforced body test blocks are cured at a constant temperature of 30°C. Then, according to the influence of the environmental temperature on the diffusion of aggressive ions in the calcified body in the Arrhenius equation, the acceleration coefficient $s_2$ can be calculated as shown in Equation 37:

$$s_2 = \frac{D_T(303)}{D_T(290.9)} = \frac{D_0 e^{\frac{E}{R}\left(\frac{1}{293}-\frac{1}{303}\right)}}{D_0 e^{\frac{E}{R}\left(\frac{1}{291}-\frac{1}{293}\right)}} = 6.95 \tag{37}$$

where $D_0$ is the diffusion coefficient of aggressive ions at temperature $T_0$ (m$^2$·s$^{-1}$); $D_T$ is the diffusion coefficient of aggressive ions at temperature $T$ (m$^2$·s$^{-1}$); $T_1$ is the reference temperature, generally taken as 293K; E/R is the activation energy, which is taken as 14,242 according to the test values in Atkinson.

Therefore, the total acceleration factor $S$ of this deterioration test is equal to the product of the acceleration factor of the external aggressive ion concentration and that of the temperature, that is, $S = 138.94$.

## 3.4 Test results and comparative analysis

In the laboratory test, the values of the model parameters are as follows: the elastic modulus $E = 20$ GPa; Poisson's ratio $\mu = 0.2$; the test constant $n$ is taken as 3.0; the hydraulic gradient $J = 12.5$ MPa; the viscosity coefficient $\eta = 1.0087$; the number of pores on the cross-section $N = 2$; the density of the grout $\rho = 1.745 \times 10^3$ kg·m$^{-3}$. Given that the water-cement ratio of the pure cement grout is 1:2, the volume of cement particles $V_c = 0.33$ m$^3$ and the volume of water $V_w = 0.67$ m$^3$ in a unit volume of the grout can be obtained. The volume of the corrosion solution $n = 0.1$ m$^3$, and the initial $pH$ value of the corrosion solution $pH_0 = 5.5$. The grouted stone specimens cured in the karst water environment for different durations were subjected to unconfined compression tests, and the results were compared with those of the theoretical model. The test results and the theoretical calculation results are presented in Table 1.

As shown in Table 1, the predicted values from the theoretical model are relatively close to the actual values obtained from experimental tests, with variances all less than 0.35. This indicates that the prediction model has good accuracy. During the accelerated erosion test, the calcified body reaches its service life after approximately 150 days of exposure to karst water curing. Using the acceleration factor of 138.94 applied in the accelerated test, we estimate its service life in a karst environment to be about 57 years. The theoretical predicted value is 63 years, with an error margin of less than 15%. This suggests that the prediction model can effectively guide engineering practice.

TABLE 1 Calculated compressive strength values of grouting stone body.

| Time | Test value of compressive strength (MPa) | Calculated value of compressive strength (MPa) | Variance |
|---|---|---|---|
| Initial state | 35.92 | 36.49 | 0.081 |
| Karst water 30d | 30.70 | 31.78 | 0.292 |
| Karst water 60d | 27.49 | 26.48 | 0.255 |
| Karst water 90d | 25.88 | 26.72 | 0.176 |
| Karst water 120d | 21.42 | 21.97 | 0.076 |
| Karst water 150d | 18.10 | 18.74 | 0.102 |

FIGURE 4
Construction photos of the site.

# 4 Application in a typical engineering project

## 4.1 Project background

The Zhumashao Reservoir is a small-sized (Type II) water conservancy project primarily intended for agricultural irrigation. It features a homogeneous earth dam with a maximum height of 9.0 m, a crest length of 110.3 m, a crest width of 3.6 m, and a crest elevation of 1359.00 m. The total storage capacity is 185,600 $m^3$. This dam site is situated in a karst depression, where the main unfavorable geological phenomenon is karst formation. Karst caves and fissures are well-developed in the area, with cave cavities often filled with clay. The dam was initially constructed in February 1970 and completed for water storage in July 1971. Due to the dam-building technology and economic conditions at that time, certain potential safety hazards were present in the project. As a result, multiple rounds of hazard removal and reinforcement work were carried out subsequently. However, after several years of operation, issues such as seepage in the dam body and at the contact zone between the dam body and the foundation, as well as seepage in the reservoir area caused by the karst-developed zone near the reservoir bank, persisted.

## 4.2 Construction scheme and effect evaluation

Curtain grouting was implemented to eliminate potential hazards and reinforce the dam. The bottom boundary of the anti-seepage curtain grouting treatment was controlled based on a permeability rate of $q \leq 10$ Lu. The axis of the curtain grouting aligned with that of the dam, and the depth of the curtain extended 5 m below the bottom boundary of the dam body. The grouting curtain consisted of single-row holes spaced 1.5 m apart, with hole depths ranging from 3.5 m to 13.97 m. The grouting material used for the dam body was a cement-clay slurry, employing conventional grouting techniques, while the dam foundation was grouted with

pure cement slurry. The anti-seepage standards for curtain grouting stipulated that the permeability coefficient of the dam body should be $k \leq 10^{\wedge -5}$ cm/s, and the permeability rate of the bedrock should be $q \leq 10$ Lu. The total length of the anti-seepage line for the curtain grouting was 118.26 m. A total of 77 production holes were drilled, resulting in a total drilling footage of 890.33 m and a total grouting section length of 752.35 m. Given that the expected service life of a small-sized water conservancy dam is approximately 100 years (t = 100 a), substituting this value into Equation 34 yields a final grouting pressure of 0.3 MPa necessary to meet the service-life requirement. The on-site construction process is depicted in Figure 4.

During the construction process, the treatment measures implemented were both reasonable and effective. Following the completion of the anti-seepage project, the anti-seepage effect was remarkable, as confirmed by the water pressure test conducted on the inspection holes. The trial water storage of the reservoir showed normal water balance analysis, indicating that the project's anti-seepage measures met the expected goals.

## 5 Conclusion

(1) Based on the deterioration law of the initial consolidation strength of the curtain body under karst erosion conditions, a service-life prediction model for the grouting curtain of dams in karst areas considering the filter-pressing effect has been established. This model is simple to calculate, and its parameters are easy to obtain. It can efficiently and accurately predict the service life of grouting curtains in karst areas, demonstrating good practicality and applicability. Furthermore, this model can not only guide the design and construction of grouting curtains for dams in karst areas, but it can also be applied to similar projects in these regions, providing a new approach for predicting the service life of grouting curtains in karst areas.

(2) An accelerated erosion test of the grouting curtain calcified body in a karst environment, under the filter-pressing effect, was conducted. This study explored the strength deterioration of the grouting curtain calcified body and verified the feasibility of a theoretical model for predicting its service life. With a water-cement ratio of 1:2 for the pure cement grout, a grouting pressure of 1 MPa, and a grouting time of 6 s, the measured service life of the calcified body was 57 years, while the theoretical predicted value was 63 years, resulting in an error of less than 15%. This indicates that the prediction model can effectively guide engineering practice.

(3) A sample-making device for dams in karst areas, which considers the filter-pressing effect, has been independently designed and developed. This device can produce standard calcified body specimens under various grouting parameters for compressive strength testing. It is easy to operate and boasts high sample-making efficiency, providing new equipment for testing the performance of grouting materials in karst environments. Additionally, by adjusting the mesh numbers of the filter paper and the permeable stone, calcified body specimens with different filter-pressing coefficients can be obtained for performance testing.

(4) The research results have been successfully applied to guide the curtain danger removal and reinforcement project of the Yingpan Reservoir in Yunnan Province, further demonstrating the feasibility and practicality of the theoretical prediction model. Based on the on-site investigation data from Yingpan Reservoir and aligned with the service life requirements stipulated in the design, the construction parameter for the curtain danger removal and reinforcement were determined using the research findings from this paper. The subsequent evaluation of the grouting effect achieved the expected goals. Given the practicality and applicability of the curtain body service life prediction model developed in this paper, this method can be further promoted and applied in the design and construction of grouting curtains in the fields of transportation, mining, and industrial and civil construction in karst areas.

(5) A sample-making device for dams in karst areas considering the filter-pressing effect was independently designed and developed. It can obtain standard calcified body specimens under different grouting parameters for compressive strength testing. This device is easy to operate and has high sample - making efficiency, providing a new piece of equipment for testing the performance of grouting materials in a karst environment. In addition, by adjusting the mesh numbers of the filter paper and the permeable stone, grouting calcified body specimens with different filter-pressing coefficients can be obtained for performance testing.

(6) The research results have been successfully applied to guide the curtain danger - removal and reinforcement project of Yingpan Reservoir in Yunnan Province, further demonstrating the feasibility and practicality of the theoretical prediction model. Based on the on-site investigation data of Yingpan Reservoir and combined with the service-life requirements stipulated in the design, the construction parameter control conditions such as the grouting material mix ratio and the designed grouting pressure value (> 0.3 MPa) for the curtain danger-removal and reinforcement were determined using the research results of this paper, and the subsequent evaluation of the grouting effect achieved the expected goals. Considering the practicality and applicability of the curtain body service-life prediction model derived in this paper, this method can be further popularized and applied in the design and construction of grouting curtains in the fields of transportation, mining, industrial and civil construction in karst areas.

## Data availability statement

The raw data supporting the conclusions of this article will be made available by the authors, without undue reservation.

## Author contributions

ZY: Writing – original draft, Data curation, Validation, Writing – review and editing. DJ: Methodology, Writing – review and editing, Conceptualization. LY: Conceptualization, Writing – review and editing. XM: Writing – original draft, Methodology. LW: Data curation, Writing – review and editing.

## Funding

The author(s) declare that financial support was received for the research and/or publication of this article. This work was supported by the Major water conservancy science and technology project of Hunan Province (XSKJ2023059-02) and the water conservancy science and technology project of Yunnan Province (Project Name: Research on Key Technologies of Intelligent Grouting in Soft Strata and System Integration). The corresponding author gratefully acknowledges this financial support.

## Conflict of interest

The authors declare that the research was conducted in the absence of any commercial or financial relationships that could be construed as a potential conflict of interest.

## Generative AI statement

The author(s) declare that no Generative AI was used in the creation of this manuscript.

## Publisher's note



## References

Axelsson, M., Gustafson, G., and Fransson, Å. (2009). Stop mechanism for cementitious grouts at different water-to-cement ratios. *Tunn. Undergr. Space Technol.* 24 (4), 390–397. doi:10.1016/j.tust.2008.11.001

Bouchelaghem, F., Benhamida, A., and Dumontet, H. (2007). Mechanical damage behaviour of an injected sand by periodic homogenization method. *Comput. Mater. Sci.* 38 (3), 473–481. doi:10.1016/j.commatsci.2005.12.044

Chen, Y., Yuan, J., Wang, G., Xu, J., Hu, R., and Yang, Z. (2022). Evaluation of groundwater flow through a high rockfill dam foundation in karst area in response to reservoir impoundment. *Int. J. Rock Mech. Min. Sci.* 160, 105268. doi:10.1016/j.ijrmms.2022.105268

Chen, W., Xing, Z., Wang, K., Fu, P., Luo, G., and Pei, X. (2021). A study on the effect of pressure filtration on the strength of cement slurry stones. *Water Resour. Hydropower Eng.* 52 (05), 196–202. doi:10.13928/j.cnki.wrahe.2021.05.021

Dafny, E., Tawfeeq, K. J., and Ghabraie, K. (2015). Evaluating temporal changes in hydraulic conductivities near karst-terrain dams: dokan Dam (Kurdistan-Iraq). *J. Hydrology* 529, 265–275. doi:10.1016/j.jhydrol.2015.07.048

Dong, J., Xie, H., Dai, Y., Zhai, J., and Dai, Y. (2022). "*Compressive strength prediction of blast furnace slag-fly ash concrete based on GA-BP algorithm*," in *International Conference on Computational Modeling, Simulation, and Data Analysis (CMSDA 2021)*. SPIE, 12160, 398–407. doi:10.1117/12.2627604

Dou, J., Zhang, G., Chen, A., Yang, B., Xin, R., Duan, J., et al. (2020). Grouting experiment in a completely weathered granite dam abutment: case study on grouting technique and test analysis. *Environ. Earth Sci.* 79, 1–15. doi:10.1007/s12665-020-9140-x

Eklund, D., and Stille, H. (2008). Penetrability due to filtration tendency of cement-based grouts. *Tunn. Undergr. Space Technol.* 23 (4), 389–398. doi:10.1016/j.tust.2007.06.011

Fazeli, M. A. (2007). Construction of grout curtain in karstic environment case study: salman Farsi Dam. *Environ. Geol.* 51 (5), 791–796. doi:10.1007/s00254-006-0397-8

Gao, X., Zhaofeng, L., Zhihao, Z., Wu, F., Huang, H., and Chen, J. (2024). Long-term erosion resistance of grouting curtain in coastal karst fracture area. *J. Build. Eng.* 85, 108721. doi:10.1016/j.jobe.2024.108721

Ge, W., Sun, H., Jing, L., Li, Z., Li, Y., Cao, B., et al. (2024). Economic life evaluation of reservoir dams based on comprehensive costs and benefits analysis considering potential dam breach: a case study of the Luhun reservoir in China. *J. Hydrology* 639, 131613. doi:10.1016/j.jhydrol.2024.131613

He, Z., Zhao, K., Yan, Y., Ning, F., Zhou, Y., and Song, Y. (2021). Mechanical response and acoustic emission characteristics of cement paste backfill and rock combination. *Constr. Build. Mater.*, 288. doi:10.1016/j.conbuildmat.2021.123119

He, X. (1990). Strength calculation of grouting curtain in porous rock formations. *Metal. Mines* (05), 25–27. (in Chinese).

Hou, J., Guo, Z., Liu, W., and Zhang, Y. (2020). Mechanical properties and meso-structure response of cemented gangue-fly ash backfill with cracks under seepage-stress coupling. *Constr. Build. Mater.* 250, 118863–211874. doi:10.1016/j.conbuildmat.2020.118863

Huo, J., Ma, F., and Xiaolei, J. I. (2019). Porosity and permeability variations of a dam curtain during dissolution. *Water Sci. Eng.* 12 (02), 155–161. doi:10.1016/j.wse.2019.05.007

Jian, J., Lu, J., Guo, Q., Wang, J., Sun, L., Mao, D., et al. (2024). Characterization and quantification of dam seepage based on resistivity and geological information. *Water* 16 (17), 2410. doi:10.3390/w16172410

Ministry of Construction of the People's Republic of China (2019). *GB/T50081-2019 standard for test methods for physical and mechanical properties of concrete*. Beijing: China Construction Industry Press. (in Chinese).

Ministry of Water Resources of the People's Republic of China (2019). *GB/T50123-2019. standard for geotechnical test methods*. Beijing: China Plan Publishing House, organized by the Institute of Standard and Quotas of the Ministry of Housing and Urban-Rural Development. (in Chinese).

Mozafari, M., Milanović, P., and Jamei, J. (2021). Water leakage problems at the Tangab Dam Reservoir (SW Iran), case study of the complexities of dams on karst. *Bull. Eng. Geol. Environ.* 80 (10), 7989–8007. doi:10.1007/s10064-021-02387-z

Muntaha, M. (2017). The effect of drying-wetting cycle's repetition to the characteristic of natural and stabilization residual soils Jawa Timur-Indonesia. *IOP Publ.* 267 (1), 012030. doi:10.1088/1757-899x/267/1/012030

Nagihara, S. (1996). Seepage-induced erosion of submarine carbonate escarpments: a numerical simulation. *Earth Planet. Sci. Lett.* 144 (1-2), 263–271. doi:10.1016/0012-821x(96)00162-8

Paglia, C., Wombacher, F., and Böhni, H. (2003). The influence of alkali-free and alkaline shotcrete accelerators within cement systems: influence of the temperature on the sulfate attack mechanisms and damage. *Cem. Concr. Res.* 33 (3), 387–395. doi:10.1016/S0008-8846(02)00967-5

Peng, T. U. (2012). *Theoretical study on durability test and evaluation of grouting stone body*. Central South University. (in Chinese).

Powers, T. C. (1960). *Physical properties of cement paste*. Washington: Fourth International Symposium on the Chemistry of Cement, 577–609.

Ran, H., Guo, Y., Feng, G., Qi, T., and Du, X. (2021). Creep properties and resistivity ultrasonic-AE response of cemented gangue backfill column under high-stress area. *Int. J. Min. Sci. Technol.* 31 (3), 401–412. doi:10.3969/j.issn.2095-2686.2021.03.006

Romanov, D., Gabrovek, F., and Dreybrodt, W. (2003). Dam sites in soluble rocks: a model of increasing leakage by dissolutional widening of fractures beneath a dam. *Eng. Geol.* 70 (1-2), 17–35. doi:10.1016/s0013-7952(03)00073-5

Wang, H., Liu, Q., Sun, S., Zhang, Q., Li, Z., and Zhang, P. (2020). Damage model and experimental study of a sand grouting-reinforced body in a seawater environment. *Water* 12 (9), 2495–2507. doi:10.3390/w12092495

Wang, H., Zhipeng, L. I., Wang, X., Zhang, Q., and Zhang, L. (2021). Study on grouted body deterioration mechanism of sand layer in seawater environment. *Adv. Mater. Sci. Eng.* 2021 (1), 1–8. doi:10.1155/2021/6329257

Xiang, Y., Sheng, J. B., Wang, L., Cai, Y., Meng, Y., and Cai, W. (2022). Research progresses on equipment technologies used in safety inspection, repair, and reinforcement for deepwater dams. *Sci. China Technol. Sci.* 65 (5), 1059–1071. doi:10.1007/s11431-021-1958-y

You, W. (2010). Performance test and application of special clay curing slurry. *J. Nanchang Eng. Coll.* 29 (03), 42–46. doi:10.3969/j.issn.1006-4869.2010.03.009

Zhang, W., Shen, Z., Chen, G., Zhang, W., Xu, L., Ren, J., et al. (2021). Optimization design and assessment of the effect of seepage control at reservoir sites under karst conditions: a case study in Anhui Province, China. *Hydrogeology J.* 29 (5), 1831–1855. doi:10.1007/s10040-021-02357-5

Zhou, R., Xiaochuan, Q. I. N., Jianfan, S. H. A., Guo, F., and Qi, W. (2022). Influence of wet or dry conditions on the fatigue life of grout cementitious materials under cyclic loading. *Geofluids* 2022 (1), 1–7. doi:10.1155/2022/3615221

Zuo, X. B., Sun, W., Li, H., and Zhao, Y. K. (2012). Modeling of diffusion-reaction behavior of sulfate ion in concrete under sulfate environments. *Comput. Concr. An Int. J.* 10 (1), 79–93. doi:10.12989/cac.2012.10.1.079

frontiers | Frontiers in Earth Science

TYPE Original Research
PUBLISHED 20 May 2025
DOI 10.3389/feart.2025.1603845



OPEN ACCESS

EDITED BY
Tongming Qu,
Hong Kong University of Science and Technology, Hong Kong SAR, China

REVIEWED BY
Jiawei Xie,
The University of Newcastle, Australia
Zarghaam Rizvi,
GeoAnalysis Engineering GmbH, Germany
Sun Rui,
Anhui University of Science and Technology, China
Jie Li,
East China Jiaotong University, China

*CORRESPONDENCE
Xinghua Fang,
xhfang95@163.com

RECEIVED 01 April 2025
ACCEPTED 05 May 2025
PUBLISHED 20 May 2025

CITATION
Tang W, Xie M, Fang X, Huang C, Mo C and Chen Y (2025) Experimental investigation on the performance degradation of grouting materials in karst erosion environment. *Front. Earth Sci.* 13:1603845. doi: 10.3389/feart.2025.1603845



# Experimental investigation on the performance degradation of grouting materials in karst erosion environment

Wang Tang[1,2], Mengshan Xie[3], Xinghua Fang[2]*, Chengxi Huang[2,4], Cuiliu Mo[2] and Yongjun Chen[2]

[1]Hunan Urban and Rural Environmental Construction Co., Ltd., Changsha, Hunan, China, [2]School of Civil Engineering, Central South University of Forestry and Technology, Changsha, Hunan, China, [3]Intelligent Construction Department, Changsha Building Engineering School, Changsha, Hunan, China, [4]Hunan Construction Investment Group Infrastructure Investment Company, Changsha, Hunan, China

The fundamental cause of leakage in grouting curtains of dams in karst areas lies in the localized damage induced by performance degradation of the curtain under seepage-induced erosion. This work investigated the degradation mechanisms of grouting curtains exposed to karst water erosion by analyzing the mechanical and microstructural evolution of cement-grouted stone (CGS) and cement-clay-grouted stone (CCGS). The results indicate that both materials experience progressive deterioration in mechanical properties, with CCGS demonstrating significantly higher vulnerability. After 120 days, the compressive strength of CGS decreased from 32.89 MPa to 20.03 MPa, while the strength of CCGS declined sharply from 3.89 MPa to 2.03 MPa. Porosity increased from 26.06% to 33.91% for CGS and from 58.04% to 77.01% for CCGS. Microstructural analysis revealed that karst water induced chemical erosion and structural damage in both materials, with CCGS exhibiting accelerated degradation due to weaker cementitious bonding and higher initial porosity, which facilitated ion penetration and reaction-induced damage. The findings highlight the inferior durability of cement-clay composites under karst water conditions and provide critical insights for optimizing grouting materials in karst-prone environments.

KEYWORDS

**karst, grouting curtain, erosion effect, performance degradation, grouted stone**

## 1 Introduction

Grout curtain grouting is the preferred construction method for anti-seepage reinforcement of dams in karst regions. However, the karst stratum contains interconnected fissures and conduits with mineral-rich groundwater, where the synergistic effects of hydrostatic pressure, chemical interactions, and geostress can readily induce deterioration and structural damage to the grouting curtain (Liu, 2004; Yu et al., 2020). Extensive engineering projects have demonstrated that the cause of seepage incidents in dam grouting curtains within karst areas lies in the performance degradation of curtain structures under seepage-induced erosion, ultimately leading to localized failures, as evidenced by the Tangab Dam (Mozafari et al., 2021), Logan Martin Dam (Bruce et al., 2017), and Teton Dam (Verma et al., 2023).

Currently, scholars primarily characterize the performance degradation of grouting curtains by investigating changes in the physical-mechanical properties of grouted stones under karst water erosion (Ahmad et al., 2019; Wei et al., 2025), a method whose feasibility has been validated. For instance, Liu (2019) conducted accelerated dissolution tests to obtain the compressive strength, cohesion, internal friction angle, permeability coefficient, and microstructural characteristics of grouted samples at different curing ages. Recent work also emphasizes the temperature field evolution in backfill materials, which could correlate with chemical and mechanical degradation pathways in similar subsurface environments (Ahmad et al., 2021). Feng (2015) compared the soft-water erosion resistance of cement-clay grouts with varying mix ratios through orthogonal experiments, analyzing the degradation patterns of cement-clay reinforcements under different erosion media and durations using strength and mass loss as performance indicators. Sha and Fan (2021) investigated the early impermeability, flexural strength, unconfined compressive strength, corrosion resistance coefficient, volume/mass variations, fracture surface characteristics, corrosion minerals, microstructure, and pore size distribution of a novel high-efficiency micro-cement grouting material in corrosive environments. Tu (2012) evaluated the durability of cement-based grouting materials in seawater using fuzzy analytic hierarchy analysis based on seawater erosion resistance tests. Wang et al. (2021) and Wang et al. (2020). addressed grouting design challenges in sand layers under seawater erosion by conducting accelerated degradation tests, establishing quantitative relationships between seawater exposure time and grouted reinforcement strength, and proposing a constitutive model for degradation damage, providing theoretical guidance for sand-layer grouting in marine environments. Fu et al. (2013) enriched durability prediction frameworks by comparing erosion rates of cement grouting curtains under low-alkalinity soft water at varying permeation pressures.

However, the initial performance of grouted stones is closely tied to grouting environments of karst dams, construction parameters, and material properties-factors often overlooked in existing studies. This oversight leads to significant discrepancies between the performance of laboratory-tested grouted stones and the behavior of real-world karst dam grouting curtains, limiting the practical applicability of experimental findings. Thus, this work simulated the erosion environment of karst dam grouting curtains by preparing high-concentration karst water curing solutions and controlling curing temperatures based on accelerated erosion principles. Specimens cured for varying durations undergo tests for compressive strength, porosity, mass loss, and microstructural morphology to elucidate the performance degradation mechanisms of karst dam grouting curtains under aggressive environmental conditions. Modeling approaches have also been applied to understand cemented geomaterial behavior under similar erosive and structural loading conditions (Rizvi et al., 2020a).

# 2 Methods

## 2.1 Raw materials and preparation

The experiment used pure cement grout and cement-clay grout to create grouted stone samples, with mix proportions corresponding to standard practices for grouting curtains in karst areas. The cement utilized was again 42.5R Ordinary Portland Cement, adhering to the national standard of normal Portland cement in China. The clay component consisted of specialized calcium-based clay from Lingshou County, Hebei Province, China. The water-cement ratio for the pure cement slurry was 1:2, while the mixing ratio for the cement-clay slurry was 2:1, with the clay content making up 50% of the cement weight. The grouting process parameters, such as pressure and duration, play a critical role in ensuring uniform penetration and minimizing head losses during injection, as highlighted in prior fluid dynamics studies (Haroon et al., 2017). During the preparation process of grouting stone bodies, a grouting pressure of 1 MPa was applied for a duration of 6 s. The samples were cured under standard conditions of 20°C ± 1°C and ≥95% humidity. Figures 1–3 illustrate the test preparation process, test equipment and grout stone samples.

## 2.2 Design of accelerated degradation test

The critical challenge in conducting laboratory accelerated degradation tests lies in constructing an accelerated erosion environment that effectively replicates the long-term service conditions of grout curtains. In this work, the degradation process of grouted specimens was accelerated by controlling the concentrations of aggressive ions in simulated karst groundwater and adjusting the curing temperature. The transport mechanisms governing the ingress of aggressive ions into grouted matrices typically include adsorption, diffusion, pressure-driven permeation, and dispersion. Among these, the diffusion of aggressive ions is generally considered to be the most important migration mechanism (Yu and Sun, 2006). When neglecting the binding capacity of aggressive ions within grouted matrices and the influence of time-dependent structural defects on diffusion coefficients, the theoretical model for ion diffusion can be derived from Fick's Second Law (Yu and Sun, 2006; Wang, 2016), as shown in Equation 1 and Equation 2.

$$c = c_0 + (c_s - c_0)\left(1 - \mathrm{erf}\frac{x}{2\sqrt{Dt}}\right) \tag{1}$$

$$erfu = \frac{2}{\pi}\int_0^u e^{-t^2}\mathrm{d}t \tag{2}$$

where $c_0$ and $c_s$ are the initial erosive ion concentration in the grouted stone and the erosive ion concentration on the exposed surface, respectively. And *erf* is the error function.

According to the test design, it can be considered that $c_0 = 0$, then Equation 1 can be simplified to Equation 3:

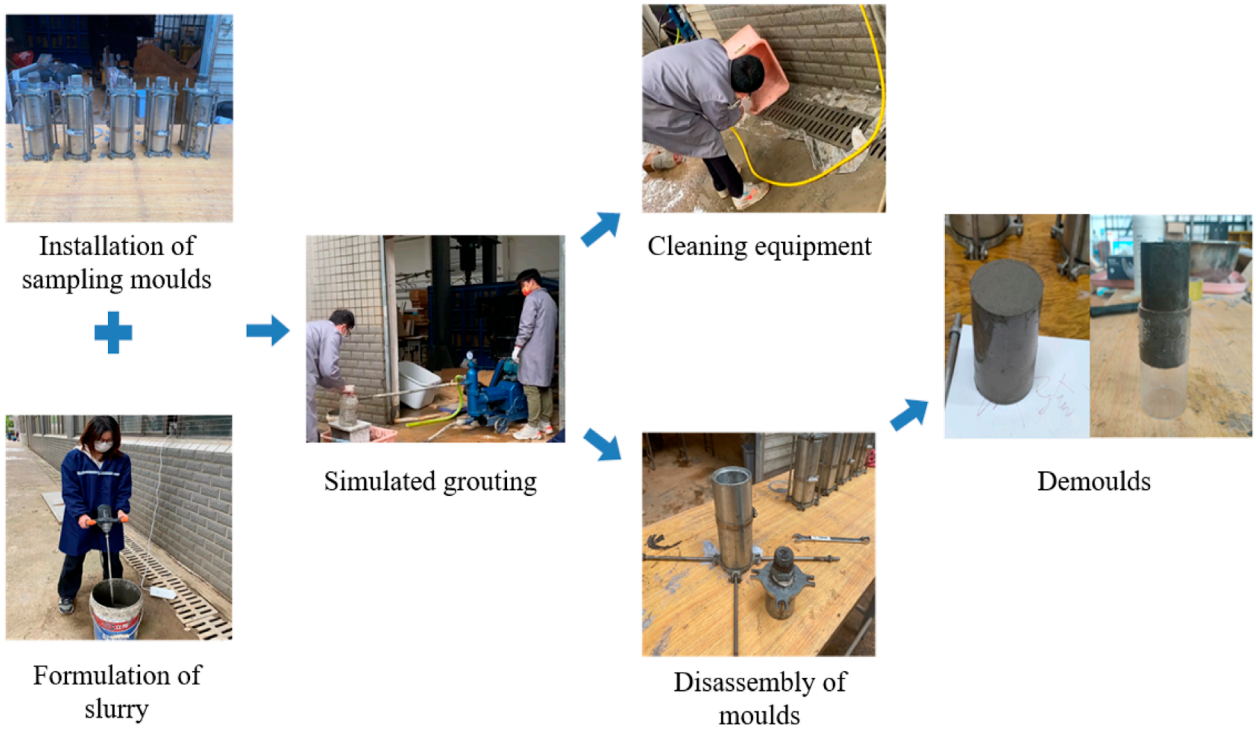


FIGURE 1
Flowchart of grouted stone samples preparation.

$$c = c_s\left(1 - \mathrm{erf}\frac{x}{2\sqrt{Dt}}\right) \tag{3}$$

Therefore, the diffusion of aggressive ions in the experiment exhibits direct proportionality to the surface concentration $c_s$. When the erosive ion concentration at the exposed surface of grouted matrices increases by a factor of 20, the corresponding acceleration factor $s_1$ for the test duration also increases by 20 times.

The fundamental mechanism of aggressive ion diffusion in grouted matrices involves random thermal motion of ions through the pore solution within the matrix. The diffusion coefficient of aggressive ions demonstrates a positive temperature dependence (Lindvall, 2007). As described by the Arrhenius equation (Zuo, 2021), the influence of ambient temperature on the diffusion of aggressive ions within grouted matrices is quantified by Equation 4:

$$D_t(T) = D_0 e^{\frac{E}{R}\left(\frac{1}{T_0} - \frac{1}{T}\right)} \tag{4}$$

where: $D_0$ is the diffusion coefficient of aggressive ions at temperature $T_0$, $m^2/s$; $D_T$ is the diffusion coefficient of aggressive ions at temperature $T$, $m^2/s$; $T_1$ is the reference temperature, generally 293 K; $E/R$ is the activation energy, which is taken as 14,242 in reference (Wang, 2019).

According to literature (Jiang et al., 2014; Pan et al., 2023), the annual average water temperature of rivers in Changsha area is about 18°C (290.9 K), and constant temperature 30°C (303 K) was used in this experiment to maintain the grouted stone test. The acceleration coefficient $s_2$ is calculated in Equation 5.

$$S_2 = \frac{D_T(303)}{D_T(290.9)} = \frac{D_0 e^{14242\left(\frac{1}{293} - \frac{1}{303}\right)}}{D_0 e^{14242\left(\frac{1}{293} - \frac{1}{291}\right)}} = 6.95 \tag{5}$$

Therefore, the total acceleration coefficient $S$ of this degradation test is equal to the product of external erosive ion concentration and temperature acceleration coefficient, that is, $S = 138.94$.

Based on the pre-determined 20 times accelerated erosion factor, the karst water curing solution was prepared at 20 times the concentration of natural karst water. According to investigations, chloride ($Cl^-$), bicarbonate ($HCO_3^-$), and sulfate ($SO_4^{2-}$) are the primary aggressive ions in karst water affecting grouted matrices. Referencing groundwater monitoring data from a karst-area dam in Hunan Province, Table 1 lists the normal and accelerated concentrations of these three ions.

The curing solution was prepared using sodium chloride, sodium bicarbonate, and potassium sulfate, with an analytical purity of ≥ 99%. Based on calculations of ion concentration, each liter of the prepared karst water curing solution contained 1.52 g of sodium chloride, 8.91 g of sodium bicarbonate, and 21.61 g of potassium sulfate. A self-made accelerated curing box was utilized to accelerate the erosion and deterioration of the stone test block. A small heater was placed at the bottom of the curing box to control the temperature of the karst water, which was set to 30°C within a control range of 20°C–35°C. The accelerated karst water erosion test is shown in Figure 4.

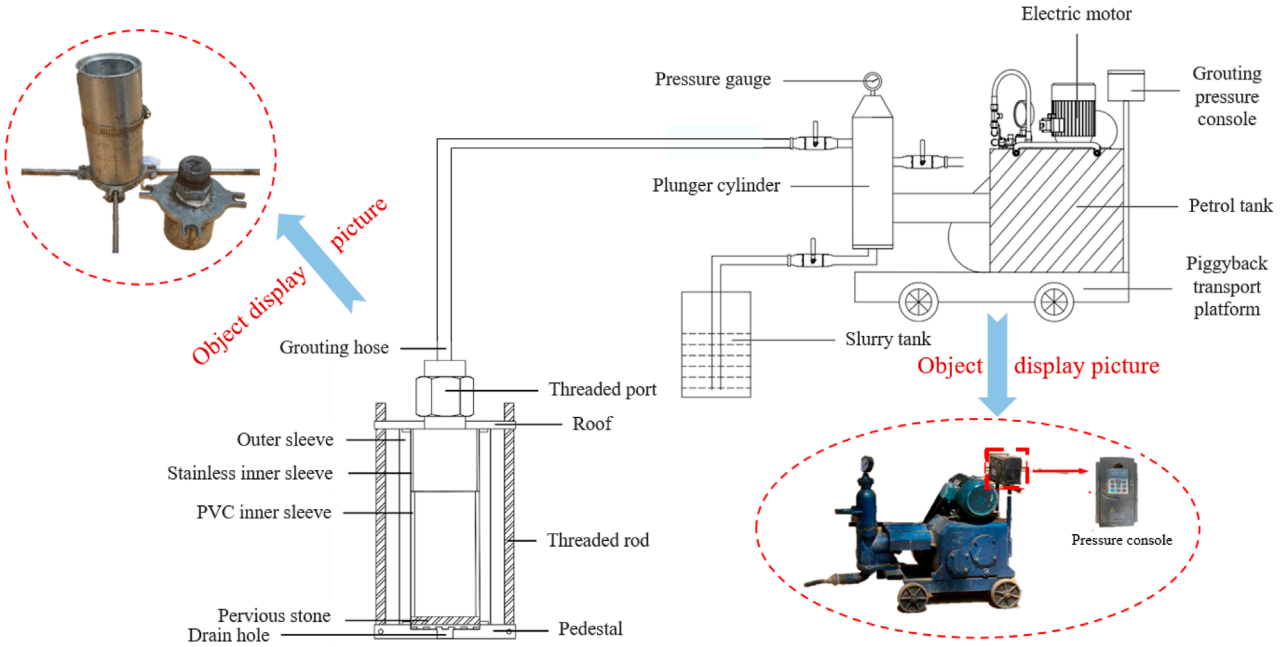


FIGURE 2
Grouting stone samples preparation equipment diagram.

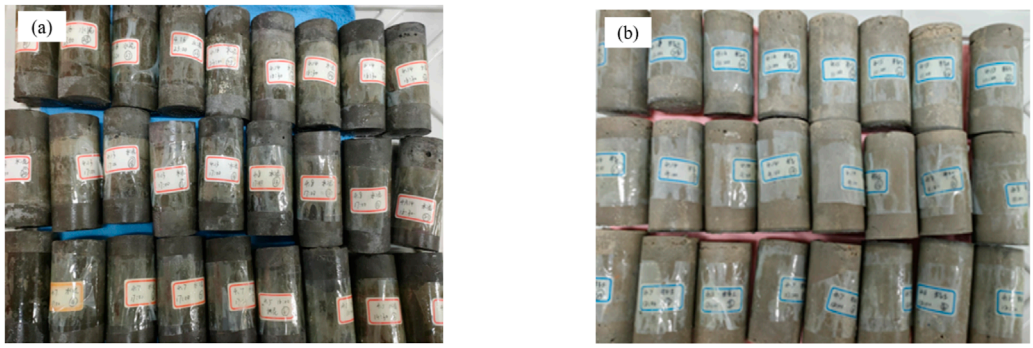


FIGURE 3
Two grouted stone samples for the tests: **(a)** CGS samples; **(b)** CCGS samples.

## 2.3 Testing methods

To investigate the degradation of physical and mechanical performance in CGS (Group A) and CCGS (Group B) specimens under karst water erosion, we conducted analyses of compressive strength, porosity, mass loss, and scanning electron microscopy (SEM) on pre-prepared specimens. The tests adhered to the technical code for testing in China (Ministry of Transport of the People's Republic of China, 2019; Ministry of Construction of the People's Republic of China, 2019). A summary of the experimental design, including test conditions, is presented in Table 2. The procedures were as follows.

(1) Specimen preparation and curing. CGS and CCGS specimens were cast, then placed in water-filled tanks for standard curing under controlled conditions (temperature: 20°C ± 1°C, humidity: ≥95%) for 28 days.

(2) Testing. After 28 days of curing, initial properties, including compressive strength, porosity, mass, and microstructural morphology, were evaluated.

(3) Accelerated erosion exposure. Specimens were transferred to a temperature-controlled accelerated erosion chamber (30°C ± 0.5°C) for grouped curing periods of 30, 60, 90, and 120 days.

(4) Post-erosion evaluation. Post-curing tests replicated baseline measurements to quantify degradation metrics: compressive strength loss (%), porosity increase (%), mass loss (%), and microcrack evolution (SEM).

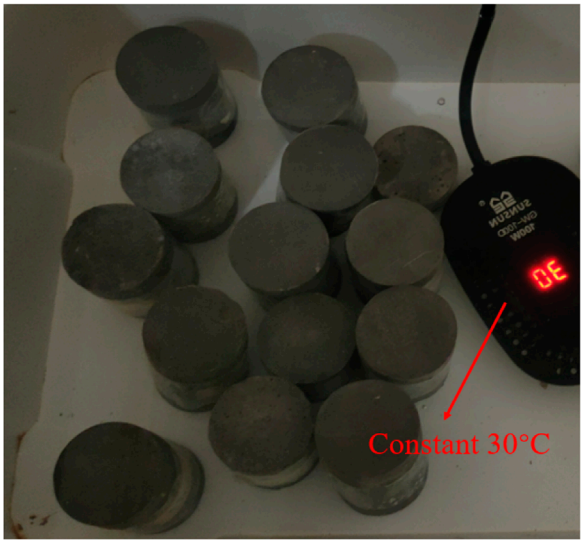


FIGURE 4
Schematic diagram of accelerated erosion conservation in karst water environments.

# 3 Results

## 3.1 Analysis of compressive strength test results

The compressive strength test results for grouted stones under accelerated karst water erosion are summarized in Figure 5. With prolonged curing time, the compressive strength of CGS (Group A) decreased from 32.89 MPa to 20.03 MPa, while CCGS (Group B) declined from 3.89 MPa to 2.03 MPa. Notably, Group A exhibited significantly higher strength than Group B. This difference stems from the charge interaction in cement-clay grout: positively charged cement hydration particles partially exchange charges with clay particles, inducing clay agglomeration to form a gel-structured skeleton. However, this skeleton demonstrates inferior mechanical performance compared to the robust particle skeleton created by cement hydration (Feng, 2015). Furthermore, both groups experienced progressive strength reduction over time due to chemical erosion from karst water. The dissolution of calcium hydroxide and degradation of hydration products (e.g., calcium silicate hydrate and calcium aluminate hydrate) into less cohesive compounds gradually compromised the structural integrity of the grouted stones, diminishing their load-bearing capacity (Zhou et al., 2022).

Figure 6 illustrates the reduction rates of compressive strength for Groups A and B grouted stones. After 120 days of curing in a karst water environment, Group A exhibited a strength reduction rate of 39.10%, while Group B showed a higher reduction rate of 47.67%, indicating that Group A experienced less strength degradation compared to Group B. This disparity arises because cement particles, with their coarser size and superior cementation properties, form a more stable granular skeleton structure in cement grout (Xie et al.,2025). This enhanced stability mitigates strength deterioration in cement grout stones relative to cement-clay grout, where the weaker clay-cement matrix is more susceptible to karst water erosion. These results further confirm that cement-clay materials exhibit inferior resistance to karst water erosion compared to pure cement materials (Bai, 2001).

Additionally, Figure 7 depicts the compressive failure morphology of grouted stone specimens cured in karst water for varying durations. Unconfined compressive strength tests revealed that failure occurred through a progressive crack propagation process: cracks initiated at the base and outer surfaces, extended upward and inward, and ultimately coalesced to cause specimen failure. The crack orientation aligned predominantly with the axial loading direction. Notably, no significant shear failure was observed during the entire unconfined compression process, demonstrating that structural disintegration was driven primarily by tensile splitting rather than shear mechanisms.

## 3.2 Analysis of porosity test results

Figure 8 shows the porosity test results of grouted stone specimens under different accelerated karst water erosion conditions. With the increase in curing time, the porosity of Group A increased from 26.06% to 33.91%, while that of Group B increased from 58.04% to 77.01%. The porosity of Group B was significantly higher than that of Group A. This is because the cement-based grouting material used in Group A exhibited better fluidity and higher density compared to the clay-cement grouting material in Group B. The porosity of both Groups A and B increased with curing time. The primary reason is that in the karst water environment, calcium hydroxide ($Ca(OH)_2$) within the grouted stones dissolves and reacts with erosive ions, reducing its concentration in the surrounding water. This process accelerates the decomposition and dissolution of other hydration products, resulting in continuous loss of chemical substances and gradual enlargement of pores within the grouted stones (Tang, 2019).

As shown in Figure 9, after 120 days of curing in the karst water environment, the porosity increase magnitude of Group A reached 30.12%, while that of Group B was 32.68%. The smaller variation in Group A's porosity aligns with its lower strength reduction compared to Group B, and the underlying mechanisms are similar. Additionally, it was observed that the porosity growth rates of both groups were relatively slow during the first 90 days of curing. However, after 90 days, the rates accelerated. This phenomenon can be attributed to calcium hydroxide being the primary dissolved component in the early stage. As pores enlarged and increased, the contact area between various hydration products and karst water increased, accelerating the dissolution and erosion rates of calcium hydroxide and other hydration products, thereby hastening porosity growth (He, 2019). Pore structure and thermal behavior of subsurface materials have been extensively modeled to assess effective thermal conductivity and degradation behavior (Rizvi et al., 2020b).

TABLE 1 Ion concentration of karst water curing solution.

| Number | Ions | Normal concentration (mmol/L) | 20x concentration (mmol/L) |
|---|---|---|---|
| 1 | Chloride ($Cl^-$) | 1.3 | 26 |
| 2 | Bicarbonate ($HCO_3^-$) | 5.3 | 106 |
| 3 | Sulfate ($SO_4^{2-}$) | 6.2 | 124 |

TABLE 2 Design of physical-mechanical tests for grouted stone under accelerated erosion by karst water.

| Number | Test type | Test method | Test conditions |
|---|---|---|---|
| 1 | Compressive strength | Hydraulic testing machine | (1) Tests were conducted after 28 days of maintenance under standard conditions (initial state)<br>(2) Based on the first condition, place the specimens into a karst water accelerated erosion environment for testing at the following intervals: 30 days, 60 days, 90 days, and 120 days |
| 2 | Porosity | Weighing | |
| 3 | Mass loss | Weighing | |
| 4 | Microstructure testing | Scanning electron microscope (SEM) | |

Note: For the mass loss test, clear water curing for 30d, 60d, 90d and 120d were added for comparison test.

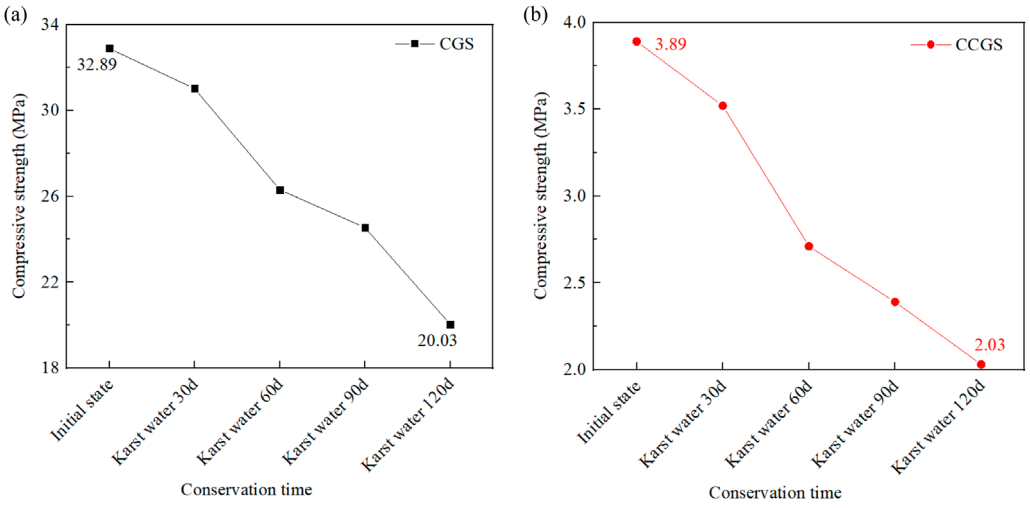


FIGURE 5
Compressive strength results of grouted stones under karst water erosion: **(a)** CGSs (Group A); **(b)** CCGSs (Group B).

## 3.3 Analysis of the results of the grouted stone mass test

The experimental study on grouted stone body specimens cured in clear water and karst water environments revealed distinct mass variation trends over different periods (as shown in Figure 10). Prior to 60 days of curing, the mass change rates of Groups A and B showed minimal differences between the two environments. However, beyond 60 days, specimens in karst water exhibited significantly greater mass variations compared to those in clear water, with the divergence amplifying over time, indicating accelerated deterioration effects from karst water. At 150 days, Group A specimens demonstrated mass change rates of 3.00% (clear water) and 4.50% (karst water), while Group B reached 4.63% and 6.44%, respectively. Notably, Group B consistently displayed higher mass variation rates than Group A. Early-stage chemical reactions between erosive ions in karst water and hydration products (e.g., calcium hydroxide dissolution) initially reduced specimen mass. However, subsequent formation of expansive minerals like gypsum and ettringite partially filled pore structures, temporarily offsetting mass loss through physical expansion while retarding further dissolution. For Group A specimens, this expansive filling initially outweighed dissolution effects, causing a slight mass gain. Prolonged exposure ultimately weakened cementitious bonding, inducing surface softening and edge spalling in both groups, thereby gradually reversing the mass trends.

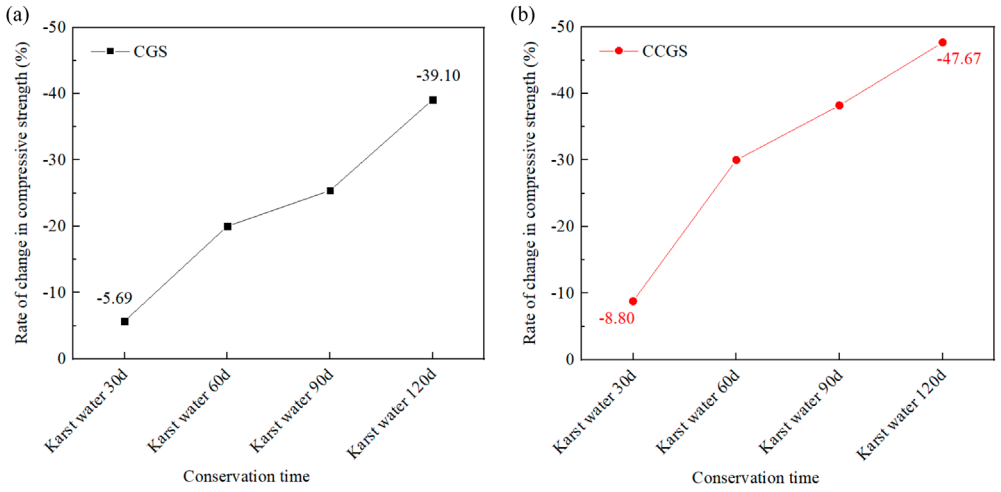


FIGURE 6
Degradation trends of compressive strength in grouted stones under karst water erosion: **(a)** CGSs (Group A); **(b)** CCGSs (Group B).

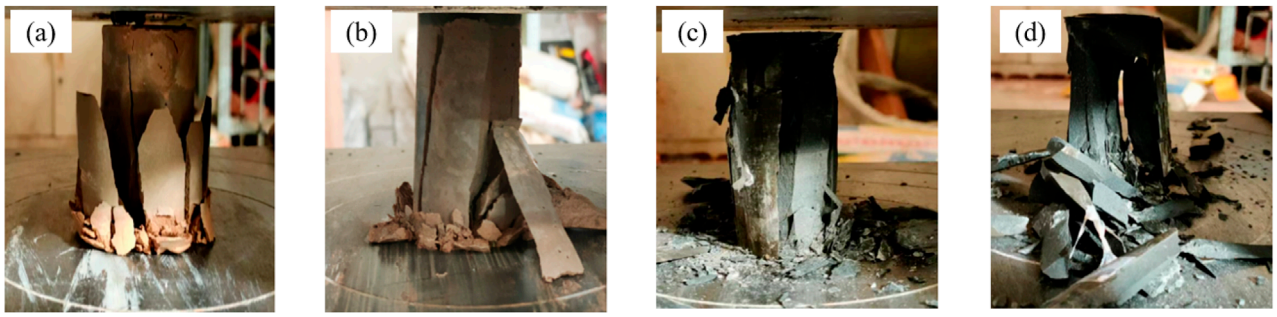


FIGURE 7
Failure mode of grouted stones under compression: **(a)** CGS cured for 28d under standard conditions; **(b)** CCGS cured for 28d under standard conditions; **(c)** CGS after 60 days of karst water erosion; **(d)** CCGS after 60 days of karst water erosion.

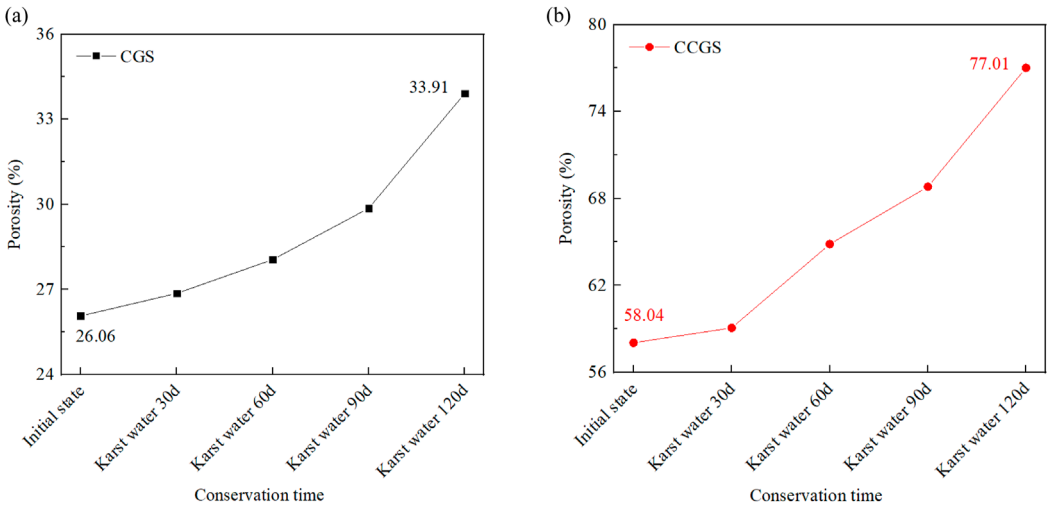


FIGURE 8
Porosity results of grouted stones under karst water erosion: **(a)** CGSs (Group A); **(b)** CCGSs (Group B).

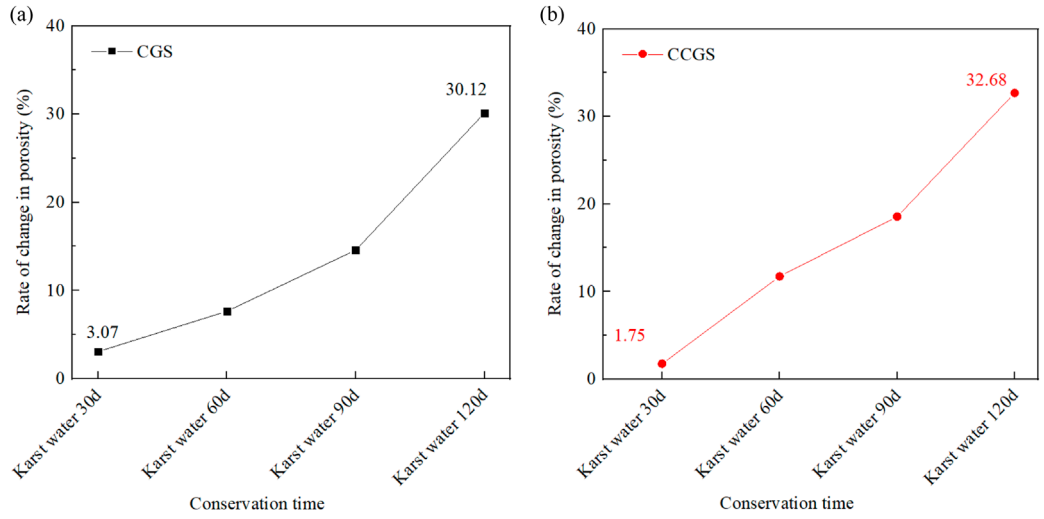


FIGURE 9
Porosity variation of grouted stones under karst water erosion: **(a)** CGSs (Group A); **(b)** CCGSs (Group B).

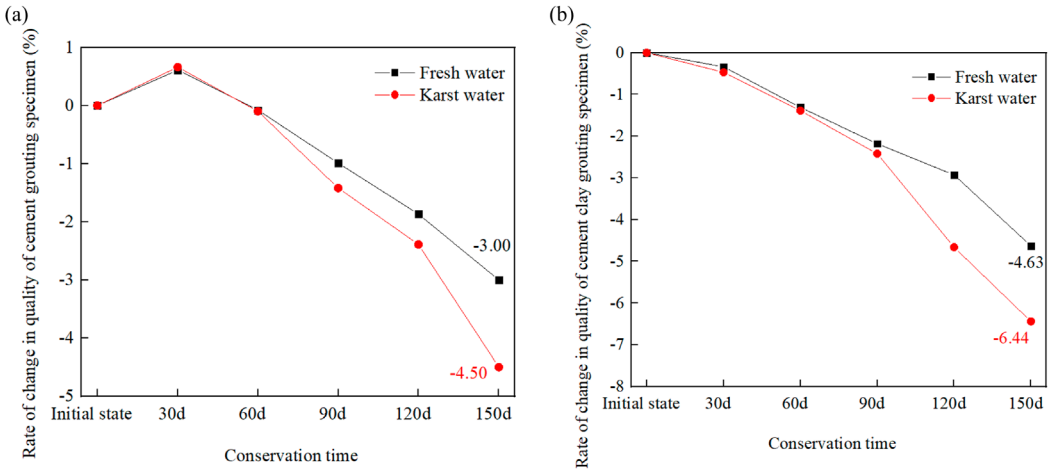


FIGURE 10
Mass loss rate of grouted stones under fresh and karst water erosion: **(a)** CGSs (Group A); **(b)** CCGSs (Group B).

Underground structural performance also varies with geometric and geomechanical parameters, as seen in tunnel stability studies (Alsabhan et al., 2021).

## 4 Discussion

Microstructural morphology serves as a critical indicator for reflecting changes in the internal composition and pore structure of grouted stones. SEM analysis was conducted on specimens cured for varying durations under karst water erosion. As shown in Figures 11, 12, the cement-grouted stone specimens (Group A) exhibited a dense structure with sufficient hydration, abundant C-S-H gels, and layered calcium hydroxide (irregular hexagonal flakes), along with minor calcium carbonate (blocky formations). In contrast, the CCGS (Group B) showed reduced cement content due to clay incorporation. Their microstructure revealed cement hydration products enveloped by clay particles, limited exposed cementitious materials, and sparse calcium hydroxide crystals and ettringite (needle-shaped). Notably, Group B specimens displayed distinct pores and microcracks, resulting in higher porosity and lower strength compared to Group A, macroscopic analysis revealed that Group A exhibited a compact microstructure, whereas Group B demonstrated pronounced porosity, consistent with macroscopic test results. Lattice element methods further enable accurate simulation of thermal transport and its relationship to geomaterial integrity (Rizvi et al., 2018).

Figures 12, 13 illustrate that after 60 days of karst water erosion, chemical reactions within the grouted stones generated secondary products such as calcium carbonate, gypsum, and

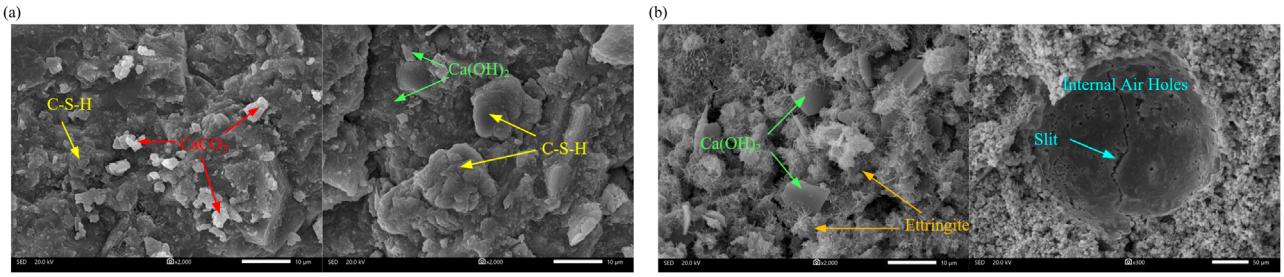


FIGURE 11
Micro-morphology of grouted stones for 28d under standard conditions (initial state): **(a)** CGSs (Group A); **(b)** CCGSs (Group B).

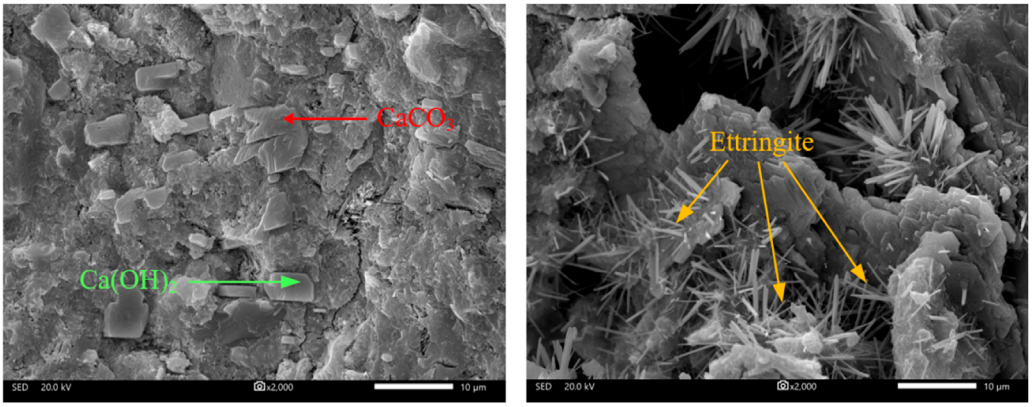


FIGURE 12
Micro-morphology of CGSs for 60d under karst water erosion.

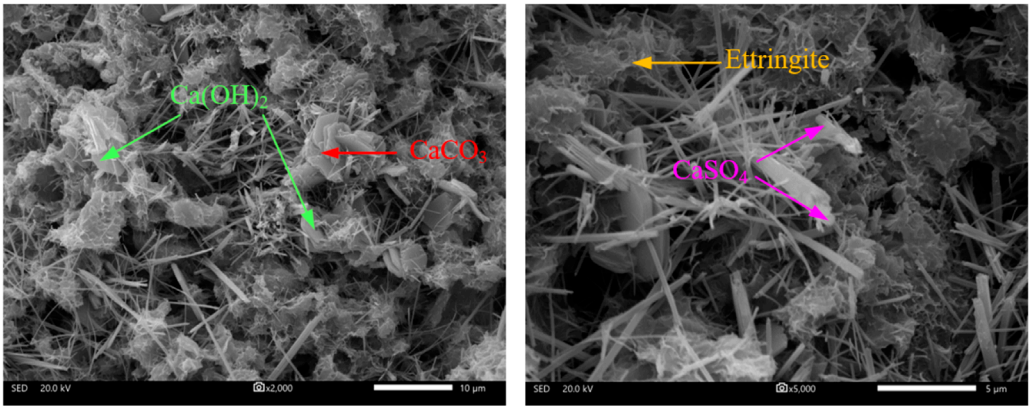


FIGURE 13
Micro-morphology of CCGSs for 60d under karst water erosion.

ettringite. Compared to the initial state after 28 days of standard curing, the 60-day eroded specimens developed pores and cracks. This deterioration arises from erosive ions reacting with calcium hydroxide to form gypsum, which subsequently interacts with aluminum phases to produce expansive ettringite. The growth of ettringite generates swelling stress at pore interfaces, fracturing the cementitious matrix. As erosion products dissolve or detach, the grouted stones become increasingly porous and fragile, leading to altered physical-mechanical properties (e.g., compressive strength, porosity) (Yu, 2017). Environmental fluctuations such as heat and moisture changes significantly influence the microstructural evolution of underground materials (Ahmad et al., 2025).

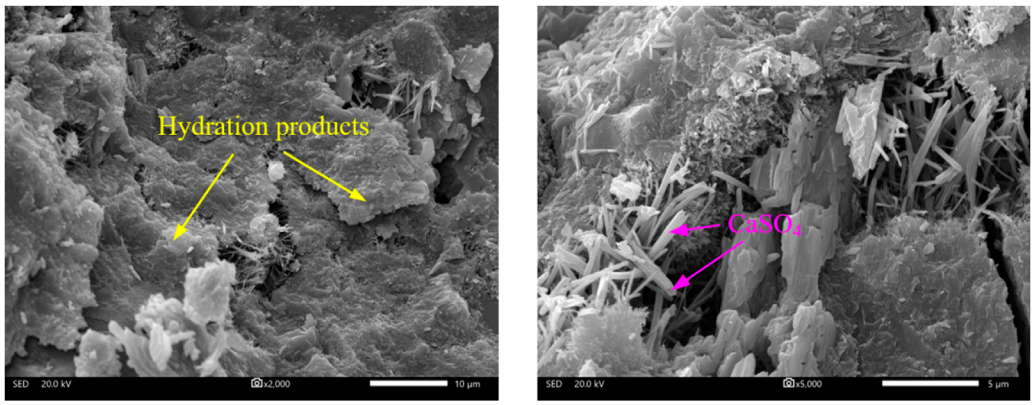


FIGURE 14
Micro-morphology of CGSs for 120d under karst water erosion.

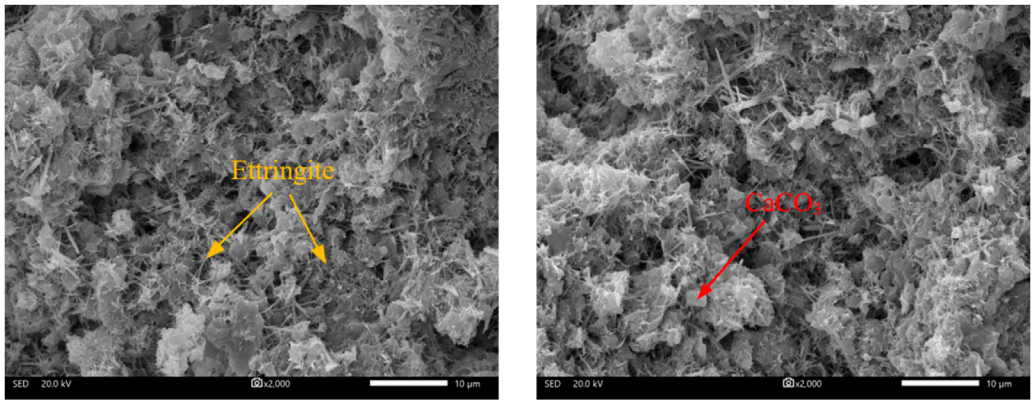


FIGURE 15
Micro-morphology of CCGSs for 120d under karst water erosion.

Figures 14, 15 demonstrate that after 120 days of karst water erosion, the grouted stones exhibited significantly increased crack density and width, indicating severe structural degradation. While calcium carbonate and gypsum continued to form, no chloride-containing compounds (e.g., calcium chloride) were detected. This absence is attributed to the low chloride ion concentration in the simulated karst water and the competitive reaction between sulfate ions (prioritized due to their higher affinity with $C_3A$ phases) and chloride ions. Consequently, chloride-related erosion products were negligible and undetectable in the sampled specimens (Wang et al., 2022).

## 5 Conclusion

Compressive strength and porosity tests were conducted on cement and CCGS specimens under varying curing durations to investigate the evolution of their mechanical and structural properties. Results demonstrated that under karst water curing, both groups exhibited progressive compressive strength reduction and porosity increase. Within 120 days, CGS specimens showed a strength decline from 32.89 MPa to 20.03 MPa, while CCGS specimens experienced a more pronounced deterioration, decreasing from 3.89 MPa to 2.03 MPa. Similarly, porosity values for CGSs rose from 26.06% to 33.91%, whereas CCGSs displayed a significantly higher porosity increase from 58.04% to 77.01% over the same period, confirming that CCGS suffered greater degradation in both strength and porosity.

Mass variation and microstructural morphology analyses were performed on cement and CCGS specimens under different curing durations and environments. Experimental findings revealed that karst water induced chemical and structural alterations in both groups through erosive effects. However, CCGSs exhibited more severe deterioration, characterized by higher mass variation rates and more drastic internal structural changes. The cement-clay matrix in CCGSs proved more vulnerable to karst water erosion, likely due to its inherently weaker cementitious bonding and higher initial porosity, which accelerated ion penetration and reaction-induced damage. The findings highlight the inferior durability of cement-clay composites under karst water conditions and provide critical insights for optimizing grouting materials in karst-prone environments.

## Data availability statement

The original contributions presented in the study are included in the article/supplementary material, further inquiries can be directed to the corresponding author.

## Author contributions

WT: Writing – original draft, Validation, Writing – review and editing, Data curation. MX: Writing – review and editing, Methodology, Conceptualization. XF: Writing – review and editing. CH: Writing – review and editing, Investigation. CM: Visualization, Writing – review and editing. YC: Writing – review and editing.

## Funding

The author(s) declare that financial support was received for the research and/or publication of this article. This work was supported by the National Natural Science Foundation of China (No.52378426), Natural Science Foundation of Hunan Province (No. 2025JJ60272), Distinguished Young Scholars of Changsha city Bureau (kq2209017), Science and technology innovation Program of Hunan Province (No. 2023RC3160), and the projects of water conservancy science and technology in Hunan Province (XSKJ2024064-48, XSKJ2023059-02). The corresponding author gratefully acknowledges this financial support.

## Conflict of interest

Author WT was employed by Hunan Urban and Rural Environmental Construction Co., Ltd. Author CH was employed by Hunan Construction Investment Group Infrastructure Investment Company.

The remaining authors declare that the research was conducted in the absence of any commercial or financial relationships that could be construed as a potential conflict of interest.

## Generative AI statement

The author(s) declare that no Generative AI was used in the creation of this manuscript.

## Publisher's note

All claims expressed in this article are solely those of the authors and do not necessarily represent those of their affiliated organizations, or those of the publisher, the editors and the reviewers. Any product that may be evaluated in this article, or claim that may be made by its manufacturer, is not guaranteed or endorsed by the publisher.

## References

Ahmad, S., Rizvi, Z., Khan, M. A., Ahmad, J., and Wuttke, F. (2019). Experimental study of thermal performance of the backfill material around underground power cable under steady and cyclic thermal loading. *Mater. today Proc.* 17, 85–95. doi:10.1016/j.matpr.2019.06.404

Ahmad, S., Rizvi, Z. H., Arp, J. C. C., Wuttke, F., Tirth, V., and Islam, S. (2021). Evolution of temperature field around underground power cable for static and cyclic heating. *Energies* 14 (23), 8191. doi:10.3390/en14238191

Ahmad, S., Rizvi, Z. H., and Wuttke, F. (2025). Unveiling soil thermal behavior under ultra-high voltage power cable operations. *Sci. Rep.* 15 (1), 7315. doi:10.1038/s41598-025-91831-1

Alsabhan, A. H., Sadique, M. R., Ahmad, S., Alam, S., and Binyahya, A. S. (2021). The effect of opening shapes on the stability of underground tunnels: a finite element analysis. *GEOMATE J.* 21 (87), 19–27. doi:10.21660/2021.87.j2267

Bai, Y. (2001). "New technologies for seepage prevention and reinforcement of Chinese dams," in *Beijing, China: water resources and electric power*. Press 404. 200109. (in Chinese).

Bruce, D. A., Greene, B. H., Craig, F. R., Williams, B. E., Williams, J. H., and Mickwee, R. L. (2017). Long-term grouting of a karst foundation at logan Martin dam, Alabama. *Grouting*, 47–57. doi:10.1061/9780784480786.005

Feng, S. (2015). *Experimental study on deterioration of clay-cement grout under erosion conditions*. Changsha, China: Changsha University of Science and Technology. (in Chinese).

Fu, P., Xing, Z., and Yang, X. (2013). "Experimental research on durability of dam foundation curtains under low-alkalinity soft water conditions," in *Foundation engineering technology for water resources and hydropower projects 2013-proceedings of the 12th national conference of Chinese hydraulic engineering society*. Editor K. F. Xia (Beijing: China Water and Power Press), 41–47. (in Chinese).

Haroon, A., Ahmad, S., and Hussain, A. (2017). *CFD prediction of loss coefficient in straight pipes development of water resources in India*. Springer International Publishing, 477–485.

He, S. (2019). *Experimental study on dissolution properties of mineral admixture concrete under soft water conditions*. Nanjing, China: Nanjing University of Science and Technology. (in Chinese).

Jiang, X., Yang, C., Wen, J., and Shi, Z. (2014). Water temperature variation and influencing factors in lakes/reservoirs of Changsha region. *J. Hunan Univ. Nat. Sci.* 41 (9), 93–99. (in Chinese). doi:10.3969/j.issn.1674-2974.2014.09.015

Lindvall, A. (2007). Chloride ingress data from field and laboratory exposure-Influence of salinity and temperature. *Cem. Concr. Compos.* 29 (2), 88–93. doi:10.1016/j.cemconcomp.2006.08.004

Liu, S. (2004). *Study on curtain grouting in karst areas*. Changchun, China: Jilin University. (in Chinese).

Liu, Y. (2019). *Mechanical performance degradation and durability of grouted soils under seawater erosion conditions*. Jinan, China: Shandong University. (in Chinese).

Ministry of Construction of the People's Republic of China (2019). *GB/T 50081-2019 Standard for test methods of concrete physical and mechanical properties*. Beijing: China Architecture and Building Press. (in Chinese).

Ministry of Transport of the People's Republic of China (2019). *TS/T 236-2019 Technical specification for concrete testing in water transport engineering*. Beijing: China Communications Press. (in Chinese).

Mozafari, M., Milanović, P., and Jamei, J. (2021). Water leakage problems at the Tangab Dam Reservoir (SW Iran), case study of the complexities of dams on karst. *Bull. Eng. Geol. Environ.* 80 (10), 7989–8007. doi:10.1007/s10064-021-02387-z

Pan, H., Cai, H., Wang, B., Zhang, P., and Yao, Y. (2023). Evolution characteristics of water temperature in Dongting Lake from 1973 to 2020. *J. Lake Sci.* 35 (1), 326–337. doi:10.18307/2023.0125 (in Chinese)

Rizvi, Z. H., Mustafa, S. H., Sattari, A. S., Ahmad, S., Furtner, P., and Wuttke, F. (2020a). "Dynamic lattice element modelling of cemented geomaterials," in *Advances in computer methods and geomechanics: IACMAG symposium 2019 volume 1* (Singapore: Springer), 655–665.

Rizvi, Z. H., Shrestha, D., Sattari, A. S., and Wuttke, F. (2018). Numerical modelling of effective thermal conductivity for modified geomaterial using lattice element method. *Heat Mass Transf.* 54, 483–499. doi:10.1007/s00231-017-2140-2

Rizvi, Z. H., Zaidi, H. H., Akhtar, S. J., Sattari, A. S., and Wuttke, F. (2020b). Soft and hard computation methods for estimation of the effective thermal conductivity of sands. *Heat Mass Transf.* 56, 1947–1959. doi:10.1007/s00231-020-02833-w

Sha, F., and Fan, G. X. (2021). Durability of a novel effective microfine cementitious grouting material in corrosion environments. *Constr. Build. Mater.* 306, 124842. doi:10.1016/j.conbuildmat.2021.124842

Tang, Y. (2019). *Failure mechanisms and performance evaluation of cement-based materials under dissolution and chloride erosion*. Nanjing, China: Nanjing University of Science and Technology. (in Chinese).

Tu, P. (2012). *Experimental study and theoretical evaluation on durability of grouted soils*. Central South University. (in Chinese).

Verma, D., Berwal, P., Khan, M. A., Alharbi, R. S., Alfaisal, F. M., and Rathnayake, U. (2023). Design for the prediction of peak outflow of embankment breaching due to overtopping by regression technique and modelling. *Water* 15 (6), 1224. doi:10.3390/w15061224

Wang, H. (2019). *Grouting diffusion reinforcement and degradation mechanisms in sand layers under seawater erosion-seepage interactions*. Shandong, China: Shandong University. (in Chinese).

Wang, H., Li, Z., Wang, X., Zhang, Q., and Zhang, L. (2021). Study on grouted body deterioration mechanism of sand layer in seawater environment. *Adv. Mater. Sci. Eng.* 2021, 1–8. doi:10.1155/2021/6329257

Wang, H. B., Liu, Q. W., Sun, S. Q., Zhang, Q., Li, Z., and Zhang, P. (2020). Damage model and experimental study of a sand grouting-reinforced body in a seawater environment. *Water* 12 (9), 2495. doi:10.3390/w12092495

Wang, P., Mo, R., Sui, X., Tian, L., Xu, J., and Jin, Z. (2022). Research progress on chemo-damage-transport models for coupled chloride-sulfate attack in concrete. *J. Chin. Ceram. Soc.* 50 (2), 512–521. (in Chinese).

Wang, T. (2016). *Numerical simulation and analysis of chloride ion diffusion in marine environment concrete*. Ganzhou, China: Jiangxi University of Science and Technology. (in Chinese).

Wei, G., Feng, F. F., Huang, S. Y., Xu, T. B., Zhu, J. X., Wang, X., et al. (2025). Full-scale loading test for shield tunnel segments:Load-bearing performance and failure patterns of lining structures. *Underground Space* 20, 197–217. doi:10.1016/j.undsp.2024.05.003

Xie, Y., Qu, T., Yang, J., Wang, S., Zhao, J., et al. (2025). Multiscale insights into tunneling-induced ground responses in coarse-grained soils. *Computers and Geotechnics* 185, 107319. doi:10.1016/j.compgeo.2025.107319

Yu, H. (2017). *Macro-micro damage mechanisms of concrete under different salt erosion types*. Changchun, China: Jilin University. (in Chinese).

Yu, H., and Sun, W. (2006). Theoretical model of chloride ion diffusion in concrete. *J. Southeast Univ. Nat. Sci. Ed.* (S2), 68–76. (in Chinese).

Yu, R., Tong, X., Ding, M., Qian, D., and Zhou, F. (2020). Degradation mechanisms and countermeasure analysis of concrete materials in underground environments. *Prot. Eng.* 42 (1), 70–78. (in Chinese).

Zhou, D., Shen, Z., Ma, B., and Zhang, K. (2022). Distribution law of mass loss in concrete dams under permeation and dissolution effects. *Adv. Sci. Technol. Water Resour.* 42 (2), 72–78. doi:10.3880/j.issn.1006-7647.2022.02.011 (in Chinese)

Zuo, C. (2021). *Service life prediction of marine concrete under multi-factor coupling effects*. Harbin, China: Harbin Engineering University. (in Chinese).

frontiers | Frontiers in Earth Science

TYPE Original Research
PUBLISHED 03 June 2025
DOI 10.3389/feart.2025.1597575



OPEN ACCESS

EDITED BY
Tongming Qu,
Hong Kong University of Science and Technology, Hong Kong SAR, China

REVIEWED BY
Xingbo Han,
Chang'an University, China
Jianyong Han,
Shandong Jianzhu University, China

*CORRESPONDENCE
Lei Cao,
815172232@qq.com

RECEIVED 21 March 2025
ACCEPTED 16 May 2025
PUBLISHED 03 June 2025

CITATION
Xu P, Song X, Cao L and Sun H (2025) Extent and control standards of grouting reinforcement for underwater karst shield tunnels.
*Front. Earth Sci.* 13:1597575.
doi: 10.3389/feart.2025.1597575



# Extent and control standards of grouting reinforcement for underwater karst shield tunnels

Peng Xu[1], Xiangshuai Song[2], Lei Cao[3]* and Heng Sun[2]

[1]CCCC South China Construction and Development Co., Ltd., Shenzhen, China, [2]CCCC Second Harbor Engineering Company Ltd., Wuhan, China, [3]School of Water Resources and Hydropower, Hunan Polytechnic of Water Resources and Electric Power, Changsha, China

In urban regions with karst developments, grouting is commonly utilized to fill cavities. However, the extent and control standards of grouting reinforcement are primarily determined through experience and field testing, which poses challenges in ensuring its effectiveness. Based on the instability mechanism of surrounding rocks in underwater karst shield tunnels, this study develops a mechanical model for analyzing the grouting reinforcement extent of such tunnels using strength theory. The reinforcement range for karst formations at various tunnel locations is clarified, and corresponding grouting reinforcement control standards are proposed based on cusp catastrophe theory. The findings indicate the following: the primary cause of surrounding rock instability in underwater karst shield tunnels is that the reduction in surrounding rock thickness during shield tunneling modifies the original constraints and boundary conditions and disrupts the initial equilibrium state. These changes influence the water content of the surrounding rocks and disturb the surrounding rock and soil mass, leading to surrounding rock instability. When grouting causes damage to the surrounding rocks between the karst and tunnel, the system is simplified into cantilever beam and plate models for analysis. It is determined that the grouting reinforcement extent is primarily influenced by factors such as karst size, properties of the karst filling material, and tunnel span. The total potential energy of the rock mass between the karst and tunnel is calculated, leading to the development of an instability and catastrophe model for the surrounding rocks. The proposed grouting reinforcement control standards are mainly dependent on factors such as the distance of the karst, characteristics of the reinforced surrounding rocks, shield machine support force, material properties post-reinforcement, and karst size.

KEYWORDS

**shield tunnel, underwater karst, instability of surrounding rocks, grouting reinforcement, control standard**

## 1 Introduction

Karst presents a significant challenge in tunnel construction, posing substantial risks and leading to serious consequences. During excavation, the exposure of previously undetected karst formations can result in mud and water inrush accidents, leading to casualties, damage to construction equipment, and severe disruptions to the project schedule (Su et al., 2025; Chen et al., 2024). In urban settings, karst tunnel construction may induce deformation in the overlying strata, potentially causing settlement, cracking, or, in severe cases, collapse of surface structures. Furthermore, the loss of large volumes of karst filling material and

the subsequent destabilization of the strata can contribute to surface collapse and roof caving (Alija et al., 2013; Huang et al., 2017; Zhao et al., 2024). Additionally, operational disruptions, including vehicle interruptions caused by karst-related issues, have been frequently reported.

For the construction of subway tunnels in urban karst areas, existing research primarily addresses the development patterns and characteristics of karst formations, the response of surface environments to disturbances caused by subway tunnel construction, the mechanisms of disturbance and instability in karst strata, and the engineering techniques for managing tunnels crossing karst regions (Liu et al., 2024; Wei et al., 2020; Su et al., 2021; Fu et al., 2020; Lan et al., 2021; Li et al., 2016). Karst grouting treatment is a widely employed engineering method that involves injecting specialized slurry into cavities to fill voids and reinforce the surrounding rock mass, thereby enhancing geological stability and load-bearing capacity. This technique relies on the fluidity and cohesiveness of the slurry to bond loose rock particles, creating an integrated structure and improving the strength of the rock mass. Current grouting applications for underwater karst shield tunnels are predominantly based on analyses of engineering case studies. For example, based on the engineering background of Guangzhou Metro shield tunneling through karst areas, Zhang et al. (2018) proposed a new controllable grouting method and two corresponding grouting materials to pre reinforce the underwater karst area before the shield tunnel passes through (Yang et al., 2020). In the Guangzhou Metro Line five karst shield tunneling project, Cui and Wang, (2008) compared the effectiveness of sleeve valve pipe grouting, perforated pipe grouting, and steel jacket grouting in typical karst regions. Ou et al. (2024) drew on the engineering experience of multiple large-scale water inrush disasters in the Dejiang Tunnel to qualitatively and quantitatively analyze the water inrush mechanism. The principle of "combining drainage and blockage" was adopted to solve the water inrush problem, and the innovative application of high-pressure grouting with membrane bags effectively solved the series connected karst pipeline. In a practical shield tunneling project through karst formations, Ma, (2018) proposed a grouting treatment method incorporating paste slurry and a combination of low-pressure pulse sealing with high-pressure pulse squeezed grouting for single karst formations, while for bead-shaped karst, a technique involving gradually segmented grouting from top to bottom with a multi-layer casing was introduced. A review of the literature indicates that control standards for grouting in underwater karst shield tunnels remain unexplored. For such grouting projects, defining reasonable reinforcement ranges is crucial to ensuring smooth construction progress and the safe operation of shield tunnels. Establishing appropriate grouting reinforcement parameters can also help optimize project costs and reduce construction timelines. However, most existing grouting projects rely on empirical methods and on-site testing to determine reinforcement ranges and requirements, which compromises engineering safety and leads to excessive consumption of manpower and financial resources.

Given these considerations, this study first examines the instability mechanism of surrounding rocks in underwater karst shield tunnels and subsequently develops a cantilever beam mechanics model. Utilizing strength theory, the grouting reinforcement range is determined for various positions of underwater karst relative to the shield tunnel. Additionally, the corresponding grouting reinforcement requirements are calculated using a fixed support plate mechanics model. The findings of this research offer a reliable approach for analyzing and establishing grouting control standards for underwater karst shield tunnels.

## 2 Instability mechanism of surrounding rocks in underwater karst shield tunnels

The formation process of underwater karst indicates that karst formations are typically in a highly stable state (Zou et al., 2025) However, when a shield tunnel passes through a karst region, the tunneling process induces stress redistribution, residual stress release, and variations in pore water pressure within a specific range around the tunnel. These changes result in deformation, displacement, and alterations in the physical and mechanical properties of the surrounding rocks, potentially leading to engineering failures such as tunnel face instabilities and water and mud inrush incidents within the tunnel (Yang et al., 2017).

Considering the alterations in the stress state of the surrounding rocks induced by shield tunneling, the primary factors contributing to the instability of surrounding rocks in underwater karst shield tunnels can be summarized as follows:

(1) During shield tunneling, a sudden reduction in the thickness of the surrounding rocks leads to substantial alterations in their initial constraints and boundary conditions, disrupting the original stress equilibrium state. This results in stress redistribution and a decrease in the strength and stiffness of the surrounding rocks. The gravitational influence of construction equipment, such as the shield tunneling machine, also affects the surrounding rock mass. When the karst is positioned above the tunnel, tensile stress acts on the surrounding rocks on the tunnel side, while compressive stress is exerted on the rocks adjacent to the karst. Conversely, when the karst is beneath the tunnel, the stress distribution is reversed. If the karst is located on the tunnel's side, significant stress concentration occurs in the surrounding rocks. Ultimately, instability failure takes place when the tensile stress generated in the surrounding rocks exceeds their tensile strength.

(2) Shield tunneling significantly influences the water content of the surrounding rocks. Tunnel excavation causes the accumulation of groundwater around the tunnel, leading to variations in pore water pressure and seepage pressure, which can compromise the structural integrity of the surrounding rocks. Additionally, the excavation process and the weight of the shield machine induce stress variations in the surrounding rocks, further altering water pressure and other influencing factors within the rock mass. Under the combined effects of fluid-solid coupling between the surrounding rocks and groundwater, the stability of the surrounding rocks near the tunnel is highly susceptible to failure.

(3) Shield tunneling induces substantial construction disturbances in the surrounding rock and soil mass. This is primarily reflected in the impact of structures such as the shield cutterhead and shield shell, which cause significant

perturbations and loosening of the surrounding rock and soil mass. Additionally, modifications in crack channels within the surrounding rocks occur, intensifying the damage caused by crack water and penetrating water. Furthermore, as the surrounding rocks loosen, previously enclosed high-pressure water and gas are partially released, further exacerbating the loosening of the rock and soil mass and, in some cases, directly leading to structural failure.

# 3 Extent of grouting reinforcement for underwater karst shield tunnels

## 3.1 Basic assumptions

The stress state of underwater karst formations positioned at various locations relative to the shield tunnel is analyzed, and the grouting reinforcement extent for these underwater karst shield tunnels is determined by assessing the safe distance between the tunnel and the karst. Based on the requirements of the analysis, the following assumptions are proposed:

(1) The surrounding rocks between the underwater karst and the shield tunnel are considered a homogeneous body, and the karst remains unchanged throughout the shield tunneling process.
(2) The arching effect of the surrounding rocks between the underwater karst and the shield tunnel is disregarded, and the surrounding rocks are simplified into beam and plate structures for elastic calculations.
(3) Before shield tunneling, the karst is assumed to be in a stable state, and the loads acting on the surrounding rocks between the underwater karst and the shield tunnel are simplified as either concentrated or uniformly distributed loads.

## 3.2 Establishment of cantilever beam and plate mechanics models

Due to the influence of drilling and grouting pressure during the grouting process in underwater karst shield tunnels, the surrounding rocks between the underwater karst and the shield tunnel experience a certain degree of damage, leading to the formation of numerous cracks and gaps. Therefore, these surrounding rocks are simplified into cantilever beam and plate models for stress analysis. In this model, let S represent the length of the cantilever and B denote the crack cutting width. Based on elastic theory, the model behaves as a cantilever beam when $S > 5B$ and transitions into a cantilever plate model when $S \leq 5B$ (Shunying et al., 2024; Rees, 2018; Carpinteri A., 2017). The mechanical model of the cantilever beam is illustrated in Figure 1a, while the cantilever plate mechanics model is depicted in Figure 1b.

## 3.3 Karst above the tunnel

When the underwater karst is positioned above the shield tunnel, the rock and soil mass between the karst and the tunnel are influenced by the surrounding rock weight, karst-filling material, and groundwater. The stress condition of the surrounding rocks in this scenario can be simplified into a cantilever beam model. Let the karst water pressure be $P_w$, the pressure exerted by the karst filling material be $P_a$, and the weight of the surrounding rocks be $P_r$. Under these conditions, the cantilever beam stress model is represented schematically in Figure 2.

According to Figure 2, the maximum shear stress $\tau_{max}$ of the cantilever beam is

$$\tau_{max} = \frac{3P_{max}}{2SB} \tag{1}$$

Where S represents the span of the surrounding rocks, and $P_{\max}$ denotes the maximum shear force of the cantilever beam.

When the shield tunneling machine remains in a stable state during excavation, the maximum shear stress should not exceed the shear strength of the surrounding rock (τ).

By combining Equation 1, it is evident that a minimum reinforcement range exists to maintain the stability of the surrounding rocks. Thus,

$$B \geq \frac{3P_{max}}{2S\tau} \tag{2}$$

According to Figure 2, the maximum shear force $P_{\max}$ satisfies

$$P_{max} = P_w + P_a + P_r \tag{3}$$

Therefore, by combining Equations 2, 3, when the underwater karst is positioned above the tunnel, the grouting reinforcement range $h_1$ is

$$h_1 = B = \frac{3P_{max}}{2S\tau} = \frac{3\left(P_w + P_a + P_r\right)}{2S\tau} \tag{4}$$

According to Equation 4, it is important to note that, since the surrounding rocks beneath the karst are in a fully saturated state, this factor must be considered when calculating the weight of the surrounding rocks.

## 3.4 Karst below the tunnel

When the underwater karst is positioned below the shield tunnel, the rock and soil mass between the karst and the tunnel are influenced by the weights of the saturated surrounding rocks and the shield machine. The stress condition of the surrounding rocks in this scenario is simplified into a cantilever beam model. Let $P_1$ represent the load of the shield tunneling machine, $P_r'$ denote the weight of the surrounding rocks, and $P_w'$ indicate the karst water pressure. Under these conditions, the cantilever beam stress model is described by the schematic shown in Figure 3.

As shown in Figure 3, similarly, by referring to Equations 1, 2, during shield excavation, a minimum reinforcement range is required to maintain the stability of the surrounding rocks.

According to Figure 3, the maximum shear force $P'_{max}$ satisfies

$$P'_{max} = P_1 + P'_r - P'_w \tag{5}$$

Therefore, based on Equation 5, when the underwater karst is located below the tunnel, the grouting reinforcement range $h_2$ is Equation 6

$$h_2 = B = \frac{3P'_{max}}{2S\tau'} = \frac{3\left(P_1 + P'_r - P'_w\right)}{2S\tau'} \tag{6}$$

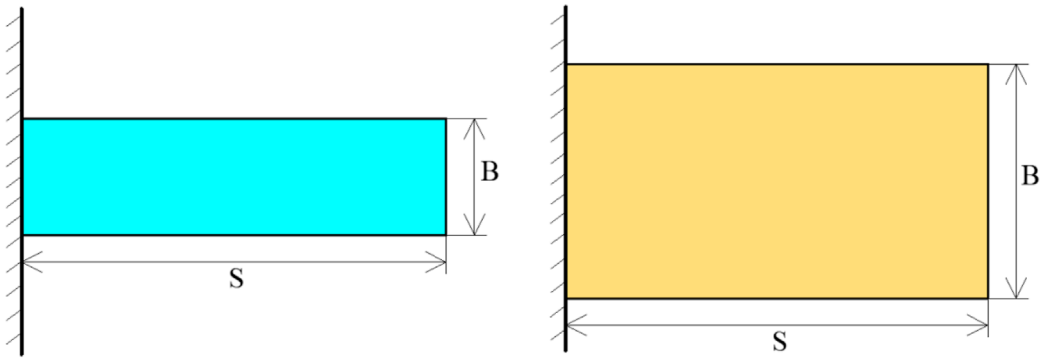


(a) Cantilever beam mechanics model (b) Cantilever plate mechanics model

FIGURE 1
Cantilever beam and cantilever plate mechanics models. **(a)** Cantilever beam mechanics model **(b)** Cantilever plate mechanics model.

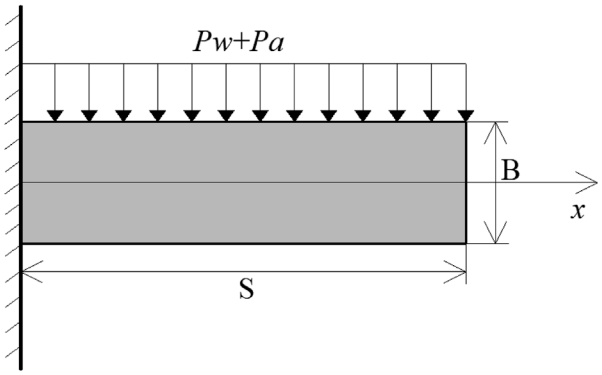


FIGURE 2
Cantilever beam stress model when the karst is above the tunnel.

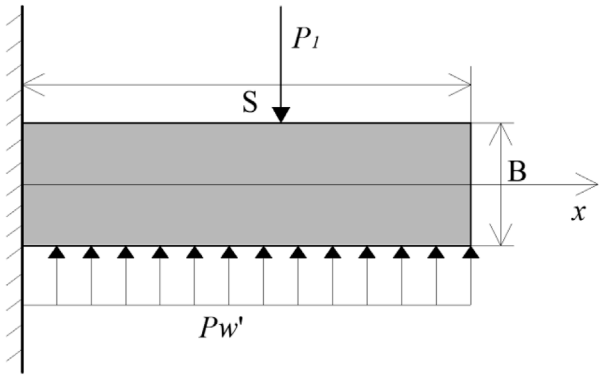


FIGURE 3
Cantilever beam stress model when the karst is under the tunnel.

## 3.5 Karst on the tunnel side

When the underwater karst is positioned on the side of the shield tunnel, the stress condition of the surrounding rocks between the underwater karst and the shield tunnel can be simplified as an elastic plate model. Let $P_w$ denote the uniformly distributed load of karst water pressure on the surrounding rock wall, and $P_a$ represent the uniformly distributed load of the karst filling material on the surrounding rock wall. Under these conditions, the elastic plate stress model shown in Figure 4 is satisfied.

According to Figure 4, similarly, by referring to Equations 1, 2, during shield excavation, a minimum reinforcement range is required to maintain the stability of the surrounding rocks.

According to Figure 4, the maximum shear force $P''_{max}$ satisfies

$$P''_{max} = P''_w + P_a \tag{7}$$

Therefore, based on Equation 7, when the underwater karst is located on the side of the tunnel, the grouting reinforcement range $h_3$ is Equation 8

$$h_3 = B = \frac{3P''_{max}}{2S\tau''} = \frac{3(P''_w + P_a)}{2S\tau''} \tag{8}$$

# 4 Control standards for grouting reinforcement of underwater karst shield tunnels

## 4.1 Grouting reinforcement model based on the cusp catastrophe theory

The cusp catastrophe theory is widely applied to analyze instability problems induced by tunnel excavation, providing both the necessary and sufficient conditions for the instability of surrounding rocks during excavation (Liao et al., 2022; Liu et al., 2024). Therefore, in the context of underwater karst shield tunnels, the instability condition of the surrounding rocks without grouting reinforcement is first determined using the cusp catastrophe theory. To ensure stability after grouting, it is essential to enhance the surrounding rock parameters to prevent an unstable state.

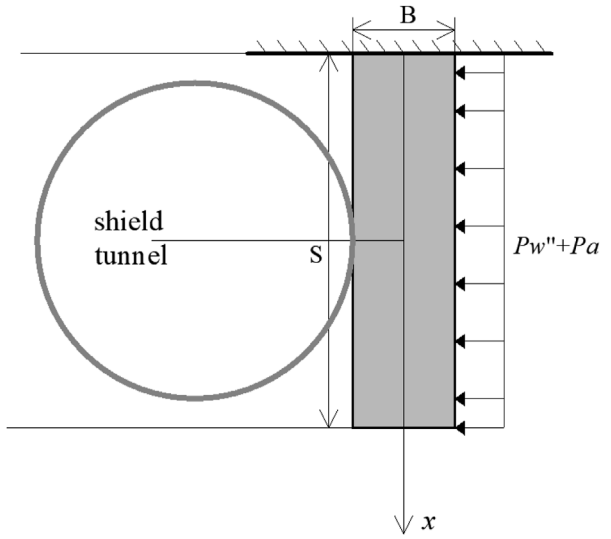


FIGURE 4
Elastic plate stress model when the karst is located on the side of the tunnel.

Consequently, the improved geological condition is established as the standard for grouting reinforcement in underwater karst shield tunnels.

After grouting reinforcement, shield tunneling is carried out. For each shield tunneling cycle step, the state variable $E_n$ of each surrounding rock unit is:

$$E_n(m) = \int_{v_n} \sigma_{ij}\varepsilon_{ij} dv_n \tag{9}$$

where $n$ represents the unit number of the model, $m$ denotes the cycle step of shield tunneling, and $E = f(t)$ expresses the variation in $E_n$ for each excavation. Expanding Equation 9 using the *Taylor* series gives, considering that the expansion of the project is mainly influenced by the first five items, while subsequent terms have negligible effects, it can be approximated as:

$$E = \sum_{n=0}^{4} \kappa_n t^n \tag{10}$$

where $\kappa_n = \frac{\partial^i f}{\partial t^i}|_{t=0}$.

Letting $\Delta$ be the control parameter, Equation 10 can be rewritten in the standard form of the cusp catastrophe theory:

$$\Pi(x) = \frac{1}{4}x^4 + \frac{1}{2}Ax^2 + Bx \tag{11}$$

where $A = \frac{\kappa_2}{\kappa_4} - \frac{3\kappa_3^2}{8\kappa_4^2}$, $B = \frac{\kappa_1}{\kappa_4} - \frac{\kappa_2\kappa_3}{2\kappa_4^2} + \frac{3\kappa_3^2}{8\kappa_4^2}$.

Taking the derivative of Equation 11 leads to the bifurcation set equation:

$$\Delta = 4A^3 + 27B^2 = 0 \tag{12}$$

According to the cusp catastrophe theory, when $\Delta > 0$, the surrounding rocks after grouting reinforcement remain in a stable state during shield tunneling. Therefore, the condition for satisfying the grouting reinforcement standard is $\Delta > 0$.

## 4.2 Karst above the tunnel

When the underwater karst is positioned above the shield tunnel, the grouting-reinforced structure between the karst and the tunnel is influenced by the weight of the surrounding rocks and groundwater. Under these loads, the surrounding rocks experience vertical displacement during shield tunneling. If this vertical displacement exceeds a critical threshold, instability occurs. Therefore, the grouting reinforcement standard is defined to ensure that the vertical displacement of the surrounding rocks remains below the critical value during shield tunneling.

### 4.2.1 Basic assumptions and model establishment

According to actual site conditions, if L represents the span between the karst and the tunnel, d denotes the distance between them, E is the elastic modulus of the formation after grouting reinforcement, $P_a$ is the weight of the reinforced structure following cave treatment, $P_w$ indicates the water pressure exerted by groundwater, $P$ be the weight of the surrounding rocks, and $q$ represents the support force provided by the shield tunnel segments. The following assumptions are made:

The formation is considered intact after grouting reinforcement, and the surrounding rocks above the shield tunnel are simplified as a beam structure for stress analysis. 2) The above loads act on the shield tunnel in the form of uniformly distributed loads. 3) The stress at both ends of the tunnel is simplified as a horizontal load $F$.

Based on these assumptions, the mechanical model depicted in Figure 5 can be established.

### 4.2.2 Calculation of the surrounding rock potential function

According to Reference (Jiang et al., 2005), the deflection of the beam axis shown in Figure 5 can be expressed as:m

$$f = \sum_{i=1}^{\infty} w_i \sin\frac{i\pi l}{L} \tag{13}$$

According to Equation 13, the initial deflection of the beam axis is:

$$f = w \sin\frac{\pi dl}{L} \tag{14}$$

where $w$ represents the deflection of the beam at $L/2$, and $l$ denotes the arc length from the endpoint of the beam to any position along the axis.

Based on the cusp catastrophe theory of grouting reinforcement, the potential function of the surrounding rocks is:

$$\Pi = U - W_x - W_y \tag{15}$$

where $U$ represents the strain energy of the beam, $W_x$ denotes the work done in the horizontal direction, and $W_y$ is the work done by vertical forces.

According to the theories of material mechanics and elasticity, based on Equation 14, the terms in Equation 15 can be expressed as:

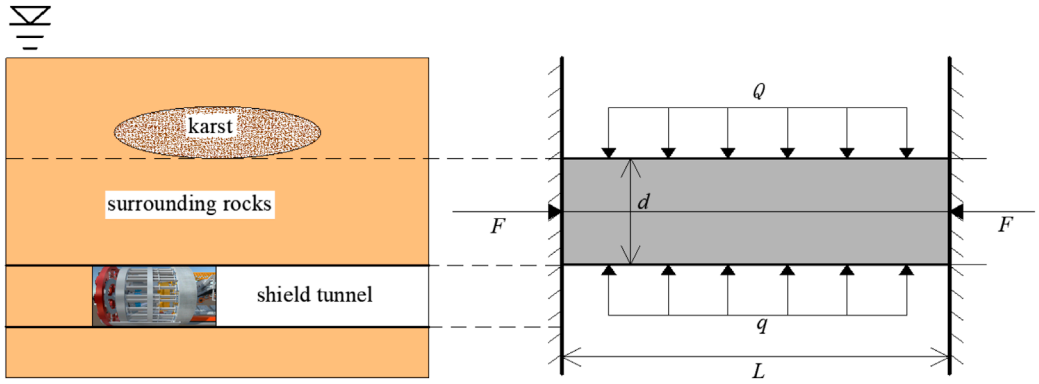


FIGURE 5
Mechanical model of the underwater karst located above the shield tunnel.

$$\begin{cases} U = \dfrac{EI}{2}\displaystyle\int_0^L \left(\frac{d^2 f}{dl^2}\right)^2 \left[1-\left(\frac{df}{dl}\right)^2\right]^{-1} ds \\ W_x = F\displaystyle\int_0^L \left(\left(\left(1-\left(\frac{df}{dl}\right)^2\right)^{\frac{1}{2}}\right)\right)^{\frac{1}{2}} \\ W_y = -(Q-q)\dfrac{2Lw}{\pi} \end{cases} \tag{16}$$

By combining Equations 15, 16, the potential function of the surrounding rocks can be obtained. After simplification, it is expressed as:

$$\prod = \frac{EI\pi^6}{16L^5}w^4 + \frac{\pi^2}{4L}\left(\frac{EI\pi^2}{L^2} - F\right)w^2 + \frac{2L(Q-q)}{\pi}w \tag{17}$$

### 4.2.3 Control standard for grouting reinforcement

Let

$$\begin{cases} w = \dfrac{L}{\pi}\left(\dfrac{4L}{EI\pi^2}\right)^{\frac{1}{4}} x \\ A = \dfrac{L}{\pi}\left(\dfrac{L}{EI}\right)^{\frac{1}{2}}\left(\dfrac{EI\pi^2}{L^2} - F\right) \\ B = \dfrac{L}{\pi}\left(\dfrac{4L}{EI\pi^2}\right)^{\frac{1}{4}}(Q-q) \end{cases} \tag{18}$$

Combining Equations 17, 18 yields:

$$\Pi(x) = \frac{1}{4}x^4 + \frac{1}{2}Ax^2 + Bx \tag{19}$$

Equation 19 represents the standard form of cusp catastrophe, which is consistent with Equation 12. When the bifurcation set satisfies $\Delta > 0$, the surrounding rocks reinforced by grouting remain stable during shield tunneling. Thus, the following condition holds:

$$\Delta = 4A^3 + 27B^2 > 0 \tag{20}$$

By substituting the terms from Equation 18 into Equation 20 and considering $I = d^3/12$ and $Q = Pa + Pw + P$, the elastic modulus $E$ of the surrounding rocks after grouting reinforcement can be determined. This is expressed in Equation 21, which serves as the grouting reinforcement standard for underwater karst formations located above the shield tunnel:

$$E > 12L^2\left(\frac{\left(\frac{-F\lambda}{2} + \left(\frac{F^2\lambda^2}{4} + \frac{\lambda^3}{27}\right)^{\frac{1}{2}}\right)^{\frac{1}{3}} - \left(\left(\frac{F\lambda}{2} + \left(\frac{F^2\lambda^2}{4} + \frac{\lambda^3}{27}\right)^{\frac{1}{2}}\right)^{\frac{1}{3}} + F\right)}{d^3\pi^2}\right. \tag{21}$$

where $\lambda = \frac{27}{2\pi^2}(P_a + P_w + P - q)^2$

According to Equation 21, the control standard for grouting reinforcement depends on factors such as the karst distance, the properties of the surrounding rocks after reinforcement, the material performance following karst reinforcement, and the influence of groundwater.

## 4.3 Karst below the tunnel

When the underwater karst is positioned below the shield tunnel, the grouting-reinforced structure between the karst and the tunnel is subjected to the weight of the surrounding rocks, groundwater pressure, and the weight of the shield machinery. Under these applied loads, vertical displacement occurs in the surrounding rocks during shield tunneling. If this vertical displacement exceeds a critical threshold, instability develops in the surrounding rocks. Therefore, the grouting reinforcement standard is established to ensure that the vertical displacement of the surrounding rocks during shield tunneling remains below the instability threshold.

### 4.3.1 Basic assumptions and model establishment

Based on the actual site conditions, we assume that the span between karst and shield tunnel is L, the distance between the two is d, the elastic modulus of the formation after grouting reinforcement is given as E, the load of the shield machine is $P_1$, the weight of the surrounding rocks is $P_r'$, and the water pressure is $P_w'$. The following assumptions are also made: The formation remains intact after grouting reinforcement, and the surrounding rocks above the shield are simplified as a fixed support beam plate for stress analysis. The above loads act on the surrounding rock mass in the form of uniformly distributed loads.

Based on these assumptions, the mechanical model illustrated in Figure 6 can be established.

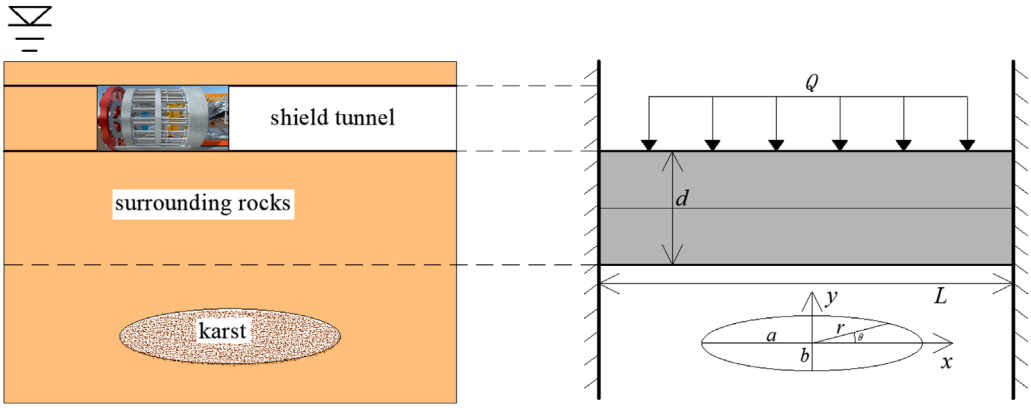


FIGURE 6
Mechanical model when the underwater karst is located below the shield tunnel.

### 4.3.2 Calculation of the surrounding rock potential function

According to References (Chen, 2002; Xu, 2024), the deflection of the fixed support beam plate shown in Figure 6 is expressed as:

$$w(x,y)=\frac{12(1-\mu^2)}{Ed^3}\frac{Q}{8\left(\frac{3}{a^4}+\frac{2}{a^2b^2}+\frac{3}{b^4}\right)}\left(\frac{x^2}{a^2}+\frac{y^2}{b^2}-1\right)^2 \tag{22}$$

where E represents the elastic modulus of the surrounding rocks after grouting reinforcement, and $\mu$ is the corresponding Poisson's ratio.

If we let $K=\frac{12(1-\mu^2)}{Ed^3}\frac{Q}{8\left(\frac{3}{a^4}+\frac{2}{a^2b^2}+\frac{3}{b^4}\right)}$, then Equation 22 can be rewritten as:

$$w(x,y)=K\left(\frac{x^2}{a^2}+\frac{y^2}{b^2}-1\right)^2 \tag{23}$$

Converting Equation 23 into a polar coordinate form, we have

$$w(x,y)=K\left(\frac{r^2}{R^2}-1\right)^2 \tag{24}$$

where $R=\frac{ab}{\sqrt{a^2sin^2\theta+b^2cos^2\theta}}$.

Additionally, based on Equation 24, considering the boundary conditions and deterministic laws, the radial displacement of the surrounding rocks is given by:

$$S_r=\frac{r}{R}\left(1-\frac{r}{R}\right)\left(\frac{1.206K^2}{R}-\frac{1.785K^2}{R}\frac{r}{R}\right) \tag{25}$$

According to the cusp catastrophe theory and the established model, combining Equation 25 for radial displacement of surrounding rock, the potential function of the surrounding rocks after grouting reinforcement is:

$$\Pi=U_1+U_2-W_1-W_2 \tag{26}$$

where $U_1$ represents the bending deformation potential energy of the surrounding rocks after grouting reinforcement, $U_2$ denotes the surface strain potential energy, $W_1$ is the axial work done by external loads, and $W_2$ represents the radial work done by external loads, respectively.

Based on elastic mechanics and the constructed model, it follows that:

$$\begin{cases} U_1=\frac{K}{2}\int_0^{2\pi}d\theta\int_0^R\left[\left(\frac{d^2K}{dr^2}\right)^2+\frac{1}{r^2}\left(\frac{dK}{dr}\right)^2\right]rdr \\ U_2=\frac{Ed}{2(1-\mu^2)}\int_0^{2\pi}d\theta\int_0^R\left\{\left[\left(\frac{dS_r}{dr}\right)+\frac{1}{2}\left(\frac{dw}{dr}\right)^2\right]^2+\frac{S_r^2}{r^2}+2\mu\frac{S_r}{r}\left[\left(\frac{dS_r}{dr}\right)+\frac{1}{2}\left(\frac{dK}{dr}\right)^2\right]\right\}rdr \\ W_1=\iint Qw(x,y)dxdy \\ W_2=\iint QS_rrd\theta dw \end{cases} \tag{27}$$

By combining Equations 26, 27 and performing term transposition, the potential function of the surrounding rocks is obtained as:

$$\prod=\frac{0.603\pi Ed}{(1-\mu^2)}\left(\frac{1}{a^2}+\frac{1}{b^2}\right)w^4+0.042Q\pi w^3+\frac{4\pi Eh^3}{9(1-\mu^2)}\left(\frac{1}{a^2}+\frac{1}{b^2}\right)w^2-\frac{abq\pi}{2}w \tag{28}$$

### 4.3.3 Control standard for grouting reinforcement

Let

$$\begin{cases} w=x+\frac{0.042Q\pi}{4\left(\frac{1}{a^2}+\frac{1}{b^2}\right)}\frac{1-\mu^2}{0.603\pi Ed} \\ A=\frac{4h}{0.603}-\frac{3}{8}\left(\frac{0.042Q\pi}{\frac{0.603\pi Ed}{(1-\mu^2)}\left(\frac{1}{a^2}+\frac{1}{b^2}\right)}\right)^2 \\ B=-\frac{abq\pi}{\frac{0.1206\pi Ed}{(1-\mu^2)}\left(\frac{1}{a^2}+\frac{1}{b^2}\right)}-\frac{0.084Qh^3(1-\mu^2)}{0.603^2\left(\frac{1}{a^2}+\frac{1}{b^2}\right)9Ed^3}+\frac{3}{8}\left(\frac{0.042Q\pi}{\frac{0.603\pi Ed}{(1-\mu^2)}\left(\frac{1}{a^2}+\frac{1}{b^2}\right)}\right)^2 \end{cases}$$

Then Equation 28 can be rewritten as,

$$\Pi(x)=\frac{1}{4}x^4+\frac{1}{2}Ax^2+Bx \tag{29}$$

Equation 29 represents the standard form of cusp catastrophe, which aligns with Equation 12. When its bifurcation set satisfies $\Delta>0$, the terms of $w$, $A$, and $B$ are substituted into Equation 20, and considering $Q=P_1+P_r'-P_w'$. The elastic modulus E of the surrounding rocks after grouting reinforcement is then determined, as expressed in Equation 30, which serves as the grouting

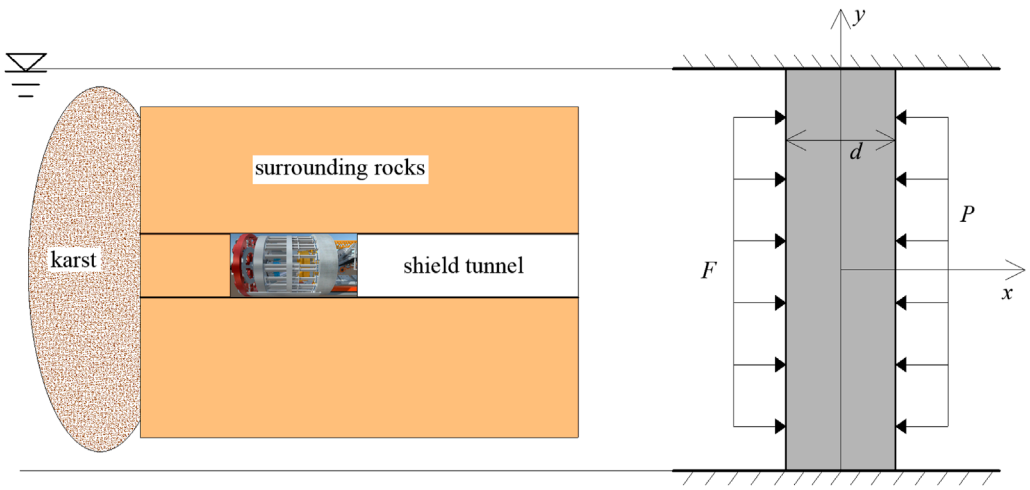


FIGURE 7
Mechanical model of underwater karst located in front of the shield tunnel.

reinforcement standard when the underwater karst is located beneath the shield tunnel.

$$E > \frac{1-\mu^2}{d^2}\sqrt{\frac{0.33\left(P_1 + P_r' - P_w'\right)}{67\left(\frac{1}{a^2}+\frac{1}{b^2}\right)}} \tag{30}$$

According to Equation 30, the control standard for grouting reinforcement depends on factors such as the karst distance, properties of the surrounding rocks after reinforcement, material performance following karst reinforcement, karst size, and the influence of groundwater.

## 4.4 Karst in front of the tunnel

When the underwater karst is positioned in front of the shield tunnel, the grouting-reinforced structure between the karst and the tunnel is subjected to external loads, leading to horizontal displacement of the surrounding rocks during the shield tunneling process. If this horizontal displacement exceeds a critical threshold, instability occurs in the surrounding rocks. Therefore, the grouting reinforcement standard is established to ensure that the horizontal displacement of the surrounding rocks during shield tunneling remains below the instability threshold.

### 4.4.1 Basic assumptions and model establishment

Based on actual site conditions, let $d$ represent the safe distance between the karst and the shield tunnel, $r$ denote the tunnel radius, $E$ be the elastic modulus of the formation after grouting reinforcement, $P$ indicate the horizontal load exerted by the karst on the tunnel face, and $F$ represent the shield support force. The following assumptions are considered: the formation remains intact after grouting reinforcement, and the karst is positioned directly in front of the tunnel axis. Horizontal loads act uniformly on the tunnel face.

Based on these assumptions, the mechanical model illustrated in Figure 7 can be established.

### 4.4.2 Calculation of the surrounding rock potential function

According to the cusp catastrophe theory and the mechanical model in Figure 7, the potential function of the tunnel face after grouting reinforcement is expressed as:

$$\Pi = U_1 + U_2 - W_1 - W_2 \tag{31}$$

where $U_1$ and $U_2$ represent the bending deformation potential energy and surface strain potential energy of the tunnel face after grouting reinforcement, respectively, and $W_1$ and $W_2$ are the axial and radial work done by external loads, respectively.

According to elastic mechanics and the constructed model, the terms in Equation 31 can be expressed as:

$$\begin{cases} U_1 = \frac{\pi E d^3}{12(1-\mu^2)}\int_0^r\left[\left(\frac{d^2u_x}{dy^2}\right)^2 + \frac{1}{y^2}\left(\frac{du_x}{dy}\right)^2\right]ydy \\ U_2 = \frac{\pi E d}{(1-\mu^2)}\int_0^r\left\{\left[\left(\frac{du_y}{dy}\right) + \frac{1}{2}\left(\frac{du_x}{dy}\right)^2\right]^2 + \frac{u_y^2}{y^2} + 2\mu\frac{u_y}{y}\left[\left(\frac{du_y}{dy}\right) + \frac{1}{2}\left(\frac{du_x}{dy}\right)^2\right]\right\}ydy \\ W_1 = \int_0^r\int_0^{2\pi}(P-F)u_x y d\theta dy \\ W_2 = \iint(P-F)u_x y d\theta du_x \end{cases} \tag{32}$$

where $u_x$ and $u_y$ represent the axial and radial displacements of the tunnel face in the grouting-reinforced structure, and $\mu$ is Poisson's ratio of the grouting-reinforced structure.

Based on elastic mechanics and the mechanical model in Figure 7, the following expression holds:

$$\begin{cases} u_x = K\left(1-\frac{y^2}{r^2}\right)^2 \\ u_y = \frac{K^2}{r^2}\left(1.206 - \frac{1.785y}{r}\right)\left(1-\frac{y}{r}\right)y \end{cases} \tag{33}$$

By combining Equations 32, 33 and performing term transposition, the potential function of the surrounding rocks is obtained as:

$$\prod = \frac{0.216\pi Ed}{\left(1-\mu^2\right)r^2}K^4 + 0.042(F-P)\pi K^3 + \frac{8\pi Eh^3}{9r\left(1-\mu^2\right)}K^2 - \frac{(F-P)a^2\pi}{3}K \quad (34)$$

### 4.4.3 Control standard for grouting reinforcement

Let

$$\begin{cases} A = -3\left(\dfrac{0.046\left(1-\mu^2\right)r^2(F-P)}{Eh}\right)^2 + 2.058h^2 \\ B = -2\left(\dfrac{0.046\left(1-\mu^2\right)r^2(F-P)}{Eh}\right)^3 \\ \quad -\left(8.33r^2 + 2.058h^2\right)\dfrac{0.046\left(1-\mu^2\right)r^2(F-P)}{Eh} \end{cases} \quad (35)$$

Then Equation 34 can be rewritten as:

$$\Pi(x) = \frac{1}{4}x^4 + \frac{1}{2}Ax^2 + Bx \quad (36)$$

Equation 36 represents the standard form of cusp catastrophe, which is consistent with Equation 12. When the bifurcation set satisfies $\Delta > 0$, substituting Equation 35 into Equation 20 again yields the elastic modulus E of the surrounding rocks after grouting reinforcement. This defines the grouting reinforcement standard when the underwater karst is positioned in front of the shield tunnel, as expressed in Equation 37.

$$E > (0.2357r)^2\frac{\left(1-\mu^2\right)(F-P)}{d^2} \quad (37)$$

According to Equation 37, the control standard for grouting reinforcement depends on factors such as the karst distance, the performance of the reinforced surrounding rocks, the support force of the shield machine, the material properties following karst reinforcement, and the karst size.

## 5 Conclusion and outlook

Targeting grouting projects in underwater karst shield tunnels, this study examines the instability mechanism of the surrounding rocks. A mechanical model for analyzing the grouting reinforcement range in underwater karst shield tunnels is developed based on strength theory, clarifying the reinforcement range as the karst location varies relative to the tunnel. Subsequently, grouting reinforcement control standards for different scenarios are determined using the cusp catastrophe theory. The main research conclusions are as follows:

(1) Considering the stress state variations in the surrounding rocks induced by shield tunneling, the primary causes of instability in underwater karst shield tunnels are summarized. During shield tunneling, a sudden reduction in the thickness of the surrounding rocks alters their initial constraints and boundary conditions, disrupting the original stress equilibrium and leading to stress redistribution. These changes influence the water content state and disturb the surrounding rock and soil mass, resulting in significant excavation.

(2) Based on the theory of karst grouting surrounding rock failure, a cantilever beam and plate analysis model was set for the surrounding rock between karst and tunnel. The grouting reinforcement range of underwater karst shield tunnel was determined to be mainly related to factors such as karst size, karst filling material performance, tunnel span, load on the surrounding rock between the two, surrounding rock performance, and the relative position between the karst and the tunnel.

(3) By establishing a sudden change model for the instability of surrounding rock, a calculation formula for grouting reinforcement to ensure that the surrounding rock remains stable after solidification is proposed. The control standards for grouting reinforcement of underwater karst shield tunnels are clarified to be related to karst distance, rock performance after reinforcement, shield machine support force, material properties after karst reinforcement, and karst size.

## Data availability statement

The original contributions presented in the study are included in the article/supplementary material, further inquiries can be directed to the corresponding author.

## Author contributions

PX: Conceptualization, Writing – review and editing, Validation, Methodology. XS: Formal Analysis, Investigation, Data curation, Software, Writing – review and editing. LC: Formal Analysis, Funding acquisition, Methodology, Writing – original draft. HS: Methodology, Writing – review and editing, Formal Analysis.

## Funding

The author(s) declare that financial support was received for the research and/or publication of this article. This work was supported by the Scientific Research Project of Hunan Education Department (23B1009).

## Conflict of interest

Author PX was employed by CCCC South China Construction and Development Co., Ltd. Authors XS and HS were employed by CCCC Second Harbor Engineering Company Ltd.

The remaining author declares that the research was conducted in the absence of any commercial or financial relationships that could be construed as a potential conflict of interest.

## Generative AI statement

The author(s) declare that no Generative AI was used in the creation of this manuscript.

## Publisher's note



## References

Alija, S., Torrijo, F., and Quinta-Ferreira, M. (2013). Geological engineering problems associated with tunnel construction in karst rock masses: the case of Gavarres tunnel (Spain). *Eng. Geol.* 157, 103–111. doi:10.1016/j.enggeo.2013.02.010

Carpinteri, A. (2017). *Structural mechanics[M]*. Oxfordshire: Taylor & Francis, 12–21. doi:10.1201/9781315274454

Chen, K., Ren, S., Li, Z., Chen, Z., Yu, B., and Zhang, H. (2024). Investigation on the seepage-stress field evolution mechanism and failure process of karst tunnels in water-rich areas. *Environ. Earth Sci.* 83 (22), 638. doi:10.1007/S12665-024-11951-1

Chen, X. (2002). *Research on instability and criteria of tunnel structures*. Chengdu: Southwest Jiaotong University.

Cui, D., and Wang, Q. (2008). Exploration of shield tunneling construction technology in karst cave strata. *Constr. Technol.* (09), 51–53+57.

Fu, H., Di, W., Yuan, F., and Min, Z. (2020). Prediction of the collapse region induced by a concealed karst cave above a deep highway tunnel. *Adv. Civ. Eng.* 2020. doi:10.1155/2020/8825262

Huang, F., Zhao, L., Ling, T., and Yang, X. (2017). Rock mass collapse mechanism of concealed karst cave beneath deep tunnel. *Int. J. Rock Mech. Min. Sci.* 91, 133–138. doi:10.1016/j.ijrmms.2016.11.017

Jiang, D., Ren, S., Liu, X., and Liu, B. (2005). Theoretical analysis of sudden changes in stability of rock salt cavern roof [J]. *Rock Soil Mech.* 26 (7), 1099–1103. doi:10.16285/j.rsm.2005.07.019

Lan, X., Zhang, X., Yin, Z., Li, X., and Yang, T. (2021). Mitigation of karst tunnel water inrush during operation in seasonal variation zone: case study in nanshibi tunnel. *J. Perform. Constr. Facil.* 35 (3). doi:10.1061/(ASCE)CF.1943-5509.0001573

Li, L., Tu, W., Shi, S., Chen, J., and Zhang, Y. (2016). Mechanism of water inrush in tunnel construction in karst area. *Geomatics, Nat. Hazards Risk* 7 (Suppl. 1), 35–46. doi:10.1080/19475705.2016.1181342

Li, W., Wang, W., Li, J., and Ouyang, M. (2020). Application of TETSP in advance prediction of water and mud inrush in karst tunnel. *IOP Conf. Ser. Earth Environ. Sci.* 617 (1), 012008. doi:10.1088/1755-1315/617/1/012008

Liao, Y., Deng, T., Zhang, W., Zhang, C., and Xu, Z. (2022). Research on the stability and support of surrounding rock in tunnel excavation based on the sharp point mutation theory [J]. *Nonferrous Met. Eng.* 12 (04), 116–123. doi:10.3969/j.issn.2095-1744.2022.04.017

Liu, D., Liu, M., Sun, H., Liu, R., and Lu, X. (2024). Detection and comprehensive treatment for giant karst caves under the tunnel floor: a case study in Guangxi, China. *Environ. Earth Sci.* 83 (23), 650. doi:10.1007/S12665-024-11959-7

Liu, G., Peng, Y., Wu, L., Cheng, Y., Dong, D., Jia, L., et al. (2024). Stability prediction of surrounding rock in tunnel crossing fault zone based on cusp catastrophe theory. *KSCE J. Civ. Eng.* 28 (9), 4146–4157. doi:10.1007/S12205-024-2478-1

Ma, F. (2018). Analysis of several key technologies for shield tunnels crossing the development zone of river bottom karst caves. *Railw. Stand. Des.* 62 (01), 93–98. doi:10.13238/j.issn.1004-2954.201703180004

Ou, X., Ouyang, L., Zheng, X., and Zhang, X. (2024). Hydrogeological analysis and remediation strategies for water inrush hazards in highway karst tunnels. *Tunn. Undergr. Space Technol. incorporating Trenchless Technol. Res.* 152, 105929. doi:10.1016/J.TUST.2024.105929

Rees, D. (2018). *Mechanics of elastic solids[M]*. World Scientific Publishing Company.

Shunying, J., Yue, M., and Dzianis, M. (2024). *Mechanics of materials[M]*. Paris: EDP Sciences, 153–171. doi:10.1051/978-2-7598-3200-2

Su, M., Liu, Y., Xue, Y., Cheng, K., Ning, Z., Li, G., et al. (2021). Detection method of karst features around tunnel construction by multi-resistivity data-fusion pseudo-3D-imaging based on the PCA approach. *Eng. Geol.* 288, 106127–127. doi:10.1016/J.ENGGEO.2021.106127

Su, X., Lai, J., Ma, E., Xu, J., Qiu, J., and Wang, W. (2025). Failure mechanism analysis and treatment of tunnels built in karst fissure strata: a case study. *Eng. Fail. Anal.* 167 (PB), 109048. doi:10.1016/J.ENGFAILANAL.2024.109048

Xu, C. (2024). *Nonlinear theory research and application of rock mass failure*. Nanjing: Hohai University.

Yang, J., Zhang, C., Fu, J., Wang, S., Ou, X., and Xie, Y. (2020). Pre-grouting reinforcement of underwater karst area for shield tunneling passing through Xiangjiang River in Changsha, China. *Tunn. Undergr. Space Technol.* 100, 103380. doi:10.1016/j.tust.2020.103380

Yang, X., Li, Z., Liu, Z., and Xiao, H. (2017). Collapse analysis of tunnel floor in karst area based on Hoek-Brown rock media. *J. Central South Univ.* 24 (4), 957–966. doi:10.1007/s11771-017-3498-5

Zhang, C., Fu, J., Yang, J., Ou, X., Ye, X., and Zhang, Y. (2018). Formulation and performance of grouting materials for underwater shield tunnel construction in karst ground. *Constr. Build. Mater.* 187, 327–338. doi:10.1016/j.conbuildmat.2018.07.054

Zhao, R., Zhang, L., Hu, A., Kai, S., and Fan, C. (2024). Risk assessment of karst water inrush in tunnel engineering based on improved game theory and uncertainty measure theory. *Sci. Rep.* 14 (1), 20284. doi:10.1038/S41598-024-71214-8

Zou, Y., Tang, Q., and Peng, L. (2025). Stability analysis and instability time prediction of tunnel roofs in a karst region based on catastrophe theory. *Appl. Sci.* 15 (2), 978. doi:10.3390/APP15020978

frontiers | Frontiers in Earth Science

TYPE Original Research
PUBLISHED 15 July 2025
DOI 10.3389/feart.2025.1620850



OPEN ACCESS

EDITED BY
Pengfei Liu,
CCCC Second Harbor Engineering Co., Ltd., China

REVIEWED BY
Fengyuan Wu,
Shenyang Jianzhu University, China
Luobin Zheng,
Wuhan University of Science and Technology, China

*CORRESPONDENCE
Jianyong Han,
hanlwb@163.com

RECEIVED 30 April 2025
ACCEPTED 30 June 2025
PUBLISHED 15 July 2025

CITATION
Wu J, Han J, Luo Y, Song H, Li H and Dong X (2025) Performance of anticorrosive coatings for photovoltaic PHC pipe piles in brine environments of saline-alkali tidal flats. *Front. Earth Sci.* 13:1620850. doi: 10.3389/feart.2025.1620850



# Performance of anticorrosive coatings for photovoltaic PHC pipe piles in brine environments of saline-alkali tidal flats

Jianxin Wu[1], Jianyong Han[2,3]*, Yong Luo[1], Hongzhu Song[1], Hai Li[2] and Xiaobin Dong[4]

[1]Shandong Electric Power Engineering Consulting Institute Corp., Ltd., Jinan, Shandong, China, [2]School of Civil Engineering, Shandong Jianzhu University, Jinan, Shandong, China, [3]Key Laboratory of Building Structural Retrofitting and Underground Space Engineering (Shandong Jianzhu University), Ministry of Education, Jinan, Shandong, China, [4]Shandong Binhai Energy Co., Ltd., Weifang, Shandong, China

This study was conducted on an integrated wind-solar-storage-transmission base project located in a saline-alkali tidal flat area. The brine formation mechanism in saline-alkali tidal flats was revealed, and the chemical composition of the brine was comprehensively characterized by on-site tests. The mechanisms and causes of corrosion of PHC pipe piles under brine exposure were revealed. Field tests of the surface morphology and thickness changes for four types of anticorrosion coatings applied to PHC pipe piles were conducted to determine the protective performance of each anticorrosion coating. The results show that PHC pipe pile corrosion in the brine environment of saline-alkali tidal flats is primarily driven by hydrogen ion erosion. After nearly 1 year of *in situ* corrosion testing, the surfaces of ZB, ZH, TD-D (double-sided application), and LC exhibited oxidation and darkening in color, with coating thickness reductions ranging from 0 to approximately 0.35 mm; however, the coatings remained largely intact. For the TD-S specimens (single-sided application), the coated surface darkened, whereas the uncoated surface experienced severe corrosion, with a thickness reduction of approximately 1.8 mm, accompanied by mortar spalling and coarse aggregate exposure. All four anticorrosive coatings demonstrated favorable protective performances. A comprehensive evaluation model was employed to grade and score the coatings based on three performance indicators, which revealed that the TD anticorrosive coating exhibited the best overall performance. This study provides essential scientific evidence and technical support for the durability design and protective measures of concrete structures under aggressive environmental conditions.

KEYWORDS

**saline-alkali tidal flats, salt-lake brine environment, PHC pipe piles, corrosion mechanism, photovoltaic power generation, anticorrosive coatings**

## 1 Introduction

In recent years, photovoltaic (PV) power generation, an important form of renewable energy, has rapidly developed globally, becoming a key driver for energy transition

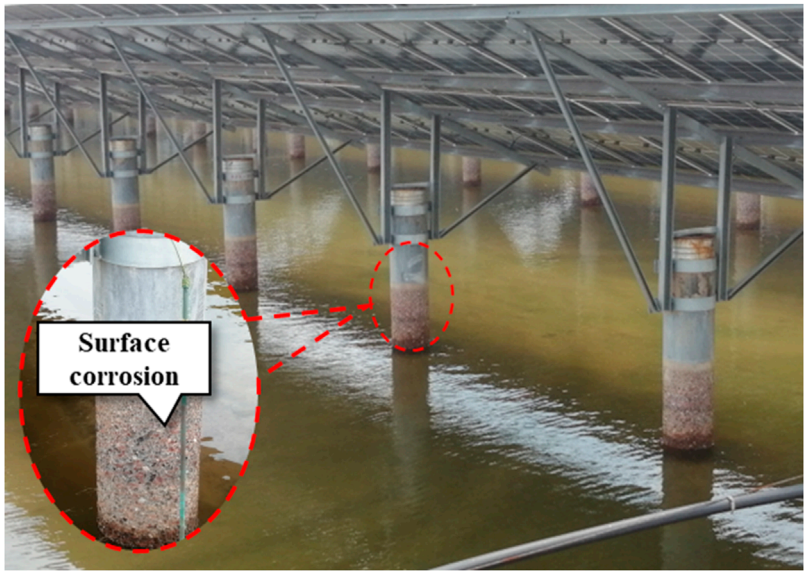


FIGURE 1
Corrosion condition of photovoltaic PHC pipe pile foundations.

and green low-carbon development. With the continuous expansion of the scale of PV projects, the application of traditional PHC pipe piles in PV foundations has become increasingly widespread, particularly in coastal seawater environments (Wang et al., 2022). In such environments, the primary factors contributing to pile corrosion are chloride and sulfate ions. However, compared with conventional seawater, brine contains much higher concentrations of corrosive substances, such as chloride and sulfate ions. These aggressive ions significantly accelerate the carbonation of the concrete surface and the corrosion of the internal steel reinforcement, resulting in a decline in the structural strength and a substantial reduction in the durability of the pipe piles. Moreover, the high permeability and electrical conductivity of brine further exacerbate the electrochemical corrosion process, rendering PHC pipe piles highly susceptible to cracking, spalling, and even fracturing during long-term service (Tian H. et al., 2023), as illustrated in Figure 1. Therefore, the corrosion of PHC pipe piles in brine environments poses a serious threat to engineering safety and significantly shortens their service life, necessitating the implementation of effective protective measures (Wang et al., 2024). Although heavy-duty anticorrosion systems developed for traditional marine engineering applications can technically address these issues, photovoltaic power generation projects differ in their structure anticorrosion. PV power generation projects are highly cost-sensitive, making such high-cost solutions impractical. Consequently, it is necessary to develop low-cost, yet highly durable, anticorrosion strategies for PHC pipe piles in brine-rich environments.

Currently, studies on the corrosion behavior of reinforced concrete have primarily focused on marine environmental conditions, with systematic investigations conducted on corrosion mechanisms, material degradation processes, and protective measures. Qian et al. (2023a) investigated the corrosion behavior of reinforced concrete beams exposed to a marine atmospheric environment for 7 years and analyzed the chloride distribution, carbonation, and corrosion products. The results indicated two distinct chloride accumulation zones located near the carbonation depth and at the boundary region, corresponding to an increasing corrosion depth. Wang and Zhang (2018) simulated harsh marine conditions through a combined "UV exposure + cyclic immersion" accelerated test to study the aging behavior of organic coatings. The experimental results revealed that, under the combined effects of ultraviolet radiation and water immersion, significant changes occurred in the coating thickness, gloss, and surface morphology. Chen et al. (2022) examined the structural performance of reinforced concrete columns in marine environments and proposed material degradation and structural strength reduction models based on the damage mechanisms induced by reinforcement corrosion. This study also estimated the service life of the corroded reinforced concrete columns under various corrosive conditions.

The aforementioned studies focused primarily on the corrosion and protection of reinforced concrete in marine environments. However, brine environments differ significantly from typical marine conditions. After bromine extraction, the brine exhibited much higher concentrations of hydrogen, chloride, and sulfate ions than conventional seawater. Zhao et al. (2018) investigated the effect of ion erosion in brine environments on the HPC strength and observed that the incorporation of mineral admixtures significantly improved the corrosion resistance of concrete. Sulfate ion erosion was identified as the main cause of concrete damage and compressive strength reduction, whereas chloride ions helped slow the progression of the sulfate attack. Tian H. et al. (2023) studied the corrosion characteristics of reinforced concrete in saline soil environments using electrochemical tests, chloride concentration measurements, and damage assessments. The results showed that the deterioration of reinforced concrete increased nonlinearly over time. Li Z. et al. (2024) explored the influence

of temperature and water–cement ratio on the corrosion of reinforcements in high-salinity lake water environments. The findings indicated that, although temperature and salinity had limited effects on the corrosion potential, the initiation of corrosion in saline lake water was much faster than that in marine environments, with the corrosion rates accelerating as the temperature and water–cement ratio increased. Currently, studies on the performance of anticorrosive coatings largely rely on laboratory simulation tests, whereas field-based studies remain limited. This limitation may reduce the applicability of the test results in real-world scenarios, particularly in complex natural environments, where the long-term protective performance of coatings is difficult to evaluate accurately.

Therefore, based on an integrated wind-solar-storage-transmission base project in saline-alkali tidal flats, the corrosion mechanism of PHC pipe pile foundations under brine exposure was investigated. Four anticorrosive coating systems were selected for comparison through the field testing of the surface morphology and thickness variation. Furthermore, a comprehensive evaluation of the durability and cost-effectiveness of the coatings was conducted using an analytic hierarchy process (AHP), leading to the recommendation of a high-cost anticorrosion solution.

## 2 Corrosion mechanism of PV PHC pipe pile foundations in brine environments

### 2.1 Brine composition analysis

Based on the typical technological process of halogen production, the procedure can generally be divided into the following key functional zones:

(1) Water Intake Zone: This area is responsible for introducing raw brine or salt lake water. The water composition is complex, with relatively low salinity but a wide range of corrosive agents, making it a source of initial corrosion.
(2) Standard Brine Evaporation Zone: Comprising a series of solar ponds and evaporation basins, this zone facilitates brine concentration. The environment here is relatively stable in terms of water fluctuation, but the gradually increasing salinity leads to long-term corrosive effects.
(3) Concentration and Crystallization Zone: At this stage, the brine approaches saturation or even undergoes crystallization. Besides the extreme salt concentration, the formation of salt crystals on concrete or reinforcement surfaces may induce crystallization pressure and pore blockage, triggering stress corrosion and the development of microcracks.
(4) Drainage Outlet Zone: This is the outlet for brine circulation or discharge. Characterized by high flow velocity, strong hydrodynamic impact, and frequent wet–dry cycles, this zone also exhibits high salinity, elevated dissolved oxygen content, and significant temperature fluctuations.

Field investigations (see Figure 1) indicate that the drainage outlet zone is the most severely corroded area, where surface concrete spalling and propagation of microcracks in PHC piles are commonly observed. Therefore, this study selects the drainage outlet zone as the representative condition for corrosion testing and performance evaluation of protective coatings, providing guidance for optimizing protection strategies in high-risk corrosion environments.

The brine in saline-alkali tidal flat areas is rich in various salts. To analyze the salt components in the brine, ion chromatography was employed to determine the concentrations of major ions, such as $Na^+$, $Ca^{2+}$, $Mg^{2+}$, $Cl^-$, and $SO_4^{2-}$ (Wang, 2024) (see Table 1). According to the Code for Investigation of Geotechnical Engineering (GB 50021-2001) (Ministry of Construction of the People's Republic of China, 2002), the environmental conditions of the site fall under the Type II classification. The site investigation results indicated that brine poses a strong corrosive threat to both the concrete structure and the embedded reinforcement. The evaluation of the corrosiveness of brine for construction materials is summarized in Table 1, and the main salt contents and corresponding corrosion grades are shown in Figure 2. The representative site conditions are shown in Figure 3.

The brine corrosion environment in saline-alkali tidal flats is similar to that of marine environments but is characterized by higher salinity and stronger corrosiveness. Based on the exposure conditions of PHC pipe piles to brine environments, the brine corrosion environment in saline-alkali tidal flats can be divided into four zones: atmospheric zone, tidal zone, immersion zone, and brine mud zone (Li Y. et al., 2024) (see Figure 4). The tidal zone refers to the transitional area where, due to periodic water level fluctuations, the surface of the test specimens is repeatedly exposed to both air and liquid. According to field observations, the tidal zone in the brine pond is primarily influenced by artificial water level regulation and wind-induced disturbances, with a typical daily fluctuation range of approximately 20–30 cm. To ensure that the specimens are located within this zone, the top of the cylindrical specimens were positioned above the highest tidal level, while the square specimens were placed near the water surface. Based on the actual operational water level records of the brine pond, the location of the tidal range zone was reasonably determined, ensuring that the zone can accurately reflect the corrosion characteristics under alternating wetting and drying conditions. Each zone exhibits a distinct corrosion mechanism. The characteristics of the corrosive environment and corrosion in each zone are summarized in Table 2.

The atmospheric zone is located above the tidal zone. As the brine evaporates, a large quantity of salt particles enters the air, forming a salt spray. Simultaneously, water vapor condenses on the surface of the PHC pipe piles, forming a water film in which salt particles dissolve, creating a strong electrolyte solution. This solution penetrates the interior of PHC piles through capillary action and diffusion, resulting in salt-spray corrosion. In addition, acidic gases, such as $CO_2$ and $SO_2$, in the atmosphere can infiltrate concrete through pores and react with alkaline components inside the PHC pipe piles, leading to carbonation reactions (Qian et al., 2023b).

The tidal zone lies above and below the immersion and atmospheric zones. In this region, PHC pipe piles undergo alternating wetting and drying cycles. Chloride ions and other salts on the concrete surface can penetrate piles through capillary adsorption, diffusion, and permeation mechanisms (Zhang et al., 2018). During high tide, the dry concrete surface comes into contact with the brine and absorbs it through capillary action until saturation is reached. During low tide, as moisture evaporates from

TABLE 1 Evaluation of the corrosiveness of brine from a typical brine pond to construction materials.

| Evaluation target | Environment type | Corrosive medium | Evaluation criteria | Measured concentration | Corrosion rating |
|---|---|---|---|---|---|
| Concrete Structure | Type II | $SO_4^{2-}$ (mg/L) (wet-dry cycles) | Severe: >3000 | 9521–34720 | Severe corrosion |
| | | $Mg^{2+}$ (mg/L) | Severe: >4000 | 5000–30747 | Severe corrosion |
| | A | pH Value | Severe: <4 | 1.85–7.07 | — |
| Steel Reinforcement in Reinforced Concrete | Wet-dry cycles | $Cl^-$ (mg/L) | Severe: >5000 | 4900–18000 | Severe corrosion |
| | Long-term immersion | $Cl^-$ (mg/L) | Severe: >20,000 | 4900–18000 | — |

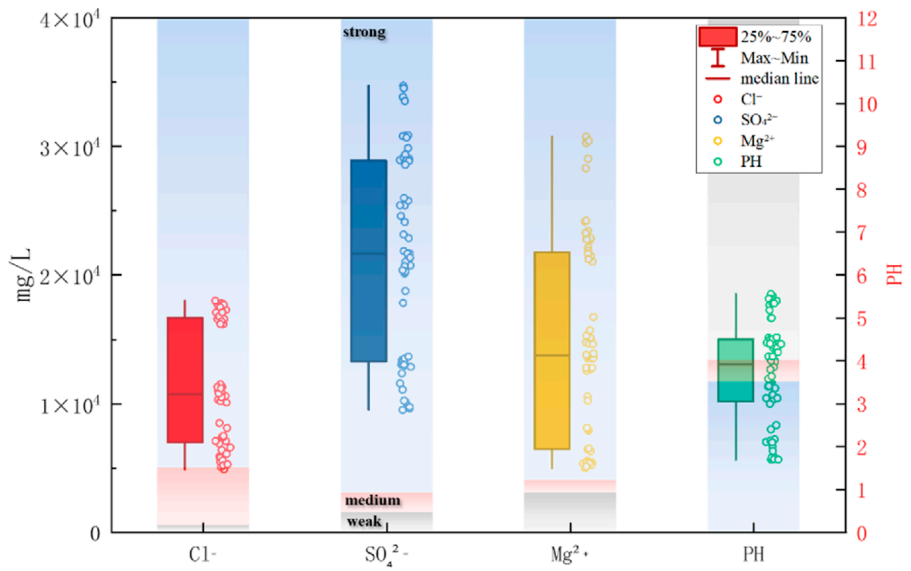


FIGURE 2
Variations in major salt content in brine from a typical brine pond.

the concrete surface, the concentration of salts in the pore solution increases, resulting in a chloride ion concentration gradient between the surface and the interior. This drives the diffusion of salts from the surface pore solution into the interior of the concrete (Qiao et al., 2017), eventually reaching the reinforcing steel and initiating electrochemical reactions that accelerate corrosion.

The immersion and brine mud zones are located below the brine level, where the concentrations of chloride and sulfate ions are high. However, owing to the limited availability of oxygen in water, the corrosion rate of the reinforcing steel in these zones is relatively slow.

## 2.2 Corrosion mechanism of PV PHC pipe pile foundations

### 2.2.1 Chloride-induced corrosion mechanism

The pH of concrete is approximately 12.5. In such a strongly alkaline environment, a dense passive film forms on the surface of the embedded reinforcement (Wu et al., 2022), which is the fundamental reason why the steel in reinforced concrete structures does not corrode under normal conditions.

In a saline-alkali tidal flat environment, brine contains a high concentration of chlorides, and the corrosion of PHC pipe piles is driven by chloride ion intrusion and electrochemical reactions (Tian Y. et al., 2023; Xu et al., 2024). Chloride ions penetrate the interior of PHC piles through mechanisms, such as capillary suction, diffusion, permeation, and electrochemical migration. The typical diffusion coefficient of concrete ranges from $1 \times 10^{-12}$ $m^2/s$ to $1 \times 10^{-10}$ $m^2/s$, with penetration depths usually between 10 mm and 50 mm. The chloride ions gradually accumulate on the reinforcement surface. As the chloride ion concentration increases, the local pH decreases. When the pH falls below 9.8, the passive film on the steel surface begins to deteriorate, exposing the reinforcement to the corrosive environment and leading to pitting or localized corrosion. The corroded regions of the reinforcement become anodic areas where oxidation reactions occur, whereas the regions still protected by the passive film act as cathodic areas where

FIGURE 3
Field measurement photograph of a typical brine pond.

reduction reactions occur, as shown in Equations 1–3:

$$\textit{anodic region}: 2Fe \rightarrow 2Fe^{2+} + 4e^{-} \quad (1)$$

$$\textit{cathodic region}: O_2 + 2H_2O + 4e^{-} \rightarrow 4OH^{-} \quad (2)$$

$$\textit{overall reaction}: 2Fe + 2H_2O + O_2 \rightarrow Fe(OH)_2 \quad (3)$$

The $Fe^{2+}$ ions generated in the anodic region react with $Cl^{-}$ to form water-soluble $FeCl_2$, which subsequently diffuses into the surrounding solution. There, it reacts with $OH^{-}$ and $O_2$ to form $Fe(OH)_2$, accompanied by the generation of $H^{+}$ ions. Throughout this process, $Cl^{-}$ is not consumed and functions essentially as a catalyst. Chloride ions not only participate in the formation of corrosion cells, but also accelerate the electrochemical reaction rate (Zuquan et al., 2018). This phenomenon is commonly referred to as anodic depolarization. The corresponding electrochemical reactions are shown in Equations 4, 5:

$$Fe^{2+} + 2Cl^{-} + 4H_2O \rightarrow FeCl_2 \cdot 4H_2O \quad (4)$$

$$FeCl_2 \cdot 4H_2O \rightarrow Fe(OH)_2 + 2Cl^{-} + 2H^{+} + 2H_2O \quad (5)$$

Meanwhile, $Fe(OH)_2$ can be further oxidized to form $Fe(OH)_3$ and $Fe_3O_4$.

### 2.2.2 Sulfate-induced corrosion mechanism

In brine environments, in addition to chloride ions, sulfate ions significantly contribute to the corrosion of PHC pipe piles. When external sulfate ions penetrate into the interior of the PHC pile, they react with calcium hydroxide ($Ca(OH)_2$) and calcium aluminate hydrate ($4CaO{\cdot}Al_2O_3{\cdot}19H_2O$) in the concrete, producing gypsum ($CaSO_4{\cdot}2H_2O$) and ettringite ($3CaO{\cdot}Al_2O_3{\cdot}3CaSO_4{\cdot}32H_2O$). As the corrosion products—gypsum and ettringite—have much larger volumes than the original reactants, expansive internal stresses develop within the concrete, leading to cracking and a reduction in compressive strength (Zhang et al., 2024). The chemical reactions are shown in Equations 6, 7:

$$Ca(OH)_2 + Na_2SO_4 \cdot 10H_2O \rightarrow CaSO_4 \cdot 2H_2O + 2NaOH + 8H_2O \quad (6)$$

$$4CaO \cdot Al_2O_3 \cdot 19H_2O + 3(CaSO_4 \cdot 2H_2O) + 8H_2O \rightarrow 3CaO \cdot Al_2O_3 \cdot 3CaSO_4 \cdot 32H_2O + Ca(OH)_2 \quad (7)$$

### 2.2.3 Corrosion mechanism in acidic environments

Bromine extraction in brine ponds generates numerous hydrogen ions, significantly lowering the pH of the brine. Hydrogen ions infiltrate the interior of the PHC pipe piles and react with hydroxide ions ($OH^{-}$), reducing the $OH^{-}$ concentration in the concrete, which lowers the pH and disrupts the alkaline environment required to stabilize various cement hydration products. When the pH drops below 10.4, these hydration products begin to decompose or the hydrogen ions directly react with the alkaline components of the hydration products. This leads to an increase in the concrete porosity, thereby reducing the strength and impermeability of the PHC pipe piles. Moreover, increased porosity facilitates the ingress of other harmful ions (Madraszewski et al., 2023; Youssari et al., 2023; Peng et al., 2022).

The investigations of the pH of brine and associated corrosion mechanisms indicate that hydrogen-ion-induced corrosion is predominant in the brine environments of saline-alkali tidal flats. Thus, anticorrosive coatings are proposed for application on the surface of PHC pipe piles to reduce the penetration rate of corrosive ions, such as $H^{+}$ and $Cl^{-}$, thereby achieving effective corrosion protection.

## 3 Field corrosion tests

### 3.1 Anticorrosive coating materials

Based on the existing concrete anticorrosion technologies and anticorrosion strategies used in similar brine environments (Vera et al., 2013), four types of coatings were selected: ZB solvent-free modified epoxy liquid coating, ZH acrylic anticorrosive coating, TD high-performance anticorrosive coating, and LC polyurea anticorrosive coating (see Table 3), considering factors, such as energy conservation and environmental protection. Field exposure tests were conducted on samples of these four coatings to establish the relationship between coating performance and natural corrosion conditions. Based on their anticorrosive performances in brine environments, the ultimate goal is to propose a cost-effective anticorrosion solution suitable for large-scale applications.

### 3.2 Experimental scheme

The drainage outlet of a brine pond was selected as the experimental site. After bromine extraction, the pH of the brine in this area was relatively low but gradually increased upon exposure to air.

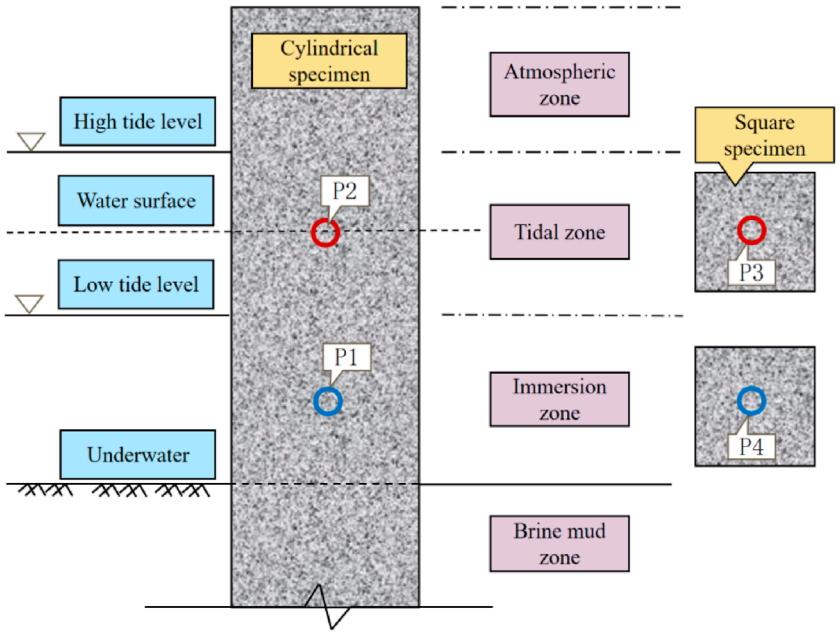


FIGURE 4
Specimen arrangement scheme for saline-alkali tidal flat brine environment.

TABLE 2 Characteristics of brine environments and corrosion in saline-alkali tidal flats.

| Brine environment zone | Environmental characteristics | Corrosion characteristics |
|---|---|---|
| Atmospheric Zone | Solar radiation; air filled with fine salt particles | Salt spray erosion, carbonation |
| Tidal Zone | Periodic immersion; abundant oxygen | Wet-dry cycling, freeze-thaw cycling, chloride/sulfate attack, electrochemical corrosion |
| Immersion Zone | Presence of various corrosive agents; low oxygen | Biological corrosion, chloride/sulfate attack |
| Brine Mud Zone | Presence of anaerobic microorganisms | Anaerobic microbial corrosion |

TABLE 3 Types and characteristics of anticorrosive coatings.

| Name | Composition | Characteristics |
|---|---|---|
| ZB Solvent-Free Modified Epoxy Liquid Coating | Compounds formed by the reaction of reactive solvents and epoxy resins | Wear-resistant, highly acid-resistant, weather-resistant, non-toxic, aesthetically pleasing |
| ZH Acrylic Anticorrosive Coating | Composed of Component A and Component B | Corrosion-resistant, environmentally friendly, acid and alkali resistant |
| TD High-Performance Anticorrosive Coating | Composed of epoxy resin, curing agent, and additives | Scratch-resistant, pitting-resistant, acid and alkali resistant, stable performance |
| LC Polyurea Anticorrosive Coating | Compounds formed by the reaction of isocyanate and amine compounds | Temperature-resistant, wear-resistant, non-toxic, corrosion-resistant |

Based on field investigation results (see Figure 1), it was found that the corrosion severity of PHC pipe piles is significantly greater in the tidal and immersion zones compared to the atmospheric and brine mud zones. To enhance the relevance and representativeness of the experiment, this study focused on conducting field exposure tests specifically in the tidal and immersion zones.

In the field test, cylindrical specimens with diameters of 120 mm, 80 mm, and 150 mm were used for ZB solvent-free modified epoxy coating, ZH acrylic anti-corrosion coating, and LC polyurea coating, respectively. These were labeled as P2 and P1 in the tidal and immersion zones. For the TD high-performance anti-corrosion coating, square specimens with a side length of 100 mm

10.3389/feart.2025.1620850

TABLE 4 Detailed information of Specimens of the field corrosion test.

| Specimen ID | Coating scheme | Measurement location | |
|---|---|---|---|
| | | P1 | P2 |
| ZB1 | Solvent-free modified epoxy liquid coating ≥300 μm | ✓ | ✓ |
| ZB2 | Solvent-free modified epoxy liquid coating ≥400 μm | ✓ | ✓ |
| ZB3 | Solvent-free modified epoxy liquid coating ≥500 μm | ✓ | ✓ |
| ZB4 | Solvent-free modified epoxy liquid coating ≥300 μm + weather-resistant 80 μm | ✓ | ✓ |
| ZB5 | Solvent-free modified epoxy liquid coating ≥400 μm + weather-resistant 80 μm | ✓ | ✓ |
| ZB6 | Solvent-free modified epoxy liquid coating ≥500 μm + weather-resistant 80 μm | ✓ | ✓ |
| ZH1 | Acrylic anticorrosive coating 800 μm | ✓ | ✓ |
| ZH2 | Acrylic anticorrosive coating 1,000 μm | ✓ | ✓ |
| ZH3 | Acrylic anticorrosive coating 1,000 μm (reinforced with fabric) | ✓ | ✓ |
| TD1-D | MP series high-performance primer 300 μm (double-sided) | ✓ | |
| TD1-S | One side MP series primer 300 μm + one untreated side | ✓ | |
| TD2-D | MP series high-performance primer 300 μm (double-sided) | | ✓ |
| TD2-S | One side MP series primer 300 μm + one untreated side | | ✓ |
| LC1 | Armored anticorrosive polyurea + LC-301 topcoat | ✓ | ✓ |
| LC2 | Sprayed polyurea LC-1138 + LC-301 topcoat | ✓ | ✓ |

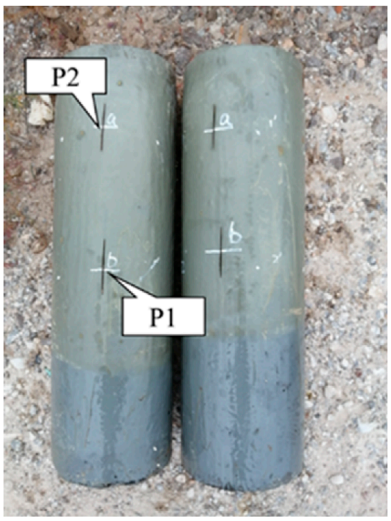


FIGURE 5
Specimen of field test (LC polyurea anticorrosive coating).

were used, with central points labeled as P3 and P4, and similarly placed in the tidal and immersion zones for testing. The specimen layout is illustrated in Figure 4.

The variation in size is mainly due to the fact that all specimens used in the experiment were provided by different anti-corrosion material manufacturers, and differences in mold fabrication led to slight inconsistencies in specimen dimensions. The square specimens were mainly used for the TD high-performance anti-corrosion coating, primarily to allow for separate investigation of different exposure zones. However, due to the larger quantity of test blocks and the inconvenience of storage, square specimens were not used for other coating materials in this study.

Considering that, under the same natural exposure conditions, the variation in corrosion resistance is mainly influenced by the type of coating and construction technique, while the geometric size and shape of the specimens have little effect on corrosion behavior. Thus, the impact of the specimen dimension can be neglected as long as other variables are properly controlled.

To ensure the consistency of the experimental results, the same specimens were used for both the surface morphology and thickness variation tests. The experimental schemes were primarily differentiated based on the coating thickness with the aim of observing the performance of coatings with varying thicknesses under the same environmental conditions. Fifteen series of tests with various anticorrosive coatings and coating schemes were performed, as listed in Table 4.

## 3.3 Corrosion test methods

The durability and anticorrosive performance of the coatings were evaluated by monitoring variations in the surface morphology and thickness under brine exposure in saline-alkali tidal flat environments during corrosion tests. The objective of the field test was to analyze the extent of coating damage after brine immersion and provide a scientific basis for material selection and the optimization of protective measures.

Surface morphology tests were conducted in accordance with the physical performance standards for Film-forming Coatings Specified In Film-forming Coatings For Concrete Structure Protection JG/T 335-2011 (2011). Each coating was uniformly applied to the surface of the concrete specimens and cured for 14 d under the specified conditions. Upon completion of the curing, the initial surface appearance of each specimen was recorded, including the coating smoothness and color uniformity. The specimens were then exposed to a brine environment, and every 120 d, the surface conditions were observed and recorded, focusing on discoloration, cracking, peeling, blistering, and other visual defects.

The thickness variation test was performed following the Pipeline Anticorrosion Coating Test Method-Part 7: Thickness Test SY/T 4113.7-2020 (2020). Each coating was applied to the specimen surface in accordance with the specified application procedures and cured for 14 d under the designated conditions. After curing, a digital caliper was used to measure the initial thickness of the coating. Two measurement locations were selected—one in the tidal zone and the other in the immersion zone—and marked using a permanent marker (see Figure 5). The specimens were then placed in a brine exposure environment, according to the experimental plan. Every 120 d, the coating thickness at the marked locations was measured using the digital caliper to assess the thickness variation over time.

# 4 Analysis of test results

## 4.1 Surface morphology analysis

Figures 6–10 show the specimens after different exposure durations. For the ZB solvent-free modified epoxy liquid coating, the surface color of specimens ZB1–ZB3 darkened, and the gloss significantly diminished. In contrast, specimens ZB4–ZB6 maintained a normal surface color, as shown in Figure 6.

On day 246, for the ZH acrylic anticorrosive coating, specimens ZH1–ZH3 exhibited a noticeably dull and nonglossy surface. Additionally, black corrosion marks were observed on the portion embedded in the brine mud, as shown in Figure 7. This is primarily because acrylic coatings are based on organic polymer matrices. A dense cross-linking of acrylic coating is difficult to form, seriously limiting its durability and anticorrosion behavior, which was demonstrated by Faccini et al. (2021) and Ładosz et al. (2024). Brine mud is a special type of soft soil characterized by high cohesion and strong hydrophilicity. The colloidal fine particles in the mud can easily penetrate the micro-pores on the coating surface. Consequently, the acrylic anticorrosive coatings exhibited surface darkening after immersion in the brine mud zone.

After 246 d of exposure, the TD high-performance anticorrosive coating showed more severe surface degradation in specimens TD1–2-D and TD1–2-S, characterized by pronounced darkening and a complete loss of gloss, as illustrated in Figure 8. Similarly, the LC polyurea anticorrosive coating exhibited a loss of surface gloss in specimens LC1–2, as shown in Figure 9.

At the same observation point, the concrete surfaces without any protective coating exhibited significantly more severe corrosion.

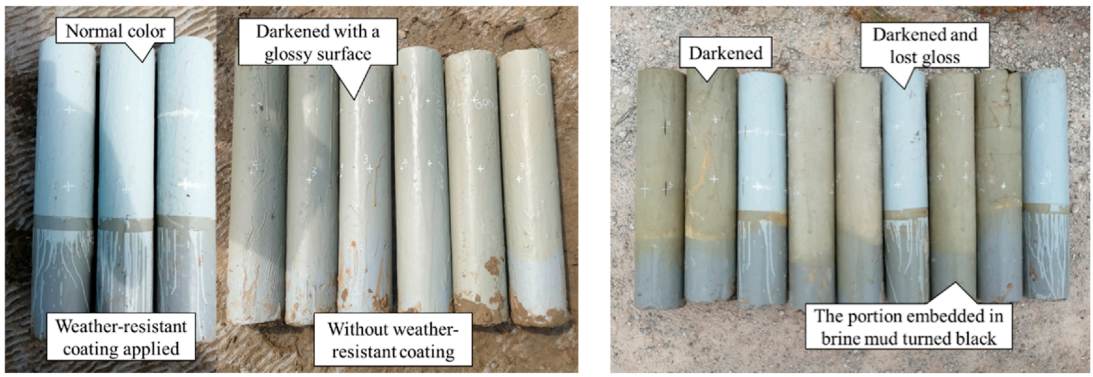


FIGURE 6
Surface morphology changes of ZB solvent-free modified epoxy liquid coating. **(a)** Day 139. **(b)** Day 246.


FIGURE 7
Surface morphology changes of ZH acrylic anti-corrosion coating. **(a)** Day 139. **(b)** Day 246.

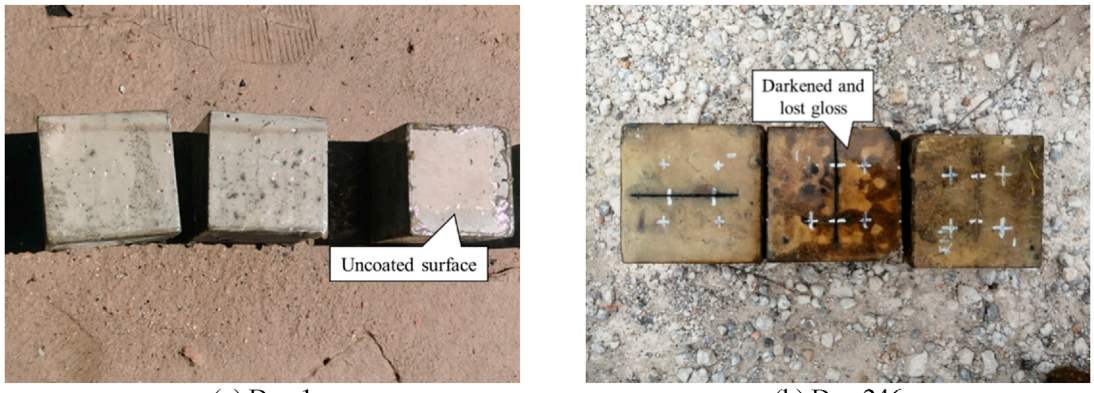


FIGURE 8
Surface morphology changes of TD high-performance anti-corrosion coating. **(a)** Day 1. **(b)** Day 246.


FIGURE 9
Surface morphology changes of LC polyurea anti-corrosion coating. **(a)** Day 139. **(b)** Day 246.

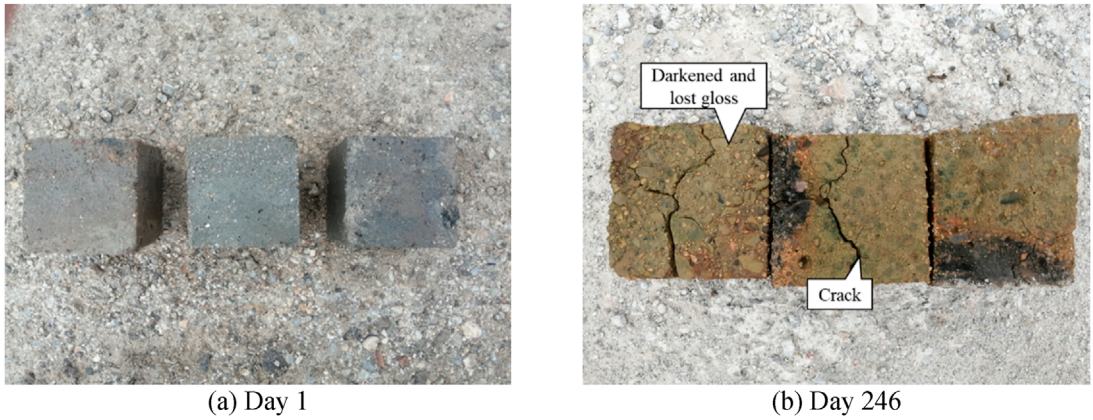


FIGURE 10
Surface morphology changes of uncoated concrete. **(a)** Day 1. **(b)** Day 246.

The coarse aggregates within the concrete were exposed, and the surface exhibited darkening, a loss of gloss, and the development of prominent cracks, as shown in Figure 10.

The test results demonstrate that anticorrosive coatings effectively mitigate the corrosion of concrete in brine environments, significantly enhancing the durability and service life of the structure.

## 4.2 Coating thickness analysis

The changes in the thicknesses of the four anticorrosive coatings are shown in Figures 11–14. The test results indicated an overall decreasing trend in the coating thickness in both the tidal and immersion zones. Moreover, the coatings experienced more severe degradation in the tidal zone than in the immersion zone.

As illustrated in Figures 11–14, the ZB, ZH, TD1, and LC coatings exhibited negligible changes in thickness during the initial 60 d of exposure. This was primarily attributed to the lower ambient temperatures during this period, which slowed the chemical corrosion processes. In addition, suspended operations at the test site during the winter season resulted in higher pH values and weaker brine acidity, thereby reducing its corrosive effect on the coatings. After 139 d, a more significant decrease in the coating thickness was observed. This can be attributed to rising temperatures, which accelerated chemical reactions and the resumption of production at the test site, leading to lower pH values and increased brine acidity, thereby intensifying coating corrosion. The annual temperature variations at the test sites are shown in Figure 15.

As shown in Figures 11–14, the reduction in coating thickness for the ZB, ZH, TD-D, and LC specimens generally ranged from 0 to 0.35 mm. By contrast, the TD-S specimens exhibited significantly more severe corrosion, with thickness reductions exceeding 1.8 mm. These results further demonstrate that anticorrosive coatings provide effective protection for concrete in brine environments.

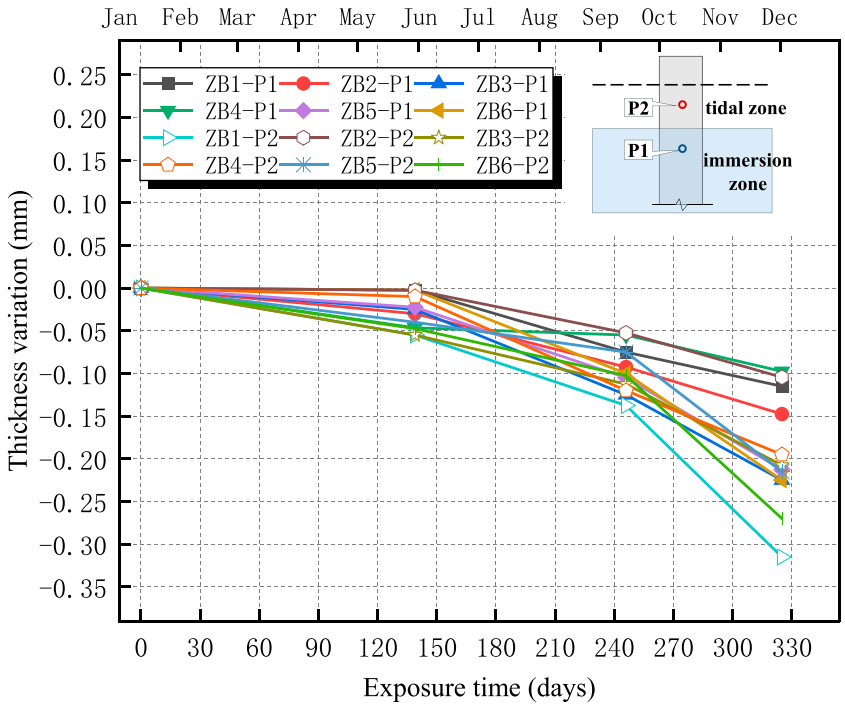


FIGURE 11
Thickness variation of ZB solvent-free modified epoxy liquid coating.

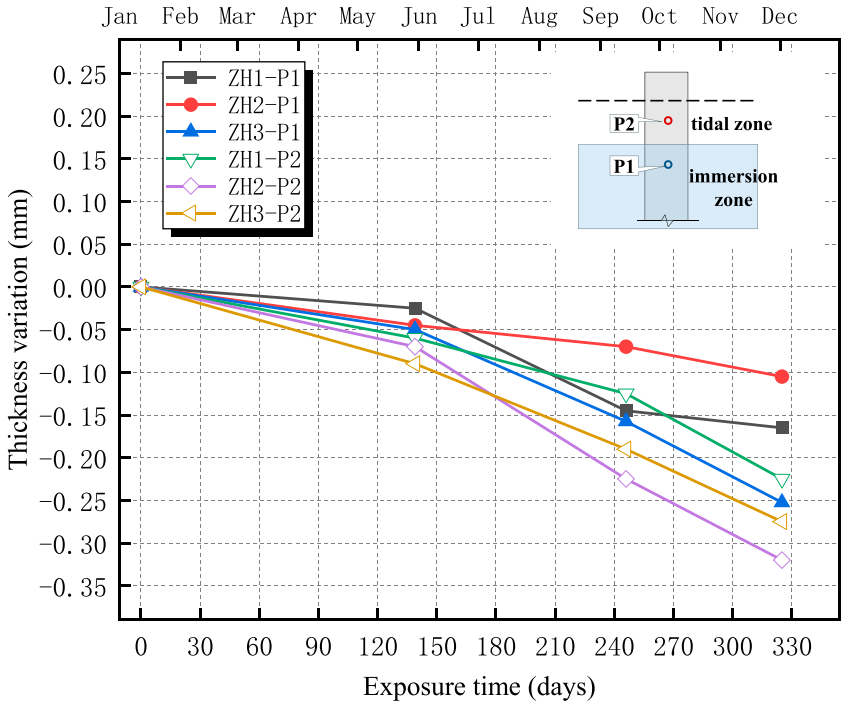


FIGURE 12
Thickness variation of ZH acrylic anti-corrosion coating.

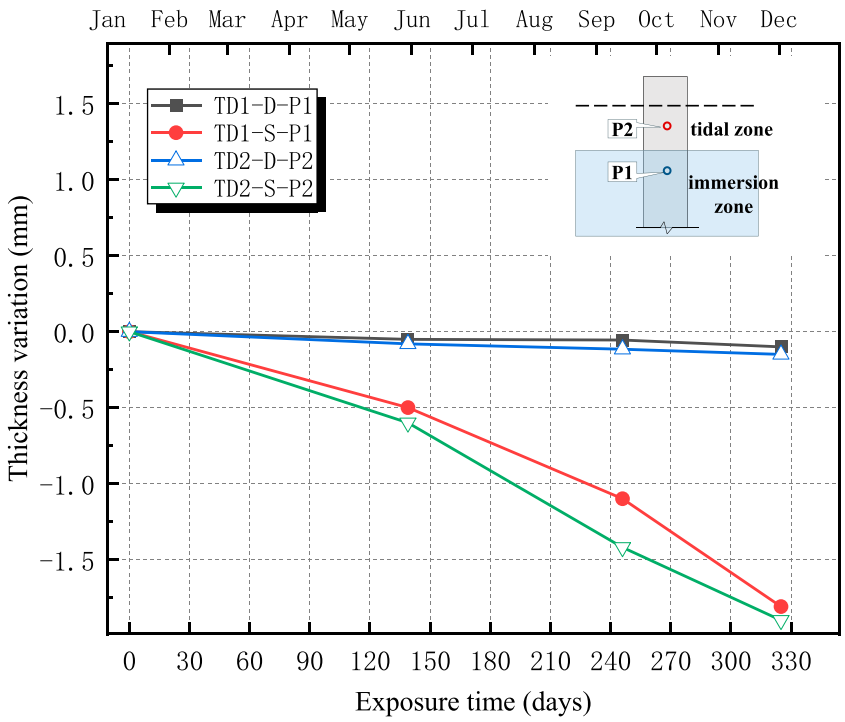


FIGURE 13
Thickness variation of TD high-performance anti-corrosion coating.

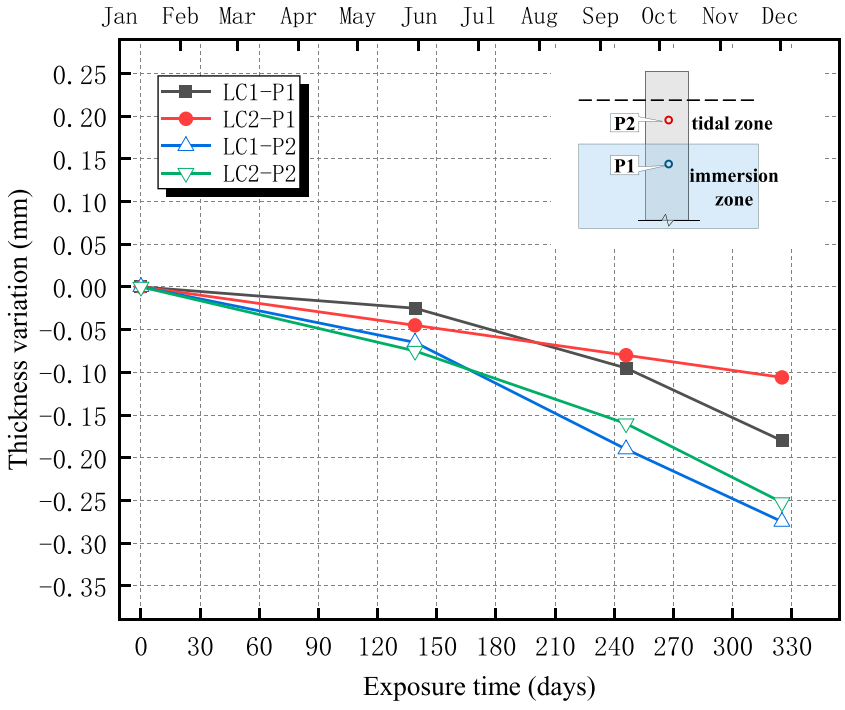


FIGURE 14
Thickness variation of LC polyurea anti-corrosion coating.

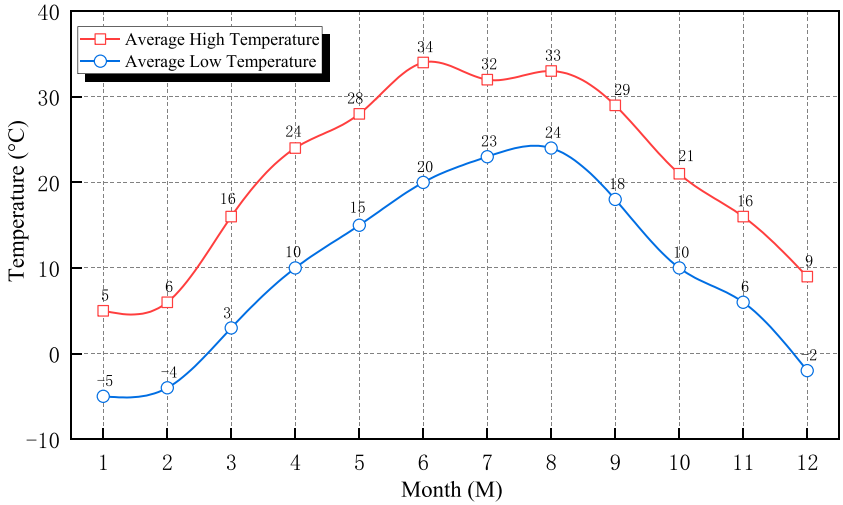


FIGURE 15
Temperature variation of the test site.

## 5 Comprehensive evaluation of anticorrosive coating schemes

This study adopted an AHP to assess the overall performance of the four anticorrosive coatings to scientifically evaluate the protective performance of different anticorrosive coatings on PHC pipe piles in brine environments, and to compare and select the optimal solution based on the comprehensive performance. The AHP method proposed by American operations researcher Thomas L. Saaty in the early 1970s (Saaty, 2013) has been widely applied to multicriteria decision-making analyses. This method decomposes complex problems into multiple components, determines the relative importance of each factor through pairwise comparisons, and combines both quantitative and qualitative analyses to derive a comprehensive priority ranking (Tavana et al., 2023; Pant et al., 2022; Panchal and Shrivastava, 2022).

The anticorrosive coatings were evaluated based on three criteria: surface morphology change, thickness variation, and cost. The relative importance of each criterion in the overall decision-making process was determined accordingly. The experimental results indicated that all four coatings demonstrated good anticorrosive performance; therefore, cost emerged as a particularly critical factor in the comprehensive evaluation (see Table 5), with the average cost value taken as the assessment metric.

Regarding the importance scale, considering that the coatings showed only minor differences in anticorrosive performance but significant differences in cost, the relative importance of cost over thickness variation was set to 5 (strong preference), and that over surface morphology changed to 6 (very strong preference). Meanwhile, the thickness variation was considered to be slightly more important than the surface morphology change, with a relative importance of 2 (weak preference), as listed in Table 6. Based on the above judgment matrix and using the eigenvalue method for the calculation, the resulting weight coefficients for each criterion were obtained as follows: surface morphology change 0.1033, thickness variation 0.1741, and cost 0.7225. To verify the consistency of the judgment matrix, the maximum eigenvalue λ_max was calculated as approximately 3.0293, yielding a consistency index (CI) of 0.0146. Referring to the random index (RI) value of 0.58 for n = 3, the consistency ratio (CR) was determined to be CR = CI/RI = 0.0252 < 0.1, indicating that the judgment matrix had good consistency, and the assigned weights were reasonable and reliable.

As shown in Table 5, a 1-to-9 scale method was adopted for scoring. The surface appearance was evaluated based on the degree of visual degradation observed after natural exposure. A score of nine was assigned to coatings with no visible changes, indicating minimal degradation; a score of six corresponded to a darkened surface, reflecting moderate deterioration; and a score of three was assigned to coatings that darkened to black, indicating severe degradation.

The thickness variation was scored using the inverse grading principle, where a smaller reduction in thickness yielded a higher score. A linear normalization method was applied, assigning a score of nine to the minimum observed thickness loss and one to the maximum thickness loss, with intermediate values interpolated proportionally. The cost score was determined using the same normalization principle as the thickness variation, where a lower cost corresponded to a higher score.

The comprehensive scores of the anticorrosive coatings are listed in Table 7. The experimental results indicate that, excluding the effects of improper application, measurement errors, and force majeure factors, the ZB1 anticorrosive coating demonstrated the best overall performance in this study and can be considered the optimal anticorrosion solution for future applications to PHC pipe piles in brine environments.

In this study, a comprehensive evaluation of the various anticorrosive coatings was conducted using the Analytic Hierarchy Process (AHP), leading to the identification of an efficient corrosion protection strategy. The evaluation results are inherently influenced by multiple factors, including the judgment matrix and scoring criteria, which may introduce certain degrees

TABLE 5 Durability performance and cost analysis of anticorrosive coating systems.

| Specimen ID | Coating scheme | Surface morphology change | Thickness variation | Cost (CNY/m$^2$) |
|---|---|---|---|---|
| ZB1 | Solvent-free modified epoxy liquid coating ≥300 μm | Darkened | 0.12~0.32 | 75 |
| ZB2 | Solvent-free modified epoxy liquid coating ≥400 μm | Darkened | 0.11~0.15 | 95 |
| ZB3 | Solvent-free modified epoxy liquid coating ≥500 μm | Darkened | 0.21~0.23 | 110 |
| ZB4 | Solvent-free modified epoxy liquid coating ≥300 μm + weather-resistant 80 μm | Slightly darkened | 0.10~0.20 | 95 |
| ZB5 | Solvent-free modified epoxy liquid coating ≥400 μm + weather-resistant 80 μm | Slightly darkened | 0.21~0.26 | 120 |
| ZB6 | Solvent-free modified epoxy liquid coating ≥500 μm + weather-resistant 80 μm | Slightly darkened | 0.23~0.27 | 130 |
| ZH1 | Acrylic anticorrosive coating 800 μm | Darkened to blackened | 0.17~0.23 | 75 |
| ZH2 | Acrylic anticorrosive coating 1,000 μm | Darkened to blackened | 0.11~0.32 | 85 |
| ZH3 | Acrylic anticorrosive coating 1,000 μm (reinforced with fabric) | Darkened to blackened | 0.25~0.27 | 95 |
| TD | MP series high-performance primer 300 μm (double-sided) | Darkened to blackened | 0.10~0.15 | 50~90 |
| LC1 | Armored anticorrosive polyurea + LC-301 topcoat | Darkened | 0.18~0.28 | 150 |
| LC2 | Sprayed polyurea LC-1138 + LC-301 topcoat | Darkened | 0.12~0.25 | 135 |

TABLE 6 Scoring matrix of anticorrosive coatings under each criterion.

| Specimen ID | Surface morphology change | Thickness variation | Cost (CNY/m$^2$) |
|---|---|---|---|
| ZB1 | 6 | 3.37 | 8.33 |
| ZB2 | 6 | 8.70 | 5.67 |
| ZB3 | 6 | 3.37 | 3.67 |
| ZB4 | 9 | 7.52 | 5.67 |
| ZB5 | 9 | 2.48 | 2.33 |
| ZB6 | 9 | 1.85 | 1.00 |
| ZH1 | 3 | 4.59 | 8.33 |
| ZH2 | 3 | 3.83 | 7.00 |
| ZH3 | 3 | 1.48 | 5.67 |
| TD | 3 | 9.00 | 9.00 |
| LC1 | 6 | 2.70 | 3.67 |
| LC2 | 6 | 5.11 | 4.33 |

TABLE 7 Comprehensive scoring results of anticorrosive coatings.

| Rank | Coating type | Composite score |
|---|---|---|
| 1 | ZB1 | 7.86 |
| 2 | ZH1 | 7.33 |
| 3 | TD | 7.01 |
| 4 | ZH2 | 6.51 |
| 5 | ZH3 | 5.97 |
| 6 | LC2 | 5.95 |
| 7 | LC1 | 5.83 |
| 8 | ZB2 | 5.79 |
| 9 | ZB4 | 5.53 |
| 10 | ZB3 | 5.12 |
| 11 | ZB5 | 4.88 |
| 12 | ZB6 | 4.77 |

of error and subjectivity. Therefore, the outcomes presented herein are intended solely for reference purposes based on the available data and scoring framework and should not be regarded as the sole basis for decision-making regarding corrosion protection strategies in saline-alkali tidal flat and brine environments.

## 6 Conclusion

To address the corrosion issues of PV PHC pipe pile foundations in saline-alkali tidal flat brine environments, the formation mechanisms and chemical composition of the brine were analyzed. The mechanisms and causes of corrosion of PHC pipe piles under brine exposure were comprehensively investigated. Four anticorrosive coating schemes were selected and evaluated using surface morphology and thickness variation tests to assess their durability. A comprehensive performance evaluation based on the AHP was conducted to determine cost-effectiveness and propose efficient anticorrosion solutions. The following conclusions were drawn:

1. The corrosion mechanisms of PHC pipe piles in brine environments are similar to those in marine environments, primarily involving chloride-, sulfate-, and acid-induced corrosion. Owing to the high concentration of hydrogen ions and the low pH of the brine, hydrogen ion erosion is the dominant mechanism. Therefore, it is recommended to apply anticorrosive coatings to the concrete surface to reduce the penetration of aggressive ions, such as $H^+$ and $Cl^-$, thereby effectively mitigating corrosion.
2. Surface morphology and thickness variation analyses revealed that, after 325 d of exposure, all the coatings experienced varying degrees of corrosion. The ZB, ZH, TD-D, and LC coatings showed signs of oxidation, yellowing, and darkening, with thickness reductions ranging approximately from 0 to 0.35 mm, though the coatings remained generally intact. By contrast, the TD-S specimens exhibited severe surface corrosion with a thickness reduction of approximately 1.8 mm, along with mortar spalling and coarse aggregate exposure.
3. A comprehensive evaluation model was used to assess the three performance indicators of the coatings. The results showed that, after 325 d of exposure, the TD high-performance coating demonstrated the best overall performance.
4. Anticorrosive coatings have proven to be an effective protective strategy for PHC pipe piles in brine environments. The following recommendations are proposed for the practical application of such coatings: Perform surface inspections every 6 months, focusing on cracks, peeling, or discoloration; promptly repair damaged areas to prevent the penetration of corrosive agents; and install corrosion sensors to monitor the real-time corrosion status of PHC piles, providing a scientific basis for maintenance decision-making.
5. The primary contribution of this study is the establishment of a systematic selection framework for anticorrosive materials tailored to high-salinity and high-humidity environments. By expanding the evaluation dimensions of PHC pile foundation materials, this study provides a quantifiable, comparable, and scalable technical basis for corrosion protection design in PV projects in saline-alkali regions. The findings not only offer practical guidance for engineering applications, but also serve as a methodological and empirical foundation for future research on protective systems for infrastructure in extreme environments.

## Data availability statement

The raw data supporting the conclusions of this article will be made available by the authors, without undue reservation.

## Author contributions

JW: Conceptualization, Data curation, Formal Analysis, Investigation, Methodology, Project administration, Resources, Supervision, Validation, Writing – original draft, Writing – review and editing. JH: Conceptualization, Data curation, Formal Analysis, Funding acquisition, Investigation, Methodology, Project administration, Validation, Visualization, Writing – original draft, Writing – review and editing. YL: Data curation, Formal Analysis, Investigation, Methodology, Resources, Validation, Visualization, Writing – original draft, Writing – review and editing. HS: Data curation, Formal Analysis, Investigation, Methodology, Resources, Validation, Writing – original draft, Writing – review and editing. HL: Data curation, Formal Analysis, Investigation, Methodology, Resources, Software, Supervision, Validation, Visualization, Writing – original draft, Writing – review and editing. XD: Data curation, Formal Analysis, Investigation, Validation, Writing – original draft, Writing – review and editing.

## Funding

The author(s) declare that financial support was received for the research and/or publication of this article. This work was supported by the Key Research and Development Program of Gansu Province (22YF7FH224); and the Open Project of the Key Joint Laboratory of the Ministry of Education (2024KFKT-YB12).

## Acknowledgments

This work was supported by the Key Research and Development Program of Gansu Province (22YF7FH224); and the Open Project of the Key Joint Laboratory of the Ministry of Education (2024KFKT-YB12). We deeply appreciate for the warm and efficient work by editors and reviewers.

## Conflict of interest

Authors, JW, YL, and HS were employed by Shandong Electric Power Engineering Consulting Institute Corp., Ltd. Author XD was employed by Shandong Binhai Energy Co., Ltd.The remaining authors declare that the research was conducted in the absence of any commercial or financial relationships that could be construed as a potential conflict of interest.

## Generative AI statement

The author(s) declare that no Generative AI was used in the creation of this manuscript.

## Publisher's note

All claims expressed in this article are solely those of the authors and do not necessarily represent those of their affiliated organizations, or those of the publisher, the editors and the reviewers. Any product that may be evaluated in this article, or claim that may be made by its manufacturer, is not guaranteed or endorsed by the publisher.

## References

Chen, H., Jiang, Y., and Markou, G. (2022). Structural performance deterioration of corroding reinforced concrete columns in marine environments. *Ocean. Eng.* 262, 112155. doi:10.1016/j.oceaneng.2022.112155

Faccini, M., Bautista, L., Soldi, L., Escobar, A. M., Altavilla, M., Calvet, M., et al. (2021). Environmentally friendly anticorrosive polymeric coatings. *Appl. Sci.* 11 (8), 3446. doi:10.3390/app11083446

JG/T 335-2011 (2011). *Film-forming coatings for concrete structure protection*.

Ładosz, Ł., Sudoł, E., Kozikowska, E., and Choińska, E. (2024). Artificial weathering test methods of waterborne acrylic coatings for steel structure corrosion protection. *Materials* 17, 1857. doi:10.3390/ma17081857

Li, Y., Tang, B., and Li, W. (2024). Durability of concrete structures in salt and freshwater confluence area. *Bull. Chin. Ceram. Soc.* 43 (12), 4389–4397.

Li, Z., Wang, Y., Sun, X., and Liu, B. (2024). Experimental investigation on the effects of temperature and w/c on corrosion characteristics of rebars in concrete exposed to salt lake environments. *J. Mater. Sci.* 59 (33), 15786–15801. doi:10.1007/s10853-024-10083-y

Madraszewski, S., Sielaff, A. M., and Stephan, D. (2023). Acid attack on concrete–Damage zones of concrete and kinetics of damage in a simulating laboratory test method for wastewater systems. *Constr. Build. Mater.* 366, 130121. doi:10.1016/j.conbuildmat.2022.130121

Ministry of Construction of the People's Republic of China (2002). *Code for investigation of geotechnical engineering*. Beijing: China Architecture and Building Press.

Panchal, S., and Shrivastava, A. K. (2022). Landslide hazard assessment using analytic hierarchy process (AHP): a case study of National Highway 5 in India. *Ain Shams Eng. J.* 13 (3), 101626. doi:10.1016/j.asej.2021.10.021

Pant, S., Kumar, A., Ram, M., Klochkov, Y., and Sharma, H. K. (2022). Consistency indices in analytic hierarchy process: a review. *Mathematics* 10 (8), 1206. doi:10.3390/math10081206

Peng, Y., Meng, X., Song, F., and Xu, G. (2022). Experimental study on the corrosion characteristics of concrete exposed to acid water containing aggressive carbon dioxide and sodium sulfate. *Constr. Build. Mater.* 321, 126397. doi:10.1016/j.conbuildmat.2022.126397

Qian, R., Li, Q., Fu, C., Zhang, Y., Wang, Y., Jin, N., et al. (2023b). Investigations on atmospheric carbonation corrosion of concrete structure beam exposed to real marine-environment for 7 years. *J. Build. Eng.* 71, 106517. doi:10.1016/j.jobe.2023.106517

Qian, R., Li, Q., Fu, C., Zhang, Y., Wang, Y., and Jin, X. (2023a). Atmospheric chloride-induced corrosion of steel-reinforced concrete beam exposed to real marine environment for 7 years. *Ocean. Eng.* 286, 115675. doi:10.1016/j.oceaneng.2023.115675

Qiao, C., Ni, W., and Weiss, J. (2017). Transport due to diffusion, drying, and wicking in concrete containing a shrinkage-reducing admixture. *J. Mater. Civ. Eng.* 29 (9), 04017146. doi:10.1061/(asce)mt.1943-5533.0001983

Saaty, T. L. (2013). The modern science of multicriteria decision making and its practical applications: the AHP/ANP approach. *Operations Res.* 61 (5), 1101–1118. doi:10.1287/opre.2013.1197

SY/T 4113.7-2020 (2020). *Pipeline anti-corrosion coating test method-Part 7:Thickness test*.

Tavana, M., Soltanifar, M., and Santos-Arteaga, F. J. (2023). Analytical hierarchy process: revolution and evolution. *Ann. Operations Res.* 326 (2), 879–907. doi:10.1007/s10479-021-04432-2

Tian, H., Qiao, H., Feng, Q., and Han, W. (2023). Corrosion deterioration of reinforced concrete in a saline soil environment. *J. Mater. Civ. Eng.* 35 (11), 4023387. doi:10.1061/jmcee7.mteng-16258

Tian, Y., Zhang, G., Ye, H., Zeng, Q., Zhang, Z., Tian, Z., et al. (2023). Corrosion of steel rebar in concrete induced by chloride ions under natural environments. *Constr. Build. Mater.* 369, 130504. doi:10.1016/j.conbuildmat.2023.130504

Vera, R., Apablaza, J., Carvajal, A. M., and Vera, E. (2013). Effect of surface coatings in the corrosion of reinforced concrete in acid environments. *Int. J. Electrochem. Sci.* 8 (10), 11832–11846. doi:10.1016/s1452-3981(23)13226-3

Wang, H., Chen, H., Yang, C., and Li, J. (2022). Durable life assessment of centrifugal stratified PHC piles in marine environment. *Eng. Struct.* 263, 114404. doi:10.1016/j.engstruct.2022.114404

Wang, H., and Zhang, H. (2018). Study on the anticorrosion performance of organic coatings in simulated marine environments. *China Coatings* 33 (09), 25–30. doi:10.13531/j.cnki.china.coatings.2018.09.005

Wang, J. (2024). Experimental study on corrosion resistance of PHC pipe pile foundation of saltern photovoltaic power station [D]. Beijing: Beijing University of Civil Engineering and Architecture. doi:10.26943/d.cnki.gbjzc.2024.000725

Wang, Y., Deng, M., Zhang, R., Yu, X., Xue, J., and Zhang, J. (2024). Durability of prestressed piles in a leachate environment. *Materials* 17 (11), 2497. doi:10.3390/ma17112497

Wu, W., He, X., Yang, W., Dai, L., Wang, Y., and He, J. (2022). Long-time durability of GFRP bars in the alkaline concrete environment for eight years. *Constr. Build. Mater.* 314, 125573. doi:10.1016/j.conbuildmat.2021.125573

Xu, Q., Liu, B., Dai, L., Yao, M., and Pang, X. (2024). Factors influencing chloride ion diffusion in reinforced concrete structures. *Materials* 17 (13), 3296. doi:10.3390/ma17133296

Youssari, F. Z., Taleb, O., and Benosman, A. S. (2023). Towards understanding the behavior of fiber-reinforced concrete in aggressive environments: acid attacks and leaching. *Constr. Build. Mater.* 368, 130444. doi:10.1016/j.conbuildmat.2023.130444

Zhang, C., Li, J., Yu, M., Lu, Y., and Liu, S. (2024). Mechanism and performance control methods of sulfate attack on concrete: a review. *Materials* 17 (19), 4836. doi:10.3390/ma17194836

Zhang, Y., Zhang, M., and Ye, G. (2018). Influence of moisture condition on chloride diffusion in partially saturated ordinary Portland cement mortar. *Mater. Struct.* 51, 36–18. doi:10.1617/s11527-018-1162-7

Zhao, X., Liu, L., and Liu, C. (2018). Influence of ion erosion on hpc strength in brine environment. *Bull. Chin. Ceram. Soc.* 37 (4), 1363–1369. doi:10.16552/j.cnki.issn1001-1625.2018.04.039

Zuquan, J., Xia, Z., Tiejun, Z., and Jianqing, L. (2018). Chloride ions transportation behavior and binding capacity of concrete exposed to different marine corrosion zones. *Constr. Build. Mater.* 177, 170–183. doi:10.1016/j.conbuildmat.2018.05.120

frontiers | Frontiers in Earth Science

TYPE Original Research
PUBLISHED 23 July 2025
DOI 10.3389/feart.2025.1647330



OPEN ACCESS

EDITED BY
Tongming Qu,
Hong Kong University of Science and Technology, Hong Kong SAR, China

REVIEWED BY
Tao Xu,
University of Macau, China
Sijie Liu,
Wuhan University, China
Xu-Yan Tan,
Chinese Academy of Sciences (CAS), China

*CORRESPONDENCE
Xin Feng,
cugfengxin@163.com

RECEIVED 15 June 2025
ACCEPTED 10 July 2025
PUBLISHED 23 July 2025

CITATION
Li T, Feng X, Li J, Qu L and Ji F (2025) Application of mold-bag sleeve valve pipe grouting technology for karst reinforcement during shield tunneling.
*Front. Earth Sci.* 13:1647330.
doi: 10.3389/feart.2025.1647330



# Application of mold-bag sleeve valve pipe grouting technology for karst reinforcement during shield tunneling

Taifeng Li[1,2], Xin Feng[3]*, Jiehua Li[4], Linjun Qu[4] and Fuquan Ji[3]

[1]Yunnan Provincial Highway Administration Corps, Kunming, China, [2]Yunnan Comprehensive Transportation Development Cente, Kunming, China, [3]CCCC Second Harbor Engineering Co., Ltd., Wuhan, China, [4]CCCC(Guangzhou) Construction Co., Ltd., Guangzhou, China

When traversing strata characterized by highly developed karst formations, shield tunneling machines are susceptible to incidents such as head sinking, surface collapse, and water inrushes. Consequently, karst reinforcement becomes a critical factor in ensuring the safety and success of shield tunneling operations in such geological conditions. However, conventional grouting technologies often face challenges, including severe grout leakage and suboptimal reinforcement outcomes, thereby introducing significant risks to tunneling activities. In this study, the limitations of traditional sleeve-valve pipe grouting technologies in reinforcing karst strata were examined, using the Dapeng Branch Line project of the Shenzhen-Huizhou Intercity Railway as a case study. To address these issues, a mold-bag sleeve-valve pipe grouting technology, specifically designed for karst reinforcement, was developed. Its construction procedures and key technical aspects were systematically investigated, and a field grouting test was performed to assess the applicability and reliability of the proposed method. The results indicated that, in karst strata with extensively developed fissures, conventional sleeve-valve pipe grouting methods encountered significant problems, including grout leakage, grout surfacing, and the inability to retrieve intact reinforced bodies from karst cavities. Consequently, the karst treatment effect failed to meet the requirements. In contrast, the proposed mold-bag grouting technology enables precise grouting in karst cave areas, reducing grout loss and forming complete reinforced bodies within the karst cave areas.

KEYWORDS

**shield tunneling, karst strata, grouting reinforcement, mold-bag sleeve valve pipe grouting, drilling and coring for inspection**

## 1 Introduction

Currently, tunnel construction is under rapid development in China. This status manifests not only as a rapid increase in the number and length of tunnels but also as large breakthroughs in construction equipment, construction technology, and environmental protection (Editorial Department of China Journal of Highway and Transport, 2022; Tan et al., 2023; Tan et al., 2024). The shield tunneling method, as a leading construction approach in contemporary China, has found widespread

application in the development of urban rail transit, highway, and railway tunnels (Dai and Ji, 2022; Meng et al., 2025).

Karst strata are extensively distributed across China, with 7 major karst regions. In southern China, many karst strata, with high water content, permeability, and susceptibility to collapse, exist (Cui et al., 2015). With the rapid development of rail transit, tunnel construction must inevitably traverse karst-developed zones. However, when passing through karst strata, shield tunneling machines can easily encounter accidents such as head sinking, surface collapse, and water bursts (Yan et al., 2021; Zhu et al., 2021). Existing studies on tunnel construction in karst strata have focused mainly on risk assessment and karst treatment. In terms of risk assessment, Li et al. (2020) established an earth pressure balance shield model test system to investigate the mechanism of water bursts in shield tunneling through karst strata. Zhang et al. (2022) normalized the evaluation indicators and determined their weights using a comprehensive weighting approach that integrated the fuzzy analytic hierarchy process (FAHP) with correlation analysis. Based on these weighted indicators, they enhanced the extended assessment method and developed a risk assessment system for ground collapse along tunnel alignments in karst strata. Sun et al. (2024) incorporated four probability models into a two-dimensional cloud model to quantify risk levels, applying the improved model to evaluate the risk probability associated with shield tunneling in karst regions. Building on the cloud model and FAHP, Meng et al. (2021) proposed a risk assessment method for shield tunneling in karst strata and established a corresponding indicator system, consisting of four primary indicators and 17 secondary indicators, along with defined risk classification criteria. In terms of karst strata treatment, grouting remains the most widely used method (Brantberger et al., 2000; Zhang et al., 2018). Qian et al. (2016) used sleeve-valve pipe grouting technology to reinforce a sandy soil-covered karst stratum and achieved good results. Yang et al. (2020) proposed a grouting reinforcement technology for underwater karst areas, in which controllable cement-bentonite fly ash and hardened cement-bentonite grouting materials were adopted. Huang et al. (2021) reported a multi-step combined control technology for karst treatment during shield tunneling in spring areas. The steps included karst exploration, multi-step grouting, and optimization of the tunneling parameters. The multi-step grouting process involved pre-grouting, as well as filling large karst caves with rubble from the ground surface, injecting a small volume of inert grout into the tunnel many times, and conducting secondary grouting at the tail of the shield tunneling machine.

The reinforcement effectiveness of karst strata before shield tunneling plays a crucial role in ensuring tunneling safety. To address this, researchers have advanced existing grouting methods and developed new technologies and materials specifically for karst reinforcement. Nevertheless, the issue of grout leakage in karst strata with developed fissures and high connectivity has yet to be fully resolved. In this study, a mold-bag sleeve-valve pipe grouting technology, adapted from Mold-bag grouting used for soft foundation reinforcement (Li et al., 2018), was introduced for application in karst strata. The construction procedure and technical parameters of this method were thoroughly investigated, and its performance was compared to that of conventional sleeve-valve pipe grouting technology, using the Dapeng Branch Line of the Shenzhen-Huizhou Intercity Railway as a practical example. The outcomes offer valuable insights for the implementation of the proposed technique.

# 2 Background of the project

## 2.1 Overview

The Dapeng Branch Line of the Shenzhen-Huizhou Intercity Railway serves as a crucial component of the intercity railway network in the Greater Bay Area. Together with the Zhongnanhu Intercity Railway and the Tanglong Intercity Railway, it forms the primary intercity corridor traversing the Pearl River Estuary, linking the eastern and western banks. According to the Greater Bay Area intercity railway development plan, the Dapeng Branch Line connects with both the Tanglong and Zhongnanhu Intercity Railways, enabling rapid transit between the eastern part of Shenzhen and the cities of Dongguan and Zhongshan. The line originates at Longcheng Station, an interchange station on the Shenzhen-Huizhou Intercity Railway, and extends to Xinda Station in the Dapeng New Area, passing through Longgang District, Pingshan District, and Dapeng New Area. The entire line, with a total length of 39.387 km, is constructed underground. It includes six stations—Longcheng, Pingshan, Yanzihu, Kuiyong, Dapeng, and Xinda—and features a parking facility at Xinda. The layout of the line is shown in Figure 1.

Work Zone 1 of the line encompasses the segment from Longcheng Station to Longping Working Shaft 1, spanning 3,064.5 m, and the segment from Longping Working Shaft 1 to Longping Working Shaft 2, extending 3,067.4 m. The shield tunneling method is utilized for construction throughout both segments (Figure 2). Longping Working Shafts 2 and 3 are interconnected by a rear pilot tunnel measuring 42.3 m in length, which is excavated using the mining method.

## 2.2 Geological condition

Along the project route in Work Zone 1, there are complex geological and hydrological conditions, a wide variety of geotechnical layers, and unfavorable geological conditions such as karst and erosion-induced fractures. The burial depth, thickness, and properties of geotechnical layers vary greatly. The sectional tunnels include moderately to slightly weathered limestone, erosion-induced fracture zones of limestone, and developed karst areas. The geological strata within the construction zone are composed mainly of plain fill, muck, silty clay, medium to coarse sand, clay, highly weathered siltstone, moderately weathered siltstone and limestone, and slightly weathered limestone. Notably, the highly and moderately weathered rock formations exhibit significant fissure development. The physical characteristics of these strata are detailed in Table 1. The groundwater system is predominantly comprised of Quaternary pore water, bedrock fissure water, and karst water. The Quaternary pore water is mainly replenished through atmospheric precipitation and surface water infiltration, leading to a high water yield. The bedrock fissure water is replenished mainly by pore water, whereas the karst water is recharged by lateral runoff and leakage. Pumping tests have revealed good connectivity

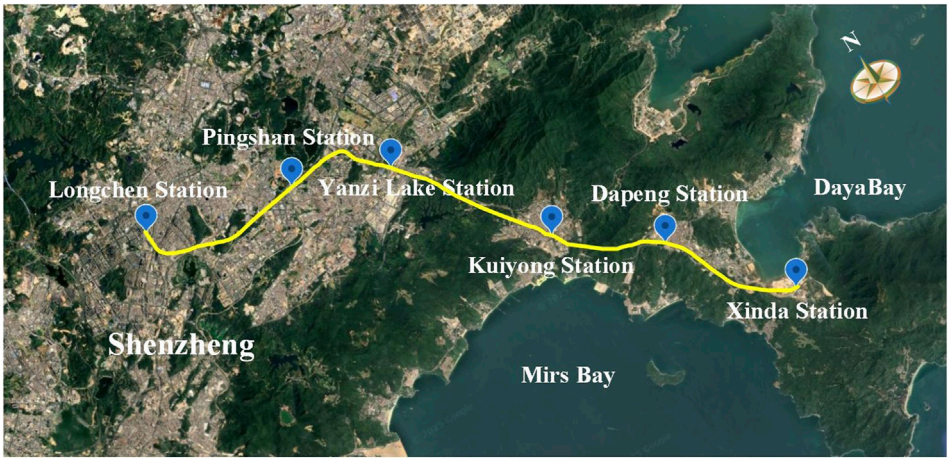


FIGURE 1
Schematic plan of the Dapeng Branch Line in the Shenzhen-Huizhou Intercity Railway.

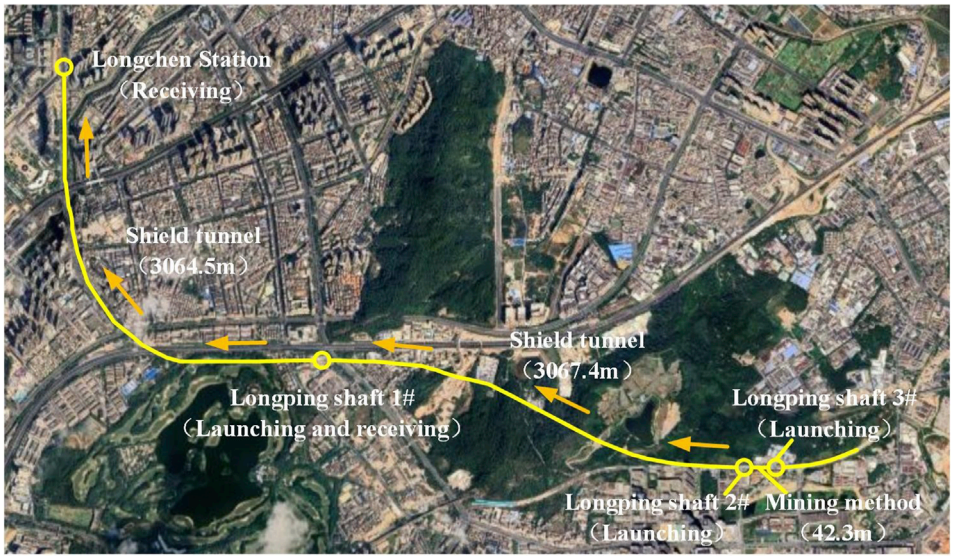


FIGURE 2
Schematic plan of the route in Work Zone 1 for the Dapeng Branch Line of the Shenzhen-Huizhou Intercity Railway.

among karsts and a large volume of fissure-karst water within the construction area.

## 2.3 Karst development characteristics and treatment principles

In this project, geological drilling and cross-hole CT methods were used for karst exploration. The exploration results indicated that the karsts in the construction area were covered and highly developed and primarily developed in the form of karst caves and dissolution fissures. The karst formations exhibited good connectivity, with some caves interconnected, forming bead-like karst caves. A total of 474 karst caves were uncovered in the shield tunneling section, including 270 empty caves, 94 semi-filled karst caves, 77 fully filled karst caves, and 33 soil caves. The karst caves were mainly filled with silty clay and gravelly soil. Karst caves were found in diverse locations relative to the shield tunnel, encompassing those within/above/below the tunnel and on both sides of the tunnel (Figure 3).

To ensure construction safety, karst caves should be treated before shield tunneling. The karst treatment principles were formulated as follows after a comprehensive consideration of the types, locations, and sizes of karsts, as well as the status of karst water (Figure 4):

1) All karst caves within 3 m on the top and both sides of the tunnel, as well as within 5 m below the tunnel bottom, should be treated;

TABLE 1 Physical and mechanical parameters of strata.

| Stratum | Natural density ρ (g/cm$^3$) | Cohesion $c$ (kPa) | Internal friction angle $\varphi$(°) | Compression modulus $E_S$ (MPa) | Deformation modulus $E_0$ (MPa) | Uniaxial compressive strength $R_c$(MPa) | Permeability coefficient $K$ (m/d) |
|---|---|---|---|---|---|---|---|
| Plain fill | 18.8 | 22.1 | 15.9 | 6.78 | / | / | 0.1 |
| Muck | 16.2 | 5 | 3.8 | 2 | / | / | 0.0001 |
| Silty clay | 18.8 | 23.68 | 15.22 | 3.3 | / | / | 0.01 |
| Medium-coarse sand | 19.6 | / | 25 | / | 30 | / | 30 |
| Clay | 19.3 | 28 | 16.51 | 4.4 | / | / | 0.1 |
| Highly weathered siltstone | 21.8 | / | / | / | 120 | 17.6 | 2.5 |
| Moderately weathered siltstone | 27.2 | / | / | / | / | 35.41 | 1.5 |
| Moderately weathered limestone | 26.9 | / | / | / | / | 31.61 | 3 |
| Slightly weathered limestone | 27.2 | / | / | / | / | 44.9 | 0.1 |

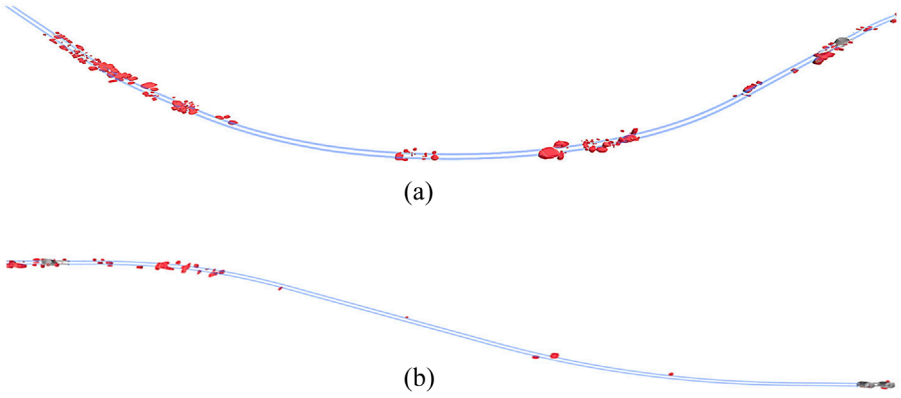


FIGURE 3
Distribution of karst caves in the shield tunneling sections. **(a)** Tunneling section from Longcheng Station to Longping Working Shaft 1. **(b)** Shield tunneling section from Longping Working Shaft 1 to Longping Working Shaft 2

2) All empty caves on the top of the tunnel should be treated;
3) Karst caves within 5 m–10 m below the tunnel bottom should be treated if the height H of the stable rock surface roof of the karst cave is less than 3 m or if the ratio of the height H of the stable rock surface roof of the karst cave to the span B of the karst cave is less than 1;
4) For any extra large karst cave (height: >5 m) found beyond the mentioned treatment ranges, a special meeting should be held to determine the necessity of treating it, considering the uncertainty of karst cave development.

According to the mentioned treatment principles, the karst caves requiring treatment within the shield tunneling section of Work Zone 1 are detailed in Table 2.

The requirements for cave treatment are as follows.

1) The unconfined compressive strength of fully filled karst caves after grouting treatment should be greater than 0.2 MPa.

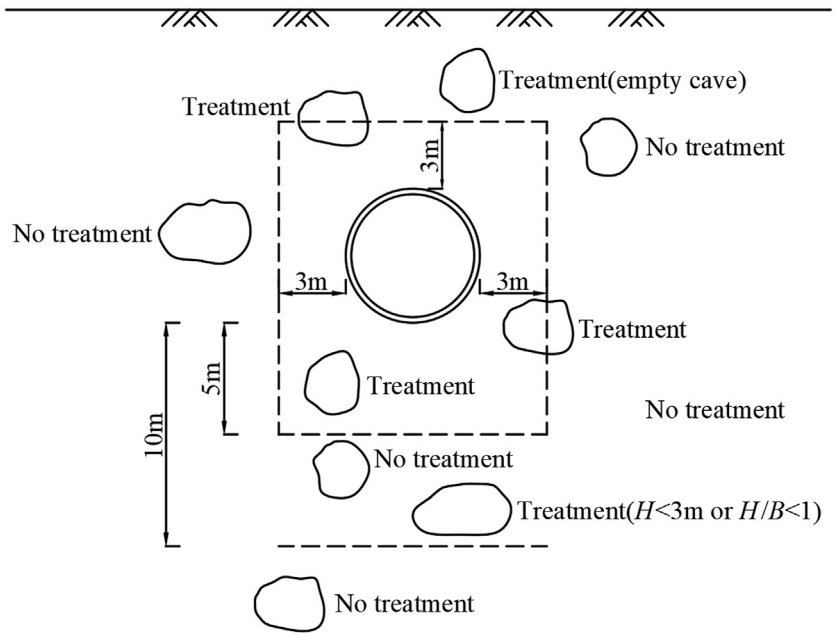


FIGURE 4
Schematic diagram of the karst cave treatment principles.

TABLE 2 Karst caves requiring treatment.

| Type | Quantity | Height *H*(m) | | |
|---|---|---|---|---|
| | | H ≤ 2 m | 2m < H ≤ 5m | H > 5m |
| Empty cave | 172 | 47 | 42 | 83 |
| Semi-filled karst cave | 58 | 22 | 19 | 17 |
| Fully-filled karst cave | 49 | 10 | 18 | 21 |
| Soil cave | 32 | 10 | 11 | 11 |
| Total | 311 | 89 | 90 | 132 |

2) For unfilled or semi filled caves, the unconfined compressive strength of the filling material should be greater than 0.8 MPa.

# 3 Conventional sleeve-valve Pipe grouting technology

## 3.1 Grouting Scheme

### 3.1.1 Treatment method

For semi-filled karst (soil) caves greater than 3 m and empty caves greater than 2 m, the first step was to fill them with C15 plain concrete; then, sleeve-valve pipe grouting technology was employed for grouting in the segments. This approach enabled loose fillings within the karst caves, as well as the voids formed after plain concrete was filled, to be compacted and permeated by cement grout, forming a consolidated mass (Figure 5). Fully-filled karst (soil) caves, semi-filled karst (soil) caves with heights less than 3 m, and empty caves not exceeding 2 m were directly treated using the sleeve-valve pipe grouting method (Figure 6). For karst caves extending beyond the specified treatment boundaries, edge sealing was performed prior to grouting by injecting a double-liquid mixture of cement and sodium silicate.

### 3.1.2 Layout of grouting holes

Before karst caves are treated, their planar ranges should be detected. First, edge exploratory boreholes were drilled along the outline of the karst caves as determined by geophysical prospecting. If a karst cave is exposed during drilling, additional boreholes should be drilled 2 m outward from the exposed point to determine the cave boundary. After the planar dimension of the karst cave is determined, the grouting holes should be arranged according to the following principles:

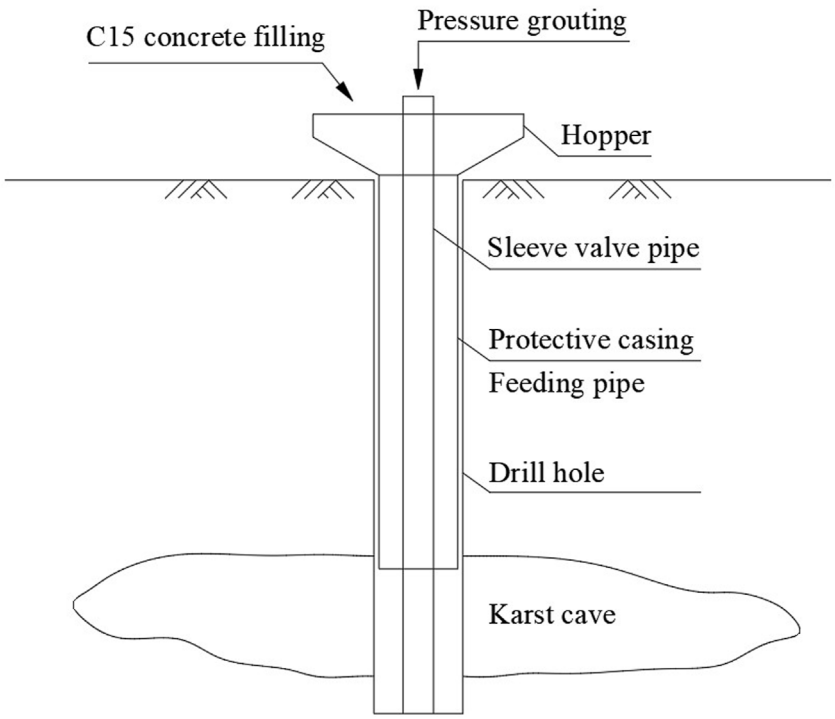


FIGURE 5
Schematic diagram of plain concrete filling and sleeve-valve pipe grouting.

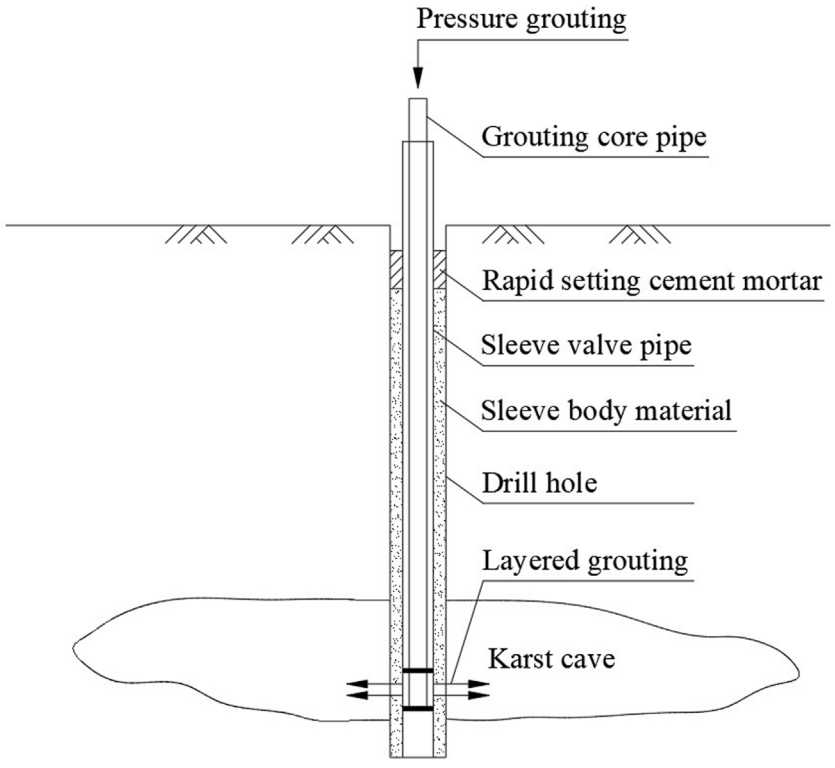


FIGURE 6
Schematic diagram of sleeve-valve pipe grouting.

1) For any karst cave exposed with a side length of less than 2 m in the projected area, one grouting hole should be arranged at the exploratory borehole uncovering it;
2) For any karst cave exposed with a side length of 2–3 m in the projected area, three grouting holes should be arranged with a spacing of 2 m × 2 m in a triangular pattern around the exploratory borehole.
3) For any karst cave exposed with a side length greater than 3 m in the projected area, grouting holes should be arranged with a spacing of 2 m × 2 m in a quincunx pattern around the exploratory boreholes uncovering it;
4) The grouting holes should extend 0.5 m below the bottom of the karst cave. When the karst cave is large in scale or has developed fissures, the drilling should be deepened to extend 0.5 m into the intact rock mass beneath the karst cave;
5) Boreholes to be filled with plain concrete should be inserted with Φ200 mm PVC pipes and distributed uniformly with a spacing of 5–6 m along the boundary of the karst cave;
6) In addition to grouting holes, vent holes should also be set aside. The number of vent holes should be determined per the scale of the karst cave.

### 3.1.3 Grouting materials and parameters

1) Grouting materials

The grouting materials consisted of two types: cement grout and double-liquid grout composed of cement and sodium silicate. The cement grout was prepared using P.O42.5 cement with a water-to-cement ratio of 1:1. The sodium silicate solution, initially having a density of 1.325 g/mL, a modulus of 3.25, and a Baume degree of 37°Bé, was diluted at a 1:1 ratio. The volume ratio between the cement grout and the diluted sodium silicate solution was maintained at 1:1.

2) Grouting parameters

After grouting commenced, the grouting core pipe pressed the grout upward from the bottom. The grouting rates at the bottom and top of the karst cave were 20–50 L/min, whereas those at the other parts were 30–70 L/min. The grouting core pipe was lifted 1 m in a single operation, and the grouting volume for each segment was controlled within 0.8–2 $m^3$. The initial grouting pressure was set at 0.2–0.3 MPa. The grouting pressure was terminated at 1.5 MPa and maintained at this value for 10 min.

## 3.2 Application effect

Owing to the presence of irregularly developed karsts, rock fissures, and loose overlaying layers, sleeve-valve pipe grouting has resulted in severe grout leakage and increased grout volume. Moreover, multiple instances of grout surfacing were observed during grouting, causing substantial pollution to the surrounding environment. After the completion of grouting, the reinforcement effect was tested via the drilling and coring methods. As a result, in many karst caves, no intact reinforced bodies were observed, or the reinforced bodies extended beyond the boundaries of the karst caves (Figures 7, 8). This required secondary treatment,

FIGURE 7
No complete reinforcement bodies.

leading to increased construction costs and elevated safety risks. Based on the field application results, the conventional sleeve-valve pipe grouting technology demonstrated notable limitations and insufficient reinforcement performance in karst strata characterized by well-developed fissures and high connectivity.

# 4 Mold-bag sleeve valve pipe grouting technology

## 4.1 Technical principles

In this method, grout leakage was mainly mitigated by wrapping a high-strength geotextile mold bag around the sleeve-valve pipe, effectively restricting grout diffusion as the solid particles were unable to penetrate the mold. The dimensions of the mold bag were tailored on-site according to the size of the karst cavity, ensuring that its height and diameter matched the vertical and horizontal measurements of the cave. The bottom of the mold bag was sealed, while the top remained open to allow insertion of the sleeve-valve pipe. Multiple loops of thin iron wire were wound around the exterior of the mold bag at intervals of 1.0–1.5 m, serving as pressure control valves during grouting. The top of the mold bag was tightly secured with iron wire to prevent grout from escaping at the upper end. The assembly was then lowered into the karst cavity, and grouting was carried out in stages using the standard sleeve-valve pipe grouting technique. This process allowed the mold bag to expand incrementally from the bottom up, ultimately creating a continuous and complete reinforced body within the karst cavity (Figure 9).

FIGURE 8
Reinforced bodies beyond the ranges of the karst caves.

## 4.2 Field test

### 4.2.1 Test site

The test site was located in the karst area in front of the entrance gate of Nanyuechun Banquet Manor. The total depth of the test borehole was 48.8 m. As discovered by coring, the upper 25 m of the borehole consisted of silty clay, whereas the lower part was composed of moderately weathered limestone. At depths of 44–46.2 m underground, a semi-filled karst cave was found (Figure 10) and treated as the primary focus of the test.

### 4.2.2 Test materials

The mold bag was made of a filamentous-woven geotextile with a diameter of 1 m, a height of 4 m, a breaking strength of 150 kN/m, an elongation rate of about 20% at break, and a weight of 550 g/m2. The sleeve valve pipes were Φ 48 mm PVC sleeve-valve pipes (length: 4 m/pcs). The grouting material was cement grout with a water:cement ratio of 1:1.

### 4.2.3 Test procedures

1) Binding of the Mold Bag

Initially, the sleeve-valve pipe was positioned within the central portion of the mold bag, with its bottom end maintained about 10 cm above the sealed base of the mold bag. The mold bag was then folded in half and rolled into a cylindrical form. Its upper end was securely tied with a Φ1.2 mm iron wire to prevent grout leakage. Pressure valves were arranged along the central section of the mold bag at intervals of 1.25 mm, created by wrapping four turns of Φ1.2 mm iron wire. During ground tests, the mold bag was able to unfold smoothly throughout the grouting process.

He measured diameter of the mold bag bound to the sleeve valve pipe was 10 cm–11 cm. Hence, the diameter of the test borehole should be more than 110 mm. In addition, the karst cave in this stratum was buried at a considerable depth and surrounded by thick and intense rock layers. Drilling operators reported that the maximum achievable borehole diameter was 110 mm; if this diameter was exceeded, drilling would be quite difficult. Therefore, the diameter of the test borehole was determined to be 110 mm.

2) Drilling

Test boreholes were drilled to a diameter of 110 mm per dimension of the bound mold bag. Coring was conducted from the entire length of the borehole during drilling, and the coring results were used to determine the location and height of the karst cave. As illustrated, there were semi-filled karst caves at depths of 44–46.2 m from the ground surface.

3) Installation of Sleeve-valve Pipes

Upon completion of drilling, the sleeve-valve pipe, wrapped with the mold bag, was positioned at the lowest section for insertion into the borehole. The target depth for the mold bag was about 20 cm below the base of the karst cavity. However, during the actual lowering process, insertion was halted after 11.5 sleeve-valve pipes had been placed, likely due to sediment buildup at the bottom of the borehole. At this point, the bottom of the mold bag was positioned roughly at the base level of the karst cavity.

4) Installation of the Grouting Pipe

After the installation of sleeve-valve pipes, the borehole was sealed. Specifically, the area from the ground surface around the borehole opening to a depth of 2 m underground was sealed using quick-setting cement mortar. The grouting pipes (DN20 steel pipe) were then installed, with the grouting head placed at the bottom and lowered to the bottom of the sleeve-valve pipe. During the actual installation, further lowering was not possible after 22 grouting pipes (each 2 m in length) had been inserted into the sleeve-valve pipes. As a result, the bottom of the grouting core pipe was positioned about 44.2 m below ground level, maintaining a distance of about 1.8 m above the bottom of the mold bag. This configuration accounted for the exposed length of the grouting pipe, the length of the grouting core pipe, and the length of the pipe joints. The spatial relationship among the karst cavity, mold bag, and grouting core pipe is illustrated in Figure 11.

5) Grouting

Following the installation of the grouting pipe, a pressure gauge was attached to its upper section. Prior to grouting, the pipes were flushed with water to ensure they remained unobstructed. Grouting was performed in segments, with the grouting core pipe being raised by 0.5–1.0 m for each segment. The grouting process was regulated by monitoring both the grouting volume and pressure. When the

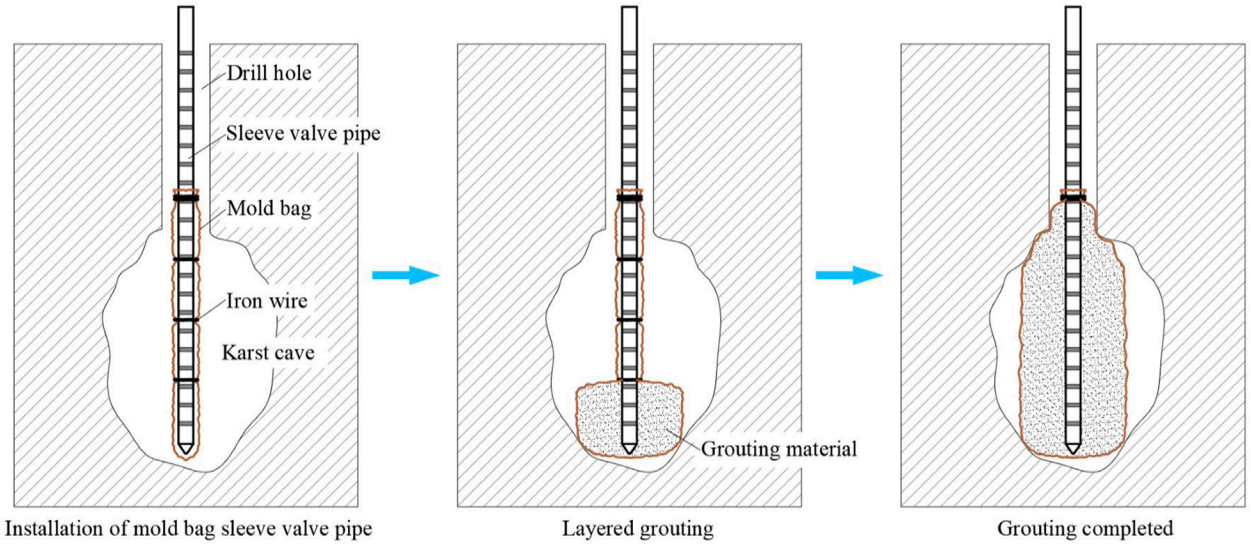


FIGURE 9
Schematic diagram of mold-bag sleeve valve pipe grouting in karst strata.

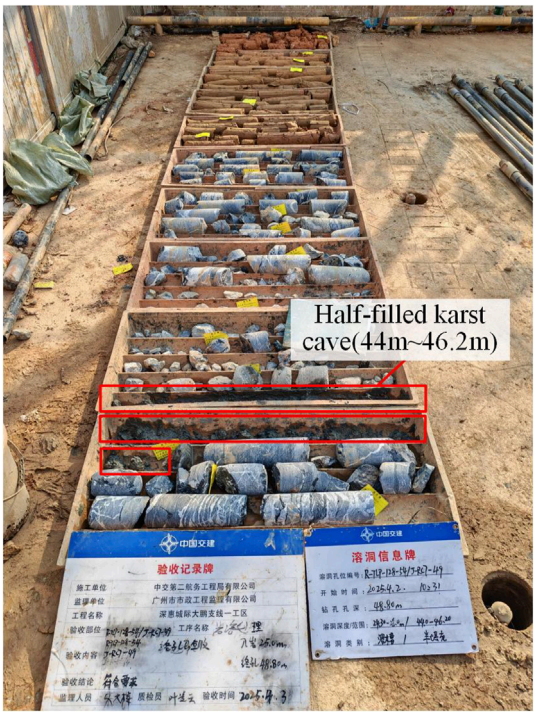


FIGURE 10
Coring from test boreholes.

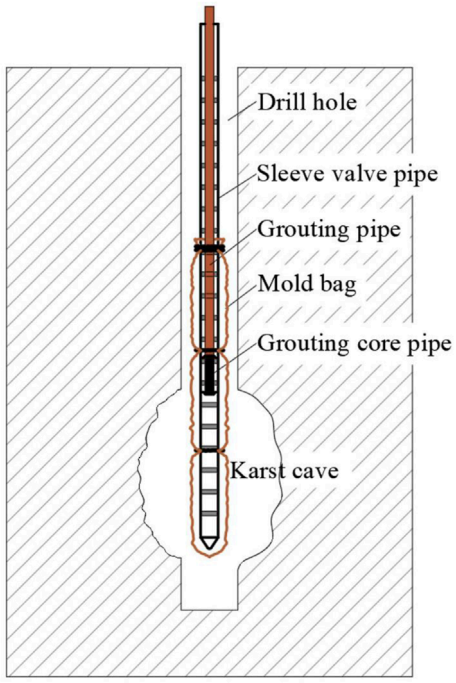


FIGURE 11
Schematic diagram showing the relative positions of the karst cave, mold bag, and grouting core pip.

size of the cave was larger than the diameter of the mold bag, the grouting amount can be controlled according to the volume of the mold bag. When the volume of the cave was small, the amount of grouting cannot be accurately estimated. Both of the above states can be judged by changes in grouting pressure. When there was a significant increase in grouting pressure, it indicates that the mold bag in this section has been basically filled, and the next section of mold bag grouting can be carried out. In this test, the volume per unit length of the mold bag was 0.7854 $m^3$, and the estimated volume of grout required within the height range of the karst cave (2.2 m) was about 1.73 $m^3$. In existing cases, the grouting pressure for mold bags is generally controlled within the range of


FIGURE 12
Comparison of rock cores before and after grouting. **(a)** Before grouting. **(b)** After grouting.

1.0–1.5 MPa. During the test, the grouting pressure was observed continuously.

Because the grouting core pipe was close to the top of the karst cave, it was not feasible to grout in segments within the karst cave area. Thus, the grouting core pipe remained stationary during grouting. In the field grouting process, the initial grouting pressure was about 0.2–0.6 MPa. After about 30 s, the grouting pressure stabilized at 0.8 MPa–1.2 MPa. The reason was that after 30 s of grouting, the slurry reached the grouting core pipe and overcomed the water pressure on the outside of the rubber sleeve to start grouting into the mold bag The grouting was halted after about 50 min of continuous grouting. In total, about 3.2 t of cement grout was grouted. Given that the specific gravity of the cement grout used on-site was 1.46 g/cm3, the volume of the grout was calculated to be 2.19 $m^3$. However, the actual grouting volume exceeded the theoretical grouting volume for the following reasons: (1) the karst cave was actually greater than 2.2 m; (2) some water in the cement grout seeped out from the mold bag, resulting in an increased grouting volume.

### 4.2.4 Grouting effect test

Two weeks after the completion of grouting, the area 20 cm away from the test borehole was drilled to a depth identical to the test borehole and then cored, with the corresponding results displayed in Figure 12. The karst cave area was filled with cement grout. In detail, the rock cores at depths of 44–45 m were complete, indicating that this segment of the mold bag was sufficiently filled with cement grout. The reason was that the grouting core pipe was positioned in the middle part of the two pressure valves, and the grouting was conducted here consistently. Additionally, the rock cores obtained from depths of 45 m–46.2 m were fragmented, indicating an unsatisfactory filling effect of the cement grout in this section. This was attributed to the loosening of the pressure valves in the upper and lower portions of the mold bag under the influence of grouting pressure after the central part had been filled. As a result, cement grout was able to flow into the upper and lower sections of the mold bag; however, the grout flow was uneven.

## 4.3 Application analysis

On the whole, it was feasible to apply mold-bag sleeve valve pipe grouting technology for karst strata reinforcement. However, the following points should be noted:

### 4.3.1 Drilling depth

Owing to sediment accumulation at the bottom of the borehole, the drilling depth should extend 2–3 m below the bottom of the karst cave to ensure that the mold bag can be lowered to the bottom of the karst cave smoothly.

### 4.3.2 Matching between the diameters of the borehole and the mold bag

As the diameter of the mold bag increases, its size, after being wrapped around the sleeve-valve pipe, also expands, necessitating a proportionally larger drilling diameter. In formations with deep karst cavities, enlarging the drilling diameter significantly raises both the complexity and the cost of drilling operations.

### 4.3.3 Lowering sleeve-valve pipes and grouting pipes

For greater drilling depths, steel sleeve-valve pipes may be employed to prevent breakage during the lowering process. Mechanical equipment can be utilized to assist in positioning both the sleeve-valve pipes and the grouting pipes.

### 4.3.4 Grouting in segments

Grouting should be performed from the bottom up to ensure that each segment of the mold bag is filled.

Owing to the characteristics of mold-bag sleeve valve pipe grouting, this technology is mainly used in the following aspects of karst strata treatment:

1) For empty caves with limited horizontal dimensions, as well as fully-filled and semi-filled karst caves, a single mold bag is sufficient for grouting reinforcement.
2) Edge sealing for karst caves. The mold-bag sleeve-valve pipe grouting technique can be applied to construct a pile-like

barrier along the edges of the karst cavity or treatment zone, thereby enhancing the effectiveness of edge sealing.

## 5 Conclusions and Suggestions

This study analyzed the use of conventional sleeve-valve pipe grouting technology for reinforcing karst strata, taking the Dapeng Branch Line project of the Shenzhen-Huizhou Intercity Railway as a reference. A mold-bag sleeve-valve pipe grouting technique, specifically designed for karst conditions, was then proposed, and its implementation process and performance were assessed. The main conclusions derived from the study are as follows:

1) In karst strata with developed fissures and good connectivity, the application of conventional sleeve-valve pipe grouting technologies could cause severe grout leakage and grout surfacing. As a result, no completely reinforced bodies were formed within the karst cave area, which necessitated secondary treatment, increasing the construction cost and safety risk.
2) The proposed grouting technology enables precise grouting within the karst cave area, reducing grout loss and improving the reinforcement effect on karst strata. This method demonstrated good applicability in karst treatment during shield tunneling.
3) When the proposed grouting technology for karst treatment was utilized, the treatment effect was critically affected by the selection of mold bag specifications, the lowering of sleeve-valve pipes and grouting pipes, and the grouting in segments. Hence, these steps should be controlled strictly.

The field test provided preliminary verification of the proposed grouting technology's effectiveness in reinforcing karst strata during shield tunneling, while also revealing areas requiring further improvement. Future research will concentrate on optimizing the construction process and refining parameter control to establish a more comprehensive and effective mold-bag sleeve-valve pipe grouting technology for karst strata reinforcement in shield tunneling applications.

## Data availability statement

The original contributions presented in the study are included in the article/supplementary material, further inquiries can be directed to the corresponding author.

## Author contributions

TL: Conceptualization, Project administration, Writing – original draft. XF: Formal Analysis, Methodology, Supervision, Writing – review and editing. JL: Data curation, Investigation, Writing – original draft. LQ: Data curation, Investigation, Writing – original draft. FJ: Resources, Validation, Writing – review and editing.

## Funding

The author(s) declare that no financial support was received for the research and/or publication of this article.

## Acknowledgments

The authors would like to thank the CCCC(Guangzhou) Construction Co., Ltd. for the cooperation in the application of grouting technology.

## Conflict of interest

Authors XF and FJ were employed by CCCC Second Harbor Engineering Co., Ltd. Authors JL and LQ were employed by CCCC(Guangzhou) Construction Co., Ltd.

The remaining authors declare that the research was conducted in the absence of any commercial or financial relationships that could be construed as a potential conflict of interest.

## Generative AI statement

The author(s) declare that no Generative AI was used in the creation of this manuscript.

## Publisher's note



## References

Brantberger, M., Stille, H., and Eriksson, M. (2000). Controlling grout spreading in tunnel grouting analyses and developments of the gin-method. *Undergr. Space Technol.* 15 (4), 343–352. doi:10.1016/S0886-7798(01)00003-7

Cui, Q. L., Wu, H. N., Shen, S. L., Xu, Y. S., and Ye, G. L. (2015). Chinese karst geology and measures to prevent geohazards during shield tunnelling in karst region with caves. *Nat. Hazards* 77, 129–152. doi:10.1007/s11069-014-1585-6

Dai, H. B., and Ji, Y. G. (2022). Statistical analysis of Chinese large-diameter shield tunnel and state-of-art and prospective of comprehensive technologies. *Tunn. Constr.* 42 (5), 757–783. doi:10.3973/j.issn.2096-4498.2022.05.002

Editorial Department of China Journal of Highway and Transport (2022). Review on China's traffic tunnel engineering research: 2022. *China J. Highw. Transp.* 35 (4), 1–40. doi:10.19721/j.cnki.1001-7372.2022.04.001

Huang, X., Li, L. F., Zhang, C. F., Liu, B., Li, K. J., Shi, H. B., et al. (2021). Multi-step combined control technology for karst and fissure water inrush disaster during shield tunneling in spring areas. *Front. Earth Sci.* 9, 795457. doi:10.3389/feart.2021.795457

Li, L. P., Sun, S. Q., Wang, J., Song, S. G., Fang, Z. D., and Zhang, M. G. (2020). Development of compound EPB shield model test system for studying the water inrushes in karst regions. *Tunn. Undergr. Space Technol.* 101, 103404. doi:10.1016/j.tust.2020.103404

Li, Q. Y., Wu, Z. Y., and Zhang, D. J. (2018). Soil compaction effect of bagged grouting piles in saturated soft clay subgrade. *J. Southwest Jiaot. Univ.* 53 (5), 1026–1032. doi:10.3969/j.issn.0258-2724.2018.05.020

Meng, F. Y., Hu, B., Chen, R. P., Cheng, H. Z., and Wu, H. N. (2025). Characteristics of deformation and defect of shield tunnel in coastal structured soil in China. *Undergr. Space* 21, 131–148. doi:10.1016/j.undsp.2024.07.007

Meng, G. W., Ye, Y. C., Wu, B., Luo, G. J., Zhang, X., Zhou, Z. Q., et al. (2021). Risk assessment of shield tunnel construction in karst strata based on fuzzy analytic hierarchy process and cloud model. *Shock Vib.* 2021, 7237136. doi:10.1155/2021/7237136

Qian, Z., Xu, Y. S., Shen, S. L., and Cui, Q. L. (2016). A case study of ground surface grouting reinforcement of shield tunnel in karst strata with sandy soil cover. *Tunn. Constr.* 36 (4), 479–484. doi:10.397.j/issn.1672–741X.2016.04.017

Sun, H. Y., Rui, Y., Lu, Y. Y., Dai, Y. M., Wang, X., and Li, X. J. (2024). Construction risk probability assessment of shield tunneling projects in karst areas based on improved two-dimensional cloud model. *Tunn. Undergr. Space Technol.* 154, 106086. doi:10.1016/j.tust.2024.106086

Tan, X. Y., Palaiahnakote, S., Chen, W. Z., Cheng, K., and Du, B. W. (2023). A novel autoencoder for structural anomalies detection in river tunnel operation. *Expert Syst. Appl.* 244 (2), 122906. doi:10.1016/j.eswa.2023.122906

Tan, X. Y., Tan, X. J., Zhang, R., Zhang, Z. X., Tarek, Z., and Du, W. B. (2024). Identification of anomaly of tunnel segment strain using an adaptive machine learning model. 2024. *GEORISK* 18 (5), 1–14. doi:10.1080/17499518.2024.2395554

Yan, F., Qiu, W., Sun, K., Jiang, S. H., Huang, H. Y., Hong, Y. Q., et al. (2021). Investigation of a large ground collapse, water inrush and mud outburst, and countermeasures during subway excavation in qingdao: a case study. *Tunn. Undergr. Space Technol.* 117, 104127. doi:10.1016/j.tust.2021.104127

Yang, J. S., Zhang, C., Fu, J. Y., Wang, S. Y., Qu, X. F., and Xie, Y. P. (2020). Pre-grouting reinforcement of underwater karst area for shield tunneling passing through xiangjiang river in changsha, China. *Tunn. Undergr. Space Technol.* 100, 103380. doi:10.1016/j.tust.2020.103380

Zhang, C., Yang, J. S., Xie, Y. P., Xie, Y. P., Gong, F. H., Liang, X., et al. (2018). Experiment and application for grouting materials for karst under conditions of underground water flow before shield tunneling. *Chin. J. Rock Mech. Eng.* 37 (9), 2120–2130. doi:10.13722/j.cnki.jrme.2018.0196

Zhang, K., Zheng, W. B., Liao, Z. Y., Xie, H. P., Zhou, C. T., Chen, S. G., et al. (2022). Risk assessment of ground collapse along tunnels in karst terrain by using an improved extension evaluation method. *Tunn. Undergr. Space Technol.* 129, 104669. doi:10.1016/j.tust.2022.104669

Zhu, W. B., Zhang, H., and Huang, H. (2021). Analysis of and prevention countermeasures for underground engineering risks in red bed areas with developed karst. *Mod. Tunn. Technol.* 58 (5), 179–186. doi:10.13807/j.cnki.mtt.2021.05.022

frontiers | Frontiers in Earth Science

TYPE Original Research
PUBLISHED 30 July 2025
DOI 10.3389/feart.2025.1644997



OPEN ACCESS

EDITED BY
Zhang Cong,
Central South University Forestry and Technology, China

REVIEWED BY
Haifeng Liu,
Chinese Academy of Sciences (CAS), China
Bing Liu,
Business School, Guilin University of Technology, China
Shasha Zhang,
Chang'an university, China

*CORRESPONDENCE
Ruiyuan Zhang,
13554082150@163.com

RECEIVED 11 June 2025
ACCEPTED 17 July 2025
PUBLISHED 30 July 2025

CITATION
Zhang R, Zhang Y, Chen P, Ji F, Luo H and Zhong Y (2025) $K_0$ test and particle flow simulation of coral sands with different gradations.
*Front. Earth Sci.* 13:1644997.
doi: 10.3389/feart.2025.1644997



# $K_0$ test and particle flow simulation of coral sands with different gradations

Ruiyuan Zhang[1]*, Yongtao Zhang[1], Peishuai Chen[1], Fuquan Ji[1], Huiwu Luo[1] and Yu Zhong[1,2]

[1]CCCC Second Harbor Engineering Company Ltd., Wuhan, China, [2]School of Civil and Architectural Engineering, Wuhan University, Wuhan, China

This paper performs a series of laboratory static lateral pressure coefficient ($K_0$) tests on coral sands with five typical gradations in dry and saturated states via water bladder type lateral pressure apparatus to investigate their ranges of $K_0$ values. The results reveal that the $K_0$ values of coral sands in dry and saturated states range from 0.22 to 0.32 and 0.27 to 0.33, respectively, and that there is an exponential function relationship between the particle gradation and the $K_0$. On this basis, a discrete element model is established with the aid of particle flow code (PFC), and the numerical simulation and laboratory test are in good agreement. The displacement field of coral sand with a narrower gradation is revealed to be more prone to exhibit a horizontally stratified compression feature at the meso-scale. The coral sand with a wider gradation exhibits a more obvious gradient distribution of internal contact forces with more uniform directional distribution and better compaction. The $K_0$ decreases and then stabilizes with increasing particle bonding strength, and the evolution law between them conforms to the exponential function form. A theoretical calculation formula of $K_0$ for coral sand based on the distribution coefficient is further proposed according to the laboratory test results. The research results of this paper can provide parameter support for construction and design of wharf retaining structures on islands and reefs.

KEYWORDS

**road engineering, static lateral pressure coefficient, laboratory tests, coral sand, particle flow code, calculation formula of K0**

## 1 Introduction

With the implementation of the 'One Belt One Road' policy and the 'Maritime Power' strategy, an increasing number of island and reef projects have been launched. Since they are far away from the mainland, they usually need to utilize coral sands formed by reclamation. Coral sand (Chen et al., 2022) is a kind of geotechnical body with special engineering properties formed by the remains of coral communities under geological action, its genesis and chemical composition are significantly similar to carbonate rocks in karst areas,and it is irregular in shape (Smith and Cheung, 2003), porous (Xu et al., 2022), easy to cement (Meng et al., 2014), and easy to fracture (Donohue et al., 2009). Its engineering mechanical properties are quite different from those of ordinary terrestrial sediments (Wang et al., 2017). In island and reef engineering and similar geological environments (such as weathered residual soil or filling materials in karst

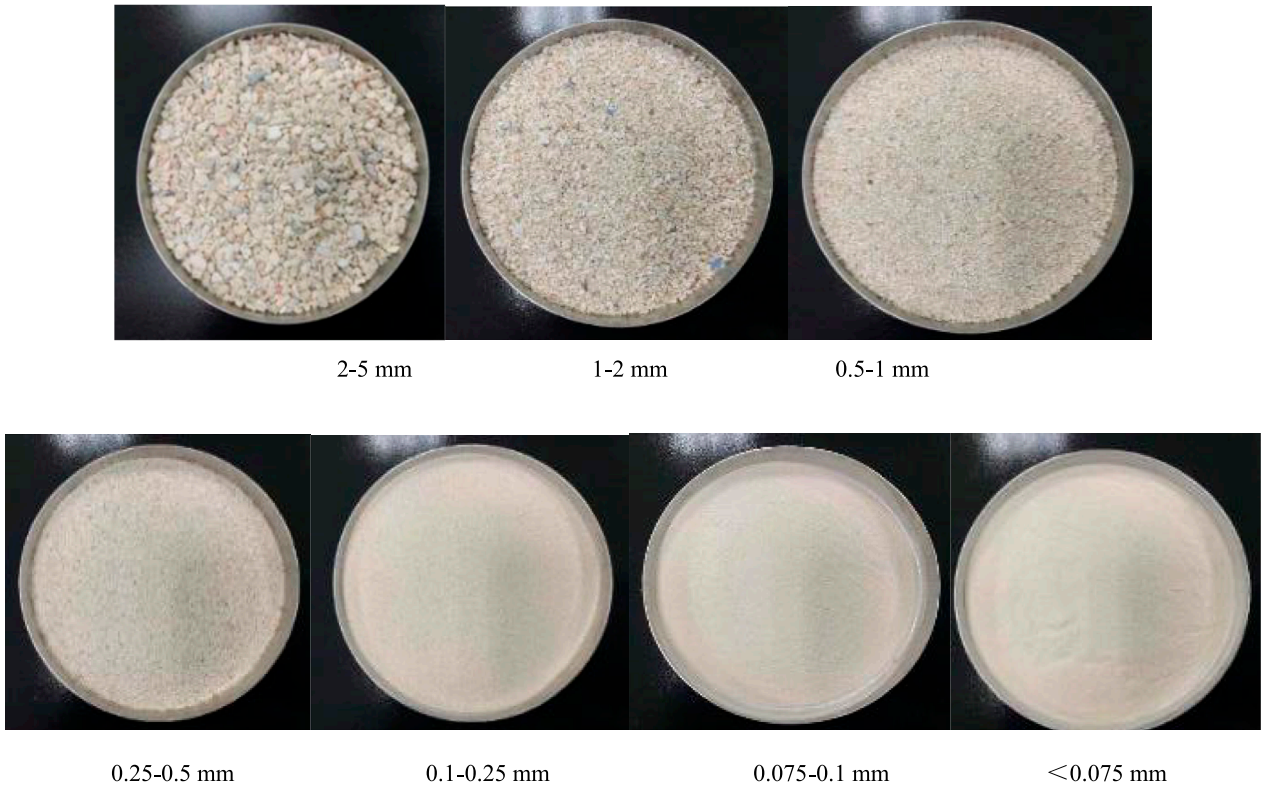


FIGURE 1
Coral sand of each particle group.

areas), the static lateral pressure coefficient ($K_0$) is a key parameter for geotechnical engineering investigation, design (such as soil pressure calculation of support structures), and construction (analyzing the horizontal stress state of the site) (Zhang et al., 1998). Its accurate control is crucial for ensuring engineering safety and preventing disasters such as foundation instability and slope collapse caused by abnormal soil stress. This study focuses on the K0 characteristics of coral sand, and its results not only directly serve the construction of islands and reefs, but also provide important theoretical basis and data support for understanding the stress evolution mechanism of similar carbonate derived soils in karst areas and disaster prevention (such as foundation treatment and slope reinforcement).

Scholars around the world have carried out a large number of theoretical and experimental studies on the $K_0$, and put forward a series of formulas for calculating the $K_0$. At present, the $K_0$ is mostly obtained by empirical formulas, *in situ* tests, and laboratory geotechnical tests (Michalowski et al., 2005; Wang et al., 2020). There are few studies on the $K_0$ of coral sand. Wang et al. (2021) determined the range of $K_0$ values of coral sands with different relative densities and water contents through laboratory tests, but they only studied coral sand with a single gradation. However, the coral sand formed by reclamation has a wide range of gradation distribution, and it is necessary to carry out research on coral sand with multiple gradations to obtain more comprehensive and practical $K_0$.

To fully study the $K_0$ of coral sands with different particle gradations, this paper measures the $K_0$ of coral sands with five typical gradations through laboratory tests, analyses the ranges of $K_0$ values in dry and saturated states, and deduces the influence laws of particle gradation on the $K_0$. A particle flow numerical model is established via PFC to reveal the macroscopic test mechanism from contact force chain and coordination number at the meso-scale. The influence law of bonding strength on $K_0$ is explored, and the formula for calculating $K_0$ based on distribution coefficient and strength parameter is further established. It is expected to clarify the stress distribution of coral sand sites and to provide mechanical parameter support for determination the earth pressure on wharf retaining structures in island and reef projects.

## 2 Test programme

### 2.1 Materials

The test sample is coral sand from an island reef in the Maldives, and the coral sand samples are sieved to obtain the particle groups of different sizes of <0.075 mm, 0.075–0.25 mm, 0.25–0.5 mm, 0.5–1 mm, 1–2 mm, and 2–5 mm, which are presented in Figure 1. According to the 'Code for Geotechnical Investigation on Port and Waterway Engineering (Partial Revision)-Geotechnical Investigation of Coral Reefs (General

TABLE 1 This is a table. Tables should be placed in the main text near to the first time they are cited.

| Parameter | Coral gravel sand | Coral coarse sand | Coral medium sand | Coral fine sand | Coral powder sand |
|---|---|---|---|---|---|
| d10 | 0.09 | 0.09 | 0.08 | 0.08 | 0.08 |
| d30 | 0.45 | 0.28 | 0.16 | 0.14 | 0.09 |
| d50 | 1.00 | 0.58 | 0.26 | 0.22 | 0.15 |
| d60 | 1.50 | 0.80 | 0.36 | 0.30 | 0.20 |
| Non-uniformity coefficient Cu | 16.67 | 8.70 | 4.80 | 4.00 | 2.67 |
| Curvature coefficient Cc | 1.50 | 1.07 | 0.95 | 0.87 | 0.54 |

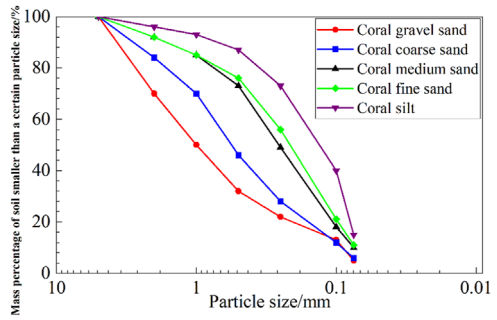


FIGURE 2
Gradation curves of coral sands.

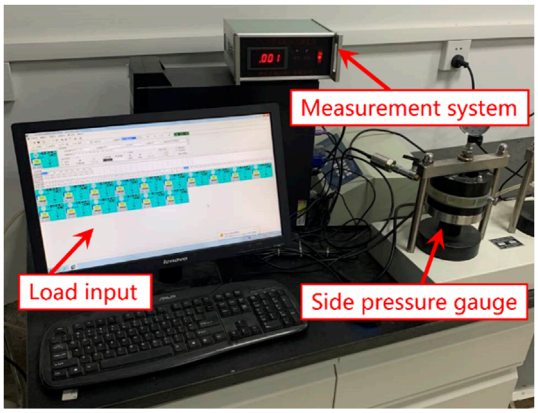


FIGURE 3
Static lateral pressure coefficient measurement test system.

Revision Draft)' (CCCC Second Navigation Engineering Survey and Design Institute, 2022), coral gravel sand, coral coarse sand, coral medium sand, coral fine sand, and coral powder sand are prepared, respectively. The five types of coral sands have a wide range of particle gradation distribution, which allows for the acquisition of all mechanical parameters of coral sands with typical representativeness.

The control particle size and gradation indexes are summarized in Table 1. The gradation curves of the five types of coral sands are depicted in Figure 2.

## 2.2 Test apparatus

The tests are carried out on GZQ-1 type fully automatic pneumatic consolidation apparatus. The equipment is produced by Nanjing Ruitai Geotechnical Testing Instrument Co., Ltd., with an axial load error of ±0.5% FS and a lateral pressure sensor nonlinearity of 0.1%. The whole system consists of a consolidation apparatus, a pneumatic pressure controller, a multi-channel communication converter, and a data acquisition system, as presented in Figure 3. The interior of the pressure chamber is inlaid with a ring-shaped rubber membrane, and the water is filled between the rubber membrane and the outer wall of pressure chamber. Coral sand squeezes the rubber membrane, leading to a varying water pressure on the side wall, which allows for the determination of the lateral pressure of coral sand sample by water pressure. The pressure chamber has a diameter of 61.8 mm and a height of 40 mm, and the maximum axial consolidation pressure it can withstand is 6 kN. It is able to provide a horizontal stress measurement range of 0–1,000 kPa and an axial displacement effective test range of 0–10 mm. The vertical load can be set freely by computer programme, and six vertical load levels of 50 kPa, 100 kPa, 150 kPa, 200 kPa, 400 kPa, and 600 kPa are designed for the tests.

## 2.3 Test procedure

The test procedure includes sample preparation, sample installation, loading, and data acquisition, while the dry and saturated scenarios are configured. For preparation of dry sample, the dried sand samples weighed according to the design density of 1.45 g/cm3 are loaded into the pressure chamber of the lateral pressure gauge for compaction in three times, and the compactness designed for the test is achieved by controlling the

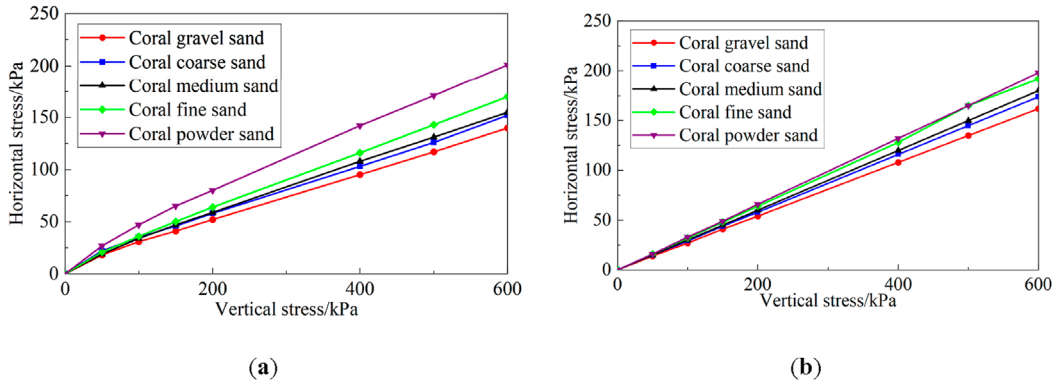


FIGURE 4
Relationship between horizontal and vertical stresses of coral sand.**(a)** Horizontal stress versus vertical stress in dry state. **(b)** Horizontal stress versus vertical stress in saturated state.

TABLE 2 K0 values of coral sands.

| Condition | Coral gravel sand | Coral coarse sand | Coral medium sand | Coral fine sand | Coral powder sand |
|---|---|---|---|---|---|
| Dry | 0.22 ± 0.01 | 0.23 ± 0.01 | 0.25 ± 0.02 | 0.27 ± 0.01 | 0.32 ± 0.02 |
| Saturated | 0.27 ± 0.02 | 0.29 ± 0.01 | 0.30 ± 0.02 | 0.32 ± 0.01 | 0.33 ± 0.01 |

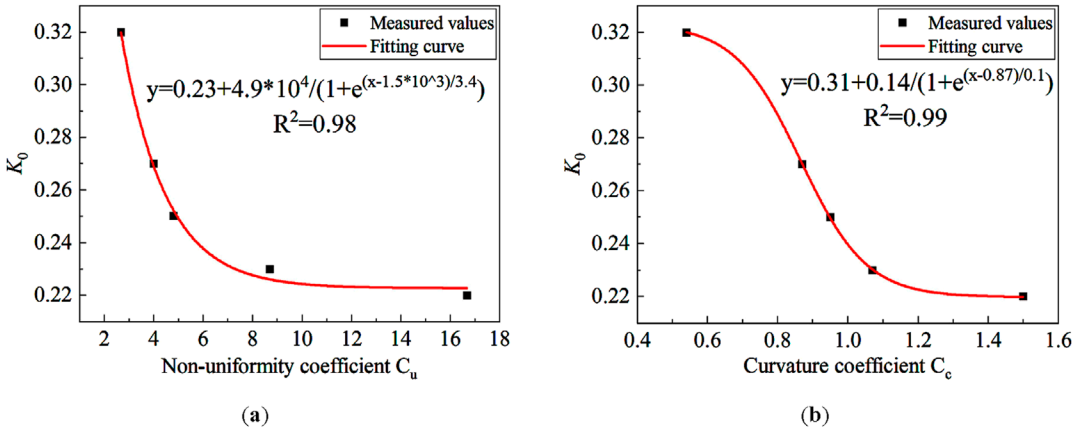


FIGURE 5
Relationship between particle gradation and K0 in dry state.**(a)** K0 versus Cu. **(b)** K0 versus Cc.

mass of sample added each time and the height of sample after compaction. The specific operation is as follows: the sample is filled in three layers, and each layer is manually compacted 10 times using a standard compaction hammer (hammer weight 2.5 kg, drop distance 200 mm). The height error of each layer after compaction is controlled to be ≤0.5 mm. For preparation of saturated sample, according to the design density, the coral sand sample of the corresponding mass is placed into the pressure chamber of the lateral pressure gauge, and then the lateral pressure gauge is put into the vacuum bucket. The vacuum pump is activated to evacuate the sample for 48 h to achieve a complete saturation.

The test adopts the rapid loading method, with a stabilization duration of 1 h for each level of loading (NSAI, 2017). The gas-free distilled water is selected for the test to ensure that no gas exists in water bladder, which results in a more accurate measurement of the horizontal pressure. The saturated coral sand sample is always covered by water during the testing process, and a certain amount of pre-pressure needs to be applied first to make the sample reach the design compactness prior to the test. The lateral pressure after

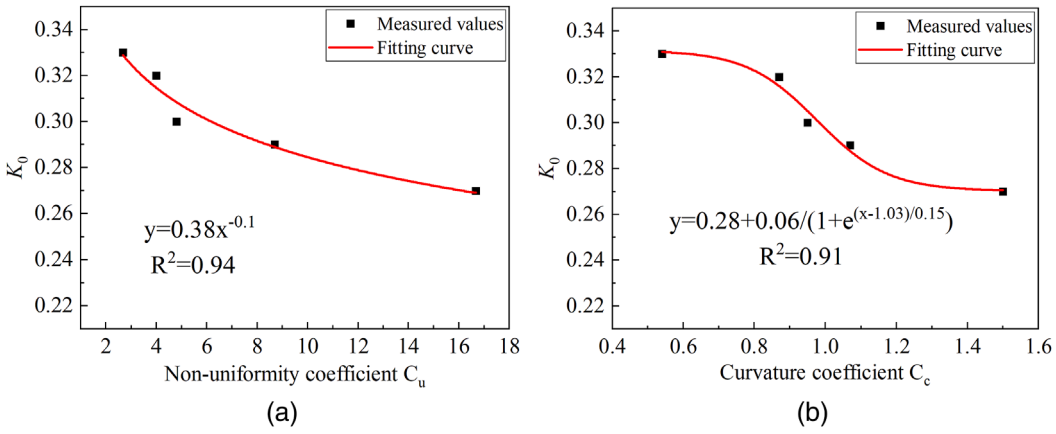


FIGURE 6
Relationship between particle grading and K0 in saturated state.**(a)** K0 versus Cu. **(b)** K0 versus Cc.

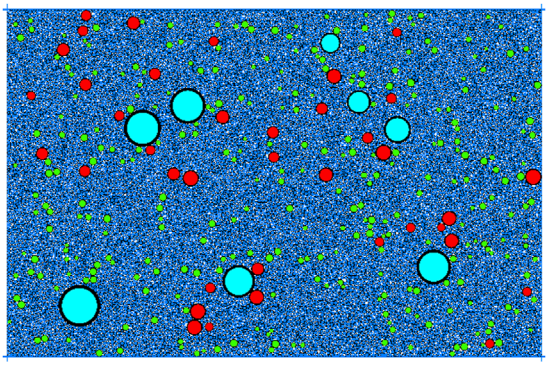

FIGURE 7
Numerical sample of coral sand.

stabilization of each level of load is continuously recorded during the test, and the test is terminated when the deformation under the last level of load is less than 0.005 mm/h. The preloading load is uniformly set at 30 kPa (equivalent to 60% of the minimum formal load of 50 kPa), which has been verified through pre testing as the optimal solution for eliminating sample gaps.

# 3 Results and analysis

## 3.1 K0

The relationships between the horizontal and vertical stresses of samples in dry and saturated states are obtained, respectively, and then the $K_0$ curves of coral sand are determined, as presented in Figure 4.

As indicated in Figure 4, the horizontal stress increases linearly with the increase of vertical stress, which demonstrates a basically constant $K_0$ along the coral sand at different depths. The $K_0$ values of coral sands in dry and saturated states are statistically obtained, as summarized in Table 2.

The values of the $K_0$ of coral powder sand, coral fine and medium sand, as well as coral coarse and gravel sands in dry state are 0.32, 0.25–0.27, and 0.22–0.23, respectively, while those in saturated state are 0.33, 0.30–0.32, and 0.27–0.27, respectively. These values are smaller than the laboratory test results of quartz sand (whose $K_0$ is 0.39–0.47) (Xu et al., 2007) (The test conditions for quartz sand are relative density Dr = 70% and dry state). Also, the $K_0$ values in saturated state are higher than those in dry state. The increase in $K_0$ of saturated coral sand is essentially due to the dual influence of water on the geotechnical system - firstly, pore water forms pressure chambers in the particle gaps, similar to a micro hydraulic system that converts vertical loads into lateral thrust, directly pushing up horizontal stress; Secondly, water molecules wrap around the edges and corners of coral sand to form a lubricating film, weakening the mechanical interlocking friction between particles and making them more prone to rolling adjustment. This lubricating effect further releases the originally locked horizontal stress. The synergistic effect of these two mechanisms results in a significantly stronger horizontal stress response in the saturated state than in the dry state.

## 3.2 Influence of particle gradation on $K_0$

Figures 5, 6 illustrate the relationships between particle gradation and $K_0$ in dry and saturated states, where the quantitative calculation formulas are also presented. The correlation coefficients are all above 0.9, indicating a good correlation between particle gradation and $K_0$ and a high calculation accuracy of the listed formulas. It is observed that the $K_0$ tends to decrease gradually with the increase of coefficient of uniformity and coefficient of curvature. This is due to the fact that with the increase in the gradation range from coral powder sand to coral gravel sand, the requirements of Cc = 1-3 and Cu ≥ 5 are gradually fulfilled, and the particle gradation changes from poor to good. Coarse particles form the skeleton, which is filled by fine particles. The occlusion between particles is

TABLE 3 Meso-scale parameters of numerical sample.

| Type of sand | Friction coefficient | Normal contact stiffness/MN·m$^{-1}$ | Stiffness ratio | Effective modulus/GPa | Cohesion/MPa | Friction angle/(°) |
|---|---|---|---|---|---|---|
| Coral gravel sand | 0.5 | 100 | 1.0 | 0.1 | 0.32 | 43.3 |
| Coral coarse sand | 0.5 | 100 | 1.0 | 0.1 | 0.26 | 43.8 |
| Coral medium sand | 0.5 | 100 | 1.0 | 0.1 | 0.3 | 45.3 |
| Coral fine sand | 0.5 | 100 | 1.0 | 0.1 | 0.28 | 43.5 |
| Coral powder sand | 0.5 | 100 | 1.0 | 0.1 | 0.22 | 41.0 |

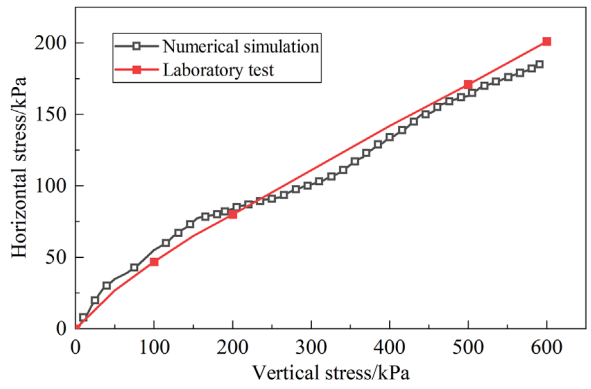


FIGURE 8
Comparison of numerical calculation and laboratory test results.

enhanced while the overall resistance to deformation is increased. Under the vertical load, the horizontal stress is smaller, which leads to a lower $K_0$ value measured. Narrow graded sand (such as silt) has uniform particles, concentrated force chains under vertical loads, and high horizontal stress transmission efficiency, resulting in a K0 of 0.32; Coarse particles form the main skeleton in wide graded sand (such as gravel sand), and fine particles fill the pores to enhance the "three-dimensional interlocking effect", converting more vertical loads into particle interlocking internal forces and reducing horizontal stress release. Therefore, K0 is reduced to 0.22. The decreasing trend of $K_0$ suggests that the magnitude of change of $K_0$ in saturated state is significantly smaller than that in dry state. This is due to the fact that the lubrication of water in coral sand in saturated state reduces the occlusal friction between the particles, which leads to a decrease in the effect of the gradation on the $K_0$.

# 4 Particle flow simulation

## 4.1 Preparation of numerical sample

The existing numerical tests report that the particle size enlargement method has less influence on the mechanical behavior of the material (Evans and Valdes, 2011; Belheine et al., 2009). The simulation in this study uniformly enlarges the particle size by 1.5 times. The numerical test procedure is as follows:

(1) Coral sand particles of the same gradations as those in laboratory tests are generated in a cylinder with a diameter of 61.8 mm and a height of 40 mm. Finally, 7,394 coral gravel sand particles, 10,263 coral coarse sand particles, 14,840 coral medium sand particles, 15,268 coral fine sand particles, and 17,196 coral powder sand particles are generated, respectively.
(2) The particle sample model with a set porosity is firstly developed. Then, a specific pressure is applied to the walls for pre-compression to achieve a homogeneous and dense sample, as illustrated in Figure 7.
(3) The contact between the particles is assigned with a parallel bond model. Relevant parameters are assigned to create a bond between the coral sand particles to simulate their occlusion.
(4) The displacements of the particles are set to zero and the upper wall is compressed with a given velocity to load the numerical sample.

## 4.2 Calibration of meso-scale parameters

This paper utilizes a parallel bond model to simulate the bonding force between the coral sand particles. The parallel bond model can describe the contact characteristics between the bonded particles, where spring components with constant normal and tangential stiffness are distributed within the contact surface of the particles. When the displacement or force between particles exceeds the critical parallel bonding strength, the parallel bonding between particles fails and fracture occurs.

Discrete element numerical simulation requires the input of meso-parameters such as contact stiffness and friction coefficient. Referring to its range in previous numerical experiments (Stratton and Wensrich, 2010; Thompson et al., 2009), the particle normal stiffness in this study is set to 100 MN/m, while the particle stiffness ratio is set to 1.0, which meets the recommended range of 1.0–1.5 by Goldenberg and Goldhirsch (2005). By reverse fitting the key characteristics of the stress-strain curve of the indoor triaxial

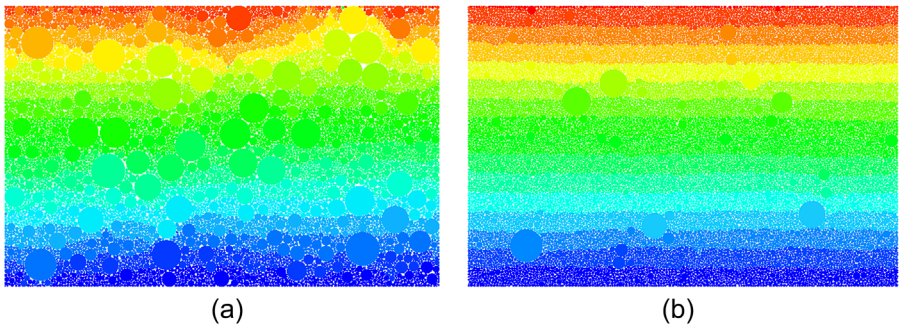


FIGURE 9
Displacement nephograms of coral sand particle.**(a)** coral gravel sand. **(b)** coral powder sand.

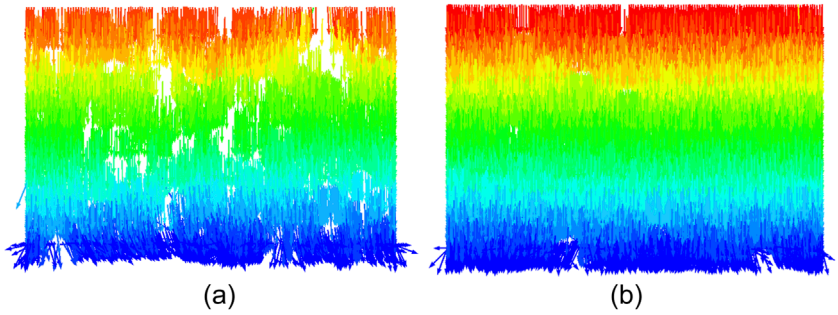


FIGURE 10
Displacement vector diagram of coral sand particles.**(a)** Coral gravel sand. **(b)** Coral powder sand.

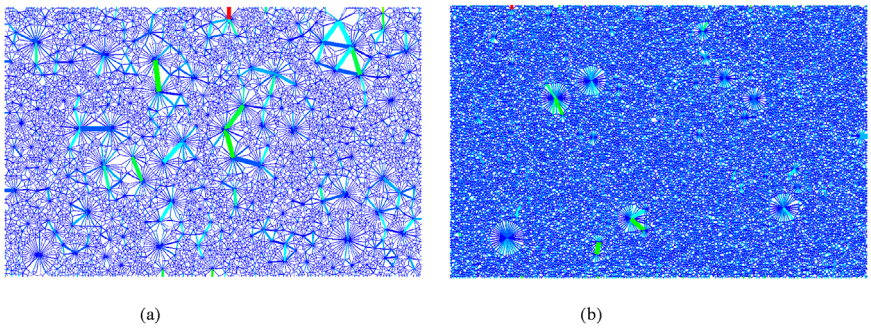


FIGURE 11
Distribution of contact force chains of coral sand particles. **(a)** Coral gravel sand. **(b)** Coral powder sand.

test, it is achieved that the basic microscopic parameters (friction coefficient, stiffness, etc.) are first fixed, and then the cohesion and friction angle are gradually adjusted to make the peak stress, residual strength trend, and elastic segment slope simulated by PFC consistent with the test curve. The iterative process aims to match the overall shape of the curve, and the final parameter values are listed in Table 3 after multiple verifications.

# 5 Numerical simulation results

## 5.1 Comparison with laboratory tests

Figure 8 presents the comparison between the numerical and experimental results regarding the relationship between the horizontal and vertical stresses for coral powder sand. It is

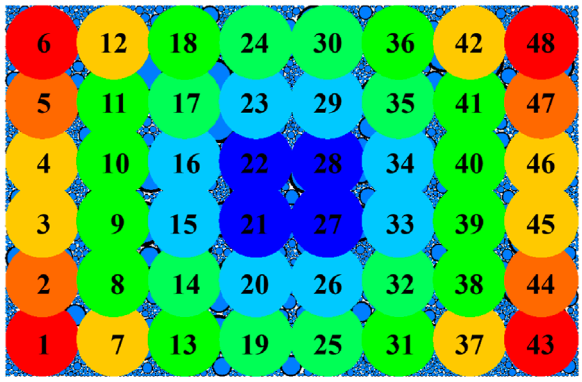


FIGURE 12
Schematic diagram of the position of measurement circles.

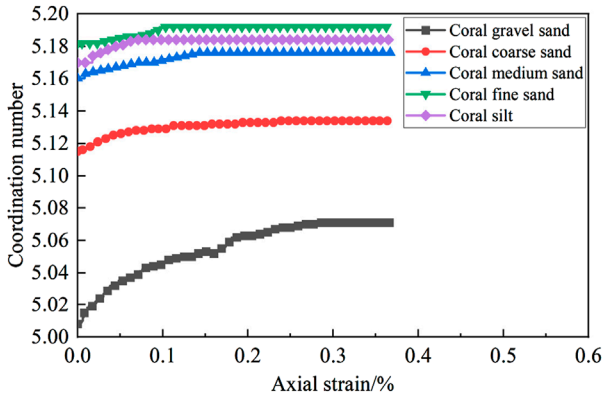


FIGURE 13
Evolution curve of coordination number.

observed that there is only a minimal discrepancy between the $K_0$ values obtained from numerical simulations and laboratory tests, indicating a high overall agreement between the two results. This verifies the feasibility of numerical simulation and the rationality of calibrated meso-parameters. An in-depth analysis of the numerical simulation results can be conducted based on this foundation.

## 5.2 Meso-scale evolutionary laws

### 5.2.1 Variation of displacement nephogram

Figure 9 displays the displacement nephograms of coral gravel sand and coral powder sand, where the red and blue regions represent the largest and smallest displacements, respectively. The applied vertical load causes the particles at the top of the sample to be continuously compressed downward, producing downward displacement. The particle displacement in the nephogram decreases gradually from top to bottom, which corresponds to the observation that the compression of the sample decreases gradually from top to bottom in the laboratory test. Comparison of the two displacement nephograms (a) and (b) in Figure 9 identifies an obvious horizontal stratification of the displacement for coral powder sand, which exhibits an overall compression characteristic. This is due to the fact that the smaller difference in particle sizes of coral sand, the weaker dislocation occlusion between particles, and the small differences in motion states of neighboring particles produce an overall downward compression feature. As the gradation of coral gravel sand becomes wider, the difference in particle size is larger. As a result, the particles are more prone to embedded dislocation occlusion, leading to a complex variation pattern of displacement field.

Figure 10 depicts the particle displacement vector diagram of coral gravel sand and coral powder sand, indicating a general downward movement trend for coral powder sand particles. In the bottom part of the sample, particles tend to move horizontally. Due to its wide grain size distribution, there is a certain amount of large-grain particles in coral gravel sand, while filling and interlocking between coarse and fine grains lead to more horizontal movements of particles. This also explains the mechanism of compressive deformation of coarse-grained soils from a meso-scale point of view, i.e., the deformation mainly consists of embedded occlusion and dislocation filling between coarse and fine particles.

### 5.2.2 Distribution of contact force chains

Figure 11 illustrates the distribution of contact force chains within the coral sand sample. The redder the color and the thicker the force chain, the greater the contact force; while the bluer the color and the thinner the force chain, the smaller the contact force. It is observed that gradient distribution of contact force inside the coral gravel sand with a wider gradation is more obvious, while magnitude range of contact force varies greatly, and the direction of contact force is distributed within 360°, which confirms a stronger embedded occlusion between the particles inside the coral gravel sand with a wider gradation. Most of the contact force chains of the internal particles of the coral gravel sand with a narrower gradation are blue, which represents a more concentrated distribution of the contact force, indicating a weaker occlusion between the internal particles of the coral gravel sand with a narrower gradation.

### 5.2.3 Evolution laws of coordination number

The coordination number reflects the average contact number per ball. The specific definition is presented in Equation 1:

$$C_{\mathrm{n}} = \frac{\sum_{N_{grain}} n_i^c}{N_{grain}} \quad i = 1, 2, \ldots, N_{grain} \tag{1}$$

To accurately obtain the number of contacts inside the sample, 48 measurement circles are arranged inside it, as depicted in Figure 12. The coordination number inside the sample is obtained by averaging the data from the measurement circles.

Figure 13 illustrates the evolution curve of coordination number inside the sample. It is observed that the coral gravel sand has the smallest coordination number, while the coral powder sand has the largest one. As the gradation of coral sand gradually narrows from coral gravel sand to coral powder sand, the coordination number gradually increases. This is mainly due to the difference in the number of particles among the five gradations of coral sands, with narrower gradations having more particles and therefore larger coordination numbers. Also, as the sample is compacted, the

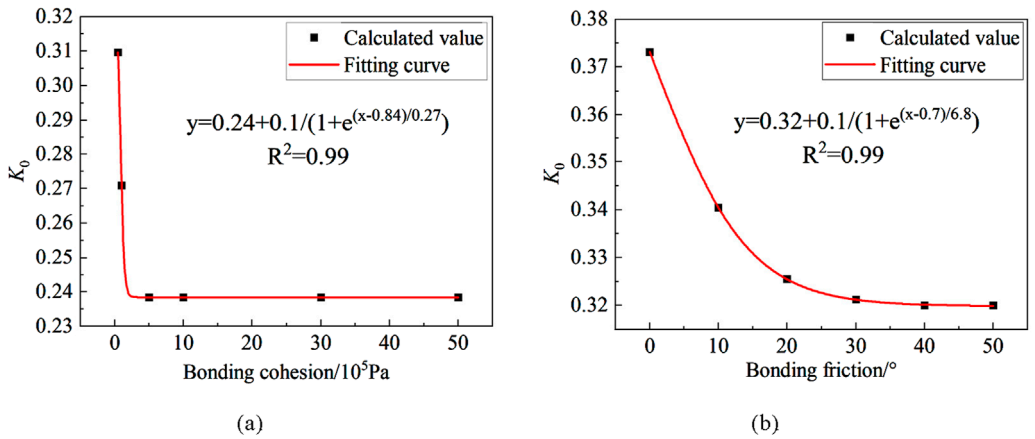


FIGURE 14
Relationship between bonding strength and K0.**(a)** K0 versus bonding cohesion. **(b)** K0 versus bonding friction angle.

TABLE 4 Calculation results of $K_0$.

| Ref. | Calculation method | Type of coral sand | Calculate results based on peak internal friction angles |
|---|---|---|---|
| Jaky (1944) | $K_0 = 1 - \sin\varphi'$ | Coral gravel sand | 0.31 |
| | | Coral coarse sand | 0.31 |
| | | Coral medium sand | 0.29 |
| | | Coral fine sand | 0.31 |
| | | Coral powder sand | 0.34 |
| Rowe (1957) | $K_0 = \tan^2\left(45° - \frac{\varphi_c}{2}\right)$ | Coral gravel sand | 0.09 |
| | | Coral coarse sand | 0.09 |
| | | Coral medium sand | 0.08 |
| | $\varphi_C = 1.5\varphi' - 9°$ | Coral fine sand | 0.09 |
| | | Coral powder sand | 0.12 |
| Hendron and Alfred (1963) | $K_0 = \frac{1+\frac{\sqrt{5}}{8}-3\frac{\sqrt{5}}{8}\sin\varphi'}{1-\frac{\sqrt{5}}{8}+3\frac{\sqrt{5}}{8}\sin\varphi'}$ | Coral gravel sand | 0.54 |
| | | Coral coarse sand | 0.54 |
| | | Coral medium sand | 0.52 |
| | | Coral fine sand | 0.54 |
| | | Coral powder sand | 0.57 |
| Sag and lamer (1975) | $K_0 = 0.97(1 - 0.97\sin\varphi')$ | Coral gravel sand | 0.32 |
| | | Coral coarse sand | 0.32 |
| | | Coral medium sand | 0.30 |
| | | Coral fine sand | 0.32 |
| | | Coral powder sand | 0.35 |

(Continued on the following page)

TABLE 4 (*Continued*) Calculation results of $K_0$.

| Ref. | Calculation method | Type of coral sand | Calculate results based on peak internal friction angles |
|---|---|---|---|
| Rymsza (1979) | $K_0 = \tan^2\left(45^o - \frac{\varphi'}{3}\right)$ 2/3 of the shear strength is exerted | Coral gravel sand | 0.35 |
| | | Coral coarse sand | 0.34 |
| | | Coral medium sand | 0.33 |
| | | Coral fine sand | 0.35 |
| | | Coral powder sand | 0.37 |
| Bloton (1979) | $K_0 = \frac{1-\sin(\varphi'-11.5^o)}{1+\sin(\varphi'-11.5^o)}$ | Coral gravel sand | 0.31 |
| | | Coral coarse sand | 0.30 |
| | | Coral medium sand | 0.29 |
| | | Coral fine sand | 0.31 |
| | | Coral powder sand | 0.34 |
| Measured values | | Coral gravel sand | 0.22 |
| | | Coral coarse sand | 0.23 |
| | | Coral medium sand | 0.25 |
| | | Coral fine sand | 0.27 |
| | | Coral powder sand | 0.32 |

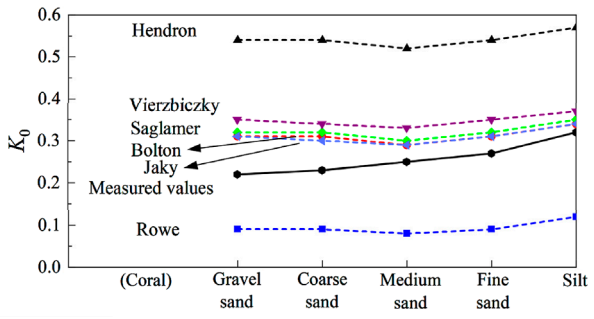


FIGURE 15
Comparison between the calculated and measured K0 values.

coordination number inside the sample increases and eventually stabilizes. The coral gravel sand with a wider gradation has the largest increase in coordination number, indicating better compaction of the sample, which corresponds to the larger compression observed in macroscopic compression tests of samples with wider gradations.

## 5.3 Influence of bonding strength on $K_0$

Coral sand particles are angular with irregular shapes, and exhibit relatively strong inter-particle cohesion, which is characterized by the bonding strength in PFC simulation. To study the influence of bonding cohesion on $K_0$, $K_0$ tests are conducted under six different bonding cohesion cases of $5 \times 10^4$, $1 \times 10^5$, $5 \times 10^5$, $1 \times 10^6$, $3 \times 10^6$, and $5 \times 10^6$ Pa. The particle gradation of coral powder sand is used for all cases, and the other meso-scale parameters are the same as those in Table 3. The obtained $K_0$ values for different bonding cohesions are presented in Figure14a. It is evident that as the inter-particle cohesion increases, the $K_0$ value of coral sand gradually decreases. Once the cohesion exceeds $1 \times 10^5$ Pa, the $K_0$ tends to stabilize gradually and finally remain unchanged as cohesion increases. The relationship between them approximately follows an exponential function relationship, as depicted by the red fitted curve.

To explore the influence of bonding friction angle on $K_0$, $K_0$ tests are conducted under six different bonding friction angle cases of 0°, 10°, 20°, 30°, 40°, and 50°. The particle gradation of coral powder sand is used for all cases, and the other meso-scale parameters are the same as those in Table 3. The obtained $K_0$ values for different bonding friction angles are displayed in Figure14b. It is observed that the $K_0$ of coral sand gradually decreases as the inter-particle bonding friction angle increases. When the friction angle is greater than 30°, the $K_0$ tends to stabilize gradually with minimal change in magnitude as friction angle increases. The relationship between the $K_0$ and the bonding friction angle approximately satisfies an exponential function relationship, as indicated by the red fitted curve.

TABLE 5 Distribution coefficient values and accuracy.

| Coral sand | Distribution coefficient $\varpi$ | Calculated value | Measured value | Error |
|---|---|---|---|---|
| Coral gravel sand | 0.4 | 0.22 | 0.22 | −0.9% |
| Coral coarse sand | 0.4 | 0.22 | 0.23 | 6.1% |
| Coral medium sand | 0.2 | 0.25 | 0.25 | 0.8% |
| Coral fine sand | 0.2 | 0.27 | 0.27 | 1.5% |
| Coral powder sand | 0.1 | 0.32 | 0.32 | 0.6% |

## 6 Calculation formula for $K_0$

A large number of research results have been achieved for calculation methods of $K_0$ for land-sourced sandy soils, which are detailed in Table 4. These $K_0$ values are generally applicable for small deformation scenarios. The peak internal friction angles gained from triaxial compression tests (Zhang et al., 2023) (see Table 3) are substituted into the six theoretical formulas mentioned to verify their applicability in the highly deformed coral reef debris layer. A comparison of the calculated $K_0$ values with the measured values is presented in Table 4 and Figure 15. Among them, the theoretical calculated $K_0$ values by five formulas are higher than the measured values, while only the theoretical formulae proposed by Rowe (based on the shear strength exertion angle) gives smaller calculated values than the measured values, which reveal that the particle occlusion and the difficulty of particle rotation are the reasons for the low $K_0$ value (Yuhang et al., 2021).

Considering that the measured $K_0$ values of coral sand are between the theoretically calculated values proposed by Rowe (1957) and Bloton (1979), a formula for calculating the $K_0$ based on the distribution coefficient and the strength parameter is proposed, as presented in Equation 2, where $\varpi$ is the distribution coefficient.

$$K_0 = (1-\varpi)\tan^2\left(45^o - \frac{\varphi_c}{2}\right) + \varpi\frac{1-\sin\left(\varphi' - 11.5^o\right)}{1+\sin\left(\varphi' - 11.5^o\right)} \quad (2)$$

Based on the measured data, the suggested values of the distribution coefficients for coral powder sand, coral fine and medium sands, as well as coral coarse and gravel sands are 0.1, 0.2, and 0.4, respectively. Table 5 presents a comparison between the calculated values obtained from the proposed formula and the measured values with the dry coral sands as examples. The maximum error observed is only 6.1%, which demonstrates the high accuracy of the calculation formula.

## 7 Conclusion

This study analyzes the influence of particle gradation on the $K_0$ by performing laboratory experiments and PFC particle flow simulations on coral sands with five typical gradations. The macroscopic test mechanism is revealed from a meso-perspective, and the influence of bonding strength on the $K_0$ is derived. A formula for calculating the $K_0$ of coral sand is established based on the experimental results. The conclusions are as follows:

(1) The $K_0$ values of coral sands in dry state range from 0.22 to 0.32, while that in saturated state range from 0.27 to 0.33. The $K_0$ in saturated state is higher than that in dry state, but the $K_0$ of coral sand is smaller than land-sourced sand. There is an exponential function relationship between the particle gradation of coral sand and the $K_0$. With the increase of the coefficient of inhomogeneity and the coefficient of curvature, the $K_0$ decreases gradually. The rate of change of $K_0$ in saturated state is obviously smaller than that in dry state.

(2) The particle flow numerical model reveals that coral sand with a narrower gradation is more likely to exhibit horizontal stratification and overall compression characteristics at meso-scale. As the gradation gradually becomes wider, the stratification and compression characteristics are gradually weakened, and the particles manifest stronger dislocation occlusion. The contact force chains demonstrate a more obvious gradient distribution for coral sand with a wider gradation, with contact forces being distributed in all directions, while the distribution of contact force chains is more concentrated for the coral sand with a narrower gradation. The coordination number inside the coral sand with a wider gradation is smaller, but it experiences a larger changing amplitude under the action of vertical force, which is macroscopically manifested as more significant volume compression effect.

(3) As the bonding strength (cohesion and friction angle) increases, $K_0$ gradually decreases, but it no longer changes after the bonding strength reaches a threshold. The relationship between the bonding strength and the $K_0$ approximately follows an exponential function. The theoretical formula with the highest computational accuracy is preferred on the basis of the existing formulas for calculating the $K_0$ of land-sourced sand and the lower $K_0$ value for coral sand. Furthermore, the distribution coefficient is introduced to propose a formula for calculating the $K_0$ based on the distribution coefficient and the strength parameter. A comparison of calculated values

with measured values demonstrates the high computational accuracy of this formula.

## Data availability statement

The original contributions presented in the study are included in the article/supplementary material, further inquiries can be directed to the corresponding author.

## Author contributions

RZ: Formal Analysis, Methodology, Software, Writing – original draft, Visualization. YoZ: Project administration, Conceptualization, Writing – review and editing, Supervision. PC: Writing – review and editing. FJ: Resources, Writing – review and editing. HL: Data curation, Writing – review and editing. YuZ: Writing – review and editing, Funding acquisition.

## Funding

The author(s) declare that financial support was received for the research and/or publication of this article. This research was funded by the Natural Science Foundation of Hubei Province of China (Grants No. 2023AFB508 and 2025AFB432).

## Conflict of interest

Authors RZ, YoZ, PC, FJ, HL, and YuZ were employed by CCCC Second Harbor Engineering Company Ltd.

## Generative AI statement

The author(s) declare that no Generative AI was used in the creation of this manuscript.

## Publisher's note

All claims expressed in this article are solely those of the authors and do not necessarily represent those of their affiliated organizations, or those of the publisher, the editors and the reviewers. Any product that may be evaluated in this article, or claim that may be made by its manufacturer, is not guaranteed or endorsed by the publisher.

## References

Belheine, N., Plassiard, J. P., Donzé, F. V., Darve, F., and Seridi, A. (2009). Numerical simulation of drained triaxial test using 3D discrete element modeling. *Comput. Geotechnics* 36 (1-2), 320–331. doi:10.1016/j.compgeo.2008.02.003

Bloton, M. (1979). *A guide to soil mechanics*. London: Macmillan.

CCCC Second Navigation Engineering Survey and Design Institute (2022). *JTS133. Specification for geotechnical investigation of water transport engineering (partial revision) - coral reef geotechnical investigation*. Beijing: Beijing People's Communications Publishing House.

Chen, Y. Y., Tang, Y., Guan, Y. F., Liu, R. M., Han, X., Zhao, X., et al. (2022). Study on the mechanical properties of coral sands with different particle gradations. *Marine Georesources and Geotechnology*, 41 (3), 327–338. doi:10.1080/1064119X.2022.2037112

Donohue, S., O'sullivan, C., and Long, M. (2009). Particle breakage during cyclic triaxial loading of a carbonate sand. *Géotechnique* 59 (5), 477–482. doi:10.1680/geot.2008.T.003

Evans, T. M., and Valdes, J. R. (2011). The microstructure of particulate mixtures in one-dimensional compression: numerical studies. *Granul. Matter* 13 (5), 657–669. doi:10.1007/s10035-011-0278-z

Goldenberg, C., and Goldhirsch, I. (2005). Friction enhances elasticity in granular solids. *Nature* 435 (7039), 188–191. doi:10.1038/nature03497

Hendron, J., and Alfred, J. (1963). *The behavior of sand in one-dimensional compression*. Illinois: University of Illinois.

Jaky, I. (1944). The coefficient of Earth pressure at rest. *J. Soc Hung. Archit. and Eng.* doi:10.1139/t93-056

Meng, Q. S., Yu, K. F., Wang, R., Qin, Y., Wei, H. Z., and Wang, X. Z. (2014). Characteristics of rocky basin structure of yongshu reef in the southern South China Sea. *Mar. Georesources and Geotechnol.* 32 (4), 307–315. doi:10.1080/1064119x.2013.764553

Michalowski, R. L. (2005). Coefficient of earth pressure at rest. *Journal of geotechnical and geoenvironmental engineering* 131 (11), 1429–1433. doi:10.1061/(ASCE)1090-0241(2005)131:11(1429)

NSAI (2017). *Code for soil test of hydropower and water conservancy engineering (DL-T5355-2006)*.

Rowe, P. (1957). "Ce = 0 hypothesis for normally loaded clays at equilibrium," in *Proceedings of the fourth international conference on soil mechanics and*. London: Foundation Engineering, 189–192.

Rymsza, B. (1979). "Earth pressure at rest in design of retaining structures," in *Proceedings of 7th European conference on Soi1 mechanics and*. Brighton: Foundation Engineering, 35–40.

Saglamer, A. (1975). "Soil parameters affecting coefficient of Earth pressure at rest of cohesionless soils," in *Proceedings of istanbul conference on soil mechanics and*. Istanbul: Foundation Engineering, 34–41.

Smith, D. A., and Cheung, K. F. (2003). Settling characteristics of calcareous sand. *J. Hydraulic Eng.* 129 (6), 479–483. doi:10.1061/(asce)0733-9429(2003)129:6(479)

Stratton, R. E., and Wensrich, C. M. (2010). Modelling of multiple intra-time step collisions in the hard-sphere discrete element method. *Powder Technol.* 199 (2), 120–130. doi:10.1016/j.powtec.2009.12.008

Thompson, N., Bennett, M. R., and Petford, N. (2009). Analyses on granular mass movement mechanics and deformation with distinct element numerical modeling: implications for large-scale rock and debris avalanches. *Acta Geotech.* 4 (4), 233–247. doi:10.1007/s11440-009-0093-4

Wang, C., Liu, H., Ding, X., Wang, C., and Ou, Q. (2021). tudy on horizontal bearing characteristics of pile foundations in coral sand. *Canadian Geotechnical Journal*, 99 (999), 1928–1942. doi:10.1139/cgj-2020-0623

Wang, X. Z., Wang, X., Jin, Z. C., Meng, Q. S., Zhu, C. Q., and Wang, R. (2017). Shear characteristics of calcareous gravelly soil. *Bull. Eng. Geol. Environ.* 76, 561–573. doi:10.1007/s10064-016-0978-z

Wang, X., Zhu, C. Q., and Wang, X. Z. (2020). Experimental study on the coefficient of lateral pressure at rest for calcareous soils. *Marine Georesources and Geotechnology*, 38 (8), 989–1001. doi:10.1080/1064119X.2019.1646361

Xu, L. J., Wang, X., Wang, R., Zhu, C. q., and Liu, X. p. (2022). Physical and mechanical properties of calcareous soils: a review. *Mar. Georesources and Geotechnol.* 40 (6), 751–766. doi:10.1080/1064119x.2021.1927270

Xu, Z.-w., Zhou, G.-q., Liu, Z.-q., Zhao, X.-d., Li, S.-s., Zhang, L., et al. (2007). Study on the Test Method of Static Earth Pressure Coefficient of Deep Soils. *Journal of China University of Mining and Technology*, 17 (3), 330–334. doi:10.1016/S1006-1266(07)60099-6

Yuhang, T., Zhong, C., Weixia, H., Zhengyu, H., Wen, Y., Xuesong, W., et al. (2021). P-wave velocity properties and its influencing factors of coral reef limestone in Nansha area. *Journal of Tropical Oceanography*, 40 (1), 133–141. doi:10.11978/2020015

Zhang, J., Shamoto, Y., and Tokimatsu, K. (1998). Evaluation of earth pressure under any lateral deformation. *Soils and foundations*, 38 (1), 15–33. doi:10.3208/sandf.38.15

Zhang, Y., Zhang, R., Yu, C., Luo, H., and Deng, Z. (2023). Study on shear characteristics of calcareous sand with different particle size distribution. *Front. Earth Sci.* 11, 1163930. doi:10.3389/feart.2023.1163930

frontiers | Frontiers in Earth Science

TYPE Original Research
PUBLISHED 08 August 2025
DOI 10.3389/feart.2025.1633717



OPEN ACCESS

EDITED BY
Pengfei Liu,
CCCC Second Harbor Engineering Co., Ltd., China

REVIEWED BY
Yipeng Xie,
Ocean University of China, China
Zhen Huang,
Guangxi University, China
Han Feng,
Shijiazhuang Tiedao University, China

*CORRESPONDENCE
Lei Cao,
m18874177214@163.com

RECEIVED 23 May 2025
ACCEPTED 16 June 2025
PUBLISHED 08 August 2025

CITATION
Zhan S, Lu L, Liu Z, Zhou J, Chen Y and Cao L (2025) Mechanism of water plugging by dynamic grouting with self-expanding slurry in karst tunnels.
*Front. Earth Sci.* 13:1633717.
doi: 10.3389/feart.2025.1633717



# Mechanism of water plugging by dynamic grouting with self-expanding slurry in karst tunnels

Shuangqiao Zhan[1], Lifeng Lu[2], Ziyan Liu[3], Jun Zhou[2], Yuncai Chen[1] and Lei Cao[4,5]*

[1]Hunan Water Resources and Hydropower Survey, Design, Planning and Research Co., Ltd., Changsha, China, [2]Hunan Provincial Water Resources Development and Investment Co., Ltd., Changsha, China, [3]School of Civil Engineering, Central South University of Forestry and Technology, Changsha, China, [4]School of Water Resources and Hydropower, Hunan Polytechnic of Water Resources and Electric Power, Changsha, China, [5]Hunan Engineering Research Center of Intelligent Inspection and Digital Maintenance for Hydraulic Engineering, Changsha, China

Clarifying the mechanism of grouting to block karst water outbursts is essential for ensuring effective sealing. This article studies the grouting blocking problem related to the prevention and control of water surge disasters in karst tunnels, focusing on the grouting blocking mechanism of efficiently plugs expanding material (EPEM) under dynamic water conditions. We propose a grouting diffusion formula and blocking criterion that take into account the self-expanding properties of the slurry. First, based on the equilibrium relationship between the friction force and anti-splitting force between the blocking body and the rock wall, we establish an effective blocking condition. Second, by combining capillary theory with Newton's fluid constitutive equation, we derive the diffusion distance formula for self-expanding slurry under dynamic water conditions. We then construct a mechanical model that uses the length of the critical blocking body as a criterion, revealing the coupling influences of groundwater pressure, grouting pressure, and grouting time. The results indicate that groundwater pressure is positively correlated with grouting pressure and grouting time, while grouting pressure is negatively correlated with grouting time. Finally, we verify the practicality of the proposed criterion through the project at Quanmutang Reservoir in Hunan Province, successfully implementing a parameter combination of 0.5 MPa grouting pressure and 20 min of grouting time to block surge water. This research provides a theoretical basis and engineering guidance for designing water surge grouting in karst tunnels.

KEYWORDS

**karst tunnel, surge water, self-expanding slurry, grouting plugging, dynamic water conditions, plugging criterion**

## 1 Introduction

The construction of transportation infrastructure has entered a phase of rapid growth in China. New projects increasingly exhibit distinctive characteristics due to harsher construction environments, more complex geological conditions, and a higher frequency of disasters and accidents. These challenges are particularly pronounced in

tunnel engineering, especially regarding adverse geological conditions. Notably, surge water disasters in karst regions have become a significant bottleneck in the development of China's transportation infrastructure due to their unpredictable nature, high potential for damage, prolonged duration, and the difficulties associated with post-disaster management. Currently, the grouting method is regarded as the most effective technical solution for preventing and controlling tunnel surge water disasters in karst areas. The key to its effectiveness lies in the careful selection of grouting parameters and the type of grouting materials used.

Extensive engineering practice has shown that surging water disasters not only threaten the safety of life and property for construction personnel but also cause serious damage to groundwater systems. Currently, scholars in China and around the world have conducted extensive research on the mechanisms of grouting and plugging. In terms of model testing, Wanghua et al. (2015) investigated the influence of four factors (fracture width, slurry gelation time, water flow rate, and grouting volume) on grouting plugging and summarized their effects. Chen et al. (2019) established a large-scale visualization experimental system based on similarity criteria, which revealed the plugging mechanism of fibers and particles in hydraulic fracturing. Liu et al. (2024) designed and constructed an experimental system to simulate the grouting plugging of surge water in karst pipelines and analyzed the influence of various factors on the effectiveness of grouting plugging. Pan et al. (2022) developed a pipeline-type grouting plugging simulation experimental system and investigated the mechanism of flowing water grouting plugging under controlled flow conditions. Shucai et al. (2020) derived numerical openness as a function of flow rate in the pipeline after implementing flow control, using their self-developed karst pipeline model test system.

Considering the shortcomings of indoor and outdoor model tests, such as size effects and the difficulty of achieving large sample sizes, researchers have conducted extensive studies on the grouting plugging mechanism of tunnel surge water using numerical simulations, which facilitate the research process. Chengyuan et al. (2021) employed the coupled computational fluid dynamics/discrete element method (CFD-DEM) method to simulate the formation of the fissure blocking zone and revealed the evolution mechanism of its structure. Haiyan et al. (2020) investigated the blocking mechanism of pipelines through numerical simulation, analyzing the changes in the slurry flow rate during the grouting process. Liu et al. (2017) used the multi-physics coupling software COMSOL Multiphysics to establish a numerical model for the diffusion of fissure grouting under dynamic water conditions, examining the influence of initial dynamic water flow rate, grouting rate, and time-varying viscosity on the diffusion process. Yang et al. (2020) utilized a CFD-DEM model for dynamic simulations, revealing the transport behavior, dynamic aggregation, and blocking mechanism of nanoparticles intruding into the pore spaces of shale. Lastly, Xu (Zhenhao et al., 2021) conducted a numerical simulation study on flow control technology for flowing water grouting plugging in karst pipes. The theoretical analysis method is straightforward due to its derivation process, allowing certain assumptions to be avoided in many cases. Consequently, more scholars are adopting this method. For example, Wang et al. (2018) proposed grouting plugging guidelines for conditions of moving water, identifying key construction parameters and processes for tunnel surge water grouting. Haiyan et al. (2021) systematically studied the dynamic water plugging mechanism under conditions of high flow rates in karst pipelines, focusing on flow control and deceleration. Additionally, Shucai et al. (2020) analyzed slurry diffusion processes at various flow rates, exploring the impacts of flow rate, grouting pressure, and countercurrent diffusion distance on slurry behavior under dynamic water conditions. Wang et al. (2018) conducted an in-depth investigation into the mechanisms of slurry diffusion and plugging in dynamic water grouting. Finally, Yalei et al. (2024) established a theoretical analytical model for grouting diffusion decay and examined the effects of the closure mechanism in multi-jointed fissured rock bodies. Scholars have conducted more in-depth research on the mechanism of tunnel surge water grouting and plugging; however, there is a lack of relevant research on the pipeline-type grouting plugging mechanism. Consequently, existing knowledge and research findings cannot directly guide tunnel surge water self-expanding material grouting projects in karst areas.

This article first analyzes the effective conditions for grouting plugging from the perspective of the relationship between the plugging body and the rock wall. It combines the single-pipe flow formula and considers the self-expansion effect of the slurry to derive the formula for the diffusion of self-expanding slurry grouting. Second, the friction between the plugging body and the contact surface of the surge water channel is used as a basis for constructing a mechanical calculation model, which proposes the grouting blocking criterion. Lastly, by examining the influence of groundwater pressure on grouting parameters, this study explores the influence mechanism of the grouting plugging criterion for tunnel surge water in karst areas.

## 2 The plugging mechanism of dynamic water grouting

### 2.1 Analysis of effective grouting plugging conditions

The efficiently plugs expanding material (EPEM) injected into the surge water pipeline will quickly undergo gelatinization and solidification to form a blocking body when it contacts water. The success of the grouting process relies primarily on the gelatinization and solidification of the EPEM after it forms the blocking body, as well as the maximum static friction ($f$) between the blocking body and the rock wall in relation to the water pressure ($P_w$).

Due to the action of water pressure, the grouting blocking body may experience splitting. Even if the maximum static friction of the blocking body is sufficient to resist the water pressure, if the water pressure exceeds the splitting force of the blocking body, cracks will form, leading to the failure of water plugging. Therefore, the rock wall should be considered in an ideal horizontal state with no bulge, and it should be analyzed under the following two conditions. The schematic diagram of blocking criterion is schematically shown in Figure 1.

(1) When the maximum static friction of the grouted plugging body ($f$) exceeds the splitting force of the plugging body ($f_p$), the grouted plugging body may crack under the action of water pressure. This cracking can cause the plugging body to split

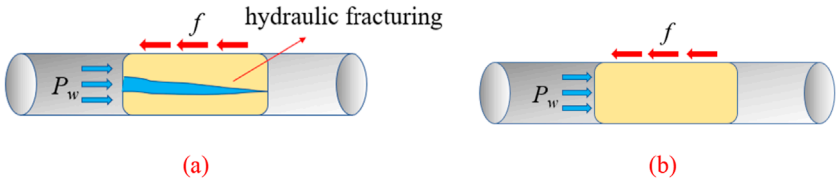


FIGURE 1
Schematic diagram of blocking criterion. **(a)** Maximum static friction $f$ > blocking body splitting force $f_p$. **(b)** Maximum static friction $f$ < blocking body splitting force $f_p$.

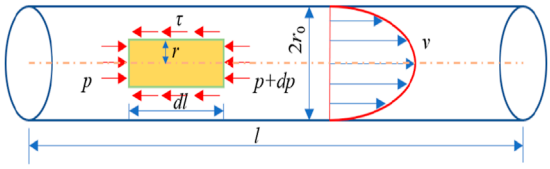


FIGURE 2
Schematic of slurry microelement forces.

and lead to failure in water blocking. Therefore, the successful criterion for grouted plugging should satisfy the condition of $f_p > P_w$.

(2) When the maximum static friction of the grouting blocking body ($f$) is less than the cleavage resistance of the blocking body ($f_p$), there will be no water pressure causing cleavage in the blocking body. In this case, the success criterion for grouting blocking should be that $f > P_w$.

## 2.2 Derivation of the grout diffusion equation for surge water

### 2.2.1 Basic assumptions

① EPEM is an incompressible Newtonian fluid, and changes in the fluid flow pattern during the grouting process are not considered
② the fluid movement in the pipeline is assumed to be laminar flow
③ the fluid is immiscible with the water body, and there exists a front at the leading edge of the fluid.

### 2.2.2 Model construction and derivation

The conduit pipe is idealized as a smooth and undulating pipe, as shown in Figure 2. In the figure, $l$ is the length of the pipe, $dl$ is a microelement segment of the slurry; is the shear stress; $r_0$ is the radius of the pipe; $v$ is the slurry flow rate; $p$ is the driving pressure; $r$ is the radius of the grout's microelement.

The Newtonian fluid slurry eigenstructure equation is as follows:

$$\tau = -\mu_s \gamma = -\mu_s \frac{dv}{dr}, \tag{1}$$

where $\mu_s$ is slurry viscosity, and Pa·s; $\gamma$ is shear rate, $s^{-1}$.

The force analysis of the EPEM microelement is carried out, and the mechanical equilibrium equation is given.

$$2\tau\pi r dl + (p + dp)\pi r^2 = p\pi r^2 \tag{2}$$

Equation 2 can be simplified as

$$\tau = -\frac{r}{2}\frac{dp}{dl} \tag{3}$$

Equations 1, 3 are obtained.

$$dv = -\frac{r}{2\mu_s}\frac{dp}{dl}dr \tag{4}$$

Integrating Equation 4 with the boundary condition $r = r_0$ gives $v = 0$, Equation 5 is obtained.

$$v = \frac{1}{4u_s}\frac{dp}{dl}(r_0^2 - r^2) \tag{5}$$

Integrating the slurry velocity in the pipe gives the slurry flow rate, Equation 6 is obtained.

$$q = \int_0^{r_0} 2\pi r v dr = \frac{\pi r_0^4}{8\mu_s}\frac{dp}{dl} \tag{6}$$

Solve for the slurry flow rate in the pipe as:

$$v = \frac{q}{\pi r_0^2} = \frac{r_0^2}{8\mu_s}\frac{dp}{dl} \tag{7}$$

The joint Equation 3, Equation 7 can be obtained as the pipe wall shear stress:

$$\tau = -v\frac{4\mu_s}{r_0} \tag{8}$$

EPEM was injected into the conduit to displace groundwater flow, as shown in Figure 3.

The force on the slurry can be analyzed using Newton's second law:

$$ma = F + f \tag{9}$$

where m is the mass of the slurry, $m = \rho_s(l_s + dl_s)\pi r_0^2$; $\rho_s$ is the density of slurry, $g/cm^3$; $\rho_w$ is the density of the groundwater; a is acceleration, $a = d^2 l_s/dt^2$; F is the differential pressure on the slurry, $F = \pi r_0^2(P_0 - P_w)$; P0 is the grouting pressure, MPa; Pw is the groundwater pressure, MPa; f is the frictional resistance, $f = 2\pi r_0 \tau_s(l_s + dl_s)$.

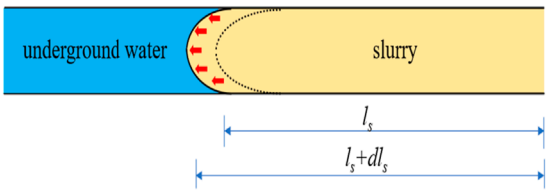


FIGURE 3
Schematic of slurry flow in the pipe.

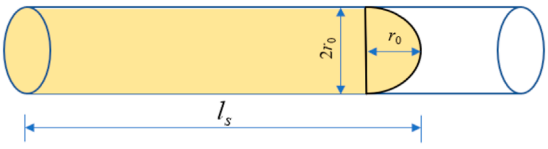


FIGURE 4
Schematic of slurry diffusion in the pipe.

Equation 9 can be written as

$$[\rho_s(l_s + dl_s)\pi r_0^2]\frac{d^2 l_s}{dt^2} = \pi r^2(P_0 - P_w) + 2\pi r_0 \tau_s(l_s + dl_s) \tag{10}$$

EPEM is moving in a laminar flow in the pipe. $a = \frac{d^2 l_s}{dt^2} \approx 0$, associative Equations 8, 10 are obtained:

$$v = \frac{r_0^2(P_0 - P_w)}{8\mu_s l_s} \tag{11}$$

Assuming that EPEM diffuses in the pipe as a column-hemisphere model, and also considering the self-expansion effect of EPEM, as shown in Figure 4, the relationship between the flow rate and the grouting volume is

$$\begin{cases} q = v\pi r_d^2 \\ Q = qt = \left[\pi r_0^2(l_s - r_0) + \frac{2}{3}\pi r_0^3\right]K \end{cases} \tag{12}$$

where $v$ is the slurry flow rate in the injection pipe, m/s; $r_d$ is the grouting pipe radius, mm; $t$ is the grouting time, min; $K$ is the volume expansion of slurry, %.

The joint Equations 11, 12 lead to the EPEM diffusion distance equation:

$$\frac{\left[\pi r_0^2(l_s - r_0) + \frac{2}{3}\pi r_0^3\right]K}{\pi r_d^2 t} = \frac{r_0^2(P_0 - P_w)}{8\mu_s l_s} \tag{13}$$

## 2.3 Derivation of grouting sealing criteria for surge water

### 2.3.1 Basic assumptions

① The blocking body is a homogeneous and isotropic medium;
② the influence of the gravity of the blocking body is not considered;
③ the wall pressure of the plugging body on the inner wall of the pipe is equal.

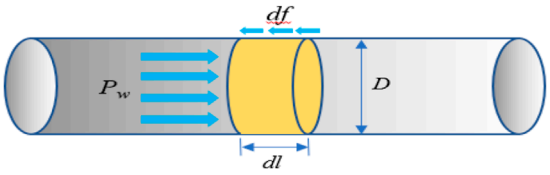


FIGURE 5
Schematic of microelement blocking calculation.

### 2.3.2 Model construction and derivation

The length of the blocking body is taken as dl, and the diameter of the blocking body is taken as D for analysis, as shown in Figure 3, 5.

The water pressure acting on the micrometric blocking body at the time of successful EPEM blocking is

$$F_w = P_w \cdot \frac{\pi D^2}{4}, \tag{14}$$

where $P_w$ is groundwater pressure, MPa; $D$ is pipeline diameter, mm.

The contact area $S$ of the blocking body with the rock wall (Equation 15) is obtained.

$$S = \pi D dl_s \tag{15}$$

The relationship between friction and water pressure is obtained from the limiting equilibrium state:

$$P_w \cdot \frac{\pi D^2}{4} = f = \mu P S = \mu P \pi D dl_s \tag{16}$$

where $\mu$ is the coefficient of friction, 1; $P$ is the average contact surface pressure, MPa.

The critical blocking body segment length required for successful blocking can then be expressed as

$$l_s = \frac{P_w D}{4\mu P} \tag{17}$$

From Equations 14, 16 when $f > F_w$, the frictional resistance of the blocking body is enough to resist the water pressure, and it can be considered that the blocking is successful. In summary, the calculation formula of the grouting plugging criterion (Equation 18) is obtained:

$$\begin{cases} \frac{\left[(\pi r_0^2 l_s - r_0) + \frac{2}{3}\pi r_0^3\right]K}{\pi r_d^2 t} = \frac{r_0^2(P_0 - P_w)}{8\mu_s l_s} \\ l_s = \frac{P_w D}{4\mu P} \end{cases} \tag{18}$$

According to Equation 17, the minimum blocking body segment length required for successful EPEM blocking can be found. Combining this with Equation 13, the grouting pressure and grouting time required for the critical blocking body length for successful EPEM blocking can be solved.

## 2.4 Parameterization and conditions of application

### 2.4.1 Determination of parameters

① EPEM volume expansion rate K.

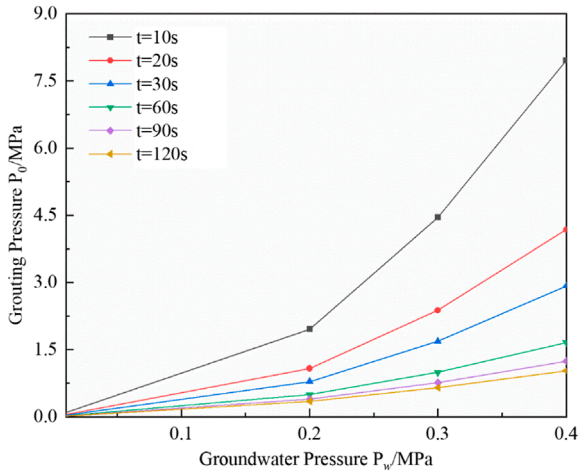


FIGURE 6
Variation curve of the effect of different grouting times.

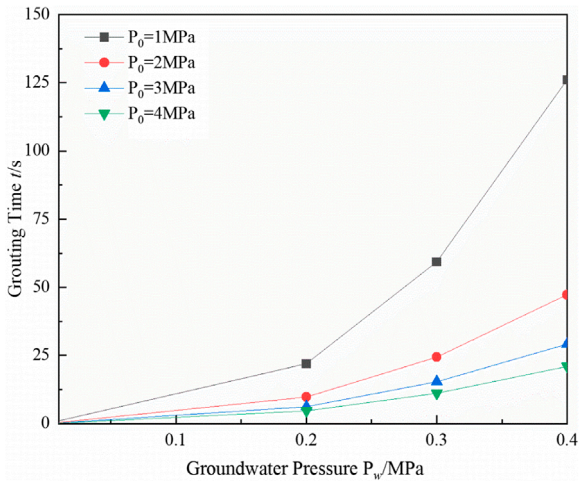


FIGURE 7
Change curve of the influence of different grouting pressures.

EPEM volume expansion rate is calculated according to Equation 19:

$$K = \frac{V_2 - V_1}{V_1} \times 100\% \tag{19}$$

where $V_1$ is the total volume of raw slurry, L; $V_2$ is the slurry colloid volume, L.

② Slurry viscosity.

Measurement, analysis, and calculation are obtained by using a fluid viscometer, such as a capillary viscometer or a rotational viscometer.

### 2.4.2 Applicable conditions

Considering that when the maximum static friction of the blocking body $f$ > the anti-splitting force of the blocking body $f_p$, the blocking body may split under the action of water pressure, so the following conditions (Equation 20) should be satisfied:

$$f_p > F_w \tag{20}$$

# 3 Influence mechanism of grouting sealing criteria of tunnel surge water

## 3.1 Analysis of the influence law of grouting time

In order to investigate the influence of grouting time on grouting plugging under the criterion model of grouting plugging of surge water, the change rule of groundwater pressure and grouting pressure under different grouting times is quantitatively analyzed. Groundwater pressures of 0.2 MPa, 0.3 MPa, and 0.4 MPa and grouting times of 10 s, 20 s, 30 s, 60 s, 90 s, and 120 s are selected, respectively, and the influence law of grouting time under the surge water grouting blocking criterion model is shown in Figure 6.

As analyzed in Figure 6, there is a positive correlation between the grouting time and groundwater pressure; that is, with increased groundwater pressure, the grouting time required for grouting and plugging increases. The reason is that with the increase of groundwater pressure, the water flow velocity increases under the same pipe diameter, and the slurry can be easily dispersed by the moving water, which leads to a decrease in the retention rate of the slurry. As a result, it is difficult to form a full-section blocking body in the pipeline, so it needs a longer grouting time to make the retention rate of the slurry increase and form a blocking body with the resistance to be scoured by the moving water inside the pipeline and then successfully block the pipe against a sudden surge of water.

## 3.2 Analysis of the influence law of grouting pressure

The change rule of groundwater pressure and grouting time under different grouting pressures is analyzed quantitatively to investigate the influence of grouting pressure on grouting plugging under the criterion model. Groundwater pressures of 0.2 MPa, 0.3 MPa, and 0.4 MPa, and grouting pressures of 1 MPa, 2 MPa, 3 MPa, and 4 MPa are selected, and the influence law of grouting pressure under the criterion model is shown in Figure 7.

Figure 7 shows a positive correlation between grouting pressure and groundwater pressure; that is, with increased groundwater pressure, the grouting pressure required for grouting plugging increases. The reason is that with the increase of groundwater pressure, the friction between the blocking body and the rock wall must be larger to resist the water pressure. The main influencing factor of the friction of the blocking body is the length of the blocking body; therefore, a higher grouting pressure is required to make the amount of grouting per unit of time increase, so that the length of the blocking body formed per unit of time will be longer and the friction will be higher to resist the groundwater pressure.

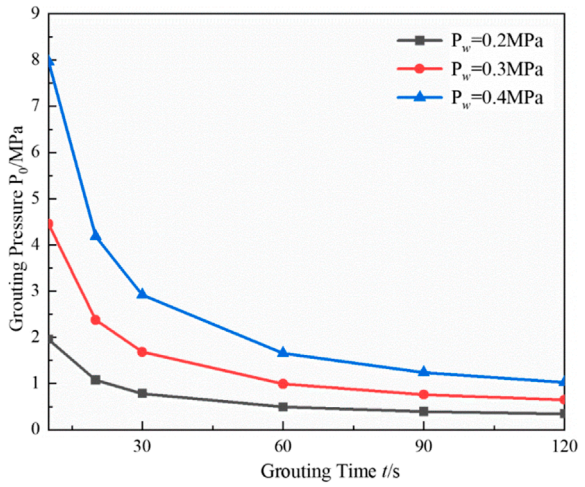


FIGURE 8
Variation curves of the impact of different groundwater pressures.

## 3.3 Analysis of groundwater pressure impact pattern

In order to investigate the influence of groundwater pressure on grouting and plugging under the criterion model, the change rule of grouting time and grouting pressure under different groundwater pressures is analyzed quantitatively. Grouting times of 30 s, 60 s, 90 s, and 120 s and grouting pressures of 1 MPa, 2 MPa, 3 MPa, and 4 MPa are selected. The results are shown in Figure 8.

Figure 8 shows that groundwater pressure, grouting pressure, and grouting time are positively correlated, while grouting pressure and grouting time are negatively correlated. That is, with the increase in grouting pressure, the grouting time required for grouting plugging is reduced. The reason is that with the increase in grouting pressure, under the same diameter of grouting pipe, the grouting volume per unit time increases, which makes the length of the blocking body formed per unit time be longer. The growth of the length of the blocking body makes the friction between the blocking body and the rock wall increase, which can realize the blocking in a shorter period of time.

# 4 Engineering applications

## 4.1 Engineering geology and hydrogeology

The total length of the Jiulongling Tunnel is 19,261.8 m. The topography is dominated by ridges and low hills and wide valleys, with gentle terrain and ground elevation of 300–350 m, and the undulation is slightly larger in the latter part of the tunnel, with a maximum height of approximately 550 m. The engineering geological conditions are complicated. The main strata traversed are the Devonian (D) and the Carboniferous (C), and the Ordovician (O) strata are traversed at the end of the tunnel. The rock properties are mainly cherts, Dolomitic tuff, dolomite, marl, charcoal shale, sandstone, slate, etc. The thickness of each rock layer ranges from thin to very thick, and there are large differences between the layers. The tunnel traverses complex hydrogeological conditions, including surface water development along the line, a groundwater level that is located above the roof of the cave, and dark rivers distributed near the axis. In terms of tectonic development, the area of the tunnel has a total of 34 faults, most of which intersect with the cave line at a large angle. The level of inclination is relatively gentle, more or less than 30°. In terms of karst development, the construction site experienced the occurrence of a sudden surge of water many times, as shown in Figure 9.

## 4.2 Construction program and effectiveness evaluation

According to the analysis of the site survey report, it is proposed to carry out curtain grouting on the side wall in the section. The holes are arranged in a plum blossom type, the designed drilling hole diameter is Φ50 mm, the hole depth is 5.0 m, the hole spacing is 1.5 m, and the ring spacing is 1.5 m. There are 10 rings in total. EPEM was chosen as the grouting material. After the field test, the slurry proportions were determined to be an alcohol-ester ratio of 0.9:1, a cement mixing amount of 70%, and a catalyst mixing amount of 3%. Through the above calculation of single-hole water influx combined with the surge water grouting blocking criterion model, the final grouting pressure is 0.5 MPa, and the single-hole grouting time reaches 20 min as the final grouting standard.

After the completion of EPEM grouting, the surge water situation improved significantly, and the flow of surge water in the section was cut off. Through the observation and analysis of the grouting holes, the surface of the grouting holes is dry, and there is no water leakage or seepage in the holes, so the grouting sealing effect is good. Subsequent on-site monitoring shows that there is no water seepage or leakage after construction using the grouting construction parameters discussed herein. The perimeter rock has been stable during subsequent excavation and lining construction, and there have been no accidents, such as a secondary surge of water.

# 5 Conclusion

(1) This article first analyzes the effective blocking conditions between the blocking body and the surge water pipe, focusing on the relationship between the blocking body and the rock wall, while also considering the water pressure splitting effect of the blocking body. Second, it deduces a formula for the grouting diffusion of the surge water by combining capillary theory with the flow formula for a single pipe. Finally, it constructs a mechanical calculation model based on the relationship between water pressure and the friction force of the blocking body, proposing the concept of grouting blocking.

(2) To reveal the influence mechanism of the grouting plugging criterion, a quantitative analysis was conducted based on the derived tunnel surge water grouting plugging criterion model, focusing on grouting time, grouting pressure, and groundwater pressure. The results indicate a positive correlation between groundwater pressure and grouting pressure; specifically, as groundwater pressure increases, the grouting pressure required for successful plugging also increases. Additionally, there

FIGURE 9
Surge of water at the site.

is a positive correlation between groundwater pressure and grouting time, meaning that higher groundwater pressure necessitates a longer grouting time for successful plugging. Conversely, there is a negative correlation between grouting pressure and grouting time; as grouting pressure increases, the time required for successful grouting and plugging decreases.

(3) The research findings on the grouting sealing mechanism for sudden water inflows in karst tunnel areas presented in this article have been successfully applied in the grouting project for the tunnel in the irrigation district of the Quanmutang Reservoir Engineering Project in Hunan Province. Based on on-site applications, a curtain grouting scheme was proposed to seal the water outburst areas. The grouting was completed when the final grouting pressure reached 0.5 MPa and the single-hole grouting time extended to 20 min, ensuring the safe excavation and support of the tunnel.

## Data availability statement

The original contributions presented in the study are included in the article/supplementary material, further inquiries can be directed to the corresponding author.

## Author contributions

SZ: writing – review and editing and writing – original draft. LL: data curation, validation, and writing – review and editing. ZL: conceptualization and writing – review and editing. JZ: writing – review and editing and conceptualization. YC: data curation, writing – review and editing. LC: writing – original draft and methodology.

## Funding

The author(s) declare that financial support was received for the research and/or publication of this article. This work was supported by the Scientific Research Project of Hunan Education Department (23B1009), the National Natural Science Foundation of China (No. 52378426), the Natural Science Foundation of Hunan Province (No. 2025JJ60272), the Distinguished Young Scholars of Changsha City Bureau (kq2209017), the Science and Technology Innovation Program of Hunan Province (No.2023RC3160), and the Water Resources Science and Technology Program of Hunan Province (XSKJ2022068-07). The corresponding author gratefully acknowledges this financial support.

## Conflict of interest

Authors SZ and YC were employed by Hunan Water Resources and Hydropower Survey, Design, Planning and Research Co., Ltd. Authors LL and JZ were employed by Hunan Provincial Water Resources Development and Investment Co., Ltd.

The remaining authors declare that the research was conducted in the absence of any commercial or financial relationships that could be construed as a potential conflict of interest.

## Generative AI statement

The author(s) declare that no Generative AI was used in the creation of this manuscript.

## Publisher's note

# References


Chen, Y., Fujian, Z., Feng, W., Tian, Z., Yuan, L., and Gao, L. (2019). Plugging mechanism of fibers and particulates in hydraulic fracture. *J. Petroleum Sci. Eng.* 176, 396–402. doi:10.1016/j.petrol.2019.01.084

Chengyuan, X. U., Zhang, J., Kang, Y., Xu, F., Lin, C., Yan, X., et al. (2021). Structural formation and evolution mechanisms of fracture plugging zone. *Petroleum Explor. Dev.* 48 (1), 232–242. doi:10.1016/s1876-3804(21)60019-8

Haiyan, L. I., Liu, J., Jing, W. U., Xu, Z., Zhang, X., Zhang, L., et al. (2021). Grouting sealing method of flow-control speed-down in karst pipelines and its engineering application. *Tunn. Undergr. Space Technol.* 108, 103695. doi:10.1016/j.tust.2020.103695

Haiyan, L. I., Zhang, Y., Jing, W. U., Zhang, X., Zhang, L., and Li, Z. (2020). Grouting sealing mechanism of water gushing in karst pipelines and engineering application. *Constr. Build. Mater.* 254, 119250. doi:10.1016/j.conbuildmat.2020.119250

Liu, J., Liu, S., Wang, M., and Peng, B. (2024). An experimental study on the sealing mechanism of a Karst pipeline by dynamic water grouting. *Appl. Sci.* 14 (4), 1381. doi:10.3390/app14041381

Liu, R., Zhang, L., Zhang, Q., Yang, L., Li, Z., Sun, Z., et al. (2017). Numerical simulation and experimental validation of diffusion of fast-setting slurry fissure dynamic water grouting. *J. Rock Mech. Eng.* 36 (S1), 3297–3306. doi:10.13722/j.cnki.jrme.2015.0815 (in Chinese)

Pan, D., Bu, Z., Haiyan, L, Xu, Z., and Liu, J. (2022). Experimental investigation of flow control technology for grouting and blocking of flowing water in karst conduits. *KSCE J. Civ. Eng.* 26 (8), 3440–3454. doi:10.1007/s12205-022-2129-3

Shucai, L. I., Pan, D., Zhenhao, X. U., Lin, P., and Zhang, Y. (2020). Numerical simulation of dynamic water grouting using quick-setting slurry in rock fracture:the Sequential Diffusion and Solidification (SDS) method. *Comput. Geotechnics* 122, 103497. doi:10.1016/j.compgeo.2020.103497

Wanghua, S. U. I., Jinyuan, L. I. U., Hu, W., Qi, J., and Zhan, K. (2015). Experimental investigation on sealing efficiency of chemical grouting in rock fracture with flowing water. *Tunn. Undergr. Space Technol.* 50 (08), 239–249. doi:10.1016/j.tust.2015.07.012

Wang, Q., Zhu, Q., Shao, T., Shu-yi, X., Qing-Li, K., Jun-Jie, Z., et al. (2018). The rheological test and application research of glass fiber cement slurry based on plugging mechanism of dynamic water grouting. *Constr. Build. Mater.*, 189–130. doi:10.1016/j.conbuildmat.2018.08.081

Yalei, Z. H. E., Hou, K., Wang, Z., Shifei, Y., Yunlin, Y., and Yong, Y. (2024). The grouting plugging mechanism of layered jointed rock mass considering the time-varying yield stress of grout. *Sci. Rep.* 14 (1), 23029. doi:10.1038/s41598-024-74583-2

Yang, X., Cai, J., Jiang, G., Xie, J., Shi, Y., Chen, S., et al. (2020). Nanoparticle plugging prediction of shale pores: a numerical and experimental study. *Energy* 208, 118337. doi:10.1016/j.energy.2020.118337

Zhenhao, X. U., Pan, D., Peng, L. I. N., Zhang, Q., Li, H., and Zhang, Y. (2021). Numerical investigation of flow control technology for grouting and blocking of flowing water in karst conduits. *Int. J. Numer. Anal. Methods Geomechanics* 45 (12), 1712–1738. doi:10.1002/nag.3221

frontiers | Frontiers in Earth Science

TYPE Methods
PUBLISHED 14 August 2025
DOI 10.3389/feart.2025.1646057



OPEN ACCESS

EDITED BY
Zhang Cong,
Central South University Forestry and Technology, China

REVIEWED BY
Ao Zheng,
China University of Mining and Technology, China
Yukai Liu,
Eindhoven University of Technology, Netherlands
Hanbo Chen,
Guilin University of Electronic Technology, China

*CORRESPONDENCE
Siyuan Wang,
1026319852@qq.com
Lei Xu,
xulei8945@163.com

RECEIVED 12 June 2025
ACCEPTED 29 July 2025
PUBLISHED 14 August 2025

CITATION
Wang S, Xu L, Li P, Wang S, Lu L and Li Z (2025) Application of geophysical prospecting methods in karst exploration.
*Front. Earth Sci.* 13:1646057.
doi: 10.3389/feart.2025.1646057



# Application of geophysical prospecting methods in karst exploration

Shaobo Wang[1,2,3,4], Lei Xu[1,2,3,4]*, Peng Li[1,2,3,4], Siyuan Wang[1,2]*, Lifeng Lu[5] and Zhengliang Li[5]

[1]Changjiang Geophysical Exploration and Testing Co., Ltd. (Wuhan), Wuhan, Hubei, China, [2]Changjiang Institute of Survey Planning Design and Research Co., Ltd., Wuhan, Hubei, China, [3]National Dam Safety Research Center, Wuhan, Hubei, China, [4]Technological Innovation Center for Health Diagnosis of Water Conservancy Project, Wuhan, Hubei, China, [5]Hunan Provincial Water Resources Development and Investment Co., Ltd., Changsha, Hunan, China

When conducting engineering construction in karst-developed regions, the presence of concealed underground karst systems can easily induce geological hazards such as ground collapse and foundation settlement, posing serious threats to engineering safety. Therefore, it is imperative to ascertain critical information including the degree of karst development and spatial distribution characteristics within the project area. Geophysical prospecting methods, characterized by high efficiency, cost-effectiveness, and strong detection accuracy, have proven to be an effective technical approach for karst exploration. This paper systematically examines several geophysical methods and their detection effectiveness for cavities with different filling states. The research outcomes can provide valuable references for karst investigation in similar engineering projects.

KEYWORDS

**geophysical prospecting, karst exploration, engineering geological exploration, cavities with different filling states, multi-electrode resistivity method**

## 1 Introduction

Karst phenomenon refers to a natural geological process characterized by the long-term dissolution and erosion of soluble rock formations, predominantly carbonate rocks such as limestone and dolomite, by groundwater (Ford and Williams, 2007). This process gradually forms distinctive geological features including karst cavities, solution grooves, and subterranean river systems. The development of karst significantly compromises the structural integrity of rock strata, resulting in reduced mechanical strength and unstable geological conditions. Such weakened formations fail to provide adequate load-bearing capacity for overlying structures, thereby posing substantial risks during tunnel construction, including cavity collapse, sudden mud inrushes, and water outbursts (White, 1988). For engineering projects in karst terrains, priority must be given to comprehensive engineering geological surveys. These investigations should systematically assess the developmental stages of subsurface karst features, delineate spatial distribution patterns of karst structures, and elucidate their evolutionary mechanisms. A thorough understanding of karst distribution characteristics and developmental patterns forms the essential foundation for mitigating geological hazards and ensuring engineering safety in such complex

geological settings (Parise and Gunn, 2007; Zhou et al., 2002; Kresic and Stevanovic, 2009). Current mainstream karst investigation methodologies primarily encompass geological mapping, engineering drilling, and geophysical prospecting (Li and Xiao, 2006; Goldscheider et al., 2011; Kaufmann, 2014). Geological mapping involves inferring karst distribution through field observations of surface exposures—such as solution grooves, sinkholes, and tiankeng—supplemented by existing geological data (Meng et al., 2019; Luo et al., 2009). While cost-effective for preliminary assessments, this approach remains heavily reliant on the expertise of field personnel and proves particularly limited in areas with complex geological settings or deeply buried karst systems, where surface manifestations poorly correlate with subsurface realities (Yin, 2009). Engineering drilling, through core sampling, enables relatively accurate characterization of lithological profiles along borehole trajectories, thereby facilitating subsurface karst interpretation. However, this method inherently provides localized insights constrained by drilling penetration points. In regions with densely clustered or interconnected karst cavities, isolated borehole data may fail to detect critical geological anomalies, potentially leading to misinterpretations of three-dimensional karst architectures. Nevertheless, implementing dense drilling grids for enhanced coverage often becomes prohibitively expensive and time-intensive (Geng and Sun, 2000; Li and Cao, 2017).

Geophysical prospecting methods operate on the principle of detecting contrasts in geophysical properties—such as body wave velocity and electrical resistivity—among distinct subsurface media objects (Telford et al., 1990). These techniques facilitate rapid, large-scale karst investigations through non-invasive means, demonstrating significant advantages in survey efficiency, cost-effectiveness, and interpretation accuracy (Mccann et al., 1987; Yang, 2017). The characteristic geophysical parameters of typical media (China Water and Power Press, 2021) in karst terrains are systematically compiled in Table 1 below. In 1990, Hohmann and Newman conducted a study on distortion attenuation curves during measurements using central-loop and coincident-loop configurations in transient electromagnetic (TEM) systems (Hohmann and Newman, 1990). In 2001, Franjo Šumanovac and Mario Weisser employed shallow seismic and electrical methods to detect karst development, achieving favorable results (Šumanovac and Weisser, 2001). In 2003, Zhang Jiagui et al. utilized audio-frequency magnetotellurics (AMT) and seismic computed tomography (CT) techniques to investigate concealed karst features in the Three Gorges Reservoir area, attaining satisfactory outcomes (Zhang et al., 2003). In 2009, Chen Binwen applied shallow seismic methods combined with high-density resistivity techniques to detect karst development along highways with notable efficacy (Chen, 2009). In 2010, Estrada-Medina Hector et al. successfully identified shallow karst structures in limestone terrains using 200 MHz ground-penetrating radar (GPR) (Estradamedina et al., 2010). In 2014, Marjana Zajc et al. investigated the influence of topographic conditions on GPR detection performance (Zajc et al., 2014). As global research on karst exploration advances, successful engineering applications continue to accumulate. Nevertheless, studies on geophysical responses to karst cavities under varying fill conditions remain limited, with most existing research confined to theoretical frameworks. Practical engineering scenarios often deviate from theoretical predictions.

Geophysical prospecting methods have been widely adopted by engineers and researchers worldwide for karst exploration with demonstrated effectiveness. However, studies on geophysical response characteristics of karst cavities with different filling conditions remain insufficient, with most research limited to theoretical analysis and numerical simulations, lacking validation through actual engineering cases. This study delineates the fundamental principles of four geophysical techniques (multi-electrode resistivity method, cross-hole electromagnetic wave computed tomography, microtremor survey, and ground penetrating radar) and establishes their standardized data processing workflows for karst detection. Through field cases verified by borehole drilling and tunnel excavation, the detection efficacy and distinctive geophysical signatures of these methods for identifying variably-filled karst cavities are comprehensively analyzed. The practical engineering applications provide crucial empirical evidence bridging the gap between theoretical models and field implementation.

# 2 Geophysical prospecting methods

As shown in the Table 1 above, significant differences exist in geophysical parameters between intact rock masses and karst cavities with different filling conditions: Air-filled cavities exhibit lower seismic wave velocity, higher electrical resistivity, and weaker electromagnetic wave attenuation compared to bedrock. Relative to bedrock, water-filled cavities exhibit lower seismic wave velocity, reduced electrical resistivity, and heightened electromagnetic signal attenuation rate.

The marked contrast in physical properties ensures the feasibility of applying the geophysical prospecting methods for karst detection. Consequently, the following section introduces several typical prospecting techniques applicable to karst surveys and their characteristics.

## 2.1 Multi-electrode resistivity method

### 2.1.1 Methodology

Multi-electrode resistivity method is an electrical exploration technique based on resistivity differences between subsurface media. It studies the distribution patterns of conductive currents under artificially applied steady-state electric fields.

The method's defining feature is deploying tens to hundreds of electrodes along a survey line simultaneously. Automated acquisition systems measure potential values between measurement electrodes and current values in circuits using predefined array configurations (Dong and Wang, 2003).

Electrode spacing is adjustable based on detection requirements. Extensive data acquisition ensures sufficient geoelectric information for inversion imaging. In field operations, current is transmitted between surface electrodes (A, B), while potentials are measured between electrodes

TABLE 1 Characteristic geophysical parameters of typical media in karst terrains.

| Medium | Shear-wave velocity (m/s) | Electrical resistivity (Ω·m) | Relative dielectric constant | Electromagnetic wave attenuation coefficient (Nper/m) |
|---|---|---|---|---|
| desiccated atmosphere (air-filled cavities) | — | ∞ | 1 | 0.001–0.01 |
| karstic groundwater | — | 1.5–30 | 81 | 0.5–2 |
| water-saturated silty sands | 100–300 | 10–100 | 23–30 | 0.4–1.8 |
| clay formation | 700–1,400 | 1–200 | 5–40 | 0.2–0.5 |
| compact limestone | 1,400–3,500 | 600–6,000 | 4–8 | 0.05–0.2 |
| compact dolomite | 1,500–3,600 | 50–6,000 | 6.8–8 | 0.03–0.15 |

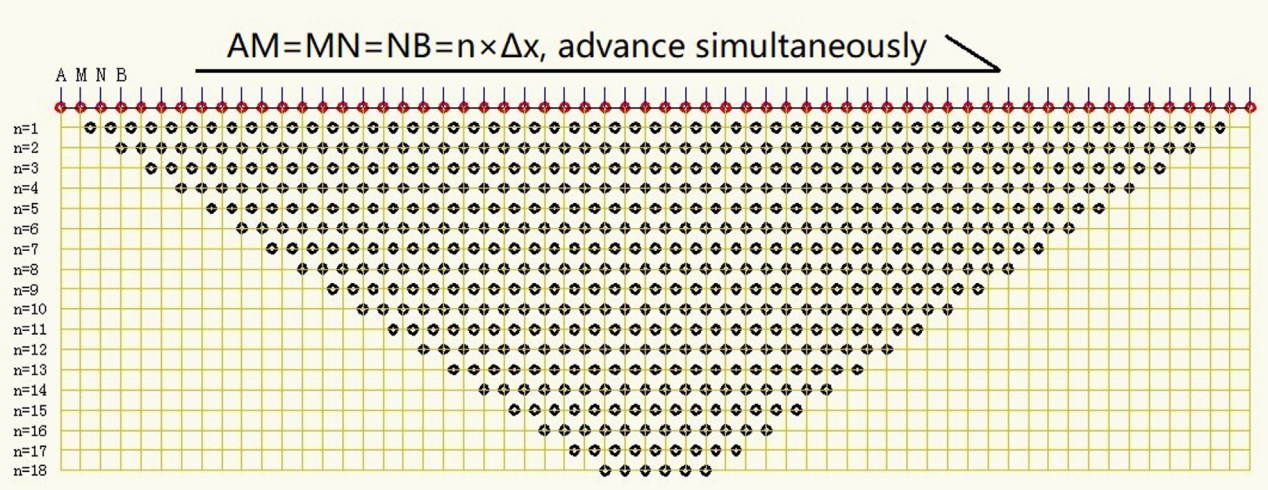


FIGURE 1
Sketch of data acquisition for Wenner array.

(M, N). The apparent resistivity formula (Equation 1) for subsurface media is:

$$\rho_s = k\frac{\Delta V}{I} \tag{1}$$

In the formula, $\rho_s$ denotes apparent resistivity (unit: Ω·m); $\Delta V$ represents the potential difference between points M and N (unit: V); $I$ indicates the loop current intensity (unit: A); and $k$, the geometric factor, is defined as $k = \frac{2\pi}{\frac{1}{AM} - \frac{1}{AN} - \frac{1}{BM} + \frac{1}{BN}}$.

In practical operations, various electrode configurations may be employed. Taking the Wenner array as an example: Electrodes A, M, N, and B are deployed sequentially along the survey line with equal spacing $n$. After each measurement cycle, all electrodes advance simultaneously to the next station until Electrode B reaches the terminus of the line. The electrode spacing $n$ is then incrementally modified, and the procedure repeats. Systematic increases in $n$ facilitate the mapping of apparent resistivity ($\rho_s$) profiles at progressively greater depths beneath the survey line (Figure 1) (Li, 2005).

### 2.1.2 Data processing workflow

Field-acquired resistivity data typically represents apparent resistivity, which requires processing to reveal subsurface geology and enable geological interpretation.

(1) Data Transfer and Format Conversion: Field data stored in the instrument console are transferred to a computer and converted into. dat format compatible with processing software using dedicated utilities.
(2) Profile Stitching: For survey lines exceeding the maximum array length, multiple overlapping arrays are deployed. All array datasets along a single profile must be merged into a continuous transect prior to subsequent processing.
(3) Bad Point Editing: Field observations may contain degraded data points due to ambient noise interference during acquisition. Extreme high/low-value outliers are discarded to prevent artifact anomalies in inversion results.
(4) Topographic Correction: Given that inversion algorithms typically assume horizontally layered media, terrain elevation

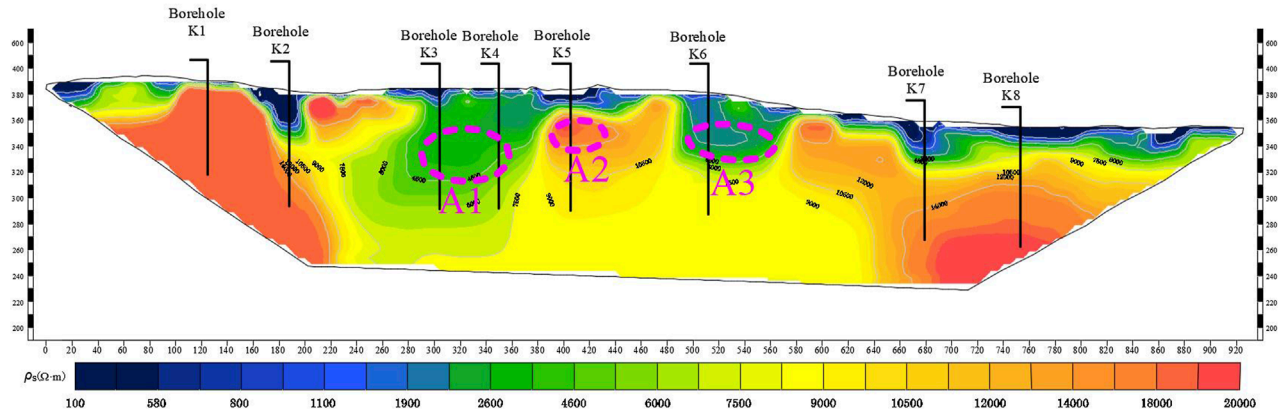


FIGURE 2
Multi-electrode resistivity method inversion section.

data are incorporated to compensate for topographic effects and enhance subsurface model fidelity.

(5) Data Inversion: Following preparatory steps, inversion parameters are configured in specialized software. Least-squares inversion (implemented in RES2DINV®) is iteratively executed until misfit errors converge below threshold criteria.

(6) Result Visualization: Inverted resistivity distributions from RES2DINV® are contoured in Surfer®. The draft plots undergo cartographic refinement in AutoCAD® for geological interpretation.

### 2.1.3 Representative case study and analysis

As tabulated in Table 1, compact limestone and dolomite demonstrate resistivities reaching 6,000 Ω m, contrasting markedly with water-saturated silty sands (<100 Ω m) and karstic groundwater (<30 Ω m), while air-filled cavities exhibit near-infinite resistivity values. This pronounced electrical contrast fundamentally enables karst cavity detection through multi-electrode resistivity method.

Illustrating with a multi-electrode resistivity method survey for karst exploration in Hunan, China (Figure 2), three prospective karst zones (A1–A3) were delineated: Zones A1 and A3 exhibiting low-resistivity anomalies indicative of water-filled cavities, while Zone A2 displayed high-resistivity signatures characteristic of air-filled cavities. Subsequent drilling operations comprising eight boreholes confirmed water-filled cavities in Borehole K3 (elev. 314–347 m), K4 (elev. 315–353 m), and K6 (elev. 325–348 m), with an air-filled cavity intercepted in K7 (elev. 298–300 m). No karst features were encountered in other boreholes.

Borehole validation demonstrates that anomalies A1 and A3 accurately predict water-filled cavities, whereas anomaly A2 yields no karst cavity—confirming multi-electrode resistivity method exhibits higher reliability in detecting water-filled cavities. Low-resistivity anomalies serve as robust indicators for filled-karst features. Notably, despite the significant resistivity contrast between air (theoretically infinite) and competent bedrock (e.g., limestone/dolomite), multi-electrode resistivity method possesses inherent limitations: its greater sensitivity to conductive targets complicates definitive identification of small air-filled cavities, primarily due to resolution constraints and signal attenuation effects.

## 2.2 Cross-borehole electromagnetic wave computed tomography

### 2.2.1 Methodology

The fundamental principle of cross-borehole computed tomography technique lies in reconstructing an object through layer-by-layer tomographic imaging. For a cross-sectional image slice of the object, defined as a function of two spatial variables $(x,y)$, this image function is designated as $f(x,y)$. When the object is illuminated by incident waves from varying directions, the measured wavefield data—constituted as a function of at least two variables: incident wave direction $\theta$ and observation point position $\rho$—is termed the projection function, denoted $u(\rho,\theta)$. In 1917, Austrian mathematician Johann Radon rigorously established that knowledge of the projection function $u(\rho,\theta)$ across all incident angles θ permits the unique reconstruction of the image function $f(x,y)$. This mathematical theorem, now recognized as the Radon transform, constitutes the theoretical foundation of tomographic imaging methodologies. The attenuation amplitude transfer equation (Equation 2) for electromagnetic waves in lossy media can be expressed as (Yue, 2007; Liu et al., 2014):

$$E = E_0 \cdot \frac{e^{-\int_R \beta(r)dr}}{R} \cdot f \tag{2}$$

In the formula, $E_0$ is the initial field strength at the transmission point (unit: V/m); $R$ denotes the distance between the transmission and reception points (unit: m); $f$ represents the directionality factor; $\beta$ stands for the absorption coefficient of the medium in the detection region (unit: Nper/m); and $E$ corresponds to the measured field strength at the reception point (unit: V/m).

### 2.2.2 Data processing workflow

(1) Field Data Acquisition: Electromagnetic wave field amplitude values are acquired, with excitation and receiver coordinates for each ray path calculated based on surveyed positional data.

(2) Model Construction: A mathematical-physical model is established considering geological/geophysical constraints, observation geometry, imaging resolution, and project objectives. Initial model parameters and constraints are derived from known geological conditions, empirical values, and field calibration tests.
(3) Data Inversion: Tomographic inversion is implemented using algorithms such as Simultaneous Iterative Reconstruction Technique (SIRT) or Algebraic Reconstruction Technique (ART), with iterative optimization to refine imaging results.
(4) Result Visualization: Absorption coefficient contour maps are generated in Surfer®, subsequently refined in AutoCAD® for geological interpretation. Final tomographic images employ pseudocolor display with either: Equal-interval classification for quantitative analysis, or Variable-interval coloring to enhance anomaly contrast.

### 2.2.3 Representative case study and analysis

As tabulated in Table 1, compact limestone and dolomite exhibit electromagnetic wave attenuation coefficients below 0.2Nper/m, contrasting markedly with air-filled cavities (0.01Nper/m), water-saturated silty sands (>0.4Nper/m) and karstic groundwater (>0.5Nper/m). This pronounced electromagnetic wave attenuation contrast fundamentally enables karst cavity detection through cross-borehole electromagnetic wave computed tomography.

Figure 3 illustrates the electromagnetic wave tomography results from a karst exploration in Hubei, China, where the profile exhibits strong electromagnetic wave attenuation in the upper section due to overburden effects, contrasting with low-attenuation bedrock zones in the lower section. Within this competent bedrock, three high-attenuation anomalies (B1–B3) were identified as potential karst features. Borehole validation confirmed cavities at all anomaly locations: B1 corresponds to an air-filled cavity, B2 to an argillaceous semi-filled cavity, and B3 to a water-filled cavity. Analysis reveals that anomalies B2 and B3 reflect highly attenuative fill materials, with B3's elevated absorption coefficient relative to B2 being consistent with the greater electromagnetic wave absorption of karstic groundwater *versus* water-saturated silty sands. Paradoxically, despite air's intrinsically low absorption coefficient, anomaly B1 exhibits strong attenuation attributable to multiple internal electromagnetic wave reflections within the air-filled cavity that dissipate wave energy. This case demonstrates that cross-borehole electromagnetic wave tomography effectively discriminates cavities with distinct infill conditions (air/water/sediment) through their characteristic attenuation signatures.

## 2.3 Microtremor survey method

### 2.3.1 Methodology

Microtremors represent persistent low-amplitude vibrations of the earth's surface, generated by natural sources (e.g., wind, oceanic waves, volcanic activity, and tidal forces) and anthropogenic activities (e.g., vehicular traffic and machinery operation). The former, characterized by frequencies typically <1 Hz, are classified as long-period microtremors; the latter, exhibiting frequencies >1 Hz, are termed short-period microtremors. These vibrations constitute a composite wavefield comprising body waves (P- and S-waves) and surface waves (Rayleigh and Love waves), with surface wave energy dominating approximately 70% of the total signal energy.

Microtremor survey entails processing ambient microtremor signals to extract Rayleigh wave dispersion curves via spatial autocorrelation (SPAC) or frequency-wavenumber (F-K) analysis. Through inversion of these dispersion characteristics, subsurface shear-wave velocity (Vs.) structures are reconstructed. Geological features are subsequently delineated by analyzing Vs. contrasts between target formations and surrounding media, thereby addressing critical engineering geological objectives such as bedrock profiling, cavity detection, and stratigraphic interface mapping (Coccia et al., 2010).

### 2.3.2 Data processing workflow

(1) Data Extraction Phase: The continuous observation files are segmented based on the precise start/end acquisition timestamps recorded at each field array station, yielding discrete datasets for individual measurement points. This process ensures temporal alignment with actual field deployment configurations while preserving original sampling characteristics.
(2) Data Standardization: Systematic implementation of baseline correction, DC component removal, and filtering operations to suppress instrument noise and anomalous interference signals. Data segments exhibiting significant interference are excluded based on predefined signal quality thresholds.
(3) Inversion Implementation: Rayleigh wave dispersion curves are extracted from array data using either Frequency-Wavenumber (F-K) spectral analysis or Spatial Autocorrelation (SPAC) method. The derived dispersion characteristics undergo nonlinear inversion via globally optimized algorithms to reconstruct 1D shear-wave velocity (Vs.) profiles with depth resolution of λ/3 to λ/4 (where λ denotes wavelength).
(4) Result Visualization: Shear-wave velocity (Vs.) distributions are contoured in Surfer®. The preliminary plots undergo graphical refinement in AutoCAD® to produce finalized interpretative sections for geophysical analysis.

### 2.3.3 Representative case study and analysis

As tabulated in Table 1, compact limestone and dolomite exhibit shear-wave velocities exceeding 1400 m/s, while shear-wave propagation is physically prohibited in air-filled cavities and karstic groundwater (effectively yielding zero velocity). Water-saturated silty sands typically register velocities below 300 m/s. This pronounced shear-wave velocity contrast between competent bedrock and cavities serves as the physical basis for microtremor survey for karst cavity detection.

Illustrating a microtremor survey for karst exploration in Jiangxi, China (Figure 4), the Vs. section delineates distinct velocity domains: surficial low-velocity layers overlie high-velocity bedrock, with embedded low-velocity anomalies (C1–C4) indicating potential karst development. Subsequent drilling confirmed cavities at all four anomalies: C1 and C3 as fully sediment-filled cavities, and C2 and C4 as partially filled cavities. Critically, microtremor methods accurately detect cavities regardless of fill saturation—since all filled cavities manifest as velocity deficits relative to intact rock—but cannot discriminate fill conditions.

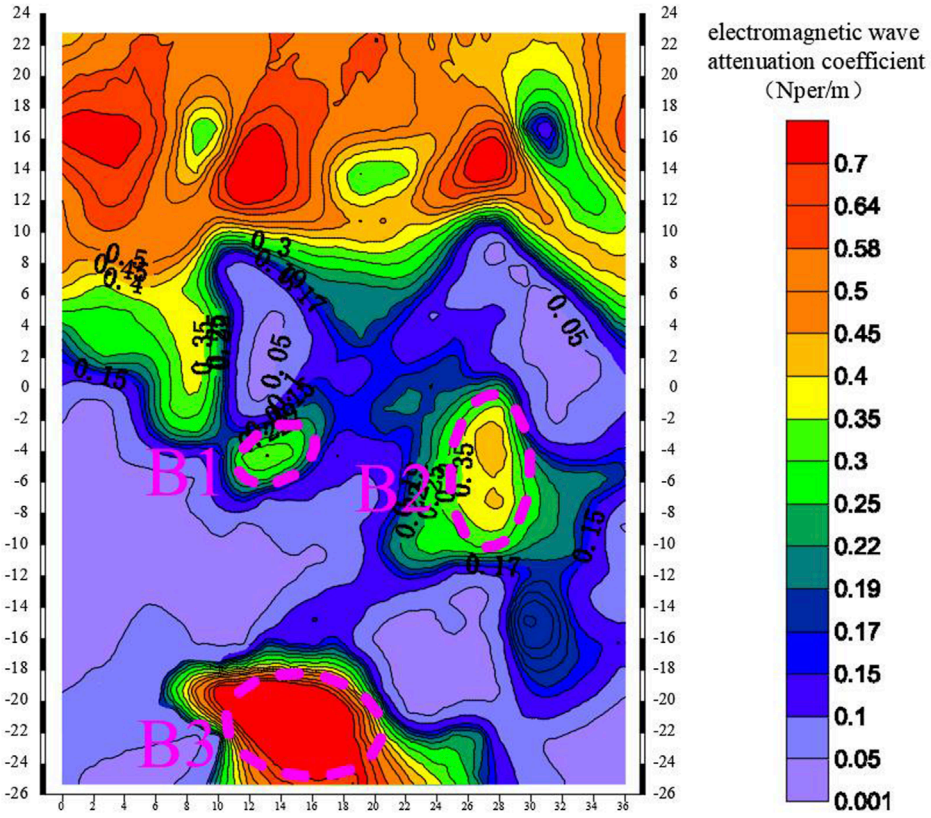


FIGURE 3
Cross-borehole electromagnetic wave computed tomography inversion section.

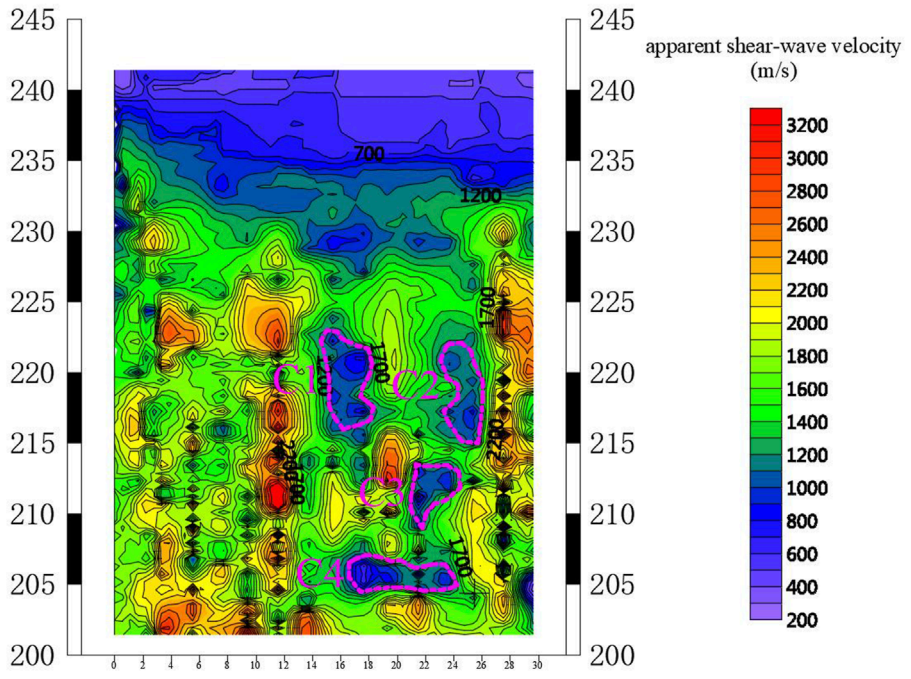


FIGURE 4
Microtremor survey inversion section.

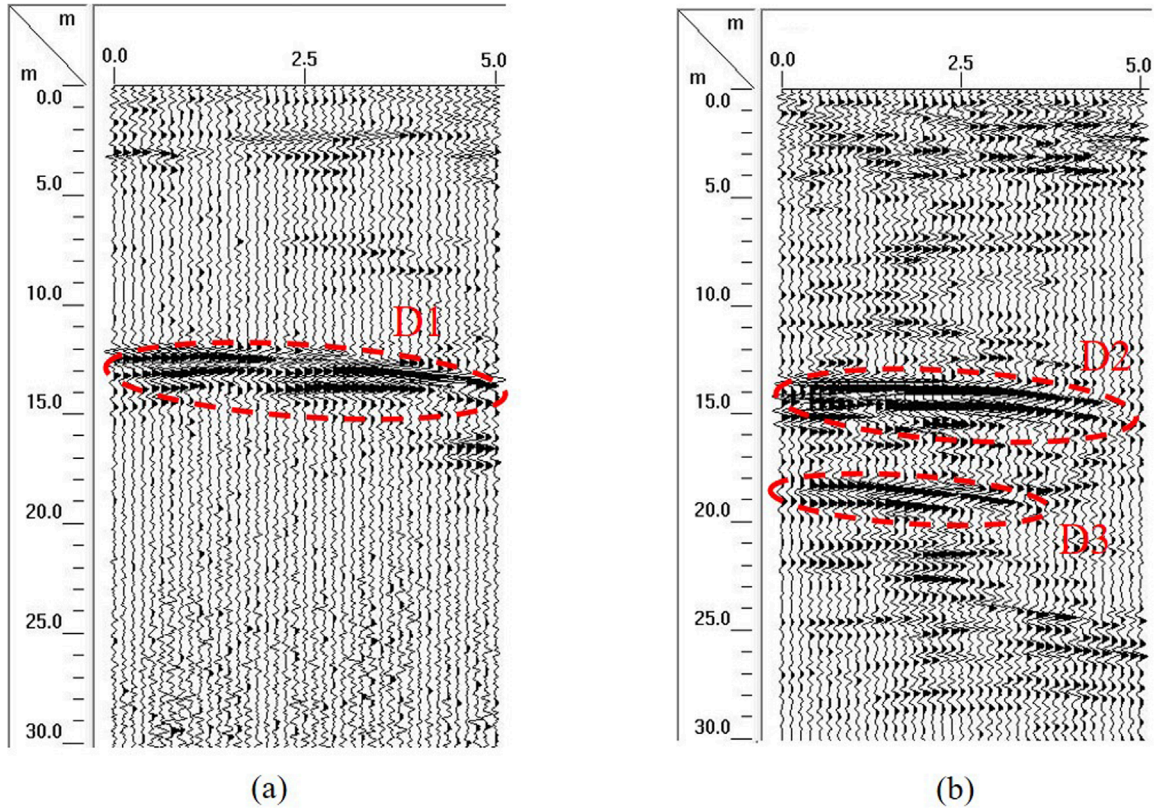


FIGURE 5
Interpreted GPR profiles for karst feature identification.

## 2.4 Ground penetrating radar

### 2.4.1 Methodology

Ground penetrating radar (GPR) operates as an electromagnetic method wherein a transmitting antenna directs high-frequency, short-pulse electromagnetic waves into subsurface interfaces. When encountering boundaries with contrasting electrical properties, these waves undergo partial reflection governed by the Fresnel equations, with reflection coefficients determined by dielectric permittivity contrasts. Reflected waves are captured by a receiving antenna, with propagation paths obeying Snell`s law and reflection amplitudes correlating to dielectric contrasts and interface geometry. Through acquisition of time-domain signals, velocity-based time-depth conversion, and waveform analysis, this technique resolves the depth, lateral position, and geometric attributes of subsurface targets or stratigraphic interfaces (Al-fares et al., 2002; Xu, 2015).

### 2.4.2 Data processing workflow

(1) Data Preprocessing: Raw data imports undergo compatibility verification in dedicated software, followed by trace editing and dead-channel removal. Direct current offsets are eliminated to normalize waveform baselines, reflection events are time-aligned, and coherent background noise (e.g., surface metallic objects, fixed interference sources) is suppressed to enhance valid signals.

(2) Filtering Operations: Bandpass/highpass/lowpass filters attenuate high-frequency noise and low-frequency drifts. Frequency-Wavenumber (F-K) filtering isolates dipping interference from target reflections, while moving-average or stacking filters mitigate lateral random noise.

(3) Gain Compensation: Amplitude recovery counteracts electromagnetic wave attenuation with depth, improving deep-target signal visibility. Localized calibration of gain functions optimizes dynamic range for anomalous zones.

(4) Time-Depth Conversion and Imaging: Input of relative permittivity (empirical or calibrated) determines electromagnetic wave velocity. Scan interval calibration and distance normalization ensure precise depth scaling, culminating in time-to-depth transformed 2D B-scan or 3D volumetric outputs for interpretable subsurface imaging.

### 2.4.3 Representative case study and analysis

The dielectric properties of materials govern their polarization capability under electric fields. Table 1 demonstrates that compact limestone and dolomite exhibit relative permittivity values typically below 8, while air-filled cavities register as 1. In contrast, water-saturated silty sands show permittivity ≥23, and karstic groundwater reaches 81. This pronounced dielectric contrast between competent bedrock and cavities, coupled with electrical conductivity

differences, serves as the theoretical basis for ground penetrating radar cavity detection by inducing measurable alterations in reflected wave amplitude and frequency.

Illustrating two representative ground penetrating radar surveys for advance geological prediction in a Hunan tunnel (Figures 5a,b), diagnostic subsurface anomalies exhibiting hyperbolic phase axes were identified.

Figure 5a reveals a high-amplitude reflection zone (D1) at 12 m behind the tunnel face, exhibiting near-parabolic waveform phase axes, interpreted as a karst cavity development zone. Subsequent excavation confirmed a clay-filled karst cavity in this location.

Figure 5b delineates two anomalies: a pronounced reflective zone (D2) at 14 m behind the face with parabolic phase axes, indicating a cavity; and a secondary zone 5 m further back (D3) showing weaker-amplitude parabolic reflections, likely attributable to multiple reflections. Excavation validated an air-filled cavity at 13 m depth (D2).

Geophysical analysis establishes that the presence of karst cavities within a ground penetrating radar survey zone invariably modifies radar wave signatures through distinct interfaces: the cavity's frontal boundary invariably generates high-amplitude reflections accompanied by waveform distortions and discontinuous phase axes, manifesting as intense reflective zones exemplified by areas D1 and D2. Critically, the infill material dictates subsequent signal behavior—cavities saturated with conductive media such as water-saturated silts or karstic groundwater induce severe electromagnetic attenuation, wholly suppressing secondary reflections. Conversely, air-filled cavities permit unimpeded wave transmission with minimal loss, enabling reflections at the rear interface that subsequently transmit through the frontal boundary; these secondary reflections exhibit waveform coherence with the primary wave but display attenuated amplitudes, as empirically documented in Area D3. Collectively, these diagnostic amplitude-phase responses and multi-reflection signatures empower ground penetrating radar to accurately detect and differentiate cavity infill conditions with high geophysical fidelity.

## 3 Conclusion

This study details the methodological principles and data processing workflows of four geophysical prospecting methods—multi-electrode resistivity method, cross-hole electromagnetic wave computed tomography, microtremor survey, and ground penetrating radar—with empirical case analyses evaluating their efficacy in detecting variably-filled karst cavities. Key findings are.

(1) Multi-electrode resistivity method accurately locates sediment-infilled cavities but exhibits limited sensitivity to open cavities; low-resistivity anomalies within high-resistivity bedrock backgrounds typically indicate infilled karst.
(2) Cross-hole electromagnetic wave computed tomography precisely identifies cavities regardless of fill conditions and discriminates fill states; strong absorption anomalies against weakly absorptive bedrock backgrounds signify cavity presence, with infilled cavities demonstrating consistently higher electromagnetic absorption than open cavities.
(3) Microtremor survey achieves reliable cavity localization but cannot differentiate fill states, as both infilled and open cavities manifest as low-velocity anomalies relative to intact bedrock.
(4) Ground penetrating radar enables precise cavity mapping and fill-state discrimination; cavities generate high-amplitude reflection zones exhibiting near-parabolic phase axes within bedrock backgrounds. Crucially, infilled cavities lack secondary reflections whereas open cavities produce distinct multiple reflections.

## Data availability statement

The original contributions presented in the study are included in the article/supplementary material, further inquiries can be directed to the corresponding author/s.

## Author contributions

SW: Data curation, Investigation, Validation, Writing – original draft, Writing – review and editing. LX: Validation, Methodology, Writing – original draft, Writing – review and editing. PL: Methodology, Validation, Writing – review and editing. SW: Data curation, Writing – original draft, Investigation. LL: Funding acquisition, Project administration, Supervision, Writing – original draft. ZL: Writing – original draft, Funding acquisition, Project administration.

## Funding

The author(s) declare that financial support was received for the research and/or publication of this article. The research was supported by Quanmutang Reservoir Project Technology Innovation Program (W-2022-72), Major Science and Technology Projects of Ministry of Water Resources (SKS-2022099), Wuhan Science and Technology Plan Project (2023030103010570) and Changjiang Survey Planning Design and Research Limited Co. Independent Innovation Research Project (CX 2022Z32). The authors declare that this study received funding from Changjiang Survey Planning Design and Research Limited Co. The funder was not involved in the study design, collection, analysis, interpretation of data, the writing of this article, or the decision to submit it for publication.

## Conflict of interest

Authors SW, LX, PL, and SW were employed by Changjiang Geophysical Exploration and Testing Co., Ltd. (Wuhan). Authors SW, LX, PL, and SW were employed by Changjiang Institute of Survey Planning Design and Research Co., Ltd. Authors LL and ZL

were employed by Hunan Provincial Water Resources Development and Investment Co., Ltd.

## Generative AI statement

The author(s) declare that no Generative AI was used in the creation of this manuscript.

## Publisher's note



## References

Al-fares, W., Bakalowicz, M., Guérin, R., and Dukhan, M. (2002). Analysis of the karst aquifer structure of the Lamalou area (Hérault, France) with ground penetrating radar. *J. Appl. Geophys.* 51:97–106. doi:10.1016/S0926-9851(02)00215-X

Chen, B. W. (2009). *Study on comprehensive geophysical exploration methods of Karst cave exploration for the highway*. Changsha, China: Central South University.

China Water and Power Press (2021). *Code for exploration of water resources and hydropower projects Part 1: geophysical exploration: SL/T 291.1-2021*. Beijing: China Water and Power Press

Coccia, S., Gaudio, V. D., Venisti, N., and Wasowski, J. (2010). Application of Refraction Microtremor (ReMi) technique for determination of 1-D shear wave velocity in a landslide area. *J. Appl. Geophys.* 71, 71–89. doi:10.1016/j.jappgeo.2010.05.001

Dong, H. B., and Wang, C. L. (2003). Development and application of 2D resistivity imaging surveys. *Earth Sci. Front.* (1), 171–176. doi:10.3321/j.issn:1005-2321.2003.01.020

Estradamedina, H., Tuttle, W., Graham, R. C., Allen, M. F., and Jiménez-Osornio, J. J. (2010). Identification of underground karst features using ground-penetrating radar in northern yucatán, méxico. *Vadose Zone J.* 9 (3), 653–661. doi:10.2136/vzj2009.0116

Ford, D., and Williams, P. (2007). *Karst hydrogeology and geomorphology*. Chichester: John Wiley and Sons, Vol. 1-30, 198–210.

Geng, R. L., and Sun, J. H. (2000). Karst and the features of drilling in the karst area. *Explor. Eng. (Rock Soil Drill. Tunneling)*(6), 3–6. doi:10.3969/j.issn.1672-7428.2000.06.002

Goldscheider, N., Plagnes, V., Guerin, R., Valois, R., and Bosch, F. P. (2011). Contribution of geophysical methods to karst-system exploration: an overview. *Hydrogeology J.* 19 (6), 1169–1180. doi:10.1007/s10040-011-0746-x

Hohmann, G. W., and Newman, G. A. (1990). Transient electromagnetic responses of surficial polarizablepatches. *Geophysics* 5, 1098–1100. doi:10.1190/1.1442921

Kaufmann, O. (2014). Geophysical mapping of solution and collapse sinkholes. *J. Appl. Geophys.* 111, 271–288. doi:10.1016/j.jappgeo.2014.10.011

Kresic, N., and Stevanovic, Z. (2009). *Groundwater hydrology of springs: engineering, theory, management, and sustainability*. Oxford: Butterworth-Heinemann. p. 325–343.

Li, D., and Xiao, K. H. (2006). High density electrical resistance exploration in the NO.2 TieFengShan tunnel. *J. Eng. Geol.* 14(3), 197–200. doi:10.3969/j.issn.1672-7940.2006.03.008

Li, J. M. (2005). *Geoelectric field and electrical prospecting*. Beijing: Geological Publishing House, 144–157.

Li, Q., and Cao, L. M. (2017). Exploration and practice of air drilling in karst areas: a case study of Well Anyie-1. *Petroleum Geol. Eng.* 31(1), 115–117+120+134. doi:10.3969/j.issn.1673-8217.2017.01.027

Liu, R. Z., Tian, Q. W., Yu, S. J., Chen, H., and Min, X. L. (2014). Triangular grid sonic computerized tomography for structural concrete. *Prog. Geophys.* 29(4), 1907–1913. doi:10.6038/pg20140458

Luo, Y. D., Liang, H., Gao, H. F., and Qin, X. X. (2009). A tentative discussion on methods for urban karst geological survey and evaluation: a case study of Hangzhou City in Zhejiang Province. *Geol. China* 36 (5), 1187–1193. doi:10.3969/j.issn.1000-3657.2009.05.023

Mccann, D. M., Jackson, P. D., and Culshaw, M. G. (1987). The use of geophysical surveying methods in the detection of natural cavities and mineshafts. *Q. J. Eng. Geol. Hydrogeology* 20, 59–73. doi:10.1144/gsl.qjeg.1987.020.01.06

Meng, F. S., Zhang, G., Chen, M. J., and Li, H. L. (2019). 3-D inversion of high density resistivity method based on 2-D high-density electrical prospecting data and its engineering application. *Geophys. Geochem. Explor.* 43(3), 672–678. doi:10.11720/wtyht.2019.1247

Parise, M., and Gunn, J. (2007). *Natural and anthropogenic hazards in karst areas: recognition, analysis and mitigation*. London: Geological Society Special Publications, Vol. 279, 101–114.

Šumanovac, F., and Weisser, M. (2001). Evaluation of resistivity and seismic methods for hydrogeological mapping in karst terrains. *J. Appl. Geophys.* 47, 13–28. doi:10.1016/s0926-9851(01)00044-1

Telford, W. M., Geldart, L. P., and Sheriff, R. E. (1990). *Applied geophysics*. Cambridge: Cambridge University Press. 2nd ed. p. 305–320.

White, W. B. (1988). *Geomorphology and hydrology of karst terrains*. New York, NY: Oxford University Press, 22–48.

Xu, L. (2015). *Forward simulation for ground penetrating radar and its application for the engineering field*. Jinan: Shandong University.

Yang, J. M. (2017). *Study and application of geophysical method in karst detection of datengxia water conservancy project*. Changchun: Jilin University.

Yin, G. R. (2009). *Survey methods and pile construction technology of bridge in karst region*. Changsha: Central South University.

Yue, C. W. (2007). *Research and application of cross-well electromagnetic tomography*. Changchun: Jilin University.

Zajc, M., Pogačnik, Ž., and Gosar, A. (2014). Ground penetrating radar and structural geological mappinginvestigation of karst and tectonic features in flyschoid rocks as geological hazard for exploitation. *Int. J. Rock Mech. Min. Sci.* 67 (2), 78–87. doi:10.1016/j.ijrmms.2014.01.011

Zhang, J. G., Chen, B. S., Yin, Y. P., Li, H. T., Sun, D. S., and Cao, F. X. (2003). Geophysical detection of concealed karst features in the Three Gorges reservoir area. *Geotechnical Investigation Surv.*(01), 64–66.

Zhou, W., Beck, B. F., and Adams, A. L. (2002). Effective engineering practice for prevention and control of sinkholes in karst areas. *Eng. Geol.* 65 (2-3), 295–315.

frontiers | Frontiers in Earth Science

TYPE Original Research
PUBLISHED 17 September 2025
DOI 10.3389/feart.2025.1674671



OPEN ACCESS

EDITED BY
Tongming Qu,
Hong Kong University of Science and Technology, Hong Kong SAR, China

REVIEWED BY
Xin Han,
Inner Mongolia University of Science and Technology, China
Yi Yang,
Dalian Jiaotong University, China

*CORRESPONDENCE
Rui Yang,
yr_swjtu@outlook.com

RECEIVED 28 July 2025
ACCEPTED 28 August 2025
PUBLISHED 17 September 2025

CITATION
Li K, Yang R, Tu W, Hu Q and Kong Q (2025) Lateral bending behavior and calculation of perforated cross-plate joints in lattice-shaped diaphragm walls.
*Front. Earth Sci.* 13:1674671.
doi: 10.3389/feart.2025.1674671



# Lateral bending behavior and calculation of perforated cross-plate joints in lattice-shaped diaphragm walls

Ke Li[1], Rui Yang[1]*, Weicheng Tu[1], Qinxin Hu[2] and Qian Kong[1]

[1]CCCC Second Harbor Engineering Company Ltd., Wuhan, China, [2]Department of Civil and Environmental Engineering, University of Strathclyde, Glasgow, United Kingdom

**Introduction:** Lattice-shaped diaphragm walls (LSDWs) are increasingly used in bridge foundations and foundation pit enclosures due to their high vertical and horizontal load-bearing capacity. Unlike conventional diaphragm walls that mainly support vertical loads, LSDWs are predominantly subjected to horizontal forces during excavation. However, the lateral bending behavior of their joints—particularly perforated cross-plate joints (PCPJs)—remains insufficiently studied. This paper aims to investigate the lateral bending performance of single- and double-cross PCPJs, a critical joint type in LSDWs.

**Methods:** An experimental program was conducted involving eight sets of PCPJ specimens and one non-jointed wall segment. Four-point bending tests were carried out to analyze the influence of the steel plate perforation ratio on the load–displacement response and ultimate bearing capacity. Typical failure modes and mechanisms were identified, and a calculation method for the lateral bending capacity of PCPJs was proposed.

**Results:** The lateral bending failure of PCPJs was characterized by separation at the web–lower flange steel–concrete interface, fracture of the concrete dowel, and tensile cracking at the end of the steel plate flange. The bending capacities during the elastic stage reached 25.5% and 44.9% of the ultimate load for single- and double-cross PCPJs, respectively. The double-cross PCPJ exhibited higher lateral bending capacity than the single-cross type—approximately 1.6 times under the same perforation ratio—though still lower than the non-jointed segment. Additionally, lateral bearing capacity correlated positively with perforation ratio, with double-cross joints showing greater sensitivity to this parameter.

**Discussion:** The proposed calculation method for lateral bending capacity showed good agreement with experimental values, with deviations ranging from −2.16% to 6.20%, demonstrating its reliability. These findings provide important insights into the structural performance of PCPJs and offer a valuable reference for the design and application of LSDWs in similar engineering applications.

KEYWORDS

**lattice-shaped diaphragm wall, perforated cross-plate joint, four-point bending test, bending bearing capacity, calculation method**

# 1 Introduction

A lattice-shaped diaphragm wall (LSDW) comprises front walls, rear walls, side walls that connect the ends of the front and rear walls, and internal partition walls. LSDWs offer a large wall-soil contact area and exhibit high vertical bearing capacity (Wu et al., 2020). Moreover, their overall bending resistance, horizontal bearing capacity, and seismic performance are significantly superior to those of pile group foundations (Japan Association of Diaphragm Wall, 2001; Wu et al., 2016a). These advantages have contributed to the growing adoption of LSDWs in bridge foundations and excavation support structures (Li W. et al., 2024; Li Z. et al., 2024).

Due to the construction characteristics of diaphragm walls, panel joints are an inevitable feature of LSDWs. However, prior research has predominantly focused on the overall stress performance of LSDWs and the wall-soil interaction mechanism, with limited attention given to the behavior of joints (Japan Association of Diaphragm Wall, 2001; Wu et al., 2016a; Li W. et al., 2024; Li Z. et al., 2024). Furthermore, unlike conventional diaphragm walls that primarily bear loads along the depth direction of the soil layer, LSDWs exhibit a distinct principal force direction. In LSDWs, the length-to-depth ratio is typically less than 1/3 (Cheng et al., 2012; Fu, 2022; Wu et al., 2016b; Zhou et al., 2011), resulting in a unidirectional plate configuration where the depth direction constitutes the long side and the horizontal direction serves as the primary load-resisting axis. Therefore, when soil excavation is involved, the LSDW joint must withstand greater lateral loads than vertical loads, which is a key reason why LSDWs typically adopt rigid joints (Wang et al., 2024). Joints can be categorized into rigid and flexible joints based on their ability to transmit bending moments and shear forces. The recommended rigid joints include I-shaped or cross-shaped perforated steel plate joints and rebar socket joints (JGJ 120-2012, 2012). However, the rigidity of these joints targets conventional diaphragm walls rather than LSDWs. In particular, more common perforated cross-plate joints (PCPJs) have rarely been studied in LSDWs.

Under horizontal loads, PCPJs are subjected to bending moments. Based on the mechanical behavior of steel-concrete composite structures, the lateral bending capacity of PCPJs may be influenced by the bond strength between the steel plates and concrete, as well as the performance of the concrete dowel. The bond strength between steel plates and concrete can be evaluated using push-out, pull-out, and splitting tests (Soh et al., 1999; Lee et al., 2011; Trad et al., 2024). Majdi et al. (Majdi et al., 2014), through pull-out tests, investigated thin-walled corrugated steel embedded in concrete with varying concrete strengths and established a bilinear bond-slip model by presenting the corresponding overall bond-slip curves. Walter et al. (Oguejiofor and Hosain, 1994) studied the normal stress-crack opening relationship at the steel-concrete interface via wedge-shaped splitting tests. They reported that the failure of the steel-concrete interface exhibited quasi-brittle characteristics. However, research on concrete dowels has focused mainly on the shear characteristics of perforated steel plate shear keys. Oguejiofor et al. (Al-Darzi et al., 2007; Ahn et al., 2010; Kim et al., 2018) derived a formula for calculating the shear bearing capacity of perforated steel plate shear keys through push-out test fitting. However, owing to the presence of transverse rebar, the shear mechanism and shear capacity of perforated steel plate shear keys are different from those of perforated steel plates. Wang (Wang et al., 2022) compared shear keys with and without transverse rebar through experiments and reported that the shear of concrete dowel dominated the failure of shear keys without transverse rebar, whereas the shear keys with transverse rebar were dominated by rebar. Moreover, the ultimate shear stiffness of the shear keys with transverse rebar was 2.12 times greater than that in the case without transverse rebar. Chen et al. (Chen et al., 2016a; Chen et al., 2016b) studied the vertical shear behavior of conventional diaphragm wall PCPJs through shear tests and numerical simulations. The results indicated that the perforation ratio influences the bearing capacity of PCPJs, the shear strength of the concrete, and the stiffness of the steel plates. The shear bearing capacity of perforated steel plate shear keys was found to be 1.8 to 4.4 times greater than that of PCPJs, and the existing shear bearing capacity formulas applicable to the former were inadequate for the latter, necessitating targeted modifications. In summary, the limited existing research on PCPJs has primarily focused on shear bearing capacity. Although factors potentially affecting the lateral bending capacity of PCPJs—such as steel-concrete interfaces and concrete dowels—have been explored, the specific mechanisms through which these factors influence bending performance remain unclear.

This study focused on the Fuchi Ship Lock project, the first in China to implement an LSDW as the lock wall. Nine sets of scaled four-point bending tests, with a similitude ratio of 1:3, were conducted on single-cross and double-cross PCPJs within the LSDW to investigate the influence of the steel plate perforation ratio on the lateral bending bearing capacity of PCPJs. The lateral bending failure mechanisms of PCPJs were identified, and a corresponding method for calculating the bending bearing capacity was proposed. The computed results aligned well with the experimental data, offering a valuable reference for the design of PCPJs in LSDWs.

# 2 Project background

The Fuchi Ship Lock chamber features a composite lock wall structure comprising an upper hollow box retaining wall and a lower LSDW. The LSDW measures 21.6 m in height, 144.4 m in length, and 1.2 m in thickness. The net spacing between the front and rear walls is either 10 m or 8.35 m. The diaphragm wall panels consist of various configurations, including I-shaped, L-shaped, T-shaped, and Z-shaped panels, with lengths ranging from 5.3 m to 11.7 m, as illustrated in Figure 1a. The diaphragm wall penetrates 5 m into the bedrock, with a 1.8 m penetration below the karst cave, as shown in Figure 1b.

The joints between the front and rear walls employ a single-cross PCPJ configuration, characterized by a 20 mm-thick cross steel plate flange, a 16 mm-thick web plate, and 32 mm-diameter horizontal and vertical rebars. The horizontal rebars of the primary panel are welded to the steel plate through equal-leg angle steel, with a 150 mm spacing between the reinforcement cages of the primary and secondary panels. Both panels have a flange length of 800 mm. The flange is perforated with eight rows of square holes, each measuring 120 mm × 120 mm, with a net spacing

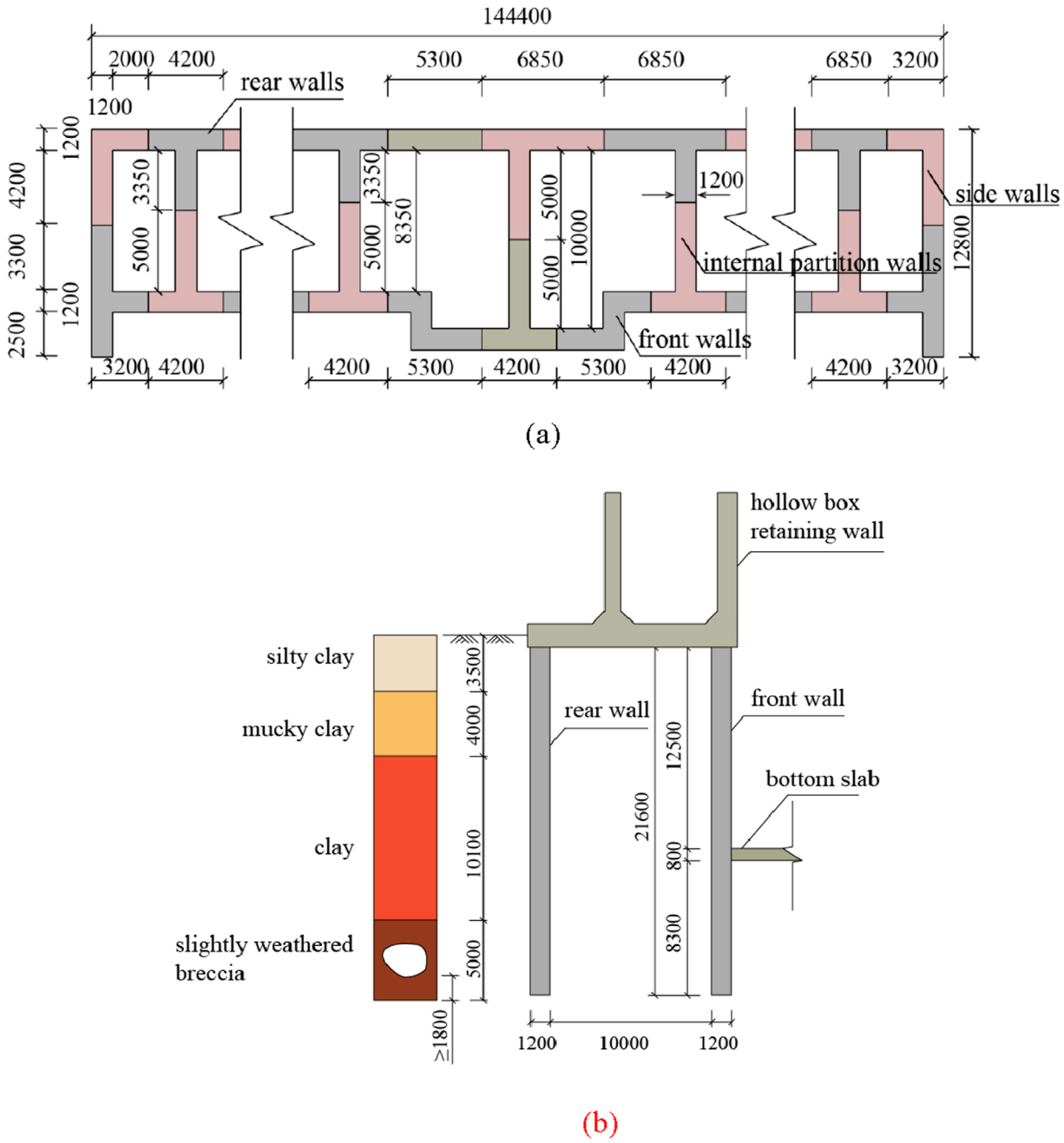


FIGURE 1
Structural diagrams of the diaphragm wall (unit: mm). **(a)** LSDW plan. **(b)** Lock wall elevation.

of 60 mm between holes. The joints of the lattice wall employ a double-cross PCPJ configuration. The double-cross steel plate flange lengths are 430 mm for the primary panel and 800 mm for the secondary panel, with a net spacing of 300 mm between the flanges in the panel width direction. The horizontal rebars of the primary panel are welded to the steel plate using connecting plates. Additionally, a stiffening plate is installed every 1,000 mm between the connecting plate and the web plate. All other structural details are consistent with those of the single-cross PCPJ, as illustrated in Figure 2.

# 3 Experimental overview

## 3.1 Experimental design and parameters

Based on the background of the Fuchi Ship Lock project, single- and double-cross PCPJs with a vertical length of 1 m. A 1:3 scale ratio was adopted in accordance with the similarity theory for structural model tests. Geometric dimensions were scaled down by 1/3. Material properties were kept consistent with the prototype: the concrete strength grade C30 and steel elastic modulus matched the

10.3389/feart.2025.1674671

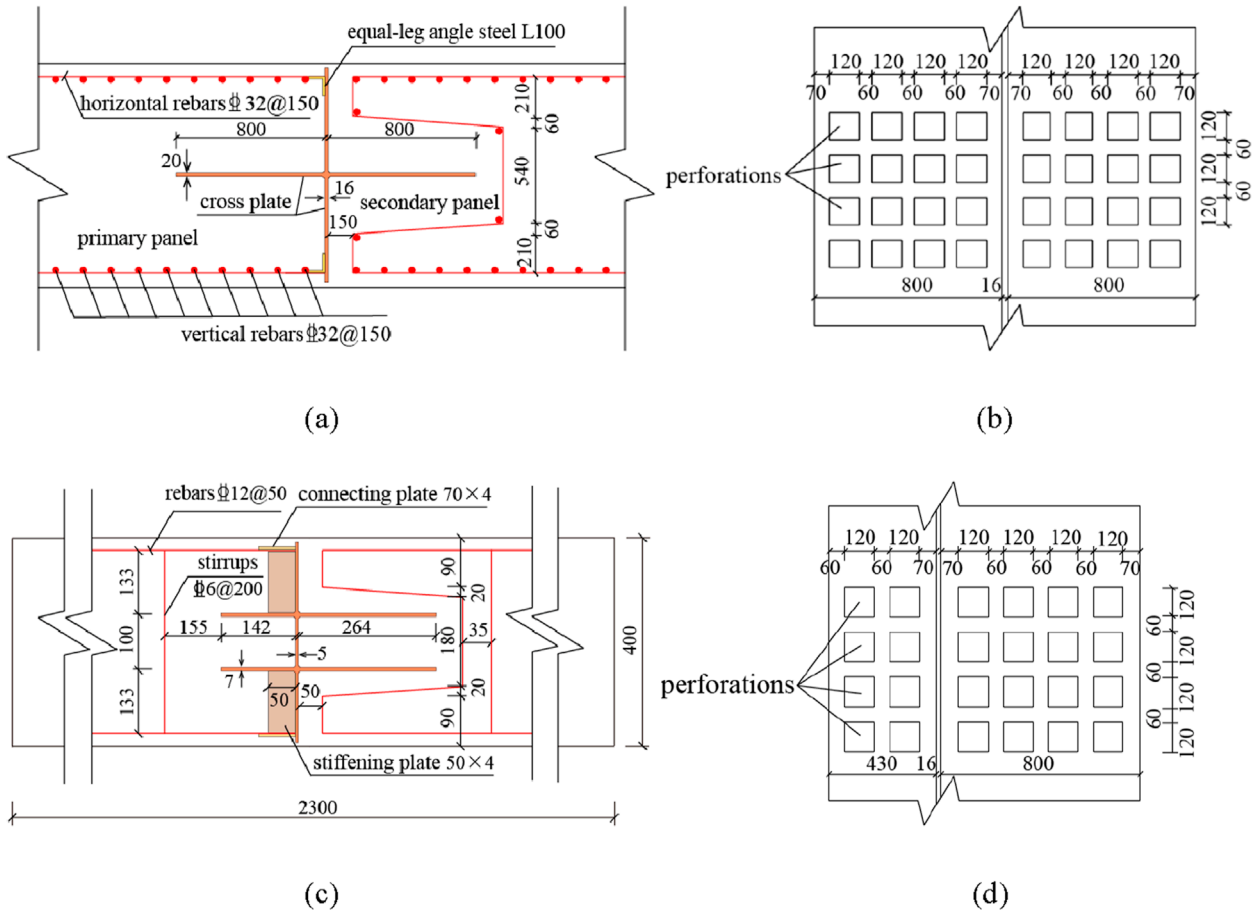


FIGURE 2
PCPJ construction drawings (unit: mm). **(a)** Schematic of a single-cross PCPJ. **(b)** Elevation of a single-cross PCPJ. **(c)** Schematic of a double-cross PCPJ. **(d)** Elevation of a double-cross PCPJ.

prototype materials, ensuring strength equivalence. The main rebar had a diameter of 12 mm and a spacing of 50 mm. The effect of the vertical reinforcement in the prototype was not considered in this study. Stirrups with a diameter of 6 mm and a spacing of 200 mm were provided and arranged to avoid the region of the cross steel plate. The steel plate flange and web had thicknesses of 7 mm and 5 mm, respectively. The vertical reinforcement was neglected in the test because the experiment focused on the lateral bending behavior of the joints, and the vertical reinforcement contributes minimally to lateral bending resistance. Both the single- and double-cross PCPJs were connected to the main reinforcement bars by welding with equal-leg angle steel, as illustrated in Figure 3.

A total of 9 specimens were prepared for the experiment, among which the r-1 specimen was a comparative non-joint specimen. Its main rebar had a diameter of 12 mm and a spacing of 50 mm, and its stirrups had a diameter of 6 mm and a spacing of 200 mm. The steel plate opening size for the secondary panel of the PCPJs was 40 mm × 40 mm. The number of openings in the primary panel remained consistent with the design, while the secondary panel included 20, 16, 8, and 0 openings for specimens s-1 to s-4 and d-1 to d-4, respectively. The dimensions of the steel plates are provided in Figure 4. The perforation ratio is defined as the ratio of the open area in the secondary panel to the total area of the steel plate flange. Accordingly, the perforation ratios for specimens s-1 to s-4 and d-1 to d-4 were 38.4%, 30.7%, 15.3%, and 0%, respectively.

## 3.2 Loading plan and layout of measuring points

The experiment utilized a 100 t multichannel servo loading system, which applied a load to the specimen via a distributing beam with a 700 mm spacing between loading points. Two hinge supports with spacings of 2,100 mm were arranged at the bottom of the specimen, as shown in Figures 5a,b.

The r-1 specimen was tested as a reinforced beam, representing a rigid joint with substantial bending capacity. The load increment for this specimen was set at 1 t per step. In contrast, the bending capacity of perforated cross-plate joints is significantly lower than that of the reinforced beam, with a load increment of 0.1 t per level for s-1–s-4 and d-1–d-4. After each load was held for 120 s and data stability was achieved, the next level of load was applied until the load on the actuator decreased.

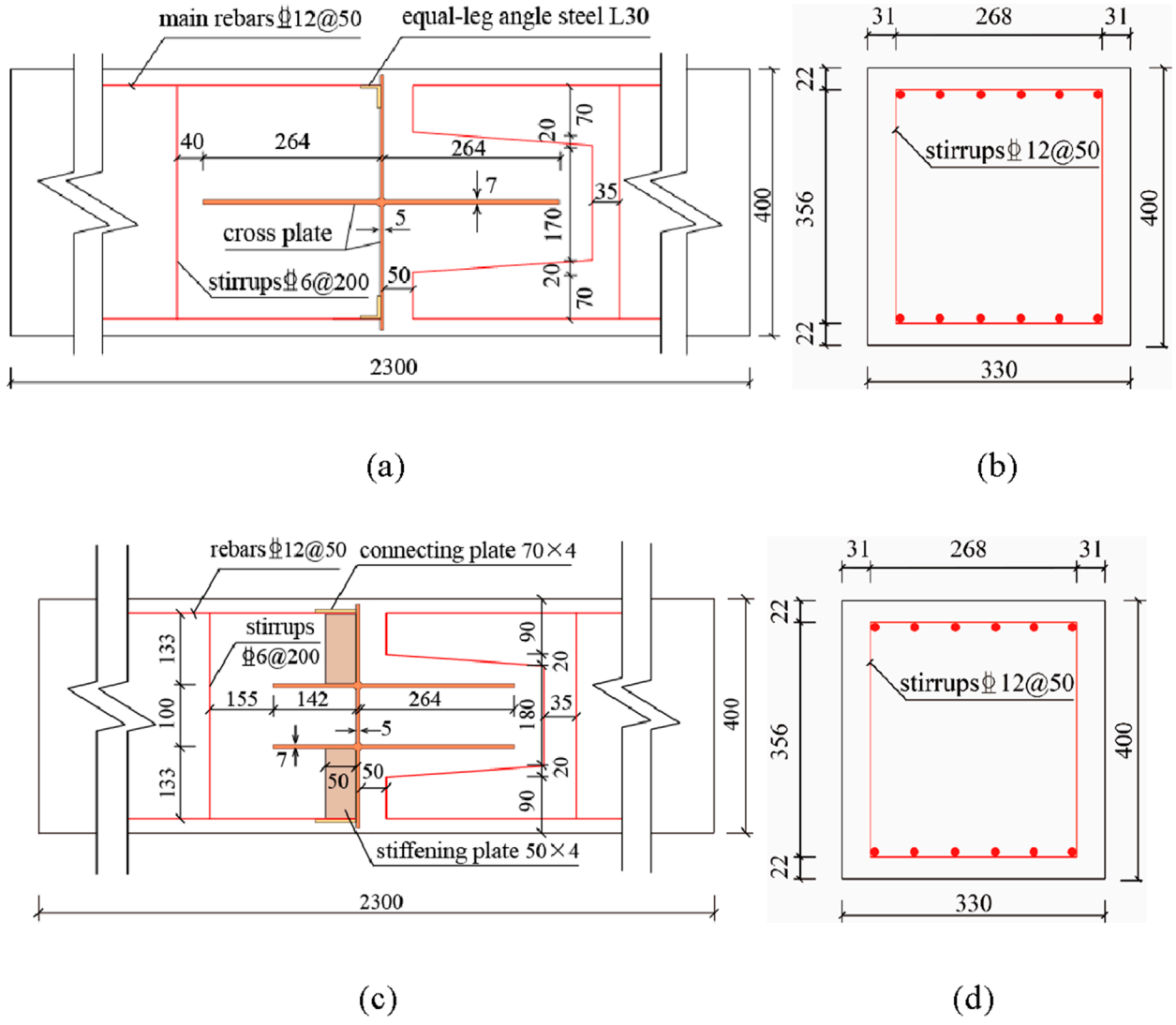


FIGURE 3
Specimen diagrams (unit: mm). **(a)** Elevation of a single-cross PCPJ specimen **(b)** Section of a single-cross PCPJ specimen. **(c)** Elevation of a double-cross PCPJ specimen. **(d)** Section of a double-cross PCPJ specimen.

The displacement sensor of the r-1 specimen was arranged in its mid-bottom, whereas the displacement sensors of the s-1–s-4 and d-1–d-4 specimens were arranged slightly right of the mid-bottom. The r-1 specimen was not equipped with strain gauges, whereas the s-1–s-4 and d-1–d-4 specimens were equipped with steel strain gauges (TS, CS, TX, CX) in the rebar area adjacent to the steel plate. One steel plate strain gauge (PL, PR) was installed on each side of the lower flange of the single-cross steel plate, adjacent to the web plate. The strain gauge arrangement for the double-cross steel plates followed the same configuration as the single-cross case, with gauges designated as PLS, PRS, PLX, and PRX. A total of four concrete strain gauges were employed: two (SG1 and SG2) were arranged horizontally at the lower part of the specimen to monitor the plain concrete between the steel plate and the M-shaped reinforcement bars; the remaining two gauges (SG3 and SG4) were positioned vertically on the right side, covering the right steel plate flange, as illustrated in Figures 5c,d.

# 4 Analysis of experimental results

## 4.1 Test phenomena and failure modes

The failure modes of the specimens are shown in Figure 6. The failure mode of the r-1 specimen is a typical failure mode of an under-reinforced beam. In the failure of single-cross PCPJ specimens, cracking initiates in the secondary panel, with a through-crack extending from the bottom of the specimen along the steel plate web to the end of the steel plate flange. This forms an L-shaped crack path that rotates 90° clockwise. Additional vertical or diagonal cracks appear at the end of the steel plate flange, as illustrated in Figures 6a–e. The failure mode of the double-cross PCPJ specimens is similar to that of the single-cross specimens, with a through-crack propagating from the specimen base along the steel plate web to the end of the lower flange, where diagonal cracks are also observed, as shown in Figures 6f–i.

10.3389/feart.2025.1674671

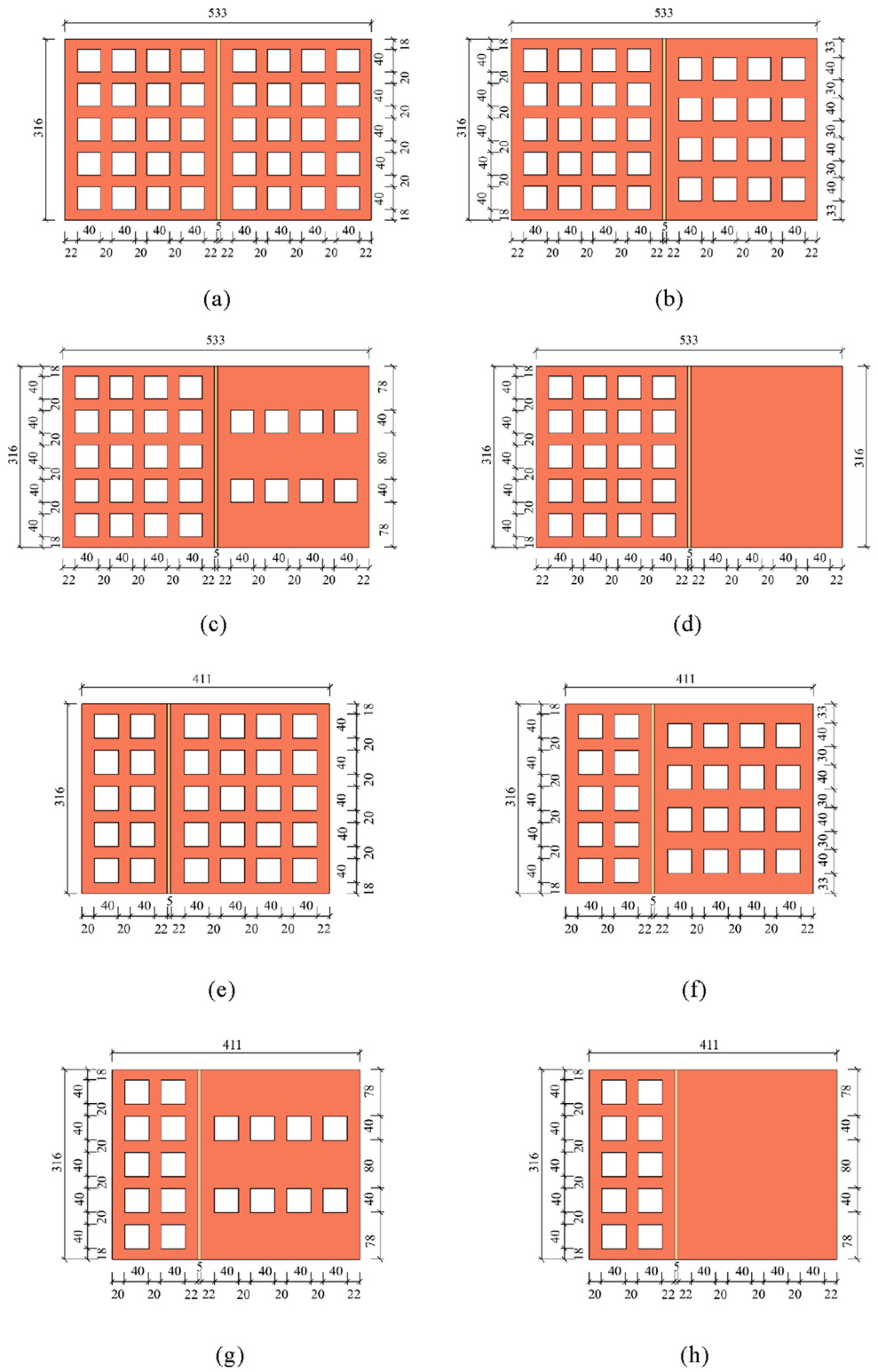


FIGURE 4
Flange dimension diagrams of the cross steel plate specimens (unit: mm). **(a)** Steel plate openings of specimen s-1. **(b)** Steel plate openings of specimen s-2. **(c)** Steel plate openings of specimen s-3. **(d)** Steel plate openings of specimen s-4. **(e)** Steel plate openings of specimen d-1. **(f)** Steel plate openings of specimen d-2. **(g)** Steel plate openings of specimen d-3. **(h)** Steel plate openings of specimen d-4.

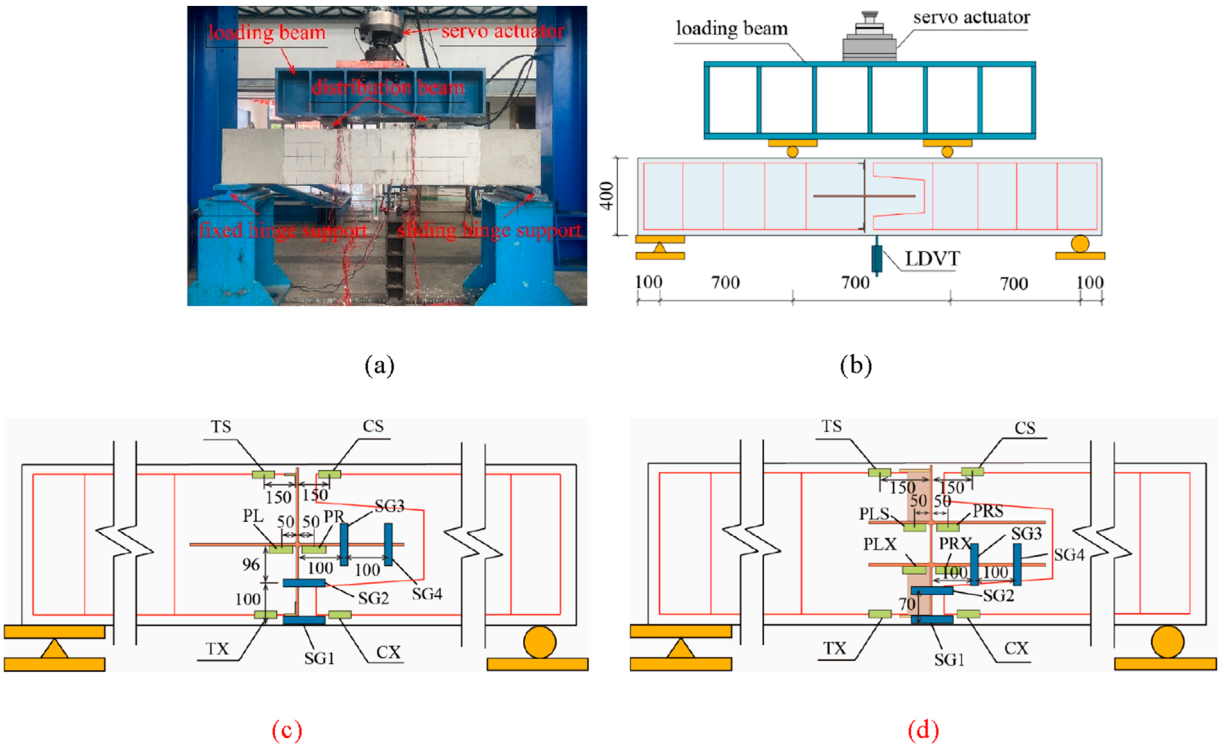


FIGURE 5
Specimen loading device and layout of the measuring points (unit: mm). **(a)** Experimental loading device. **(b)** Loading schematic. **(c)** Layout of measuring points for single-cross PCPJ specimens. **(d)** Layout of measuring points for double-cross PCPJ specimens.

Here, we take s-1 as an example to explain the test phenomenon in the single-cross PCPJ loading process. First, initial cracks appear on the concrete surface near the lower steel plate web of the specimen (Figure 7a). As the load increases, the steel-concrete interface at the bottom of the specimen separates (Figure 7b). Lateral cracks develop near the interface between the lower surface of the steel plate flange and the adjacent concrete, extending toward the end of the flange (Figure 7c). Upon failure, the lower web of the steel plate detaches entirely from the concrete, forming a smooth splitting surface (Figure 7d). Complete separation occurs at the steel-concrete interface beneath the steel plate flange, accompanied by fracture of the concrete dowel within the flange opening and the formation of vertical cracks at the flange end (Figures 7e,f).

The test phenomena of the double-cross d-1 specimen during the loading process are similar to those of the single-cross s-1 specimen. The core difference is that failure of the flange steel-concrete interface occurs on the lower surface of the lower flange, and the fracture position of the concrete dowel is inside the lattice hole of the lower flange as shown in (Figures 8a–f).

## 4.2 Analysis of load-vertical displacement curves

The PCPJ loading process in the four-point bending test can be divided into four stages: elastic, elastoplastic, failure descending, and residual, as shown in Figure 9a. The measured values of the critical loads for adjacent stages are denoted as $P_e$, $P_u$, and $P_r$, and the corresponding measured values of the mid-span deflections are $\Delta_e$, $\Delta_u$, and $\Delta_r$, as shown in Table 1.

1. Elastic stage (OA): During this stage, the load displacement curve is almost a straight line, the specimen does not show any cracks, and no slip exists between the cross steel plate and the concrete.
2. Elastoplastic Stage (AB): This stage begins with the onset of separation at the steel plate-concrete interface near the bottom of the specimen, marked by a distinct step-like inflection point on the load-displacement curve. As the applied load increases, the lower web of the steel plate progressively detaches from the concrete, eventually leading to complete separation. Concurrently, the lower surface of the steel plate flange (the lower flange) begins to separate from the concrete. During this process, the slope of the load-displacement curve gradually decreases, continuing until the specimen reaches its ultimate bearing capacity.
3. Failure descending stage (BC): significant separation occurs between the steel plate and the concrete, with the separation surface forming an L shape that rotates clockwise by 90°. Moreover, the concrete dowel fractures in the hole of the steel plate flange (lower flange), resulting in vertical or diagonal tensile cracks near the flange end, and the specimen's bearing capacity rapidly decreases.
4. Failure residual stage (CD): The width of the cracks in the concrete increases, and the measured mid-span deflection rapidly increases until the bearing capacity of the specimen becomes stable.

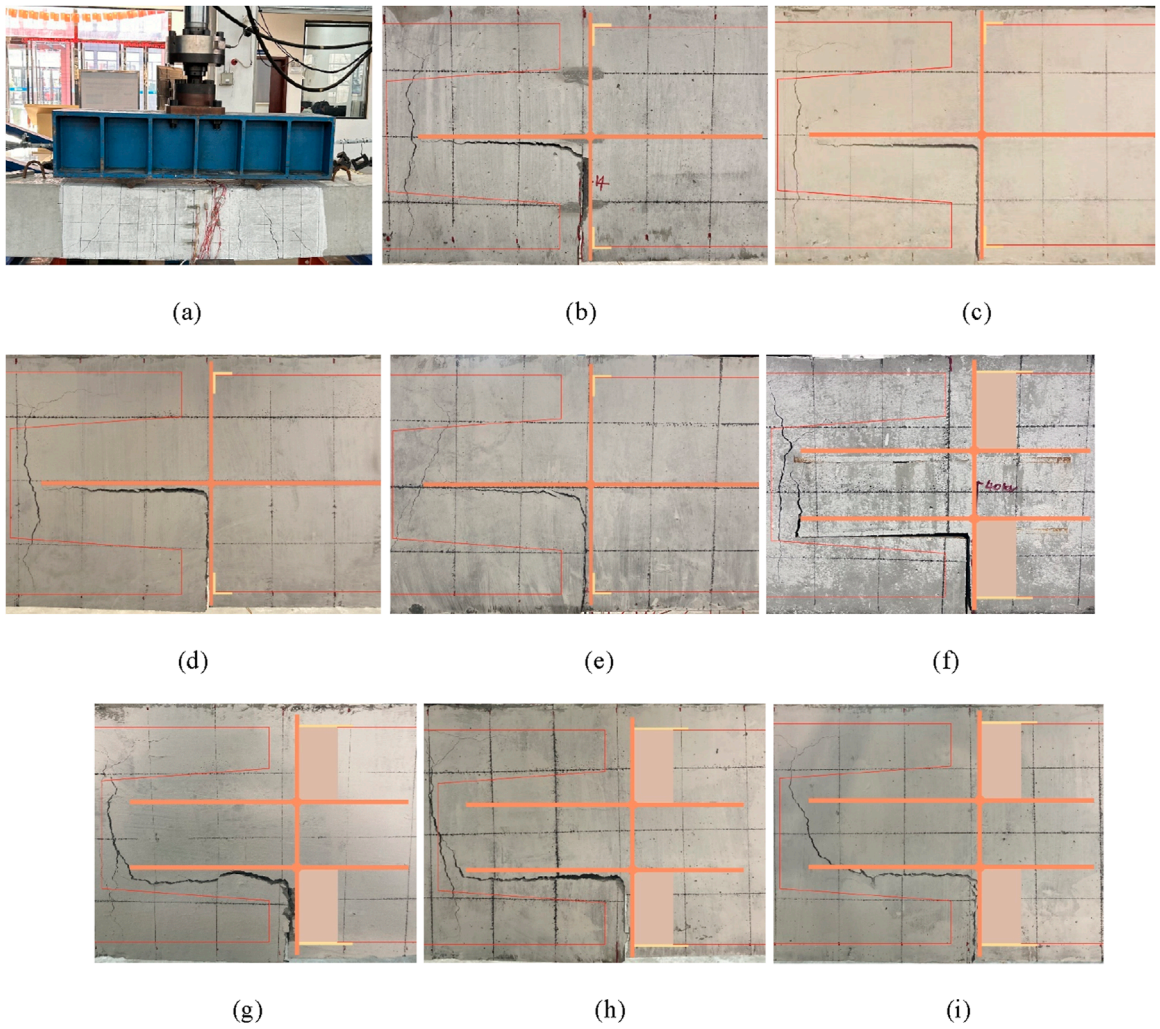


FIGURE 6
Specimen failure patterns. **(a)** Specimen r-1. **(b)** Specimen s-1. **(c)** Specimen s-2. **(d)** Specimen s-3. **(e)** Specimen s-4. **(f)** Specimen d-1. **(g)** Specimen d-2. **(h)** Specimen d-3. **(i)** Specimen d-4.

Figure 9 and Table 1 show that, compared with those of the nonperforated steel plate, with increasing perforation ratio, the bending capacities of the single-cross PCPJs increase by 41.67%, 70.83%, and 95.83%, respectively, whereas the bending capacities of the double-cross PCPJs increase by 60.0%, 97.14%, and 122.86%, respectively. This finding indicates that an increase in the perforation ratio can significantly improve the lateral bending capacity of joints, and the improvement is greater in the double-cross PCPJ case. The reason is that the concrete dowel has a greater bending contribution than the steel-concrete interface.

The bearing capacity ratios between the double-cross PCPJs and the single-cross PCPJs are 1.66, 1.68, 1.65, and 1.30 from high to low perforation ratios. These results reveal that double-cross PCPJs exhibit a greater bearing capacity than single-cross PCPJs, with an average of 1.57 times that of single-cross PCPJs. This is because the lower flange of the double-cross steel plate is further away from the neutral axis, where the bending contribution of the steel-concrete interface and concrete dowel is more significant.

The stiffness and $P_e$ values in the elastic stage are basically the same for s-1–s-4, whereas the stiffness and $P_e$ of d-1–d-4 decrease with decreasing perforation ratio. This is because the single-cross PCPJ flange is located near the neutral axis in the elastic stage, and there is almost no need for coordinated deformation between the steel plate and the concrete. The lower flange of the double-cross PCPJ is in the tensile zone and needs to undergo coordinated deformation through the steel-concrete interface and concrete dowel. The coordinated deformation ability is strengthened with increasing perforation ratio, thereby improving the bending stiffness of the component.

The $P_u$ values of s-1 and d-1 are 13.8% and 22.9% of that of r-1, and their $\Delta_u$ values are 9.23% and 14.6% of that of r-1. These results indicate that the ultimate bearing capacity and deformation capacity of the PCPJs are weaker than those of the non-joint segment, as shown in Figure 9C. In addition, after the ultimate bearing capacity is reached, the bearing capacity of the PCPJs sharply decreases, and the failure mode approaches brittle failure.

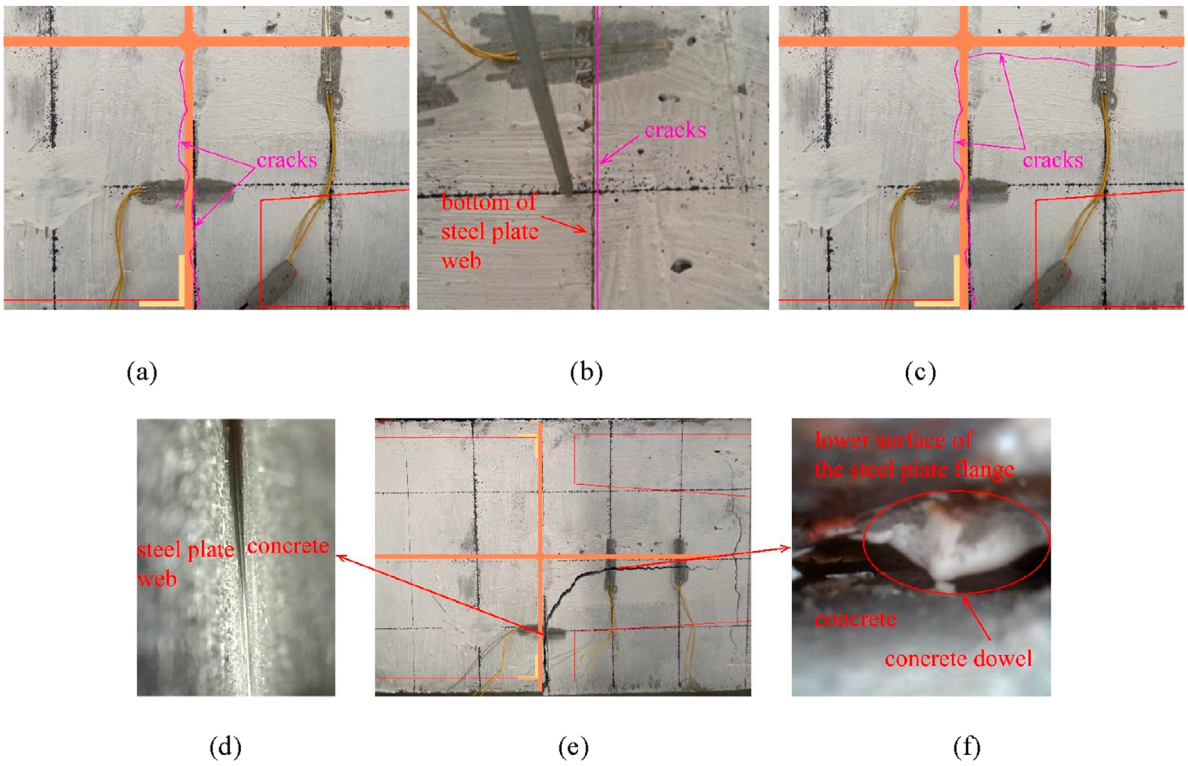


FIGURE 7
Typical test phenomena in a single-cross steel plate specimen. **(a)** Initial cracks. **(b)** Bottom cracks. **(c)** Cracks propagation. **(d)** Web-concrete interface. **(e)** Failure pattern. **(f)** Steel-concrete interface beneath the steel plate flange.

## 4.3 Steel plate strain analysis

The load-steel plate strain curves of each specimen in the elastic and elastoplastic stages are shown in Figure 10.

As shown in Figure 10, the load-steel plate strain curves exhibit bilinear characteristics, and the load corresponding to the inflection point is almost the same as the $P_e$ value of the specimen. The slopes of the load-steel plate strain curves in the elastic stage are consistent for the s-1–s-4 specimens, whereas the slopes of the d-1–d-4 specimens are positively correlated with the perforation ratio. These trends are consistent with the stiffness conclusions from the load-displacement curves for the elastic-stage specimens. The slope of the load-displacement curve in the elastoplastic stage is lower than that observed in the initial elastic stage. This reduction is attributed to the upward shift of the neutral axis as the lower web of the steel plate progressively separates from the concrete, leading to increased stress in the steel plate flange (lower flange). For specimens d-1 through d-4, the strain readings of PLS and PLR on the upper flange transition from negative to positive. Specifically, as the load increases, the lower web and flange progressively separate from concrete, reducing their contribution to resistance. This forces the neutral axis to rise, shifting the upper flange from the compressive zone to the tensile zone. When the neutral axis exceeds the upper flange elevation, tensile strains dominate, reflecting the transfer of tensile forces to the upper flange as the lower components lose efficacy.

At a given load level, the load is $P_u$, the PR microstrains of the s-1 to s-4 steel plates are 410, 365, 308, and 204, respectively, while the corresponding PL microstrains are 440, 408, 349, and 223. For the d-1 to d-4 steel plates, the PRX microstrains are 392, 368, 339, and 213, and the PLX microstrains are 442, 406, 378, and 240, respectively. The strain measured on the left edge of the steel plate is generally greater than that on the right edge of the same component, which may be attributed to better contact between the left edge and the concrete, whereas slight slippage is observed on the right edge. Before the separation of the steel plate and concrete, the strain of the structure can be approximated as the strain at the steel-concrete interface. The strains of the steel plate specimens with the same perforation ratio are similar, with a maximum difference of only 9.1%, indicating that the ultimate strain at the interface is primarily affected by the perforation ratio and is not significantly related to the specific PCPJ form.

The maximum stress of the steel plate is 91 MPa, and the entire loading process is in the elastic stage.

## 4.4 Concrete strain analysis

The strains of the concrete in the elastic and elastoplastic stages are shown in Figure 11. The strain overflow in the figure is caused by the development of cracks in the concrete, leading to the fracture of the strain gauges.

Figure 11 shows that under the same load increment, the strain slopes of SG2, SG3, and SG4 increase with increasing perforation ratio, indicating that the concrete dowel can delay the development

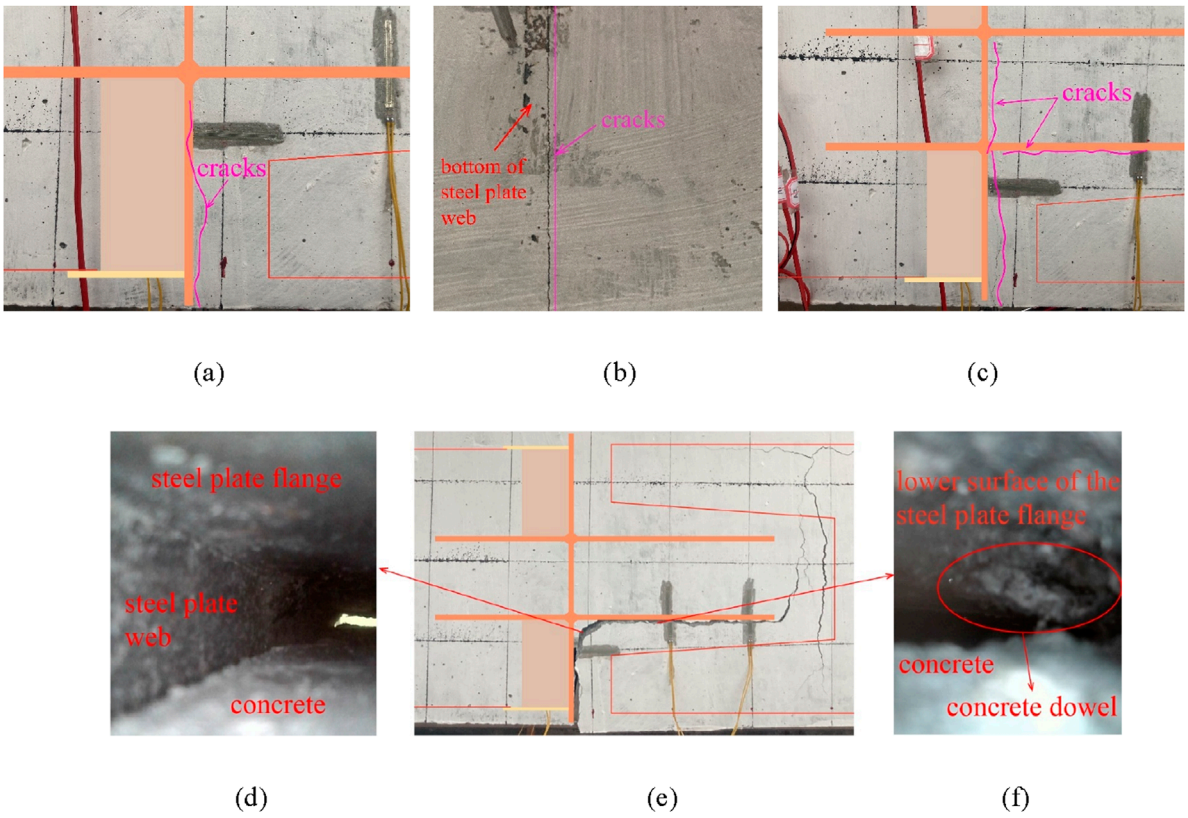


FIGURE 8
Typical test phenomena in a double-cross steel plate specimen. **(a)** Initial cracks. **(b)** Bottom cracks. **(c)** Cracks propagation. **(d)** Web-concrete interface. **(e)** Failure pattern. **(f)** Steel-concrete interface beneath the steel plate flange.

of steel-concrete interface cracks. The strains recorded by SG4 do not exceed the measurement range, indicating that the steel plate flange does not fully detach from the concrete at the point of ultimate bearing capacity. Additionally, the load corresponding to the strain overflow of SG1 aligns with the transition point to the elastoplastic stage, confirming that the end of the elastic stage is marked by the separation of the lower web of the steel plate from the concrete.

Under identical loading conditions and with the same number of steel plate openings, the strains recorded by SG1–SG4 in double-cross PCPJs are lower than those observed in the single-cross PCPJ specimens. This can be attributed to the greater distance between the lower flange of the double-cross PCPJ and the neutral axis, as well as the tensile forces acting on the upper flange, which help to delay the separation of the interface between the lower flange steel plate and the concrete.

# 5 Calculation method for bending bearing capacity

## 5.1 Failure mechanisms

According to the experimental phenomena and data, the lateral bending failure mechanisms of the PCPJs are as follows:

1. The normal bonding strength at the steel-concrete interface is lower than the bonding strength between concrete aggregates. Under the action of bending moments, the lower web of the steel plate progressively detaches from the surrounding concrete. As a result, the neutral axis gradually shifts upward from the mid-height of the specimen, ultimately subjecting the cross steel plate flange to tensile forces.
2. When the steel plate flange-concrete region is subjected to bending and tensile forces, the strains in the steel plate and the concrete are equal. However, due to the elastic modulus of the steel plate being about seven times that of the concrete, the resulting stress difference is primarily resisted by two components: the tangential stress at the steel-concrete interface of the steel plate flange, and the shear resistance provided by the concrete dowel within the flange opening. As the stress differential increases, the concrete dowel undergoes shear failure, and the concrete begins to slide relative to the lower surface of the steel plate flange. This continues until the tangential cohesion at the interface reaches its maximum, at which point the corresponding bending moment defines the ultimate bearing capacity.
3. As the relative sliding between the concrete and the lower surface of the steel plate flange continues to increase, the tangential cohesion at the steel-concrete interface decreases.

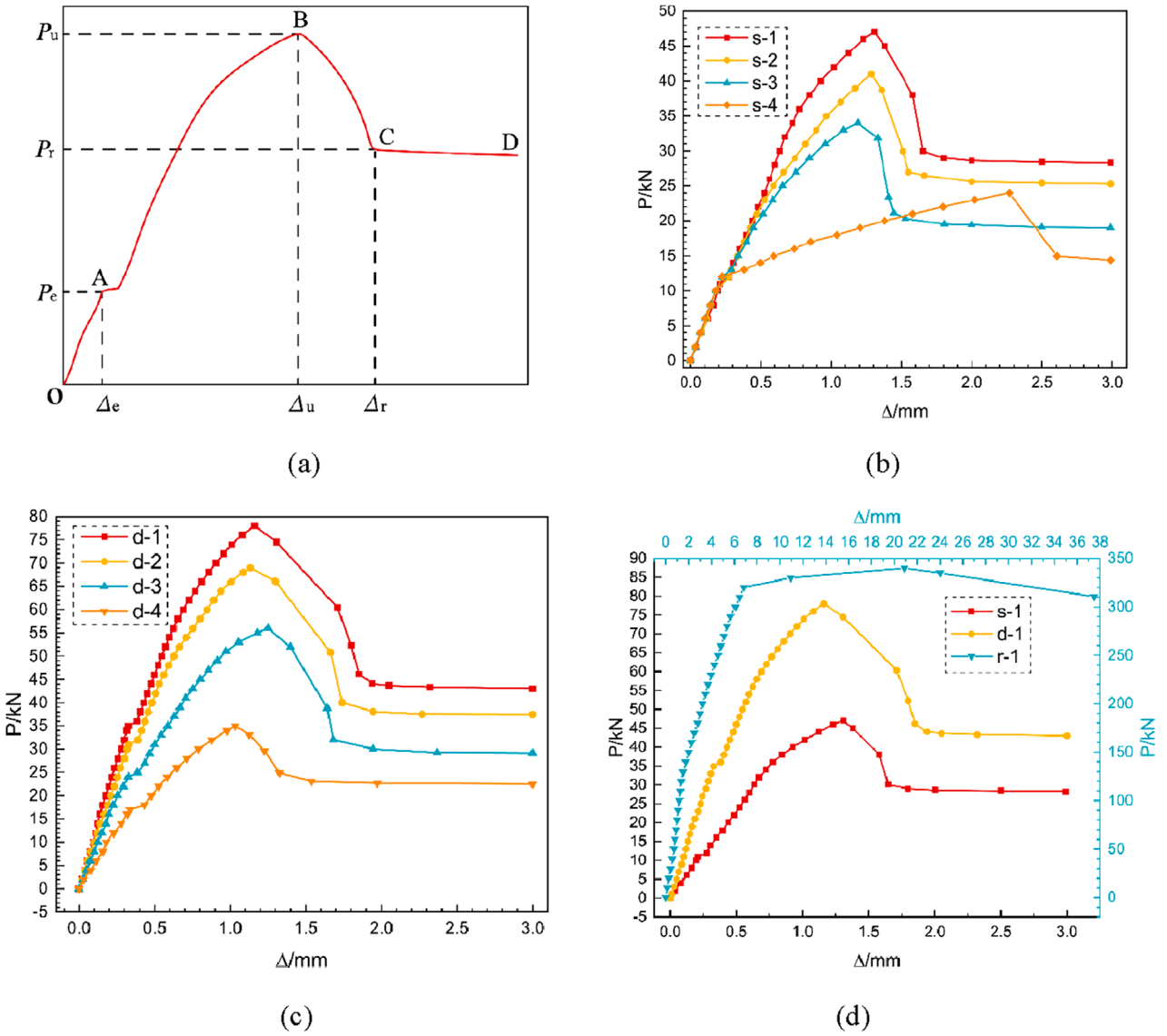


FIGURE 9
Load–displacement curves. **(a)** Typical load-displacement curves of PCPJs specimens. **(b)** Load-displacement curves of single PCPJs specimens. **(c)** Load-displacement curves of double PCPJs specimens. **(d)** Load-displacement curves of s-1, d-1 and r-1.

Concurrently, cracking develops in the concrete at the end of the flange, resulting in a rapid decline in bearing capacity until a stable residual value is achieved.

## 5.2 Simplified calculations and assumptions

We simplify the bearing capacity into the sum of two parts. Part I separates the steel plate web and the concrete, considering only the influence of the normal stress at the interface between the steel plate web and the concrete. Part II involves the separation between the lower surface of the steel plate flange and the concrete, as well as the tensile cracking of the concrete at the flange end. Considering the end section of the steel plate flange as the object of analysis, equilibrium is achieved through the combined effects of concrete stress, steel-concrete interface stress at the flange, and rebar stress, as illustrated in Figure 12. Due to the detachment of the steel plate web from the concrete, the stress level in the concrete beneath the flange (lower flange) is relatively low and therefore excluded from the analysis.

The following simplifications and assumptions are used when calculating the bearing capacity:

1. The influence of the differential biting force between the steel plate flange and the concrete on the bearing capacity of Part I is not considered.
2. The normal stress at the interface between the steel plate flange and the concrete is neglected.
3. The end section of the Part II flange is assumed to satisfy the plane section hypothesis.

TABLE 1 Test results of the PCPJ lateral bending bearing capacity.

| 编号No. | $P_e$ (kN) | $P_u$ (kN) | $P_r$ (kN) | $\Delta_e$ (mm) | $\Delta_u$ (mm) | $\Delta_r$ (mm) | $P_e/\Delta_e$ (kN·mm$^{-1}$) |
|---|---|---|---|---|---|---|---|
| r-1 | 130.00 | 340.00 | 310.32 | 1.51 | 20.87 | 37.46 | 86.09 |
| s-1 | 12.00 | 47.00 | 30.00 | 0.21 | 1.31 | 1.65 | 57.14 |
| s-2 | 12.00 | 42.00 | 27.00 | 0.23 | 1.29 | 1.55 | 52.17 |
| s-3 | 12.00 | 34.00 | 21.12 | 0.22 | 1.19 | 1.45 | 54.55 |
| s-4 | 12.00 | 27.00 | 15.00 | 0.22 | 2.27 | 2.60 | 54.55 |
| d-1 | 35.00 | 78.00 | 46.20 | 0.33 | 1.16 | 1.85 | 106.06 |
| d-2 | 31.00 | 69.00 | 40.04 | 0.33 | 1.13 | 1.74 | 93.94 |
| d-3 | 24.00 | 56.00 | 32.01 | 0.32 | 1.25 | 1.68 | 75.00 |
| d-4 | 18.00 | 35.00 | 24.94 | 0.34 | 1.03 | 1.33 | 52.94 |

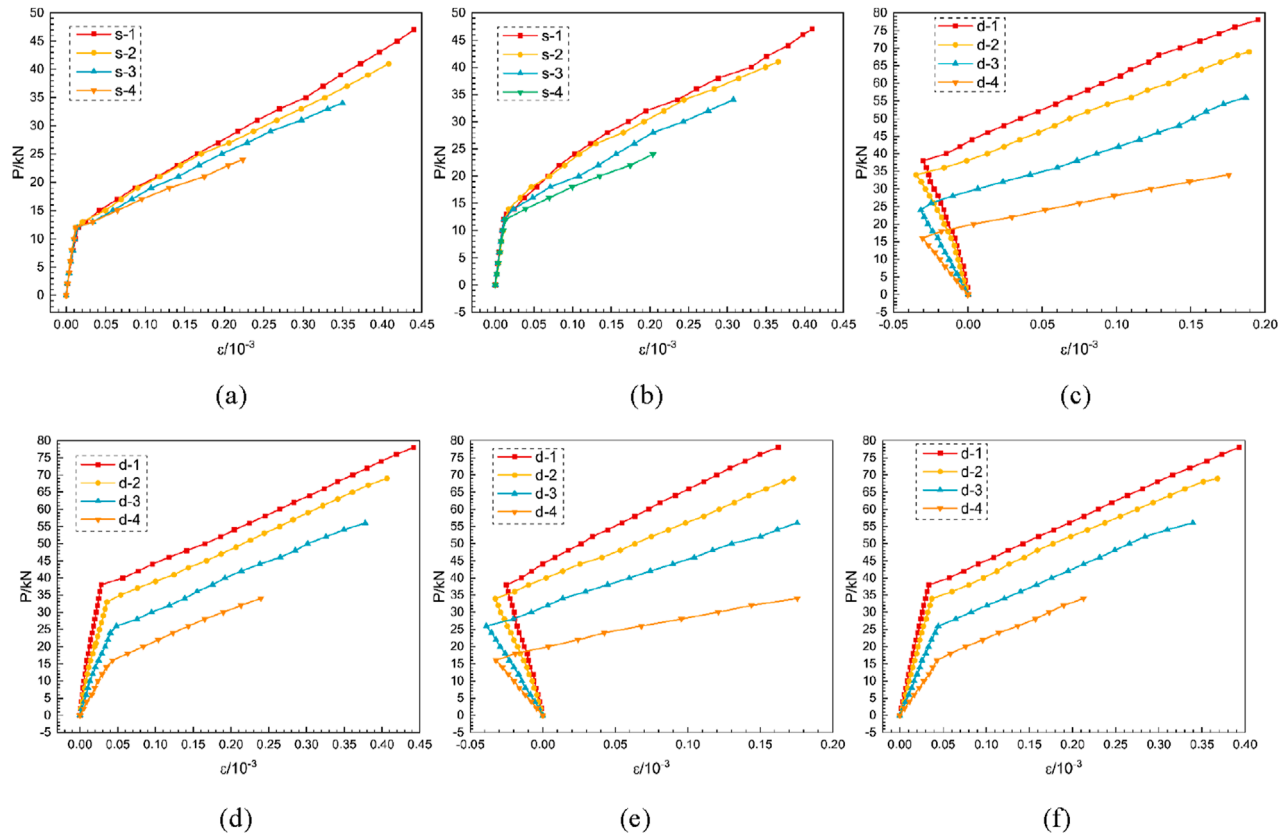


FIGURE 10
Load-steel plate strain curves. **(a)** PL. **(b)** PR. **(c)** PLS. **(d)** PLX. **(e)** PRS. **(f)** PRX.

4. When a PCPJ reaches its ultimate state, the biting force between the flange (lower flange) and the concrete attains its maximum value, and the stress distribution in the compressive and tensile zones of the concrete section is triangular.

## 5.3 Calculation method

The bearing capacity $M_u$ is calculated according to Equation 1.

$$M_u = M_{\mathrm{I}} + M_{\mathrm{II}}; \tag{1}$$

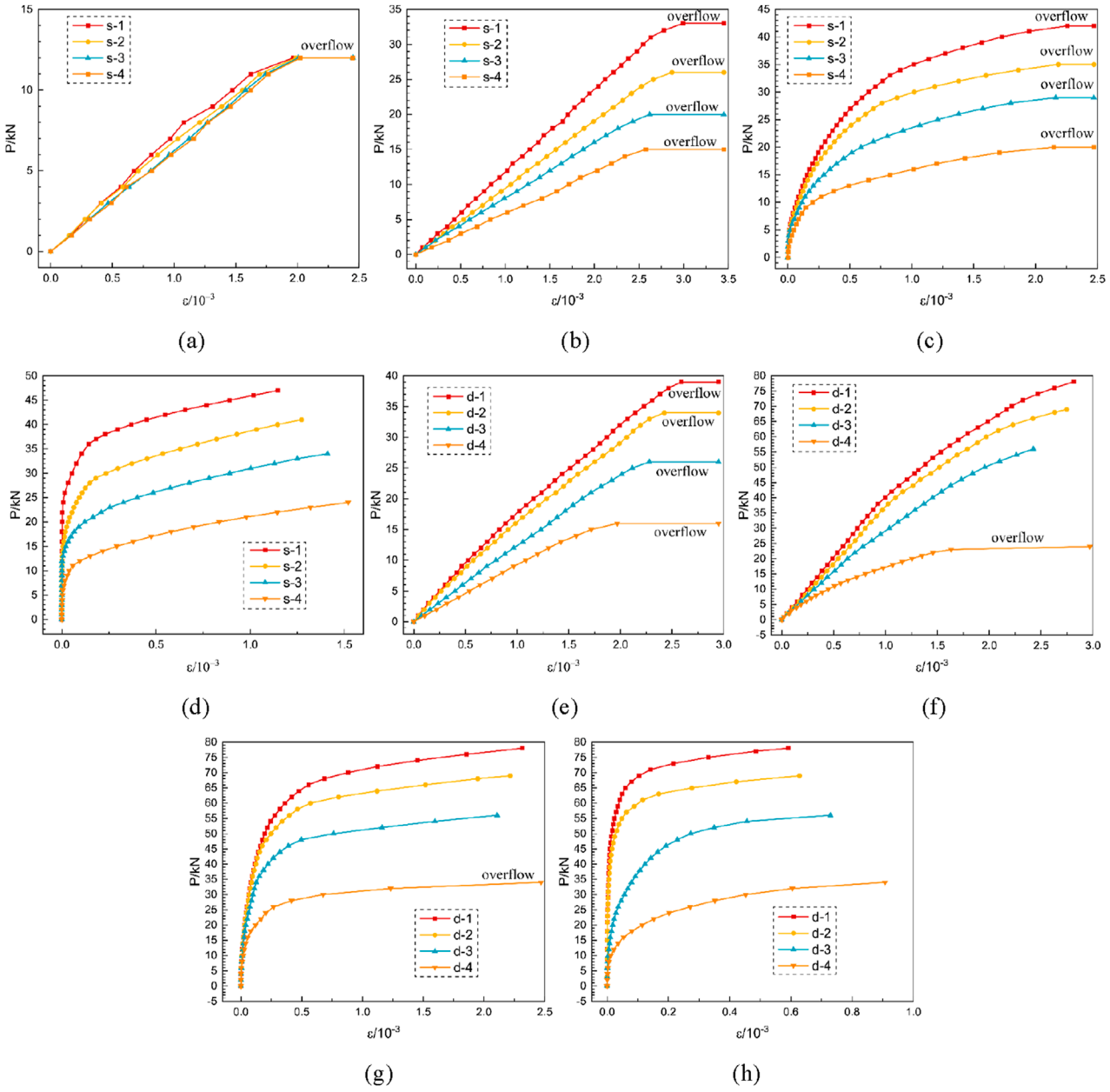


FIGURE 11
Load-concrete strain curves. **(a)** Single-cross steel plate SG1. **(b)** Single-cross steel plate SG2. **(c)** Single-cross steel plate SG3. **(d)** Single-cross steel plate SG4. **(e)** Double-cross steel plate SG1. **(f)** Double-cross steel plate SG2. **(g)** Double-cross steel plate SG3. **(h)** Double-cross steel plate SG4.

The Part I bearing capacity $M_{\mathrm{I}}$ is calculated according to Equation 2.

$$M_{\mathrm{I}} = \sigma_u W \tag{2}$$

where $\sigma_u$ represents the maximum normal stress at the steel-concrete interface, which is 0.17 MPa (Xue et al., 2022), and where $W$ is the section modulus obtained via the equivalent section method.

The simplified stress-strain distribution of Part II is shown in Figure 13.

The strain $\varepsilon_{cs}$ at the interface between the lower surface of the steel plate flange (lower flange) and the concrete is calculated according to Equation 3.

$$\varepsilon_{cs} = \Delta_s / l_p \tag{3}$$

where $\Delta_s$ is the slip corresponding to the peak shear stress at the steel plate-concrete interface, which is 0.014 mm (Song et al., 2020), and where $l_p$ is the length of the steel plate flange.

The maximum tensile strain $\varepsilon_t$ of the section concrete is calculated according to Equation 4.

$$\varepsilon_t = \left(h - x - h_p\right)\varepsilon_{cs}/(h - x) \tag{4}$$

where $h$ is the height of the section, $x$ is the height of the compression zone, and $h_p$ is the thickness of the steel plate flange.

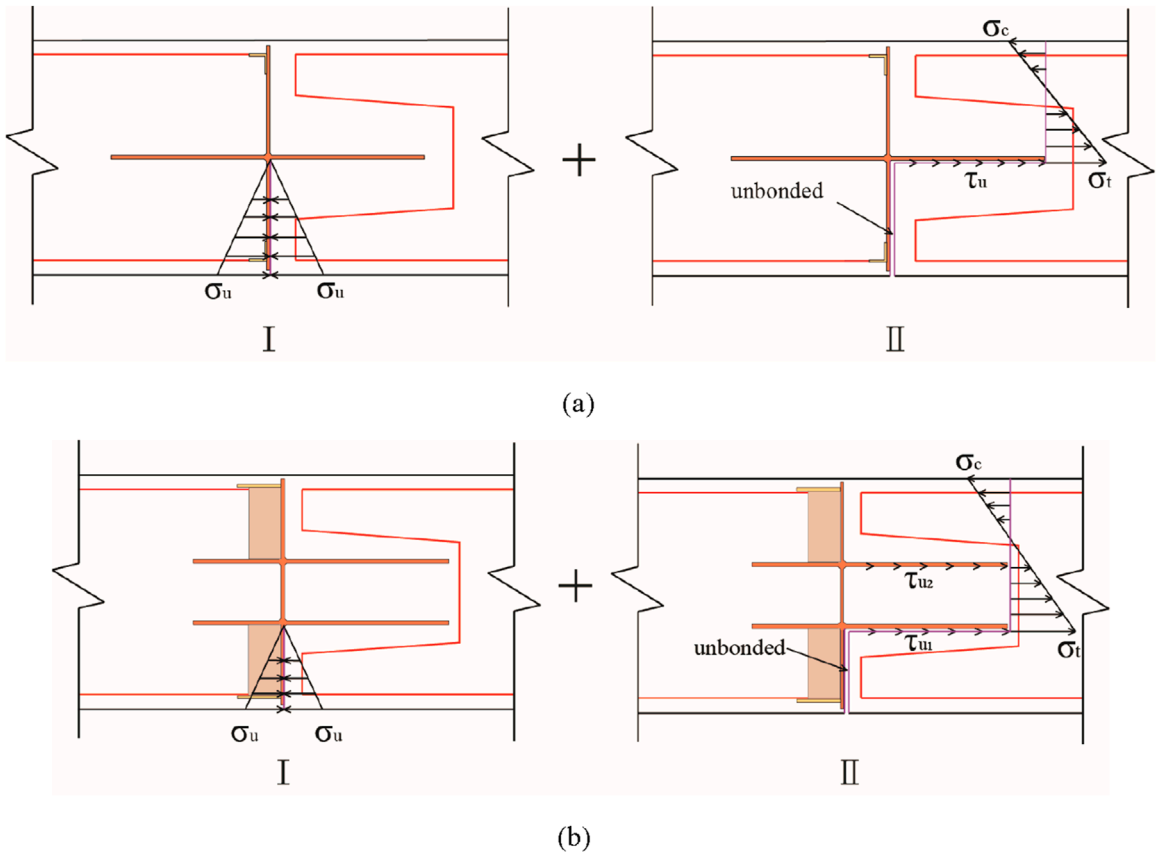


FIGURE 12
Simplified bearing capacity calculation models. **(a)** Single-cross PCPJ. **(b)** Double-cross PCPJ.

The strain $\varepsilon_s$ of the tensile rebar is calculated according to Equation 5.

$$\varepsilon_s = a_s\varepsilon_{cs}/(h-x) \tag{5}$$

where $a_s$ is the distance from the tensile rebar to the section bottom.

he strain $\varepsilon_s'$ of the compressed rebar is calculated according to Equation 6.

$$\varepsilon_s' = (x-a_s')\varepsilon_{cs}/(h-x) \tag{6}$$

where $a_s'$ is the distance from the compressed rebar to the section top.

The maximum compressive strain $\varepsilon_c$ of the section concrete is determined according to Equation 7.

$$\varepsilon_c = x\varepsilon_{cs}/(h-x) \tag{7}$$

For a double-cross PCPJ, the strain $\varepsilon_{cs}'$ at the interface between the upper flange and the concrete is calculated following to Equation 8.

$$\varepsilon_{cs}' = a_{cs}\varepsilon_{cs}/(h-x) \tag{8}$$

The ultimate biting force $f_{cs}$ between the steel plate flange and the concrete is calculated using Equation 9.

$$f_{cs} = A_p\tau_{cs} + A_c\tau_c \tag{9}$$

where $A_p$ is the contact area between the lower surface of the steel plate flange (lower flange) and the concrete; $A_c$ is the area of openings for the steel plate flange; $\tau_{cs}$ is the peak shear stress at the steel plate-concrete interface, which is 0.27 MPa (Song et al., 2020); and $\tau_c$ is the peak shear stress of the concrete, which is computed via Equation 10 (Yoshitake et al., 2011).

$$\tau_c = 0.21 f_c^{2/3} \tag{10}$$

where $f_c$ is the compressive strength of the cylindrical concrete.

For a double-cross PCPJ, the biting force $f_{cs}'$ between the upper flange and the concrete is calculated according to Equation 11.

$$f_{cs}' = 2a_{cs}f_{cs}/(h-x) \tag{11}$$

The tensile and compressive rebar forces $f_s$ and $f_s'$ are calculated according to Equations 12, 13, respectively.

$$f_s = nA_s\varepsilon_s E_s \tag{12}$$

$$f_s' = nA_s\varepsilon_s' E_s \tag{13}$$

where $n$ and $A_s$ are the number and cross-sectional area of the M-shaped rebar, respectively, and where $E_s$ is the elastic modulus of the rebar.

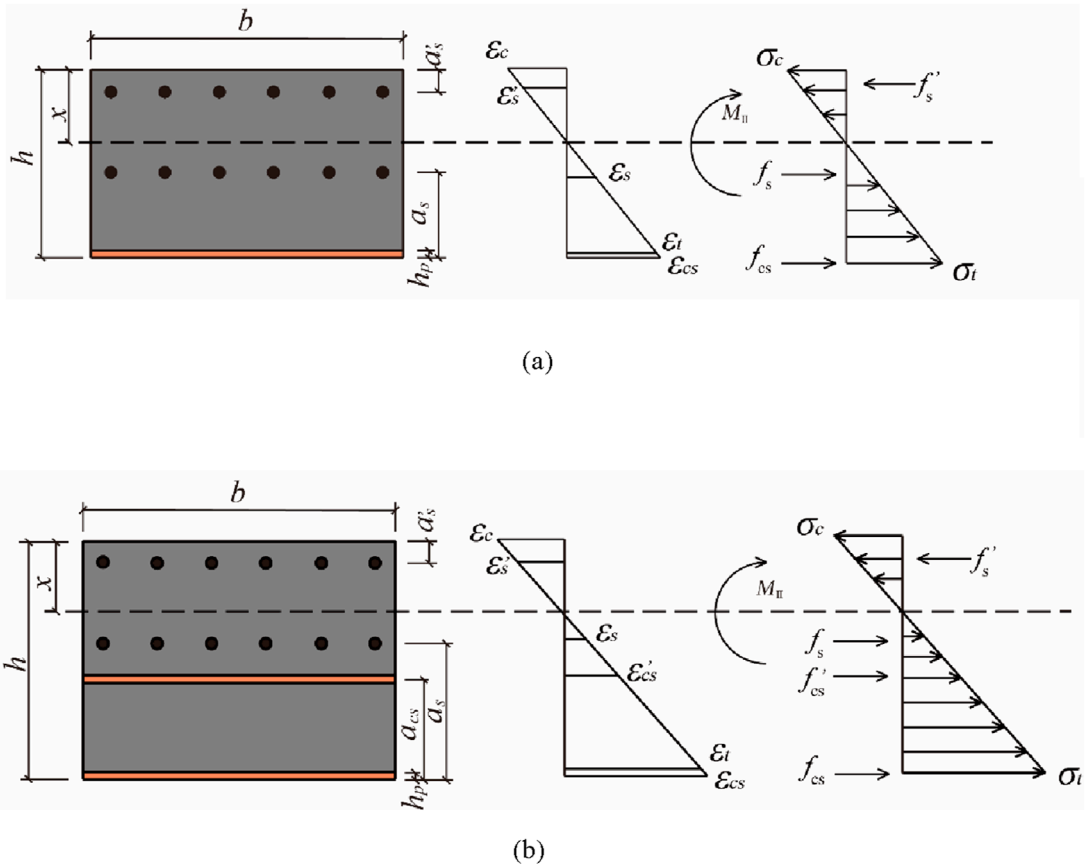


FIGURE 13
Stress-strain distribution maps of the failure sections. **(a)** Single-cross PCPJ. **(b)** Double-cross PCPJ.

The resultant force $f_t$ of the concrete in the tensile zone is calculated according to Equations 14–18 (GB50010, 2010).

$$f_t = \sigma_t(h-x)b/2 \tag{14}$$

$$\sigma_t = (1-d_t)E_c\varepsilon_t \tag{15}$$

$$d_t = \begin{cases} 1-\rho_t(1.2-0.2\eta_t^5) & \eta_t \le 1 \\ 1-\dfrac{\rho_t}{\alpha_t(\eta_t-1)^{1.7}+\eta_t} & \eta_t > 1 \end{cases} \tag{16}$$

$$\eta_t = \frac{\varepsilon_t}{\varepsilon_{tr}} \tag{17}$$

$$\rho_t = \frac{f_{tr}}{E_c\varepsilon_{tr}} \tag{18}$$

where $\alpha_t$ is the parameter of the descending segment in the uniaxial tensile stress-strain curve of the concrete, which has a value of 1.25; $d_t$ is the Concrete uniaxial tension damage evolution parameters, $f_{tr}$ is the uniaxial tensile strength of the concrete; $\varepsilon_{tr}$ is the peak tensile strain of the concrete; and $E_c$ is the elastic modulus of the concrete.

The resultant force of the concrete in the compression zone is calculated according to Equations 19–24.

$$f_c = \sigma_c x b/2 \tag{19}$$

$$\sigma_c = (1-d_c)E_c\varepsilon_c \tag{20}$$

$$d_c = \begin{cases} 1-\dfrac{\rho_c\mu}{\mu-1+\eta_c^{\mu}} & \eta_c \le 1 \\ 1-\dfrac{\rho_c}{\alpha_c(\eta_c-1)^2+\eta_c} & \eta_c > 1 \end{cases} \tag{21}$$

$$\rho_c = \frac{f_{cr}}{E_c\varepsilon_{cr}} \tag{22}$$

$$\mu = \frac{E_c\varepsilon_{cr}}{E_c\varepsilon_{cr}-f_{cr}} \tag{23}$$

$$\eta_c = \frac{\varepsilon_c}{\varepsilon_{cr}} \tag{24}$$

where $\alpha_c$ is the parameter of the descending segment in the uniaxial compressive stress-strain curve of the concrete, which has a value of 0.74; $d_c$ is the Concrete uniaxial compression damage evolution parameters, $f_{cr}$ is the uniaxial compressive strength of the concrete; and $\varepsilon_{cr}$ is the peak compressive strain of the concrete.

According to the force equilibrium condition, the height $x$ of the compression zone for the single- and double-cross PCPJs is calculated based on Equations 25, 26.

$$f_s + f_{cs} + f_t = f_s' + f_c \tag{25}$$

TABLE 2 Comparison of the calculated and tested bending bearing capacities.

| Specimen no. | $M_u$ (kN·m) | $M'_u$ (kN·m) | $(M'_u - M_u)/M'_u$ % |
|---|---|---|---|
| s-1 | 18.04 | 18.25 | 1.17 |
| s-2 | 16.50 | 16.15 | −2.16 |
| s-3 | 13.40 | 13.70 | 2.21 |
| s-4 | 10.27 | 10.20 | −0.68 |
| d-1 | 27.71 | 29.10 | 4.76 |
| d-2 | 25.23 | 25.95 | 2.76 |
| d-3 | 20.07 | 21.40 | 6.20 |
| d-4 | 13.55 | 14.05 | 3.53 |

$$f_s + f'_{cs} + f_{cs} + f_t = f'_s + f_c \tag{26}$$

The moment $M_{II;}$ at the point of application of the resultant force in the tensile zone of the single- and double-cross PCPJ specimens is calculated according to Equations 27, 28.

$$\begin{aligned} M_{II;} = {} & f_s(h - x - a_s + (f'_s(x - a'_s) + 2f_c x/3)/(f'_s + f_c)) \\ & + f_{cs}(h - x + (f'_s(x - a'_s) + 2f_c x/3)/(f'_s + f_c)) \\ & + f_t(2(h - x)/3 + (f'_s(x - a'_s) + 2f_c x/3)/(f'_s + f_c)) \end{aligned} \tag{27}$$

$$\begin{aligned} M_{II;} = {} & f_s(h - x - a_s + (f'_s(x - a'_s) + 2f_c x/3)/(f'_s + f_c)) \\ & + f_{cs}(h - x + (f'_s(x - a'_s) + 2f_c x/3)/(f'_s + f_c)) \\ & + f_t(2(h - x)/3 + (f'_s(x - a'_s) + 2f_c x/3)/(f'_s + f_c)) \\ & + f'_{cs}(h - a_{cs} + (f'_s(x - a'_s) + 2f_c x/3)/(f'_s + f_c)) \end{aligned} \tag{28}$$

The bearing capacity $M_u$ of specimens s-1–s-4 and d-1–d-4 is calculated according to Equation 1 and compared with $M'_u$, as shown in Table 2. Here, $M'_u$ is the sum of the measured bending moment and the mid-span bending moment caused by gravity.

According to Table 2, the relative error between the calculated and experimental values falls within a range of −2.16%–6.20%. The small discrepancies stem from three main factors: (1) Simplified assumptions in the calculation model, such as neglecting differential biting forces at the steel-concrete interface and assuming triangular stress distribution in concrete, which slightly underestimates compressive zone contributions. (2) Material property variability: Concrete tensile strength in tests varied from the design value, affecting dowel shear resistance. (3) Measurement errors in strain gauges and displacement sensors, contributing to minor deviations in ultimate load recording. Overall, the errors are within acceptable limits, validating the model's reliability.

## 6 Conclusion and discussion

This study focused on the PCPJs of the first LSDW ship lock wall constructed in China. Scaled four-point bending tests were conducted to investigate the lateral bending performance and failure mechanisms of PCPJs across varying perforation ratios. Based on the observed failure mechanisms, a calculation method for determining the lateral bending bearing capacity of PCPJs was developed. The conclusions are as follows:

1. The lateral bending failure mode of the PCPJs manifested as follows: (a) The separation of the steel-concrete interface between the cross steel plate web and the flange (lower flange), with the separation interface forming an L shape rotated clockwise by 90°; (b) the concrete dowel between the holes of the cross steel plate flange (lower flange) broke, causing tensile cracks in the end concrete.
2. The load-displacement curve of the PCPJ under lateral bending moments can be divided into four distinct stages: elastic, elastoplastic, descending, and residual. The bending capacities of the single- and double-cross PCPJs (with a perforation ratio of 38.3%) in the elastic stage were 25.5% and 44.9% of the ultimate bearing capacity, respectively, whereas the bending capacities in the residual stage were 63.8% and 59.2% of the ultimate bearing capacity, respectively. Throughout all four stages, the steel plates and bars of the joints were in the elastic stage.
3. The lateral bending capacity of the double-cross PCPJ was greater than that of the single-cross PCPJ; however, both were lower than that of the non-joint segment. The ultimate bearing capacities of the single- and double-cross PCPJs, with a perforation ratio of 38.3%, were 13.8% and 22.9% of the ultimate capacity of the non-joint segment, respectively. For double-cross PCPJs with perforation ratios of 0%, 15.3%, 30.7%, and 38.4%, their lateral bending capacities were 1.30, 1.65, 1.68, and 1.66 times greater than those of single-cross PCPJs, respectively.
4. The lateral bending capacity of the PCPJs was positively correlated with the perforation ratio of the steel plate. Relative to PCPJ with a perforation ratio of 0%, single-cross PCPJ with perforation ratios of 15.3%, 30.7%, and 38.4% increased its bearing capacity by 25.9%, 55.6%, and 74.1%, respectively. In comparison, the bearing capacity of the double-cross PCPJ increased by 60.0%, 97.1%, and 122.9%, respectively.
5. The lateral bending capacity of PCPJs comprises the combined contributions of the web plate and the flange. Calculation formulas for the bending bearing capacity of each component were established. The deviation between the sum of the calculated values and the experimental results ranged from −2.16% to 6.20%.

Compared to conventional diaphragm walls, LSDWs have greater requirements for the transverse bearing capacity of their joints. The research findings of this paper provide a reliable design basis and an important reference for the practical application of PCPJs in LSDWs. The primary factors that influence the lateral bending capacity of PCPJs include the strength of the steel-concrete interface, the ratio of perforations, concrete shear strength, and the arrangement of the web. Modifying these factors can improve the lateral bending capacity of these joints. These results support the use of perforated cross-shaped steel plate joints in LSDWs, especially in situations where LSDWs primarily bear horizontal loads, such

as in lock gate walls, dry dock walls, and foundation pit retaining structures.

Scaled model physical tests serve as an effective method for investigating the lateral bearing mechanism of perforated cross-plate joints (PCPJs); however, they exhibit significant limitations compared to actual engineering projects, primarily stemming from size effects that impact critical mechanical behaviors. These inherent size-dependent limitations manifest in three key aspects: (1) The bond strength at the steel-concrete interface displays size dependence, where smaller specimens tend to overestimate bond strength, potentially inflating the measured bearing capacity of the joints. (2) Concrete shear strength exhibits a decreasing trend with increasing specimen size, meaning that the 1:3 scale adopted in the tests may lead to an overestimation of dowel shear resistance when compared to full-scale prototypes. (3) Additionally, transverse axial forces which are present in full-scale LSDWs due to soil pressure were not simulated in the scaled tests, resulting in conservative measurements of structural stiffness. To address these size-related discrepancies and refine the analytical model, future full-scale tests and long-term field monitoring are necessary to account for these size-dependent effects comprehensively. Additionally, the tests did not account for the transverse axial forces acting on the joints, which may have resulted in overly conservative test outcomes. In the future, conducting full-scale model tests along with on-site measured data is expected to refine the research findings and enhance the reliability of the conclusions.

## Data availability statement

The original contributions presented in the study are included in the article/supplementary material, further inquiries can be directed to the corresponding author.

## Author contributions

KL: Writing – original draft. RY: Resources, Supervision, Validation, Writing – review and editing. WT: Data curation, Formal Analysis, Investigation, Writing – review and editing. QH: Methodology, Resources, Writing – review and editing. QK: Methodology, Supervision, Writing – original draft.

## Funding

The author(s) declare that financial support was received for the research and/or publication of this article. The financial support from the Hubei Natural Science Foundation Youth Project (Grant No. 2024AFB409) and the National Natural Science Foundation of China (Grant No. 42462029) are acknowledged and appreciated.

## Conflict of interest

Authors KL, RY, WT, and QK were employed by CCCC Second Harbor Engineering Company Ltd.

The remaining author declares that the research was conducted in the absence of any commercial or financial relationships that could be construed as a potential conflict of interest.

The handling editor TQ declared a past co-authorship with the author QH.

## Generative AI statement

The author(s) declare that no Generative AI was used in the creation of this manuscript.

Any alternative text (alt text) provided alongside figures in this article has been generated by Frontiers with the support of artificial intelligence and reasonable efforts have been made to ensure accuracy, including review by the authors wherever possible. If you identify any issues, please contact us.

## Publisher's note



## References

Ahn, J., Lee, C., Won, J., and Kim, S. (2010). Shear resistance of the perfobond-rib shear connector depending on concrete strength and rib arrangement. *J. Constr. Steel. Res.* 66 (10), 1295–1307. doi:10.1016/j.jcsr.2010.04.008

Al-Darzi, S., Chen, R., and Liu, Y. (2007). Finite element simulation and parametric studies of perfobond rib connector. *Am. J. Appl. Sci.* 4 (3), 122–127. doi:10.3844/ajassp.2007.122.127

Chen, J., Wang, J., Qiao, P., Hou, Y., and Gu, Q. (2016a). Shear bearing of cross-plate joints between diaphragm wall panels – I: model tests and shear behaviour. *Mag. Concr. Res.* 68 (17), 902–915. doi:10.1680/jmacr.15.00325

Chen, J., Hou, Y., Wang, J., and Qiao, P. (2016b). Shear bearing of cross-plate joints between diaphragm wall panels – II: numerical analysis and prediction formula. *Mag. Concr. Res.* 68 (20), 1025–1039. doi:10.1680/jmacr.15.00326

Cheng, Q., Wu, J., Song, Z., and Wen, H. (2012). The behavior of a rectangular closed diaphragm wall when used as a bridge foundation. *Front. Struct. Civ. Eng.* 6, 398–420. doi:10.1007/s11709-012-0175-5

Fu, Z. (2022). "A case study on determining the optimal supporting structure scheme in deep excavation in river channels by 3D FEM analysis," in *2022 8th international conference on hydraulic and civil engineering: deep space intelligent development and utilization forum (ICHCE)* (Xi'an, China), 804–817. doi:10.1109/ICHCE57331.2022.10042635

GB50010 (2010). *Code for design of concrete structures*. Beijing, China: China Architecture and Building Press. (In Chinese).

Japan Association of Diaphragm Wall (2001). Outlook of underground continuous wall foundation, found (In Japanese). *Eng.* 29 (1), 60–65. Available online at: https://ndlsearch.ndl.go.jp/books/R000000004-I5625364 (Accessed January 01, 2001).

JGJ 120-2012 (2012). *Technical specification for retaining and protection of building foundation excavations*. Beijing, China: China Architecture and Building Press. (In Chinese).

Kim, S., Han, O., Kim, K., and Park, J. (2018). Experimental behavior of double-row Y-type perfobond rib shear connectors. *J. Constr. Steel. Res.* 150, 221–229. doi:10.1016/j.jcsr.2018.08.012

Lee, Y., Joo, Y., Lee, T., and Ha, D. (2011). Mechanical properties of constitutive parameters in steel–concrete interface. *Eng. Struct.* 33 (4), 1277–1290. doi:10.1016/j.engstruct.2011.01.005

Li, W., Tao, Q., Li, C., Wang, X., Gong, W., and Dai, G. (2024a). *In-Situ* experimental study of closed-diaphragm wall foundations for cross-sea suspension bridges. *Mar. Sci. Eng.* 12 (12), 2304. doi:10.3390/jmse12122304

Li, Z., Zhao, G., Zhang, Y., Hao, Z., Niu, K., and Liu, R. (2024b). Numerical modelling of sand liquefaction via a weakly coupled approach between lattice spring and discrete element methods. *Comput. Geotech.* 172, 106461. doi:10.1016/j.compgeo.2024.106461

Majdi, Y., Hsu, C., and Punurai, S. (2014). Local bond–slip behavior between cold-formed metal and concrete. *Eng. Struct.* 69, 271–284. doi:10.1016/j.engstruct.2014.03.025

Oguejiofor, E., and Hosain, M. (1994). A parametric study of perfobond rib shear connectors. *Can. J. Civ. Eng.* 21 (4), 614–625. doi:10.1139/l94-063

Soh, C., Chiew, S., and Dong, Y. (1999). Damage model for concrete-steel interface. *J. Eng. Mech.* 125 (8), 979–983. doi:10.1061/(ASCE)0733-9399(1999)125:8(979)

Song, J., Wang, W., Su, S., Ding, X., Luo, Q., and Quan, C. (2020). Experimental study on the bond-slip performance between concrete and a corrugated steel plate with studs. *Eng. Struct.* 224, 111195. doi:10.1016/j.engstruct.2020.111195

Trad, M., Bitar, I., Grange, S., and Richard, B. (2024). A multiscale steel–concrete interface model for structural applications. *Structures* 68, 107137. doi:10.1016/j.istruc.2024.107137

Wang, X., Liu, Y., Lu, Y., and Li, X. (2022). Shear transfer mechanism of perforated web connection for concrete encased steel structures. *Eng. Struct.* 252, 113418. doi:10.1016/j.engstruct.2021.113418

Wang, J., Xiong, W., and Cai, C. (2024). Flexural performance of rigid joints for diaphragm walls: experimental investigation and numerical analysis. *Case Stud. Constr. Mater.* 20, e02936. doi:10.1016/j.cscm.2024.e02936

Wu, J., Cheng, Q., Wen, H., Li, Y., Zhang, J., and Wang, L. (2016a). Comparison on the horizontal behaviors of lattice-shaped diaphragm wall and pile group under static and seismic loads. *Shock Vib.* 2016, 1–17. doi:10.1155/2016/1289375

Wu, J., Cheng, Q., Wen, H., Wang, L., Li, Y., and Zhang, J. (2016b). A load transfer approach to rectangular closed diaphragm walls. *Geotech. Eng.* 169 (6), 509–526. doi:10.1680/jgeen.15.00156

Wu, J., Naggar, M., Cheng, Q., Wen, H., Li, Y., and Zhang, J. (2020). Iterative load transfer procedure for settlement evaluation of lattice-shaped diaphragm walls in multilayered soil. *Comput. Geotech.* 120, 103409. doi:10.1016/j.compgeo.2019.103409

Xue, X., Hu, S., Qi, H., and Shan, C. (2022). Study on the normal bonding performance of the steel-concrete interface. *Eng. Mech.* 39 (5), 65–74. (In Chinese). doi:10.6052/j.issn.1000-4750.2021.03.0182

Yoshitake, I., Uno, T., Scanlon, A., and Hamada, S. (2011). Simplified test of cracking strength of concrete element subjected to pure shear. *J. Mater. Civ. Eng.* 23 (7), 999–1006. doi:10.1061/(ASCE)MT.1943-5533.0000259

Zhou, G., Wei, X., and Yu, C. (2011). Analyses of Earth pressure on gridding concrete retaining wall in the excavation of deep foundation pit in soft soil area. *Appl. Mech. Mater.* 52–54, 2181–2186. doi:10.4028/www.scientific.net/amm.52-54.2181

frontiers | Frontiers in Earth Science

TYPE Original Research
PUBLISHED 18 September 2025
DOI 10.3389/feart.2025.1691323



OPEN ACCESS

EDITED BY
Pengfei Liu,
CCCC Second Harbor Engineering Co., Ltd., China

REVIEWED BY
Yang Cao,
Fuzhou University, China
Pei Huang,
Chang'an University, China
Wei HE,
North China University of Water Resources and Electric Power, China

*CORRESPONDENCE
Jingxi Zhang,
zjx_adhere@gs.zzu.edu.cn

RECEIVED 23 August 2025
ACCEPTED 03 September 2025
PUBLISHED 18 September 2025

CITATION
Wang R, Li S, Li C, Bian K and Zhang J (2025) Mechanistic analysis of TBM cutterhead-ground interaction under mud build-up effect.
*Front. Earth Sci.* 13:1691323.
doi: 10.3389/feart.2025.1691323



# Mechanistic analysis of TBM cutterhead-ground interaction under mud build-up effect

Renchong Wang[1], Shiwei Li[2,3], Congshi Li[1], Ke Bian[2,3] and Jingxi Zhang[4]*

[1]Henan Qianping Reservoir Irrigation District Project Company, Luoyang, Henan, China, [2]Henan Provincial Water Conservancy Technology Application Center, Zhengzhou, Henan, China, [3]Henan Key Laboratory of Safety Technology for Water Conservancy Project, Zhengzhou, Henan, China, [4]School of Water Conservancy and Transportation, Zhengzhou University, Zhengzhou, Henan, China

**Introduction:** In tunnel construction using TBMs, the complex mineral composition of strata and hydrogeological conditions often induce cutterhead mud build-up, which results in sharp increases in torque and thrust, thereby reducing excavation efficiency. Understanding the interaction between the TBM cutterhead and the surrounding ground under cutterhead blockage conditions is therefore a critical challenge for improving tunnelling efficiency.
**Methods:** This study develops a cutterhead load model that explicitly incorporates both aperture ratio and mud coating effects, and establishes a load-prediction framework for TBM excavation in composite strata.
**Results:** The validity of the proposed model is verified using field monitoring data. On this basis, the influence of aperture ratio on excavation loads is systematically analysed.
**Discussion:** An optimization strategy—maintaining a relatively large aperture ratio—is proposed to enhance TBM tunnelling efficiency, providing effective theoretical support and practical guidance for addressing cutterhead mud build-up.

KEYWORDS

**composite strata, cutterhead mud build-up, cutterhead load, aperture ratio, TBM excavation efficiency**

## 1 Introduction

With the advantages of safety and efficiency, tunnel boring machines (TBMs) have been widely used in tunnelling tunnels of various sizes (Hassanpour et al., 2011). Its performance largely depends on the rock breaking efficiency induced by its cutterhead, which bears complex loads due to the difficult grounds, such as fault zone, blocky rock mass and mixed face (Zhao et al., 2007). Many tunnelling projects driven by different types of TBMs suffered from inadequate cutterhead loads (Bilgin and Algan, 2012; Jancsecz et al., 1999; Nelson et al., 1992). Therefore, calculation and prediction of cutterhead loads are crucially important for a successful TBM tunnelling.

Precise control of shield tunneling loads relies on understanding the cutterhead-soil interaction. This interaction comprises two main components: the cutting action between the cutter and the soil, and the extrusion between the cutterhead faceplate and the soil

(Han et al., 2017; Li et al., 2022). The resistance encountered by the tool while cutting the soil primarily contributes to the cutterhead torque, while the interaction between the cutterhead faceplate and the soil mainly generates thrust resistance for the shield (Hasanpour et al., 2018; Wang et al., 2022).

Researchers have conducted extensive work on cutterhead-soil interaction to establish a reasonable theoretical calculation model for tunneling loads (Guo et al., 2018; Ramoni and Anagnostou, 2010) employed numerical simulation to study the thrust force requirements for tunnel boring machines (TBMs) in squeezing ground (Shi et al., 2011). further determined the composition of cutterhead torque and proposed a calculation method considering cutterhead structure, cutting principle, and the interaction between the cutterhead and soil (Wang et al., 2012). improved the Krause model for estimating cutterhead thrust by incorporating five main components, validating it through laboratory tests with a U1.8 m EPB shield tunneling machine.

To analyze the excavation load of layered soil (Sun et al., 2018; Zhang et al., 2015; Zhang et al., 2014; Zhang et al., 2016), proposed a load model that considers the properties and thickness of each soil layer. Ates et al. (2014) established a statistical model between cutterhead diameter and total installed load on the basis of a database containing 262 types of TBMs and emphasized the key role of geological parameters in the prediction of total loads. Zhou and Zhai, (2018) presented a theoretical model for the cutterhead torque of an EPB TBM in soft ground. Geng et al. (2016), Liu et al. (2018) developed a load prediction model on the basis of the CSM model and the disc cutter layout. Jing et al. (2019), Zhao et al. (2019) reported a power function relationship between rock breaking load and joint parameters on the basis of *in-situ* data and full-scale rotary cutting tests, and established a load prediction model. Liu et al. (2020) conducted a series of novel rolling cutting tests on layered sandstone, and the influence of dip angle, strata, normal force, and rotational speed on the reliability of the disc cutter were analyzed. Wang et al. (2022) propose a novel thrust model that incorporates soil properties, shield operating parameters, pose parameters, and geometric parameters to estimate total and grouped thrusts, and its effectiveness is validated through a case study. Shen et al. (2025) significantly contributes to the understanding and quantification of shield tunneling thrust and cutterhead torque by establishing a refined three-dimensional cutter-soil interaction model. Zhang et al. (2025) incorporated the mud build-up effect into the load model in their study.

Although numerous studies have focused on load prediction models in shield tunnelling, few have explicitly considered the effects of mud build-up, which decreases the cutterhead aperture ratio and consequently alters excavation loads. To address this limitation, this study develops a load prediction model that incorporates the effective aperture ratio of the cutterhead, quantitatively evaluates its impact on excavation loads, and proposes corresponding optimization strategies. The proposed model is applicable to various ground conditions, and the findings provide theoretical support and practical guidance for improving excavation efficiency and ensuring construction safety under mud build-up scenarios.

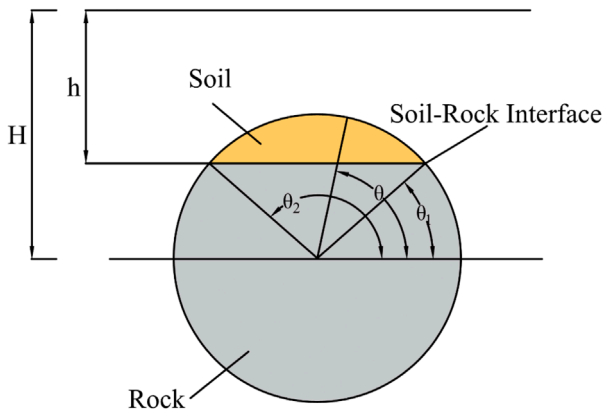


FIGURE 1
Schematic diagram of composite strata at the TBM excavation face.

# 2 Interaction between the TBM cutterhead and the strata considering mud build-up

## 2.1 TBM thrust force

The load analysis of cutterhead mud build-up is critical for tunnel design and construction. The mud build-up effect causes raised deposits on the cutterhead surface, altering the contact area and pressure distribution between the cutterhead and the ground, which in turn affects both torque and thrust. By analyzing the load characteristics under mud build-up conditions, the influence on cutterhead torque and thrust can be quantified, providing a basis for the rational determination of design and construction parameters to ensure tunneling safety and efficiency.

### 2.1.1 Shield TBM cutterhead thrust considering mud clogging

Kong et al. (2022), using a soft-over-hard stratum as an example, conducted a mechanical analysis of TBM tunneling considering factors such as ground composition, cutter geometry, TBM advance rate, and cutterhead torque (Figure 1). Based on this, a thrust calculation method for TBM tunneling in composite strata was proposed, yielding expressions $F_1$ and $F_2$.

The lateral earth pressure acting on the cutterhead faceplate is discussed based on the position of the soil–rock interface on the TBM excavation face, as shown in Equations 1–3.

$$F_{1s} = \int_{\theta_1}^{\theta_2} \int_{\frac{H-h}{\sin\theta}}^{\frac{D}{2}} (H - r\sin\theta)\lambda_1\gamma_1 r\mathrm{d}r\mathrm{d}\theta \tag{1}$$

$$F_{1r} = \lambda_2 \left\{ \begin{aligned} &\int_0^{2\pi} \int_0^{\frac{D}{2}} \left[\gamma_1\left(H - \frac{D}{2}\right) + \gamma_2\left(\frac{D}{2} - r\sin\theta\right)\right] r\mathrm{d}r\mathrm{d}\theta - \\ &\int_{\theta_1}^{\theta_2} \int_{\frac{H-h}{\sin\theta}}^{\frac{D}{2}} \left[\gamma_1\left(H - \frac{D}{2}\right) + \gamma_2\left(\frac{D}{2} - r\sin\theta\right)\right] r\mathrm{d}r\mathrm{d}\theta \end{aligned} \right\} \tag{2}$$

Based on the above equation, the lateral pressure acting on the cutterhead faceplate in the soil and rock zones can be calculated. Considering the influence of mud build-up on the actual aperture ratio during cutterhead excavation, the resulting force $F_1$ can be expressed as:

$$F_1 = (1\text{-}\xi')(F_{1s} + F_{1r}) \tag{3}$$

Where:

$F_1$ is the lateral earth pressure acting on the cutterhead faceplate in composite strata.

$F_{1s}$ is the lateral earth pressure from the upper soil layer acting on the faceplate.

$F_{1r}$ is the lateral earth pressure from the lower rock layer acting on the faceplate.

$\xi'$ is the actual aperture ratio of the cutterhead during excavation, considering the effect of mud build-up.

$\theta$ is the dip angle between the soil-rock interface on the excavation face and the horizontal direction through the shield center.

$\theta_1$, $\theta_2$ are angular parameters related to the soil–rock interface.

$r$ is the distance from a point on the cutterhead to the cutterhead center.

$D$ is the diameter of the cutterhead.

$h$ is the burial depth of the soil-rock interface on the excavation face.

$H$ is the burial depth of the shield's central axis.

$\lambda_1$ is the lateral earth pressure coefficient of the soil.

$\lambda_2$ is the lateral earth pressure coefficient of the rock.

$\gamma_1$ is the unit weight of the soil.

$\gamma_2$ is the unit weight of the rock.

### 2.1.2 Shield–stratum frictional resistance

The frictional force between the upper soil and the shield casing can be expressed as Equation 4:

$$F_{2s} = \mu_1 DL \int_{\theta_1}^{\frac{\pi}{2}} p_{s1} \sin\theta + p_{s2} \cos\theta \mathrm{d}\theta \tag{4}$$

The frictional force between the lower rock mass and the shield casing can be expressed as Equation 5:

$$F_{2r} = \mu_2 DL \left[ \int_0^{\theta_1} P_{r1} \sin\theta + P_{r2} \cos\theta \mathrm{d}\theta + \int_{-\frac{\pi}{2}}^{0} P_{r2} \cos\theta\text{-}P_{r1} \sin\theta \mathrm{d}\theta \right] \tag{5}$$

The value of $F_2$ can be expressed as Equation 6:

$$F_2 = F_{2s} + F_{2r} \tag{6}$$

Where:

$F_2$ is the frictional resistance between the shield shell and the ground during shield advancement.

$F_{2s}$ is the frictional force between the upper soil layer and the shield shell.

$F_{2r}$ is the frictional force between the lower rock layer and the shield shell.

$P_{s1}$ and $P_{s2}$ are the vertical and horizontal pressures exerted by the upper soil layer on the shield shell.

$P_{r1}$ and $P_{r2}$ are the vertical and horizontal pressures exerted by the lower rock layer on the shield shell.

$\mu_1$ is the friction coefficient between the soil and the shield shell.

$\mu_2$ is the friction coefficient between the rock and the shield shell.

$L$ is the length of the shield shell.

### 2.1.3 Penetration resistance acting on the cutters mounted on the cutterhead

In composite strata, the TBM cutterhead no longer only considers its interaction with a single soil type. Depending on the stratigraphic conditions during TBM tunneling, both the rolling cutters and disc cutters interact with the soil and rock during the cutting and rock-breaking process. Zhang et al. (2025) considered the cutter forces under mud build-up conditions as shown in Equation 7.

$$F_3 = \sum_{i=1}^{n} f_{ni} \tag{7}$$

Where:

$F_3$ is the resistance force acting on the cutter during penetration.

$f_{ni}$ is the penetration resistance force acting on a single cutter under mud build-up conditions in contact with the rock stratum.

## 2.2 Cutterhead torque

### 2.2.1 Cutterhead face–stratum frictional resistance torque

Zhu et al. (2014) calculated based on the soil and rock masses in the TBM excavation interface region, as shown in Equations 8–10:

$$T_{1s} = (1\text{-}\xi')\mu_1\lambda_1\gamma_1 \int_{\theta_1}^{\theta_2} \int_{\frac{H\text{-}h}{\sin\theta}}^{\frac{D}{2}} (H\text{-}r\sin\theta) r^2 \mathrm{d}r\mathrm{d}\theta \tag{8}$$

$$T_{1r} = (1\text{-}\xi')\mu_2\lambda_2 \left\{ \begin{array}{l} \int_0^{2\pi} \int_0^{\frac{D}{2}} \left[ \gamma_1 \left( H\text{-}\frac{D}{2} \right) + \gamma_2 \left( \frac{D}{2}\text{-}r\sin\theta \right) \right] r^2 \mathrm{d}r\mathrm{d}\theta - \\ \int_{\theta_1}^{\theta_2} \int_{\frac{H\text{-}h}{\sin\theta}}^{\frac{D}{2}} \left[ \gamma_1 \left( H\text{-}\frac{D}{2} \right) + \gamma_2 \left( \frac{D}{2}\text{-}r\sin\theta \right) \right] r^2 \mathrm{d}r\mathrm{d}\theta \end{array} \right\} \tag{9}$$

The resistive torque $T_1$ between the cutterhead faceplate and the surrounding geological formation is given by:

$$T_1 = T_{1s} + T_{1r} \tag{10}$$

Where:

$T_1$ is the torque generated by friction between the cutterhead front face and the surrounding ground.

$T_{1s}$ is the torque generated by friction between the cutterhead front face and the soil.

$T_{1r}$ is the torque generated by friction between the cutterhead front face and the rock.

$b$ is the thickness of the cutterhead.

### 2.2.2 Cutterhead side–stratum frictional resistance torque

Liu et al. (2015) and Zhu et al. (2014) calculated based on the soil and rock masses in the TBM excavation interface region, as shown in Equations 11–13:

$$T_{2s} = \frac{\mu_1 \gamma_1 b D^2}{4} \int_{\theta_1}^{\theta_2} \left[ \left( H - \frac{D}{2} \sin\theta \right) \sin^2\theta + \lambda_1 \left( H - \frac{D}{2} \sin\theta \right) \cos^2\theta \right] \mathrm{d}\theta \tag{11}$$

$$T_{2r} = \frac{\mu_2 \gamma_2 b D^2}{4} \left\{ \begin{array}{l} \int_{0}^{\theta_1} \left[ \left( H - \frac{D}{2} \sin\theta \right) \sin^2\theta + \lambda_2 \left( H - \frac{D}{2} \sin\theta \right) \cos^2\theta \right] \mathrm{d}\theta + \\ \int_{\theta_2}^{2\pi} \left[ \left( H - \frac{D}{2} \sin\theta \right) \sin^2\theta + \lambda_2 \left( H - \frac{D}{2} \sin\theta \right) \cos^2\theta \right] \mathrm{d}\theta \end{array} \right\} \tag{12}$$

The resistive torque $T_2$ between the cutterhead side and the surrounding geological formation is given by:

$$T_2 = T_{2s} + T_{2r} \tag{13}$$

Where:

$T_2$ is the torque generated by friction between the cutterhead side and the surrounding ground.

$T_{2s}$ is the torque generated by friction between the cutterhead side and the soil.

$T_{2r}$ is the torque generated by friction between the cutterhead side and the rock.

$T_3$ is the torque generated by friction between the back of the cutterhead and the muck.

### 2.2.3 Cutterhead back–excavated material frictional resistance torque

As shown in Equation 14.

$$T_3 = (1 - \xi') \int_0^{2\pi} \int_0^{\frac{D}{2}} \mu_1 F_{\mathrm{li}} r^2 \mathrm{d}r\mathrm{d}\theta \tag{14}$$

Where:

$F_{\mathrm{li}}$ is the muck pressure acting on a micro-element at the back of the cutterhead (Liu et al., 2015).

$R_{\mathrm{i}}$ is the contact radius of the disc cutter, i.e., the distance from the disc cutter contact point to the rotation axis.

$R_{\mathrm{j}}$ is the contact radius of the scraper, i.e., the distance from the scraper contact point to the rotation axis.

### 2.2.4 Cutterhead torque induced by ground resistance during cutter excavation

As shown in Equation 15.

$$T_{41} = \sum_{i=1}^{n} f_{\mathrm{ti}} R_{\mathrm{i}} \tag{15}$$

Where:

$T_4$ is the torque generated by the resistance of the ground against cutter penetration on the cutterhead (Zhang et al., 2025).

$f_{\mathrm{ni}}$ is the tangential force acting on a single cutter under mud build-up conditions in contact with the stratum.

# 3 Engineering case verification

## 3.1 Project overview

This study takes a TBM tunnel section in Shenzhen as the engineering background. The tunnel was excavated by an earth pressure balance (EPB) shield through strata composed of cobble soil, gravel soil, coarse sand, sandy strongly weathered granite, and moderately weathered granite, forming a typical "soft-over-hard" composite ground. During excavation, frequent mud build-up was observed on the cutterhead, particularly when crossing the interface between gravel soils and sandy strongly weathered granite. Such composite strata share similarities with karst-affected geological conditions in southern China, where unconsolidated sediments overlie hard bedrock, often accompanied by groundwater activity and localized dissolution features. A composite cutterhead was adopted for the TBM, with an overall aperture ratio of 35% and a central aperture ratio of 38%. The cutterhead was equipped with six 18-inch double-edged disc cutters at the center and thirty-two 18-inch single-edged disc cutters. In addition, ninety-four scrapers were installed, along with twelve edge scrapers.

## 3.2 Engineering data analysis

### 3.2.1 Load model verification

Using the load calculation formulas presented in Chapter 2, the thrust and torque were calculated, and the relationships between the measured and theoretical values of thrust and torque within the cutterhead mud build-up zone were plotted, as shown in Figures 2, 3.

Within the actual cutterhead mud build-up zone, the average measured total thrust of the TBM machine was 16,372.05 kN, while the theoretical value was 17,499.55 kN, approximately 6.8% higher. This discrepancy arises because the theoretical thrust calculation assumes simultaneous contact between all cutters and the ground, whereas in practice, due to vertical differences between disc cutters and scrapers and variations in installation positions even among the same cutter type, cutter-ground contact does not occur simultaneously. The average measured total torque was 3,585.67 kN m, while the theoretical value was 4,113.32 kN m, about 14.7% higher. This larger deviation is primarily related to the axial coverage of the mud build-up on the cutterhead: when the mud build-up completely covers the cutters and prevents them from cutting the ground, the torque required for cutting must be comprehensively reconsidered.

For the analysis of forces acting on the cutterhead face, variations in aperture ratio under different levels of mud build-up are introduced to more accurately evaluate the cutterhead loading. In the cutter load calculation, this study considers the cutter forces under mud build-up conditions. In summary, the proposed load calculation model is applicable to various typical ground conditions and demonstrates strong generality and engineering adaptability.

### 3.2.2 Formation process of mud build-up

During the tunneling process from ring 0 to ring 165, the TBM advance rate is shown in Figure 4, in conjunction with the thrust and torque variations illustrated in Figures 2, 3. Based on the variation curves of relevant parameters during excavation, the formation

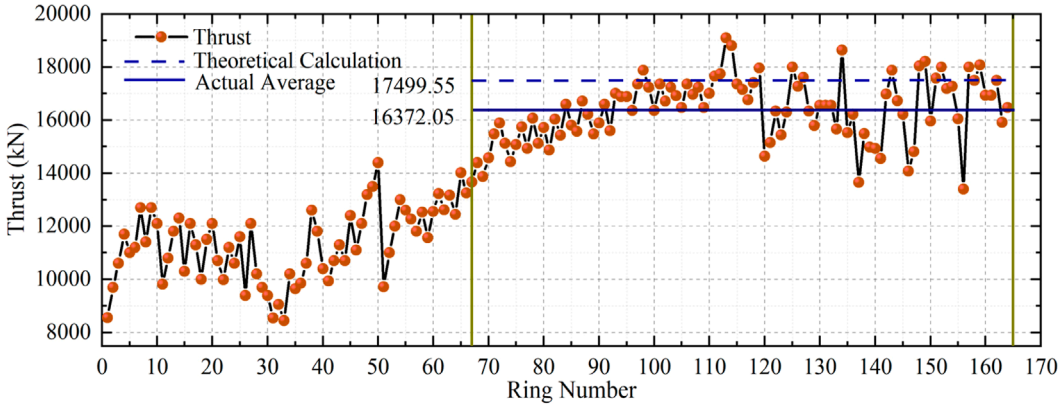


FIGURE 2
Thrust comparison curve.

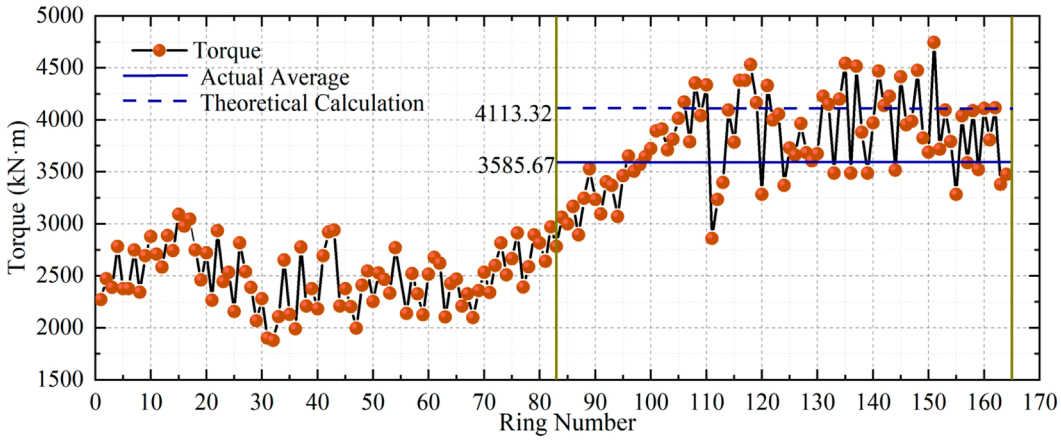


FIGURE 3
Torque comparison curve.

process of cutterhead mud build-up can be divided into five stages, as analyzed below:

#### 3.2.2.1 Normal Excavation Stage

From ring 0 to ring 67, excluding the initial increase in advance rate and thrust caused by TBM start-up, all tunneling parameters remained stable with relatively small fluctuations. During this stage, the TBM advance rate ranged from 20 to 40 mm/min, the thrust ranged from 8,000 to 15,000 kN, and the cutterhead torque ranged from 1,750 to 3,000 kN m.

#### 3.2.2.2 Mud Build-up Formation Stage

Between rings 67 and 68, abnormal changes in tunneling parameters were observed. Except for the cutterhead torque, which remained stable, the advance rate dropped sharply while the thrust increased and showed a tendency to exceed the stable range observed during rings 0 to 67. At this stage, mud build-up began to form on the cutterhead, particularly around the openings, reducing the aperture ratio and impeding the discharge of excavated muck. Meanwhile, mud build-up on the spokes and faceplates of the cutterhead introduced additional resistance, resulting in increased thrust. However, since the degree of cutterhead mud build-up was still relatively low, its impact on cutting performance was limited, allowing the cutterhead torque to remain stable despite the reduced advance rate.

#### 3.2.2.3 Expansion Stage of Mud Build-up on Cutterhead Face

From ring 68 to ring 81, the advance rate no longer declined but fluctuated within a relatively stable range of 10–25 mm/min. The thrust continued to increase but at a slower rate than in the previous stage, ranging from 14,000 to 18,000 kN. The cutterhead torque remained stable during this phase.

#### 3.2.2.4 Full Coverage Stage of Cutterhead Mud Build-up

From ring 81 to ring 90, the cutterhead torque rose sharply from 2,196 kN m to 4,274 kN m. At this point, extensive mud build-up had formed on the cutterhead, accumulating in thickness along the tunneling direction. The build-up gradually extended inward from the periphery, covering previously unobstructed openings. As

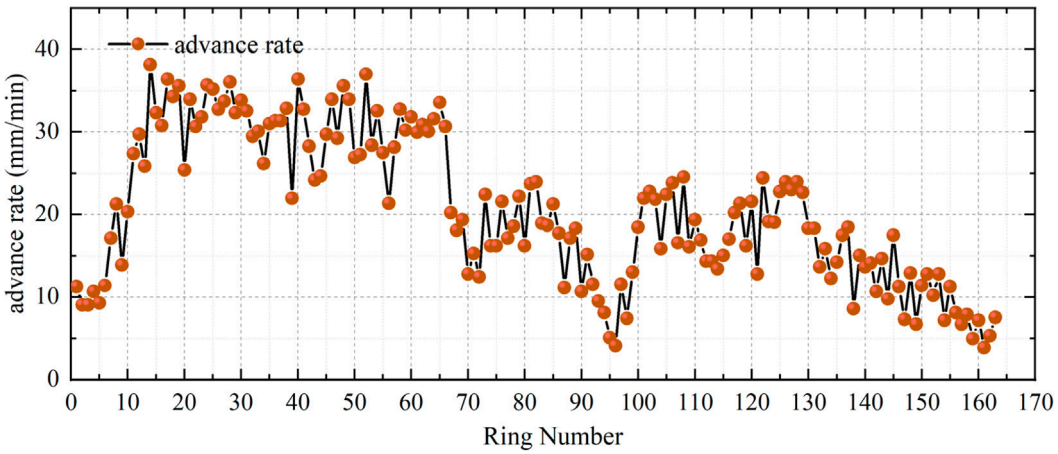


FIGURE 4
Advance rate variation curve.

a result, the cutters experienced reduced cutting capacity due to the mud coverage, and the excavated muck became increasingly difficult to discharge through the blocked openings. These combined effects led to a rapid and significant increase in cutterhead torque.

#### 3.2.2.5 Stabilized Mud Build-up Stage

After ring 90, the thrust stabilized within the range of 14,000 to 19,000 kN, and the cutterhead torque remained between 3,000 and 4,500 kN m. Analysis indicates that by this stage, the cutterhead face and openings were completely covered by mud build-up, effectively forming a secondary "cutterhead" composed of the accumulated mud. Under the combined effects of adhesion and friction with the excavation face, the mud build-up reached a mechanical equilibrium, and its scale ceased to grow. The contact condition between the cutterhead, cutters, and the surrounding soil mass became stable, resulting in a steady state of thrust and torque during excavation.

Based on the variation of tunneling parameters during the cutterhead mud build-up process, rings 56 to 110-covering the transitional phases-were selected for further analysis of thrust and torque.

The thrust variation curve for rings 56 to 110 is shown in Figure 5.

Within this interval, the TBM thrust exhibited a gradual increase with the tunneling progress. Around ring 90, the growth trend of thrust approached zero and remained stable thereafter. This indicates that in the earlier stage, the increasing thrust was caused by the progressive accumulation of mud build-up on the cutterhead surface, which led to greater resistance between the cutterhead face, cutters, and the excavation face. To maintain excavation, the TBM thrust was gradually increased. Once the mud build-up on the cutterhead surface reached its maximum extent, it effectively replaced direct contact between the cutterhead and the ground, resulting in a stabilized interaction and consistent thrust in the subsequent stage.

The variation curve of cutterhead torque for rings 56 to 110 is shown in Figure 6.

The cutterhead torque within this interval showed a gradual increase with the tunneling progress, with the rate of increase becoming more pronounced over time. This suggests that cutterhead mud build-up had a greater impact on torque than on thrust. Due to the presence of mud build-up on the cutterhead surface, the cutting performance of the shield cutters was significantly impaired. Meanwhile, the accumulated mud intensified friction between the cutterhead and the excavation face. To maintain excavation, the cutterhead had to generate higher torque to meet the basic cutting requirements.

## 3.3 Analysis of cutterhead aperture ratio variation

### 3.3.1 Relationship between cutterhead aperture ratio and loads

According to the stages of cutterhead mud build-up defined in Section 3.2.2, both the cutterhead aperture ratio and the mud build-up coverage ratio on the cutterhead vary continuously throughout the TBM tunneling process. Based on this, the corresponding variation curves can be plotted as follows:

Since the cutterhead remains in constant contact with the excavation face during actual tunneling, it is not possible to monitor the aperture condition of the cutterhead in real time. Therefore, the following assumptions are made:

1. The mud build-up coverage on the cutterhead openings and faceplates is assumed to increase linearly and uniformly, without considering abrupt changes in adhesion due to specific strata conditions;
2. The mud build-up on the cutterhead surface is considered to be in a dynamic equilibrium between detachment and adhesion. In other words, the mud already adhered to the cutterhead is assumed to remain unchanged as tunneling progresses, ensuring that the amount of mud build-up on the openings and faceplates increases monotonically.

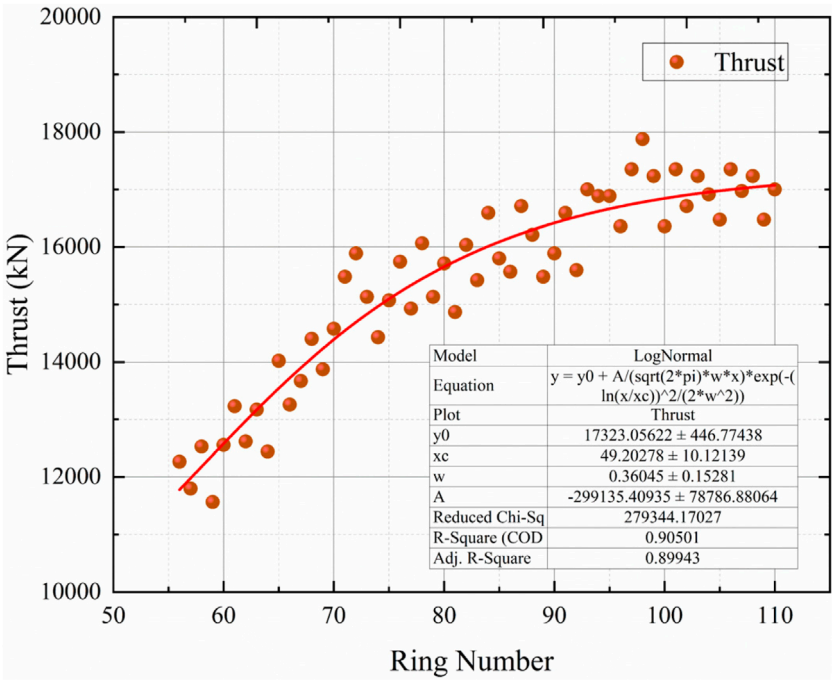


FIGURE 5
Fitted curve of TBM thrust for rings 56 to 110.

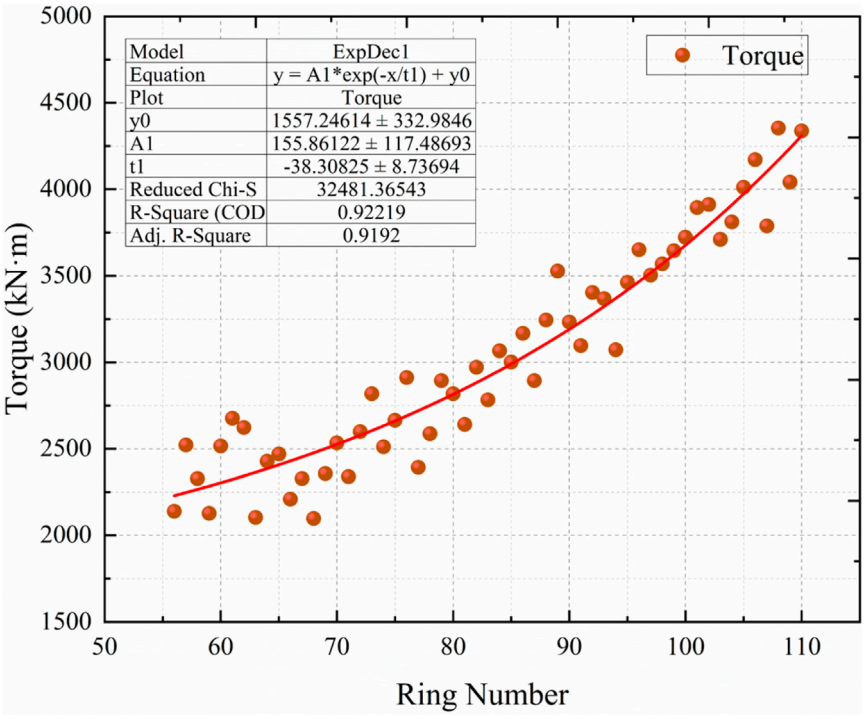


FIGURE 6
Fitted curve of cutterhead torque for rings 56 to 110.

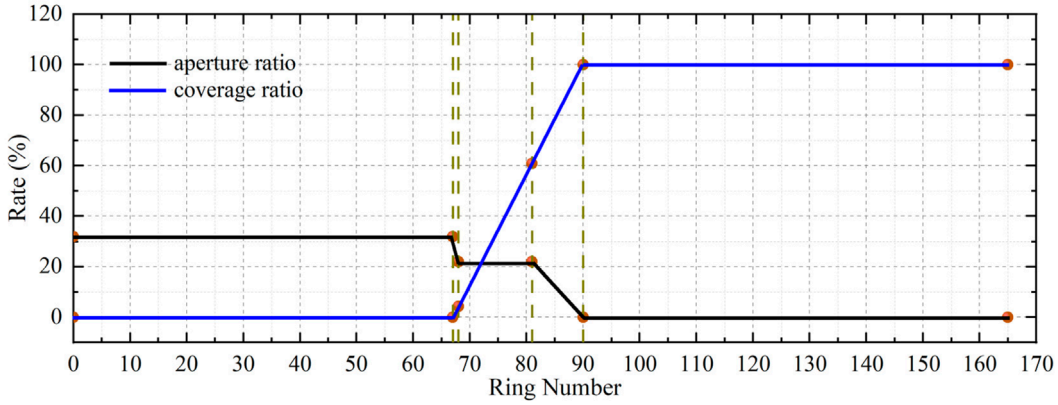


FIGURE 7
Evolution of cutterhead mud build-up.

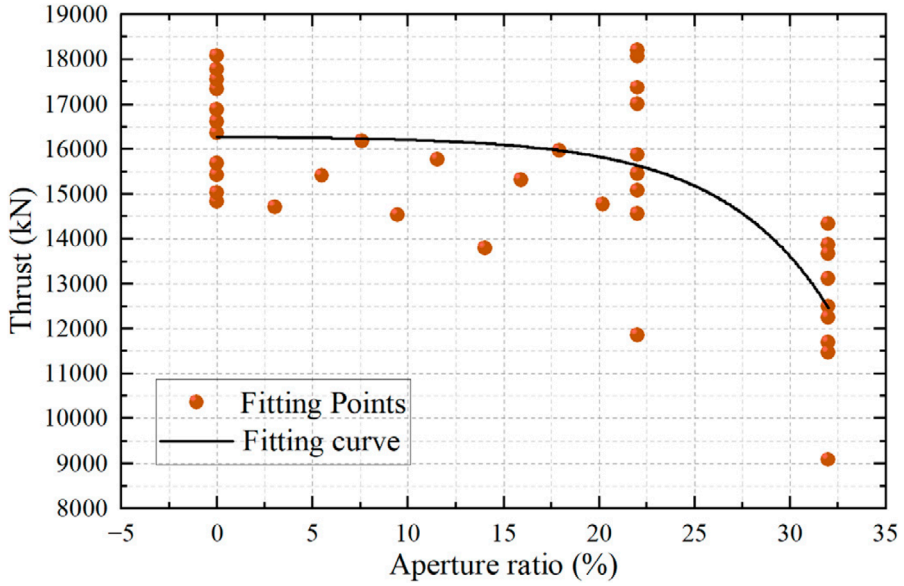


FIGURE 8
Correlation between TBM thrust and aperture ratio in presence of cutterhead mud build-up.

Based on the above assumptions, the variation curves of the aperture ratio in the presence of cutterhead mud build-up and the mud build-up coverage ratio on the cutterhead during rings 0 to 165 are shown in Figure 7.

As shown in Figure 7, significant changes in the cutterhead aperture ratio in the presence of mud build-up and the mud build-up coverage ratio occurred between rings 67 and 90. During this interval, the overall mud build-up coverage on the cutterhead continuously increased, as the mud coating on the faceplate expanded radially outward from the center of the cutterhead. The aperture ratio in the presence of cutterhead mud build-up exhibited two stages of decline and one stage of stabilization. According to the mud build-up obstruction model at the cutterhead openings (Ruyong, 2018; Yongjian, 2020), the mud coating over the openings may undergo bending failure. Once the mud build-up in the openings reaches an upper limit, the aperture ratio becomes stable due to mechanical equilibrium at the openings. However, when thick mud build-up accumulates around the opening areas, it gradually expands axially along the cutterhead, eventually filling all remaining openings.

To further analyze the relationship between the aperture ratio in the presence of cutterhead mud build-up and tunneling parameters during TBM excavation, the correlation between TBM thrust and the aperture ratio is illustrated in Figure 8.

As shown in Figure 8, there is a clear correlation between TBM thrust and the aperture ratio in the presence of cutterhead mud build-up. When the cutterhead face is only partially covered by mud build-up-i.e., when the aperture ratio is relatively high-the TBM thrust remains low. As the aperture ratio decreases and

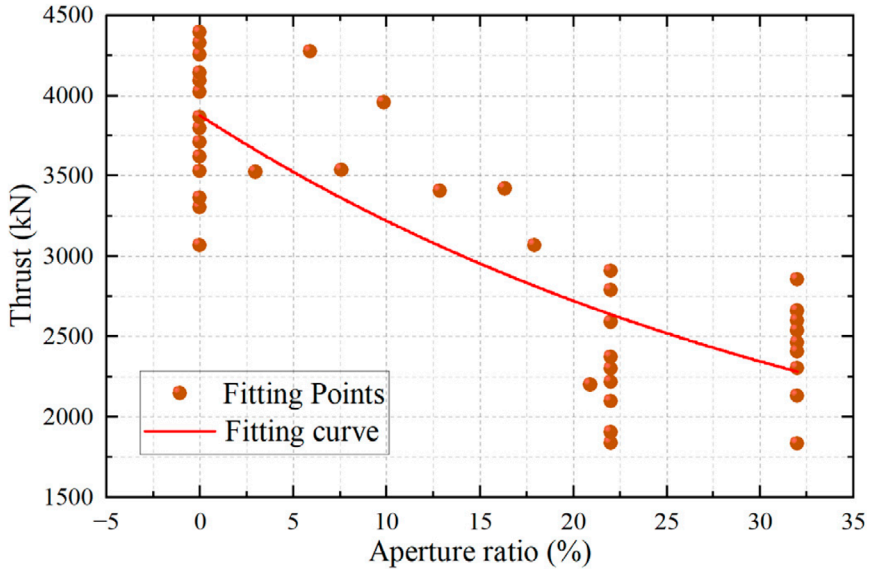


FIGURE 9
Correlation between cutterhead torque and aperture ratio in presence of cutterhead mud build-up.

the cutterhead becomes fully covered by mud build-up, the thrust approaches its maximum value.

To further analyze the relationship between the aperture ratio in the presence of cutterhead mud build-up and tunneling parameters during TBM excavation, the correlation between cutterhead torque and the aperture ratio is illustrated in Figure 9.

As shown in Figure 9, a clear negative correlation is observed between cutterhead torque and the aperture ratio. When the aperture ratio is relatively high, the cutterhead torque remains low. As the aperture ratio decreases to its minimum—indicating complete coverage of the cutterhead by mud build-up—the cutterhead torque reaches its maximum value.

These results suggest that the aperture ratio under cutterhead mud build-up conditions provides valuable insight into the behavior of tunneling parameters. Selecting a cutterhead design with a relatively large aperture ratio during the planning stage can effectively reduce the risk of cutterhead mud build-up.

### 3.3.2 Optimization recommendations based on aperture ratio

The cutterhead aperture ratio not only affects muck discharge efficiency but is also closely related to the stability of mud build-up formation at the openings. Based on the aperture ratio analysis, it is recommended to maximize the aperture ratio within the structural constraints of the cutterhead to reduce the likelihood of muck accumulation and subsequent mud build-up in the opening areas. From a topological perspective, the location of the openings also influences mud build-up formation. The central region of the cutterhead poses a higher risk of cutterhead mud build-up; therefore, it is advisable to allocate larger openings near the center, while closed structural elements such as spokes, ribs, and faceplates-hich are essential for maintaining excavation face stability-hould be arranged closer to the cutterhead perimeter.

## 4 Conclusion

The mud build-up effect can cause abrupt changes in TBM loads, thereby reducing tunneling efficiency. In this study, a load prediction framework for TBM tunneling in composite strata under mud build-up conditions was established, and a cutterhead load model incorporating both the aperture ratio and mud coverage was proposed. Field monitoring data were employed to validate the framework, and the influence of aperture ratio on tunneling efficiency was systematically analyzed. The main conclusions are as follows:

A cutterhead load calculation model that accounts for the actual aperture ratio was developed, which effectively captures the influence of mud build-up on cutterhead loads.

Mud build-up was incorporated into the analysis of cutterhead–strata interaction, demonstrating its significant impact on cutter forces and excavation loads.

Increasing the cutterhead aperture ratio is shown to improve tunneling efficiency, providing an effective strategy to mitigate the adverse impacts of mud build-up.

The proposed model and findings not only enhance the understanding of mud build-up mechanisms in TBM tunneling but also offer theoretical support and practical guidance for safe and efficient construction in karst-affected composite strata.

## Data availability statement

The original contributions presented in the study are included in the article/supplementary material. Further inquiries can be directed to the corresponding author.

## Author contributions

RW: Conceptualization, Validation, Writing – original draft. SL: Resources, Writing – original draft. CL: Software, Writing – original draft. KB: Writing – review and editing, Visualization. JZ: Writing – review and editing.

## Funding

The author(s) declare that financial support was received for the research and/or publication of this article. This research was supported by the Henan Qianping Irrigation District North Trunk Canal Ruyang Water Supply Project (Grant No. QPRY-ZX-2024-01), the 2024 Henan Water Conservancy Science and Technology Project (Grant No. GG202455), and the National Natural Science Foundation of China (Grant No. 52079128).

## Conflict of interest

Authors RW and CL were employed by Henan Qianping Reservoir Irrigation District Project Company. Authors SL and KB were employed by Henan Provincial Water Conservancy Technology Application Center. Authors SL and KB were also employed by Henan Key Laboratory of Safety Technology for Water Conservancy Project. Author JZ was employed by the School of Water Conservancy and Transportation, Zhengzhou University.

## Generative AI statement

The author(s) declare that no Generative AI was used in the creation of this manuscript.

Any alternative text (alt text) provided alongside figures in this article has been generated by Frontiers with the support of artificial intelligence and reasonable efforts have been made to ensure accuracy, including review by the authors wherever possible. If you identify any issues, please contact us.

## Publisher's note



## References

Ates, U., Bilgin, N., and Copur, H. (2014). Estimating torque, thrust and other design parameters of different type TBMs with some criticism to TBMs used in Turkish tunneling projects. *Tunn. Undergr. Space Technol.* 40, 46–63. doi:10.1016/j.tust.2013.09.004

Bilgin, N., and Algan, M. (2012). The performance of a TBM in a squeezing ground at Uluabat, Turkey. *Tunn. Undergr. Space Technol.* 32, 58–65. doi:10.1016/j.tust.2012.05.004

Geng, Q., Wei, Z., Meng, H., and Macias, F. J. (2016). Mechanical performance of TBM cutterhead in mixed rock ground conditions. *Tunn. Undergr. Space Technol.* 57, 76–84. doi:10.1016/j.tust.2016.02.012

Guo, K., Xu, Y., and Li, J. (2018). Thrust force allocation method for shield tunneling machines under complex load conditions. *Automation Constr.* 96, 141–147. doi:10.1016/j.autcon.2018.08.016

Han, M. D., Cai, Z. X., Qu, C. Y., and Jin, L. S. (2017). Dynamic numerical simulation of cutterhead loads in TBM tunnelling. *Tunn. Undergr. Space Technol.* 70, 286–298. doi:10.1016/j.tust.2017.08.028

Hasanpour, R., Rostami, J., Thewes, M., and Schmitt, J. (2018). Parametric study of the impacts of various geological and machine parameters on thrust force requirements for operating a single shield TBM in squeezing ground. *Tunn. Undergr. Space Technol.* 73, 252–260. doi:10.1016/j.tust.2017.12.027

Hassanpour, J., Rostami, J., and Zhao, J. (2011). A new hard rock TBM performance prediction model for project planning. *Tunn. Undergr. Space Technol.* 26 (5), 595–603. doi:10.1016/j.tust.2011.04.004

Jancsecz, S., Krause, R., and Langmaack, L. (1999). "Advantages of soil conditioning in shield tunneling: experiences of LRTS Izmir," in Proceedings of the World Tunnel Congress '99, Oslo, June 1999, 865–875.

Jing, L.-j., Li, J.-b., Yang, C., Chen, S., Zhang, N., and Peng, X.-x. (2019). A case study of TBM performance prediction using field tunnelling tests in limestone strata. *Tunn. Undergr. Space Technol.* 83, 364–372. doi:10.1016/j.tust.2018.10.001

Kong, X., Tang, L., Ling, X., Tang, W., and Zhang, Y. (2022). Thrust calculation method for earth pressure balance shield in Compound strata. *Chin. J. Undergr. Space Eng.* 18 (06), 1805–1813.

Li, J., Zhang, B., Lyu, D., Guo, J., Su, K., and Hu, B. (2022). Fatigue reliability analysis of tunnelling boring machine cutterhead with cracks. *Eng. Fail. Anal.* 141, 106669. doi:10.1016/j.engfailanal.2022.106669

Liu, Y., Sun, Z., and Zhou, R. (2015). On driving torque calculation of EPBM cutter head in complex strata. *Track Traffic and Undergr. Eng.* 33 (06), 83–85+90. doi:10.3969/j.issn.1009-7767.2015.06.027

Liu, J., Bin, H., and Guo, W. (2018). Load characteristics of the TBM cutterhead under mixed-face rock ground condition. *Harbin Gongcheng Daxue Xuebao/Journal Harbin Eng. Univ.* 39 (3), 575–583. doi:10.11990/jheu.201609049

Liu, B., Yang, H., and Karekal, S. (2020). Reliability analysis of TBM disc cutters under different conditions. *Undergr. Space* 6 (2), 142–152. doi:10.1016/j.undsp.2020.01.001

Nelson, P. P., Al-Jalil, Y. A., and Laughton, C. (1992). "Analysis of performance measures of tunnel boring machines," in *Rock characterization: ISRM symposium, eurock '92* (Chester, UK), 408–413.

Ramoni, M., and Anagnostou, G. (2010). Thrust force requirements for TBMs in squeezing ground. *Tunn. Undergr. Space Technol.* 25 (4), 433–455. doi:10.1016/j.tust.2010.02.008

Ruyong, D. (2018). *Study on the Mechanism and disposal Measures of clay Clogging in TBM cutter-head.* Master's thesis. Southwest jiaotong university.

Shen, X., Yuan, D., Jin, D., Chen, X., Luo, W., Peng, Y., et al. (2025). Model test on cutterhead-soil interaction during shield tunneling and its theoretical model. *Undergr. Space* 20, 46–68. doi:10.1016/j.undsp.2024.03.006

Shi, H., Yang, H., Gong, G., and Wang, L. (2011). Determination of the cutterhead torque for EPB shield tunneling machine. *Automation Constr.* 20 (8), 1087–1095. doi:10.1016/j.autcon.2011.04.010

Sun, W., Shi, M., Zhang, C., Zhao, J., and Song, X. (2018). Dynamic load prediction of tunnel boring machine (TBM) based on heterogeneous *in-situ* data. *Automation Constr.* 92, 23–34. doi:10.1016/j.autcon.2018.03.030

Wang, L., Gong, G., Shi, H., and Yang, H. (2012). Modeling and analysis of thrust force for EPB shield tunneling machine. *Automation Constr.* 27, 138–146. doi:10.1016/j.autcon.2012.02.004

Wang, X., Yuan, D., Jin, D., Jin, H., Yang, Y., and Wu, J. (2022). Determination of thrusts for different cylinder groups during shield tunneling. *Tunn. Undergr. Space Technol.* 127, 104579. doi:10.1016/j.tust.2022.104579

Yongjian, T. (2020). *Study on large-diameter slurry shield Tunneling with half-chamber Air pressure Method in Clay strata.* Master's thesis. Shanghai Jiaotong University.

Zhang, Q., Qu, C., Cai, Z., Kang, Y., and Huang, T. (2014). Modeling of the thrust and torque acting on shield machines during tunneling. *Automation Constr.* 40, 60–67. doi:10.1016/j.autcon.2013.12.008

Zhang, Q., Hou, Z., Huang, G., Cai, Z., and Kang, Y. (2015). Mechanical characterization of the load distribution on the cutterhead–ground interface of shield tunneling machines. *Tunn. Undergr. Space Technol.* 47, 106–113. doi:10.1016/j.tust.2014.12.009

Zhang, Q., Su, C., Qin, Q., Cai, Z., Hou, Z., and Kang, Y. (2016). Modeling and prediction for the thrust on EPB TBMs under different geological conditions by considering mechanical decoupling. *Sci. China Technol. Sci.* 59 (9), 1428–1434. doi:10.1007/s11431-016-6096-0

Zhang, J., Kou, L., Wang, J., and Xu, J. (2025). Load model for shield tunneling in composite strata considering mud build-up effects. *Tunn. Undergr. Space Technol.* 165, 106918. doi:10.1016/j.tust.2025.106918

Zhao, J., Gong, Q. M., and Eisensten, Z. (2007). Tunnelling through a frequently changing and mixed ground: a case history in Singapore. *Tunn. Undergr. Space Technol.* 22 (4), 388–400. doi:10.1016/j.tust.2006.10.002

Zhao, Y., Yang, H., Chen, Z., Chen, X., Huang, L., and Liu, S. (2019). Effects of jointed rock mass and mixed ground conditions on the cutting efficiency and cutter wear of tunnel boring machine. *Rock Mech. Rock Eng.* 52 (5), 1303–1313. doi:10.1007/s00603-018-1667-y

Zhou, X.-P., and Zhai, S.-F. (2018). Estimation of the cutterhead torque for earth pressure balance TBM under mixed-face conditions. *Tunn. Undergr. Space Technol.* 74, 217–229. doi:10.1016/j.tust.2018.01.025

Zhu, L., Zheng, Z., and Li, R. (2014). Calculation of shield cutter head torque in mix ground. *Mech. Eng. and Automation* (06), 110–111. doi:10.3969/j.issn.1672-6413.2014.06.044

frontiers | Frontiers in Earth Science

TYPE Original Research
PUBLISHED 13 October 2025
DOI 10.3389/feart.2025.1692577



OPEN ACCESS

EDITED BY
Zhang Cong,
Central South University Forestry and Technology, China

REVIEWED BY
Jiawei Xie,
The University of Newcastle, Australia
Yipeng Xie,
Ocean University of China, China
Jie Li,
East China Jiaotong University, China

*CORRESPONDENCE
Jingjing Yu,
2150471020@email.szu.edu.cn

RECEIVED 25 August 2025
ACCEPTED 15 September 2025
PUBLISHED 13 October 2025

CITATION
Dang P, Chang L, Tang P, Yu J and Li Z (2025) Intelligent recognition of surrounding rock grades based on TBM tunneling parameters. *Front. Earth Sci.* 13:1692577. doi: 10.3389/feart.2025.1692577



# Intelligent recognition of surrounding rock grades based on TBM tunneling parameters

Pengliang Dang[1], Le Chang[1], Peishuo Tang[1], Jingjing Yu[2]* and Zeliang Li[2]

[1]Sinohydro Bureau 14 Co., Ltd., Kunming, Yunnan, China, [2]College of Civil and Transportation Engineering, Shenzhen University, Shenzhen, Guangdong, China

Rapid, accurate, and efficient prediction of surrounding rock grades is crucial for ensuring the safety and enhancing the efficiency of tunnel boring machine (TBM) construction. To achieve intelligent perception of surrounding rock grades based on TBM tunneling parameters, this study leverages data from the TBM1 construction phase of the Luotian Reservoir-Tiegang Reservoir Water Diversion Tunnel Project, integrating geological records and tunneling parameters to establish models for different rock grades. First, raw data were cleaned and denoised using box plots, followed by the selection of eight critical parameters—including thrust, torque, penetration rate (PR), rotation speed (RS), et al—through a hybrid approach combining "knowledge-driven" and "data-driven" criteria. The dataset was partitioned into training, testing, and validation sets at a 7:2:1 ratio. Three data processing methods were applied, and machine learning algorithms (XGBoost, Random Forest, CatBoost, and LightGBM) were employed to construct surrounding rock classification models, with Optuna hyperparameter optimization implemented to enhance model performance. The result reveals that the CatBoost model, optimized via SMOTE (Synthetic Minority Oversampling Technique) and hyperparameter tuning, delivered superior performance, achieving 99% validation accuracy with no misclassification across adjacent surrounding rock grades. This research provides actionable insights for advancing intelligent TBM construction practices.

KEYWORDS

**TBM tunneling parameters, surrounding rock classification, ensemble learning algorithms, hyperparameter optimization, model performance**

## 1 Introduction

Under the continuous impetus and leadership of China's informatization and digitization, intelligent construction and smart tunneling are inevitably becoming the mainstream development direction in the tunnel engineering field (Fang et al., 2025; Aston et al., 1988; Xie et al., 2025), particularly for shield tunnels (Barton, 2012; Fang et al., 2023; Zheng et al., 2016). Shield tunnels, constructed using tunnel boring machines (TBMs), are equipped with numerous sensors that monitor and collect various mechanical, electrical, and environmental parameters in real time at specific frequencies during construction. This establishes a foundation for data-driven intelligent TBM construction. Furthermore, with the rapid advancement of computer technology, artificial intelligence (AI) has been widely applied across numerous fields such as finance, healthcare,

TABLE 1 The Main characteristic parameters of TBM.

| Parameter | Value | Parameter | Value |
|---|---|---|---|
| TBM type | Earth Pressure/TBM Dual Mode Shield | Maximum cutterhead rotation speed $n_{max}$ (r/min) | 6.1 |
| Diameter of cutterhead $D$ (mm) | 6,730 | Data acquisition frequency (Hz) | 1 |
| Maximum thrust $F_{max}$ (kN) | 40860 | Number of disc cutter $N$ (pcs) | 43 |
| Maximum torque $T_{max}$ (kN·m) | 9,818 | Breakout torque $T$ (kN·m) | 11781 |
| Maximum advance speed $v_{max}$ (mm/min) | 100(Earth Pressure)/120(TBM) | Drive Power (kW) | 2000 |

transportation, and manufacturing. The emergence of open-source machine learning libraries (e.g., Scikit-learn, PyTorch, TensorFlow) has also provided more accessible channels for researchers in tunneling to learn and apply AI algorithms.

Currently, AI technologies based on big data are increasingly being introduced into tunnel engineering to assist TBM construction. Key research focuses include TBM efficiency optimization, intelligent perception of surrounding rock grades, tunneling performance prediction, and adverse geological condition forecasting (Tang et al., 2024; Chen et al., 2021; Li et al., 2023a; Li et al., 2023b). In the domain of surrounding rock grade classification, existing studies have employed various machine learning algorithms (Afradi and Ebrahimabadi, 2020; Guo et al., 2022a; Guo et al., 2022b; Ghorbani and Yagiz, 2024; Feng et al., 2021; Hou et al., 2022; Kohestani et al., 2017; Liu et al., 2020; Xiong, 2014; Zhu et al., 2021)—such as ensemble methods (Stacking, Random Forest, Adaboost/Adacost, Decision Trees, GBDT), clustering techniques (KNN, SVM), and deep learning models (MLP, DNN)—to develop intelligent surrounding rock grade perception models based on TBM tunneling parameters. These models incorporate parameters such as gripper pressure, gear seal pressure, advance displacement, cutterhead power, shield pressure and rolling force (Zhu et al., 2020; Mao et al., 2021; Zhang et al., 2019; Wu et al., 2021; Liu et al., 2021; Yin et al., 2022; Prechelt, 2002; Chen et al., 2015). However, due to data imbalance, these models exhibit poor prediction accuracy for Grade II and V surrounding rocks. Although the SMOTE oversampling method has been applied to balance datasets, its effectiveness remains limited (Wu et al., 2021; Liu et al., 2021; Yin et al., 2022; Prechelt, 2002; Chen et al., 2015). Current feature selection methods generally fall into two categories: "data-driven" and "knowledge-driven." Data-driven approaches analyze correlations between input tunneling parameters and target variables using techniques like Random Forest, Pearson correlation analysis, PCA, and XGBoost, ultimately selecting modeling parameters based on correlation strength. Knowledge-driven methods rely on personal expertise and experience to choose input parameters, which introduces subjective biases. While using averaged stable-phase data for modeling can improve accuracy to some extent, it conflicts with real-time prediction requirements, rendering such models inadequate for guiding actual construction. Although AI technologies have advanced in TBM applications, existing models lack universality due to variations in tunneling parameters across different TBM types (e.g., cutterhead diameter, tool configuration) and geological conditions.

In summary, this study is based on the Luotian Reservoir-Tiegang Reservoir Water Diversion Tunnel Project (hereafter referred to as the Luotie Project), utilizing comprehensive geological data and tunneling parameters from its TBM1. First, feature parameters were selected by integrating data-driven and knowledge-driven criteria according to data characteristics and prediction targets. The raw data were then cleaned using box plots and partitioned into training (70%), testing (20%), and validation (10%) sets. Subsequently, three data imbalance mitigation strategies were applied to construct surrounding rock classification models using XGBoost, RF, CatBoost, and LightGBM algorithms. This research enables rapid, efficient, and intelligent perception of surrounding rock grades, guiding shield drivers to make parameter adjustments, ensuring safer and more efficient tunneling.

# 2 Luotie Project

## 2.1 Description of the project

This study is based on the Luotie Project, a component of the Shenzhen section of the Pearl River Delta Water Resources Allocation Project. The project has a total water delivery capacity of 2.6 million $m^3$/day, with a main tunnel spanning 21.68 km. The target study section is TBM Construction Section 1, starting and ending at chainage K0+486.74 to K5+108.64. This section employs a dual-mode TBM (designated TBM1) with a diameter of 6,730 mm. Key technical specifications are summarized in Table 1.

## 2.2 Data sources and composition

In the Luotie Project, four TBMs are deployed concurrently, with TBM1 operating in a heterogeneous geological formation predominantly composed of quartz gneiss and sandstone, and characterized by significant groundwater presence. The alignment and longitudinal geological profile of TBM1 are presented in Figure 1. The dataset for this study includes tunneling parameters and geological records derived from the completed excavation segments of TBM1. The tunneling parameters were recorded at

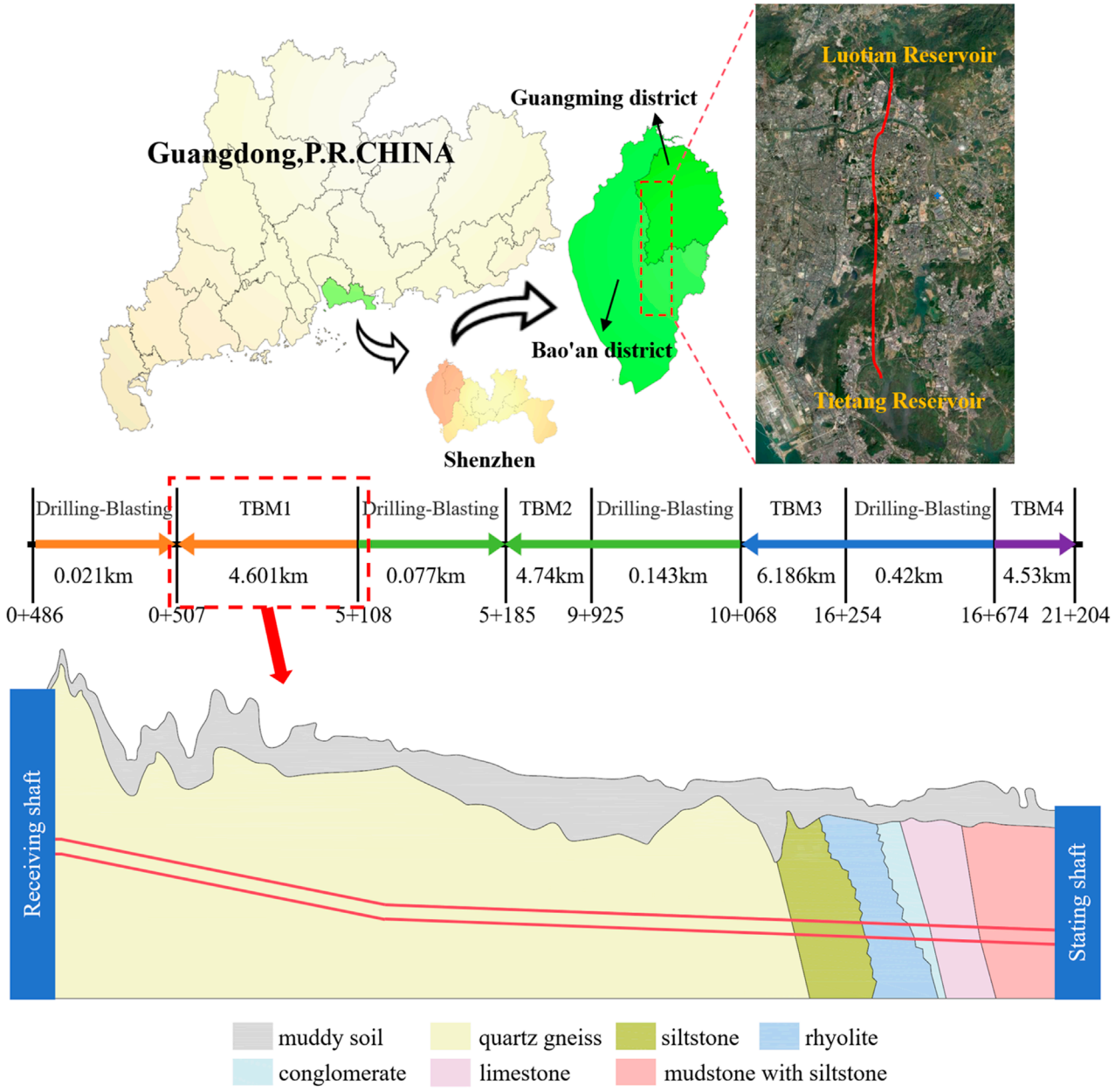


FIGURE 1
Construction alignment and geological profile of TBM1 in the luotie project.

a frequency of 1 Hz, and the distribution of surrounding rock grades along the tunnel is depicted in Figure 2. As shown, the majority of the tunnel encounters SR-IV (Surrounding Rock Grade IV), which constitutes 50.3% (774 segments) of the total excavation. This is followed by SR-III (Surrounding Rock Grade III), representing 34.5% (532 segments), while SR-V (Surrounding Rock Grade V) is the least encountered, comprising only 15.2% (234 segments). This distribution highlights that the tunnel primarily traverses SR-IV, followed by SR-III, with SR-V occurring in a smaller portion of the excavation. Subsequent model development and analysis were based exclusively on the tunneling parameters collected from these segments.

# 3 Data processing

## 3.1 Data cleaning

Invalid data were removed from the collected tunneling parameters by retaining only non-zero entries, i.e., any data row containing a zero value in any parameter was deleted according to the criterion defined in Equation 1. After preliminary data cleaning, boxplots were used for secondary outlier removal. A boxplot eliminates abnormal data based on the median, lower quartile (Q1), upper quartile (Q3), maximum value (Q3+1.5 (Q3-Q1)), and minimum value (Q1-1.5 (Q3-Q1)). In this study, the stable

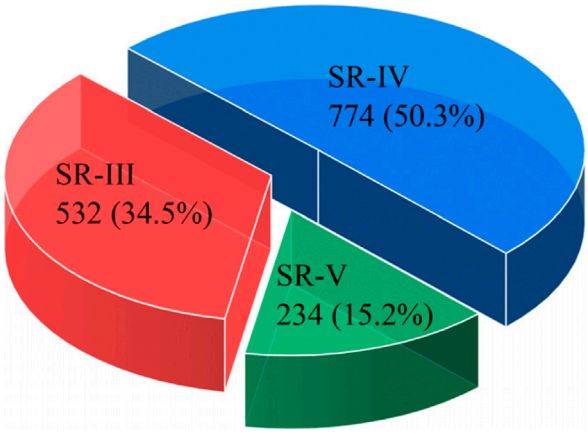


FIGURE 2
Percentage of different surrounding rock grades.

excavation phase was specifically extracted to analyze tunneling parameter variations. Notably, even during stable excavation, manual operational decisions introduce fluctuations in two critical parameters—thrust and rotation speed—which subsequently affect other operational indicators. To address this challenge, a refined segmentation method for the stable excavation phase was implemented using a stopping criterion method (Breiman, 2001), as defined in Equation 2. The processed distributions of four key tunneling parameters are shown in Figure 3, where distinct unimodal distributions under different surrounding rock grades demonstrate the effectiveness of the data cleaning methodology.

$$f(F) \cdot f(T) \cdot f(N) \cdot f(v) = 0 \tag{1}$$

$$P_k(t) := 1000 \cdot \left( \frac{\sum_{t_0=t-k+1}^{t} E(t_0)}{k \cdot \min_{t_0+k-1}^{t} E(t_0)} - 1 \right) \tag{2}$$

## 3.2 Feature parameter selection and dataset spliting

Pearson correlation analysis was first conducted to assess the linear relationships between all tunneling parameters and surrounding rock classification. The objective of this analysis was to quantify the strength of correlation between each parameter and the surrounding rock grade, facilitating the identification of the most relevant features. Based on the results of this analysis, and employing a hybrid "knowledge-driven" and "data-driven" approach, eight critical feature parameters were selected: Thrust, Rotation Speed (RS), Torque, Penetration Rate (PR), 1# Middle Shield Retracting Gripper Shoe Pressure (1#SSP), 2# Middle Shield Retracting Gripper Shoe Pressure (2#SSP), Foam Pressure (1#FP), and Surrounding Rock Classification (SR). The Pearson correlation coefficients for these parameters are presented in Figure 4. Notably, the absolute correlation coefficients for the other seven features with surrounding rock grade were all greater than 0.15, indicating a significant linear relationship. In contrast, Thrust exhibited a correlation coefficient of only 0.05, reflecting a weak association with surrounding rock grade. However, given that Thrust is a critical control parameter in TBM tunneling, it was retained in the final set of features. Following data cleaning and feature selection, the dataset was partitioned into training, testing, and validation sets in a 7:2:1 ratio. The partitioning process involved categorizing the data samples by surrounding rock grade (III, IV, V), and then, within each grade group, randomly selecting 70% of the data for the training set, 20% for the testing set, and the remaining 10% for the validation set.

## 3.3 Model training methods

Based on the selected feature parameters and processed data, modeling is performed using the following three methods:

Method (1): Using raw data with default hyperparameters and no additional processing; Method (2): Applying hyperparameter optimization to the data; Method (3): Combining hyperparameter optimization with SMOTE for data processing. The SMOTE oversampling method was specifically employed to address severe data imbalance issues across Grades III, IV, and V surrounding rocks.

Surrounding rock grade classification models were developed using XGBoost, CatBoost, RF, and LightGBM algorithms based on these three modeling methods. Model performance was evaluated using key metrics—Precision, Recall, and F1_score—to assess the effectiveness of each strategy. The formulas for these metrics are defined in Equations 3–5.

$$PRE = \frac{TP}{TP + FP} \tag{3}$$

$$REC = \frac{TP}{TP + FN} \tag{4}$$

$$F_1 = \frac{2 \times PRE \times REC}{PRE \times REC} \tag{5}$$

In the equations, TP denotes the number of true positive samples (correctly predicted positive instances), FP represents false positive samples (negative instances incorrectly predicted as positive), and FN indicates false negative samples (positive instances incorrectly predicted as negative).

# 4 Machine learning algorithms

## 4.1 eXtreme gradient boosting (XGBoost)

The Extreme Gradient Boosting (XGBoost) algorithm, proposed by Chen and Guestrin et al. (Zhang et al., 2022), is a composite algorithm formed by combining base functions and weights to achieve superior data fitting. It belongs to the category of Gradient Boosting Decision Tree (GBDT). The core principle of GBDT lies in combining multiple weak learners (decision trees) to form a stronger predictive model. During training, GBDT iteratively adds new decision trees to correct errors from previous models until convergence or reaching predefined iteration limits [Prokhorenkova et al. (2017) and

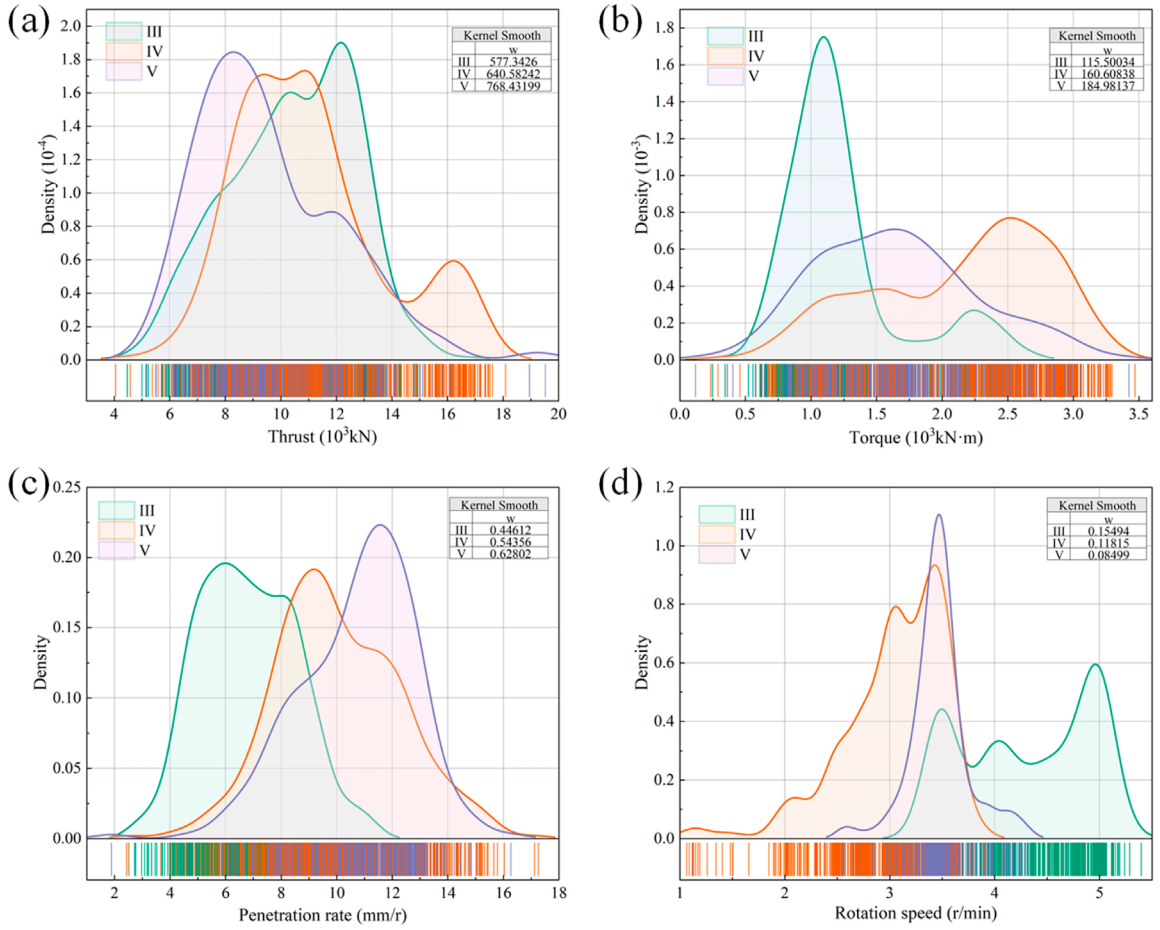


FIGURE 3
Kernel Density Curves of Different Feature Parameters under Corresponding surrounding rock Grades: **(a)** Thrust; **(b)**Torque; **(c)** Penetration rate; **(d)** Rotation speed.

35]. Unlike traditional GBDT, XGBoost enhances the objective loss function by incorporating regularization terms. To address challenges in calculating derivatives for certain loss functions, XGBoost approximates the loss function using a second-order Taylor expansion, improving computational precision. Additionally, XGBoost employs shrinkage strategies and feature subsampling to prevent overfitting and introduces a sparsity-aware algorithm to handle missing data. It also supports greedy algorithms and approximate learning for node splitting in tree models.

Due to its efficiency in processing large-scale data and complex models, as well as its robustness against overfitting, XGBoost has gained widespread attention and application since its inception.

## 4.2 Random Forest (RF)

Random Forest (RF), proposed by Breiman in 2001 (Hancock and Khoshgoftaar, 2020), is an ensemble learning method based on decision tree algorithms. The RF model employs a Bagging aggregation strategy, utilizing bootstrapping (a random sampling method with replacement) for data sampling. These techniques effectively mitigate overfitting risks during model construction. By integrating the results of multiple base estimators, RF achieves superior predictive performance compared to single-estimator models, demonstrating enhanced generalization capability and robustness. Additionally, the model reduces classification errors in imbalanced datasets and exhibits high training efficiency. Consequently, it has been widely applied to both regression and classification problems (Bentéjac et al., 2021).

## 4.3 Categorical boosting (CatBoost)

The CatBoost algorithm, proposed by Prokhorenkova et al. (2017), Ke et al. (2017), Shen et al. (2025a), is an advanced gradient boosting decision tree (GBDT) algorithm. Building upon GBDT, CatBoost introduces two key enhancements: adaptive learning rates and categorical feature processing, which enable superior performance in both classification and regression tasks. The adaptive learning rate optimizes the contribution of decision trees in each iteration, thereby improving overall model

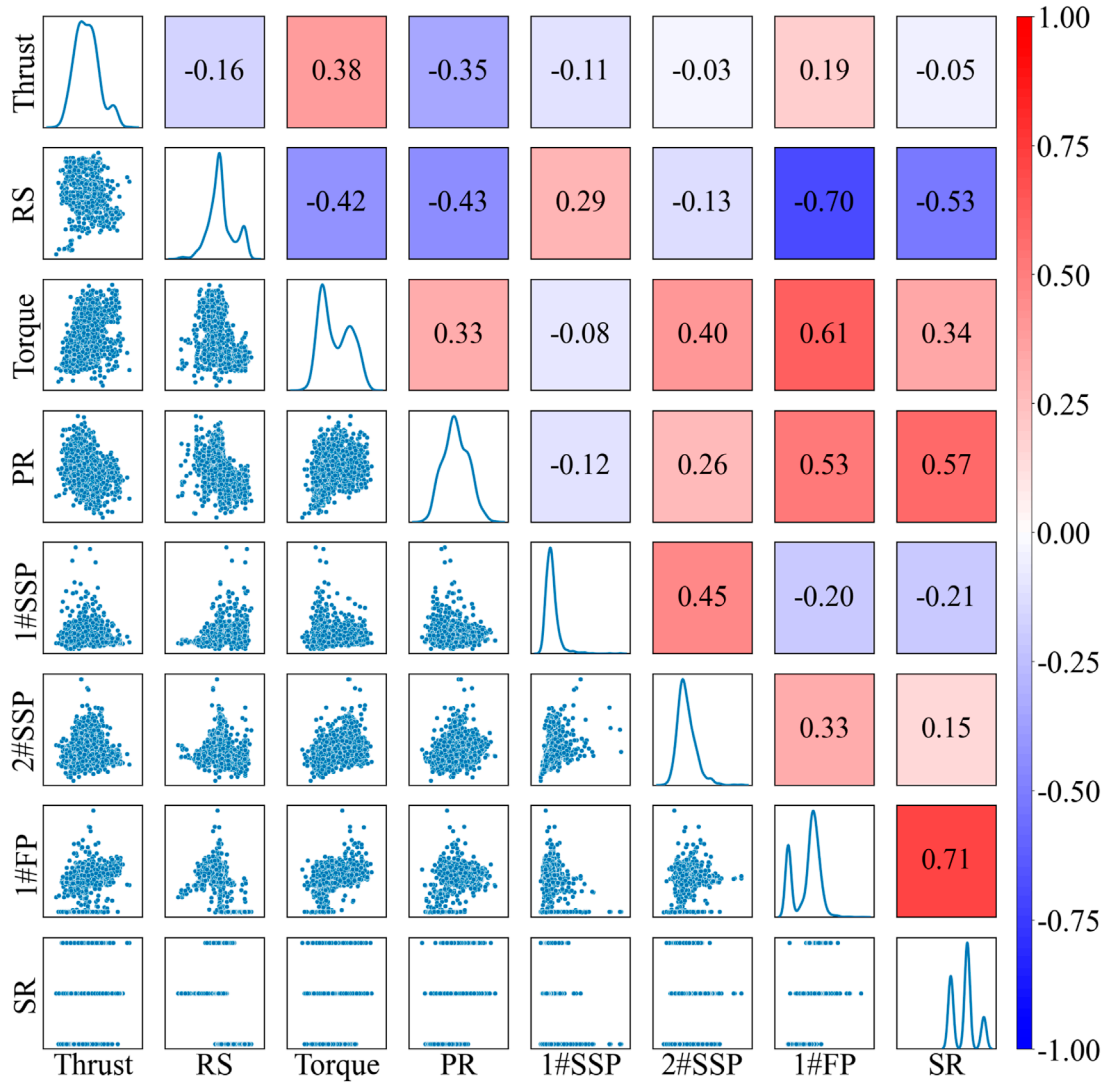


FIGURE 4
Pearson correlation analysis results of tunneling parameters.

accuracy. Its calculation method is detailed in Equations 6, 7. Categorical feature processing employs the Ordered Target Statistics encoding technique to convert categorical features into numerical representations. This method applies hash encoding to categorical values and maps the resulting hash values to numerical equivalents, effectively capturing the influence of categorical features.

Compared to XGBoost, CatBoost exhibits the following advantages.

1. Higher Model Accuracy: CatBoost often achieves high precision without requiring extensive hyperparameter tuning.
2. Faster Training Speed: Outperforms XGBoost in training efficiency.
3. Superior Prediction Speed: Delivers significantly faster inference times than XGBoost.
4. Lower Memory Consumption: Requires less memory usage on computational hardware.
5. Native Categorical Feature Support: Unlike XGBoost, which relies on OneHot encoding for categorical features, CatBoost directly handles string-type categorical features without preprocessing.

$$\eta_t = \frac{1}{\sqrt{1+t}} \tag{6}$$

$$\alpha_t = \frac{\sum_{i=1}^{t} \eta_i}{t} \tag{7}$$

In the equations, $t$ denotes the iteration number, $\eta_t$ represents the learning rate at the $t$th iteration, and $\alpha_t$ is the average learning rate from the previous iteration.

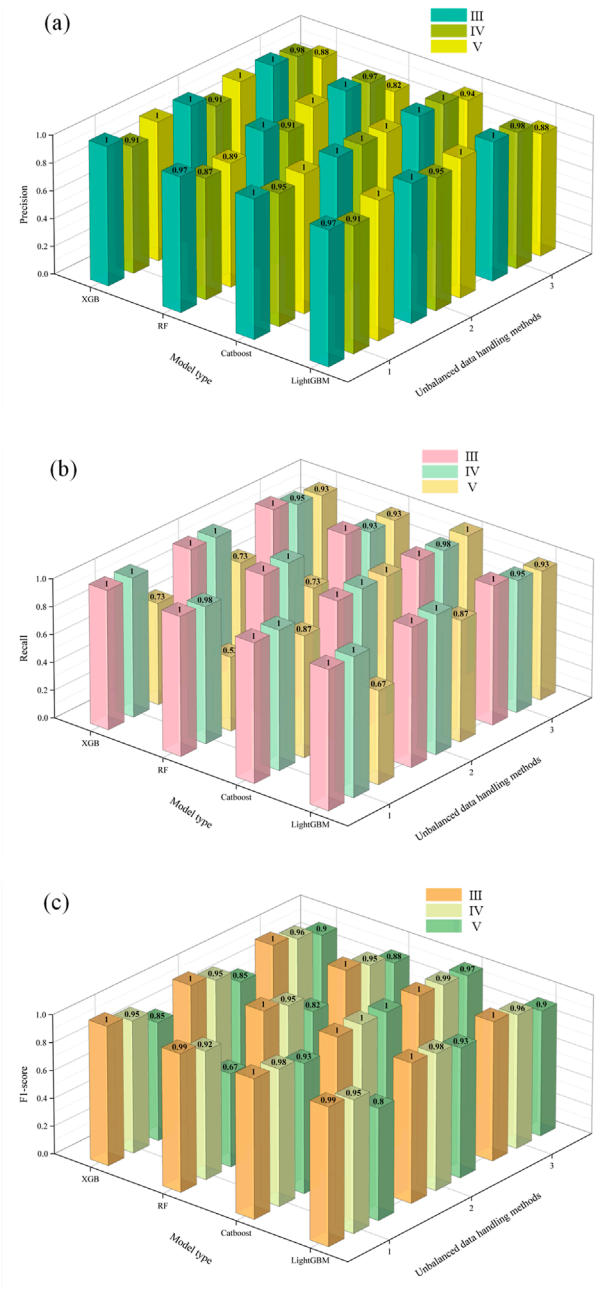


FIGURE 5
Evaluation metrics for intelligent diagnostic models: **(a)** Precision; **(b)** Recall; **(c)** F1_score.

## 4.4 Light Gradient Boosting Machine (LightGBM)

Light Gradient Boosting Machine (LightGBM), proposed by Ke et al. (2017), Shen et al. (2025b), is an efficient framework for implementing GBDT algorithms. Compared to XGBoost, LightGBM significantly reduces time complexity by converting sample-wise traversal into bin-wise calculations via the histogram algorithm (optimizing from sample-level to bin-level traversal). Additionally, LightGBM employs Gradient-based One-Side Sampling (GOSS), which retains samples with large gradients while randomly selecting a subset of low-gradient samples, thereby reducing computational load while maintaining gradient distribution stability. Furthermore, its leaf-wise growth strategy prioritizes splitting leaf nodes that yield the greatest loss reduction during the tree-building process, generating deeper asymmetric tree structures to minimize redundant computations. LightGBM also combines optimized feature parallelism and data parallelism methods to accelerate training and introduces the Exclusive Feature Bundling (EFB) algorithm, which merges sparse and mutually exclusive features into single composite features to reduce dimensionality and memory consumption. These innovations enable LightGBM to achieve high efficiency and low resource utilization when processing large-scale, high-dimensional data.

# 5 Predictive models and results

## 5.1 Surrounding rock classification model

Surrounding rock classification models were developed using XGBoost, CatBoost, RF, and LightGBM algorithms. First, eight TBM tunneling parameters—Thrust, Rotation Speed (RS), Torque, Penetration Rate (PR), 1#SSP, 2#SSP, 1#FP, and SR—were selected through a hybrid "data-driven" and "knowledge-driven" approach. The data were cleaned according to Equation 1 and denoised using boxplots. The preprocessed dataset was partitioned into training, testing, and validation sets at a 7:2:1 ratio. Three imbalanced data processing methods were applied, with the input parameters being the eight selected TBM tunneling parameters and the output being the surrounding rock grades (III, IV, V), labeled as 3, 4, and 5, respectively.

Before model training, the training set was standardized using Equation 8. The Optuna hyperparameter optimizer was employed for automated hyperparameter tuning, with the optimization cycle set to 100 iterations, yielding final hyperparameters for models based on the three imbalanced data processing methods. Training was then conducted using these optimized hyperparameters. Finally, the trained models were validated using the testing set to obtain the final surrounding rock classification results.

$$x_{new} = \frac{x - \mu}{\sigma} \tag{8}$$

In the equation, $x_{new}$ represents the standardized data, $x$ denotes the raw data, $\mu$ is the mean of the sample data, and $\sigma$ is the standard deviation of the sample data.

## 5.2 Model performance evaluation

Surrounding rock classification models under three data processing methods were established using XGBoost, CatBoost, RF, and LightGBM ensemble learning algorithms. The prediction results of these models were evaluated using three key metrics: Precision, Recall, and F1_score, as shown in Figure 5. The optimal hyperparameters obtained via Optuna optimization are summarized in Table 2. The results indicate: Method (1)

TABLE 2 The hyperparameter optimization results of the intelligent diagnostic model.

| Model type | XGBoost | RF | CatBoost | LightGBM |
|---|---|---|---|---|
| Unbalanced data handing methods (2) | *n_estimators*: 1855<br>*max_depth*: 9<br>*learning_rate*: 0.0468<br>*subsample*: 0.8663<br>*colsample_bytree*: 0.8882<br>*gamma*: 0.5033<br>*min_child_weight*: 5<br>*reg_alpha*: 0.1713<br>*reg_lambda*: 2.6573 | *n_estimators*: 1,559<br>*max_depth*: 18<br>*min_samples_split*: 3<br>*min_samples_leaf*: 3 | *iterations*: 1,142<br>*depth*: 4<br>*learning_rate*: 5.38e-2<br>*l2_leaf_reg*: 0.0188<br>*bagging_temperature*: 0.2057<br>*random_strength*: 2.3258<br>*border_count*: 252 | *n_estimators*: 1,241<br>*max_depth*: 0<br>*learning_rate*: 0.1681<br>*subsample*: 0.7184<br>*colsample_bytree*: 0.9625<br>*num_leaves*: 55<br>*min_child_samples*: 35<br>*reg_alpha*:0.0187<br>*reg_lambda*: 1.1492 |
| Unbalanced data handing methods (3) | *n_estimators*: 455<br>*max_depth*: 18<br>*learning_rate*: 8.36e-3<br>*subsample*: 0.9832<br>*colsample_bytree*: 0.9238<br>*gamma*: 0.3049<br>*min_child_weight*: 9<br>*reg_alpha*: 1.003e-4<br>*reg_lambda*: 1.181e-4 | *n_estimators*: 1,023<br>*max_depth*: 11<br>*min_samples_split*: 3<br>*min_samples_leaf*: 3 | *iterations*: 542<br>*depth*: 6<br>*learning_rate*: 2.63e-2<br>*l2_leaf_reg*: 0.0610<br>*bagging_temperature*: 0.5349<br>*random_strength*: 3.6250<br>*border_count*: 35 | *n_estimators*: 1,511<br>*max_depth*: 14<br>*learning_rate*: 9.30e-3<br>*subsample*: 0.9086<br>*colsample_bytree*: 0.8780<br>*num_leaves*: 130<br>*min_child_samples*: 4<br>*reg_alpha*:0.0024<br>*reg_lambda*: 5.2011 |

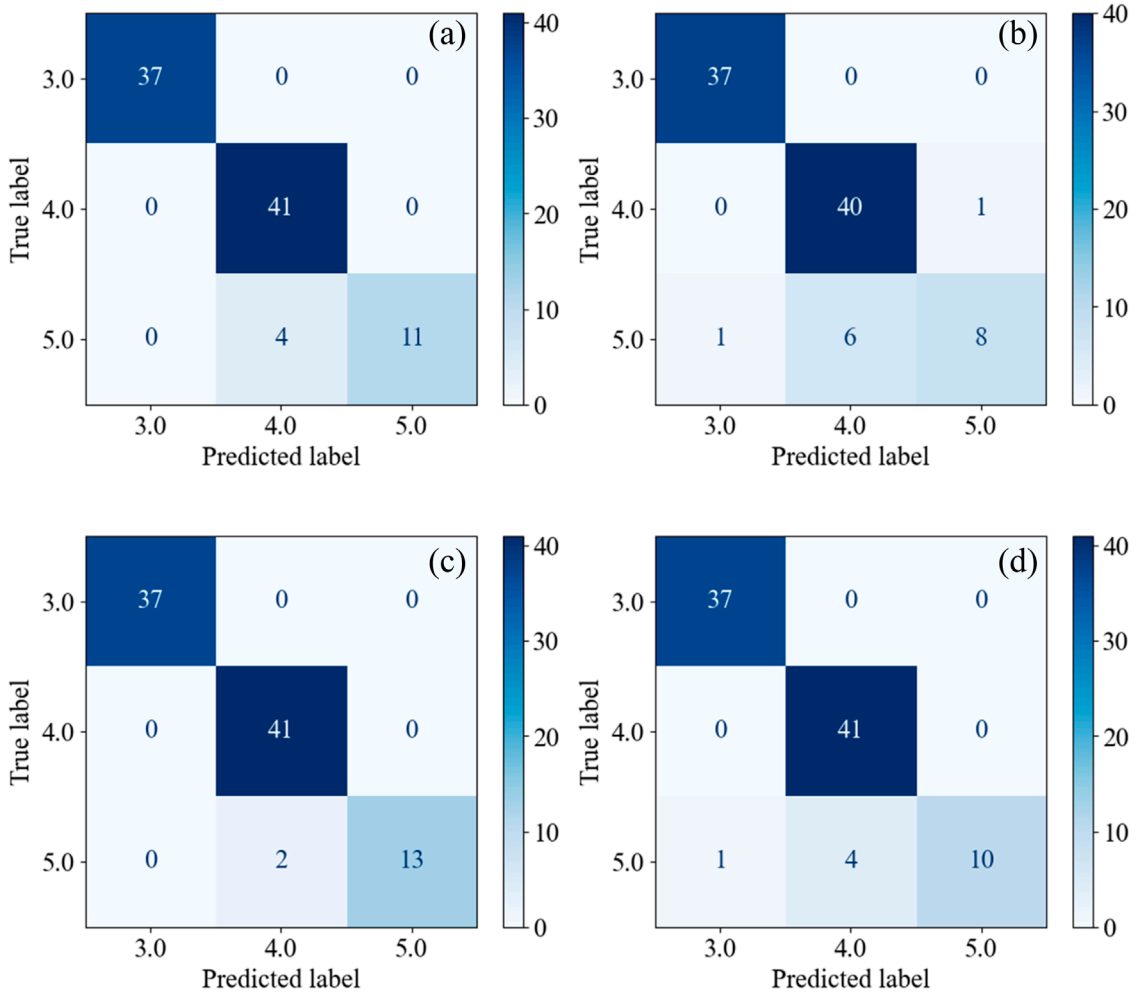


FIGURE 6
Classification prediction results with default raw parameters: **(a)** XGBoost; **(b)** RF; **(c)** CatBoost; **(d)** LightGBM.

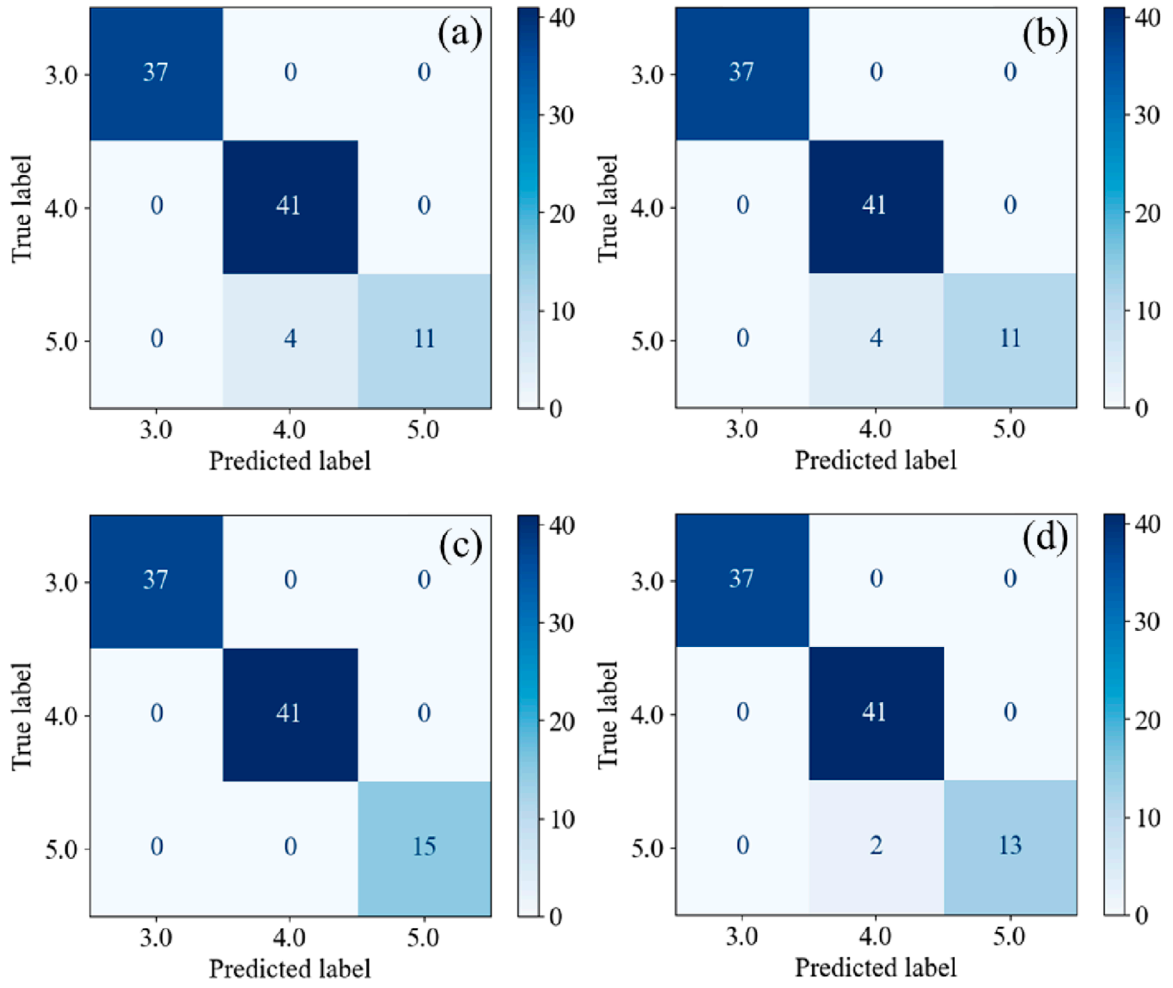


FIGURE 7
Classification prediction results with hyperparameter optimization: **(a)** XGBoost; **(b)** RF; **(c)** CatBoost; **(d)** LightGBM.

(raw data only): All four models exhibited poor performance. The RF model performed worst for Grade V surrounding rock (Precision:0.67, Recall:0.53, F1:0.89). Method (2) (hyperparameter optimization): Significant accuracy improvements were achieved compared to Method (1). The CatBoost model satisfied all evaluation criteria, indicating reliable predictions, while RF and XGBoost models still underperformed. Method (3) (hyperparameter optimization + SMOTE): All models showed further accuracy gains, with the CatBoost model achieving the best prediction performance.

Performance analysis revealed varying degrees of classification confusion among all models using raw data, as demonstrated by the confusion matrix of the validation set in Figure 6. The RF model exhibited a misclassification rate of 1.92% (1/52) between Grades III and V, with cross-grade misclassifications observed. The misclassification rate between Grades IV and V reached 10.71% (6/56). The XGBoost and LightGBM models showed improved performance, reducing the IV-V misclassification rates to 7.14% (4/56) and 7.27% (4/55), respectively. The CatBoost model outperformed others, achieving a IV-V misclassification rate of 3.57% (2/56), with prediction accuracies of 100% for Grade III, 100% for Grade IV, and 86% for Grade V. These results confirm that the CatBoost model delivers the best predictive performance under raw data conditions.

After hyperparameter optimization, the confusion matrices of different models on the validation set are shown in Figure 7. The results indicate: RF and XGBoost models exhibited no misclassification between Grades III and V, while the misclassification rate between Grades IV and V decreased to 7.14% (4/56). LightGBM model further reduced the IV-V misclassification rate to 3.57% (2/56). CatBoost model achieved zero misclassification with 100% prediction accuracy for Grades III, IV, and V, demonstrating its superior effectiveness.

When combining SMOTE with hyperparameter optimization, the classification prediction results of the validation set confusion matrix are shown in Figure 8. The results demonstrate: The XGBoost model achieved further improvement, reducing the misclassification rate between Grades IV and V to 5.36% (3/56). The RF and LightGBM models increased the prediction accuracy for Grade V to

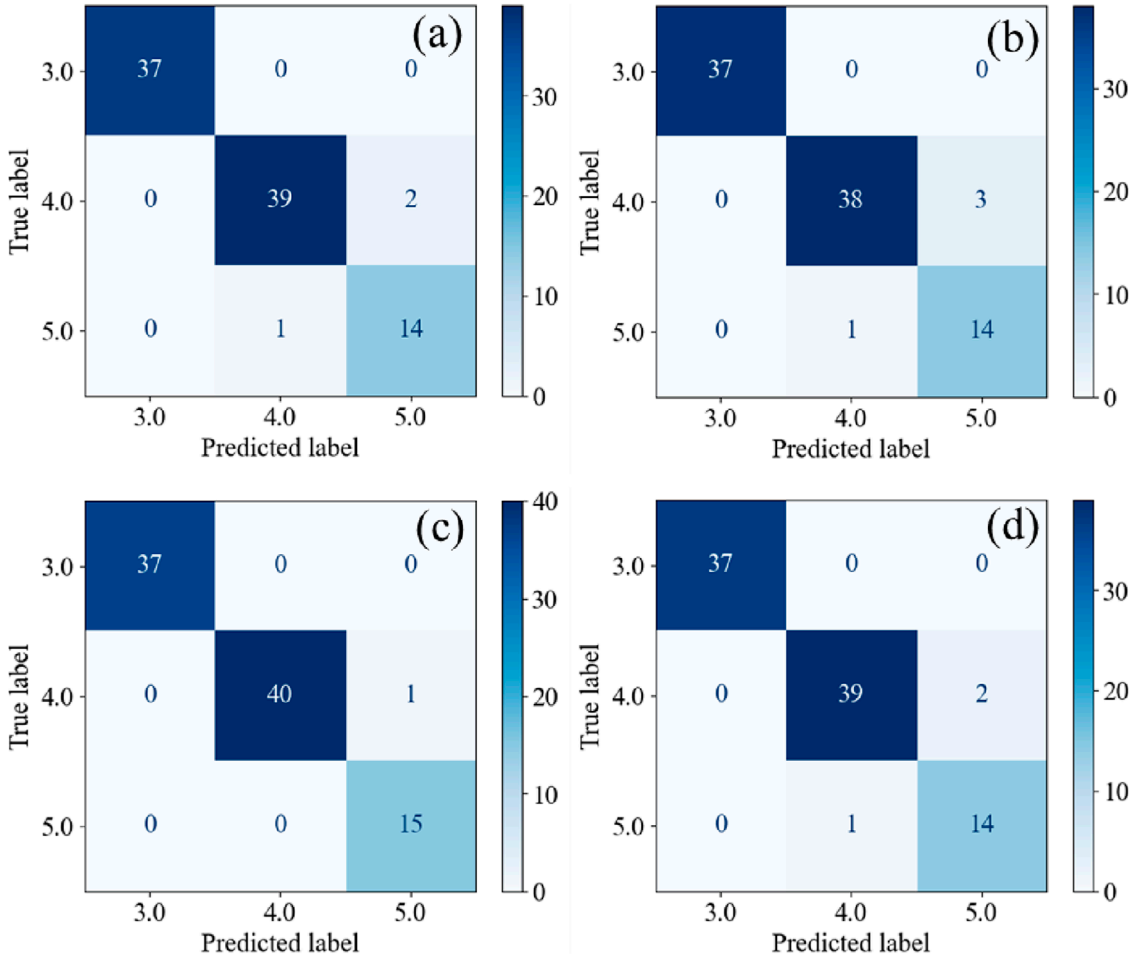


FIGURE 8
Classification prediction results with SMOTE and hyperparameter optimization: **(a)** XGBoost; **(b)** RF; **(c)** CatBoost; **(d)** LightGBM.

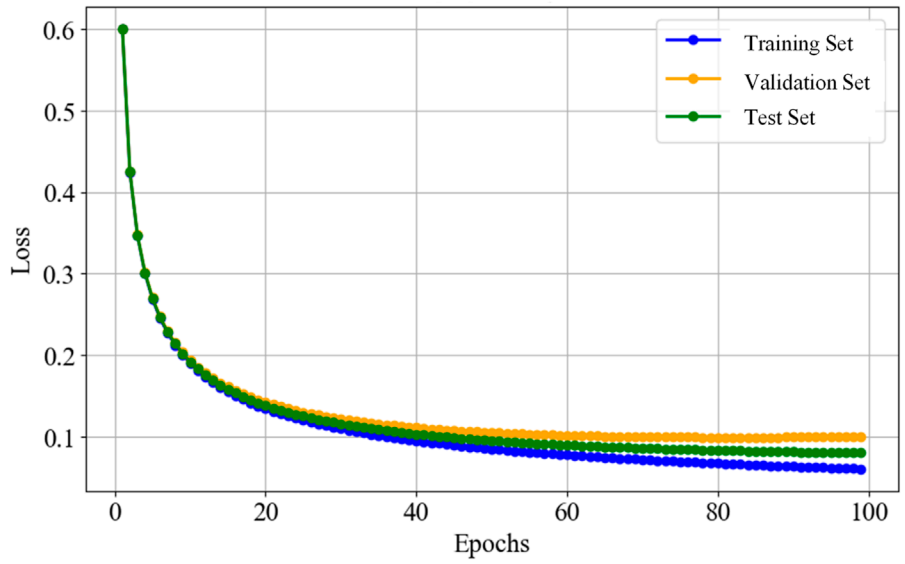


FIGURE 9
Convergence curve of CatBoost model.

93.3% (14/15) with no cross-grade misclassifications. These results indicate that SMOTE-enhanced hyperparameter optimization further improves model accuracy. The CatBoost model, which already achieved excellent performance with hyperparameter optimization alone, showed negligible differences after SMOTE integration.

Therefore, through comprehensive consideration of prediction accuracy, the CatBoost model integrated with SMOTE and hyperparameter optimization was selected as the optimal intelligent diagnostic model in this study. Without further validating the performance curves of the CatBoost model, its convergence curve was plotted as shown in Figure 9. The results indicate that the model exhibits only slight overfitting, and its overall performance remains acceptable.

## 6 Conclusion

TBM tunneling efficiency and construction safety are highly dependent on real-time perception of surrounding rock conditions and parameter optimization. This study, based on TBM construction data from the Luotie Project, established intelligent diagnostic models for surrounding rock classification using XGBoost, RF, CatBoost, and LightGBM algorithms. These models integrate feature selection methods combining data-driven and knowledge-driven approaches, along with three data processing techniques. Model performance was evaluated using three key metrics: Precision, Recall, and F1_score. The conclusions are as follows.

1. Feature-selected tunneling parameters from TBM1 in the Luotie Project were processed using three methods to develop surrounding rock classification models. The CatBoost model with SMOTE-enhanced hyperparameter optimization achieved the highest prediction accuracy (average 99%).
2. The RF model using raw data exhibited a 1.92% (1/52) misclassification rate between Grades III and V, involving cross-grade errors. Other models (XGBoost, CatBoost, LightGBM) and the hyperparameter-optimized RF model with SMOTE eliminated cross-grade misclassifications, demonstrating perfect differentiation between Grades III and V. This confirms that SMOTE-enhanced hyperparameter optimization significantly improves prediction accuracy.
3. The CatBoost model achieved optimal prediction accuracy with hyperparameter optimization alone, showing negligible performance differences when combined with SMOTE. Both approaches satisfied all key evaluation criteria.

## Data availability statement

The original contributions presented in the study are included in the article/supplementary material, further inquiries can be directed to the corresponding author.

## Author contributions

PD: Writing – review and editing. LC: Writing – review and editing. PT: Writing – review and editing. JY: Writing – original draft, Writing – review and editing. ZL: Writing – review and editing.

## Funding

The author(s) declare that no financial support was received for the research and/or publication of this article.

## Conflict of interest

Authors PD, LC, and PT were employed by Sinohydro Bureau 14 Co., Ltd.

The remaining authors declare that the research was conducted in the absence of any commercial or financial relationships that could be construed as a potential conflict of interest.

## Generative AI statement

The author(s) declare that no Generative AI was used in the creation of this manuscript.

Any alternative text (alt text) provided alongside figures in this article has been generated by Frontiers with the support of artificial intelligence and reasonable efforts have been made to ensure accuracy, including review by the authors wherever possible. If you identify any issues, please contact us.

## Publisher's note



## References

Afradi, A., and Ebrahimabadi, A. (2020). Comparison of artificial neural networks (ANN), support vector machine (SVM) and gene expression programming (GEP) approaches for predicting TBM penetration rate. *SN Appl. Sci.* 2 (12), 2004. doi:10.1007/s42452-020-03767-y

Aston, T. R. C., Gilby, J. L., and Yuen, C. M. K. (1988). A comparison of rock mass disturbance in TBM and drill and blast drivages at the donkin Mine, Nova Scotia. *Int. J. Min. Geol. Eng.* 6 (2), 147–162. doi:10.1007/bf00880804

Barton, N. (2012). Reducing risk in long deep tunnels by using TBM and drill-and-blast methods in the same project–the hybrid solution. *J. Rock Mech. Geotechnical Eng.* 4 (2), 115–126. doi:10.3724/sp.j.1235.2012.00115

Bentéjac, C., Csörgő, A., and Martínez-Muñoz, G. (2021). A comparative analysis of gradient boosting algorithms. *Artif. Intell. Rev.* 54 (3), 1937–1967. doi:10.1007/s10462-020-09896-5

Breiman, L. (2001). Random forests. *Mach. Learn.* 45 (1), 5–32. doi:10.1023/a:1010933404324

Chen, T. Q., He, T., Benesty, M., Khotilovich, V., Tang, Y., Cho, H., et al. (2015). Xgboost: extreme gradient boosting. *R. package version 0.4-2* 1 (4), 1–4.

Chen, Z. Y., Zhang, Y. P., Li, J. B., Li, X., and Jing, L. (2021). Diagnosing tunnel collapse sections based on TBM tunneling big data and deep learning: a case study on the Yinsong Project, China. *Tunn. Undergr. Space Technol.* 108, 103700. doi:10.1016/j.tust.2020.103700

Fang, X. H., Yang, J. S., Zhang, X. M., Zhang, C., Wang, S., and Xie, Y. (2023). Numerical modeling of open TBM tunneling in stratified rock masses using a coupled FDM-DEM method. *Comput. Geotechnics* 156, 105251. doi:10.1016/j.compgeo.2023.105251

Fang, X. H., Yang, L. Q., Zhang, C., Yang, J., and Zhou, W. (2025). Large diameter shafts in fractured strata: equipment and construction procedures. *J. Constr. Eng. Manag.* 151 (9), 06025001. doi:10.1061/jcemd4.coeng-16745

Feng, S. X., Chen, Z. Y., Luo, H., Wang, S., Zhao, Y., Liu, L., et al. (2021). Tunnel boring machines (TBM) performance prediction: a case study using big data and deep learning. *Tunn. Undergr. Space Technol.* 110, 103636. doi:10.1016/j.tust.2020.103636

Ghorbani, E., and Yagiz, S. (2024). Predicting disc cutter wear using two optimized machine learning techniques. *Archives Civ. Mech. Eng.* 24 (2), 106. doi:10.1007/s43452-024-00911-y

Guo, D., Li, J. H., Jiang, S. H., Li, X., and Chen, Z. (2022a). Intelligent assistant driving method for tunnel boring machine based on big data. *Acta Geotech.* 17 (4), 1019–1030. doi:10.1007/s11440-021-01327-1

Guo, D., Li, J. H., Li, X., Li, Z., Li, P., and Chen, Z. (2022b). Advance prediction of collapse for TBM tunneling using deep learning method. *Eng. Geol.* 299, 106556. doi:10.1016/j.enggeo.2022.106556

Hancock, J. T., and Khoshgoftaar, T. M. (2020). CatBoost for big data: an interdisciplinary review. *J. big data* 7 (1), 94. doi:10.1186/s40537-020-00369-8

Hou, S. K., Liu, Y. R., and Yang, Q. (2022). Real-time prediction of rock mass classification based on TBM operation big data and stacking technique of ensemble learning. *J. Rock Mech. Geotechnical Eng.* 14 (1), 123–143. doi:10.1016/j.jrmge.2021.05.004

Ke, G., Meng, Q., Finley, T., Wang, T. F., Chen, W., Ma, W. D., et al. (2017). Lightgbm: a highly efficient gradient boosting decision tree. *Adv. neural Inf. Process. Syst.*, 30. doi:10.5555/3294996.3295074

Kohestani, V. R., Bazarganlari, M. R., and Asgari Marnani, J. (2017). Prediction of maximum surface settlement caused by earth pressure balance shield tunneling using random forest. *J. AI Data Min.* 5 (1), 127–135. doi:10.22044/jadm.2016.748

Li, J. B., Chen, Z. Y., Li, X., Jing, L. J., Zhang, Y. P., Xiao, H. H., et al. (2023a). Feedback on a shared big dataset for intelligent TBM part I: feature extraction and machine learning methods. *Undergr. Space* 11, 1–25. doi:10.1016/j.undsp.2023.01.001

Li, J. B., Chen, Z. Y., Li, X., Jing, L. J., Zhang, Y. P., Xiao, H. H., et al. (2023b). Feedback on a shared big dataset for intelligent TBM Part II: application and forward look. *Undergr. Space* 11, 26–45. doi:10.1016/j.undsp.2023.01.002

Liu, B., Wang, R., Zhao, G., Guo, X., Wang, Y., Li, J., et al. (2020). Prediction of rock mass parameters in the TBM tunnel based on BP neural network integrated simulated annealing algorithm. *Tunn. Undergr. Space Technol.* 95, 103103. doi:10.1016/j.tust.2019.103103

Liu, Z. B., Li, L., Fang, X. L., Qi, W., Shen, J., Zhou, H., et al. (2021). Hard-rock tunnel lithology prediction with TBM construction big data using a global-attention-mechanism-based LSTM network. *Automation Constr.* 125, 103647. doi:10.1016/j.autcon.2021.103647

Mao, Y. Z., Gong, G., Zhou, X., Hu, X. Q., and Chen, Z. Y. (2021). Identification of TBM surrounding rock based on Markov process and deep neural network. *J. Zhejiang Univ. Eng. Sci.* 55 (3), 448–454. doi:10.3785/j.issn.1008-973X.2021.03.004

Prechelt, L. (2002). *Early stopping-but when?[M]//Neural networks: tricks of the trade*. Berlin, Heidelberg: Springer Berlin Heidelberg, 55–69.

Prokhorenkova, L., Gusev, G., Vorobev, A., Dorogush, A. V., and Gulin, A. (2018). CatBoost: unbiased boosting with categorical features. *Adv. neural Inf. Process. Syst.*, 31. doi:10.5555/3327757.3327770

Shen, J., Bao, X. H., Chen, X. S., Wu, X. L., Qiu, T., and Cui, H. Z. (2025a). Seismic resilience assessment method for tunnels based on cloud model considering multiple damage evaluation indices. *Tunn. Undergr. Space Technol.*157, 106360. doi:10.1016/j.tust.2024.106360

Shen, J., Bao, X. H., Li, J. H., Chen, X. S., and Cui, H. Z. (2025b). Study on the mechanism of EPWP dissipation at the joints of shield tunnel in liquefiable strata during seismic events. *Soil Dyn. Earthq. Eng.* 188, 109089. doi:10.1016/j.soildyn.2024.109089

Tang, Y., Yang, J. S., You, Y. Y., Fu, J., Zheng, X., and Zhang, C. (2024). Multi-output prediction for TBM operation parameters based on stacking ensemble algorithm. *Tunn. Undergr. Space Technol.* 152, 105960. doi:10.1016/j.tust.2024.105960

Wu, Z. J., Wei, R. L., Chu, Z. F., and Liu, Q. (2021). Real-time rock mass condition prediction with TBM tunneling big data using a novel rock–machine mutual feedback perception method. *J. Rock Mech. Geotechnical Eng.* 13 (6), 1311–1325. doi:10.1016/j.jrmge.2021.07.012

Xie, Y. P., Qu, T. M., Yang, J. S., Wang, S., and Zhao, J. (2025). Multiscale insights into tunneling-induced ground responses in coarse-grained soils. *Comput. Geotechnics* 185. doi:10.1016/j.compgeo.2025.107319

Xiong, X. (2014). Research on prediction of rating of rockburst based on BP neural network. 8, 463, 469. doi:10.2174/1874149501408010463

Yin, X., Liu, Q. S., Huang, X., and Pan, Y. (2022). Perception model of surrounding rock geological conditions based on TBM operational big data and combined unsupervised-supervised learning. *Tunn. Undergr. Space Technol.* 120, 104285. doi:10.1016/j.tust.2021.104285

Zhang, N., Li, J. B., Jing, L. J., Liu, C., and Gao, J. (2019). Prediction method of Rockmass parameters based on tunnelling process of tunnel boring machine. *J. Zhejiang Univ. Eng. Sci.* 53 (10), 1977–1985. doi:10.3785/j.issn.1008-973X.2019.10.015

Zhang, W. G., Zhang, R. H., Wu, C. Z., Goh, A. T., and Wang, L. (2022). Assessment of basal heave stability for braced excavations in anisotropic clay using extreme gradient boosting and random forest regression. *Undergr. Space* 7 (2), 233–241. doi:10.1016/j.undsp.2020.03.001

Zheng, Y. L., Zhang, Q. B., Zhao, J., Du, J. H., Yin, J. B., and Li, H. Q. (2016). Challenges and opportunities of using tunnel boring machines in mining. *Tunn. Undergr. Space Technol.* 57, 287–299. doi:10.1016/j.tust.2016.01.023

Zhu, M. Q., Zhu, H. H., Wang, X., and Cheng, P. P. (2020). Study on CART-based ensemble learning algorithms for predicting TBM tunneling parameters and classing surrounding rockmasses. *Chin. J. Rock Mech. Eng.* 39 (9), 1860–1871. doi:10.13722/j.cnki.jrme.2020.0555

Zhu, M. Q., Gutierrez, M., Zhu, H. H., Ju, J. W., and Sarna, S. (2021). Performance Evaluation Indicator (PEI): a new paradigm to evaluate the competence of machine learning classifiers in predicting rockmass conditions. *Adv. Eng. Inf.* 47, 101232. doi:10.1016/j.aei.2020.101232

frontiers | Frontiers in Earth Science

TYPE Original Research
PUBLISHED 22 October 2025
DOI 10.3389/feart.2025.1684101



OPEN ACCESS

EDITED BY
Zhang Cong,
Central South University Forestry and Technology, China

REVIEWED BY
Haifeng Liu,
Chinese Academy of Sciences (CAS), China
Erlei Yao,
Yangtze River Scientific Research Institute, China

*CORRESPONDENCE
Songlin Peng,
ylshanwang86@163.com

RECEIVED 12 August 2025
ACCEPTED 30 September 2025
PUBLISHED 22 October 2025

CITATION
Tu M, Tang X, He G, Peng S, Yang L and Xu J (2025) Experimental study on blasting with a short straight hole + wedge compound cut scheme in hard rock tunnels.
*Front. Earth Sci.* 13:1684101.
doi: 10.3389/feart.2025.1684101



# Experimental study on blasting with a short straight hole + wedge compound cut scheme in hard rock tunnels

Meng Tu[1], Xianglong Tang[2], Guidao He[1], Songlin Peng[3]*, Lin Yang[3] and Jinxing Xu[3]

[1]Wenshan Tianwen Expressway Investment and Development Co., Ltd., Wenshan, China, [2]CCCC Rail Transit Branch, Beijing, China, [3]CCCC Second Harbor Engineering Co., Ltd., Wuhan, China

**Introduction:** In drill-and-blast excavation for small- and medium-sized tunnels, the conventional wedge-cut blasting method is often constrained by the limited maneuvering space of construction equipment. This restriction can result in excessive inclination of wedge-cut holes relative to the tunnel face. Consequently, the rock in the cut zone is subjected to strong confinement, leading to reduced advance per round, low blasthole utilization efficiency, and an increased specific charge.

**Methods:** In this study, theoretical analysis and formula derivation were conducted to evaluate the respective advantages and limitations of wedge cutting and straight-hole cutting. Based on these analyses, optimal layout parameters for straight holes were determined. A combined short straight-hole + wedge compound cut blasting scheme was subsequently proposed and tested in a hard rock tunnel.

**Results:** When calculating the spacing between charge holes and relief holes, the influence of high strain rates on the rock's tensile strength should be incorporated to ensure that theoretical parameters are both accurate and applicable. Compared with the original blasting scheme, the designed compound cut method increased the advance per round from 1.7–1.8 m to 2.0–2.1 m and improved blasthole utilization from 73.91%–78.26% to 86.96%–91.30%. The specific charge remained nearly unchanged, while detonator consumption decreased by approximately 0.4 detonators/$m^3$, demonstrating clear economic benefits. The application of the short straight-hole + wedge compound cut technique also resulted in fewer remaining holes and finer rock fragmentation at the tunnel face, thereby enhancing the efficiency of muck removal and drilling operations in subsequent cycles.

**Discussion:** The short straight-hole + wedge compound cut technique has been successfully applied in small and medium-sized section hard rock tunnels,These results offer valuable guidance for optimizing drill-and-blast design parameters and construction practices in small- and medium-scale hard rock tunneling projects.

KEYWORDS

**water conveyance tunnel, compound cut blasting, blasting parameters, circular tunnel, experiment**

# 1 Introduction

Drilling and blasting are the most commonly used construction methods for excavating underground spaces, particularly hard rock tunnels. Tunnel blasting excavation involves only one free surface, which is subjected to a large confinement effect and is therefore not conducive to blasting (Ren-Shu et al., 2022; Bao-Long, 2014a). As the "vanguard" of tunnel blasting excavation, cut holes provide compensation spaces and free surfaces for delayed blastholes, exerting a decisive influence on the blasting effect (Xin-Han, 2024). A well-designed cut blasting scheme can significantly improve excavation efficiency (Xiao-Ming and Shi-Hai, 2019). The most common cut configurations in tunnel blasting are straight-hole cuts and wedge cuts. In small tunnels, wedge cuts are restricted by limited working space, whereas straight-hole cuts are generally free from such spatial constraints but require a larger number of blastholes and higher explosive consumption (Yuan-Li et al., 2020). Yi et al. (2024) investigated the mechanical behavior of wedge-cut blasting in deep-buried karst tunnels, finding that substantial tensile stresses developed near the cave. Xia Zhiyuan et al. (Zhiyuan et al.) optimized the existing charge structure for blasting in karst caves, improving rock damage and fragmentation. Ping (2021) summarized the principles and influencing factors of straight-hole cutting and, through experimental comparison of three cut schemes, determined that the highest blasthole utilization rate was achieved with three relief holes. Bao-Long (2014b) applied a quasi-parallel cutting method in tunnel blasting by adding an extra row of straight charge holes along the tunnel centerline, which significantly increased blasting advance. Yu-Yin (2013) expanded the cut zone area in field experiments, effectively reducing the burden and confinement effect on surrounding break holes while lowering the specific charge. Qi-Yue et al. (2018) improved the traditional straight-hole cut design, achieving greater advance per round. Yue-Yang and Su-Peng (2016) implemented a double-wedge cut combined with smooth blasting, markedly reducing unit explosive consumption in large hard rock tunnels. Yang Yueyang (Gang et al., 2018) conducted on-site blasting trials using a spiral cut with relief holes, obtaining favorable results. Hu Gang (Xing-Jun et al., 2016) performed numerical simulations of straight-hole cut blasting in tunnels and, through complementary field tests, demonstrated that the inclusion of relief holes improved both blasthole utilization and specific charge efficiency.

Extensive research has been carried out to enhance progress per round in small- and medium-sized hard rock tunnels. However, there are few studies on compound cut blasting technology involving short straight holes for such tunnels. Therefore, based on the relief hole effect, cut blasting theory, and the rock-breaking mechanisms of straight-hole and wedge cutting, this study developed a short straight-hole + wedge compound cut scheme and presents its application in the blasting of small- and medium-sized hard rock tunnels.

# 2 Theory

## 2.1 Common cutting structures

In tunnel construction using the drill-and-blast method, common cut blasting schemes include straight-hole cut blasting and inclined cut blasting. As shown in the schematic layout of blastholes in Figure 1, a straight-hole cut structure is typically employed in small- and medium-sized tunnels, whereas inclined cuts are generally used in large tunnels. However, the mechanisms of rock throw differ significantly between these two methods.

The single-hole blasting funnel theory shows that rock crushing includes compression stage, stress wave reverse tensile stage and explosive gas expansion stage. During the trough blasting, the rock mass cracks and breaks under the action of explosive stress waves, and then the explosion gas invades the rock mass cracks, overcoming the resistance of the broken rock mass, causing it to throw and fly out, and finally forming a trough cavity.

The inclined cut operates through a two-stage mechanism. The straight hole groove blasting holes are arranged perpendicular to the free surface, and a certain number of empty holes are arranged at the same time. The main blasting holes are continuously charged, and the functions of the empty holes are: (a) the explosion-induced stress wave impacts the relief hole wall, creating stress concentration and inducing plastic deformation in the surrounding rock mass; (b) reflection of stress waves from the free surface produces tensile stresses that cause rock failure; and (c) the relief holes provide additional free space, facilitating cavity formation and ensuring complete rock fragmentation.

## 2.2 Short straight hole + wedge compound cut

Owing to the limited working space, the use of large machinery is not feasible in small- and medium-sized tunnels. The angle of wedge-cut blastholes is difficult to control manually, often resulting in a large inclination between the cut holes and the tunnel face. The rock structure in the cut zone is highly confined, leading to poor cutting performance and reducing the blasthole utilization rate per round. Consequently, the straight-hole cut blasting scheme is often employed in small- and medium-sized tunnels, although it requires a greater number of holes and a higher specific charge than the inclined cut approach. Moreover, the remaining holes in the straight-hole cut zone are deeper, and the cutting efficiency is suboptimal, thereby reducing the advance per blast and conflicting with production requirements on site. Hence, efficient cutting with fewer holes and higher blasthole utilization is urgently required for construction.

In this study, a modified compound cut design was tested, as illustrated in Figure 2, in which short straight holes were incorporated into the conventional wedge-cut blasthole pattern. The addition of these short straight charge holes, together with multiple centrally positioned relief holes, created an auxiliary free surface

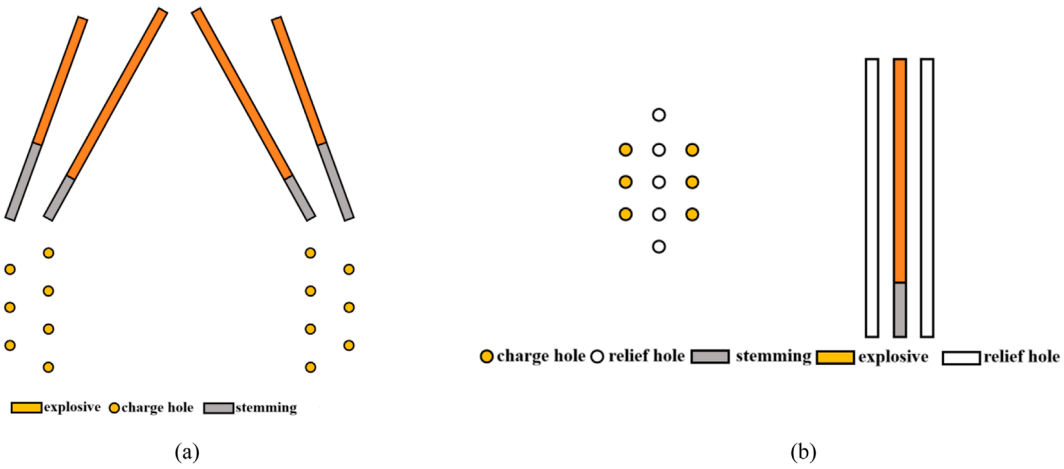


FIGURE 1
Layout diagram of common cutting structures. **(a)** Inclined cut. **(b)** Straight-hole cut.

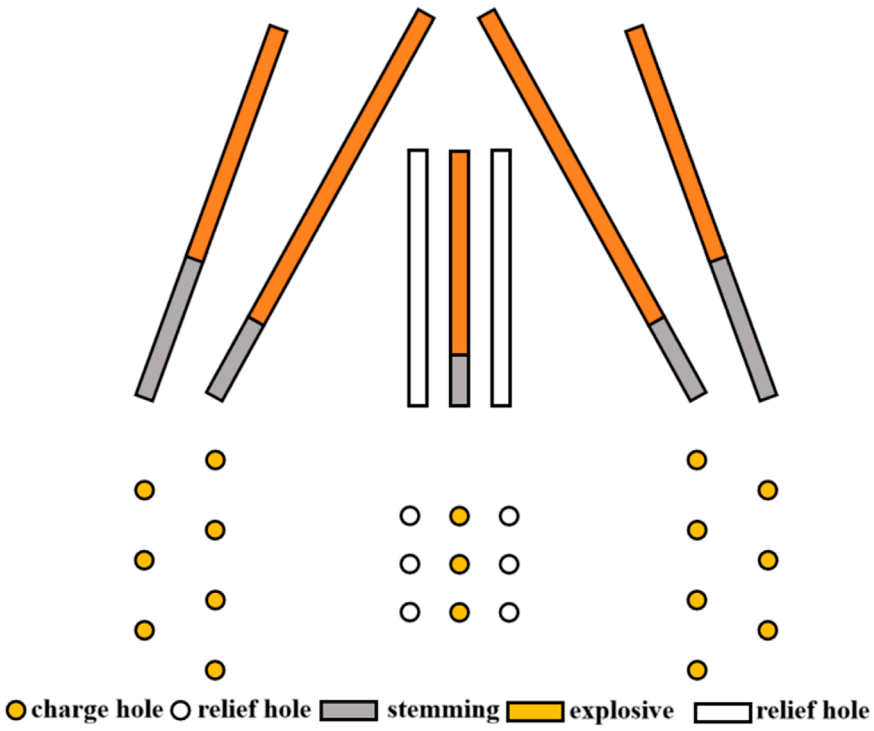


FIGURE 2
Short straight hole + wedge compound cut.

for the detonation of subsequent blastholes. This configuration effectively mitigated the limited rock throw caused by the large inclination of cut holes relative to the tunnel face in small- and medium-sized tunnels. When the tunnel face is relatively small, perforation is more likely to occur. However, setting explosives in the middle can expand the empty hole while minimizing the impact on the inclined cut. Therefore, a short straight hole + wedge-shaped cut structure is adopted for field testing in small and medium-sized circular water conveyance tunnels in hard rock.

# 3 Project overview

## 3.1 Surrounding rocks and geological conditions

The tunnel has a total length of 769.5 m, with burial depths ranging from 11.7 m to 108.7 m, and employs a combined pressurized and free-flow discharge system. The primary lithology along the main section is slightly weathered arkose (J2s2--3). The

10.3389/feart.2025.1684101

strata display a monoclinic structure, dipping downstream toward the left bank, with a measured orientation of 235°∠10°. No faults are present in the rock mass, and its main structural characteristics are tectonic fractures and unloading joints. The predominant surrounding rock in the tunnel's main section is Class III (79.5% of the alignment), with an excavation diameter of 4.4 m. The physical and mechanical parameters of the rock mass are listed in Table 1.

TABLE 1 Physical and mechanical parameters of the tunnel rock mass.

| Lithology | Natural unit weight (kN/m3) | Uniaxial compressive strength (MPa) | | Deformation parameters (MPa) | | Shear strength (MPa) | Poisson's ratio | Softening coefficient |
|---|---|---|---|---|---|---|---|---|
| | | Natural | Saturated | Deformation modulus | Elastic modulus | | | |
| Arkose | 24.9 | 50–55 | 40–45 | 7–8 | 9–10 | 0.8–1.0 | 0.20–0.25 | 0.85 |

## 3.2 Original blasting construction scheme

The tunnel excavation section was designed to be circular with a diameter of 4.4 m and an excavation area of 15.2 $m^2$. The original blasting scheme used a wedge cut structure, and the emulsion explosive cartridge specification was $\phi$ 32 mm × 300 mm, with a unit weight of 300 g. The rock drilling equipment used was a YT-28 pneumatic leg drill, with a drill rod length of 2.5 m and a drilled hole diameter of 40 mm. Considering the actual drilling efficiency of the on-site equipment, the cut holes were drilled to a depth of 2.4 m, while the auxiliary and perimeter holes were each 2.3 m deep. The spacing between adjacent perimeter holes was 45 cm, with a smooth blasting layer thickness of 50 cm. A total of 67 blastholes were arranged, all of which were continuously charged. The charge weights were 0.9 kg for perimeter holes, 1.2–1.5 kg for auxiliary holes, and 1.5–1.8 kg for cut holes. The detonation delay between successive firing periods was set at 50 ms. The blasthole arrangement for the original blasting construction scheme is illustrated in Figure 3.

## 3.3 Blasting effect of the original scheme

In accordance with the original wedge cut blasting scheme, 10 rounds of excavation were conducted in the hard rock section, with a single-round advance of 1.7–1.8 m and yielding a total advance of 17.6 m. A single round consumed 72 kg of explosives and 70 detonators, the data are presented in Table 2. After the explosion, a half-hole pattern was visible in the post-blasting profile, and minor unstable blocks appeared in the surrounding rock of the tunnel face. The cut zone exhibited stepped recesses with partial remaining holes, and the depths of the remaining holes are shown in Figure 4. The cut structure did not sufficiently throw the rock mass, the muck pile contained a small number of oversized rocks, and the overbreak/underbreak met the prescribed standards. The rock surrounding the tunnel face was rigid, the blasthole utilization rate remained low at 74%–88%, and the specific charge was relatively high, ranging from 2.63 to 2.79 kg/$m^3$.

# 4 Blasting (cutting) parameters in the compound scheme

## 4.1 Drilling parameters

On the basis of the original blasting scheme, short straight holes were added at the diameter position of the central axis of the tunnel face. According to the blasting mechanism of straight holes cut with relief holes, the tensile stress reflected from the post-explosion stress

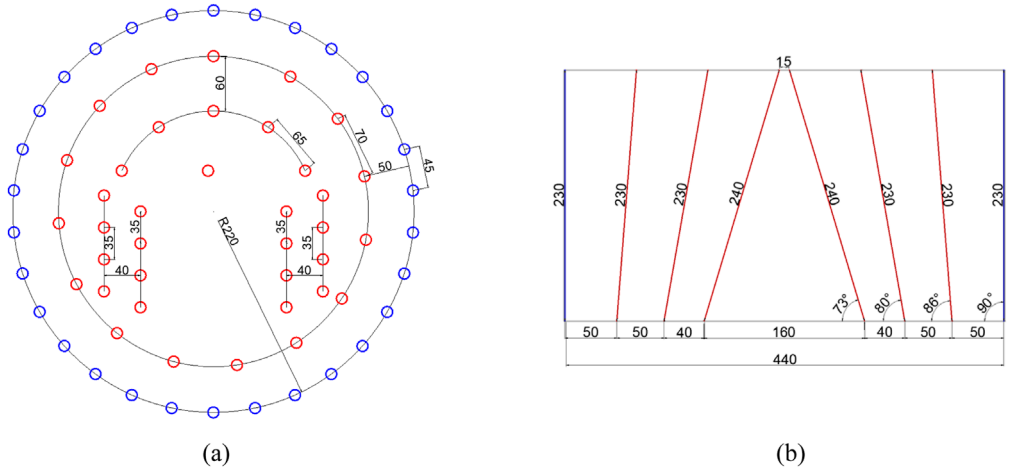


FIGURE 3
Blasthole layout in the original blasting construction scheme (unit: cm). **(a)** Layout plan of blastholes. **(b)** Blasthole profile (perimeter hole depth: 2.3 m).

TABLE 2 Statistical data of the original wedge-shaped excavation blasting site.

| Mileage station number of the tunnel body | | Surrounding rock classification | Single cycle footage(m) | 2 # Explosive dosage (kg) | Detonator consumption |
|---|---|---|---|---|---|
| Starting point | Destination | | | | |
| Y0+020.7 | Y0+022.5 | III | 1.8 | 72 | 70 |
| Y0+022.5 | Y0+024.3 | III | 1.8 | 72 | 70 |
| Y0+024.3 | Y0+026.0 | III | 1.7 | 72 | 70 |
| Y0+026.0 | Y0+027.7 | III | 1.7 | 72 | 70 |
| Y0+027.7 | Y0+029.5 | III | 1.8 | 72 | 70 |
| Y0+029.5 | Y0+031.2 | III | 1.7 | 72 | 70 |
| Y0+031.2 | Y0+032.9 | III | 1.7 | 72 | 70 |
| Y0+032.9 | Y0+034.7 | III | 1.8 | 72 | 70 |
| Y0+034.7 | Y0+036.5 | III | 1.8 | 72 | 70 |
| Y0+036.5 | Y0+038.3 | III | 1.8 | 72 | 70 |
| Total | | | 17.6 | 720 | 700 |

wave on the relief hole wall must be greater than the tensile strength of the rock. That is, $\sigma_{\theta\max} \geq \sigma_\theta$ must be satisfied when determining the distance between the charge hole and the relief hole (Yu-Jie, 2018) to ensure effective breaking of the relief hole wall under tensile stress. The spacing between the charge hole and the relief hole (Hai-Bo et al., 2015) must meet the following condition:

$$L \leq r_A \left[ \frac{(1+3\lambda)p}{[\sigma_\theta]} \right]^{\frac{1}{\alpha}} + r_B \tag{1}$$

where

$$\left.\begin{aligned} \alpha &= 2 - \mu_{动}/(1-\mu_{动}) \\ \lambda &= \mu_{动}/(1-\mu_{动}) \end{aligned}\right\} \tag{2}$$

where $r_A$ is the radius of the charge hole, which has a value of 20 mm; $r_B = 20$ mm is the radius of the relief hole; $[\sigma_\theta]$ is the tensile strength of the rock; and $\lambda$ and $\alpha$ are the lateral stress coefficient and stress wave attenuation coefficient, respectively, which are related to the dynamic Poisson's ratio ($\mu_d$) of the rock. Research by Ying-song et al. (1998) has shown that $\mu_d = \mu$. $p$ is the transmitted pressure at the wall

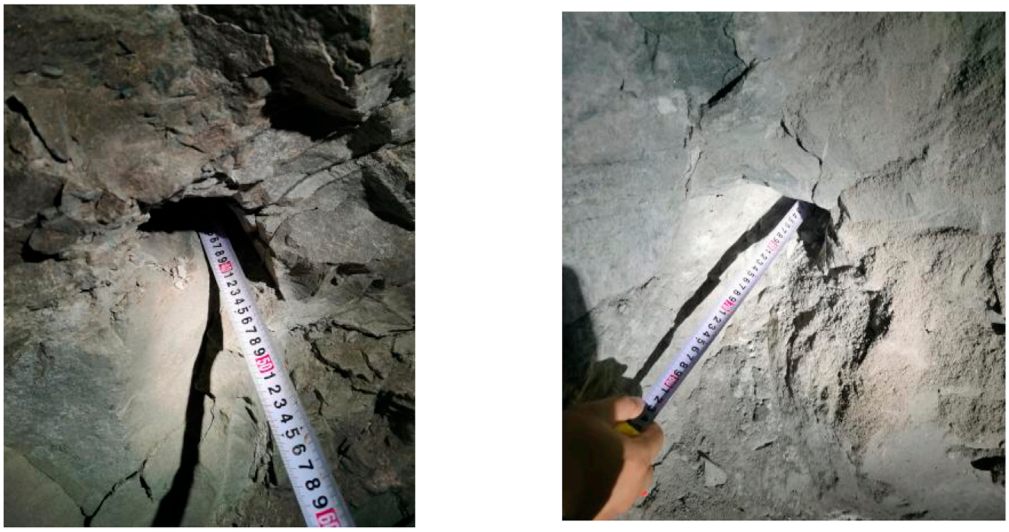


FIGURE 4
Post-blast hole remnants in the original scheme. **(a)** 40 cm deep cut hole remnant. **(b)** 50 cm deep perimeter hole remnant.

of the hole (Geglio, 1997), which is calculated as Equation 3:

$$p = \frac{1}{8}\rho_e \mathrm{D}^2 \left(\frac{r_e}{r_h}\right)^{2n} \tag{3}$$

where $r_e$ is the cartridge diameter, which is 32 mm; $r_h = 40$ mm is the blasthole diameter; $\rho_e$ is the charge density, which is 1.10 g/cm$^3$; $D$ is the detonation velocity, which is 3,500 m/s; and $n$ is the polytropic index, which is generally 3. It can be calculated that $p = 441.55MPa$.

In general, the tensile strength of a rock is 1/20–1/10 of its compressive strength. Based on the physical and mechanical parameters of the tunnel rock mass in Table 1, the tensile strength here can reach 5 MPa. However, blasting is extremely rapid and is a dynamic process with a high strain rate. Therefore, the rock tensile strength $[\sigma_\theta]$ in Equation 1 should be replaced with the dynamic tensile strength. Mao Rongrong (Rong-rong, 2018) studied the tensile properties of coal-measure sandstone using a split Hopkinson pressure bar (SHPB) and reported that when the strain rate increased from 30.93 s$^{-1}$ to 108.93 s$^{-1}$, the tensile strength of the rock sample increased by 125.34%, whereas the blasting strain rate $\varepsilon$ was $10^3$–$10^4$ s$^{-1}$. However, there is still a lack of relevant research on the increase in the dynamic tensile strength of rocks under blasting loads. Therefore, based on the conclusion of Ref. (Rong-rong, 2018), this study considered a 200% dynamic tensile strength increase under blasting loads, set $[\sigma_\theta]$ to 15 MPa, and adopted $\mu_\mathrm{d} = \mu = 0.225$. Substituting the above calculation parameters into Equations 1, 2 yields $L \leq 443$mm.

Based on relevant production experience and previous studies, excessively small spacing can cause premature leakage of detonation gases, thereby diminishing the throw effect (Yi et al., 2024). In practice, the burden for straight-hole cuts is typically around 20 cm. To enhance the reliability of short straight-hole cutting, the calculated values were further reduced with reference to proven applications. In the test, the burden between the charge hole and the relief hole was set to 20 cm, with a hole spacing of 15 cm and a vertical distance of 1.5 m from the floor excavation line. Three rows of blastholes were arranged, comprising a total of 15 holes. The central row consisted of charged holes, whereas the relief holes on either side provided both compensation space and a secondary free surface, allowing the rock to move toward the relief holes and the tunnel face. The rock at the bottom of the tunnel experienced the greatest confinement, making post-fragmentation displacement most difficult; thus, the charge holes were overdrilled by 10 cm. To prevent breakthrough between these holes and the inclined cut, the charge hole depth was set at 1.6 m, and the relief hole depth was set at 1.5 m. The blasthole layout for the proposed compound scheme is illustrated in Figure 5.

## 4.2 Charge and detonation parameters

In the compound test scheme, the charging parameters were increased relative to those of the original wedge-cut blasting design, with a total of 84 kg of explosives per round and an additional 12 kg of half-cartridge explosives, all charged continuously. Five central charge holes were added, and the number of detonators remained at 70. Following the method outlined by Wei-Yi et al. (2024), the explosive distribution was determined according to the type and arrangement of the blastholes. The quantity, charge, and firing sequence of each blasthole type are presented in Table 3. These parameters were verified and adjusted through field trials until an optimal blasting effect was obtained. The initiation system employs digital electronic detonators to precisely control delay timing, with a total of eight delay periods set, each with an interval of 50 ms, which is consistent with the original scheme. After repeated trials and considering the rules governing the allocation of explosives and detonators, satisfactory blasting performance could still be

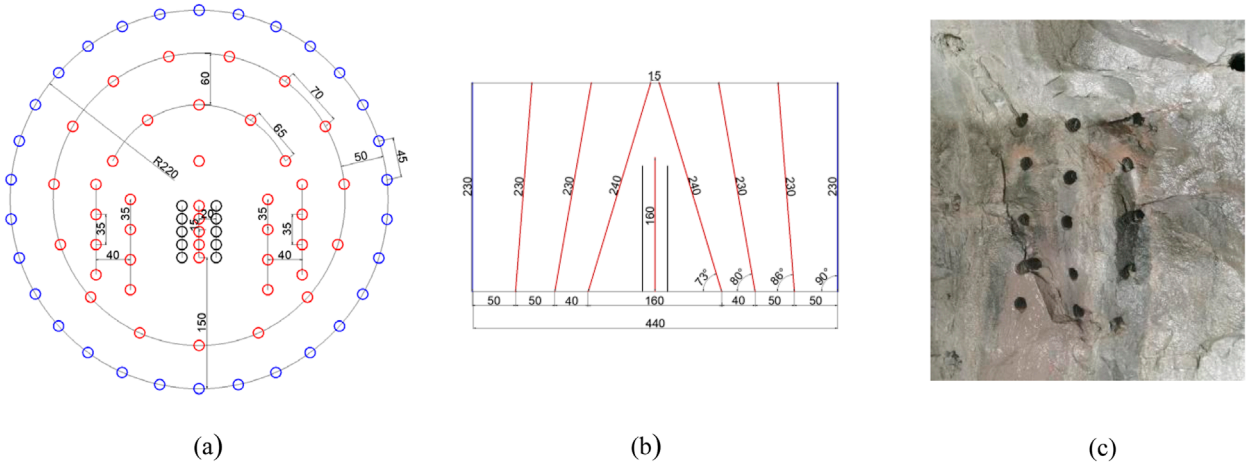


FIGURE 5
Blasthole layout in the proposed blasting scheme (unit: cm). **(a)** Layout plan of blastholes. **(b)** Blasthole profile. **(c)** On-site drilling of short straight holes.

TABLE 3 Design of the test blasting parameters.

| Blasthole type | Hole number | Charge per hole/kg | Total charge/kg | Interhole delay/ms | Firing sequence schematic (unit: cm) |
|---|---|---|---|---|---|
| Cut hole (straight) | 5 | 0.9 (3 cartridges) | 4.5 | 25 (1#) | 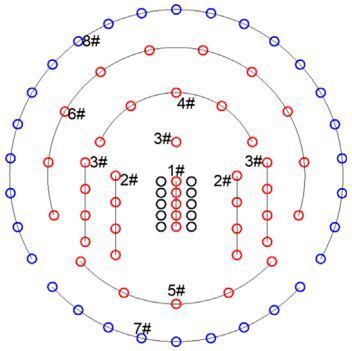 |
| Cut hole (wedge) | 8 | 1.5 (5 cartridges) | 12 | 75 (2#) | |
| Auxiliary cut hole | 9 | 1.2 (4 cartridges) | 10.8 | 125 (3#) | |
| Auxiliary hole 1 | 5 | 1.2 (4 cartridges) | 6 | 175 (4#) | |
| Auxiliary hole 2 | 5 | 1.2 (4 cartridges) | 6 | 225 (5#) | |
| Auxiliary hole 3 | 10 | 1.2 (4 cartridges) | 12 | 275 (6#) | |
| Floor hole | 9 | 1.5 (5 cartridges) | 13.5 | 325 (7#) | |
| Perimeter hole | 21 | 0.9 (3 cartridges) | 18.9 | 375 (8#) | |
| Total | 72 | — | 83.7 | — | |



achieved when detonators were issued integer multiples of ten and two perimeter holes that remained uncharged.

# 5 Blasting effect analysis for the compound scheme

## 5.1 Comparison of efficacy

In terms of the number of blastholes, the original wedge-cut design included 67 holes, whereas the proposed short straight-hole + wedge-cut design included 82 holes, representing an increase of 15 holes, or 22.39%. All additional holes were shallow, averaging 1.5 m in depth, adding 22.5 m to the total drilling length. Given that the total blasthole depth in the original scheme was 154 m, this represented a 14.61% increase. Drilling was carried out by six workers operating five YT-28 pneumatic leg drills simultaneously. In the original arrangement, one drilling cycle required 2.5 h, and boring a shallow hole of 1.5–1.6 m typically took 2 min. If a single drill was used, adding 15 shallow holes would extend the drilling time by nearly 20% compared with the original scheme. However, as the equipment operated in parallel, the actual increase in total drilling time was minimal, and the overall number of cycles for drilling, charging, and blasting was largely unaffected, the comparison of work efficiency is shown in Table 4. With respect to pyrotechnic consumption, the modified scheme required 12 kg more explosives. Repeated field trials revealed that effective blasting results could still be achieved when two perimeter holes were left uncharged without altering the total number of detonators, which remained the same as in the original scheme. The blasting performance obtained under the new arrangement is shown in Figure 6.

TABLE 4 Comparison of work efficiency.

| Category | Design blast holes (number) | Total hole depth (m) | Single cycle drilling duration (h) | Single cycle explosive consumption (kg) | Single-cycle detonator consumption |
|---|---|---|---|---|---|
| Original wedge-shaped cutting design scheme | 67 | 154 | 2.5 | 72 | 70 |
| Short straight hole + wedge-shaped composite cutting test plan | 82 | 176.5 | 3 | 84 | 70 |
| Increase situation | 15 | 22.5 | 0.5 | 12 | 0 |

FIGURE 6
Blasting effect of the proposed test scheme.

## 5.2 Comparison of the main technical indicators

A series of experiments was carried out on the two cutting methods in a flat tunnel section with Class III surrounding rock, and the primary technical and economic indicators were compared, as summarized in Table 5. In terms of single-round advance, the original wedge-cut method achieved 1.7–1.8 m per round, with a blasthole utilization rate of 73.91%–78.26%. In contrast, the short straight-hole + wedge compound cut scheme reached 2.0–2.1 m per round, with utilization rates ranging from 86.96% to 91.30%. This represents an increase of 0.3 m in advance per round and an improvement in blasthole utilization of more than 10%. With respect to single-round pyrotechnic consumption, the specific charge for both schemes was nearly identical; however, the compound cut method reduced detonator usage by 0.4 detonators/$m^3$ compared with the original design, offering greater economic efficiency. While the compound cut increased the total drilling length by 22.5 m, the cost impact was minimal. Nonetheless, the slightly longer single-round drilling time introduced a marginally greater operational risk for blasting personnel.

## 5.3 Comparison of blasting fragmentation rates

From the perspective of the blasting effect, there was a serious phenomenon of remnant holes in the original wedge cut blasting plan, with insufficient cuts in the middle, which affected the throw of auxiliary holes and occasionally resulted in large-sized blocks. The proposed short straight hole + wedge compound cut scheme could break the fragments more evenly, making it easier for the raking machine to remove slag. The compound scheme also had fewer remaining holes on the tunnel surface, making it easier to perform the next round of drilling. Moreover, the dam filling works of the key hub project required transitional materials, so the blasted fragments from the emptying tunnel were screened by removing the small number of oversized blocks exceeding 30 cm in diameter. The gradation curve is shown in Figure 7 below. According to the screening data, the mass percentage of fragments smaller than 200 mm in diameter was 92%, whereas those smaller than 60 mm accounted for 39.3%.The grading curve of explosive slag is between the upper and lower envelope lines of the source material. Based on this analysis, the processed blasting residue could be used as a transitional material for dam filling.

# 6 Conclusion

Based on drill-and-blast excavation of hard rock tunnels, combined with theoretical analysis and formula derivation, this study employed a short straight-hole + wedge compound cut scheme and conducted blasting tests. The blasting performance of the compound scheme was analyzed and compared with that of the original wedge-cut scheme in terms of blasting efficacy, key technical indicators, and fragmentation. The following conclusions were drawn.

1. In designing blasting parameters for the compound cut scheme in hard rock tunnels, accounting for the high strain rate effect on rock tensile strength ensured the accuracy of calculated parameters such as the distance between charge holes and relief holes.
2. Implementation of the compound cut scheme increased the single-round advance from 1.7 to 1.8 m in the original design to 2.0–2.1 m—an improvement of 0.3 m—and

TABLE 5 Comparison of the main technical and economic indicators.

| Category | Advance per round (m) | Blasthole utilization rate (%) | Specific charge (kg/m$^3$) | Unit detonator consumption (/m$^3$) | Total length of single-round drilling (m) |
|---|---|---|---|---|---|
| Original wedge cut | 1.7–1.8 | 73.91–78.26 | 2.79–2.63 | 2.56–2.71 | 154 |
| Short straight hole + wedge compound cut | 2.0–2.1 | 86.96–91.30 | 2.76–2.63 | 2.19–2.30 | 176.5 |
| Difference | +0.3 m | Above +10% | Almost unchanged | About −0.4 | +22.5 m |

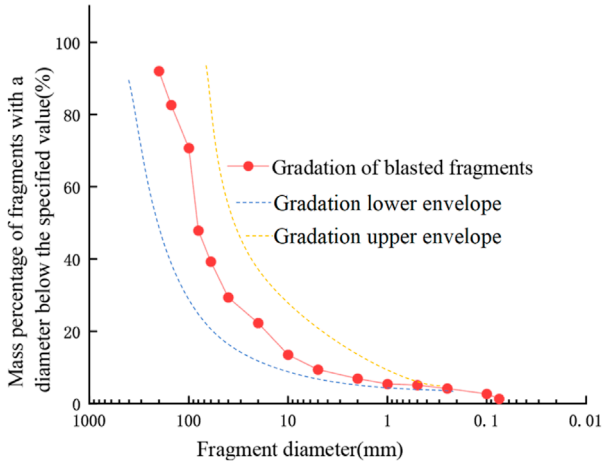


FIGURE 7
Gradation curve of blasted fragments.

enhanced the blasthole utilization rate from 73.91%–78.26% to 86.96%–91.30%, representing a gain of more than 10%. Although the specific charge remained nearly unchanged, detonator consumption was reduced by about 0.4 detonators/m$^3$, reflecting improved economic efficiency.

3. Adoption of the compound cut scheme resulted in fewer remaining holes and finer fragmentation at the tunnel face, thereby facilitating subsequent mucking and drilling operations. On-site fragment size screening data indicated that, in small tunnels within Class III surrounding rock, the slag produced by this blasting scheme could serve as a transitional material for dam filling.
4. The compound cut scheme involved a slight increase in the number of shallow straight holes. However, given the drilling efficiency, its effect on overall construction efficiency was minimal compared with the original scheme.

## Data availability statement

The original contributions presented in the study are included in the article, further inquiries can be directed to the corresponding author.

## Author contributions

MT: Writing – original draft, Writing – review and editing. XT: Writing – review and editing. GH: Writing – review and editing. SP: Writing – review and editing. LY: Writing – review and editing. JX: Writing – review and editing.

## Funding

The author(s) declare that financial support was received for the research and/or publication of this article. Yunnan Provincial Department of Transport Technology Innovation and Demonstration Project (2025--16), CCCC Key R&D Project (No. 2023--ZJKJ--14).

## Conflict of interest

Authors MT and GH were employed by Wenshan Tianwen Expressway Investment and Development Co., Ltd. Author XT was employed by CCCC Rail Transit Branch. Authors SP, LY, and JX were employed by CCCC Second Harbor Engineering Co., Ltd.

The authors declare that this study received funding from CCCC. The funder had the following involvement in the study: participated in the design of blasting parameters and analysis of blasting effects in the experimental plan.

## Generative AI statement

The author(s) declare that no Generative AI was used in the creation of this manuscript.

Any alternative text (alt text) provided alongside figures in this article has been generated by Frontiers with the support of artificial intelligence and reasonable efforts have been made to ensure accuracy, including review by the authors wherever possible. If you identify any issues, please contact us.

## Publisher's note

All claims expressed in this article are solely those of the authors and do not necessarily represent those of their affiliated organizations, or those of the publisher,

the editors and the reviewers. Any product that may be evaluated in this article, or claim that may be made by its manufacturer, is not guaranteed or endorsed by the publisher.

## References

Bao-Long, H. (2014a). Research progress on theory and technology of trenching and blasting in rock roadway excavation. *China Min. J.* 23 (10), 103–106. doi:10.3969/j.issn.1004-4051.2014.10.024

Bao-Long, H. (2014b). Application of collimated hole grooving technology in large-section tunnel excavation. *Blasting Blasting* 31 (1), 65–68. doi:10.3963/j.issn.1001-487X.2014.01.014

Gang, H., Hong-Lu, F., and Zhi-Yu, G. (2018). Mechanical mechanism and numerical simulation analysis of large hollow compound cylindrical straight-hole cut. *China Saf. Prod. Sci. Technol.* 14 (9), 129–135. doi:10.11731/j.issn.1673-193x.2018.09.021

Geglio, M. (1997). Spherical vessel subjected to explosive detonation loading. *Int. J. Press. Vessel and Pip.* 74 (2), 83–88. doi:10.1016/s0308-0161(97)00024-0

Hai-Bo, W., Qi, Z., and Yao-Cai, Z. (2015). Numerical simulation analysis and application of explosion stress field of vertical cut with large diameter hollow hole in vertical shaft. *J. Rock Mech. Eng.* 34 (S1), 3223–3229. doi:10.13722/j.cnki.jrme.2014.0296

Ping, W. (2021). Straight cut blasting test and control measures of an underground metal mine. *Metal. Mine* 8, 52–56. doi:10.19614/j.cnki.jsks.202108009

Qi-Yue, L., Zheng-Yu, W., and Wu-Lin, H. (2018). Improvement and analysis of the calculation model of hole effect in straight cut. *J. Min. Saf. Eng.* 35 (5), 925–930. doi:10.13545/j.cnki.jmse.2018.05.007

Ren-Shu, Y., Yan-Bing, W., Zhao-Ran, Z., Jin-jing, Z., Chang-Da, Z., and Shu-Xuan, L. (2022). New technology and application of trench excavation and blasting in urban engineering. *Chin. Sci. Found.* 36 (1), 120–127. doi:10.16262/j.cnki.1000-8217.2022.01.028

Rong-rong, M. (2018). *Study on tensile properties and damage and fracture mechanism of coal-bearing sandstone under high strain rate*. Xuzhou: China University of Mining and Technology.

Wei-Yi, G., Ying-Kang, Y., and Yu-Xiang, D. (2024). Field test on blasting excavation and over-under-excavation control of long-cut straight hole in medium-section tunnel. *Blasting* 41 (2), 32–39. doi:10.3963/j.issn.1001-487X.2024.02.005

Xiao-Ming, L., and Shi-Hai, C. (2019). Waveform prediction of surface vibration caused by slotting hole blasting in tunnel excavation. *Chin. J. Geotechnical Eng.* 41 (9), 1731–1737. doi:10.11779/CJGE201909018

Xin-Han, L. I. (2024). Field test of blasting trenching method in small cross-sectional geological exploration. *Henan Sci. Technol.* 51 (17), 46–49. doi:10.19968/j.cnki.hnkj.1003-5168.2024.17.010

Xing-Jun, F., Bin, C., Jun, X., and Jin-Xi, D. (2016). Numerical simulation of cavity-forming process by straight cut blasting with intermediate interval charge. *Min. Res. Dev.* 36 (9), 88–92. doi:10.13827/j.cnki.kyyk.2016.09.021

Yi, L., Yun-Chen, D., Cheng, L., Ya-Qiao, Y., Xin, L., Hang-Li, G., et al. (2024). Influence of blasting excavation of deep karst tunnel on damage and seepage characteristics of surrounding rock mass. *Blasting* 41 (03), 85–94. doi:10.3963/j.issn.1001-487X.2024.03.011

Ying-Song, L., Hong-Kui, G., and Shun-Chang, W. (1998). Experimental study on dynamic and static mechanical parameters of rock. *J. Rock Mech. Eng.* 17 (2), 216–222.

Yu-Jie, W. (2018). *Blasting engineering*. 2nd Edition. Wuhan: Wuhan University of Technology Publishing House.

Yu-Yin, Y. (2013). Experimental study on the influence of cut area on the utilization rate of tunnel excavation. *Blasting* 30 (2), 100–103. doi:10.3963/j.issn.1001-487X.2013.02.020

Yuan-Li, C., Yu-Hua, F., Li-Yan, G., Qing, W., and Kang-Kang, Z. (2020). Experimental study on trenching and blasting under complex rock conditions. *Min. Res. Dev.* 40 (6), 23–27. doi:10.13827/j.cnki.kyyk.2020.06.006

Yue-Yang, Y., and Su-Peng, M. O. (2016). Application of large hole spiral cut blasting in tongkeng mine. *Min. Technol.* 16 (3), 80–82. doi:10.3969/j.issn.1671-2900.2016.03.031

Zhi-Yuan, X., Peng-Fei, G., Ming-Yuan, Q., Lu, C., Zheng-Wei, Y., and Zi-Heng, C. (2022). Optimization of charging structure and numerical simulation of blasting of rock mass containing karst cave. *Metal mine* 2, 42–47. doi:10.19614/j.cnki.jsks.202202006

frontiers | Frontiers in Earth Science

TYPE Original Research
PUBLISHED 29 October 2025
DOI 10.3389/feart.2025.1707062



OPEN ACCESS

EDITED BY
Tongming Qu,
Hong Kong University of Science and Technology, China

REVIEWED BY
Quan Xue,
Xi'an University of Technology, China
Yuna Cai,
Wuhan University, China

*CORRESPONDENCE
Yu Zhong,
zhongyu1216@163.com

RECEIVED 17 September 2025
ACCEPTED 16 October 2025
PUBLISHED 29 October 2025

CITATION
Zhong Y, Zhang Y, Yu C, Ji F and Chen P (2025) Construction techniques for cross-sea bridges in coral reef and island environments. *Front. Earth Sci.* 13:1707062. doi: 10.3389/feart.2025.1707062



# Construction techniques for cross-sea bridges in coral reef and island environments

Yu Zhong[1,2]*, Yongtao Zhang[1], Chengcheng Yu[1], Fuquan Ji[1] and Peishuai Chen[1]

[1]CCCC Second Harbor Engineering Co., Ltd., Wuhan, China, [2]CCCC Wuhan Harbour Engineering Design & Research Company Ltd., Wuhan, China

Coral islands and reefs serve as the sole land-based foundations in the open ocean, and their unique engineering characteristics pose significant challenges for cross-sea bridge construction. This study focused on the China-Maldives Friendship Bridge to investigate the load-bearing mechanisms and construction techniques of pile foundations on coral islands and reefs. Field and laboratory tests on coral reef debris and reef limestone yielded a method to evaluate the compactness of coral reef debris using dynamic penetration test (DPT) blow count. Different classification methods were employed to perform engineering classification and evaluation of the coral reef debris and reef limestone strata. Shear tests on the coral reef debris-pile interface and model tests on driven steel pipe piles clarified the mechanism underlying low pile side friction resistance in coral reef debris strata, while a modified formula for calculating side friction resistance was provided. Shear tests of reef limestone-concrete interfaces with different surface morphologies, combined with field pile testing, yielded recommended mobilization coefficient ($c_2$) of side friction resistance for cast-in-place piles in reef limestone strata. A hydraulic automatic opening and closing chuck for driven piles, a large cantilever guiding frame system with a fuse mechanism, and specialized drilling heads for cast-in-place piles, were developed to ensure pile construction quality.

KEYWORDS

**coral reef, bridge engineering, pile foundation, load-bearing mechanism, construction equipment**

## 1 Introduction

The ocean's abundant resources have made marine development a strategic priority for coastal countries worldwide. The 21st century has therefore been termed the "Century of the Ocean" (Chortis et al., 2020; Lin et al., 2019; Yu et al., 2014). Cross-sea bridges provide critical connections between coastal cities, the mainland, and remote islands, and their construction has important implications for marine resource development. Natural coral reef islands are the sole land foundations in the open ocean, and their physical and mechanical properties differ substantially from those of typical geological settings (Zhong et al., 2020; Gao and Ye, 2023). Moreover, the complex and exposed open-sea environment presents major challenges for the construction of cross-sea island-connecting bridges.

Given their high load-bearing capacity and reliability, pile foundations remain a competitive choice for cross-sea bridges (Shan and Wang, 2000; Höppner and Boley, 2022;

Ho et al., 2022; Xu et al., 2023; Schmüdderich et al., 2020). However, pile foundation construction in coral reef regions faces multiple challenges. Carter et al. (1988) reported that the pile foundations installed for the North Rankin A oil and gas platform in Australia exhibited actual load-bearing capacities significantly below their design values. Furthermore, the unique depositional patterns and karstic characteristics of reef limestone also promote occurrences of "pile slippage" during driving (Ghazali et al., 1988; King and Lodge, 1988; Lu and Luo, 2016; Zhou, 2014).

To address geotechnical challenges in coral reef settings, several studies have defined the unique characteristics of reef geology. Coral reef strata are predominantly distributed in tropical and subtropical marine regions. They feature a typical dual-layer structure: an upper layer of coral reef debris and a lower layer of reef limestone with occasional soft-hard interbedded layers (Wang, 2001; Beger et al., 2014). Coral reef strata and their physical-mechanical properties, along with the load-bearing mechanisms of pile foundations, have been studied through theoretical analysis, field investigations, and laboratory testing. Clark and Walker (1997) and Wang et al. (1997) found through field investigations and experiments that coral reef strata experienced complex biological sedimentary evolution and diagenesis, resulting in high porosity, fragility, and compressibility (Nansha Integrated Scientific Expedition Team and Chinese Academy of Sciences, 1992). Zhu et al. (2016) and Wan et al. (2018) identified the cementation components of reef limestone as granular calcite, biogenic microcrystals, and acicular aragonite, which have low strength and contain extensive dissolution pores. Yao et al. (2024) examined the shear behavior of coral sand and found substantial differences across particle sizes. The engineering properties of coral reef rock-soil masses remain unclear. Jiang (2009) revealed low side friction resistance for driven piles in coral sand strata through model tests. However, large-scale model test validation is challenging, and calculation methods for side friction resistance in driven steel pipe piles within coral sands remain undeveloped. Additionally, $C_2$ used for cast-in-place piles in terrigenous strata are not applicable to coral reef strata, and research on their load-bearing mechanisms is limited. Nevertheless, the engineering behavior of coral reef soils and rock masses is still poorly constrained. Consequently, studies on techniques for constructing cross-sea bridges on coral reef substrates are limited (Xu et al., 2022; Liu et al., 2021; Qin et al., 2019), and focused research is needed to bridge this knowledge gap.

This study focused on the China-Maldives Friendship Bridge to investigate the causes of low side friction resistance in driven piles and the cementation behavior of cast-in-place pile interfaces through a combination of laboratory tests, model tests, and mechanism analyses. It examined pile foundation load-bearing mechanisms and develops improved equipment for driven steel pipe piles and cast-in-place piles in coral reef strata to enable safe and efficient construction. This research provides a theoretical and practical foundation for the construction of cross-sea bridges in coral reef geological formations and offers scientific value and practical significance.

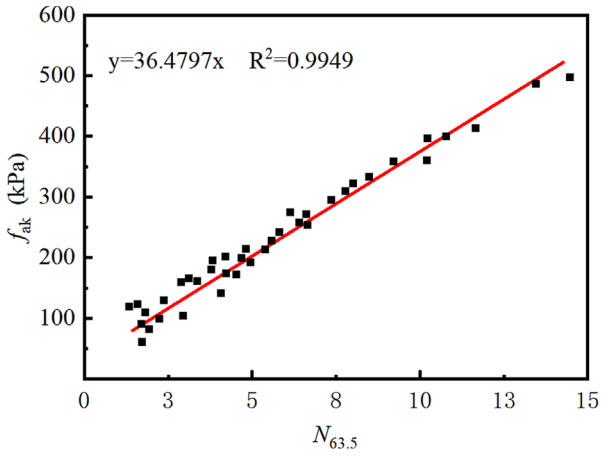


FIGURE 1
Relationship between DPT blow count and foundation load-bearing capacity.

## 2 Physical and mechanical properties of coral reef strata

Coral reef strata, formed through marine biological sedimentation, differ significantly from conventional terrigenous sediments. Existing design and construction techniques often overlook their unique and complex engineering properties. Therefore, it is necessary to study their classification and physical-mechanical parameters to provide fundamental data for bridge foundation design and construction in coral reef strata. Therefore, field samples were collected and tested to study the characteristics of coral reef strata.

### 2.1 Classification of coral reef soils

#### 2.1.1 Classification of coral debris

Coral reef debris is categorized into four types based on particle size distribution: coral gravel, coral sand, coral silt, and coral mud. Coral sand is specifically defined as material where particles larger than 0.075 mm account for more than 50% of the total mass. Coral sand is specifically defined as material where particles larger than 0.075 mm account for more than 50% of the total mass.

Static load tests and heavy cone dynamic penetration tests were conducted at 47 selected test sites. As illustrated in Figure 1, the DPT blow count ($N_{63.5}$) for coral soil exhibited a strong linear relationship with the characteristic value of foundation load-bearing capacity ($f_{ak}$): $f_{ak} = kN_{63.5}$, where the $k$-value for coral debris is approximately 36.5. Additionally, the compaction degrees of coral sand were categorized based on dynamic penetration test results, as summarized in Table 1.

#### 2.1.2 Classification of reef limestone

The compressive strength of reef limestone is primarily influenced by coral species, rock structure, and the degree and

TABLE 1 Classification of coral sand compaction degrees.

| Compaction degrees | Loose | Slightly dense | Moderately dense | Dense |
|---|---|---|---|---|
| DPT blow count/$N_{63.5}$ | $N_{63.5} \leq 6$ | $6 < N_{63.5} \leq 8$ | $8 < N_{63.5} \leq 12$ | $N_{63.5} < 12$ |

TABLE 2 Classification of reef limestone cementation degrees.

| Cementation degrees | Strong cementation | Relatively strong cementation | Moderately weak cementation | Weak cementation |
|---|---|---|---|---|
| Saturated uniaxial compressive strength ($f_{rk}$/MPa) | $f_{rk}$>20 | $20 \geq f_{rk} > 10$ | $10 \geq f_{rk} > 5$ | $f_{rk} \leq 5$ |

TABLE 3 Classification of reef limestone compaction degrees.

| Compaction degrees | P-wave velocity ($V_P$/m·s$^{-1}$) | Porosity ($n$/%) |
|---|---|---|
| Loose | $2{,}000 < V_P \leq 3{,}000$ | $n \geq 30$ |
| Slightly loose | $3{,}000 < V_P \leq 4{,}000$ | $15 \leq n < 30$ |
| Moderately dense | $4{,}000 < V_P \leq 5{,}500$ | $5 \leq n < 15$ |
| Dense | $V_P > 5{,}500$ | $n < 5$ |

type of cementation, where the cementation degree is the most significant factor. Therefore, the degree of cementation is employed as the classification standard for assessing the engineering properties of reef limestone. Table 2 categorizes reef limestone into five types: strong cementation, relatively strong cementation, moderate cementation, weak cementation, and very weak cementation. The compaction degree of the rock is related to porosity, which in turn is correlated with the velocity of P-waves. Table 3 provides classifications of reef limestone compaction degree based on P-wave velocity or porosity. In cases where evaluations based on P-wave velocity and porosity are inconsistent, the results based on P-wave velocity take precedence.

## 2.2 Physical and mechanical properties of coral sand

The surface layer of coral islands and reefs is typically composed of coral sand, which can be divided into five types based on particle size: coral gravel sand, coarse sand, medium sand, fine sand, and silty sand. Laboratory triaxial shear tests and lateral earth pressure coefficient tests were performed to analyze the mechanical behaviors of these sand types.

Triaxial tests on coral sand revealed that shear bands consistently formed after shear failure, as depicted in Figure 2. This failure mode differs from the "dilation" failure observed in terrigenous siliceous sand. Table 4 summarizes the shear strength parameters for various coral sand types obtained from triaxial tests. Sands with larger particle sizes exhibited higher peak and residual strengths. The ratio of peak strength to residual strength across the five types of coral sand ranged from 0.63 to 0.83.

The lateral earth pressure coefficient ($K_0$) refers to the ratio of horizontal principal stress to vertical stress for soil consolidated under conditions without lateral deformation. $K_0$ tests were performed on coral sand samples in both dry and saturated states to analyze the relationship between horizontal and vertical stresses, as illustrated in Figures 3a,b. Coral silty sand exhibited the highest $K_0$ value, ranging from 0.31 to 0.33, while other coral sand types showed $K_0$ values between 0.22 and 0.31. The $K_0$ values in saturated coral sand samples were slightly higher than those in dry samples, while the $K_0$ value remained consistent across different depths.

# 3 Pile foundation load-bearing mechanism in coral reef strata

Bridge foundations typically consist of driven steel pipe piles and cast-in-place concrete piles. The study focused on the vertical load-bearing capacity characteristics of driven steel pipe piles in coral sand strata and cast-in-place concrete piles in reef limestone strata.

## 3.1 Side friction resistance load-bearing mechanism of driven steel pipe piles in coral sand strata

The physical and mechanical properties of coral sand differ significantly from those of traditional quartz sand. This results in lower load-bearing efficiency of driven steel pipe piles in this stratum. Direct shear tests and model tests were conducted to analyze the side friction resistance load-bearing mechanism

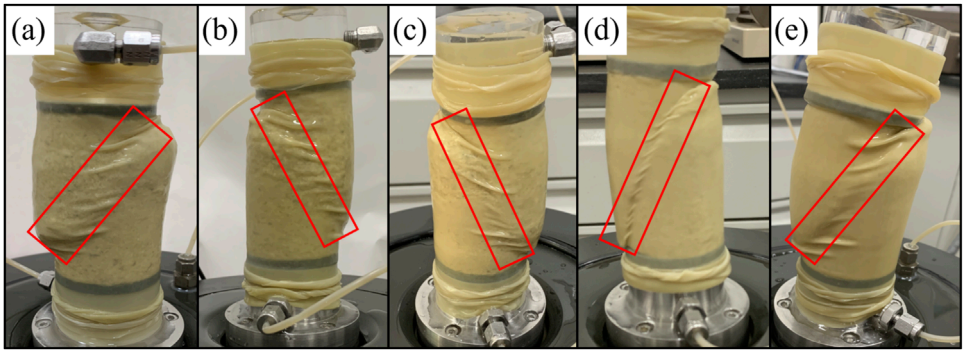


FIGURE 2
Shear failure modes of coral sand. **(a)** Gravel sand. **(b)** Coarse sand. **(c)** Medium sand. **(d)** Fine sand. **(e)** Silty sand.

TABLE 4 Strength parameters of different sand types.

| Category | Peak strength | | Residual strength | |
|---|---|---|---|---|
| | Internal friction angle ($\varphi$/°) | Cohesion (c/kPa) | Internal friction angle ($\varphi$/°) | Cohesion (c/kPa) |
| Coral gravel sand | 43.3 | 25.6 | 36.9 | 15.9 |
| Coral coarse sand | 43.8 | 24.7 | 37.1 | 15.0 |
| Coral medium sand | 45.3 | 22.4 | 38.5 | 13.6 |
| Coral fine sand | 43.5 | 20.2 | 38.0 | 11.3 |
| Coral silty sand | 41.0 | 19.8 | 36.6 | 10.9 |

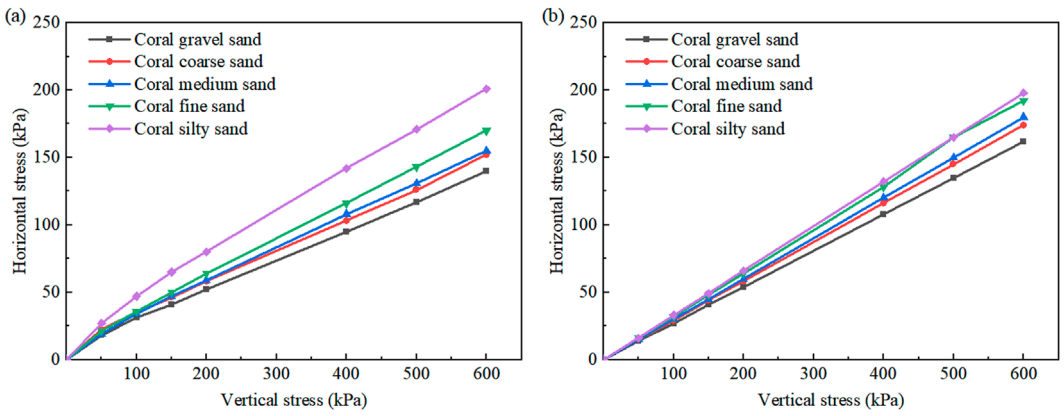


FIGURE 3
Vertical stress-horizontal stress relationship curves for coral sand. **(a)** Dry state. **(b)** Saturated state.

for driven piles in coral sands, and the calculation method for side friction resistance of steel pipe piles in coral sand strata was modified.

### 3.1.1 Interface shear tests

Interface shear tests were conducted between coral reef debris and steel piles under constant normal stiffness conditions, as illustrated in Figure 4. Results indicated that during the initial shear stage, shear strain increased significantly while normal stress decreased sharply. As shear continued, normal stress stabilized. As a result, the sample demonstrated a general tendency towards shear contraction. This behavior was attributed to the relative sliding between steel pipe piles and coral sand, which caused particle overturning, fragmentation, and redistribution. This reorganization

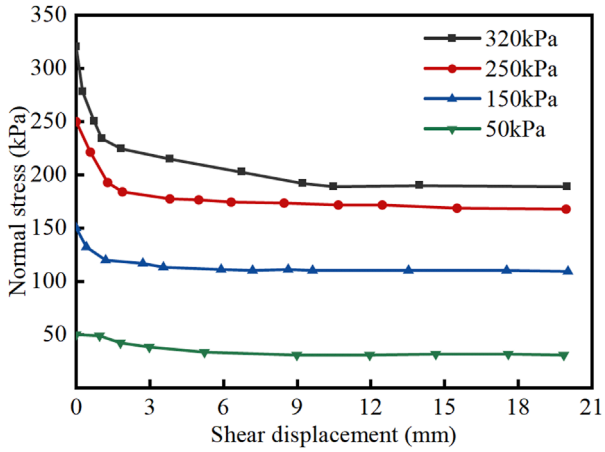


FIGURE 4
Shear contraction behavior of coral reef debris.

filled voids, reduced lateral pressure around the pile, and limited the development of side friction resistance.

### 3.1.2 Model tests of driven steel pipe piles

Model tests were conducted to investigate the distribution of pile side friction resistance in coral reef strata and evaluate the interaction between coral sand and steel pipe piles. The samples used in the model tests were sourced from the uncemented coral medium sand in Maldives, characterized by a uniformity coefficient ($C_u$) of 4.87 and a curvature coefficient ($C_c$) of 0.9, which indicates poorly graded sand. The model box used in this study was a cylindrical structure with a diameter of 2 m and a height of 3 m. The model piles were designed as steel pipe piles with a maximum outer diameter of 0.25 m and a length of 2.0 m. As illustrated in Figures 5a,b, the testing system consisted of a loading plate, a transmission column, a confining pressure loading jack, and an actuator. Eight loading levels were established at 24 kPa, 36.5 kPa, 49 kPa, 74 kPa, 99 kPa, 124 kPa, 174 kPa, and 224 kPa to investigate the ultimate side friction resistance of driven piles and its distribution under varying effective vertical stress conditions.

The variation in side friction resistance of piles embedded in quartz sand under different effective vertical stress conditions was calculated based on the model test results for driven piles using the recommended methods from the American Petroleum Institute (API) standards (Institute, 2000). These results were then compared with those obtained from coral medium sand, as depicted in Figure 6. Both types of strata exhibited a parabolic distribution of pipe side friction resistance. Coral sand exhibited a lower pile side friction resistance of approximately 17.5 kPa, which is 21.4% of the pile side friction resistance in quartz sand. This is close to the 27% observed in Jiang's experimental results (King and Lodge, 1988). The stress conversion showed that the ultimate side friction resistance for coral sand corresponded to an embedding depth of approximately 9.3 m, while for quartz sand, it was about 25 m. This difference was primarily attributed to higher internal friction angle and cohesion in coral sand, which led to an arching effect during deformation and consequently resulted in smaller increments in lateral pressure.

### 3.1.3 Calculation method for side friction resistance of driven steel pipe piles in coral sand strata

Currently, there is no effective method for calculating side friction resistance of pile foundations in coral reef strata in China. Internationally, the recommended methods from API standards are typically used, which only modify parameters such as the lateral pressure coefficient ($k$), the friction angle ($\delta$) between the soil and the pile wall, the ultimate unit side friction resistance ($f_{max}$), and the ultimate unit end resistance ($q_{max}$) (Institute, 2000). However, these methods do not account for the unique properties of coral sand, which makes them unsuitable for calculating pile side friction resistance in coral sand strata. The distribution of side friction resistance for driven piles was simplified to a "triangle + rectangle" configuration based on the model test results. A calculation method for side friction resistance of driven steel pipe piles in coral reef strata was proposed based on API standards, as indicated in Equation 1.

$$q_s = \begin{cases} \sigma_n' \tan\delta = K_0 \sigma_V' \tan\delta & (h < H_0) \\ \eta \dfrac{Y}{1+\alpha} \tan\delta & (h \geq H_0) \end{cases} \tag{1}$$

where $\sigma_n'$ denotes the vertical effective self-weight stress of the soil surrounding the pile; $\delta$ refers to the interface friction angle; $K_0$ represents the static lateral earth pressure coefficient; $\sigma_V'$ is the horizontal stress of the soil surrounding the pile; $\alpha$ and $Y$ are the slope and intercept of the shear strength line of the coral sand, respectively. $\eta$ is the comprehensive correction factor for pile-soil contact and the soil layer compressed by the pile foundation. It can be taken as two for coral medium sand. $H_0$ indicates the critical depth, which is defined as the depth at which the theoretical values of shallow and deep side friction resistance are equal. Given the complexity of calculating the circumferential compressive stress coefficient, the depth at which the theoretical values of shallow side friction resistance equal those of deep side friction resistance is designated as the critical depth for simplifying calculations. Equation 2 can be employed for this calculation.

$$H_0 = \frac{\eta Y}{(1+\alpha)\gamma K_0} \tag{2}$$

The study selected 32 protective tubes of the China-Maldives Friendship Bridge as the research subjects and conducted *in situ* high-strain testing on the pile foundations, as depicted in Figure 7. The proposed calculation method for side friction resistance in coral reef strata was applied to evaluate the side load-bearing capacity of driven piles in the China-Maldives Friendship Bridge. The computation results were compared with the field test results, as illustrated in Figure 8. The average error between the two was 10.3%. Additionally, the theoretical values were consistently lower than the measured values. This indicates that the calculation method proposed in this study is conservative and validates the rationality of the modified calculation approach.

## 3.2 Vertical load-bearing mechanism of cast-in-place piles in reef limestone strata

The vertical load-bearing capacity of cast-in-place piles in reef limestone strata primarily depends on the mechanical

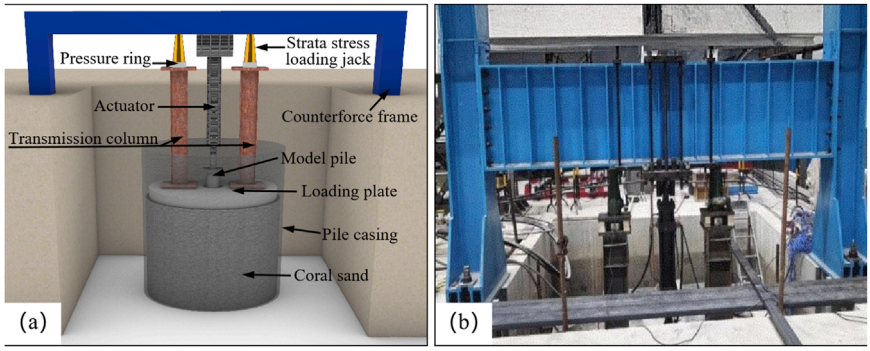


FIGURE 5
Driven pile model test. **(a)** Schematic diagram of the model. **(b)** Model test photo.

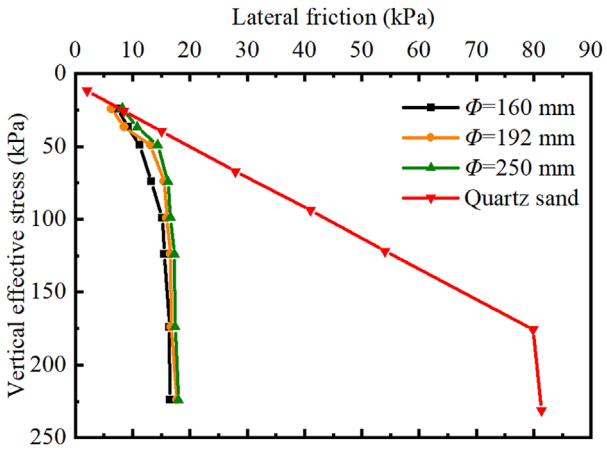


FIGURE 6
Distribution of pile side friction resistance.

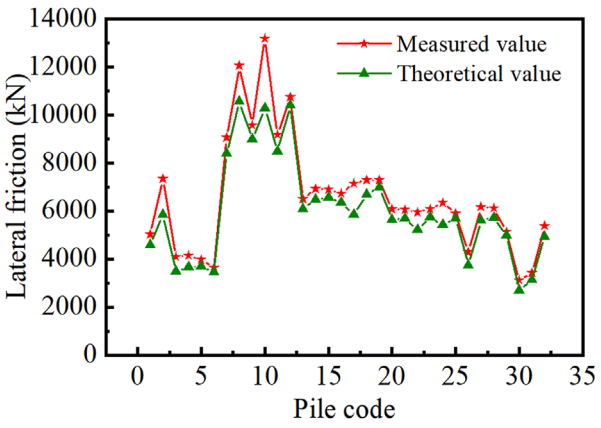


FIGURE 8
Comparison of theoretical and measured friction resistance.


FIGURE 7
High-strain hammer test on pile foundations.

characteristics of the pile-rock interface and the rock strength. Currently, research on the mechanical response of reef limestone is still in its infancy, and there is a lack of systematic studies on its cementation strength and mechanical properties at the micro-scale. Additionally, there are currently no constitutive models applicable to reef limestone. The unclear failure mechanisms at the pile-reef limestone interface, along with insufficient consideration of factors such as interface morphology, have prevented a thorough understanding of the load-bearing mechanism of cast-in-place piles. Moreover, there is currently no calculation method for determining the load-bearing capacity of cast-in-place piles in reef limestone strata.

### 3.2.1 $C_2$ of cast-in-place piles in reef limestone strata

The influence mechanism of clean-water borehole wall morphology and the interface condition between reef limestone and cast-in-place piles on the $c_2$ has not been thoroughly investigated. The borehole walls depicted in the reef limestone detection images were simplified into seven different casting interface morphologies, as illustrated in Figure 9. Shear tests

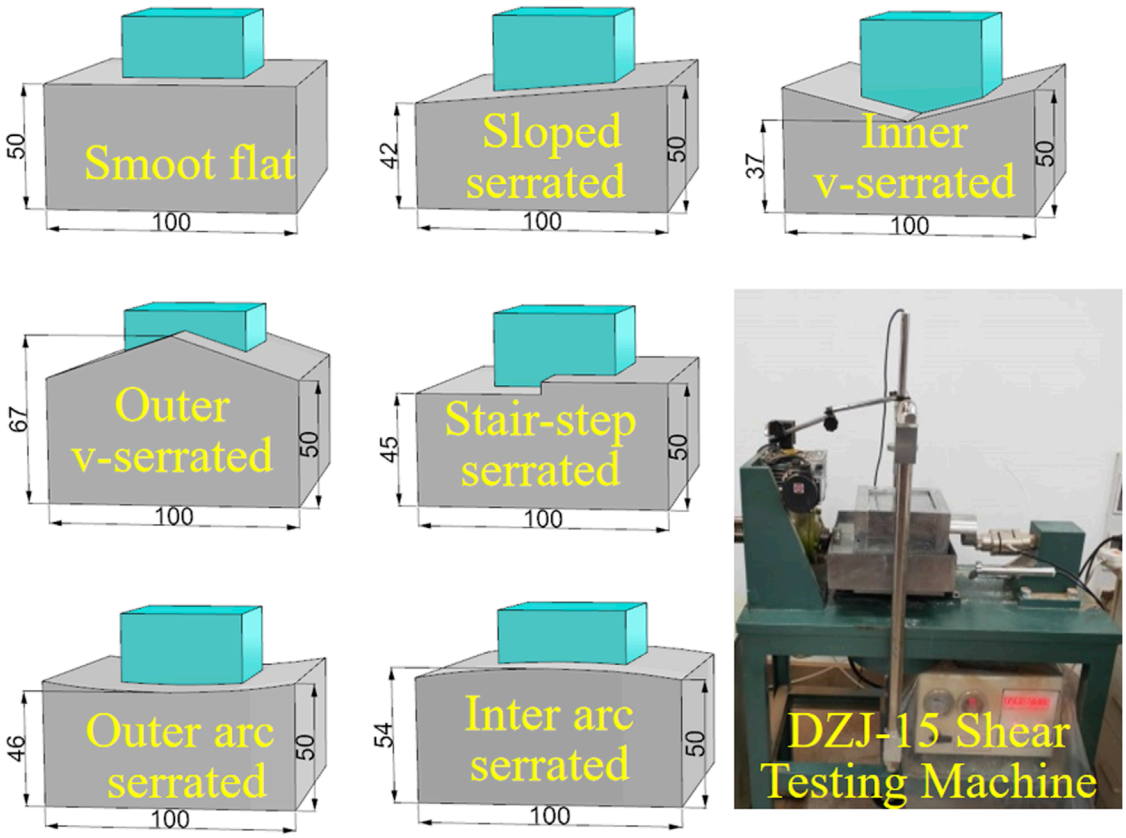


FIGURE 9
Shear test of reef limestone-concrete interface.

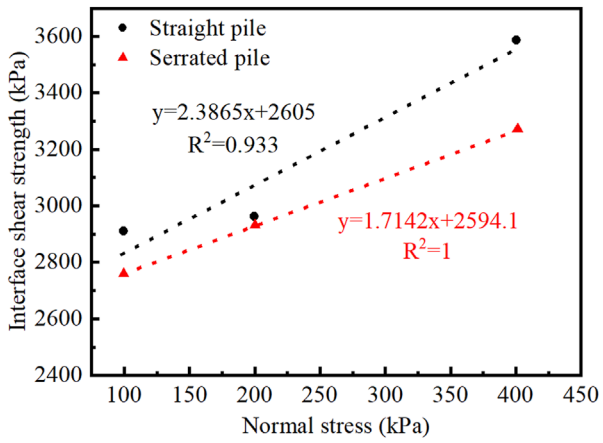


FIGURE 10
Shear strength of straight pile interfaces and average shear strength of serrated interfaces.

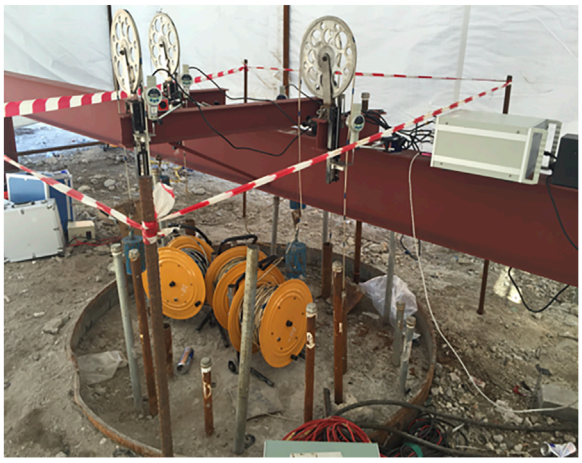

FIGURE 11
Field self-balancing pile test.

were conducted on the reef limestone-concrete interface to investigate the impact of borehole wall morphology on side friction resistance.

The average shear strength of all serrated pile interfaces was calculated and compared with that of straight piles, as depicted in Figure 10. The average shear strengths at both the straight pile and serrated interfaces were found to be comparable under different normal stress conditions, with values of approximately 2.6 MPa. This suggested that the filling state of the interface had a more significant effect on shear strength than the interface morphology. The saturated

TABLE 5 Measured $c_2$ from pile testing.

| Test pile number | Rock layer name | Elevation | Measured maximum side friction resistance (kPa) | Ratio of ultimate side friction resistance to saturated uniaxial compressive strength | $c_2$ values for terrestrial rocks |
|---|---|---|---|---|---|
| SZ1 | ⑥reef limestone | −37.70 to −58.70 | 447–597 | 0.053–0.108 | 0.032–0.04 |
| | ⑦reef limestone | −72.20 to −82.20 | 577 | 0.056 | 0.032–0.04 |
| SZ2 | ⑥reef limestone | −52.23 to −65.53 | 498 | 0.059–0.091 | 0.032–0.04 |
| | ⑦reef limestone | −78.83 to −82.83 | 747 | 0.072 | 0.032–0.04 |
| SZ3 | ④reef limestone | −9.4 to −19.6 | 606–710 | 0.057–0.070 | 0.024–0.032 |
| | $⑤_{1b}$ reef limestone | −19.6 to −25.4 | 962 | 0.128 | 0.024–0.032 |
| | $⑤_{1c}$ reef limestone | −25.4 to −28.4 | 312–465 | 0.053–0.079 | 0.024–0.032 |

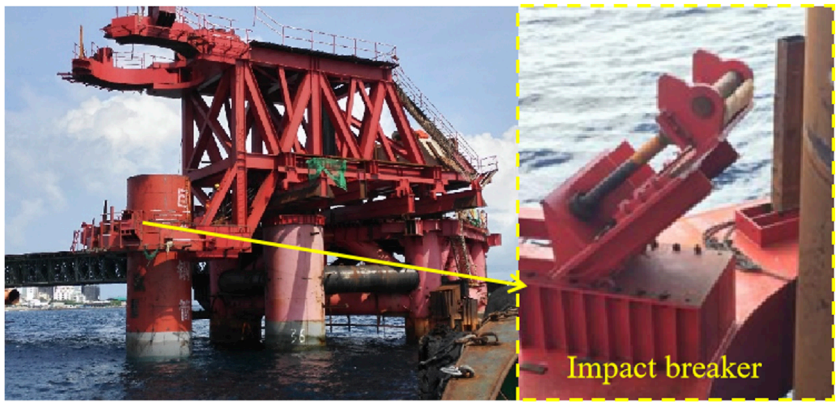


FIGURE 12
Guide frame with hydraulic automatic opening and closing chuck and impact breaker.

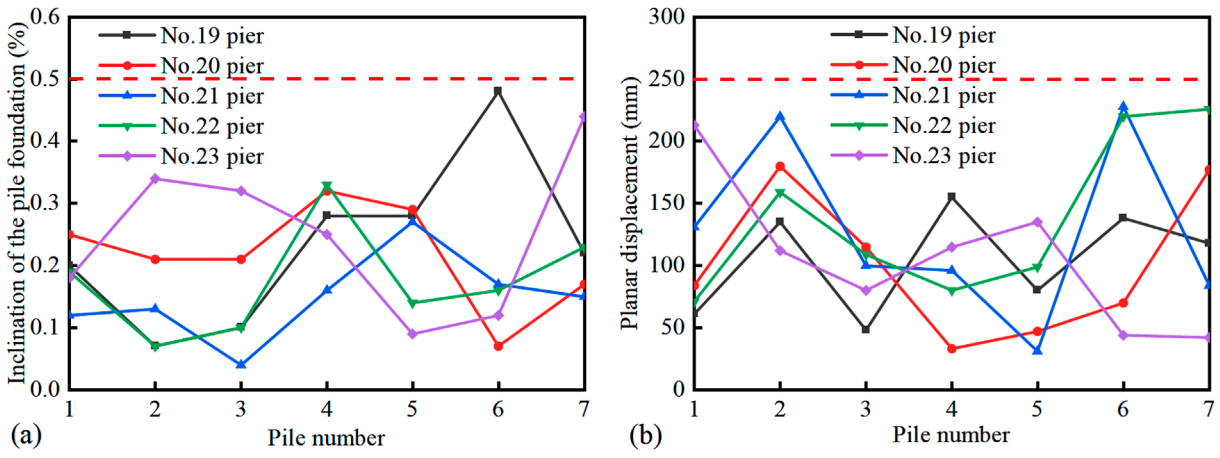


FIGURE 13
Precision of pile installation. **(a)** Inclination of the pile foundation. **(b)** Planar displacement of the pile foundation.

TABLE 6 Control parameters for clean-water rotary drilling.

| Stratum name | Drilling speed (m/h) | Drilling pressure (bar) | Pressure relief (bar) |
|---|---|---|---|
| Coral sand | 0.6–0.8 | 3–8 | 8–9 |
| Coral gravel | 0.4–0.6 | 4–12 | 5–8 |
| Weakly cemented reef limestone | 0.3–0.5 | 7–10 | 5–7 |
| Moderately cemented reef limestone | 0.2–0.4 | 7–15 | 4–6 |
| Strongly cemented reef limestone | 0.2–0.3 | 10–15 | 1.5–3 |

uniaxial compressive strength of the reef limestone samples ranged from 5.8 to 7.5 MPa. The $c_2$ is defined as the ratio of side friction resistance to saturated uniaxial compressive strength of the pile-side rock, and serves as an important indicator of the efficiency of side friction resistance. Shear tests indicated that the $c_2$ for the embedded segments of cast-in-place piles in reef limestone strata ranged from 0.33 to 0.43, which is significantly higher than the recommended value of 0.05 for terrestrial rocks as specified in the standard (Zhou, 2014). Hence, the differences in the $c_2$ between cast-in-place piles in reef limestone and terrestrial rock strata should be considered in the design process.

### 3.2.2 Calculation method for cast-in-place piles in limestone strata

The "Specifications for Design of Foundation of Highway Bridges and Culverts" (Zhou, 2014) specifies the formula for calculating the allowable axial compressive capacity of a single rock-socketed bored pile, which is expressed in Equation 3.

$$[R_a] = c_1 A_p f_{rk} + u \sum_{i=1}^{m} c_{2i} h_i f_{rk_i} + \frac{1}{2} \zeta_s u \sum_{j=1}^{n} l_j q_{sj} \quad (3)$$

where $[R_a]$ is the allowable vertical load-bearing capacity of a single pile ($k_N$); $c_1$ denotes the mobilization coefficient of end friction resistance depending on various factors such as rock integrity; $A_p$ is the cross-sectional area of the pile end ($m^2$); $f_{rk}$ represents the standard saturated uniaxial compressive strength of the rock at the pile end (kPa); $c_{2i}$ is the mobilization coefficient of side friction resistance for the ith rock layer determined by rock integrity and compaction degree; $u$ refers to the perimeter of the pile shaft within each soil or rock layer (m); $h_i$ indicates the thickness of the pile embedded in each rock layer (m); $m$ is the number of rock layers, $l_i$ is the thickness of each coral reef layer (m); $q_{sj}$ is the standard side friction resistance for the ith soil layer surrounding the pile (kPa); and $n$ is the number of soil layers.

The study of the side friction resistance mechanism of cast-in-place piles in reef limestone strata and the porous characteristics of reef limestone highlighted a necessity to modify the $c_2$. Field tests were conducted using the self-balancing method to determine the ultimate side friction resistance of cast-in-place piles in reef limestone at the bridge site, as illustrated in Figure 11. As depicted in Table 5, field test results revealed that the ratio of measured ultimate side friction resistance to the saturated uniaxial compressive strength of the pile-side rock ranged from 0.05 to 0.11, with localized values up to 0.128. Terrestrial limestone typically exhibits $c_2$ values varying between 0.024 and 0.04 (CCCC Highway Consultants Co. and Ltd, 2007). The $c_2$ value for clean-water boreholes in reef limestone is approximately 2–3 times that in terrestrial limestone, yet remains lower than the values obtained from laboratory shear tests for rock-socketed segments. This is likely because laboratory reef limestone samples are finely processed with minimal damage, whereas on-site drilling produces unavoidable damage to borehole wall rock layers. Moreover, design code-recommended values are established through extensive practical applications and include safety factors. Therefore, during the design phase, the $c_2$ value for rock-socketed segments of cast-in-place piles in reef limestone can be appropriately increased based on the rock's integrity and mechanical properties. A recommended range for the $c_2$ is 0.05–0.11.

## 4 Construction techniques and equipment development for driven steel pipe piles in coral debris strata

### 4.1 Construction techniques and equipment development for driven steel pipe piles in coral debris strata

For offshore bridge projects, the construction of driven steel pipe piles is affected by ocean currents and waves, which can result in low accuracy in pile positioning and increased construction safety risks. Furthermore, the presence of cavities or weak layers in the coral reef strata poses a risk of "pile slippage" during installation. Figure 12 illustrates the developed guide frame equipped with hydraulic automatic opening and closing chuck, which effectively mitigates safety risks associated with excessive swaying during the hoisting of the steel casing. The cantilever guiding frame system with a fuse mechanism can prevent impact on the guiding frame by triggering the fuse in case of "pile slipping." These methods ensured that the installation precision of steel pipe piles under ocean current and wave conditions met the necessary standards (as depicted in Figure 13): planar displacement <25 cm and inclination <0.5%.

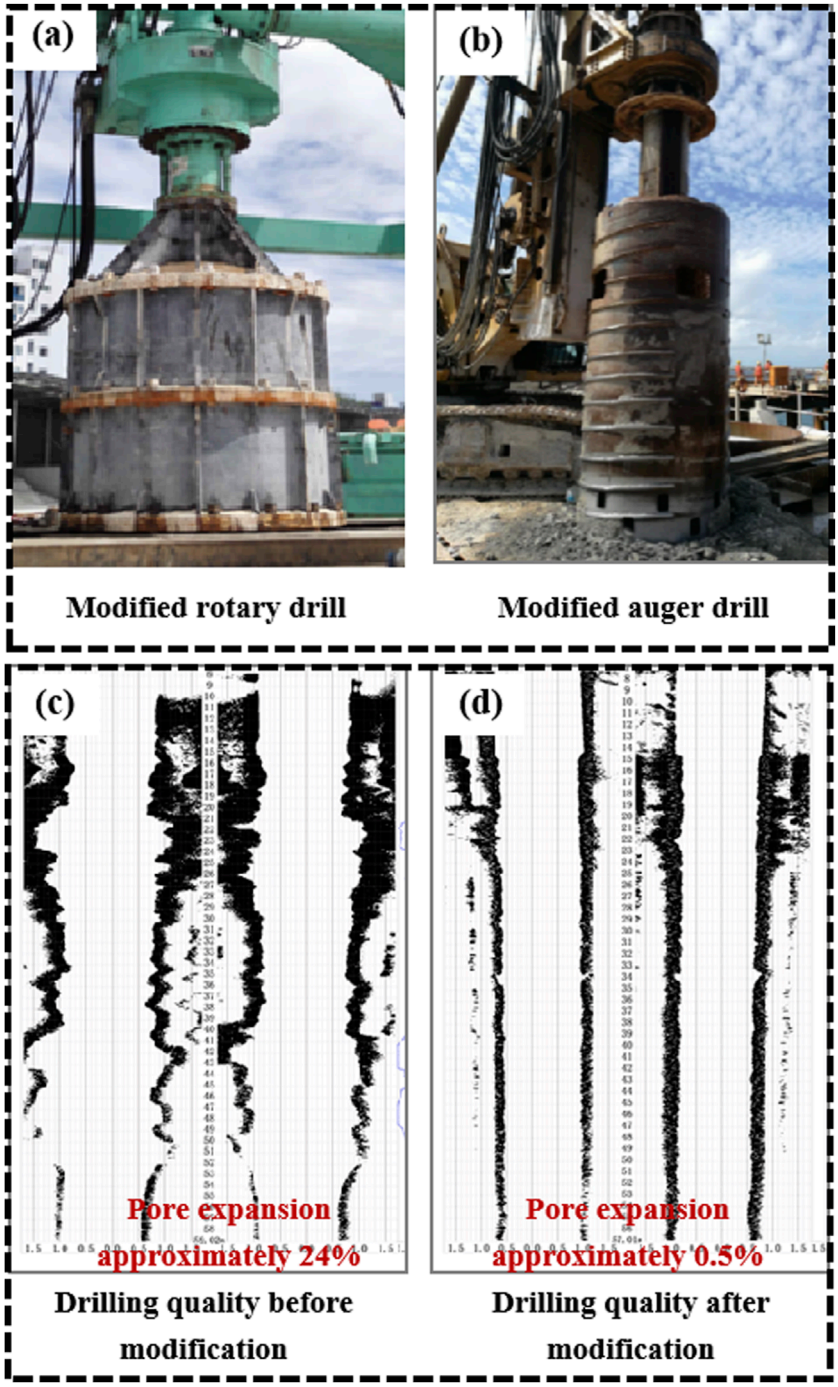


FIGURE 14
The modified drilling equipment and a comparison of its effects. **(a)** Modified rotary drill. **(b)** Modified auger drill. **(c)** Drilling quality before modification. **(d)** Drilling quality after modification.

## 4.2 Construction techniques and equipment development for cast-in-place piles in reef limestone strata

The porous and heterogeneous characteristics of reef limestone strata pose challenges to traditional drilling methods for cast-in-place piles, including excessive hole enlargement and significant deviations in vertical alignment. Clean-water drilling experiments have established control parameters for various coral reef strata, which ensure safe and efficient drilling. The detailed control parameters are presented in Table 6. The methods for controlling borehole diameters, such as extended barrel drilling for circular cuts and tooth-cutting drill bits for hard-soft interbedded reef limestone strata, were employed to mitigate borehole wall collapse

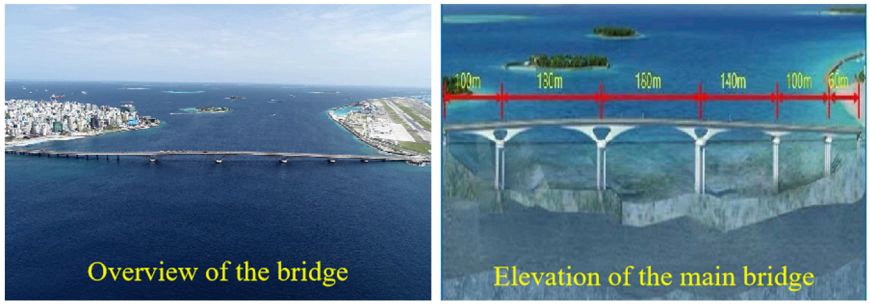


FIGURE 15
The China-Maldives friendship bridge.

and address the prevalence of voids in coral reef strata. These approaches effectively controlled hole enlargement. Additionally, modifications to rotary and reverse circulation drill bits ensured high-quality drilling in hard-soft interbedded reef limestone strata. The modified drilling equipment can be seen in Figures 14a,b. This resulted in a vertically smooth borehole wall morphology, as illustrated in Figures 14c,d.

## 5 Engineering applications

The China-Maldives Friendship Bridge (see Figure 15) is located in the North Malé Atoll of the Maldives. It spans the Gaadhoo Koa Strait and connects three adjacent islands: Malé Island, Airport Island, and Hulhumalé Island. The total route length is 2.0 km, where the bridge segment measures 1.39 km. The main bridge is a six-span hybrid beam rigid frame bridge with a length of 760 m. Piers 19 to 23 of the main bridge utilize variable cross-section steel pipe composite pile foundations. The diameters of steel casings range from 3.2 m to 3.6 m, and the maximum length of the cast-in-place piles is 110 m. The Maldives islands are surrounded by open waters with strong ocean currents, high waves, and long periods, which present significant challenges to construction.

Relevant research findings and technologies have been successfully applied in the design and construction of the pile foundations and superstructure of the China-Maldives Friendship Bridge. The load-bearing mechanism of pile foundations under coral reef geological conditions has been defined. The developed hydraulic automatic opening and closing chuck guide frame with a fusing mechanism allows for driven pile placement with a planar displacement of less than 25 cm and an inclination of less than 0.5%. The construction technique for cast-in-place piles in soft-hard interbedded reef limestone strata results in a verticality error of less than 0.5%. By applying these cross-sea bridge construction technologies, the project team improved efficiency and ensured successful project execution.

## 6 Conclusion and suggestions

This study addressed construction challenges for cross-sea bridges on coral reef substrates. Additionally, we proposed an engineering classification system for coral reef soils and rock masses exhibiting binary sedimentation fabrics through theoretical analysis, field investigations, and laboratory experiments. The load-bearing mechanisms and construction techniques of pile foundations in coral reef strata were explored. The findings have been applied in the China-Maldives Friendship Bridge. The main conclusions are as follows:

1. The engineering properties of coral reef soils and rock masses differed markedly from those of typical rock and soil types. The coral debris strata can be categorized according to particle size distribution, while their engineering compactness should be determined from dynamic penetration test results. Furthermore, the static lateral earth pressure coefficient ($K_0$) of various coral sands varied significantly, with values ranging from 0.22 to 0.33.
2. The construction of driven piles in coral sand strata resulted in fragmentation and redistribution of coral sand particles. This led to lower pile side friction resistance of approximately 17.5 kPa, which is about 21.4% of that found in quartz sand. A calculation formula for side friction resistance of driven piles in coral sand strata was proposed based on the model test results.
3. Seven simplified casting interface shear characteristics at the reef limestone-pile interface were analyzed. The recommended range for the *c2* of cast-in-place piles embedded in reef limestone strata is between 0.05 and 0.11, which is 2–3 times that observed in terrestrial limestone.
4. A hydraulic automatic opening and closing chuck guide frame system with a fusing mechanism was developed. Additionally, methods for controlling borehole diameters, such as extended barrel drilling for circular cuts and tooth-cutting drill bits for hard-soft interbedded reef limestone strata, were proposed. These advancements enhance both the efficiency and quality of pile foundation construction in coral strata.

## Data availability statement

The original contributions presented in the study are included in the article/supplementary material, further inquiries can be directed to the corresponding author.

## Author contributions

YuZ: Conceptualization, Project administration, Writing – original draft. YoZ: Formal Analysis, Methodology, Supervision, Writing – review and editing. CY: Data curation, Investigation, Writing – original draft. FJ: Data curation, Investigation, Writing – original draft. PC: Resources, Validation, Writing – review and editing.

## Funding

The author(s) declare that financial support was received for the research and/or publication of this article. This work was supported by Hubei Provincial Natural Science Foundation of China (Grant No. 2023AFB508).

## Conflict of interest

Authors YuZ, YoZ, CY, FJ, and PC were employed by CCCC Second Harbor Engineering Co., Ltd.

Author YuZ was employed by CCCC Wuhan Harbour Engineering Design & Research Company Ltd.

## Generative AI statement

The author(s) declare that no Generative AI was used in the creation of this manuscript.

Any alternative text (alt text) provided alongside figures in this article has been generated by Frontiers with the support of artificial intelligence and reasonable efforts have been made to ensure accuracy, including review by the authors wherever possible. If you identify any issues, please contact us.

## Publisher's note



## References

Beger, M., Sommer, B., Harrison, P. H., Smith, S. D., and Pandolfi, J. M. (2014). Conserving potential coral reef refuges at high latitudes. *Divers. Distributions* 20 (3), 245–257. doi:10.1111/ddi.12140

Carter, J. P., Johnston, I. W., and Fahey, M. (1988). *Triaxial testing of north rankin calcarenite. Proceeding of the international conference on calcareous sediments*. Perth, Rotterdam: Balkema Publishers, 515–530.

CCCC Highway Consultants Co., Ltd. (2007). *JTG D63-2007 code for design of ground base and foundation of highway bridges and culverts*. Beijing: China Communications Press.

Chortis, G., Askarinejad, A., Prendergast, L., Li, Q., and Gavin, K. (2020). Influence of scour depth and type on p-y curves for monopiles in sand under monotonic lateral loading in a geotechnical centrifuge. *Ocean. Eng.* 197, 106838. doi:10.1016/j.oceaneng.2019.106838

Clark, A. R., and Walker, B. F. (1997). A proposed scheme for the classification and nomemclature for use in the engineering description on Middle Eastern sedimentary rocks. *Géotechnique* 27 (1), 93–99. doi:10.1680/geot.1977.27.1.93

Gao, R., and Ye, J. H. (2023). Mechanical behaviors of coral sand and relationship between particle breakage and plastic work. *Eng. Geol.* 316, 107063. doi:10.1016/j.enggeo.2023.107063

Ghazali, F. M., Sotiropoulos, E., and Mansour, O. A. (1988). Large-diameter bored and grouted piles in marine sediments of the Red Sea. *Can. Geotechnical J.* 25 (4), 826–831. doi:10.1139/t88-090

Ho, H. M., Malik, A. A., Kuwano, J., Brasile, S., Tran, T. V., and Mazhar, M. A. (2022). Experimental and numerical study on pressure distribution under screw and straight pile in dense sand. *Int. J. Geomech.* 22 (9), 04022139. doi:10.1061/(asce)gm.1943-5622.0002520

Höppner, R., and Boley, C. (2022). Erkenntnisse zum tragverhalten von fertigschraubpfählen unter axialer belastung. *Bautechnik* 99 (9), 656–664. doi:10.1002/bate.202200030

Institute, A. P. (2000). Recommended practice for planning, designing and constructing fixed offshore platforms (RP 2A-WSD).

Jiang, H. (2009). *Research on bearing behavior of pile foundations in calcareous sand*. Wuhan: University of the Chinese Academy of Sciences Institute of Rock and Soil Mechanics.

King, R., and Lodge, M. (1988). *North west shelf development—The foundation engineering challenge. Proceeding of the international conference on calcareous sediments*. Perth, Rotterdam: Balkema Publishers, 555–564.

Lin, X., Zhang, J., Wang, R., Liu, W., and Zhang, Y. (2019). Scour around a mono-pile foundation of a horizontal axis tidal stream turbine under steady current. *Ocean. Eng.* 192, 106571. doi:10.1016/j.oceaneng.2019.106571

Liu, H. F., Zhu, C. Q., Wang, R., Cui, X., and Wang, T. (2021). Characterization of the interface between concrete pile and coral reef calcarenite using constant normal stiffness direct shear test. *Bull. Eng. Geol. Environ.* 80, 1757–1765. doi:10.1007/s10064-020-02039-8

Lu, J. C., and Luo, H. (2016). Enhineering geological characteristic and evaluation for construction site of cross-sea bridge in male-airport island. *Constr. Des. Eng.* 5, 71–74. doi:10.13616/j.cnki.gcjsysj.2016.05.017

Nansha Integrated Scientific Expedition Team and Chinese Academy of Sciences (1992). *Quaternary coral reef geology of the yongshu reef, nansha islands*. Beijing: China Ocean Press.

Qin, W., Dai, G. L., and Ma, L. Z. (2019). *In-situ* static loading tests of prestressed high strength concrete (PHC) pile in coral strata. *Rock Soil Mech.* 40, 381–389. doi:10.16285/j.rsm.2019.0149

Schmüdderich, C., Shahrabi, M. M., Taiebat, M., and Alimardani Lavasan, A. (2020). Strategies for numerical simulation of cast-in-place piles under axial loading. *Comput. Geotech.* 125, 103656. doi:10.1016/j.compgeo.2020.103656

Shan, H. G., and Wang, R. (2000). Development of study on pile in calcareous sand. *Rock Soil Mech.* 21 (3), 299–304. doi:10.16285/j.rsm.2000.03.027

Wan, Z. H., Dai, G. L., and Gong, W. M. (2018). Enhanced mechanism of post-grouting pilein coral-reef limestone formations. *Rock Soil Mech.* 39 (2), 467–473. doi:10.16285/j.rsm.2017.1124

Wang, G. (2001). *Sedimentology of coral reef areas in the South China Sea*. Beijing: China Ocean Press.

Wang, R., Song, C. J., and Zhao, H. T. (1997). *Coral reef engineering geology of nansha islands*. Beijing: Science Press.

Xu, X. L., Lei, X., and Wang, T. L. (2022). Experimental study on shear mechanical properties of pile-coral sand interface. *Chin. J. Undergr. Space Eng.* 18, 1891–1897+1905.

Xu, M., Zhang, F., Ni, P., and Mei, G. (2023). Load–settlement behaviour of membrane-confined grouted pile: experimental and analytical study. *Acta Geotech.* 18 (5), 2777–2793. doi:10.1007/s11440-022-01711-5

Yao, T., Cao, Z. W., and Li, W. (2024). On the mechanical behaviour of a coral silt from the South China Sea. *Géotechnique*, 1–14. doi:10.1680/jgeot.24.00012

Yu, K. F., Zhang, G. X., and Wang, R. (2014). Studies on the coral reefs of the South China Sea: from global change to oil-gas exploration. *Adv. Earth Sci.* 29 (11), 1287–1293.

Zhong, Y., Wang, R., and Li, Q. (2020). Physical and engineering characteristics of reef limestone: a review. *Sci. Technol.* 38, 57–70.

Zhou, Y. (2014). *Teoretical analysis and experimental studies on residual stress of jacked open-ended concrete pipe piles*. Hangzhou: Zhejiang University.

Zhu, C. Q., Liu, H. F., and Zhou, B. (2016). Micro-structures and the basic engineering properties of beach calcarenites in South China Sea. *Ocean. Eng.* 114, 224–235. doi:10.1016/j.oceaneng.2016.01.009

# Frontiers in Earth Science

**Investigates the processes operating within the major spheres of our planet**

Advances our understanding across the earth sciences, providing a theoretical background for better use of our planet's resources and equipping us to face major environmental challenges.

---

## Discover the latest Research Topics

See more →


**Frontiers**

Avenue du Tribunal-Fédéral 34
1005 Lausanne, Switzerland
frontiersin.org

**Contact us**

+41 (0)21 510 17 00
frontiersin.org/about/contact